

Fall 2013

Synthesis and Molecular Modeling Studies of Bicyclic Inhibitors of Dihydrofolate Reductase, Receptor Tyrosine Kinases and Tubulin

Sudhir Raghavan

Follow this and additional works at: <https://dsc.duq.edu/etd>

Recommended Citation

Raghavan, S. (2013). Synthesis and Molecular Modeling Studies of Bicyclic Inhibitors of Dihydrofolate Reductase, Receptor Tyrosine Kinases and Tubulin (Doctoral dissertation, Duquesne University). Retrieved from <https://dsc.duq.edu/etd/1080>

This Immediate Access is brought to you for free and open access by Duquesne Scholarship Collection. It has been accepted for inclusion in Electronic Theses and Dissertations by an authorized administrator of Duquesne Scholarship Collection. For more information, please contact phillips@duq.edu.

SYNTHESIS AND MOLECULAR MODELING STUDIES OF BICYCLIC
INHIBITORS OF DIHYDROFOLATE REDUCTASE,
RECEPTOR TYROSINE KINASES AND TUBULIN

A Dissertation

Submitted to the Graduate School of Pharmaceutical Sciences

Duquesne University

In partial fulfillment of the requirements for
the degree of Doctor of Philosophy

By

Sudhir Raghavan

2013

Copyright by
Sudhir Raghavan

2013

Name: Sudhir Raghavan

Dissertation: Synthesis and Molecular Modeling Studies of Bicyclic Inhibitors of Dihydrofolate Reductase, Receptor Tyrosine Kinases and Tubulin

Degree: Doctor of Philosophy

Date: November 15, 2013

APPROVED &
ACCEPTED

Aleem Gangjee, Ph. D. (Dissertation Committee Chairperson)
Professor of Medicinal Chemistry
Mylan School of Pharmacy Distinguished Professor
Graduate School of Pharmaceutical Sciences, Duquesne University, Pittsburgh, PA

APPROVED

Marc W. Harrold, Ph. D.
Professor of Medicinal Chemistry,
Graduate School of Pharmaceutical Sciences, Duquesne University, Pittsburgh, PA

APPROVED

Patrick T. Flaherty, Ph. D.
Associate Professor of Medicinal Chemistry,
Graduate School of Pharmaceutical Sciences, Duquesne University, Pittsburgh, PA

APPROVED

David J. Lapinsky, Ph. D.
Associate Professor of Medicinal Chemistry,
Graduate School of Pharmaceutical Sciences, Duquesne University, Pittsburgh, PA

APPROVED

Lawrence H. Block, Ph. D.
Emeritus Professor of Pharmaceutics
Graduate School of Pharmaceutical Sciences, Duquesne University, Pittsburgh, PA

APPROVED

James K Drennen III, Ph. D.
Associate Dean for Research and Graduate Programs
Graduate School of Pharmaceutical Sciences, Duquesne University, Pittsburgh, PA

APPROVED

J. Douglas Bricker, Ph. D.
Dean, Mylan School of Pharmacy and the Graduate School of Pharmaceutical Sciences, Duquesne University, Pittsburgh, PA

ABSTRACT

SYNTHESIS AND MOLECULAR MODELING STUDIES OF BICYCLIC INHIBITORS OF DIHYDROFOLATE REDUCTASE, RECEPTOR TYROSINE KINASES AND TUBULIN

By

Sudhir Raghavan

December 2013

Dissertation supervised by Dr. Aleem Gangjee

The results from this work are reported into two sections listed below:

Synthesis:

Following structural classes of compounds have been designed, synthesized and studied as inhibitors of p_jDHFR, RTKs and tubulin:

1. 2,4-Diamino-6-(substituted-arylmethyl)pyrido[2,3-*d*]pyrimidines
2. 4-((3-Bromophenyl)linked)-6-(substituted-benzyl)-7*H*-pyrrolo[2,3-*d*]pyrimidin-2-
amines
3. 6-Methyl-5-((substitutedphenyl)thio)-7*H*-pyrrolo[2,3-*d*]pyrimidin-2-
amines

A total of 35 new compounds (excluding intermediates) were synthesized, characterized and submitted for biological evaluation. Results from these studies will be presented in due course. Bulk synthesis of the potent lead compound **170** was carried out to facilitate *in vivo* evaluation.

Docking Studies

Docking studies were performed using LeadIT, MOE, Sybyl or Flexx for target compounds listed above and for other compounds reported by Gangjee *et al.* against the following targets:

1. Dihydrofolate reductase: human, *P. carinii*, *P. jirovecii* (pjDHFR) and *T. gondii* (tgDHFR)
2. Thymidylate synthase: human (hTS) and *T. gondii* (tgTS)
3. Receptor tyrosine kinases: VEGFR2, EGFR and PDGFR- β
4. Colchicine binding site of tubulin.

Novel homology models were generated and validated for pjDHFR, tgDHFR, tgTS, PDGFR- β and the F36C L65P pjDHFR double mutant. The tgTS homology model generated in this study and employed to design novel inhibitors shows remarkable similarity with the recently published X-ray crystal structures. Docking studies were performed to provide a molecular basis for the observed activity of target compounds against DHFR, RTKs or tubulin. Results from these studies support structure-based and ligand-based medicinal chemistry efforts in order to improve potency and/or selectivity of analogs of the docked compounds against these targets.

Novel topomer CoMFA models were developed for tgTS and hTS using a set of 85 bicyclic inhibitors and for RTKs using a set of 60 inhibitors reported by Gangjee *et al.* The resultant models could be used to explain the potency and/or selectivity differences for selected molecules for tgTS over hTS. Topomer CoMFA maps show differences in steric and/or electronic requirements among the three RTKs, and could be used, in conjunction with other medicinal chemistry approaches, to modulate the selectivity and/or potency of

inhibitors with multiple RTK inhibitory potential. Drug design efforts that involve virtual library screening using these topomer CoMFA models in conjunction with traditional medicinal chemistry techniques and docking are currently underway.

DEDICATION

Dedicated to My Family and Friends

ACKNOWLEDGEMENTS

I would like to express my sincere gratitude to everyone whose help and support have made this work possible.

I am very fortunate to have had Dr. Gangjee as my mentor for this work. His advice, his untiring patience, constant support, encouragement and willingness to share his knowledge have helped develop my skills and knowledge as a medicinal chemist. He has always been, and will always be a source of inspiration to me. I admire his zeal for research and passion for science and hope to excel in my research just the way he has always taught me.

Thank you, Dr. Patrick T Flaherty, Dr. Marc W. Harrold, Dr. David J Lapinsky, and Dr. Lawrence H Block for serving on my committee. Thank you for your time, sharing your knowledge, your suggestions and your advice. What I have learned from you over the years is invaluable.

I would like to specially thank Nancy Hosni for all her help, her welcoming smile and all the candy I have taken! You have always made everything so simple for us. Thank you so much!

I would like to thank Jackie Farrer, Deb Willson and Mary Caruso for their help. I would also like to thank the Department of Pharmaceutical Sciences at Duquesne University for giving me the opportunity to be here and for their financial support. The support staff at Duquesne University – the friendly folks in the purchasing department, EHS, instrument maintenance department and the janitorial staff – plays a critical role in making research life at Duquesne University such a breeze.

My work at Duquesne University would have been impossible without my lab mates. In particular, I would like to mention Dr. Nilesh Zaware for being an extraordinary room mate, colleague and friend. Your encouragement and insights made these years of research memorable and enjoyable.

To all my friends in Pittsburgh, especially Lavanya Jayaraman and Sabarish Sethuraman, I am very grateful for all your help, support and encouragement.

Last, but not the least, this work would not have been possible without the unconditional and unending love and support from my parents Mr. P. G. Raghavan and Mrs. Sudha Raghavan, my wife Dr. Prashi Jain and my sister Rashmi Nair. You are the reason I try to achieve everything I can. You have been with me every step of the way. Thank you for everything.

TABLE OF CONTENTS

Abstract	iv
Dedication	vii
Acknowledgements	viii
List of Tables	x
List of Figures	xii
List of Schemes	xx
List of Abbreviations	xxiii
A. Biochemical review	1
B. Chemical review	84
C. Statement of the problem	100
D. Chemical discussion	147
E. Summary	252
F. Experimental	262
G. Bibliography	294
H.1. Appendix-1	327
H.2. Appendix-2	347

LIST OF TABLES

Table 1	X-ray crystal structures of pcDHFR available in the PDB.	21
Table 2	Pyrrolo[2,3-d]pyrimidines as classical and nonclassical inhibitors of TS	35
Table 3	RTK Inhibitors Approved for Use in the U.S.	42
Table 4	Small-molecule protein kinase inhibitors and their targets along with the target conformation	48
Table 5	Pyrrolo[2,3- <i>d</i>]pyrimidine inhibitors of RTKs	52
Table 6	Selected X-ray crystal structures of EGFR complexed with small molecule inhibitors	58
Table 7	Selected X-ray crystal structures of VEGFR-2 complexed with small molecule inhibitors	59
Table 8	Structures and inhibitory concentrations (IC ₅₀ , nM) of 192a and 192b- e against pjDHFR, pcDHFR and hDHFR	110
Table 9	Ki values (M) against wild type pjDHFR and F36C L65P double mutant resistant pjDHFR	112
Table 10	Biological activities of 193a-j against pcDHFR, tgDHFR, rIDHFR, pjDHFR and hDHFR	113
Table 11	Structure of 194a-c and inhibition concentration (IC ₅₀ , μM) against isolated TS.	115
Table 12	Inhibitory concentrations of 194a-d (IC ₅₀ , μM) against TS and DHFR	117
Table 13	Structure and IC ₅₀ (μM) values of kinase inhibition, A 431 cytotoxicity and inhibition of CAM assay	121
Table 14	IC ₅₀ values (μM) of kinase inhibition, A431 cytotoxicity, and inhibition of the CAM assay of 195 , 212a-k .	136
Table 15	IC ₅₀ Values (μM) of kinase inhibition and A431 cytotoxicity assay of 213b-c .	138
Table 16	IC ₅₀ values for inhibition of proliferation of MDA-MB-435 cells and EC ₅₀ s for cellular microtubule loss.	145

Table 17	Docking scores for the best docked pose of TMP and 168	173
Table 18a	Topomer CoMFA Statistics – tgTS	198
Table 18b	Topomer CoMFA Statistics – hTS	199
Table 19	IC ₅₀ values (μM) of kinase inhibition and the A431 cytotoxicity assay of 195 , 196a-k and 211a-k .	215
Table 20	Model generated from fragments generated using Method A	234
Table 21	Model generated from fragments generated using Method B	234
Table 22	Model generated from fragments generated using Method C	235
Table 23	Model generated from fragments generated using Method D	236

LIST OF FIGURES

Figure 1	Structure of folic acid	1
Figure 2	Folate metabolism pathway	2
Figure 3	Folic acid pathway	3
Figure 4	<i>De novo</i> synthesis of purines	4
Figure 5	De novo synthesis of dTMP	5
Figure 6	Structures of Trimethoprim (TMP), Trimetrexate (TMQ), Piritrexim (PTX) and Sulfamethoxazole (SMX)	5
Figure 7	Folic acid (white) bound to the active site of hDHFR. (PDB:DRF38)	7
Figure 8	Interaction of Glu30 in the active site of human DHFR with A) DHF (PDB: 1DRF), and B) MTX (PDB: 1DLR)	10
Figure 9	The structures of pyrimethamine, DDMP and DAMP	14
Figure 10	The structures of MZPES and Methylbenzoprim	15
Figure 11	Structures of TMQ and 1-3	15
Figure 12	Tetrahydroquinazoline analogues 4-6	16
Figure 13	The structure of PTX and 7 and 8	16
Figure 14	Structures of 9 and 10	17
Figure 15	Structures of 11 – 13	17
Figure 16	Structures of 14 – 16	18
Figure 17	Structures of 17 – 20	18
Figure 18	Structures of 21 – 23	19
Figure 19	Structures of 24 and 25	19
Figure 20	Structures of ligands cocrystallized with pcDHFR available in the PDB	22
Figure 21	Structure of ligand WR99210 in <i>P. falciparum</i> DHFR (PDB: 1J3I)	24
Figure 22	The mechanism of catalysis by TS	33
Figure 23	Structure of PDDE.	34
Figure 24	Process of angiogenesis	37
Figure 25	Structures of RTK inhibitors currently marketed in the U.S.	43

Figure 26	Crystal structure an inhibitor dasatinib bound to Abelson tyrosine kinase (Abl) (PDB: 2GQG)	44
Figure 27	Binding site comparisons of active and inactive forms of different kinases	47
Figure 28	X-ray crystal structure of 34 bound to EGFR (PDB: 2ITT)	50
Figure 29	X-ray crystal structure of 35 bound to VEGFR-2 (PDB: 3CJF)	51
Figure 30	X-ray crystal structure of 36 bound to VEGFR-2 (PDB: 3CJG)	51
Figure 31	Compounds used as standards in RTK inhibition assays	54
Figure 32	Structures of ligands co-crystallized with EGFR available in the PDB	59
Figure 33	Structures of ligands co-crystallized with VEGFR-2 available in the PDB	60
Figure 34	Structure of a microtubule	62
Figure 35	Different stages of mitosis	64
Figure 36	The process of dynamic instability	66
Figure 37	The process of treadmilling	67
Figure 38	Antimitotic agents	68
Figure 39	X-ray crystal structure of tubulin. (PDB ID: 1JFF)	71
Figure 40	X-ray crystal structure of colchicine bound to tubulin. (PDB: 3UT5)	72
Figure 41	Predicted binding modes of CSAs (blue) in the colchicine binding pocket of tubulin	73
Figure 42	Overlay of docked poses of CSAs (blue) form roughly a 45° angle between the bisecting planes in the colchicine binding pocket	74
Figure 43	Agents reversing Pgp mediated MDR in cancer	76
Figure 44	Pyrrolo[2,3- <i>d</i>]pyrimidines that act as antimitotics and reverse resistance exhibited by tumors to vinblastine and vincristine	77
Figure 45	5,7-Disubstituted-4-methyl-7 <i>H</i> -pyrrolo[2,3- <i>d</i>]pyrimidin-2-amines as microtubule inhibitors	79
Figure 46	Pyrrolo[2,3- <i>d</i>]pyrimidines and cyclopenta[2,3- <i>d</i>]pyrimidines that	80

	act as antimitotic agents	
Figure 47	Pyrrolo[3,2- <i>d</i>]pyrimidines as antimitotic agents	81
Figure 48	Sequence alignment of hDHFR (DYR_HUMAN) ¹ , pjDHFR (Q9UUP5_PNEJ)	102
Figure 49	Structures of 168 and 169	102
Figure 50	Docked pose of 168 in the active site of the homology model for pjDHFR	103
Figure 51	Docked pose of 168 in the pjDHFR homology model	104
Figure 52	Structures of target compounds 170 – 180	105
Figure 53	Docked pose of 173 in the active site of the homology model for pjDHFR	106
Figure 54	Structures of compounds 181 – 185	107
Figure 55	Structures of target compounds 186 – 191	108
Figure 56	Docked pose of 186 in the active site of the homology model for pjDHFR	109
Figure 57	Sequence alignment of DHFR from <i>T. gondii</i> (DRTS_TOXGO), <i>T. cruzii</i> (DRTS_TYRCR), <i>Cryptosporidium hominis</i> (Q5CGA3_CRYHO), <i>Plasmodium falciparum</i> (A7UD81_PLAFA), <i>Leishmania major</i> (DRTS_LEIMA) and hDHFR (DYR_HUMAN) using Protein BLAST (BLASTP)	114
Figure 58	General structures of bicyclic non-classical pyrrolo[2,3- <i>d</i>]pyrimidines and thieno[2,3- <i>d</i>]pyrimidines for topomer CoMFA analysis	118
Figure 59	Proposed binding modes for pyrrolo[2,3- <i>d</i>]pyrimidine RTK inhibitors	122
Figure 60	Proposed pyrrolo[2,3- <i>d</i>]pyrimidine RTK inhibitors	124
Figure 61	Comparison of C-N-C, C-S-C and C-O-C bond angles in energy minimized conformations of 195 , 197 and 205 respectively	125
Figure 62	Docked conformation of 195 in the ATP binding pocket of EGFR.	127
Figure 63	Docked conformation of 197 in the ATP binding pocket of EGFR	128
Figure 64	Docked conformation of 205 in the ATP binding pocket of EGFR	129

Figure 65	Docked conformation of 207 in the ATP binding pocket of EGFR	129
Figure 66	Sequence alignment of PDGFR- β (P09619), FLT3 (PDB: 1PKG), FLT-3 kinase (PDB: 1RJB), LCK (PDB: 1QPD) and FGFR (PDB: 1FGI)	131
Figure 67	N4-(3-bromophenyl)-7-(substituted benzyl)-7 <i>H</i> -pyrrolo[2,3- <i>d</i>]pyrimidine-2,4-diamines 211a-k as potential multiple RTK inhibitors	132
Figure 68	General pharmacophore model of pyrrolo[2,3- <i>d</i>]pyrimidines with five potential binding modes	133
Figure 69	Structures of lead compounds (195 , 212a-b) and analogues (212c-k)	134
Figure 70	Proposed binding modes for pyrrolo[2,3- <i>d</i>]pyrimidine RTK inhibitors	135
Figure 71	Design and structures of pyrimido[4,5- <i>b</i>]indoles 213b-c	137
Figure 72	General structures of pyrrolo[2,3- <i>d</i>]pyrimine and furo[2,3- <i>d</i>]pyrimidine based RTK inhibitors	139
Figure 73	Structures of pyrrolo[2,3- <i>d</i>]pyrimines 214a-e	141
Figure 74	Structures of pyrrolo[2,3- <i>d</i>]pyrimines 215	142
Figure 75	Superimposition of the proposed binding mode of 215 (green) with DAMA-colchicine (yellow) in the colchicine binding site	143
Figure 76	Structures of tubulin inhibitors 218a,b and 219a-e	144
Figure 77	Reductive amination mechanism	154
Figure 78	Docked pose of 192b in pcDHFR binding pocket (PDB:1LY3)	160
Figure 79	Ramachandran plot and Procheck analysis of the pjDHFR homology model generated using MOE 2008.10	162
Figure 80	ProSA analysis of the pjDHFR homology model generated using MOE 2008.10	163
Figure 81	Superimposition of pjDHFR homology models generated using MOE 2008.10, Swiss-Model, Phyre2 and CPHmodel 3.0	165
Figure 82	Docked pose of 192d in the pjDHFR homology model	167
Figure 83	N-Me of 192d interacts with Ile123 (pjDHFR model, red) but not	167

	as well with Val115 (superimposed hDHFR, green)	
Figure 84	Docked pose of TMP in the pjDHFR homology model	169
Figure 85	Docked structure of TMP in the F36C L65P double mutant pjDHFR homology model.	170
Figure 86	Docked structure of 168 in the pjDHFR homology model	171
Figure 87	Docked structure of 168 in the double mutant pjDHFR homology model.	172
Figure 88	Docked structure of 192d in the double mutant pjDHFR homology model	173
Figure 89	Docked pose of 193f in the pjDHFR active site model	175
Figure 90	Steric clash of phenyl side chain of 193f with Phe31 in hDHFR	176
Figure 91	Superimposition of docked pose of 194a and 194b in the active site of the tgDHFR model showing similar docked conformations	180
Figure 92	Docked pose of 194a in the active site of the tgDHFR model	180
Figure 93	Superimposition of 194a on the furo[2,3- <i>d</i>]pyrimidine ligand in hDHFR	181
Figure 94	Sequence alignment of <i>T. cruzii</i> TS (DRTS_TRYCR), hTS (TYSY_HUMAN), pcTS (TYSY_PNECA), tgTS (DRTS_TOXGO) and <i>P. falciparum</i> TS (DRTS_PLAFK) using Clustal W	183
Figure 95	Superimposition of homology models generated using <i>T. cruzi</i> (blue), <i>T. cruzi</i> (brown) and swissmodel (magenta) showing good overlap of the models. C α -RMSD: 0.855 Å	184
Figure 96	Ramachandran plot and Procheck analysis of the tgTS homology model generated using MOE 2008.10	185
Figure 97	Prosa analysis of the tgTS homology model generated using MOE 2008.10	185
Figure 98	Docked pose of 194e (white) in the tgTS homology model	189
Figure 99	Docked pose of 194e (white) in hTS (PDB: 1JU6)	189
Figure 100	Docked pose of 194d (white) in the tgTS active site homology	190

	model	
Figure 101	Ribbon depiction of the superimposition of the docked pose of 194d and the X-ray crystal structure	191
Figure 102	Docked pose of 194d (white) in the tgTS active site homology model	192
Figure 103	Docked pose of 194f (white) in the tgTS active site homology model.	193
Figure 104	Superimposition of the docked conformation of 194f in the tgTS homology model (white) and its X-ray crystal structure	194
Figure 105	Difference in the predicted (white) and crystal structure (red) pose of 194f	194
Figure 106	Fragmentation methods for compounds used in this study	197
Figure 107	CoMFA predictions for the training set of tgTS inhibitors using Method A	198
Figure 108	CoMFA predictions for the training set of tgTS inhibitors using Method C	199
Figure 109	Structures and biological activities of 221a-b	200
Figure 110	Topomer COMFA maps representing steric and electrostatic contributions for 221a (left) and 221b (right)	200
Figure 111	Structures and biological activities of 222a-b against tgTS and hTS	201
Figure 112	Topomer COMFA maps representing steric and electrostatic contributions for 222b in the hTS model	202
Figure 113	Topomer COMFA maps representing steric and electrostatic contributions for 222b in the tgTS model	202
Figure 114	Topomer COMFA maps representing steric and electrostatic contributions for 222a in the tgTS model	203
Figure 115	Topomer COMFA maps representing steric and electrostatic contributions for 222b in the tgTS model	203
Figure 116	Docked pose of 222b (white) in the active site of the tgTS homology model	204

Figure 117	DISOPRED analysis of PDGFR- β kinase domain amino acid sequence	211
Figure 118	Superimposition of the PDGFR- β homology model (brown) with the c-KIT crystal structure (magenta).	212
Figure 119	Ramachandran plot of the PDGFR- β homology model	213
Figure 120	ProSA analysis of the PDGFR- β homology model	214
Figure 121	Superimposition of docked poses of 196c (red) and 211c (white) in the ATP binding site of VEGFR2. (PDB: 1YWN)	216
Figure 122	Docked pose of 196c (red) and 211c (white) in the putative binding site of the PDGFR β homology model	218
Figure 123	Superimposition of the best scored pose (white) and alternate docked pose (blue) of 211e in the putative binding site of PDGFR β	220
Figure 124	Overlay of docked poses of 195 (red), 212a (white) and 212b (blue) in EGFR active site (PDB: 1M17)	220
Figure 125	Ligand interaction plots of docked poses of 195 (red), 212a (white) and 212b (blue) in EGFR active site	221
Figure 126	Overlay of docked poses of 195 (red) and 212c (white) in EGFR active site	223
Figure 127	(A) Ligand interaction plots of docked pose of 212c in the EGFR active site. (B) Overlay of ligand interaction plots of docked poses of 212c (red) and 195 (green) in the EGFR active site	223
Figure 128	Overlay of docked poses of 212k (red) and 212b (white) in EGFR active site	224
Figure 129	(A) Ligand interaction plots of docked pose of 212k in the EGFR active site. (B) Overlay of ligand interaction plots of docked poses of 212k (red) and 212b (green) in the EGFR active site	224
Figure 130	Docked pose of 212b (white) in PDGFR- β homology model	226
Figure 131	Overlay of docked poses of 212i (red) and 212b (white) in PDGFR- β homology model	226
Figure 132	(A) Ligand interaction plots of docked pose of 212b in the PDGFR-	227

	β model. (B) Overlay of ligand interaction plots of docked poses of 212b (red) and 212i (green) in the PDGFR- β model	
Figure 133	Stereoview of the docked pose of 213b in the putative PDGFR- β active site model	228
Figure 134	Results from the flexible alignment of the 60 compounds using MOE 2009.10	231
Figure 135	Fragmentation methods for pyrrolo[2,3- <i>d</i>]pyrimidines (A – C) and furo[2,3- <i>d</i>]pyrimidines (D).	232
Figure 136	Stdev*coefficient contour maps for EGFR	238
Figure 137	Stdev*coefficient contour maps for VEGFR2	238
Figure 138	Stdev*coefficient contour maps for PDGFR- β	239
Figure 139	Docked pose of (<i>R</i>)- 219a (white) overlaid with DAMA colchicine	246
Figure 140	Superimposition of the docked poses of (<i>R</i>)- 219a (white) and 219b (magenta) in the colchicine binding site of tubulin	248
Figure 141	Superimposition of the docked poses of (<i>R</i>)- 219a (white), (<i>S</i>)- 219a (cyan) and DAMA colchicine (red) in the colchicine binding site of tubulin	248
Figure 142	Docking mode of (<i>R</i>)- 219a (white) overlaid with docked poses of 15 ligands (blue) in the colchicine binding site of tubulin	249
Figure 143	Superimposition of the final docked conformations of (<i>R</i>)- 219a (blue) and (<i>S</i>)- 219a (white) in the colchicine site of tubulin	250

LIST OF SCHEMES

Scheme 1	Synthesis of pyrido[2,3- <i>d</i>]pyridines from substituted pyridines	85
Scheme 2	Synthesis of pyrido[2,3- <i>d</i>]pyrimidines from 2,4-dioxypyrimidine derivatives	86
Scheme 3	Synthesis of 6-methyl pyrido[2,3- <i>d</i>]pyrimidine-2,4-diamine	86
Scheme 4	Synthesis of 7-substituted-pyrido[2,3- <i>d</i>]pyrimidine-6-carbonitrile-2,4-diamines	87
Scheme 5	Synthesis of N ⁶ -substituted-benzylpyrido[2,3- <i>d</i>]pyrimidine-2,4,6-triamine	87
Scheme 6	Synthesis of 6-(ethylthio)-5-substituted-pyrido[2,3- <i>d</i>]pyrimidine-2,4,7-triamine	88
Scheme 7	Synthesis of pyrido[2,3- <i>d</i>]pyrimidine-6-carboxaldehyde-2,4-diamine from 2-cyanothioacetamide	88
Scheme 8	Synthesis of pyrido[2,3- <i>d</i>]pyrimidine-6-carboxaldehyde-2,4-diamine from 2,4,6-triaminopyrimidine	89
Scheme 9	Synthesis of 6-methyl pyrido[2,3- <i>d</i>]pyrimidine-2,4-diamine	90
Scheme 10	Conversion of pyrimidine-2,4,6-triamine to di-tert-butyl (6-bromopyrido[2,3- <i>d</i>]pyrimidine-2,4-diyl)dicarbamate	90
Scheme 11	Synthesis of <i>N</i> -(4-amino-6-bromopyrido[2,3- <i>d</i>]pyrimidin-2-yl)pivalamide	91
Scheme 12	Synthesis of various 4- <i>N</i> -substituted 7-(2-trifluoromethylphenyl)pyrido[2,3- <i>d</i>]pyrimidine-2,4-diamines	91
Scheme 13	Synthesis of (<i>S</i>)-2-(4-(((2,4-diaminopyrido[2,3- <i>d</i>]pyrimidin-6-yl)methyl)amino) benzamido)pentanedioic acid	92
Scheme 14	Synthesis of 6-(thioarylmethyl)pyrido[2,3- <i>d</i>]pyrimidine-2,4-diamines	92
Scheme 15	Synthesis of pyrrolo[2,3- <i>d</i>]pyrimidines from 4-(alkoxycarbonylmethylamino)-6-chloro-2-methylthiopyrimidine-5-carbonitriles	93
Scheme 16	Synthesis of pyrrolo[2,3- <i>d</i>]pyrimidines from 6-amino-2-	94

	(dimethylamino)pyrimidin-4-(3 <i>H</i>)-one	
Scheme 17	Synthesis of pyrrolo[2,3- <i>d</i>]pyrimidines by Paal Knorr reaction	95
Scheme 18	Synthesis of 6-butyl-2,4-dimethyl-7 <i>H</i> -pyrrolo[2,3- <i>d</i>]pyrimidine	96
Scheme 19	Synthesis of pyrrolo[2,3- <i>d</i>]pyrimidines using Fisher-Indole reaction	96
Scheme 20	Synthesis of 7-benzyl-4-methyl-7 <i>H</i> -pyrrolo[2,3- <i>d</i>]pyrimidin-2-amine	97
Scheme 21	Synthesis of pyrrolo[2,3- <i>d</i>]pyrimidines from 1-benzyl-2-amino-3-cyanopyrroles	98
Scheme 22	Conversion of a 2-amino pyrroles to pyrrolo[2,3- <i>d</i>]pyrimidines	98
Scheme 23	Synthesis of target compounds 171 – 173	147
Scheme 24	Modified synthesis of 174 , 174 – 179	148
Scheme 25	Synthesis of lead compound 170 from 91a	150
Scheme 26	Synthesis of 170 from 92a	151
Scheme 27	Optimization of reductive amination conditions	153
Scheme 28	Optimized reaction conditions for synthesis of 170	155
Scheme 29	Synthesis of 2,4-diamino-6-[(arythio)methyl]pyrido[2,3- <i>d</i>]pyrimidines 186 - 188	156
Scheme 30	Synthesis of 2,4-diamino-6-[(aryloxo)methyl]pyrido[2,3- <i>d</i>]pyrimidines 189 - 191	157
Scheme 31	Synthesis of 2-amino-4-substituted-6-arylmethyl-7 <i>H</i> -pyrrolo[2,3- <i>d</i>]pyrimidines 197-210	206
Scheme 32	Synthesis of target compounds 197-200	207
Scheme 33	Synthesis of target compounds 205-210	209
Scheme 34	Attempted synthesis of 203-204	209
Scheme 35	Synthesis of target compound 234	210
Scheme 36	Attempted synthesis of target compound 235	210
Scheme 37	Synthesis of compound 236	239
Scheme 38	Synthesis of compounds 216a-c , 216f-g , 217a-c , 217f-g	240
Scheme 39	Optimization of reaction conditions for conversion of 216b to 216c	241

Scheme 40	Synthesis of target compounds 216d and 216h	242
Scheme 41	Synthesis of target compounds 217a-h	243

LIST OF ABBREVIATIONS

5-FU	5-Fluorouracil
A7UD81_PLAFA	<i>Plasmodium falciparum</i> dihydrofolate reductase sequence
ABC	ATP-binding cassette
Abl	Abelson kinase
AICAR	Amino-imidazolecarboxamide ribosyl-5-phosphate
AICART	Aminoimidazole carboxamide formyltransferase
AIDS	Acquired immunodeficiency syndrome
AML	Acute myeloid leukemia
AMT	Aminopterin
ALL	Acute lymphoblastic leukemia
AOS	All orientation search
ASM	Aggressive systemic mastocytosis
ATP	Adenosine triphosphate
BCR	Breakpoint cluster
BHMT	Betaine-homocysteine methyltransferase
BLAST	Basic local alignment search tool
BLASTP	Protein Basic local alignment search tool
CAM	Chorioallantoic membrane
cFMS	Colony-stimulating factor-1 receptor
chDHFR	chicken liver dihydrofolate reductase
c-Kit	Mast-stem cell growth factor receptor
CA4P	Combretastatin A-4 phosphate

CL	Catalytic loop
CML	chronic myeloid leukemia
CoMFA	Comparative molecular field analysis
CoMSIA	Molecular Similarity Indices in a Comparative Analysis
CMPD	Chronic myeloproliferative disorders
CSAs	Colchicine site binding agents
CSA4	Combretastatin A-4
DAMA-	
colchicine	<i>N</i> -deacetyl- <i>N</i> -(2-mercaptoacetyl) colchicine
dATP	2'-Deoxyadenosine-5'-triphosphate
DDQ	Dihydrodicyano quinone
DFG	Aspartate-Phenylalanine-Glycine
DFSP	Dermatofibrosarcoma protruberans
dGTP	2'-Deoxyguanosine-5'-triphosphate
DHF	Dihydrofolate
DHFR	Dihydrofolate reductase
DHPS	Dihydropteroate synthetase
DMF	Dimethyl formamide
DMG	Dimethylglycine
DNA	Deoxyribonucleic acid
DRTS_LEIMA	<i>Leishmania major</i> DHFR-TS sequence
DRTS_PLAFK	<i>Plasmodium falciparum</i> DHFR-TS sequence
DRTS_TOXGO	<i>Toxoplasma gondii</i> DHFR-TS sequence

DRTS_TYRCR	<i>Trypanosoma cruzi</i> DHFR-TS sequence
dTMP	Deoxythymidine monophosphate
dUMP	Deoxyuridine monophosphate
DYR_HUMAN	Human dihydrofolate reductase sequence
ec	<i>Escherichia coli</i>
ecDHFR	<i>Escherichia coli</i> dihydrofolate reductase
EdAM	Edatrexate
EGF	Epidermal growth factor
EGFR	Epidermal growth factor receptor
fAICAR	Formyl-amino-imidazolecarboxamide ribosyl-5-phosphate
FBP	Folate binding protein
FDA	Food and drug administration
FdUMP	5-Fluorodeoxyuridine monophosphate
fGAR	Formyl-glycinamide ribosyl-5-phosphate
FGFR	Fibroblast growth factor receptor
FPGS	Folylpoly- γ -glutamate synthetase
FR	Folate receptor
GAR	Glycinamide ribosyl-5-phosphate
GART	Glycinamide ribonucleotide formyltransferase
GIST	Gastrointestinal stromal tumor
GTP	Guanosine-5'-triphosphate
hDHFR	Human dihydrofolate reductase

hTS	Human thymidylate synthase
IMP	Inosine-5'-monophosphate
ma	<i>Mycobacterium avium complex</i>
MAPs	Microtubule associated proteins
MD	Molecular dynamics
MDR	Multidrug resistance
MOE	Molecular Operating Environment
MRP1	Multidrug resistance associated protein 1
MTHFR	Methylenetetrahydrofolate reductase
MTOCs	Microtubule organizing centers
MTR	Methionine synthase
MTX	Methotrexate
MZPES	Meta-azidopyrimethamine ethanesulphonate
NADPH	Nicotinamide adenine dinucleotide phosphate
NMP	N-methyl-2-pyrrolidinone
NSCLC	non-small-cell lung cancer
ONC	Optimum number of components
pc	<i>Pneumocystis carinii</i>
pcDHFR	<i>Pneumocystis carinii</i> dihydrofolate reductase
pj	<i>Pneumocystis jirovecii</i>
pjDHFR	<i>Pneumocystis jirovecii</i> dihydrofolate reductase
PCC	Pearson correlation coefficients
PCFT	Proton-coupled folate receptor

PcP	<i>Pneumocystis carinii</i> pneumonia
PDB	Protein data bank
PDGF	Platelet derived growth factor
PDGFR	Platelet derived growth factor receptor
Pgp	P-glycoprotein
ProSA	Protein Structure Analysis
PTX	Piritrexim
q ² -GRS	Modified cross-validated r ² -guided region selection
RFC	Reduced folate carrier
RMSD	Root-mean-square deviation
RNA	Ribonucleic acid
RTK	Receptor tyrosine kinase
SAH	S-adenosylhomocysteine
SAR	Structure-activity relationship
SMX	Sulfamethoxazole
tg	<i>Toxoplasma gondii</i>
tgDHFR	<i>Toxoplasma gondii</i> dihydrofolate reductase
THF	Tetrahydrofolate
TLC	Thin layer chromatography
TMP	Trimethoprim
TMQ	Trimetrexate
TS	Thymidylate synthase
VEGF	Vascular endothelial growth factor

VEGFR Vascular endothelial growth factor receptor

BIOCHEMICAL REVIEW

A. 1. ANTIFOLATES

A.1.1. The folate metabolism pathway:

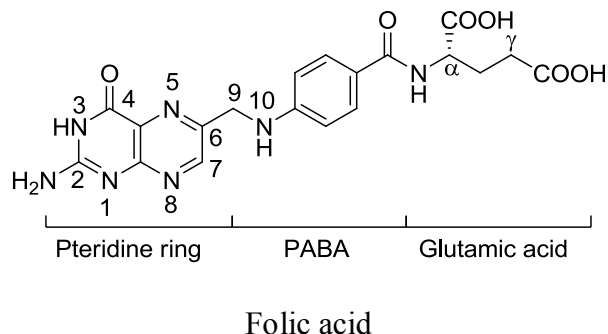


Figure 1. Structure of folic acid

The term folate represents a group of water-soluble compounds composed of a pterioic acid (pteridine ring linked to *p*-aminobenzoic acid) and one or more L-glutamate residues. In nature, folate exists as a mixture of different forms that have variable bioavailability and stability.²⁻⁵ The most common source of folates is folic acid (Figure 1), an oxidized and chemically stable derivative. Folates play a vital role in cell proliferation and amino acid metabolism. Folate deficiency leads to anemia, impaired growth and dermatitis. Under normal conditions a high concentration of the folate pool is present in the cell.⁶ Unlike mammalian cells, which get their folic acid from the diet, higher plants, fungi and bacteria synthesize folates *de novo*.⁷

Derivatives of folic acid substituted at the N5- and N10-positions serve as substrates for single-carbon transfer reactions in the production of nucleotides and methionine (Figure 2). The reduced folate carrier (RFC) is the primary means for the transport of folates into cells.^{8,9} Another transporter of folates are the folate receptors (FR),

a cell membrane associated folate binding protein (FBP).^{8, 10, 11} Additionally, proton-coupled folate receptor (PCFT) was recently reported to contribute to folate absorption in the duodenum.¹² The tissue specificity and overall role of PCFT in folate transport and homeostasis are currently being investigated.

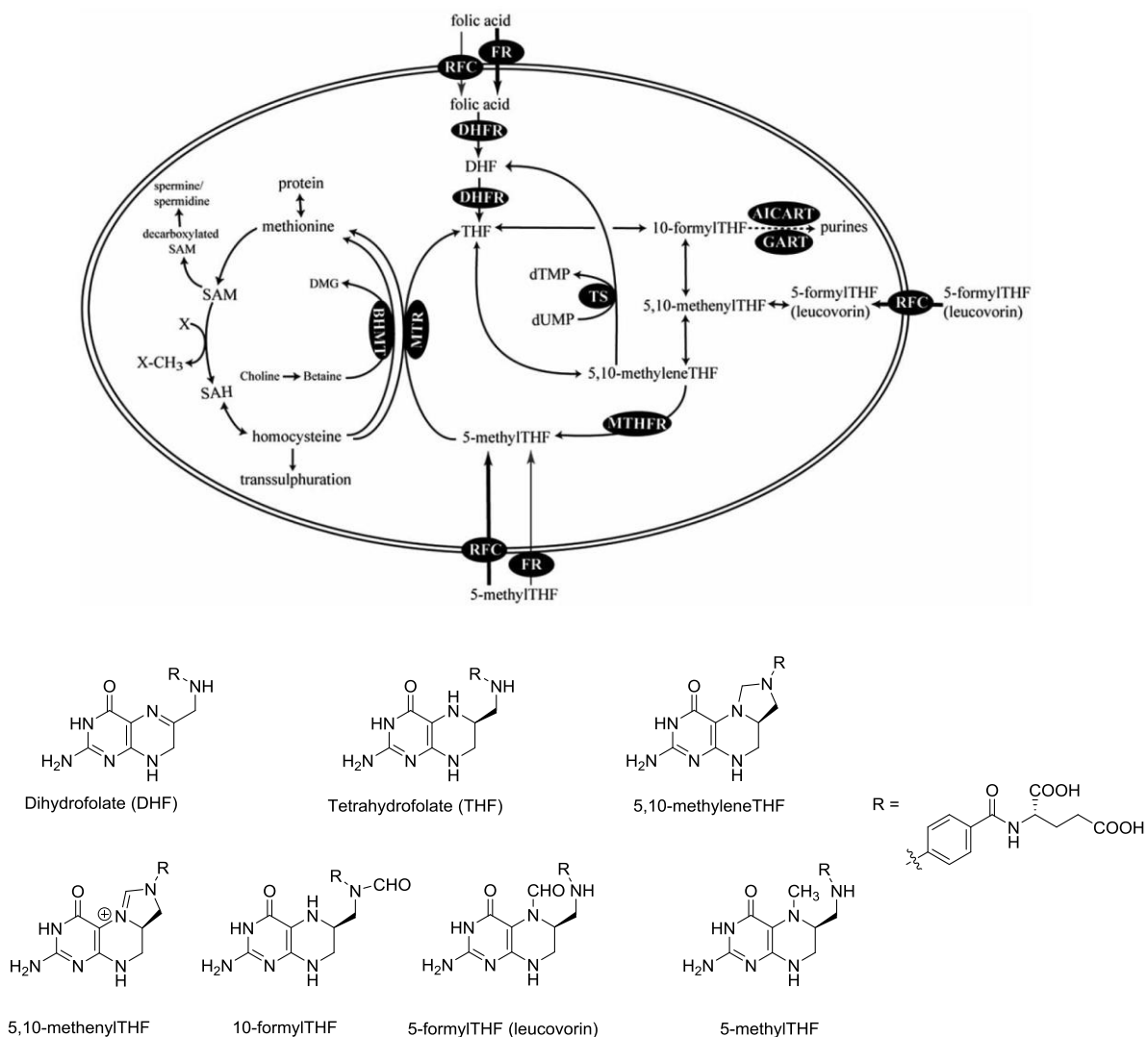


Figure 2. Folate metabolism pathway. (modified from ref.¹³) Aminoimidazole carboxamide formyltransferase, AICART; betaine-homocysteine methyltransferase, BHMT; dihydrofolate reductase, DHFR; deoxythymidine monophosphate, dTMP; deoxyuridine monophosphate, dUMP; dimethylglycine, DMG; folate receptor, FR; glycinamide ribonucleotide formyltransferase, GART; methylenetetrahydrofolate reductase, MTHFR; methionine synthase,

MTR; reduced folate carrier, RFC; S-adenosylhomocysteine, SAH; S-adenosylmethionine, SAM; thymidylate synthase, TS.

The enzyme folylpoly- γ -glutamate synthetase (FPGS) sequentially adds up to eight L-glutamic acid residues to the folate monoglutamate within the cell.¹⁴ This has the following important consequences: (a) it greatly increases the affinity of the folates to some folate-metabolizing enzymes, and (b) prevents efflux of the folates and increases their intracellular retention.

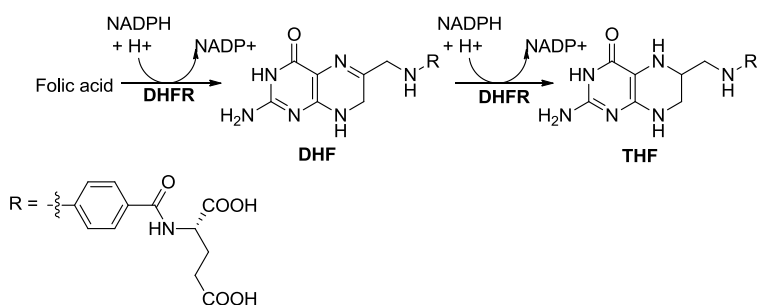


Figure 3. Folic acid pathway

The various enzymes of the folate metabolism pathway (Figure 3) perform the crucial role of utilizing the folate cofactors for the biosynthesis of DNA. Folate cofactors and the folate metabolizing enzymes are also critical for amino acid metabolism.¹⁵⁻¹⁷ To act as cofactors, folates have to be reduced to tetrahydrofolate (THF). This reduction reaction is catalyzed by the enzyme dihydrofolate reductase (DHFR) and occurs from dietary folates in two steps (Figure 3). The first step is the intracellular reduction of the pyrazine portion of the pteridine ring of folic acid, in presence of reductant nicotinamide adenine dinucleotide phosphate (NADPH) which leads to the formation of 7,8-dihydrofolate (DHF) followed by the reduction of DHF to THF.¹⁸

The *de novo* synthesis of purines is described in Figure 4. In presence of the enzyme

glycinamide-ribonucleotide formyl transferase (GARFTase), another cofactor, 10-formylTHF and glycinamide ribosyl-5-phosphate (GAR) are converted to THF and formyl-glycinamide ribosyl-5-phosphate (fGAR) respectively. The fGAR formed is further transformed to amino-imidazolecarboxamide ribosyl-5-phosphate (AICAR) in five steps.

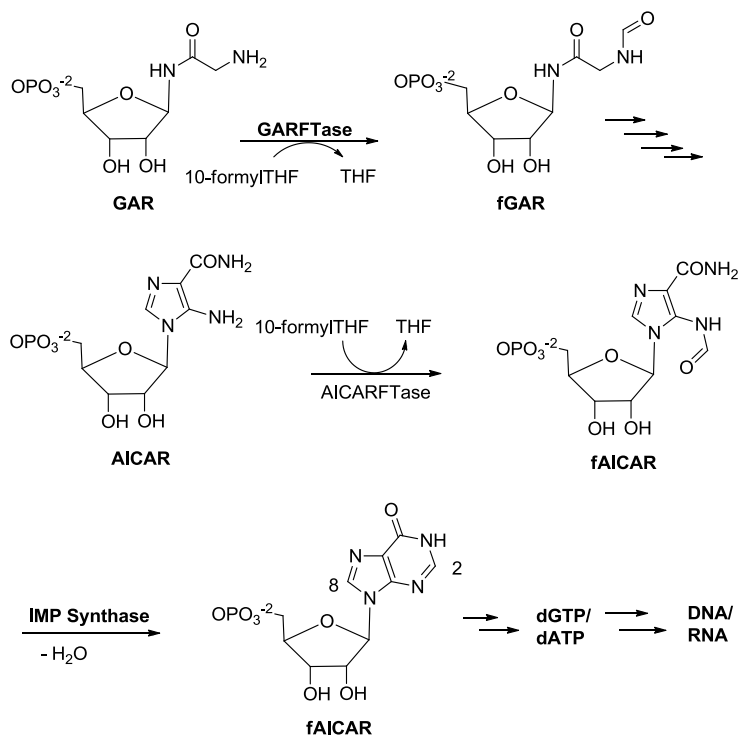


Figure 4. *De novo* synthesis of purines.

The enzyme AICARFTase uses 10-formylTHF to convert AICAR to formyl-amino-imidazolecarboxamide ribosyl-5-phosphate (fAICAR) releasing THF in this process. The fAICAR formed continues along the purine biosynthetic pathway leading to the formation of inosine-5'-monophosphate (IMP), the precursor of adenosine-5'-triphosphate (ATP) and guanosine-5'-triphosphate (GTP) necessary for ribonucleic acid (RNA) synthesis and of 2'-deoxyadenosine-5'-triphosphate (dATP) and 2'-deoxyguanosine-5'-triphosphate (dGTP) essential for DNA synthesis.^{19, 20}

Folates are key components for the formation of 2'-deoxythymidylate-5'-monophosphate (dTMP) from 2'-deoxyuridylate-5'-monophosphate (dUMP) (Figure 5). This process is catalyzed by thymidylate synthase (TS), and uses 5,10-methylene THF to transfer a methylene to the 5-position of dUMP to form the 5-methyl group of dTMP. This reaction is the sole *de novo* source of dTMP and is the rate-limiting step in mammalian DNA synthesis.²¹ Hence inhibition of the folate pathway by targeting enzymes such as DHFR or TS is a viable target for therapeutic intervention and has been successfully employed in the clinic for the treatment of different cancers and pathogenic infections.

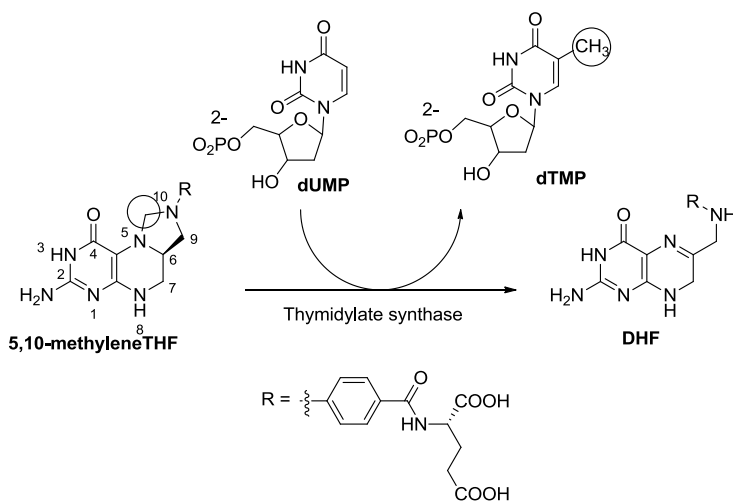


Figure 5. De novo synthesis of dTMP

A.1.2. Opportunistic infections

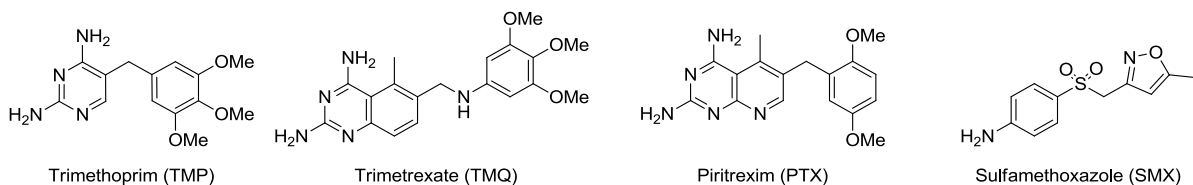


Figure 6: Structures of Trimethoprim (TMP), Trimetrexate (TMQ), Piritrexim (PTX) and

Sulfamethoxazole (SMX)

Opportunistic infections caused by organisms such as *Pneumocystis carinii* (pc), *Pneumocystis jirovecii* (pj), *Toxoplasma gondii* (tg), and *Mycobacterium avium complex* (ma) often cause life threatening infections in immunocompromised patients such as HIV patients and post-transplant patients on immunosuppressant drugs.²²⁻²⁶ These infections are a major cause of morbidity and severely decrease the quality of life of such patients. While bacteria, fungi, yeasts and protozoa obtain dihydrofolate by de-novo synthesis from simple precursors, humans obtain the required folates from diet, mostly as folic acid, which is reduced sequentially to FH₂ and FH₄. Additionally, mammalian cells contain active folate transport systems such as reduced folate carrier (RFC) while pathogens lack such specialized transport systems.²⁷ This provides an excellent opportunity to selectively target pathogen DHFR by means of lipophilic, non-classical DHFR inhibitors such as trimethoprim (TMP), trimetrexate (TMQ), and piritrexim (PTX) (Figure 6). These agents, which lack the glutamate chain of classical DHFR inhibitors, do not require specialized transport systems for uptake into cells, passively diffuse across cell membranes. Mammalian cells can be selectively protected from the resultant toxic effects of such lipophilic agents by the co-administration of a folic acid precursor, leucovorin, which is taken up by mammalian cells by active transport and provides the necessary folate precursor for normal cellular function.²⁸ Several excellent reviews that detail the development of agents that target DHFR from opportunistic infections are present in the literature.^{27, 29-32} X-ray crystal structures of human DHFR (hDHFR) and pathogen DHFR have aided in drug development efforts and are discussed below.

A.1.3. Structure of DHFR

A.1.3.1. Human DHFR

DHFR (EC 1.5.1.3) is one of the best studied enzymes in the folate metabolism pathway.³³⁻³⁵ DHFR is found in all organisms except archaeobacteria and few parasitic protozoa. Currently the protein data bank (PDB)³⁶ comprises of 323 DHFR structures bound to cofactors as well as inhibitors. Bacterial DHFR shows lower homology (25-40%) relative to vertebrate DHFR (75-90%). Homology at the N-terminal is much higher than that at the C-terminal.^{37, 38} DHFR is a monomeric enzyme with a sequence of 159-204 amino acid residues and a molecular weight in the range of 18000-22000 daltons. The tertiary structure of DHFR, an α/β structure, contains a eight stranded β -sheet and atleast four α -helices. The β -sheet consists of seven parallel strands, and one antiparallel strand.

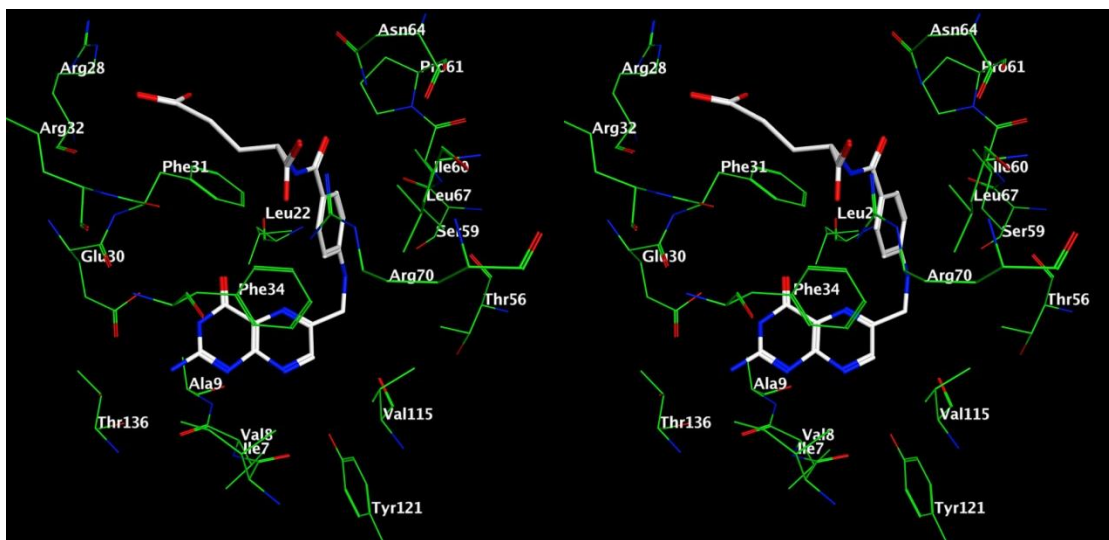


Figure 7: Stereoview. Folic acid (white) bound to the active site of hDHFR. (PDB: 1DRF³⁹)

The active site of the enzyme is located in a Hydrophobic pocket and shows the presence of a conserved acid residue (Glu30 in vertebrate DHFR⁴⁰ and Asp27 in *Escherichia coli* (*ec*) DHFR).⁴¹ The Hydrophobic pocket acts as the binding site for the

substrate or the antifolates and nicotinamide portion of NADPH.⁴⁰ The pteridine portion and the glutamate side chain portions of folates interact with the polar side chains and backbone carbonyls in the active site (Figure 7). Additionally, the binding site contains hydrophobic flanking amino acids such as Phe31 and Phe34 which bind to the pteridine scaffold of folic acid and other scaffolds of antifolates.⁴⁰

A.1.3.2.*Pneumocystis carinii* DHFR (pcDHFR)

pcDHFR consists of 206 amino acid residues and is similar to rat liver (rl) DHFR in size with a molecular weight of 26000 Dalton. The optimum pH for pcDHFR is 7.0 and its K_m for FH_2 is four-fold higher ($17.6 \pm 3.9 \mu M$) than rat liver DHFR ($4.0 \pm 2.2 \mu M$).⁴²

The size of the cavity of pcDHFR active site is smaller than that of hDHFR but larger than that of bacteria such as *E. coli* DHFR.⁴² X-ray crystal structures⁴²⁻⁴⁴ have shown that most residues of DHFR involved in catalysis and binding are conserved in both hDHFR and pcDHFR with the exception of the polar Asn64 residue in hDHFR, located just outside the binding site, being replaced by a nonpolar Phe69 in pcDHFR. The more potent pcDHFR inhibitors like PTX ($IC_{50} = 19.3 \text{ nM}$) and TMQ ($IC_{50} = 42 \text{ nM}$) lack selectivity.

A.1.3.3.*Pneumocystis jirovecii* (pjDHFR)

It was recently shown that *P. jirovecii* is the actual opportunistic pathogen that infects humans, while *P. carinii* is the pathogen that is derived from and infects rats.^{45, 46} It has recently been reported that patients with rheumatoid arthritis undergoing first line

therapy with methotrexate (MTX) are at increased risk of contracting *P. jirovecii* pneumonia (PCP).⁴⁷ Cody *et al*⁴⁸ reported that the recombinant human-derived pjDHFR differs from rat-derived pcDHFR by 38% in amino acid sequences. There are no reported crystal structures for DHFR from pjDHFR.

A.1.3.4. *Toxoplasma gondii* (tgDHFR)

T. gondii is a DHFR-TS bifunctional enzyme with the DHFR domain located at the N-terminus and the TS domain is at the C-terminus.⁴⁹ A junction polypeptide separates the two domains. The protozoan parasite is a ubiquitous organism capable of infecting a wide range of vertebrate hosts, including man. Toxoplasmosis is a leading opportunistic pathogen associated with AIDS.^{50, 51} Although the crystal structures of tgDHFR are not yet available, the primary structure of the DHFR-TS gene from tg has been reported by Roos.⁴⁹

The K_m for tgDHFR ($IC_{50} = 4.6 \pm 4.3 \mu M$) is similar as that for rat liver (rl) DHFR ($IC_{50} = 20 \mu M$). Several DHFR inhibitors such as TMQ ($IC_{50} = 10 \text{ nM}$), PTX ($IC_{50} = 4.3 \text{ nM}$) and TMP ($IC_{50} = 2.8 \mu M$) are active against isolated *T. gondii* enzyme and against the growth of *T. gondii* cells in culture.^{27, 52}

A.1.4.DHFR inhibitors

DHFR inhibitors have been successfully used in the clinic in anticancer, antibacterial and antiprotozoal treatment regimens. DHFR inhibitors commonly replace the 2-amino-4-oxo system in folate with a 2,4-diamino system, which increases the basicity of the nitrogen of the 1,3-diazine.⁵³ This modification results in protonation at N1 rather than N8 of the pteridine core.^{39, 54-56} Resultantly, this intermediate cannot accept a hydride ion and be converted to the product. Additionally, the intermediate is commonly bound through a salt bridge to a conserved acidic residue (Glu or Asp) in the DHFR active site.⁵⁶

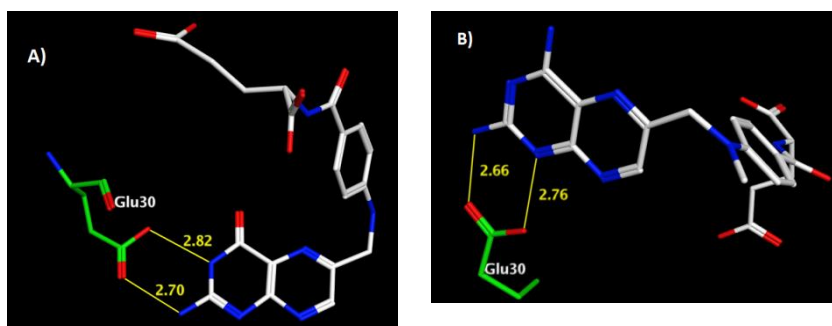


Figure 8. Interaction of Glu30 in the active site of human DHFR with (A) DHF (PDB: 1DRF³⁹), and (B) MTX (PDB: 1DLR⁵⁷).

Analysis of various crystal structures indicates that MTX binds to DHFR such that the *para*-aminobenzoyl group and the pteridine moiety are oriented perpendicular to each other (Figure 8).^{39, 40} The N1 atom of MTX is protonated in its bound state (studied by spectroscopic,^{54, 55} calorimetric,⁵⁵ theoretical and NMR⁵⁶ methods) and forms an ionic bond with an ionized carboxylic acid of a conserved acidic residue (Glu or Asp; e.g. Asp26 in *L. casei*, Glu30 in mammalian DHFR). In *L. casei* the Oδ2 of Asp26 is interacts with N¹ and

the Oδ1 is hydrogen bonded to the 2-amino group. This binding mode is found in a majority of reported DHFR inhibitors and forms the basis for its activity against the enzyme.

Antifolates with a pteridine, pyridopyrimidine, or quinazoline core and a 2,4-diamino moiety have been shown to bind to the active site of human DHFR (hDHFR) similar to MTX. Additional interactions include a water mediated hydrogen bonding network between the conserved residues of human DHFR – Thr136, Trp24 and the 2-NH₂ and N8-nitrogen respectively.^{42, 58-60} The 4-NH₂ group of MTX is the part of a hydrogen bonding network between the conserved residues Ile7, Val115 and Tyr121. This framework of hydrogen bonds is characteristic of all crystal structures reported for DHFR complexes.^{61, 62} A comparison of the crystal structure of DHFR with folic acid and that with the antifolate MTX indicates that they bind with their pteridine ring rotated 180° from each other which is responsible for their different active site interactions.

The differences of the amino acid sequences in the active site of DHFR from different species accounts for the differences in the binding affinity of inhibitors and has been exploited to design inhibitors that are selective for pathogen DHFR over human DHFR. Thus the binding affinity of TMP (Figure 6) is five orders of magnitude greater than mammalian DHFR and hence TMP can function as a potent and selective antibacterial agent.

A.1.4.1.Nonclassical DHFR inhibitors

Currently, different DHFR inhibitors including trimethoprim (TMP), trimetrexate (TMQ) and piritrexim (PTX) (Figure 8) are used for treatment of opportunistic infections caused by pc and tg.

A.1.4.1.Monocyclic DHFR inhibitors

The following section briefly summarizes selected important monocyclic DHFR inhibitors and their analogs.

Trimethoprim

TMP (Figure 6) is a highly selective DHFR inhibitor ($IC_{50} = 7$ nM for ecDHFR compared to $IC_{50} = 490000$ nM for rat liver DHFR (rDHFR)) and is approved for use as an antibacterial and antipneumocystitis agent in combination with sulfamethoxazole (SMX). SMX blocks the conversion of PABA to FH_2 through the inhibition of dihydropteroate synthase.²² Dapsone is often used in the prophylaxis of pneumocystis pneumonia (PCP) in patients with AIDS who are unable to tolerate TMP/SMX. Severe hematologic effects such as agranulocytosis, aplastic anemia, and hemolytic anemia have been reported with the use of dapsone.^{63, 64} TMP lacks the glutamic acid side-chain, which is the characteristic feature of the nonclassical antifolate.

Comparison of crystal structures of TMP in chicken liver (ch) DHFR and ecDHFR was performed to explain the observed selectivity of TMP.⁴¹ TMP was observed to bind deeper in chDHFR compared to ecDHFR. This binding led to the loss of two hydrogen bonds. Additionally, the benzyl side chain of TMP is oriented towards the NADPH binding site in ecDHFR, whereas in chDHFR the side chain of TMP points away from the cofactor binding site. This difference in binding of TMP in ecDHFR and chDHFR leads to a significant difference in the torsion angle about the C5-C7 and C7-C1' bonds for TMP.⁴¹ However, comparison of TMP bound to hDHFR, both in the crystal and solution, showed no loss of hydrogen bonding. Crystal structures of a TMP analog that contained a 3'-methoxy in the side chain phenyl ring indicated that the 3'-methoxy substituent could form additional interactions with the γ -glutamate binding pocket of

DHFR, thereby enhanced its inhibitory property.⁶⁵

In contrast, the hydrophobic pocket of pcDHFR is larger than that of ecDHFR.⁴² In the crystal structure of TMP bound to pcDHFR, the 4-amino group of TMP forms two hydrogen bonds with the backbone carbonyls of Ile10 and Ile123. The benzyl group of TMP occupies a hydrophobic pocket formed by Ile23, Leu25, Ile33, Phe36, Pro65, Ile66 and interacts with the nicotinamide ribose of the cofactor through hydrophobic interactions.

TMQ and PTX (Figure 6) are potent and non-selective DHFR inhibitors and are co-administered with leucovorin for host rescue^{66, 67} due to the high rate of myelosuppression associated with high doses of these agents.^{67, 68} However, the DHFR inhibitor/leucovorin combination therapy also has several drawbacks including, the high cost of leucovorin and the inconsistent effect of leucovorin under all clinical conditions.⁶⁹ Thus, there is a considerable interest to incorporate selectivity of TMP and potency of TMX/PTX into a single agent that can be used alone to treat these infections and is the target of several ongoing research endeavours. An analysis of the literature indicates that the issue of potency has been addressed in several studies, however selectivity over hDHFR remains a significant challenge. The structural requirements for potential DHFR inhibitors have been summarized in recent publications.^{31, 32, 53} The availability of high resolution crystal structures of pcDHFR and human DHFR has aided rational drug design in the development of highly potent and specific DHFR inhibitors. However, crystal structures of pjDHFR, tgDHFR and maDHFR have not been solved yet. In these cases, comparative modeling techniques have been used to generate models which have been used in rational drug design efforts. Additionally, ligand based drug design efforts using

3D-QSAR techniques, such as CoMFA, have been successfully applied in the design of newer agents.^{53, 70, 71}

The discovery of TMQ and pyrimethamine as potential antibacterial and antimalarial agents stimulated the research for new nonclassical antifolates, which lack the benzoylglutamate side chain of classical compounds such as MTX. These agents have found utility in anti-infective therapy since bacteria and protozoa synthesize folic acid *de novo* without using preformed folate. In addition, these compounds do not utilize the folate active transport systems such as FR or RFC. They are taken up by passive and/or facilitated diffusion and are not substrates for FPGS. Thus they overcome resistance encountered with classical inhibitors like PTX, which are associated with a defect in transport or FPGS activity. The main drawback of these new potent antifolates is their lack of selectivity against DHFR derived from pathogens and hDHFR.

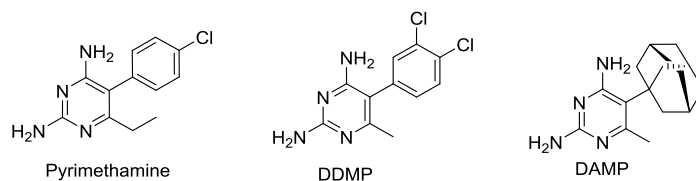


Figure 9. The structures of Pyrimethamine, DDMP and DAMP

Pyrimethamine (Figure 9) is a potent selective inhibitor of plasmodia DHFR used in the treatment and prophylaxis of malarial. Two small structural changes to the pyrimethamine: changing the 6-ethyl group to a methyl group and introducing an additional chlorine on the phenyl ring, led to 2,4-diamino-5-(3,4-dichlorophenyl)-6-methylpyrimidine (DDMP, Figure 9), which is a potent vertebrate DHFR inhibitor and was clinically used to treat MTX resistant tumors along with the structurally related DAMP (Figure 9)^{169, 170}

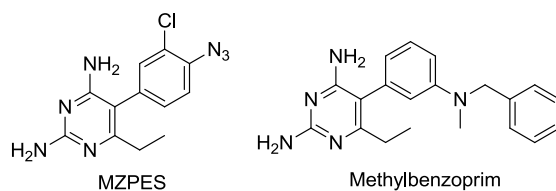


Figure 10. The structures of MZPES and Methylbenzoprim

Analogues of pyrimethamine that vary in the 5-phenyl ring substitutions include meta-azidopyrimethamine ethanesulphonate (MZPES, Figure 10), which completed Phase I clinical trials as an antitumor agent. Methylbenzoprim is one of the most potent nonclassical DHFR inhibitor ($K_i = 9$ pM against rat liver DHFR) reported in the literature.¹⁷²

A.1.4.2. 6,6-Fused Bicyclic DHFR Inhibitors

The following section deals with selected 6,6-fused bicyclic inhibitors of hDHFR and pathogen DHFR.

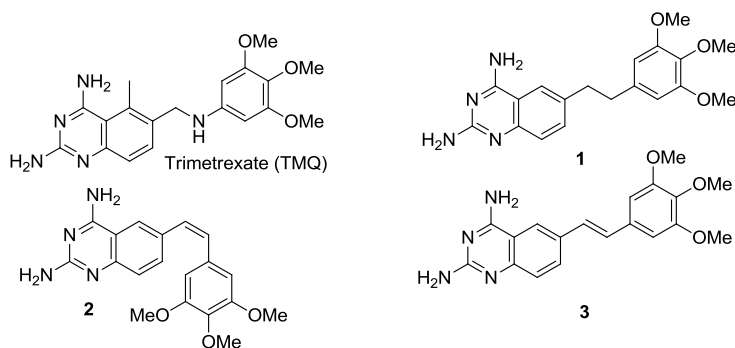


Figure 11. Structures of TMQ and 1-3

Trimetrexate (TMQ) (Figure 11) is a potent inhibitor of hDHFR and pcDHFR and displays better antitumor activity than MTX but its lack of selectivity for pcDHFR over hDHFR limits its clinical applications. TMQ has been approved for the treatment of PCP. Replacement of the nitrogen in the linker region of TMQ with a carbon affords **1** (Figure

11), which is a potent *ec*DHFR inhibitor. The Z-isomer (**2**, cis) is more potent than the E-isomer (**3**).

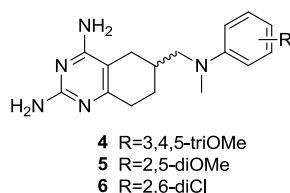


Figure 12. Tetrahydroquinazoline analogues **4-6**

Gangjee *et al.*⁷² reported a series of 6-substituted tetrahydroquinazoline analogues of TMQ. Compounds **4-6** (Figure 12) showed nanomolar inhibition of tgDHFR with 5-11 fold selectivity ratios (IC_{50} rDHFR/ IC_{50} tgDHFR) as compared to rDHFR.

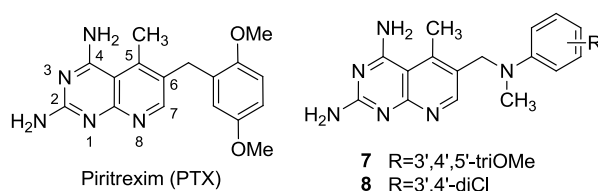


Figure 13. The structure of PTX and **7** and **8**

PTX is a potent 2,4-diaminopyrido[2,3-*d*]pyrimidine inhibitor of pcDHFR (IC_{50} = 31 nM, 40 – 1000 fold more potent than TMP⁷³) but lacks selectivity. It is utilized as a second-line therapy in the clinic for moderate to severe PCP. The 5-methyl group of PTX was important for high potency. The removal of the 5-methyl group and/or the 2',5'-dimethoxy substituent both resulted in the decrease of activity.

Gangjee *et al.*⁷⁴ reported **7** and **8** which replaced the methylene bridge of PTX with CH_2NCH_3 (Figure 13). Compound **7** shows extremely potent inhibitory activity against tgDHFR (IC_{50} = 0.58 nM) whereas **8** had excellent antitumor activity.

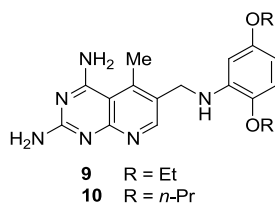


Figure 14. Structures of **9** and **10**

Suling *et al.*⁷⁵ reported a series of 5-methyl-6-substituted pyrido[2,3-*d*]pyrimidines as potential maDHFR inhibitors. The most potent compound in this series was **9** (Figure 14, maDHFR IC₅₀ = 0.84 nM) with excellent selectivity (2378-fold) over hDHFR. Compound **10** exhibited the highest selectivity in this series (maDHFR IC₅₀ = 1 nM, 7300-fold selective). Additional compounds that varied in the nature of the linker at the 6-position of the pyrido[2,3-*d*]pyrimidine scaffold (-CH₂-S- or -CH₂-CH₂- instead of -CH₂-NH-) were reported.⁷⁵ These compounds displayed excellent selectivity (> 2500-fold) for maDHFR over hDHFR.

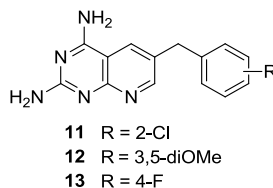


Figure 15: Structures of **11** – **13**.

PTX analogs **11** – **13** (Figure 15) were designed by Rosowski *et al.*⁷⁶ as a part of a series of compounds. While these compounds displayed fair selectivity, none were more potent than PTX in targeting pathogen DHFR. Compound **11** was the most potent inhibitor of *tg*DHFR (IC₅₀ = 14 nM) and was modestly selective for *tg*DHFR (4-fold) over rIDHFR. Compound **12** was the most selective inhibitor of *tg*DHFR (IC₅₀ = 36 nM; 10.3-fold selective) as well as *ma*DHFR (IC₅₀ = 41 nM; 9-fold selective) over rIDHFR. Compound **13** exhibited good potency and moderate selectivity against *tg*DHFR and

maDHFR over rIDHFR. All the compounds of the series displayed submicromolar inhibition of pcDHFR, displaying the importance of the 5-methyl group for activity.

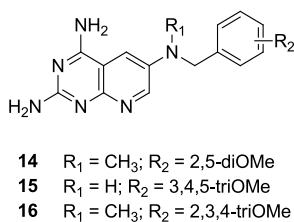


Figure 16: Structures of **14** – **16**

Gangjee *et al.*⁷⁷ published **14** – **16** (Figure 16) as part of a series of compounds that lack the 5-methyl group (from PTX and TMQ) and contains a reversed C9-N10 bridge leading to the transposition of the N9-nitrogen. Compound **14** was 304-fold selective for tgDHFR versus hDHFR. Compound **14** was also a potent inhibitor of pcDHFR ($\text{IC}_{50} = 84 \text{ nM}$) and was 101-fold selective for pcDHFR over hDHFR. Compound **15** was 192-fold selective for tgDHFR over hDHFR, but was much less potent compared to PTX against all the DHFRs tested and exhibited an IC_{50} in micromolar range. The corresponding N9-methyl analog **16** was a potent but nonselective inhibitor of pcDHFR and tgDHFR.

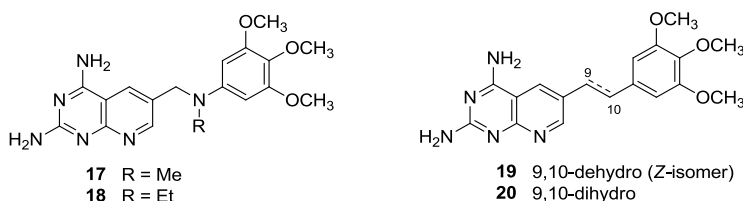


Figure 17: Structures of **17** – **20**

Gangjee *et al.*⁷⁸ also designed **17** and **18** (Figure 17) in an attempt to explore the effect of substitution at the N10-position on DHFR activity. Compounds **19** and **20** were designed as analogs in which the N10-nitrogen was replaced with a carbon. Further, the effect of conformational restriction was analyzed by **20**. Compound **17** was an excellent

inhibitor of tgDHFR ($IC_{50} = 9$ nM, 31-fold selective over rIDHFR). Compared to TMP, compound **17** was only slightly less selective but displayed a vastly improved 300-fold increased potency against tgDHFR. Compound **18** was a potent inhibitor of pcDHFR and tgDHFR but lacked selectivity. Compounds **19** and **20** did not display potent DHFR inhibition (μ M IC_{50} s).

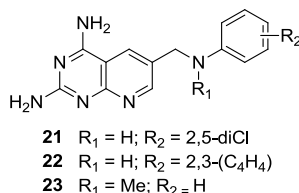


Figure 18: Structures of **21** – **23**

Gangjee *et al.*⁷⁹ further reported **21** – **23** (Figure 18) as a part of a series of pyrido[2,3-*d*]pyrimidines designed to investigate the effect of variation in the substitution and the size of the side chain on activity and/or selectivity for DHFR. Analog **21** was the most selective inhibitor of both pcDHFR ($IC_{50} = 440$ nM; 15.7-fold selective) and tgDHFR ($IC_{50} = 300$ nM; 23-fold selective) in this series. Compound **22** was the most potent compound in this series against both pcDHFR ($IC_{50} = 70$ nM; 8.6-fold selective) and tgDHFR ($IC_{50} = 96$ nM; 6.3-fold selective). The N10-methylated analog **23** displayed a loss of potency against all three tested DHFRs.

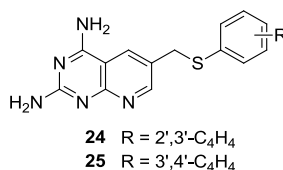


Figure 19: Structures of **24** and **25**

Gangjee *et al.*⁸⁰ reported the synthesis of **24** and **25** (Figure 19) as a part of a series of six 2,4-diaminopyrido[2,3-*d*]pyrimidines with a 6-methylthio bridge to an aryl

group as inhibitors of pcDHFR and tgDHFR. Compound **24** showed the highest selectivity ratios of 3.6 and 8.7 against pcDHFR and tgDHFR, respectively, against rat liver (rl) DHFR. The β -naphthyl analogue **25** exhibited the highest potency within the series with an IC₅₀ value of 0.17 and 0.09 μ M against pcDHFR and tgDHFR, respectively. Compound **24** was evaluated for *in vitro* antimycobacterium activity and was shown to inhibit the growth of *M. tuberculosis* H37Rv cells by 58% at a concentration of 6.25 mg/mL.

A.1.5. Molecular modeling approaches employed for designing selective DHFR inhibitors

This review summarizes modeling efforts for the design of selective DHFR inhibitors against opportunistic agents and generation of homology models for pathogen DHFR. These areas have been reviewed extensively in the literature by Tawari *et al.*⁵³

Multiple high resolution (< 2.5 Å) X-ray crystal structures of DHFR from pathogens such as *P. carinii* (17 structures), *Cryptosporidium hominis* (chDHFR, 5 structures), *Leishmania major* (3 structures) and *T. cruzi* (9 structures) among others can be accessed in the protein data bank. Additionally, the presence of multiple hDHFR crystal structures has aided in comparison of active sites, and aided in the design of inhibitors selective for pathogen DHFR.^{81, 82} This review will cover modeling studies with pcDHFR and tgDHFR.

A.1.5.1. Molecular Modeling studies with pcDHFR

pcDHFR is a 206 amino acid chain and shares 34% identity with human DHFR.⁸³ Table **1** provides a list of the 17 X-ray crystal structures of pcDHFR that can currently be

accessed in the PDB.

Chamness *et al.*⁴² described, 1.86 Å resolution crystal structure of ternary complex of pc DHFR with TMP and NADP, similarly with PTX and NADP along with a binary complex holoenzyme at 2.5 Å resolution. Cody *et al.*⁸⁴ reported the crystal structure (PDB: 1HFQ) of a classical furopyrimidine inhibitor, MOT (Figure 20, pcDHFR IC₅₀: 6.5 nM; hDHFR IC₅₀: 2.7 nM), with pcDHFR and recombinant wild-type human DHFR. These studies provided the first direct comparison of the binding interactions of the same antifolate inhibitor in the active site for pcDHFR and human DHFR.

Table 1: X-ray crystal structures of pcDHFR available in the PDB

	PDB	Resolution (Å)	Ligand	Reference
1	1DYR	1.86	TMP, NDP	⁴²
2	3OAF	1.70	OAG	⁸⁵
3	3L3R	2.00	OAG, NDP	⁸⁵
4	1E26	2.00	GPB, NAP	⁴³
5	1DAJ	2.30	MOT, NDP	⁸⁶
6	1CD2	2.20	FOL, NAP	⁴³
7	2CD2	1.90	FOL, NAP	⁴³
8	3CD2	2.50	MTX, NAP	⁴³
9	4CD2	2.00	FOL	⁴³
10	1VJ3	2.10	TAB, NDP	⁸⁷
11	1KLK	2.30	PMD, NDP	⁸²
12	1S3Y	2.25	TQT, NAP	⁸¹
13	1LY3	1.90	COG, NAP	⁸²
14	1LY4	2.10	COQ, NAP	⁸²
15	2FZH	2.10	DH1, NAP	⁴⁴
16	2FZI	1.60	DH3, NAP	⁴⁴
17	2FZJ	2.00	DH3, NAP	⁴⁴

Comparison of the pcDHFR crystal structure with folic acid and those of the apo enzyme by Cody *et al.*⁸⁶ revealed a >7 Å movement of the loop region near Asn23 that

results in a “flap-open” position for the binary complex, and a “closed” position in the ternary complexes, similar to that reported for ecDHFR complexes.

Cody *et al.*⁸⁸ reported structural data for PT653 (Figure 20, PDB: 1KLK) with pcDHFR. The crystal structure explained that the observed 21-fold selectivity of PT653 for pcDHFR over rIDHFR could be the result of a ligand-induced fit of the hydrophobic dibenzazepine ring of PT653, which occupied regions of the enzyme active site not occupied by other antifolates and due to conformational differences between the structures of human and pcDHFR.

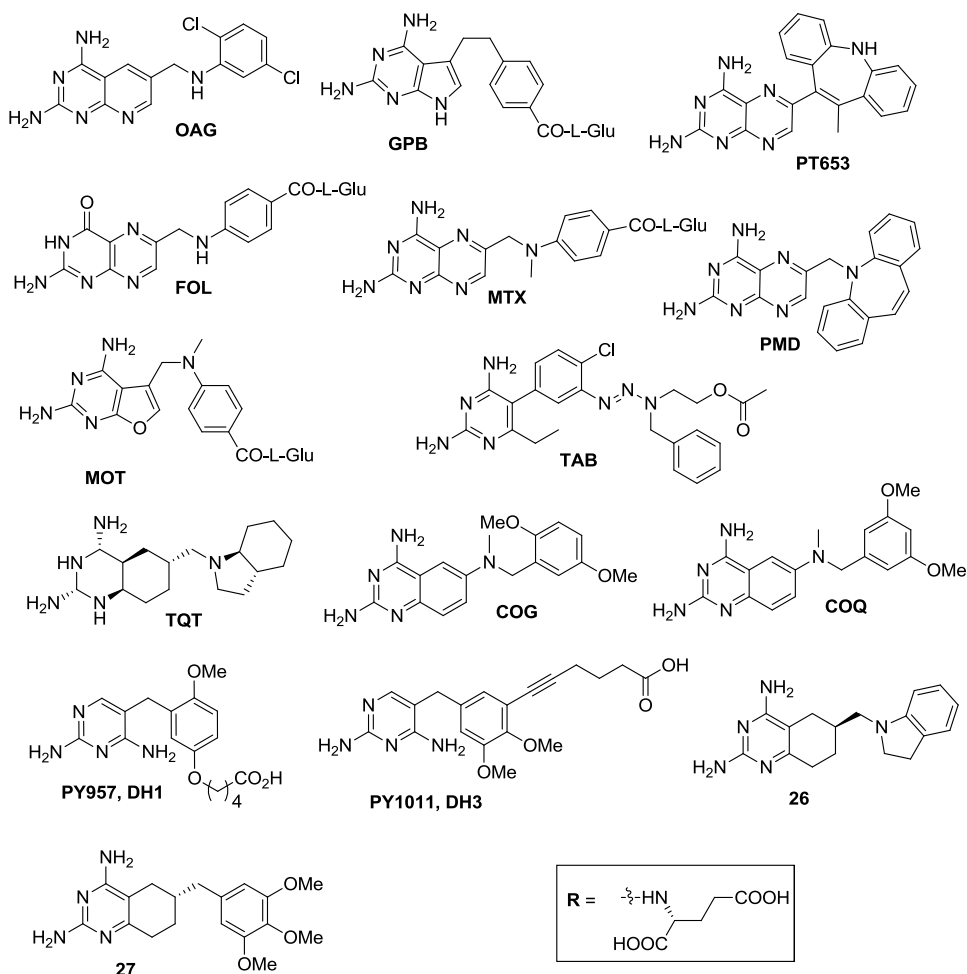


Figure 20: Structures of ligands cocrystallized with pcDHFR available in the PDB

High resolution crystal structures of two ternary complexes of pcDHFR with the cofactor NADPH and potent antifolates: the *N*9-10 reversed-bridge quinazoline inhibitor COG (Figure 20) and its 3,5-dimethoxypyrido[2,3-*d*]pyrimidine analog, COQ (Figure 20) were reported by Cody *et al.*⁸⁹ These studies revealed the first observation of an unusual conformation for the reversed-bridge geometry (C5-C6-N9-C10 torsion angle) in this antifolate. Structures of tetrahydroquinazoline antifolate **9** and its trimethoxy analogue **10** (Figure 20) as inhibitor complexes with hDHFR and pcDHFR and correlations between enzyme selectivity and stereochemistry have been described by Cody *et al.*⁹⁰ Structural analysis of these potent and selective DHFR inhibitor complexes revealed preferential binding of the 6*S*-equatorial isomer in each structure. Cody *et al.*⁴⁴ reported structural data for two highly potent antifolates, PY1011 (DH3, Figure 20), with a 5000-fold selectivity for pcDHFR, relative to rIDHFR refined to 2.0 Å resolution and PY957, (DH1, Figure 20) that has 80-fold selectivity for pcDHFR was refined to 2.2 Å resolution. From these structures it was observed that carboxylate of the γ -carboxyalkoxy side chain of these inhibitors form ionic interactions with the conserved Arg in the substrate binding pocket of DHFR. The structural data further revealed reasons for differences in potency of two inhibitors.

Thus, the available crystal structures allow direct comparison of potent and selective inhibitors of pathogen DHFR with human DHFR. Furthermore, some of the structures indicate ligand induced specific conformational changes, which could be exploited for the design of better inhibitors.

A.1.5.2. Homology Modeling

There are no reported crystal structures of pjDHFR and tgDHFR. Thus, homology models were required for these enzymes to aid structure based drug design of molecules against these enzymes. Very recently Cody *et al.*⁹¹ described the generation of a homology model of pjDHFR based on the crystal structure of pcDHFR complexed with MTX.

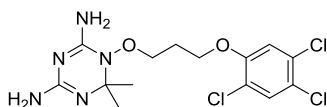


Figure 21: Structure of ligand WR99210 in *P. falciparum* DHFR (PDB: 1J3I)⁹²

Cody *et al.*⁴⁴ reported a model of the tgDHFR active site based on the crystal structures of ecDHFR-MTX complexes and MtbDHFR-TMP ternary complex. The homology model was generated using sequence alignments between the two crystal structures. Popov *et al.*⁹³ reported a homology model of the first 300 residues of tgDHFR-TS sequence using the automated JIGSAW server and refined using Sybyl 7.0. Based on the superimposition with crystal structure of *P. falciparum* DHFR (PDB ID: 1J3I⁹²), cofactor, NADPH and ligand, WR99210 (Figure 21), were added to the model. This model was further used for correlating the docking scores from ensemble of poses for 11 docked inhibitors with their binding affinity. A correlation of 50.2% between docking score and activity was obtained in these studies. Thus, in absence of experimentally determined crystal structure, comparative modeling techniques provide an understanding of DHFR inhibition.

A.1.5.3. Structure-based Approaches: Molecular Docking and Binding Affinity

Prediction

Availability of a large number of high resolution crystal structures of both

pcDHFR and hDHFR has enabled structure-based design studies for potent and selective DHFR inhibitors. Due to similarities in the binding pocket, inhibitors designed against pcDHFR are usually screened against DHFR from other opportunistic agents such as maDHFR and tgDHFR. Molecular docking involves two steps: (a) initial placement of the inhibitor in the active site, also known as pose prediction and (b) prediction of binding affinity of the inhibitor based on the placement in the pocket. In general, majority of docking algorithms show high accuracy (~ 2 Å root-mean-square deviation (RMSD) to that of observed crystal structure) in pose prediction but lack similar accuracy in scoring of poses in order to prioritize the docked poses. Ideally, a scoring function should be able to reproduce binding energy and be able to rank the ligands according to their binding affinity. However, the majority of scoring functions have been reported to often perform poorly in reproduction of binding affinity; hence, use of these scoring functions is limited to screening of databases of large number of ligand.^{94, 95} Different postdocking methods have been used in the literature to predict binding affinity of small molecule inhibitors.^{70, 94, 95} These methods range from simple consensus scoring to free energy perturbation.^{96, 97} This section of the review is limited to molecular modeling efforts reported for predicting the binding affinity of opportunistic and hDHFR inhibitors. Graffner-Nordberg *et al.*⁸⁸ calculated relative binding affinities from free energy perturbation simulations and employed it for the selection of four esters with quinazoline and pteridine core as inhibitors of human DHFR. Simulations were carried out using the protonation state of the bound ligands with the free energy for protonation in water added as a correction to account for the differences in protonation states of quinazoline and pteridine nuclei. The results of the study demonstrated that the estimation of relative binding free energies by

FEP simulations could be useful for the selection of target compounds to be synthesized for biological evaluation against DHFR; it further revealed the importance and viability of ester linkage in the MTX scaffold as potential DHFR inhibitors. Furthermore, molecular dynamics (MD) simulations of three ligands in complex with pcDHFR and the human DHFR enzyme were conducted to understand the molecular basis for the observed selectivity. The LIE method⁹⁸ was employed to predict the absolute binding free energies of molecules against pcDHFR and human DHFR. The predicted binding affinity and the selectivity ratio were well correlated with the experimental observations.

A series of compounds in which the methylenamino-bridge of non-classical inhibitors was replaced with an ester function to provide potential inhibitors for inhalation use against PCP was reported by Graffner-Nordberg *et al.*⁹⁹ In this study, the selection of the target compounds for synthesis was partly guided by an automated docking and scoring procedure using AutoDock 3.0¹⁰⁰ as well as MD simulations. Even though, the AutoDock scores overestimated the magnitude of the binding free energies (-16 to -11 kcal/mol), the relative comparison was possible. As predicted by their AutoDock scores, the compounds were not selective versus human DHFR. Five of the docked compounds were selected for studies using the more time consuming LIE method. Compounds were again predicted to be non-selective by the LIE method. Thus, this study provided compounds with only slight preference for the fungal enzyme; furthermore, modest selectivity of the synthesized inhibitors was reasonably well predicted using the employed computational methods, although a correct ranking of the relative affinities was not successful in all cases.⁴⁵

Gorse *et al.*¹⁰¹ reported MD simulations on hDHFR in order to determine the

putative stable binding conformers of selected deazapterin analogs. Method based on standard thermodynamics cycles and linear approximation of polar and non-polar free energy contributions from MD averages was used to correlate the binding affinities of the different ligands in each binding site with experimental dissociation constants. The study provided insights into structure-activity-relationships (SAR) for use in the design of modified inhibitors of DHFR. Pitts *et al.*⁶⁶ reported interaction energy calculations for various pcDHFR inhibitors including PTX, TMX, TMP and epiroprim using explicit solvent model. Each inhibitor was divided into different substructural regions and the minimized complexes were then used to calculate interaction energies for each intact antifolate and its corresponding substructural regions with the pcDHFR binding site residues. Substructural regions containing pteridyl, pyridopyrimidinyl and diaminopyrimidinyl subregions contributed most to the stability of antifolate interactions, while interaction energies for the hydrocarbon aromatic rings, methoxy and ethoxy groups were much less stable.

Recently, Bag *et al.*²² described the design, synthesis and biological evaluation of fourteen structurally diverse compounds. The top five docked poses using Glide-XP²⁸ score were minimized using the local optimization feature in Prime²⁸ and the energies were calculated using the OPLSAA force field¹⁰² and the GBSA continuum model.⁶³ The docking scores from Glide-XP method and MM-GBSA predicted Gbind were able to distinguish between the active and poorly active compounds. Furthermore, a good correlation coefficient of 0.797 was obtained between the IC₅₀ values and MM-GBSA predicted Gbind.

Thus, a variety of methods ranging from simple docking scores, to

computationally expensive and accurate methods like FEP, have been employed to rank order DHFR inhibitors according to their binding energy, with varying success. However, accurate prediction of binding affinity for a larger dataset of DHFR inhibitors still remains a challenge.

A.1.5.4. Ligand Based Approaches - QSAR and Pharmacophore Modeling

Availability of large number of active and inactive ligands has aided rational ligand based drug design. These methods vary from simple 2D descriptor based methods to more complex and advanced receptor based 3D-QSAR methods. Furthermore, the DHFR inhibitor dataset is often used to validate newly proposed ligand based approaches. A survey of various ligand based models developed for inhibitors of pcDHFR, tgDHFR and maDHFR is presented in this section.

Agrawal *et al.*⁶⁴ reported development of QSAR models using a series of nineteen 2,6-substituted 2,4-diaminopyrido[3,2-*d*]pyrimidine derivatives against pcDHFR using topological indexes. Mattioni *et al.*⁶⁷ used a data set of 345 diverse DHFR inhibitors to build QSAR models using artificial neural networks to correlate chemical structure and inhibition potency for pcDHFR, tgDHFR and rIDHFR. Classification models were also built using linear discriminant analysis (LDA) to predict the selectivity for pcDHFR and tgDHFR. A set of new nitrogen and oxygen-specific descriptors were developed to better encode structural features. The developed neural network models were able to accurately predict log IC₅₀ values for the three types of DHFR to within ± 0.65 log units. The best LDA models were able to correctly predict DHFR selectivity for approximately 70% of the external prediction set compounds.

Gangjee *et al.*^{50, 103} reported 3D-QSAR model development using three methods,

conventional CoMFA, all orientation search (AOS) CoMFA, and CoMSIA, using a dataset of 179 structurally diverse compounds from their previous publications. Low energy conformation of 5-((naphthalen-2-ylthio)methyl)furo[2,3-*d*]pyrimidine-2,4-diamine (Figure 10), one of the most potent and selective inhibitor was used as template for the flexible alignment using Molecular Operating Environment (MOE) suite. The models were derived against pcDHFR, tgDHFR and rlDHFR. AOS CoMFA models gave the best internal predictions ($q^2 = 0.604, 0.600$, and 0.634 for pcDHFR, tgDHFR, and rlDHFR respectively). CoMSIA models gave the best external predictions (predictive $r^2 = 0.544, 0.648$, and 0.488 for pcDHFR, tgDHFR, and rlDHFR respectively). Both AOS CoMFA and CoMSIA analyses were used to construct $\text{stdev} \times \text{coeff.}$ contour maps which provide an insight into SAR.

Jain *et al.*⁸⁵ described QSAR analysis using 2D and 3D descriptors on a series of DHFR analogs of 2,4-diaminopyrido[2,3-*d*]pyrimidines and 2,4-diaminopyrrolo[2,3-*d*]pyrimidines. The QSAR model indicated importance of the hydrogen bond between the hydroxyl group of Tyr129 and the cofactor NADPH. The major difference between the earlier pharmacophore hypothesis developed using Catalyst and the one proposed in this study was that the hydrogen bond acceptor feature corresponding to 3-nitrogen of 2,4-diaminodeazapteridin ring was missing in this pharmacophore. Also, one hydrogen bond acceptor feature corresponding to 8-nitrogen was present in Catalyst pharmacophore while in the one proposed in this study, hydrogen bond acceptor feature corresponding to nitrogen at 1-position in 2,4-diaminodeazapteridin ring was present. Moreover, the proposed new pharmacophore had two new donor features mapped to N-H bonds of two amino groups of 2,4-diaminodeazapteridin ring system. The proposed

pharmacophore was used to refine the earlier pharmacophore and was in agreement with mechanism of the reaction catalyzed by the enzyme. The alignment from pharmacophore model was used to develop CoMFA and CoMSIA models from 68 compounds taken from a dataset of 90 compounds. Each model was further validated using a test set of 22 compounds not included in the training set. Of the various models evaluated CoMSIA model with a combination of steric, electrostatic, hydrophobic, and H-bond fields produced a statistically significant model with good correlation and predictive power. Furthermore, analysis of various contours provided details about the SAR.

Gangjee *et al.*⁵⁰ recently described CoMFA analysis of tgDHFR and rIDHFR based on 80 antifolates with 6-5 fused ring system using the all-orientation search (AOS) routine and a modified cross-validated r^2 -guided region selection (q^2 -GRS) routine. In this study, two modifications of q^2 -GRS routine were suggested to improve the predictability of models. In the first modification, the lowest corner of each modified subregion was the lowest grid point of the conventional CoMFA grid enclosed by the original q^2 -GRS subregion, and the highest corner of each modified subregion was the highest grid point of the conventional CoMFA grid enclosed within the subregion of the original q^2 -GRS routine. In the second modification, the region box was divided into 125 equal-sized subregions and the distance between the adjacent subregions was 1 Å, whereas in the original routine, the adjacent subregions touch each other. Among the various generated models, the q^2 -GRS model using the second modification showed the best external predictive r^2 (0.499) along with a satisfactory internal cross-validated q^2 at 0.647 (optimum number of components (ONC) = 3). On the basis of the steric contour maps of the models, four new compounds were designed belonging to the 2,4-diamino-5-

methyl-6-phenylsulfanyl-substituted pyrrolo[2,3-*d*]pyrimidine series. It was observed that, as predicted, the new compounds were potent and selective inhibitors of tgDHFR. One of them, 2,4-diamino-5-methyl-6-(2',6'-dimethylphenylthio)pyrrolo[2,3-*d*]pyrimidine, showed nanomolar tgDHFR inhibitory activity.

Thus, the QSAR models derived from the homologous series (e.g. 2,4-diaminopyrido[3,2-*d*]pyrimidine, 2,4-diamino-5-methyl-6-[(substituted anilino)methyl]pyrrolo [2,3-*d*]pyrimidines, 2,4-diaminopyrido[2,3-*d*]pyrimidines and 2,4-diaminopyrrolo[2,3-*d*]pyrimidines), for DHFR inhibition, have applicability domains restricted to specific chemotypes. Furthermore, these models and even some of the models derived from larger datasets, provide no information about the binding site. On the other hand, the 3DQSAR models derived using methods such as, CoMFA and CoMSIA, have distinct advantage of stdev*coeff. contour maps, which provides an insight into SAR and generation of SAR in context of active site. However, these models lack inherent ability to mine 3D databases in search of potent/selective DHFR inhibitors. The models developed using receptor residue interaction energy, quantify the binding contribution of active site residues. Pharmacophore models are reported for maDHFR, however, there are no reports for development of pharmacophore models for pcDHFR and tgDHFR.

A.1.6. Thymidylate synthase:

The enzyme TS (EC 2.1.1.45) is present in almost every living organism including humans, bacteria and protozoa.¹⁰⁴ Currently the protein data bank (PDB)¹⁰⁵ lists 165 TS structures. The crystal structures depict the enzyme in different molecular states

and reaction intermediates: apoprotein, binary and ternary complexes with one or both substrates, dUMP and mTHF, products, dTMP and DHF, inhibitors or substrate analogs, such as FdUMP, 2'-deoxyguanosine-5'-monophosphate (dGMP), 2'-deoxycytidine-5'-monophosphate (dCMP) or classical or nonclassical antifolates.¹⁰⁶

The TS enzyme is active as a homodimer consisting of two identical subunits each having a molecular weight of 30-35 kDa.^{21, 107} It has two active sites, each formed by residues from the monomers. In each monomer, there are two main domains: one larger, conserved domain (residues 1-98 and 130-313 in human TS (hTS)) and one smaller, variable domain (the small domain (SD), residues 99-129 hTS). Each monomer shows an alpha and beta fold ($\alpha+\beta$) with 8 β -strands and 5 α -helices in the large domain. A five stranded β -sheet in each large domain forms the dimer interface. C195 in the catalytic loop (CL, residues 184-199 hTS) is the catalytic amino acid that reacts with carbon C6 of dUMP, forming the covalent complex. Other important regions that can be recognized in the enzyme structure are the loop at the interface (HIL, residues 144-158 hTS), the loop around R50 and the C-terminal region (CT, residues 308-313 hTS).

The longest sequence of TS is found in *Lactobacillus casei* with 316 amino acids, whereas the shortest sequence of TS is in *E.coli* with 264 amino acids. There are 6 major insertions: *Homo sapiens* and *Rattus norvegicus* have an extended N-terminal with 24 and 18 residues, respectively. *Bacillus subtilis* has 10 amino acids inserted into the loop around Arg50. *P. carinii* and *Cryptosporidium hominis* have a 6 and 1 residue insertion respectively at residue 206. However, the most variable regions are the small domain and the loop at the interface. The small domain varies in number from 20 to 70 residues from *E.coli* to the *L. casei* sequence.

The mechanism of catalysis by TS is well studied¹⁰⁸ and is depicted in Figure 22. Cys 195 (hTS) attacks C6 of dUMP to form an enolate which then abstracts a proton from an unidentified basic residue of the protein to form an enol in step (A).

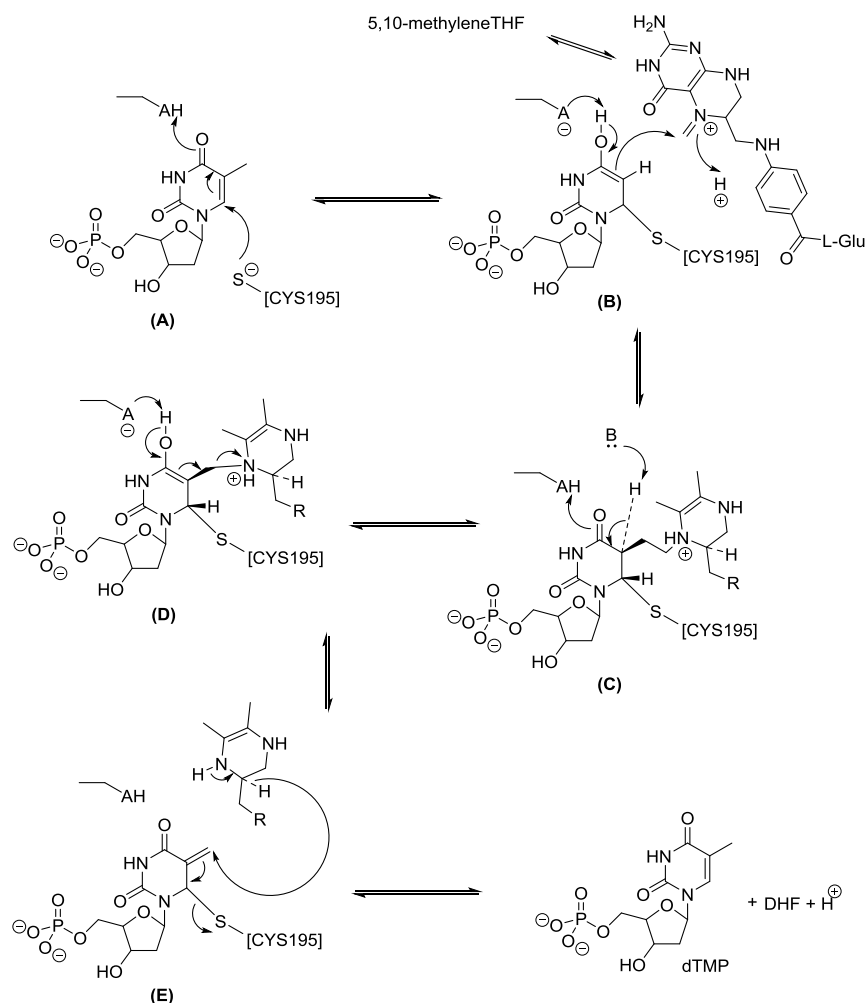


Figure 22. The mechanism of catalysis by TS (Modified from ref.¹⁰⁹)

The co-factor, 5,10-methyleneTHF is activated by iminium ion formation at N5. The C5 position of dUMP, activated by enol formation, reacts with the methylene of the activated co-factor in step (B). H5 of dUMP is abstracted and the enol is regenerated in (C). Abstraction of a proton from O4 of the enol in (D) results in formation of an exocyclic methylene and release of the catalytic Cys (Cys 195). The methylene is then reduced by the modified cofactor to produce dTMP. The modified cofactor, which has

served as methylene donor and reductant, is released from the active site of TS followed by release of product, dTMP.

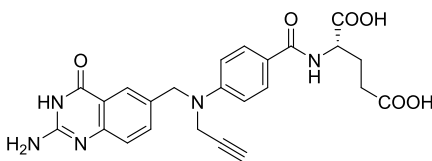


Figure 23. Structure of PDDF.

A 2.3 Å X-ray crystal structure of the ternary complex of *E. coli*

TS:FdUMP:PDDF was reported by Oatley *et al.*¹¹⁰ In this structure a covalent bond is formed between Cys146 at C6 of the nucleotide analog FdUMP by a thioether bond. Another key interaction of FdUMP is the charge-mediated interaction of the 5'-phosphate group in the dianionic state with four conserved arginine residues (Arg21, Arg166, Arg126, and Arg127), two from each subunit. In addition, the polar atoms in both the pyrimidine and ribosyl moieties of FdUMP form hydrogen bonds with side chains of binding pocket amino acid and ordered solvent molecules.

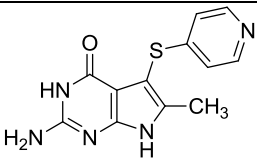
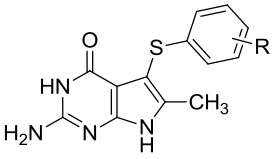
The cofactor analog PDDF binds in a partially folded conformation with its *para*-aminobenzoyl group inclined at a 65 ° angle to the heterocycle and the L-glutamate tail exposed at the entrance to the active site cleft. Formation of the ternary complex induces a large conformational change in which the active site is capped by four carboxylic acid-terminal amino acids and the bound ligands are sequestered from the bulk solvent. PDDF sits directly above the substrate analog FdUMP and the B-ring of PDDF forms a charge transfer complex with the pyrimidine portion of FdUMP. The N1, N3 and the 2-NH₂ groups of PDDF are involved in hydrogen bonds with side-chain residues of TS either *via* direct hydrogen bonds or by water mediated hydrogen bonds. The C5 and C8 atoms of

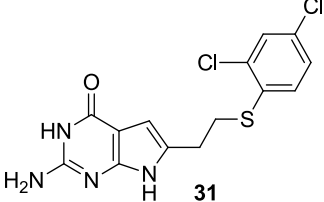
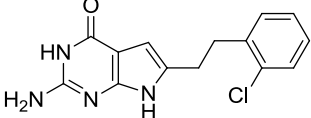
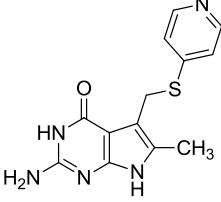
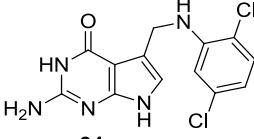
the quinazoline B-ring do not have hydrogen bond donor or acceptor side chain residues within a distance of 5 Å. This could explain the improvement in inhibition produced by quinazoline antifolates compared to pteridine antifolates, which require desolvation of the polar N5 and N8 groups. The quinazoline ring also interacts *via* hydrophobic bonds with Trp83 and Leu43. The hydrophobic interaction between the C6- methylene moiety of the quinazoline and the conserved Trp80 is an important interaction. The 4-oxo group of PDDF is not involved in hydrogen bonding interactions with side chain residues or ordered water molecules of TS. In addition to the quinazoline backbone, the L-glutamate moiety also contributes to binding by having interactions with Lys 50 and several backbone residues including His53, Leu224 and Ile310 via the bridging of two conserved water molecules.

A.1.6.1 TS Inhibitors

This review will cover bicyclic non-classical inhibitors of TS.

Table 2. Pyrrolo[2,3-*d*]pyrimidines as nonclassical inhibitors of TS

Non-classical compounds		
 <p>28</p>	<p>IC₅₀ in nM against hTS</p> <p>28 340</p> <p>MTX 36</p>	111
 <p>29 3',4'-diCl</p> <p>30 4'-NO₂</p>	<p>IC₅₀ in μM against hTS</p> <p>29 0.13</p> <p>30 0.15</p> <p>PDDF 0.18</p>	112

 <p>31</p>	<p>Compound 31 exhibited 25% inhibition of hTS at 23 μM</p>	<p>113</p>
 <p>32</p>	<p>No inhibition of hTS at >10 μM</p>	<p>114</p>
 <p>33</p>	<p>IC₅₀ in μM against hTS 33 >25 (20% inhibition) PDDF 0.036</p>	<p>115</p>
 <p>34</p>	<p>Inactive against TS</p>	<p>116</p>

A.2. RECEPTOR TYROSINE KINASE INHIBITORS

A.2.1. Angiogenesis:

The term angiogenesis is used to describe the physiological process of formation of new blood vessels from pre-existing vasculature.¹¹⁷ Angiogenesis is critically important for growth and development of the body and normally occurs only during embryonic and post-embryonic development, reproductive cycle, and wound healing. However, an upregulated angiogenesis has been observed as one of the hallmarks of cancer, playing an essential role in tumor growth, invasion, and metastasis.¹¹⁸ Furthermore, many other diseases – diabetic retinopathy, hemoangioma, arthritis,

psoriasis and atherosclerosis among others – are also dependent on upregulated angiogenesis.^{119, 120}

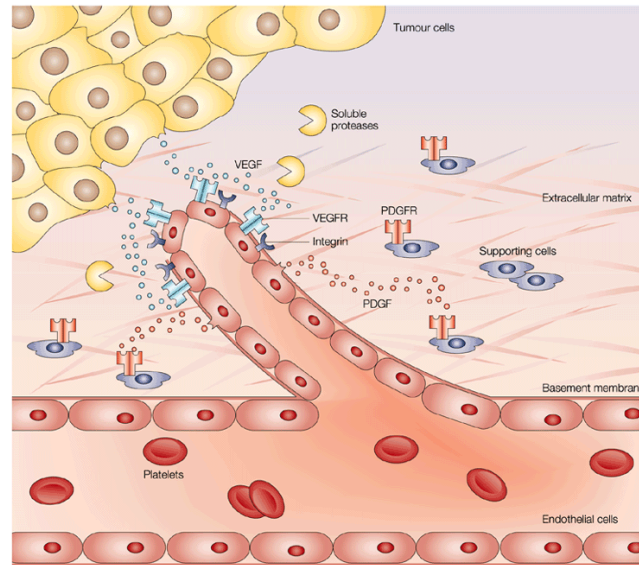


Figure 24. Process of angiogenesis. (Modified from ref.¹¹⁹)

(1) An activating, proangiogenic signal induces the switching on of the angiogenic phenotype of resting endothelial cells, which become activated. (2) These activated cells acquire an invasive potential, involving basal membrane degradation, (3) extracellular matrix remodeling, proliferation, and migration. (4) Finally, morphogenesis contributes to the alignment of endothelial cells forming a new microvessel, and (5) this microvessel is stabilized by eventual recruitment of pericytes and acquisition of a new basal membrane.

The process of angiogenesis starts an angiogenic signal activates resting endothelial cells. This initiates the release of degrading enzymes from endothelial cells and initiates a sequence of migration, proliferation and cell differentiation to form new vessels as depicted in Figure 1.¹¹⁹

Angiogenesis is critical for tumor growth beyond 1-2 mm and for tumor invasion and metastasis.¹¹⁹ As a tumor grows in size, it becomes increasingly hypoxic, and triggers the release of growth factors, particularly, vascular endothelial growth factor (VEGF),

epidermal growth factor (EGF), and platelet derived growth factor (PDGF) among others, which act as proangiogenic signals (Figure 24) and initiate angiogenesis. Leading from this observation, Folkman, in 1971, proposed that inhibition of angiogenesis could serve as a potential approach in cancer treatment.¹¹⁷

Anti-angiogenic therapy, directed to activated endothelial cells presents a series of advantages over therapies targeted to tumor cells.¹¹⁹ First, due to the fact that endothelial cells are homogeneous, diploid, genetically stable targets; spontaneous mutations rarely occur in them relative to tumor cells. Second, the turnover of endothelial cells in tumoral tissues is usually fifty-fold higher than that of quiescent endothelia in normal tissues. The activated endothelium overexpresses specific markers – integrin $\alpha_v\beta_3$, E-selectin, Tie, and vascular endothelial growth factor receptor (VEGFR) – that could be used as targets for the development of specific therapies directed to these cells. In addition, the contact between endothelial cells and blood makes this target easily accessible to systemically administered drugs, therefore avoiding the problem of low penetration of antitumor agents into the solid tumors.¹²¹ Finally, because a single vascular net may support the growth of different populations of tumor cells, the inhibition of the vascular growth may affect the survival of many tumor cells.¹²²

Any of the steps involved in angiogenesis may be a potential target for developing novel anticancer agents.¹¹⁹ The present review will focus only on Receptor Tyrosine Kinases (RTKs) as potential targets for the abrogation of cancer induced angiogenesis.

A.2.2. Receptor tyrosine kinases (RTKs):

Protein kinases are enzymes that transfer a phosphate group from ATP to the hydroxyl group of serine, threonine, or tyrosine of specific proteins inside cells.¹²³ The

phosphorylation by these enzymes achieves an important function of signal transduction in eukaryotic cells, and controls the processes of cell proliferation metabolism, survival and apoptosis. A misregulation of these tightly controlled processes results in the overexpression of kinases and/or mutations and is associated with a variety of disease states including cancer.¹²⁴

For angiogenesis to occur, the pro-angiogenic growth factors have to bind to transmembrane receptors of the protein kinase family identified as RTKs. At present, 58 RTKs are known, grouped into 20 subfamilies.¹²⁵ The structural composition of RTKs consists of an extracellular ligand binding domain, a transmembrane hydrophobic domain, and an intracellular catalytic domain. Following binding of the growth factor to the extracellular domain, these receptors commonly undergo dimerization, resulting in autophosphorylation of tyrosine residues within the catalytic domain. This triggers a cascade of events through phosphorylation of intracellular proteins that ultimately transmit the extracellular signal to the nucleus, causing changes in gene expression eventually leading to angiogenesis.¹²⁶

A number of RTKs have been recognized to be involved in tumor induced angiogenesis. The key RTK families in cancer include the platelet derived growth factor receptor (PDGFR), epidermal growth factor receptor (EGFR), and the VEGFR families of RTKs.¹²⁷

PDGFR. Members of the PDGFR family – PDGFR α and PDGFR β have been implicated, indirectly, in inducing VEGF secretion and hence in angiogenesis.¹²⁸ Although PDGFR plays a role in the development and maintenance of tumors due to its role in blood vessel growth, the validity of PDGFR as a drug target itself is still unclear,

as it is not usually the main factor in tumor development. However, there are several cancers that exhibit an upregulation of PDGFR, namely, chronic myelomonocytic leukemia (CMML), gastrointestinal stromal tumor (GIST), acute myeloid leukemia (AML), chronic myeloproliferative disorders (CMPD), and dermatofibrosarcoma protruberans (DFSP), a soft tissue sarcoma.^{129, 130}

EGFR. The ligand for EGFR, EGF, controls a pathway that is linked to cell proliferation, migration, and differentiation. There are four subtypes of EGFR receptors: EGFR-1 (later referred to as EGFR; also identified as erythroblastic leukemia viral oncogene homologue 1, Erb-B1, or human EGF receptor HER-1), HER-2 (Erb-B2, or neuroglioblastoma neu), HER-3 (Erb-B3), and HER-4 (Erb-B4). Among these, HER-2 lacks a known endogeneous ligand and HER-3 lacks kinase activity. Abnormal activity, either by overexpression or constitutive action, has been linked to a number of cancers, including lung, breast (especially HER-2/neu), and prostate cancers.¹³¹ EGFR inhibitors have been recommended as first line therapy for patients with advanced or metastatic NSCLC.¹³²

VEGFR. In the VEGFR family, VEGFR-2 (Flk-1/KDR) has been recognized as the principal receptor that mediates VEGF stimulation in angiogenesis. VEGFRs are almost exclusively expressed on endothelial cells. Targeted inhibition or disruption of VEGFR-2 produces an abrogation of angiogenesis and tumor growth.^{133, 134} In addition, VEGFRs are overexpressed on many tumor types.¹³⁵⁻¹³⁷ Reports suggest that VEGFR-1 (Flt-1) shows promise as a therapeutic target not only for tumor angiogenesis but also for the inflammation associated with tumors.¹³⁸

A.2.3. RTK inhibitors approved for use in the U.S. and the importance of multi kinase inhibition:

A list of kinase inhibitors approved (till 2012) for various cancer indications within the U.S. is provided in Table 3. Imatinib mesylate (Figure 25) was the first RTK inhibitor approved in the U.S. for Philadelphia chromosome (Ph)-positive chronic myeloid leukemia (CML) patients^{130, 139}. In addition, imatinib mesylate has been approved for multiple cancers such as Gastrointestinal stromal tumors (GIST), Acute lymphoblastic leukemia (ALL), myelodysplastic diseases associated with PDGFR gene rearrangements, aggressive systemic mastocytosis (ASM), Dermatofibrosarcoma protuberans (DFSP).

Early research suggests that imatinib has shown potential in the treatment of plexiform neurofibromas.¹⁴⁰ The use of imatinib has been associated with the development of resistance mediated either by mutations within the kinase domain of BCR-ABL or, to a lesser degree, amplification of the BCR-ABL genomic locus.¹⁴¹ Ruxolitinib was approved in 2011 for the treatment of intermediate or high-risk myelofibrosis and is currently in clinical trials for the treatment of pancreatic cancer, polycythemia vera and plaque psoriasis.⁹⁸ More recently, vemurafenib, which targets B-raf kinase, was approved for the treatment of late stage melanoma in 2012.¹⁰⁰

Table 3. RTK Inhibitors Approved for Use in the U.S.

Brand Name	Year Approved	Generic Name	US FDA Approved Indications	Target kinase(s)
Gleevec	2001	imatinib mesylate	chronic myeloid leukemia (CML)	Abl, c-Kit, PDGFR α , PDGFR β
Iressa	2003	gefitinib	non-small-cell lung cancer (NSCLC)	EGFR
Tarceva	2004	erlotinib	NSCLC, pancreatic cancers	EGFR
Nexavar	2005	sorafenib tosylate	hepatocellular carcinoma, renal cell carcinoma (RCC)	Raf, VEGFR2, VEGFR3, c-Kit, PDGFR β
Sutent	2006	sunitinib malate	GIST, renal cell carcinoma	c-Kit, VEGFR, PDGFR, FLT3
Sprycel	2006	dasatinib	CML (especially imatinib-resistant)	Abl, c-Kit, PDGFR, Src
Tasigna	2007	nilotinib	CML (imatinib resistant and intolerant)	Abl, c-Kit, PDGFR β , Src, Ephthrin
Tykerb	2007	lapatinib	breast cancer	EGFR, Her-2
Votrient	2009	pazopanib	RCC, soft tissue sarcoma	VEGFR1, VEGFR2, VEGFR3, PDGFR α , PDGFR β , c-Kit
Jakafi	2011	ruxolitinib	myelofibrosis	JAK1, JAK2
Xalkori	2011	crizotinib	NSCLC with Alk mutation	Alk/Met
Zelboraf	2012	vemurafenib	late stage melanoma	B-raf

Gefitinib and erlotinib (Figure 25), two inhibitors of EGFR kinase, were the second and the third kinase inhibitors to be approved for clinical use. These drugs showed remarkable effects in a subpopulation of patients with non-small-cell lung cancer (NSCLC) harboring activating mutations.¹⁴²⁻¹⁴⁹ Unfortunately, drug resistant tumors were observed within a year or so of initiating treatment. Lapatinib (Figure 2) was approved in 2007 for use in breast cancer in combination with a cytotoxic agent. Lapatinib is a dual inhibitor of both EGFR and human EGF receptor-2 (HER-2)

Although most of the early work in the area of RTK inhibitor discovery was focused on producing inhibitors of single RTKs, recent data shows that tumors treated with specific RTK inhibitors can develop resistance through an upregulation of alternate

kinase mediated pathways.¹⁵⁰

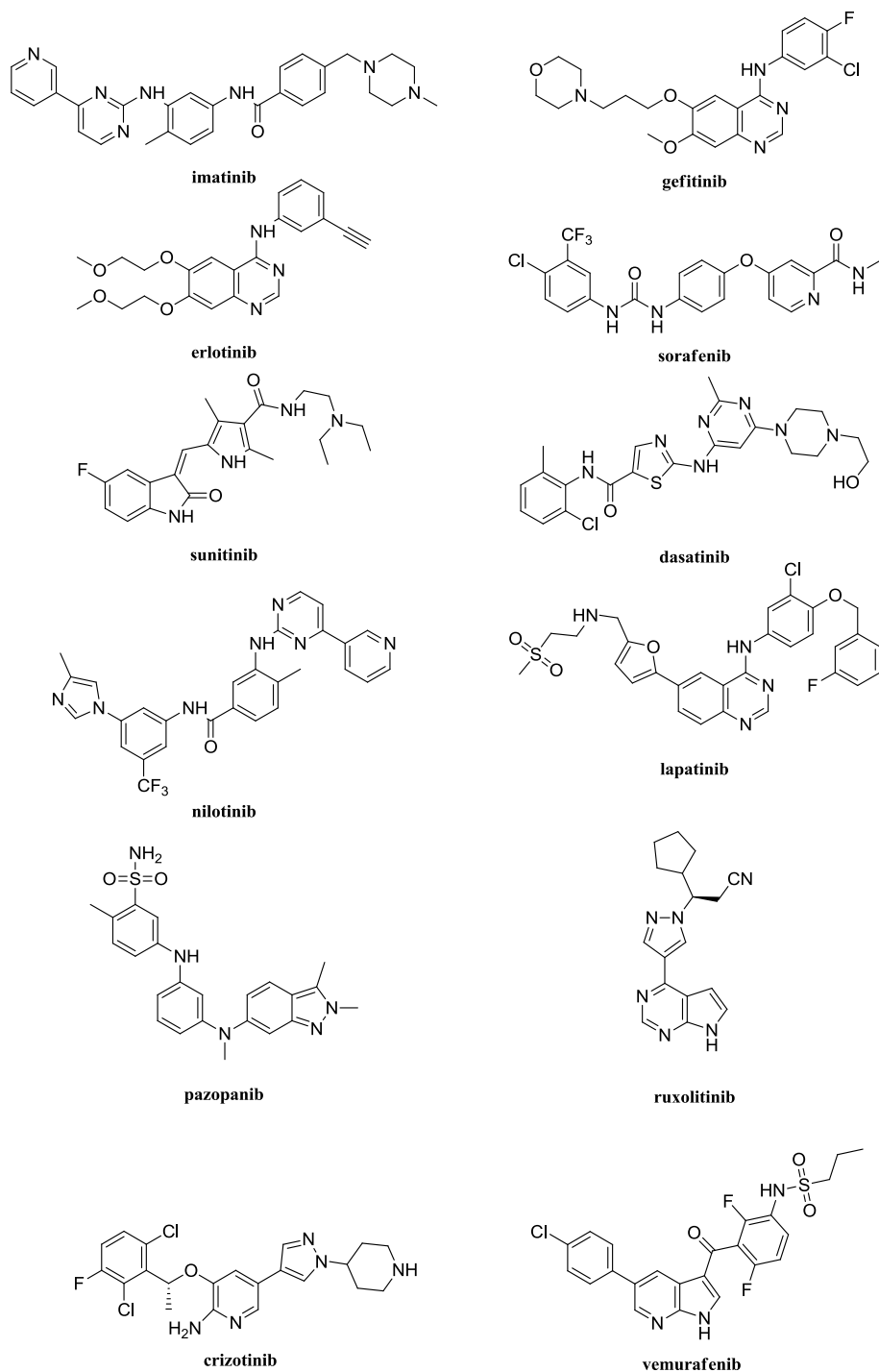


Figure 25. Structures of RTK inhibitors currently marketed in the U.S.

There are a number of RTK mediated processes that can promote angiogenesis,

thus inhibitors targeting a broader range of RTKs may lead to a more robust antitumor response and prevent resistance by targeting two or more angiogenic pathways.^{151, 152} This is underlined by the fact that the newly approved inhibitors of RTKs – sorafenib and sunitinib (Figure 25) – target multiple RTKs. Sorafenib inhibits multiple vascular endothelial growth factor receptor kinases, the mast-stem cell growth factor receptor (c-Kit) kinase, and the proto-oncogene c-Raf kinase. Sunitinib inhibits VEGF and PDGF receptor kinases, in addition to c-Kit and FMS-like tyrosine kinase 3 (Flt3). These drugs are expected to act by arresting the development of blood supplies to the growing tumors, in addition to specifically blocking an oncogenic kinase within a tumor type (e.g., c-Kit).¹⁵³⁻¹⁵⁵

A.2.4. RTK activation relevant to the design of clinical inhibitors: DFG dynamics and C-Helix dynamics:

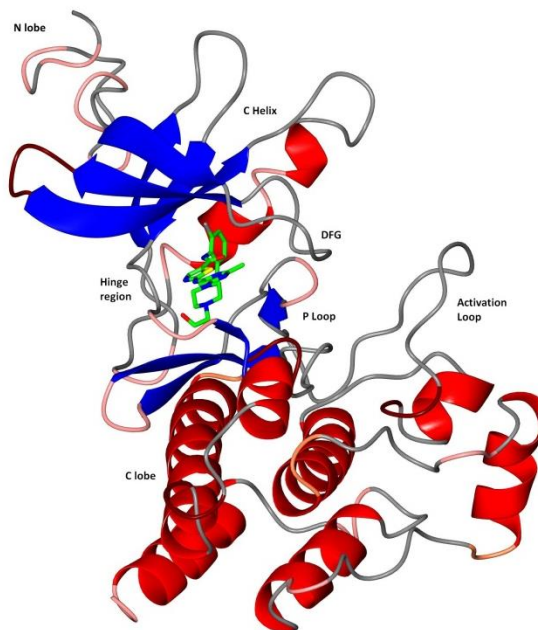


Figure 26. Crystal structure an inhibitor dasatinib bound to Abelson tyrosine kinase (Abl) (PDB: 2GQG).¹⁵⁶

All RTKs share a characteristic ATP binding structure as shown in Figure 26.¹⁵⁷ The

kinase or catalytic domain consists of an N-terminal lobe, which consists mainly of β strands but contains one α helix, helix C. The C-terminal lobe is mainly α -helical in nature. A short strand termed the hinge region connects the two lobes. The ATP binding site is sandwiched between the two lobes. ATP forms critical hydrogen bonds with the hinge region.

Early on, in the development of kinase inhibitors selectivity was identified as a challenge when designing inhibitors that bound to the ATP pocket. This was a formidable challenge because evolutionary pressure exerted to maintain a general common shape and chemical similarity of the ATP binding site in different kinases. Hence, drug design efforts have sought to exploit regions of the active site that are not directly involved in ATP binding, or conformations of the kinase that show greater structural and chemical heterogeneity.

The RTK active site is known to exist in multiple conformational states as a consequence of the activation and inactivation mechanism of kinases.¹⁵⁷ The P-loop (or phosphate-binding loop or glycine-rich loop) plays a key role in the dynamics of the kinase domain where its conformation is a determining factor in the shape of the ATP-binding site (Figure 26). In the active form of a kinase, a characteristic Asp-Phe-Gly motif (DFG motif), located immediately above the activation loop, adopts a conformation with Asp and Phe both oriented toward the binding site (DFG-in) (Figures 24 and 25a).

While the active form of the kinase catalytic domain is fairly homogeneous structurally, the inactive forms are less so. The greater structural variations of the inactive form exist because the inactive form of the kinase does not have to obey the requirement of binding to the common substrate ATP. Hence numerous inactive states have been

identified, which can be related to the mechanism of activation of the kinase.¹⁵⁸ One of these states is called the “DFG-out” state and is associated with kinases that activate by phosphorylation of residues on the activation loop. In the DFG-out state, the phenylalanine of the DFG motif is positioned in the ATP-binding site so that it effectively blocks ATP access to the binding site (Figure 27b). Phosphorylation of tyrosine, threonine, or serine residues of the activation loop by another kinase is incompatible with this conformation and consequently leads to activation of the kinase. Phosphorylation can occur as the activation loop can act as a substrate for other kinases or can even be phosphorylated autocatalytically.¹⁵⁸

Kinase inhibitors that bind to the active form of the kinase are called type I inhibitors, and those that bind to the inactive form of the kinase are called type II inhibitors.¹⁵⁹ Imatinib, the first kinase inhibitor to make it to market, binds to the inactive form of Abl, c-Kit, and PDGF kinases.¹⁶⁰

A second inactive form of the kinase retains the general DFG-in form but rotation and shifting of the C-helix out leads to inactivation of the kinase (Figure 27d-e).^{161, 162} This rotation of the C-helix can alter the nature of the ATP binding site. A number of activation mechanisms have been associated with the helix-C-out inactive conformation. In c-Src, activation of the kinase is effected by phosphorylation of a tyrosine in the activation loop similar to the phosphorylation in Abl that destabilizes the DFG-out inactive form. In CDK2, activation results from binding of the protein cyclin to the kinase.

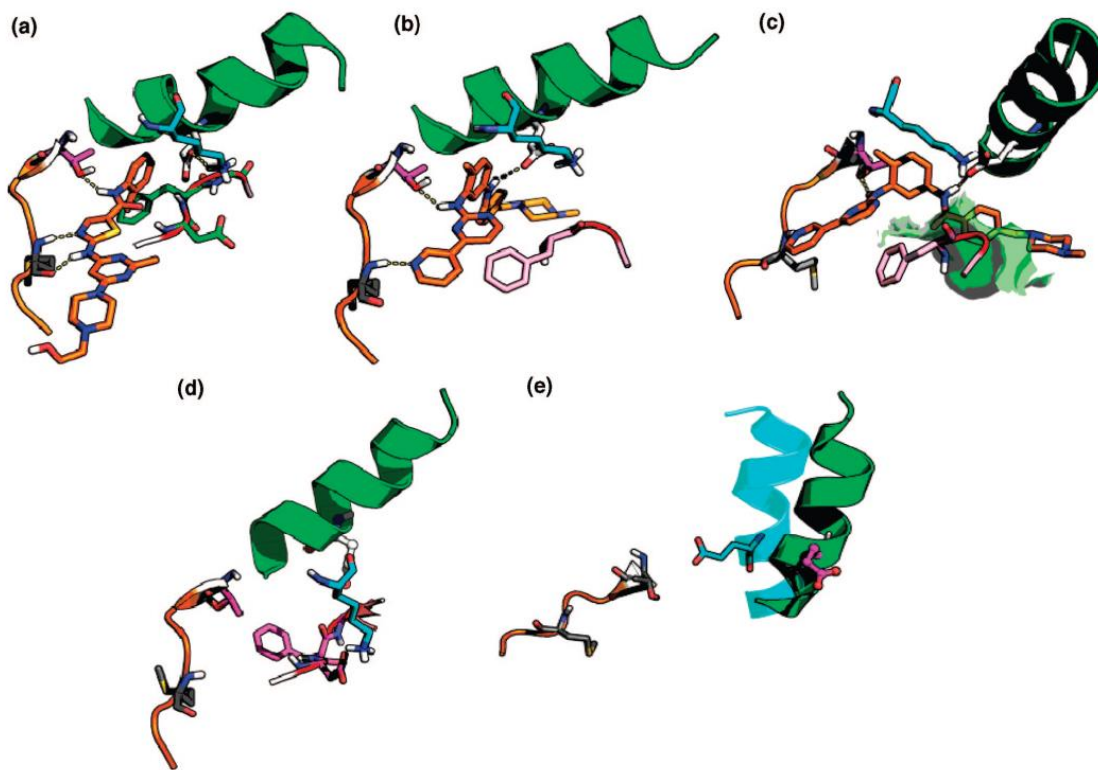


Figure 27.¹⁵⁷ Binding site comparisons of active and inactive forms of different kinases. (a) The Abl active form in complex with dasatinib (PDB: 2GQG). The phenylalanine of the DFG motif (green carbons) is shown to point away from the binding site and is buried in the interior of the protein. (b) The Abl DFG-out inactive form in complex with imatinib (PDB: 1IEP). The phenylalanine of the DFG motif points into the binding pocket. (c) Rotation of ~90 degrees of (b) to highlight the depth of the DFG-out pocket (surface representation). (d) Helix-C-out inactive form of EGFR (PDB: 1XKK). The catalytic lysine (cyan carbons) is far removed from Helix C's glutamic acid (white carbons). (e) Helix-C movement from active (cyan helix) to inactive form (green helix) from an overlay of the Abl (PDB: 2GQG, helix in) and EGFR (PDB: 1XKK, helix out). (a)-(c) show the catalytic lysine (cyan carbons) and the salt bridge formed with the glutamic acid from Helix C (white carbons).

In EGFR, formation of an asymmetric kinase domain homo- or heterodimer following the extracellular binding of EGF results in kinase activation.^{163, 164} Although the EGFR kinases have a tyrosine in the activation loop that gets phosphorylated, this does not appear to be necessary for activation.¹⁶³ The C-helix-out form of the kinase has been shown

to bind to lapatinib.¹⁶²

The nature of the ATP binding site can be altered by the C-helix-out inactive form. On rotation of helix C in EGFR, a conserved glutamic acid points towards solvent rather than towards the ATP binding site (Figure 27d). Such a conformation disrupts the salt bridge between glutamic acid and the conserved catalytic lysine residue. This salt bridge is required to position the α and β phosphate groups of ATP and is therefore critical for catalytic activity. The key structural changes associated with the movement from C-helix-out inactive form to the active form are shown in Figure 27d and Figure 27e. Crystal structures of EGFR bound to ATP analogs in the DFG-in/C-helix-out conformation have been solved for EGFR.¹⁶³ A crystal structure of the C-helix-out conformation of an inhibitor bound to Abl has also been solved.¹⁶⁵

Table 4. provides a list of approved inhibitors and the conformation of the RTKs which these inhibitors target.¹⁶⁶

Table 4. Small-molecule protein kinase inhibitors and their targets along with the target conformation. [Modified from ref¹⁶⁶]

<i>Inhibitor</i>	<i>Primary Targets</i>	<i>Targeted Conformation</i>
Imatinib	Abl, Kit, PDGFR	Inactive (DFG-out and C-helix in)
Gefitinib	EGFR	Active (DFG-in and C-helix in)
Erlotinib	EGFR	Active (DFG-in and C-helix in)
Sorafenib	Raf	Inactive (DFG-out and C-helix in)
Sunitinib	Kit, VEGFR-2, PDGFR, Flt3	Active (DFG-in and C-helix in)
Dasatinib	Abl, PDGFR β , Src	Active (DFG-in and C-helix in)
Lapatinib	EGFR	Inactive (DFG-in and C-helix out)

Hence substantial information is available on the dynamics of kinases and can be exploited for drug design.

A.2.5. Emergence of drug resistance:

The appearance of drug resistant tumors was an unwelcome addition to the already substantial challenges to kinase drug discovery. Kinases were anticipated to be difficult targets partly because the conservation of shape and character of the ATP binding site posed a selectivity issue and partly because the high endogeneous concentration of ATP indicates that inhibitors would have to be very potent to be successful as drugs. Notably, after the first RTK inhibitors were used clinically, it became clear that various amino acid mutations, some in the kinase domain, could lead to drug resistance.^{144, 145, 167, 168} Following this observation, addressing drug resistance has become a defining challenge of kinase drug discovery.

Repeating patterns of mutations seem to appear at the activation loop, the P-loop, and at the “gatekeeper” residue within the ATP binding sites.¹⁵⁷ A “gatekeeper,” is a residue that flanks a highly variable Hydrophobic pocket at the rear of the ATP binding site and can act as a selectivity filter.¹⁶⁹ Individual kinases have additional mutations that result in alterations of ligand binding or kinase activation. Crystallographic data for complexes of key protein-ligand pairs with mutations in Abl¹⁷⁰⁻¹⁷² and EGFR^{162, 173} has helped in interpretation of the effect of these mutations.

Some general trends are clear. Mutations in the P-loop and activation loop can produce active states of kinases by destabilizing the inactive forms. Hence, this can reduce or eliminate the binding of inhibitors targeted at the inactive forms of kinases (cf. c-Kit¹⁷⁴ and PDGFR^{175, 176}). The effects of numerous mutations can also be rationalized by their

direct action on ligand binding within the ATP-binding cleft or occupation of additional accessible space in the inactive form of the kinase. Most prominent of this type of mutation is that of the gatekeeper threonine in Bcr-Abl and c-Kit, which confer resistance to imatinib. This has been explained as a direct loss of a critical hydrogen bond to the ligand (Figure 27b).

A.2.6. Binding of inhibitors in the RTK active site:

In this section the binding interactions of inhibitors to the ATP binding site of EGFR and VEGFR2 are discussed to present an idea of the interaction patterns seen between the ligand and the active site residues.

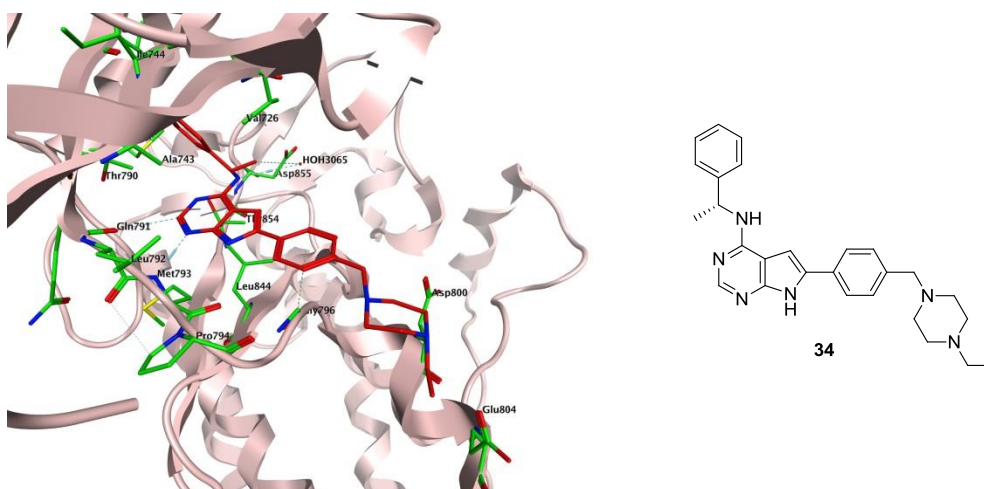


Figure 28 X-ray crystal structure of **34** bound to EGFR (PDB: 2ITT)¹⁷³

Yun *et al.*¹⁷³ reported a X-ray crystal structure of a pyrrolo[2,3-*d*]pyrimidine compound **34** (AEE788)¹⁷⁷ (Figure 28). Compound **34** displayed potent inhibition of VEGFR and ErbB family of kinases. It has low nanomolar potency against EGFR and was advanced to phase I clinical trials for treating relapsed glioblastoma multiforme.⁵⁹ The crystal structure indicates that the pyrrolo[2,3-*d*]pyrimidine core of **34** hydrogen bonds with the hinge region, and the N3 atom interacts with the hydroxyl of Thr854. The 4-

phenylethylamine moiety extends into the Hydrophobic pocket defined by Thr790, Leu788, Lys745, and Met766. The 6-phenyl substituent is sandwiched between Leu718 above and Gly796 below. Finally the ethylpiperazine group extends towards solvent near Asp800 and Glu804 at the edge of the active site.

Harris *et al.*¹⁷⁸ reported indazolylpyrimidine **35** (Figure 29) with good potency against VEGFR-2 ($IC_{50} = 6.3$ nM). In addition, **35** had an oral bioavailability of 85% in the rat at a dose of 10 mg/kg. A crystal structure of **35** with VEGFR-2 indicated that the pyrimidine N-1 and the C-2 anilino N-H making hydrogen acceptor and donor bonds with the peptide backbone of Cys919.

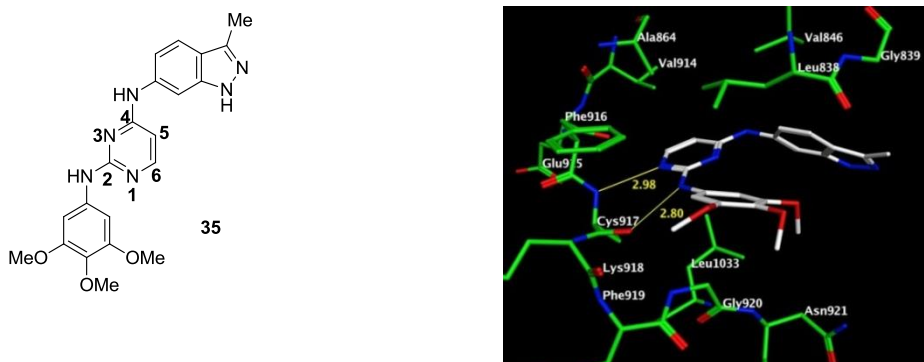


Figure 29. X-ray crystal structure of **35** bound to VEGFR-2 (PDB: 3CJF)¹⁷⁸

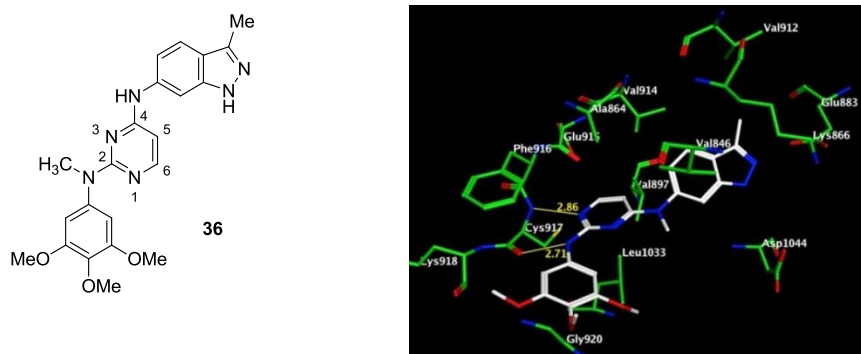


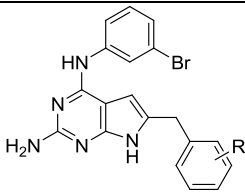
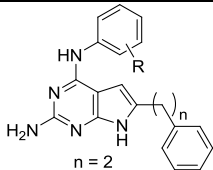
Figure 30. X-ray crystal structure of **36** bound to VEGFR-2 (PDB: 3CJG)¹⁷⁸

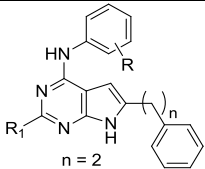
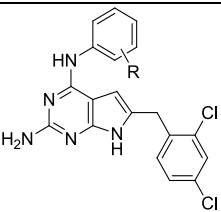
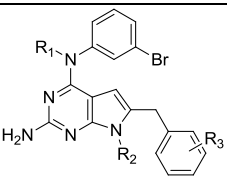
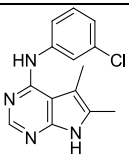
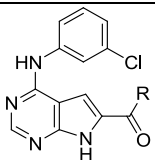
The N-methylated analog of **35**, compound **36** (Figure 30) had an oral bioavailability of 65%. The crystal structure of **36** with VEGFR-2 revealed the inhibitor in a “S-shaped” conformation in contrast to **35** which exists in a “U-shaped” conformation. The S-shaped conformation was preferred most likely to avoid an unfavorable steric interaction between the methyl group and the pyrimidine C-5 hydrogen.

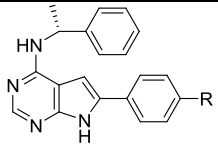
A.2.7. RTK inhibitors:

The design and synthesis of RTK inhibitors have been extensively reviewed in the literature. The following review will cover the pyrrolo[2,3-d]pyrimidine class of RTK inhibitors

Table 5. Pyrrolo[2,3-d]pyrimidine inhibitors of RTKs

Structure	Compound	RTK inhibitory activity	Ref
	37 R=2'-Me	Whole cell assays	179
	38 R=2',5'-diOMe	41 IC ₅₀ =0.25μM (VEGFR-2)	
	39 R=2',4'-diCl	41 IC ₅₀ =1.21μM (A431)	
		42 IC ₅₀ =0.62μM (VEGFR-2)	
		42 IC ₅₀ =8.92μM (PDGFR-β)	
		43 IC ₅₀ =0.23μM (EGFR)	
		43 IC ₅₀ =2.8μM (A431)	
	40 R=3'-Br	Whole cell assays	180
	41 R=2'F,4'-Cl	37 IC ₅₀ =0.3μM (EGFR)	
	42 R=4'-Cl	38 IC ₅₀ =1.4μM (A431)	
	43 R=3'-CF ₃	39 IC ₅₀ =1.6μM (A431)	
		40 IC ₅₀ =0.03μM (CAM)	

	<p>44 R₁=H, R = 3'-Br</p> <p>45 R₁=H, R = 3'-CF₃</p> <p>46 R₁=H, R = 3'-Br, 4'-F</p> <p>47 R₁=H, R = 3'4'-(C₂H₃N)</p>	<p>Whole cell assays</p> <p>44 IC₅₀ = 8.5 μM (PDGFR-β)</p> <p>45 IC₅₀ = 22.1 μM (VEGFR-2)</p> <p>46 IC₅₀ = 25.2 μM (VEGFR-2)</p> <p>47 IC₅₀ = 31.6 μM (VEGFR-2)</p>	181
	<p>48 R = 4'-Br, 2'-Cl</p> <p>49 R = 3'-F</p> <p>50 R = 4'-iPr</p>	<p>Whole cell assays</p> <p>48 IC₅₀ = 0.1 μM (VEGFR-2)</p> <p>48 IC₅₀ = 16.2 μM (A431)</p> <p>49 IC₅₀ = 0.3 μM (VEGFR-2)</p> <p>50 IC₅₀ = 1.4 μM (VEGFR-2)</p>	182
	<p>51 R₁= CH₃, R₂=CH₃, R₃=2'-CH₃</p> <p>52 R₁= CH₃, R₂=CH₃, R₃=2',5'-diOCH₃</p> <p>53 R₁= CH₃, R₂=H, R₃=2'-CH₃</p>	<p>Whole cell assays</p> <p>51 IC₅₀ = 1.2 μM (EGFR)</p> <p>52 IC₅₀ = 0.5 μM (EGFR)</p> <p>53 IC₅₀ = 1.3 μM (PDGFR-β)</p>	183
	54	<p>Isolated enzyme assay</p> <p>IC₅₀ = 27 nM (EGFR)</p>	184-186
	<p>55 R= OCH₃</p> <p>56 R= NHCH₃</p>	Potent EGFR inhibition	187, 188

	57 R=NHCOCH ₃ 58 R=NHSO ₂ CH(CH ₃) ₂ 59 R=OCH ₃	Isolated enzyme assay IC ₅₀ = 1-3 nM (EGFR)	187, 188
	60 R= <i>p</i> -NH ₂ 61 R= <i>p</i> -OH 62 R= <i>p</i> -COOH	Isolated enzyme assay IC ₅₀ = 1-5 nM (EGFR)	187, 188

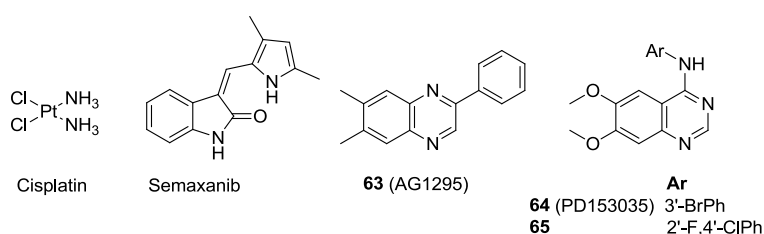


Figure 31. Compounds used as standards in RTK inhibition assays

Gangjee *et al.*¹⁷⁹ reported the design, synthesis and biological evaluation of N⁴-(3-bromophenyl)-6-(substituted benzyl) pyrrolo[2,3-*d*]pyrimidines, **37–39** (Table 5) as RTK inhibitors. These compounds were tested in human tumor cells known to over express high levels of RTKs such as EGFR, VEGFR-1, VEGFR-2 and PDGFR-β. Compound **37** exhibited toxicity against A431 cells, which depend on EGFR for survival¹⁸⁹ at values ten-fold better than standard cisplatin (Figure 31) used in this assay. Additionally, **37** also exhibited a ten-fold better VEGFR-2 inhibition than the standard agent semaxanib, thereby demonstrating dual kinase inhibition. The EC₅₀ values of **38** against VEGFR-2 and PDGFR-β were four-fold better than and comparable to standard agents semaxanib and **27** (AG1295) respectively. Inhibition of EGFR and A431 cell lines by **39** was comparable to or five-fold better than the standard **58** (PD153035). Thus, Gangjee *et al.* demonstrated that the substitution pattern in the N⁴-(3-bromophenyl)-6-

(substituted benzyl) pyrrolo[2,3-*d*]pyrimidine scaffold strongly influences the observed multikinase inhibition and affords potencies equivalent to or better than standard agents.

Gangjee *et al.*¹⁸⁰ reported a series of N4-phenylsubstituted-6-(2-phenylethylsubstituted)-7*H*-pyrrolo[2,3-*d*]pyrimidine-2,4-diamines as a homologated series of their previously published RTK inhibitors.¹⁷⁹ These compounds retained activity against EGFR and VEGFR-2 and showed improved PDGFR- β inhibition compared to the previous series of compounds. Compounds **40-43** are the best compounds from this series. Compound **40** showed EGFR inhibition similar to the standard **63** used in this assay. While the 2'-F, 4'-Cl- and 4'-Cl- analogs (**41** and **42**) did not display significant EGFR inhibition, they were about 5- fold more active than the standard cisplatin in the A431 cytotoxicity assay. Compound **43**, the 3'-CF₃ analog of **40**, was 3-fold better than semaxanib in the chicken choriallantoic membrane (CAM) assay which is a standard test for angiogenesis.¹⁹⁰

Gangjee *et al.*¹⁸¹ reported a series of compounds that showed variation in the substitutions at the 2-position in order to determine the validity of their hypothesis that the 2-NH₂ group affords improved potency against RTKs by potentially providing additional means of hydrogen bonding to the hinge region in the ATP binding site. With the exception of **44**, the 2-NH₂ analogs showed better inhibition of EGFR, PDGFR- β and in whole cell inhibition assays against A431 cells. Interestingly, the 2-desamino analogs such as **45 – 47** were more potent against VEGFR-2 than the 2-NH₂ analogs. However, the 2-Desamino analogs were only micromolar inhibitors in the CAM assay and were less potent than the standard semaxinib in these assays, proving the importance of the 2- NH₂ moiety in this scaffold.

Gangjee *et al.*¹⁸² reported eight N4-phenylsubstituted-6-(2,4-dichlorophenyl-methyl)-7*H*-pyrrolo[2,3-*d*]pyrimidine-2,4-diamines as VEGFR-2 inhibitors with variations in the phenyl ring of the 4-anilino moiety. Compounds **48** - **50** were potent VEGFR-2 inhibitors and were 100-fold, 40-fold and 8-fold more potent than the standard semaxanib, respectively. Compound **48** was a potent inhibitor of A431 cells with inhibition comparable to standard cisplatin in the assay.

In an effort to substantiate the three proposed binding modes against RTKs, Gangjee *et al.*¹⁸³ proposed a series of pyrrolo[2,3-*d*]pyrimidine analogs of three potent lead compounds with strategically placed methyl substitutions at the N7- and/or N4-positions and evaluation of the resulting analogues for RTK activity. It was hypothesized that, depending on the preferred binding mode of the compounds in RTK, selective methylation should lead to a loss of hydrogen bonding with the hinge region, and consequently, should result in a decrease in activity of the compound against the particular kinase. Additionally, if all the three proposed binding modes were viable, the compounds with methyl groups at the N7- and N4-positions, which would lack hydrogen bonding capabilities, should be poorly active. The biological evaluation results indicated that dimethylation of both the N4- and N7-positions (**51** and **52**) afforded whole cell EGFR inhibitors that are more cytotoxic than the standard erlotinib. In addition, mono-methylation at the N4- or N7-positions (**53**) afforded increased PDGFR- β inhibition than the standard sunitinib. Methylation at either the 4-N or N7 position was detrimental to VEGFR-2 inhibition. The biological evaluation results in this study demonstrated that methylation of the 4-NH and/or the 7-NH influences both the specificity and potency of RTK inhibition.

Compound **54** (CGP59326) was designed as a part of an effort to improve the EGFR activity of 7*H*-pyrrolo[2,3-*d*]pyrimidines by using a pharmacophore model for the ATP binding site of EGFR.¹⁸⁴⁻¹⁸⁸ It was proposed that the NH of the pyrrole ring and the N1 of the pyrimidine ring form a bidentate hydrogen bond donor acceptor system with Gln767 and Met769 in the hinge region of EGFR, and the substituted aniline moiety at the C-4 position binds in the Sugar pocket and interacts with Cys773. In addition, the substituents at the 5 and 6 positions form van der Waals interactions with the Hydrophobic pocket not accessed by ATP. Compound **54** showed good potency and selectivity for isolated EGFR (IC₅₀ = 27 nM). Modifying the 4- and 6-positions of the pyrrolo[2,3-*d*]pyrimidine scaffold afforded compounds with improved biological and physicochemical properties. Variation of substituents at the 6-position including esters (**55**), amides (**56**), were introduced in order to increase hydrophobic interactions with residues such as Thr76 and Thr860 in the active site. These modifications resulted in improvement of activity against EGFR (IC₅₀ = 1-5 nM). Replacement of the *m*-chloroanilino moiety at the 4-position by a (*R*)-phenylethylamino led to potent compounds (**57-59**, IC₅₀ range of 1-3 nM) with improved pharmacokinetic properties. Similar variations at the 6-position of the pyrrolo[2,3-*d*]pyrimidine scaffold with *p*- or *m*-substituted aromatic rings (**60 – 62**) led to compounds with potent EGFR inhibition.

A.2.8. Molecular Modeling Studies with Receptor Tyrosine Kinases

The presence of multiple high-resolution X-ray crystal structures of RTKs such as EGFR, VEGFR-1 and VEGFR-2 complexed with various small molecule inhibitors or peptides has enabled structure based drug-design strategies. The following section lists selected high-resolution ($< 2 \text{ \AA}$) crystal structures in the PDB complexed with small molecule inhibitors of EGFR (Table 6 and Figure 32) and VEGFR-2 (Table 7 and Figure 33).

A.2.8.1 EGFR Crystal Structures

There are 89 X-ray crystal structures of human EGFR currently in the PDB. The 11 high resolution ($< 2 \text{ \AA}$) crystal structures co-crystallized with small molecule inhibitors are listed in Table 6.

Table 6: Selected X-ray crystal structures of EGFR complexed with small molecule inhibitors:

Sr.No.	PDB	Resolution	Ligand	Reference
1	3POZ	1.50	TAK-285	97
2	3VRP	1.52	PTR	96
3	3W33	1.70	19B	26
4	4I22	1.71	Gefitinib	25
6	4I24	1.80	Dasitinib	25
7	2RGP	2.00	HYZ	24
8	3W2Q	2.20	HKI-272	91
9	1XKK	2.40	GW572016	191
10	1M17	2.60	Erlotinib	192
11	2ITO	3.25	Iressa	173

A.2.8.2. VEGFR-2 Crystal Structures

There are 40 X-ray crystal structures of human EGFR currently in the PDB. The 10 high resolution ($< 2 \text{ \AA}$) crystal structures co-crystallized with small molecule inhibitors are listed in Table 7.

Table 7: Selected X-ray crystal structures of VEGFR-2 complexed with small molecule inhibitors:

Sr.No.	PDB	Resolution (Å)	Ligand	Reference
1	3VO3	1.52	OKF	193
2	4AG8	1.95	Axitinib	194
3	4ASE	1.83	Tivozanib	194
4	3VNT	1.64	OJA	195
6	3VHE	1.55	42Q	196
7	2XIR	1.50	PF-00337210	197
8	3EWH	1.60	K11	198
9	3BE2	1.75	RAJ	199
10	1YWN	1.71	LIF	200

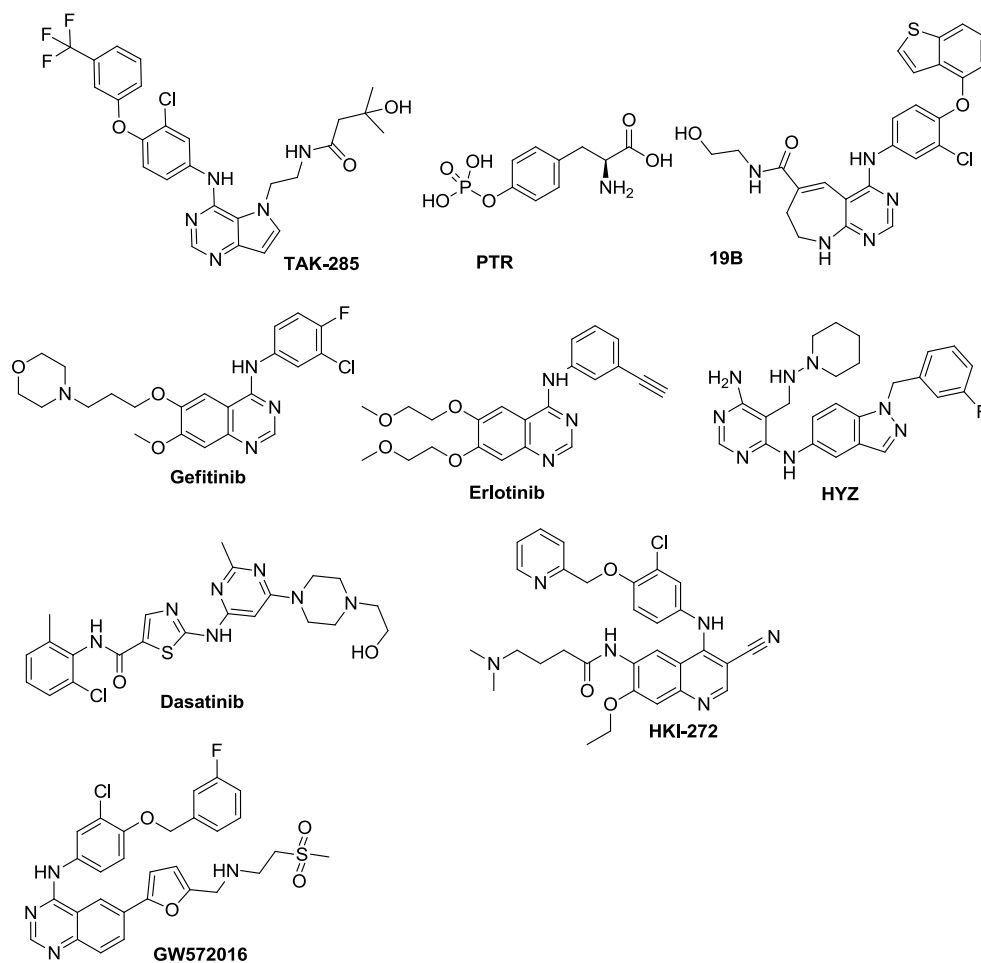


Figure 32. Structures of ligands co-crystallized with EGFR listed in Table 6.

KDR. CoMFA and CoMSIA models were developed based on the docking conformations.

The CoMFA model produced statistically significant results with the cross-validated correlation coefficient (q^2) of 0.504 and the non-cross-validated correlation coefficient (r^2) of 0.913. The predictive abilities of the two models were further validated by 14 test compounds ($r^2 = 0.727$ for CoMFA and $r^2 = 0.624$ for CoMSIA). In addition, the CoMFA and CoMSIA models were used to guide the design of a series of new inhibitors of this class with predicted excellent activities.

Lu *et al.*²⁰⁶ reported the development of CoMFA and CoMSIA models from a set of 47 compounds composed of 3-aminoindazole ureas, 7-aminopyrazolo[1,5-*a*]pyrimidine ureas and 5-aminoquinoxaline ureas against VEGFR2. To account for the flexibility of the molecules a pharmacophore based alignment was used to construct the 3D-QSAR models. The constructed CoMFA models ($r^2 = 0.982$, $q^2 = 0.507$) were validated by a test set of 16 compounds ($r^2 = 0.540$).

Recently, Zhang *et al.*²¹⁰ reported 3D-QSAR modeling and docking studies of arylphthalazines and 2-((1H-azol-1-yl)methyl)-*N*-arylbenzamides-based VEGFR2 inhibitors. Two statistically relevant 3D-QSAR models (CoMFA $r^2 = 0.969$; $q^2 = 0.671$; CoMSIA $r^2 = 0.936$, $q^2 = 0.608$) were developed to predict the biological activity of new compounds. Analogs were designed using molecular fragment replacement was virtually screened using Glide (docking) and further evaluated with CoMFA prediction, and ADMET analysis. Forty four novel *N*-(pyridin-4-ylmethyl)aniline derivatives were developed using this approach.

In 2009 Du *et al.*²¹² reported the CoMFA and CoMSIA analysis studies of a series of 82 selective inhibitors of KDR with either a quinazoline, naphthalene or phenyl core scaffold. Docking studies were performed to explore the binding mode and predict the bioactive conformations of the 82 inhibitors in KDR. Two conformer-based alignment strategies were employed to construct reliable 3D-QSAR models. The docked conformer-based alignment strategy gave the best 3D-QSAR models ($r^2 = 0.936$ and 0.961 ; $q^2 = 0.546$ and 0.715). The information obtained from these models were coupled with molecular modeling studies to design 8 novel highly potent (low nanomolar), selective inhibitors of KDR.

A.3. COLCHICINE SITE BINDING ANTI-MITOTIC AGENTS

A.3.1. Tubulin and microtubules

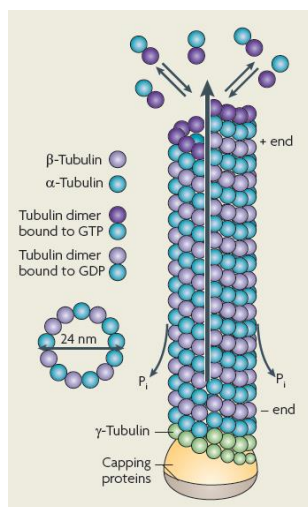


Figure 34. Structure of a microtubule.²¹³

Every nucleated cell in the human body contains two similar spherical proteins – α and β -tubulin (Figure 34), each with a molecular weight of 50 kDa. Through a series of events these proteins come together to form an α - β heterodimer about 8 nm in length.

Two molecules of energy rich guanosine triphosphate (GTP) are bound to these heterodimers. While one of these GTP molecules is tightly bound and cannot be removed without denaturing the heterodimer, the other GTP molecule is freely exchangeable with unbound GTP. The α - β tubulin heterodimers, at 37 °C can combine in a head-to-tail arrangement to give a long protein fiber composed of alternating α and β -tubulin, known as protofilaments. The protofilaments can group together to form a C-shaped protein sheet, which then curls around to give a pipe-like structure known as a microtubule. Microtubules typically consist of 12 or 13 protofilaments with an external diameter of around 24 nm and internal diameter of around 15 nm. A number of proteins, known as Microtubule Associated Proteins (MAPs), each with a mass of about 200 kDa, are associated with microtubules. Although the exact purpose of MAPs is unclear, microtubules form faster in their presence and the MAPs appear to protect the microtubule from agents which induce depolymerization, namely low temperature and Ca^{2+} ions.

Another key component associated with microtubules are Microtubule Organizing Centers (MTOCs). MTOCs form a focus for microtubule growth, and all microtubules initially begin to grow from one of these centers. A major type of MTOC in most cells is known as the cell center or centrosome which contains two major microtubule structures known as centrioles. It seems that the organization of microtubule growth at the MTOC involves a third type of tubulin protein known as γ -tubulin. The presence of γ -tubulin is vital for microtubule growth in vivo.²¹⁴ It appears that an aggregation of γ -tubulin occurs on the surface of the MTOC, perhaps forming a ring or short cylinder and that this aggregate acts as the site of nucleation for incoming α - β tubulin heterodimers.

After formation, microtubules are not static. They exist in an equilibrium with heterodimers continuously adding to one end of the microtubule [known as the “plus” (+) end], and leaving at the other [the “minus” (–) end]. A fine balance of this equilibrium and the resting control of the length of the microtubules is vital for numerous cellular functions.

Microtubules are required for a number of crucial cellular functions. Amongst the known functions are the maintenance of cell shape, cellular transport and transporting organelles around the interior of the cell. The most crucial function of microtubules however is the formation of the mitotic spindle which eventually makes replication possible.

A. 3. 2. Role of microtubules in mitosis:²¹⁵

One of the most complex and demanding processes undertaken by the human body is the process of cell division. During this process, the cell must completely duplicate its internal components including its DNA, such that it can form two identical daughter cells.

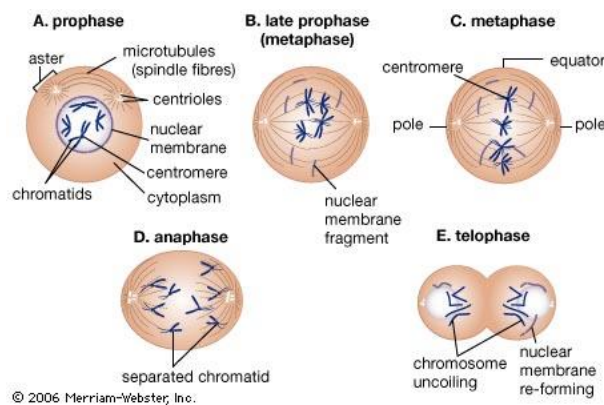


Figure 35. Different stages of mitosis²¹⁶

Once the duplication of the internal components is complete, the cell assembles its DNA into two identical sets of chromosomes and separates them into two individual parcels at opposite ends of the cell, ready to form the two nuclei in the daughter cells.

Following the separation of the new nuclei, the cell is ready to split into two new daughter cells. This ordering and relocation of the genetic material is known as mitosis. Mitosis can be divided into five separate processes (Figure 35)

The first phase of mitosis is termed prophase. In prophase, the DNA in the nucleus is replicated and two sets of genetic material are organized into two identical daughter sets of chromosomes. Towards the end of prophase, the microtubules needed for cell division begin to form and grow toward the newly formed chromosomes. The bundle of microtubules this generates in the cellular space is known as the mitotic spindle. This spindle grows concomitantly from two MTOCs, which begin to separate and migrate toward opposite ends of the cell.

In the next stage, the prometaphase, the nuclear envelope rapidly disintegrates and the microtubules attach themselves to the chromosomes at a point known as the kinetochore, which is the center of the chromosomes.

The cell then enters metaphase. In this phase, the chromosomes gradually become arranged in the plane between two centrosomes. After an accurate arrangement of these chromosomes, the cell abruptly enters anaphase. The daughter chromosomes then start to separate slowly as the microtubules depolymerize, slowly drawing and guiding the daughter chromosomes to opposite ends of the cell.

The final phase of cell division is the telophase. During this phase, the chromosomes reach the opposite ends of the cell and new nuclear envelopes form around them. This completes the process of mitosis, and it only remains for the cytoplasm surrounding the nuclei to begin to divide, in a process known as cytokinesis. The nuclei thus become partitioned, finally dividing to give two new daughter cells. The importance

of microtubules in mitosis makes them an attractive target for the drug development process.

A.3.3. Microtubule dynamics:

The functional diversity of microtubules is dependent on their intrinsic non equilibrium dynamic behaviors.²¹⁷⁻²²⁶ Microtubules exhibit two types of dynamic behaviors; one such behavior is called “dynamic instability” (Figure 36). In dynamic instability, microtubule ends alternate between phases of growth and shortening.^{218-221, 223-}

226

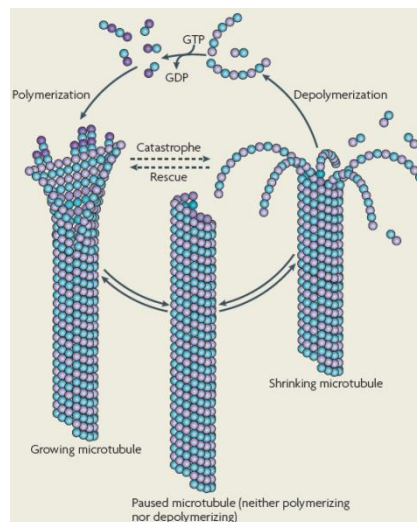


Figure 36. The process of dynamic instability.²¹³

Usually microtubules display slow growth phases and rapid shortening phases. They also undergo a pause phase when there is no detectable growth or shortening at the microtubule ends. The transition from a growth or a pause state to a shortening phase is called a “catastrophe” and the transition from a shortening phase to a growth or a pause state is called “rescue”. The transition frequencies are important for regulating microtubule dynamics for diverse cellular tasks.²¹⁹⁻²²⁶

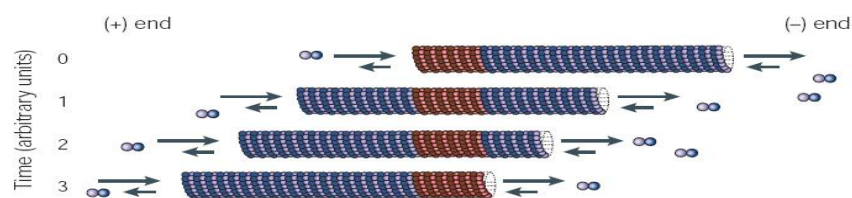


Figure 37. The process of treadmilling.²²¹

Another type of dynamic behavior exhibited by microtubules is called “treadmilling” (Figure 37). Treadmilling involves a net growth at the plus end and a net shortening at the minus end of the microtubule.^{217, 223}

A microtubule population may exhibit one or both of these dynamic behaviors. The polymerization dynamics of microtubules depends on the loss or gain of a stabilizing cap composed of either tubulin-GTP or tubulin-GDP-Pi at their ends.^{219, 226} The assembly dynamics is finely regulated by several proteins including stabilizing microtubule-associated proteins (MAPs) such as tau, MAP1, MAP2, MAP4, and destabilizing MAPs such as stathmin.^{219, 223, 226-228} Microtubule dynamics is specifically important for the proper attachment and movement of chromosomes during various stages of the mitotic phase.²¹⁹⁻²²¹ Suppression of microtubule dynamics in cells by small molecule inhibitors block the cell division machinery at mitosis leading to cell death. Hence, the assembly dynamics of microtubule represents a potential target for finding anticancer drugs. The small molecule inhibitors usually imitate the action of the natural regulators of microtubule assembly and disassembly kinetics making these agents a valuable tool for probing the roles of microtubule dynamics in different cellular processes.

A.3.4. Antimitotic agents:

Agents which induce cell death by inhibiting the function of microtubules are known as antimitotics. Cancer cells are relatively sensitive to these drugs relative to normal cells because many cancer cells divide more frequently than normal cells and thus frequently pass through a stage of vulnerability to mitotic poisons. However it is likely that other mechanisms, such as expression of a variety of checkpoint and apoptotic proteins and differential uptake and retention drugs, can also distinguish the differential responses of tumor and normal cells to antimitotics drugs.

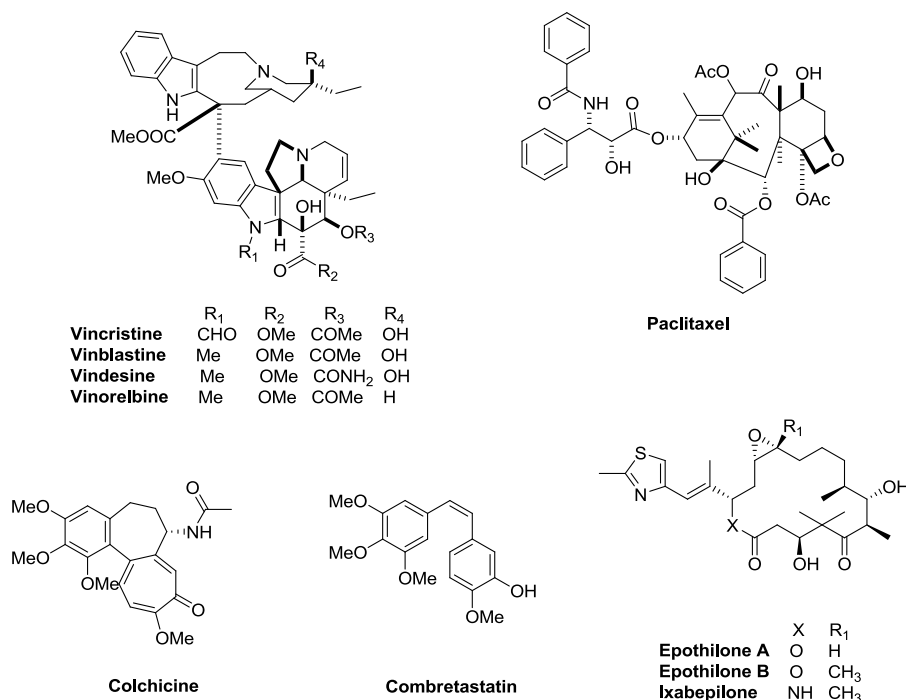


Figure 38. Antimitotic agents.²²⁹

Antimitotics can be broadly divided into three distinct classes. The vinca alkaloids are represented by vincristine, vinblastine, vindesine, and vinorelbine (Figure 38). These agents bind to β -tubulin and interfere with proper mitotic spindle formation by preventing the normal dynamics of polymerization of microtubules. *Vinca* alkaloids are important

agents for the treatment of leukemias, lymphomas, small cell lung cancer, and other cancers.^{221, 230} These agents are also designated as microtubule-destabilizing agents or microtubule polymerization inhibitors or depolymerizers.

The second class of antimitotics, taxanes, is represented by paclitaxel and docetaxel (Figure 38). Paclitaxel binds to β -tubulin as well; however its location is different from that of the vinca alkaloids. As determined in tubulin protofilaments in Zn sheets, paclitaxel binds on the inside surface of the β -subunit of microtubules.^{231, 232} Paclitaxel induces an increase in microtubule polymerization, thereby interfering with spindle microtubule dynamics and preventing the progression of cell division. Hence the agents of this class are termed microtubule-stabilizing agents or polymerizing agents. The taxanes are important for the treatment of breast, lung, ovarian, head and neck, and bladder carcinomas among others.

The third class is typified by colchicines (Figure 38) and comprises of a diverse collection of small molecules that bind to the colchicines binding site. Although the nature of this binding site has not been determined with certainty, insights into colchicines binding sites are available from homology models.²³³ The agents from this class also act by an inhibition of microtubule polymerization like the vinca alkaloids, but along with a difference in the binding site, their depolymerization mechanism is also different from the vinca alkaloids. The combretastatins are a class of drugs that bind to the colchicine binding site and are in clinical trials as antitumor agents.²²¹

The epothilones, produced by the myxobacterium *Sorangium cellulosum*, and discovered in the early 1990s,²³⁴⁻²³⁶ are a novel class of microtubule-stabilizing agents. These agents bind at the taxane binding site and have a mechanism of action similar to

the taxanes. Epothilones A and B were found to have potent in vitro anticancer activity, including activity against taxane-resistant cell lines, but their in vivo activity is modest, owing to issues such as poor metabolic stability and unfavourable pharmacokinetics.²³⁴⁻²³⁶ Synthesis and testing of more than 300 semisynthetic epothilone analogs with the aim of addressing these issues led to the identification of ixabepilone.²³⁴⁻²³⁶ Ixabepilone has been approved for the treatment metastatic breast cancer in 2007.^{237, 238} The epothilones are considered more superior to taxanes because their less susceptibility to multiple mechanisms of resistance.^{236, 239}

It has been observed that most microtubule-targeted drugs, including *Vinca* alkaloids, taxanes and epothilones, also act by suppression of microtubule dynamics in cells at concentrations that inhibit proliferation and block mitosis.²⁴⁰

Microtubule targeted drugs can act by two more mechanisms. One is to inhibit the process of angiogenesis, and the second is to shut down existing tumor vasculature by vascular disruption.²⁴⁰

A. 3.5. Structure of tubulin:

A detailed description of the tubulin protein helps in the analysis of the mechanistic aspect of drug-tubulin interaction. Electron crystallography of zinc-induced 2D crystals of tubulin were obtained with a 6.5 Å resolution.²⁴¹ The atomic model of $\alpha\beta$ tubulin dimer was further obtained at 3.7 Å resolution by using electron crystallography of zinc-induced tubulin sheet. In this structure, α and β share an identical principal structure: each monomer is composed of a core of two β sheets surrounded by α helices.

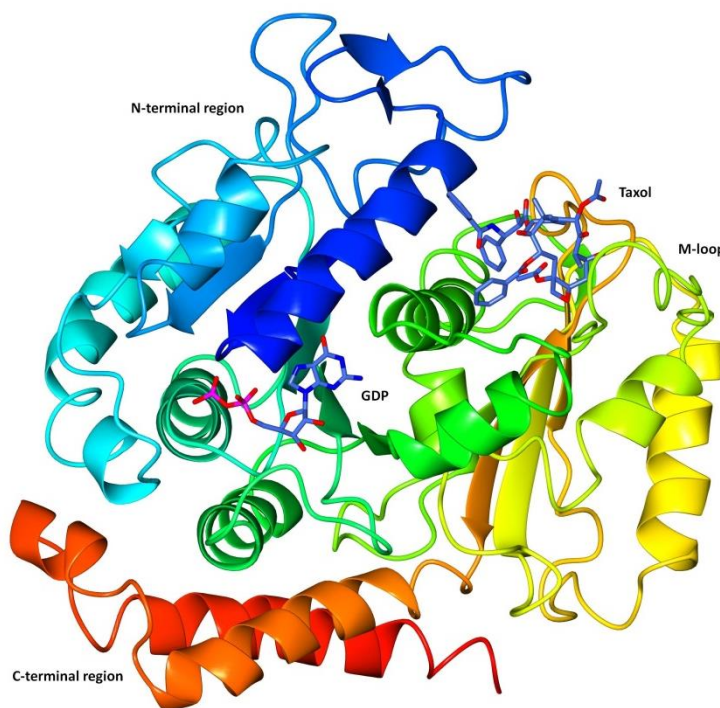


Figure 39. X-ray crystal structure of tubulin. (PDB ID: 1JFF⁹²)

The monomer has a compact structure and can be divided into three functional domains: the amino-terminal domain possessing a nucleotide-binding region, an intermediate domain where lies the taxol-binding site, and the carboxy-terminal domain comprising the binding site for motor proteins. The model was further refined using standard X-ray crystallography methods (Figure 39).²³¹ This model indicates that each monomer was composed of an N-terminal, nucleotide-binding domain, having six parallel β -strands (S1-S6) alternating with helices (H1-H6). Loops T1-T6 connect each strand with the strand of the next helix in binding the nucleotide. This structure provides a detailed description of lateral contacts in zinc-sheets and the nucleotide and taxol binding sites.

A.3.6. Colchicine binding site on tubulin:

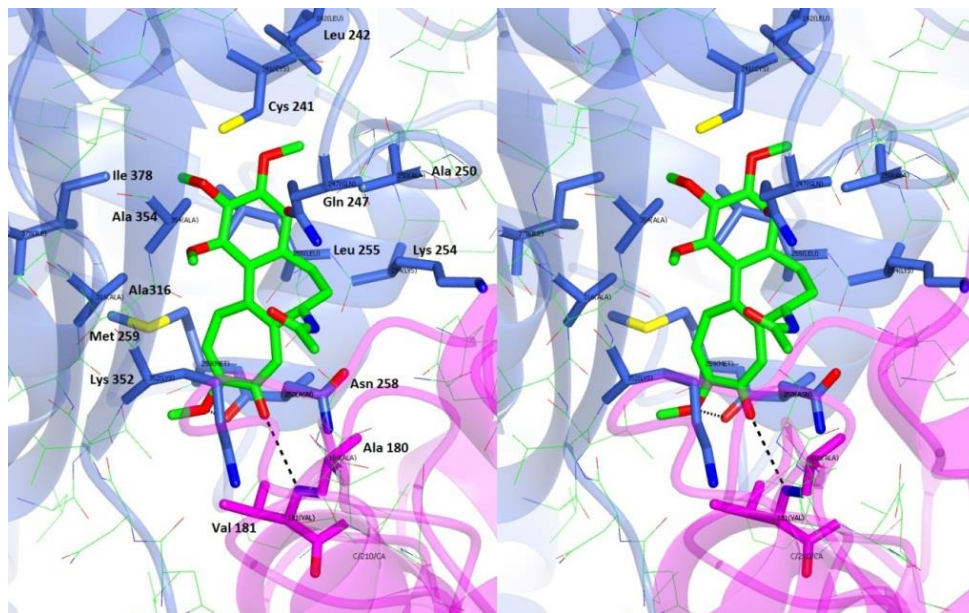


Figure 40: Stereoview. X-ray crystal structure of colchicine (green) bound to tubulin. (PDB: 3UT5).²⁴² Secondary structures colored according to chain. (pink: chain A; blue: chain B). Binding site amino acids highlighted and colored according to chain.

The colchicine site is located mostly in the β -subunit of tubulin and is bordered by helix 7, which contains Cys β 241, and helix 8. The colchicine binding site has a volume of $\sim 10 \text{ \AA} \times \sim 10 \text{ \AA} \times 4\text{--}5 \text{ \AA}$ and borders the α -tubulin monomer, which forms crucial interactions at the colchicine site, notably the loop connecting sheet 5 and helix 5.²⁴² Thr α 179 and Val α 181 interact with colchicine and have also been implicated in formation of hydrogen bonds with other colchicine site binding agents (CSAs). The molecular volume and electrostatic properties of the colchicine site play an important role on the conformations of colchicine site binding agents and have proved useful in elucidating the bioactive conformations of colchicine site binding agents.²⁴³

A.3.7. Binding mode prediction of colchicine site agents

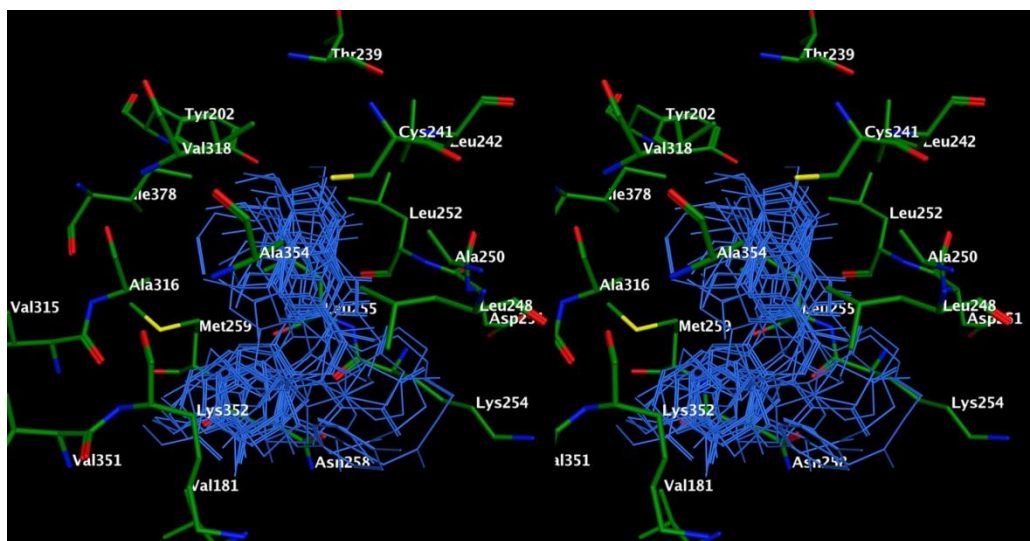


Figure 41:²⁴³ Stereoview. Predicted binding modes of CSAs (blue) in the colchicine binding pocket of tubulin.

Nguyen *et al.*²⁴³ used docking studies to determine the binding modes of a set of 15 structurally diverse colchicine site inhibitors. These binding models were subsequently used to construct a comprehensive, structure-based pharmacophore that was used in combination with molecular dynamics simulations to understand binding interactions at the colchicine site of tubulin. Figure 41²⁴³ shows the superimposition of the docked structures of the 15 CSAs. It was observed that, despite the variations in the chemical nature of the 15 CSAs, the CSAs occupied similar Cartesian space in the binding site. The overlaid poses of the compounds can be bisected by two planes (Figure 42) which are roughly at 45 degrees to each other. Since the typical CSA contains a biaryl system, the relative orientations of the two aryl chains in each molecule lie roughly along the two bisecting planes. However, even among CSAs that lack the biaryl system, the binding architecture was conserved.

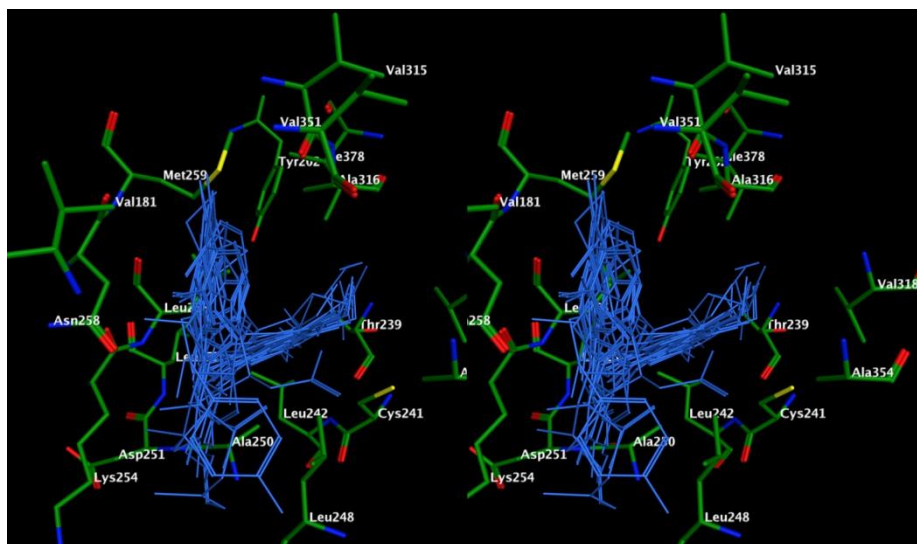


Figure 42:²⁴³ Stereoview. Overlay of docked poses of CSAs (blue) form roughly a 45° angle between the bisecting planes in the colchicine binding pocket.

All 15 CSIs were found to form a hydrogen bond with the thiol group of Cys β 241. In addition, a hydrogen bond was observed between 11 CSIs and the backbone NH of Val α 181. Molecular modeling further indicated that hydrogen bonds could be formed between the CSIs and backbone NH atoms of Ala β 250, Asp β 251, and Leu β 252 due to conformational changes in the loop or due to the presence of structured water molecules. Thr α 179 was found to be involved in the formation of hydrogen bonds with 4 CSIs in their binding models.²⁴³ This publication highlighted the important residues in the colchicine binding pocket and the key interactions with these residues. Further, the authors utilized this data to build a 7-point pharmacophore model (three hydrogen bond acceptors, one hydrogen bond donor, two hydrophobic centers, and one planar group) of the binding of these CSIs in the colchicine binding site. It was observed that none of the 15 CSIs individually utilized all the 7 points, suggesting that binding affinities for each

chemotype could be improved by appropriate chemical modifications that target the pharmacophore point not utilized by that chemotype.

A.3.8. Targeting multidrug resistance in cancer:

The emergence of multidrug resistance (MDR) is a major concern for contemporary cancer chemotherapy. There are three major mechanisms by which MDR usually occurs.²⁴⁴ First, decreased uptake of water-soluble drugs such as folate antagonists and nucleoside analogs which require transporters to enter cells; second, various changes in cells that affect the capacity of cytotoxic drugs to kill cells, including alterations in cell cycle, increased repair of DNA damage, reduced apoptosis and altered metabolism of drugs. The third, and the major mechanism responsible for MDR, is the increased efflux of hydrophobic cytotoxic drugs mediated by a family of energy-dependent transporters, known as ATP-binding cassette (ABC) transporters. ABC transporters were discovered in 1973 by Dano *et al.*²⁴⁵ They noticed the active outward transport of the drug daunomycin in multidrug-resistant Ehrlich ascites tumor cells. Subsequent work indicated that the ‘reduced drug permeation’ in multidrug-resistant cells is associated with the presence of a cell surface glycoprotein known as P-glycoprotein (Pgp).²⁴⁶ Based on the presence of specific conserved sequences, Pgp was recognized to be an ABC transporter protein.²⁴⁷⁻²⁵¹

A human small-cell lung cancer cell line (H69), that shows resistance to doxorubicin without increasing expression of Pgp was later discovered.²⁵² Similar to the cells overexpressing Pgp, H69 displayed deficient combined drug accumulation and resistance to a broad range of anticancer agents, including vinca alkaloids and

epipodophyllotoxins.^{253, 254} Analysis indicated the increased expression of a novel ABC transporter, termed multidrug resistance associated protein 1 (MRP1).²⁵⁵

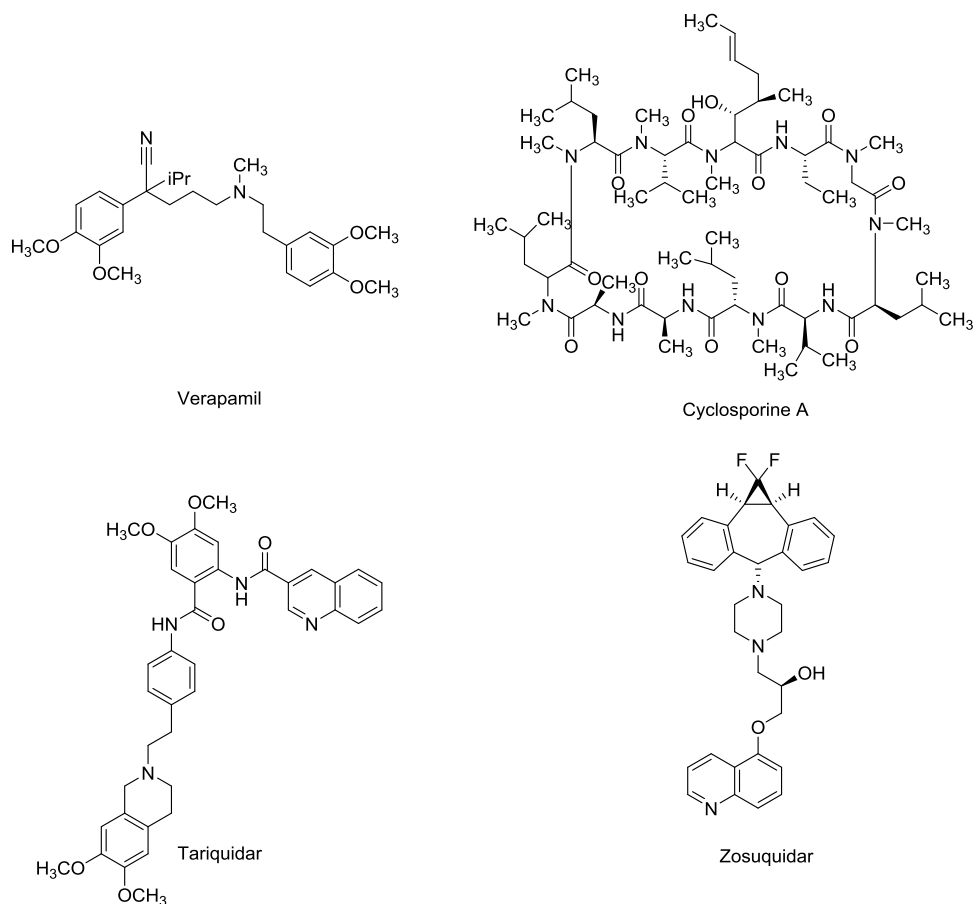


Figure 43. Agents reversing Pgp mediated MDR in cancer.^{229, 256}

Several agents have been investigated for their ability to reverse Pgp mediated MDR. Examples include verapamil,²⁵⁷ cyclosporine A,²⁵⁷ tariquidar^{258, 259} and zosuquidar²⁶⁰ (Figure 43). Excellent reviews of efforts to reverse MDR inhibitory effects have been recently published.^{261, 262} Although a large number of compounds possessing diverse chemical structures and biological activities, are able to reverse MDR, there are currently no approved reversal agents available in the clinic.^{263, 264} A 3.80 Å X-ray crystal structure of Pgp has recently been reported.²⁶⁵ In order to address MDR, new

agents that possess antimitotic and antitumor activities without substrate activity for Pgp are highly coveted and would be useful antitumor agents as single agents or in combination with other antitumor agents.

A.3.9. Antimitotic agents that also reverse tumor resistance:

The following section will provide a brief summary of 6,5-fused bicyclic agents that act as antimitotic agents by targeting the colchicine binding pocket of tubulin.

Gangjee *et al.*²⁶⁶ reported a series of pyrrolo[2,3-*d*]pyrimidine antimitotics **63** – **68** (Figure 44) that are not substrates for Pgp and MRP1, and in addition, are capable of reversing the resistance exhibited by tumors to vinblastine and vincristine.

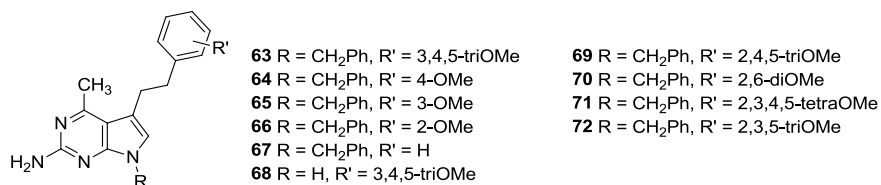


Figure 44.²⁶⁶ Pyrrolo[2,3-*d*]pyrimidines that act as antimitotics and reverse resistance exhibited by tumors to vinblastine and vincristine.

Compounds **63-68** were originally designed as potential RTK inhibitors. These compounds displayed antitumor activity against a variety of tumor cells but were not inhibitors of RTKs. In the NCI 60 cell line panel compound **63**, displayed potent inhibition (GI₅₀ of single to two digit nanomolar) of 16 tumor cell lines. Compound **68**, the corresponding debenzylated analog of **63**, showed a loss of potency of 100- to 10,000- fold against 56 tumor cell lines, suggesting that the N7-benzyl group is critical for activity. The 2-OMe and 3-OMe analogs, **64** and **65** respectively GI₅₀ values in the micromolar - millimolar range against the tumor cells in culture. The 4-OMe compound **66** had GI₅₀s similar to **65**, indicating the importance of the 3- and/or 5-OMe groups. The

unsubstituted phenyl analog **67** displayed GI₅₀ in the millimolar or lower range for 52 tumor cells. The corresponding debenzylated analogs of **64-67** showed substantially decreased activity against the 60 cell line panel. The biological evaluation results from this series indicated that a 3,4,5-triOMe substitution along with the presence of the N7-benzyl moiety was important for potent inhibitory activity against tumor cells in culture.

An NCI COMPARE analysis²⁶⁷ was performed to elucidate the possible mechanism of action of **63**. The first five compounds whose cell type selectivity profile showed the highest Pearson correlation coefficients (PCC)^{268, 269} with **63** were all well-known antimitotic agents. Hence compound **63** was suspected to exhibit its actions microtubule targeting agent. It was later determined from binding studies that **63** bound to tubulin at a site different from the colchicines, *Vinca*, and taxane binding sites.

Compound **63** exhibited subnanomolar IC₅₀s against both, drug sensitive (cell lines that do not express Pgp or MRP1) as well as drug resistant tumor cell lines (cell lines that express Pgp or MRP1)²²⁹ indicating that it is not a substrate for Pgp and MRP1. The 2-OMe substituted compound **66** displayed best results when tested for its ability to reverse Pgp mediated MDR to vinblastine. Compounds **64**, **65** and **67** also induced a dose dependent sensitization of the tumor cells to vinblastine. The ability of compound **63** to display similar effect could not be determined due to its high cytotoxicity.

Gangjee *et al.*²⁷⁰ reported compounds **69 – 72** (Figure 44) as a part of a series of compounds based on **63** that varied in the nature of substitutions on the phenyl ring of the 5-phenylethyl side chain in an attempt to optimize the antitubulin, antitumor, and resistance reversal activities of the parent compounds. All the compounds in this series showed two-digit micromolar IC₅₀ values against MCF-7 cells. Compound **69** was the

most potent compound against MCF-7 cells with an IC₅₀ value of 15 μ M. Compounds **70** – **72** inhibited Pgp activity, making NCI/ADR cells more sensitive to vinblastine. Compound **72** remarkably caused sensitization of tumor cells resistant due to both Pgp and MRP1 and is the only known pyrrolo[2,3-*d*]pyrimidine analog that has native antitumor activity and restores sensitivity of antitumor agents to tumor cells resistant to these agents due to both Pgp and MRP1.

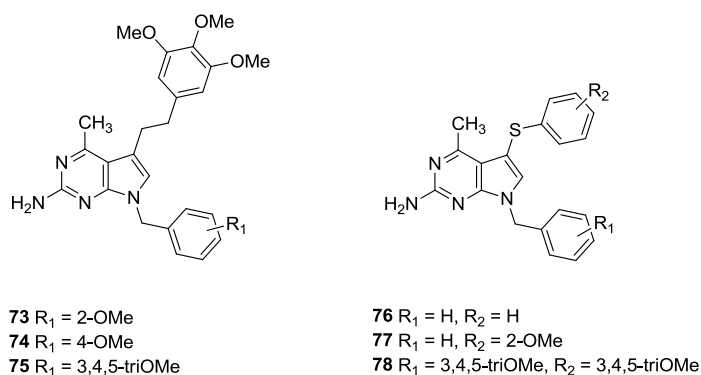


Figure 45.²⁷¹ 5,7-disubstituted-4-methyl-7*H*-pyrrolo[2,3-*d*]pyrimidin-2-amines as microtubule inhibitors

Since the N7-benzyl moiety of **63** (Figure 44) was shown to be critical for its antitumor activity,²⁶⁶ Gangjee *et al.*²⁷¹ designed **73** – **78** (Figure 45) as a part of an effort to optimize antitumor potential and Pgp modulatory effects. In these compounds **73** – **75** methoxy substitutions were varied on the 7-benzyl moiety while maintaining the 3,4,5-triOMe phenethyl substitution at C5. Compounds **76** – **78** were designed as 5-thio analogs, with the large sulfur atom anticipated to mimic the two-carbon bridge of **73** and its analogs. In addition, the 5-thio linker permits the side chain phenyl distance somewhere between a one- and two-carbon-atom bridge and also cause a decrease in the C–S–C angle (98 °) compared to a C–C–C angle (109 °), consequently altering the orientation of the C5 phenyl ring relative to the parent scaffold.

Compounds **73–75** with variations in the *N*7-benzyl moiety showed potent inhibition ($IC_{50} = 0.6$ to $3\ \mu\text{M}$) in the cytotoxicity assay. Compound **74** was the most potent compound in this series and was four-fold less potent than the standard compound Taxol. In addition, **74** demonstrated a significant increase in the intracellular accumulation of [^3H] Taxol in the drug accumulation assay for determination of Pgp activity.

The 5-thiosubstituted compounds **76–78** demonstrated micromolar cytotoxicity in JC cells. . Compound **76** was the most potent compound in this series ($IC_{50} = 4\ \mu\text{M}$) Compound **77** displayed an increase in the intracellular accumulation of [^3H] Taxol below its IC_{50} . Compound **78**, which had a 3,4,5-triOMe substitution on the phenyl ring at the C5 phenyl and the benzyl at the *N*7 position was inactive in the biological evaluation studies.

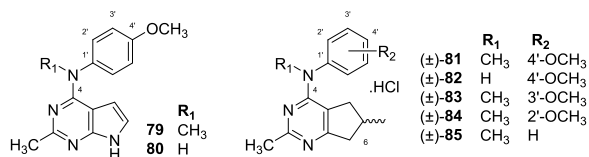


Figure 46.⁵⁰ Pyrrolo[2,3-*d*]pyrimidines and cyclopenta[*d*]pyrimidines that act as antimetabolic agents

As a part of a continued effort to develop 6,5-fused bicyclic agents that act as antimetabolic agents, Gangjee *et al.*^{50, 272} reported the synthesis and biological evaluation of pyrrolo[2,3-*d*]pyrimidines (**79** and **80**) (Figure 46) and cyclopenta[*d*]pyrimidines ((±)-**81** - (±)-**85**) (Figure 46). Compounds **79** and (±)-**81**.HCl displayed potent antiproliferative activities in the nanomolar range with (±)-**81**.HCl displaying significantly higher potency than **79**. Mechanistic studies showed that both **79** and (±)-**81**.HCl cause loss of cellular microtubules and inhibit the polymerization of purified tubulin. Additionally, both compounds inhibit colchicine binding and were thus shown to exhibit their antimetabolic

activity by binding to the colchicine site on tubulin. Gangjee *et al.*²⁷³ later reported the synthesis and evaluation of the individual *R*- and the *S*-enantiomers of **81**. It was seen that both enantiomers were potent inhibitors of cell proliferation and caused microtubule loss in cells and mitotic arrest. Additionally, both compounds inhibited purified tubulin assembly and the binding of [³H]colchicine to tubulin, with (*S*)-**81** being about twice as potent as (*R*)-**81**. However, in cytotoxicity studies against 60 tumor cell lines, (*S*)-**81** was 10- to 88-fold more potent than (*R*)-**81**.

Gangjee *et al.*²⁷⁴ designed **82** – **85** (Figure 47) as regioisomers of the pyrrolo[2,3-*d*]pyrimidine **79** and as isostere of the cyclopenta[*d*]pyrimidine (±)-**81**.HCl. The compounds in this series were designed to explore the nature and importance of substitutions at the 2-, N4- and 6- positions and/or the aniline ring of the pyrrolo[3,2-*d*]pyrimidine scaffold.

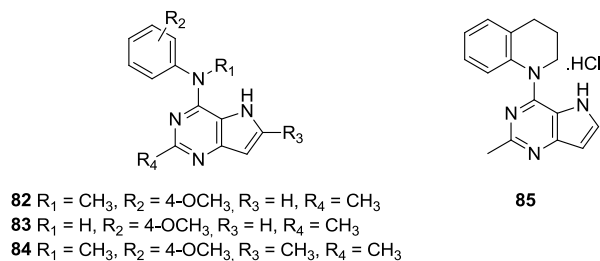


Figure 47.²⁷⁴ Pyrrolo[3,2-*d*]pyrimidines as antimetabolic agents

Compound **85** was designed as a conformationally restricted analog of **82**. The biological evaluation studies indicated that **82** (MDA-MB-435 $\text{IC}_{50} = 96.6 \text{ nM}$), was about 2-times more potent than its lead **79** (MDA-MB-435 $\text{IC}_{50} = 183 \text{ nM}$). Compound **82** ($\text{EC}_{50} = 1.2 \text{ }\mu\text{M}$), was about 5-times more potent than **79** ($\text{EC}_{50} = 5.8 \text{ }\mu\text{M}$) in the microtubule depolymerization assay. In addition, the 4'-OMe moiety and the methyl group attached to the nitrogen bridge both were crucial for activity. Removal of the 2-Me

group of **82** caused a 2-fold reduction in cytotoxicity in the MDA-MB-435 cell line but only a small loss in ability to cause microtubule disassembly in the A-10 cells. Addition of a 6-Me group of **82** gave **84** which displayed a 3-fold improvement in activity against MDA-MB-435 cells ($IC_{50} = 1.2 \mu M$) and improved ability to disassemble microtubules in the A-10 cells 5-6-fold ($EC_{50} = 0.22 \mu M$). The conformationally restricted analog **85** showed 3-fold improved potency in the cellular assays compared to **82** and equivalent to **84**. Compounds **84** and **85** showed equivalent activity against microtubule depolymerization ($EC_{50} = 0.22 \mu M$), but were significantly less active than the standard combretastatin A4 ($EC_{50} = 0.0131 \mu M$). Compounds **84** and **85** were shown to inhibit binding of colchicine to tubulin, thus suggesting that they likely act as an antimitotic by binding to the colchicine site on tubulin.

A.4. COMPARITIVE MOLECULAR FIELD ANALYSIS (CoMFA)

A.4.1 Topomer CoMFA

A topomer is defined as as a molecular fragment having a single internal geometry or “pose” (conformation plus position).²⁷⁵ Topomer CoMFA applies conventional CoMFA methodologies to fragments attached to a central core. By definition, fragments have at least one open valence (point of attachment to the core), which can be fixed in Cartesian space and can be used to align other fragments.^{275, 276} Topomers provide a reproducible way of generating consistent, automatic alignments. Additionally, ligands assembled from shape similar fragment sets tend to share biological activities.²⁷⁷ Topomer CoMFA is thus insensitive to the initial conformation of the molecules, which is a major limitation of traditional CoMFA methodology.²⁷⁷ Several recent reports have shown the utility of

topomer CoMFA in lead optimization studies²⁷⁸, design of novel highly active analogs of targets such as HIV-1 integrase²⁷⁹, HCV NS5b polymerase,²⁸⁰ renin inhibitors²⁸¹ and other targets.^{282, 283}

B. CHEMICAL REVIEW

This section will review synthetic approaches to the following ring systems –

B. 1. Pyrido[2,3-*d*]pyridines

B. 2. Pyrrolo[2,3-*d*]pyrimidines

B. 1. Pyrido[2,3-*d*]pyridines

B. 1. 1. Condensation of substituted 2-amino-3-cyano pyridines with guanidine

B. 1. 2. From substituted pyridines

B. 1. 3. Miscellaneous methods

B. 2. Pyrrolo[2,3-*d*]pyrimidines

B. 2. 1. From substituted pyrimidines

B. 2. 2. From substituted pyrroles

B. 2. 3. Miscellaneous methods

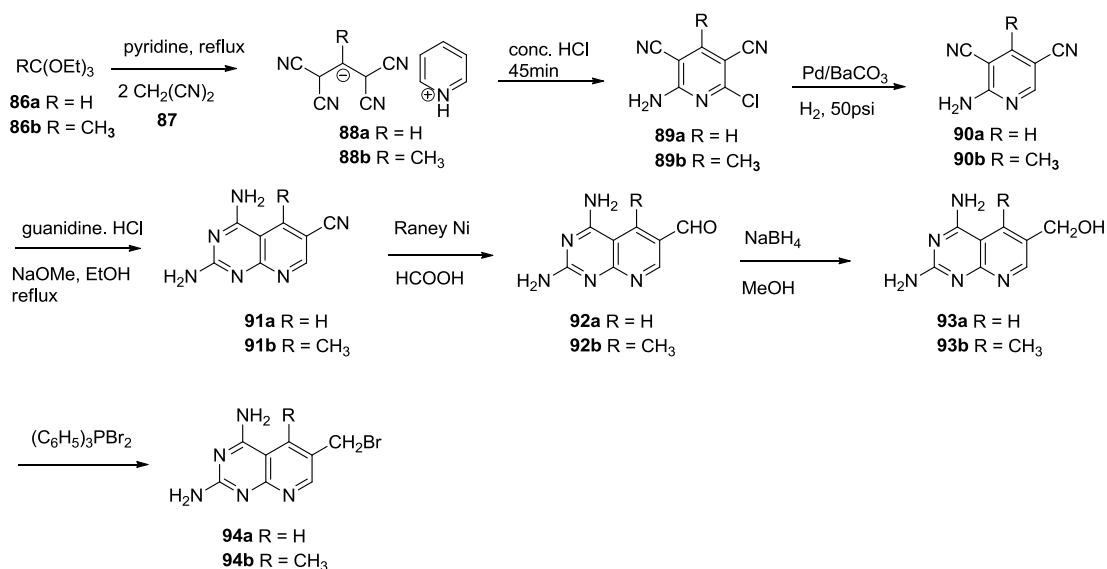
B. 1. Pyrido[2,3-*d*]pyridines

B. 1. 1. Condensation of substituted 2-amino-3-cyano pyridines with guanidine

Piper *et al.*²⁸⁴ reported the synthesis of a series of pyrido[2,3-*d*]pyridines as 5-deaza analogues of aminopterin, MTX, folic acid and N¹⁰-methylfolic acid. The key intermediate for the synthesis of these analogs were 2,4-diamino-5-substituted-pyrido[2,3-*d*]pyrimidine-6-carboxaldehydes **92a-b** (Scheme 1). Intermediate **90** was synthesized starting from condensation of malononitrile **87** with **86** to readily give the salt **88** which, on reflux in presence of conc. HCl gave the substituted chloropyridine intermediate **89**. Reductive dechlorination of **89** afforded **90**. Alternate methods²⁸⁵ for the

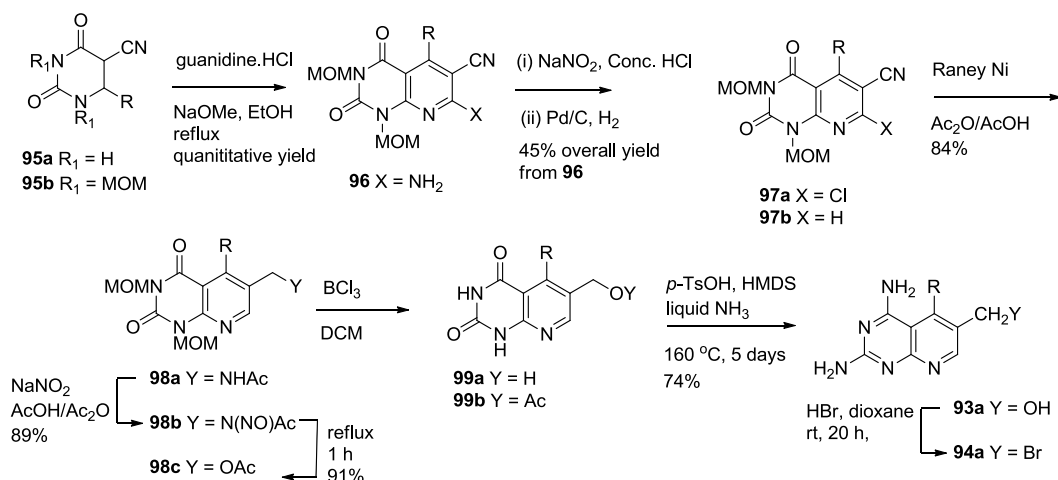
dechlorination of **89** reported in the literature involve treatment of **89** with PdCl₂ and DMF with NEt₃ as the HCl scavenger.

Scheme 1: Synthesis of pyrido[2,3-*d*]pyridines from substituted pyridines²⁸⁴



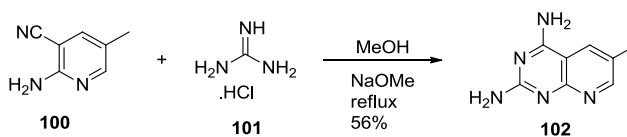
The pyrido[2,3-*d*]pyridine scaffolds were synthesized by condensation of substituted pyridines **90** with guanidine.HCl under basic conditions at reflux in EtOH in 95% yield. The key intermediate **92a-b** were obtained from the nitriles **90a-b** by treatment with Raney Ni in aqueous formic acid. Compounds **92a-b** were reduced by NaBH₄ to the corresponding alcohols **93a-b**. The 6-bromomethyl compounds **94a-b** were synthesized by bromination of **93a-b** with dibromotriphenylphosphorane.

Scheme 2: Synthesis of pyrido[2,3-*d*]pyrimidines from 2,4-dioxypyrimidine derivatives.²⁸⁶



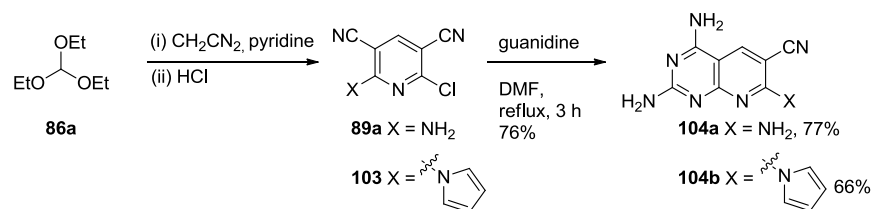
Su *et al.*²⁸⁶ reported the synthesis of intermediate **93a** (Scheme 2) by amination of the acetylated intermediate **99b** using a method developed by Vonbruggen and Krolkiewicz.²⁸⁷ The pyrido[2,3-*d*]pyrimidine scaffold was synthesized from the methoxymethyl (MOM) -protected uracil **95b** by condensation with guanidine.HCl. Diazotization of the 7-NH₂ group of **96** followed by reflux with conc. HCl provided the 7-chloro compound **97a** which was subjected to reductive dehalogenation using Pd/C and H₂ to give **97b**. Reduction of the cyano group of **97b** over Raney Ni in Ac₂O/AcOH afforded the acetamide **98a** in high yield.

Scheme 3: Synthesis of 6-methyl pyrido[2,3-*d*]pyrimidine-2,4-diamine



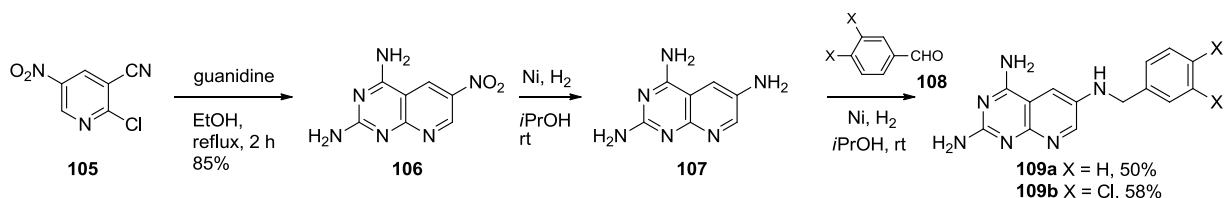
DeGraw *et al.*²⁸⁸ reported the synthesis of 6-methylpyrido[2,3-*d*]pyrimidine-2,4-diamine **102** (Scheme 3) by condensation of 2-amino-5-methylnicotinonitrile **100** with guanidine.HCl **101** under basic conditions at reflux in 56% yield.

Scheme 4: Synthesis of 7-substituted-pyrido[2,3-*d*]pyrimidine-6-carbonitrile-2,4-diamines



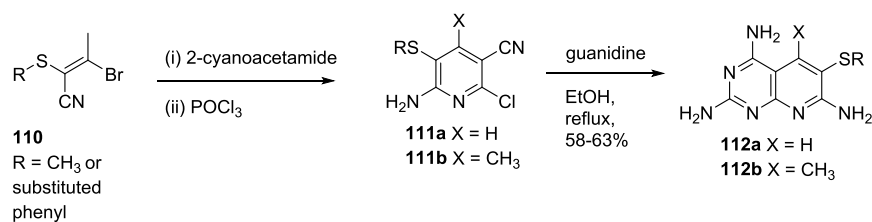
Recently, Soliman *et al.*²⁸⁹ reported the synthesis of 2,4,7-triaminopyrido[2,3-*d*]pyrimidine-6-carbonitriles **104a-b** (Scheme 4) by condensation of 2-amino-6-chloropyridine-3,5-dicarbonitrile **89a**^{284, 290} or 2-pyrrolo-6-chloropyridine-3,5-dicarbonitrile **103**²⁸⁹ with guanidine at reflux using DMF as the solvent in 76% and 66% yields respectively.

Scheme 5: Synthesis of N⁶-substituted-benzylpyrido[2,3-*d*]pyrimidine-2,4,6-triamine



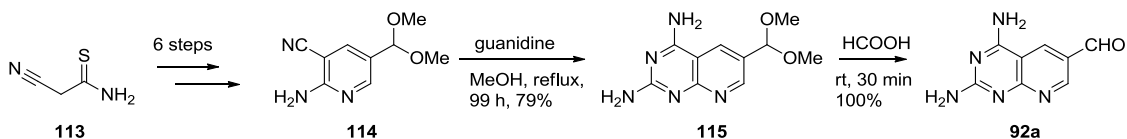
Davoll *et al.*²⁹¹ reported N⁶-substituted-benzylpyrido[2,3-*d*]pyrimidine-2,4,6-triamines **109a-b** (Scheme 5) as folate antagonists and as antimalarial agents. The key intermediate **106** was synthesized by condensation of nitropyridine compound **105** with guanidine at reflux in EtOH in 85% yield. *In situ* reduction of **106** with Raney Ni afforded the amino intermediate **107** which was condensed without isolation with benzaldehydes **108** to afford the target compounds **109a-b** in 50 – 58% yield.

Scheme 6: Synthesis of 6-(ethylthio)-5-substituted-pyrido[2,3-*d*]pyrimidine-2,4,7-triamine



Pochat *et al.*²⁹² described the synthesis of 6-(substituted thio)-5-substituted-pyrido[2,3-*d*]pyrimidine-2,4,7-triamines **112a-b** (Scheme 6) from substituted pyridines **111a-b** by condensation with guanidine under reflux in 58 – 63% yields. Intermediates **111a-b** were synthesized by condensation of *E*-3-bromo-2-(4-substituted thio)-2-butenenitriles **110**²⁹³ with 2-cyanoacetamide to form an intermediate 2-pyridone derivative and further conversion by reaction with POCl₃.

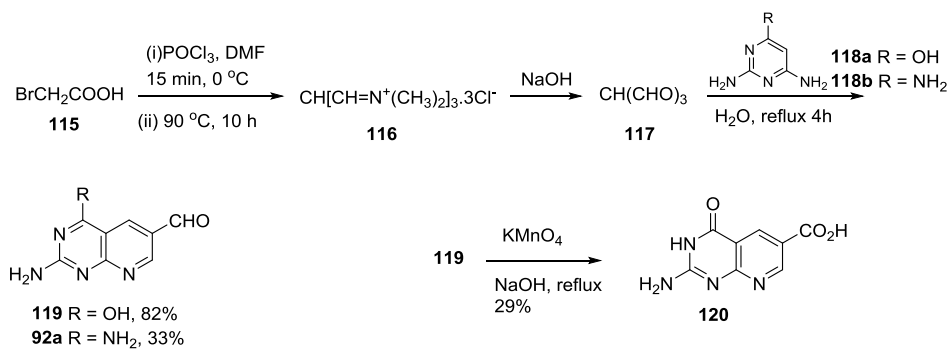
Scheme 7: Synthesis of pyrido[2,3-*d*]pyrimidine-6-carboxaldehyde-2,4-diamine from 2-cyanothioacetamide



Harrington *et al.*²⁹⁴ reported the synthesis of **92a** in quantitative yields by the hydrolysis of intermediate **115** (Scheme 7) by formic acid at room temperature. Compound **115** was synthesized by a six-step sequence starting from 2-cyanothioacetamide **113** to form the substituted pyridine intermediate **114**. Compound **114** condensed with guanidine in MeOH at reflux to give **115** in 79% yield.

B. 1. 2. From substituted pyrimidines:

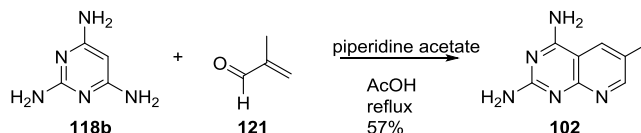
Scheme 8: Synthesis of pyrido[2,3-*d*]pyrimidine-6-carboxaldehyde-2,4-diamine from 2,4,6-triaminopyrimidine



Temple *et al.*²⁹⁵ described the synthesis of pyrido[2,3-*d*]pyrimidine-6-carboxaldehydes **119** (Scheme 8) and **92a** from 2,4,6-triaminopyrimidine. The reaction involved a one-pot generation of trimethylmethane **117** using the method described by Arnold, A.²⁹⁶ Bromoacetic acid **115** is treated by a Vilsmeier reagent, initially at 0 °C and then at 90 °C for 10 h to give the complex **116** which is decomposed under basic conditions to give trimethylmethane **117**. Analogous to condensation of 4-aminopyrimidines with malonaldehyde derivatives to give pyrido[2,3-*d*]pyrimidines, the reaction of **117** with 2,6-diamino-4-oxopyrimidine **118a** or 2,4,6-triaminopyrimidine **118b** in water at reflux afforded **119** or **92a** in 82% and 33% yields respectively. The presence of the formyl group on **92a** was confirmed by condensation with 2,4-dinitrophenylhydrazine to give the corresponding hydrazone. In addition, the aldehyde moiety of **119** was oxidized to the corresponding acid **120** by potassium permanganate. The ¹HNMR of **120** prepared by this method matched the previously reported²⁹⁷ ¹HNMR spectra of **120** prepared by an independent route. Although the mechanism for the condensation is unknown, it was speculated that the initial reaction occurs through the

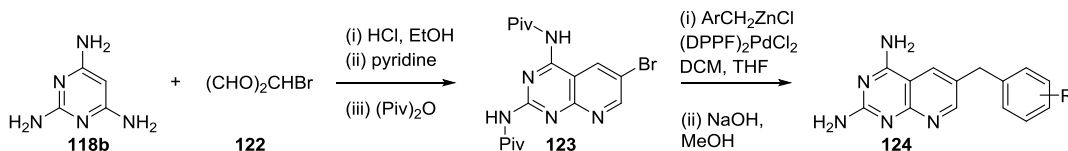
electrophilic attack of one formyl group of **117** with the 5-position of the pyrimidine ring or with the 6-NH₂ group on the pyrimidine to give the Schiff base followed by cyclization of the resulting intermediate to give the pyrido[2,3-*d*]pyrimidine scaffold.

Scheme 9: Synthesis of 6-methyl pyrido[2,3-*d*]pyrimidine-2,4-diamine



Gangjee *et al.*²⁹⁸ reported the synthesis of 6-methylpyrido[2,3-*d*]pyrimidine-2,4-diamine **102** (Scheme 9) by condensation of 2,4,6-triaminopyrimidine **118b** with methacrolein **121** using piperidine acetate as a catalyst in AcOH at reflux in 57% yield.

Scheme 10: Conversion of pyrimidine-2,4,6-triamine to di-tert-butyl (6-bromopyrido[2,3-*d*]pyrimidine-2,4-diyl)dicarbamate

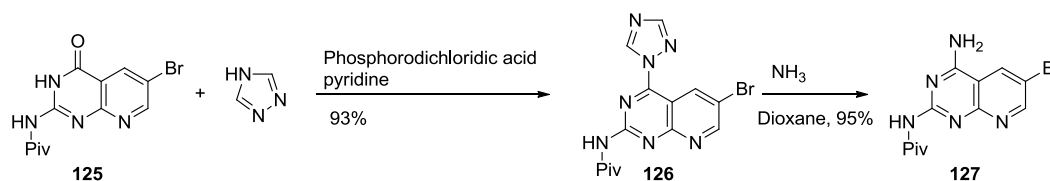


Gangjee *et al.*^{299 300} described the synthesis of di-tert-butyl (6-bromopyrido[2,3-*d*]pyrimidine-2,4-diyl)dicarbamate **124** (Scheme 10) by the condensation of freshly prepared bromomalonaldehyde **122** with pyrimidine-2,4,6-triamine. Upon further reaction with pivalic anhydride leads to the formation of the dipivaloylated compound **123** in 29% overall yield after silica gel chromatography. Rosowski *et al.*³⁰¹ described the coupling of commercially available benzyl zinc chlorides with **123** using a catalytic amount (2.5 mol%) of 1,1-bis(diphenylphosphino)ferrocene]

dichloropalladium(II)·CH₂Cl₂ in THF. The desired compounds **124** were obtained in <40% overall yield from **123** after deprotection of the pivaloyl groups using NaOH in MeOH and recrystallization from mixtures of aqueous DMF, mixtures of MeOH, EtOH, and H₂O, or mixtures of DMF, EtOH, and H₂O.

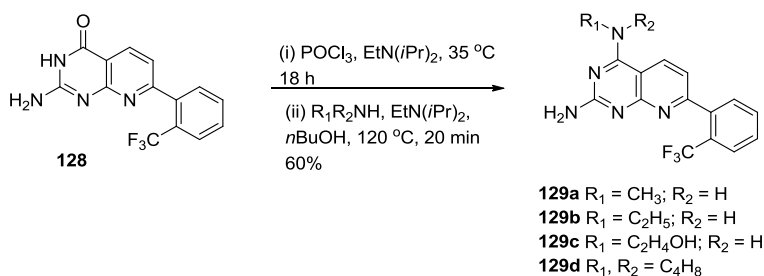
B. 1. 3. Miscellaneous methods

Scheme 11: Synthesis of *N*-(4-amino-6-bromopyrido[2,3-*d*]pyrimidin-2-yl)pivalamide



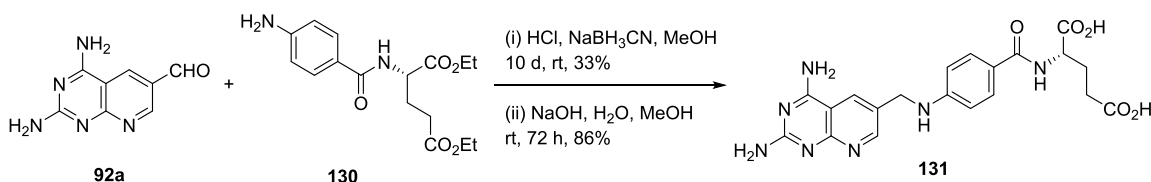
Taylor *et al.*³⁰² reported the conversion of the *N*-(6-bromo-4-oxo-3,4-dihydropyrido[2,3-*d*]pyrimidin-2-yl)pivalamide **125** (Scheme 11) into *N*-(4-amino-6-bromopyrido[2,3-*d*]pyrimidin-2-yl)pivalamide **127**. The two-step process conversion of the 4-oxo moiety of **125** into its triazole derivate **126** by reaction with 4*H*-1,2,4-triazole using phosphorodichloridic acid as a catalyst. The triazole moiety then acts as a good leaving group for the subsequent attack by NH₃ to afford the target compound **127** in excellent yields.

Scheme 12: Synthesis of various 4-*N*-substituted 7-(2-trifluoromethyl-phenyl)pyrido[2,3-*d*]pyrimidine-2,4-diamines



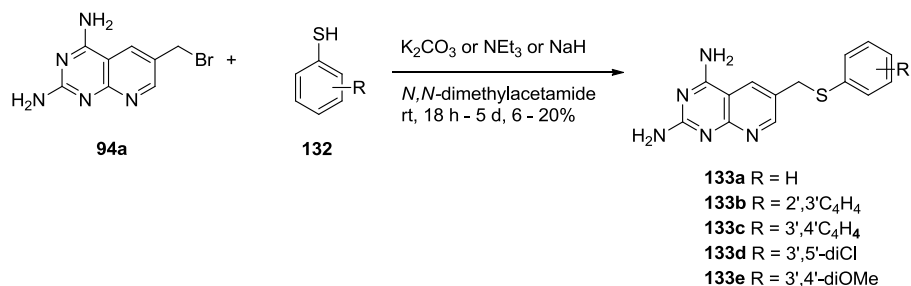
Cheung *et al.*³⁰³ recently published the conversion of N-(4-oxo-7-(2-trifluoromethyl)phenyl)-3,4-dihydropyrido[2,3-*d*]pyrimidin-2-yl)pivalamide **128** (Scheme 12) into an intermediate 4-chloro derivative by reaction with POCl₃ which was subjected to reaction with various primary and secondary alkylamines under microwave irradiation to afford various 4-*N*-substituted 7-(2-trifluoromethyl-phenyl)pyrido[2,3-*d*]pyrimidine-2,4-diamines **129a-d** in around 60% yield over two steps.

Scheme 13: Synthesis of (*S*)-2-(4-(((2,4-diaminopyrido[2,3-*d*]pyrimidin-6-yl)methyl)amino) benzamido)pentanedioic acid



Harrington, P. J.²⁹⁴ described the synthesis of the classical compound **131** (Scheme 13) by the reductive alkylation of **92a** using benzoyl glutamic acid and NaBH₃CN as the reducing agent. The one-step reaction involves the formation of an intermediate Schiff base by the condensation of the aldehyde moiety of **92a** and the aniline of **130** which is reduced by NaBH₃CN. The reaction however, was slow (10 days) with poor yields (33%). Subsequent ester hydrolysis afforded the target compound **131** in 86% yield.

Scheme 14: Synthesis of 6-(thioaryl)methylpyrido[2,3-*d*]pyrimidine-2,4-diamines

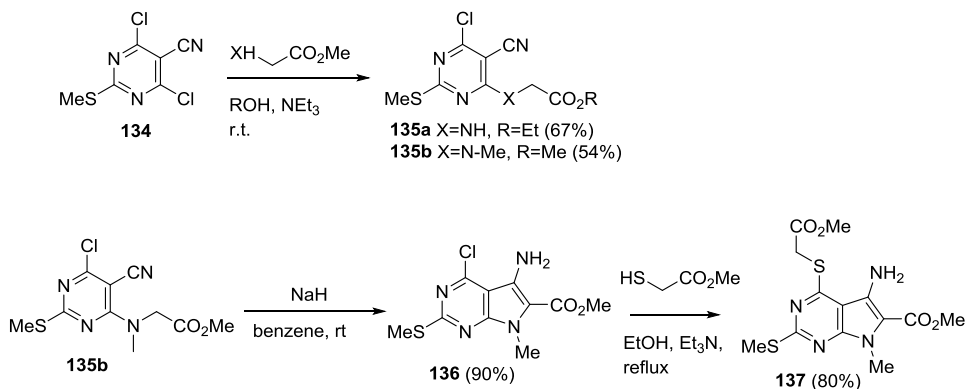


Gangjee *et al.*⁸⁰ reported the synthesis of 6-(thioaryl)methylpyrido[2,3-*d*]pyrimidine-2,4-diamines **133a-c** by the nucleophilic displacement of the bromide of **94a** with various arylthiols using K₂CO₃, NEt₃ or NaH as the base in 6-20% yields. All three bases were effective at promoting the nucleophilic displacement by the thiols.

B. 2. Pyrrolo[2,3-*d*]pyridines

B. 2.1 From substituted pyrimidines:

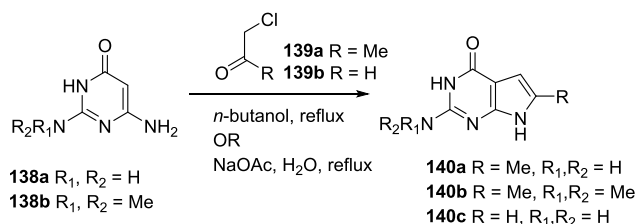
Scheme 15. Synthesis of pyrrolo[2,3-*d*]pyrimidines from 4-(alkoxycarbonylmethylamino)-6-chloro-2-methylthiopyrimidine-5-carbonitriles



Using the common intermediate 4-(alkoxycarbonylmethylamino)-6-chloro-2-methylthiopyrimidine-5-carbonitriles **135a, b** (Scheme 15) Tumkevicius *et al.*³⁰⁴ reported the synthetic route for pyrrolo[2,3-*d*]pyrimidine-6-carboxylates **136** and **137**. Reaction of

4,6-dichloro-2-methylthiopyrimidine-5-carbonitrile **134** with methyl or ethyl esters of glycine and sarcosine at room temperature in the presence of NEt_3 provided the corresponding 4-(alkoxycarbonylmethylamino)-6-chloro-2-methylthiopyrimidine-5-carbonitriles **135a-b**. The reaction of mercaptoacetic acid esters with 6-chloropyrimidine-5-carbonitriles under basic conditions and subsequent cyclization has been previously reported to afford thienopyrimidine derivatives.³⁰⁵⁻³¹¹ It was found that compounds **135a** when heated at reflux under basic conditions afforded the pyrrolo[2,3-*d*]pyrimidine derivative **136**, instead of the corresponding thieno[2,3-*d*]pyrimidine. Displacement of the chloride of **136** by mercaptoesters under basic conditions provided the target **137** in 80% yield.

Scheme 16. Synthesis of pyrrolo[2,3-*d*]pyrimidines from 6-amino-2-(dimethylamino)pyrimidin-4-(3*H*)-one

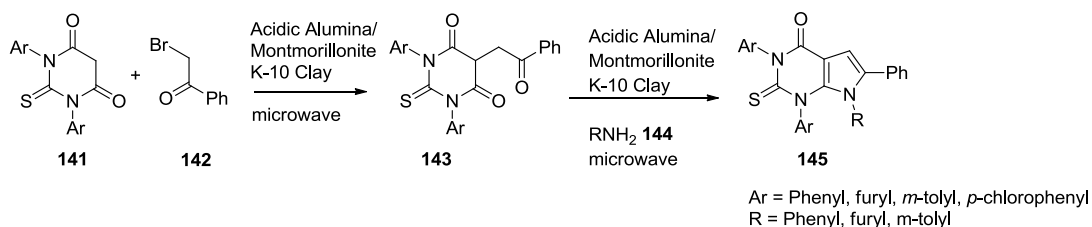


Gangjee *et al.*³¹² reported the synthesis of **140a** (Scheme 16) by the condensation of an aqueous solution of α -chloroacetone **139a** in presence of NaOAc in 70% yield. Linz *et al.*³¹³ also reported the synthesis of a series of pyrrolo[2,3-*d*]pyrimidines from 6-amino-2-(dimethylamino)pyrimidin-4(3*H*)-ones **138b** (Scheme 16). Compound **138b** on treatment with α -chloroacetone **139a** or α -chloroacetaldehyde **139b** provided the corresponding pyrrolo[2,3-*d*]pyrimidines **140a** or **140b** in 68% and 75% yields

respectively. This methodology has been previously used in the synthesis of several substituted pyrrolo[2,3-*d*]pyrimidines^{114, 179, 180, 314, 315} and has been utilized in the synthesis of pemetrexed, which is a multitargeted antifolate.³¹⁶ Secrist *et al.*³¹⁵ reported the generation of a furo[2,3-*d*]pyrimidine-2,4-diamine derivative in addition to the pyrrolo[2,3-*d*]pyrimidin-4-one when this methodology was used.

Yoneda *et al.*³¹⁷ reported the reaction of α -bromoketones with 6-amino-1,3-dimethyluracil to form pyrrolo[2,3-*d*]pyrimidines. When DMF was used as the reaction solvent the desired pyrrolo[2,3-*d*]pyrimidine product was obtained. However, when the same reaction was repeated in acetic acid instead of DMF, a mixture of pyrrolo[2,3-*d*]pyrimidine (major product) and furo[2,3-*d*]pyrimidine (minor product) was obtained.

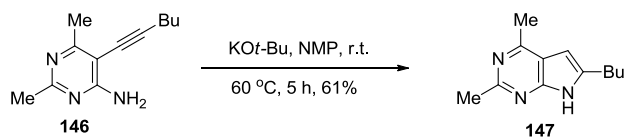
Scheme 17. Synthesis of pyrrolo[2,3-*d*]pyrimidines by Paal Knorr reaction



Kidwai *et al.*³¹⁸ reported the solid supported synthesis of a series of twelve 1,3,7-triaryl-6-phenyl-2-thioxo-1,2,3,7-tetrahydropyrrolo[2,3-*d*]pyrimidin-4-ones **145** from readily accessible *N,N*-disubstituted thiobarbaturic acids **141** using microwave conditions by the Paal Knorr reaction (Scheme 17). Compound **141** on treatment with phenacyl bromide **142** over basic alumina or anhydrous potassium carbonate as solid support under microwave irradiation affords the corresponding 1,4-diketone intermediates **143** which were cyclized with various aromatic/heteroaromatic amines **144** over acidic

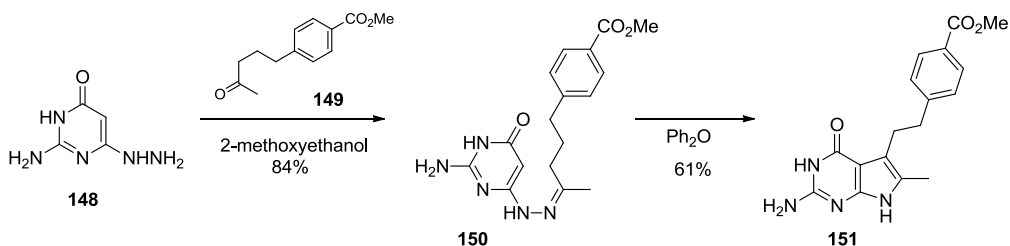
alumina/montmorillonite K-10 clay to provide the target compounds **145** in 65-88% yields.

Scheme 18. Synthesis of 6-butyl-2,4-dimethyl-7*H*-pyrrolo[2,3-*d*]pyrimidine



Rodriguez *et al.*³¹⁹ reported the synthesis of 6-butyl-2,4-dimethyl-7*H*-pyrrolo[2,3-*d*]pyrimidine **147** (Scheme 18) by Sonogashira coupling and 5-*endo-dig* cyclization. The precursor **146** was prepared by a Sonogashira coupling reaction. Compound **146** on treatment with excess potassium *tert*-butoxide in polar solvent NMP undergoes 5-*endo-dig* cyclization to afford the target **147** in 61% yield.

Scheme 19: Synthesis of pyrrolo[2,3-*d*]pyrimidines using Fisher-Indole reaction

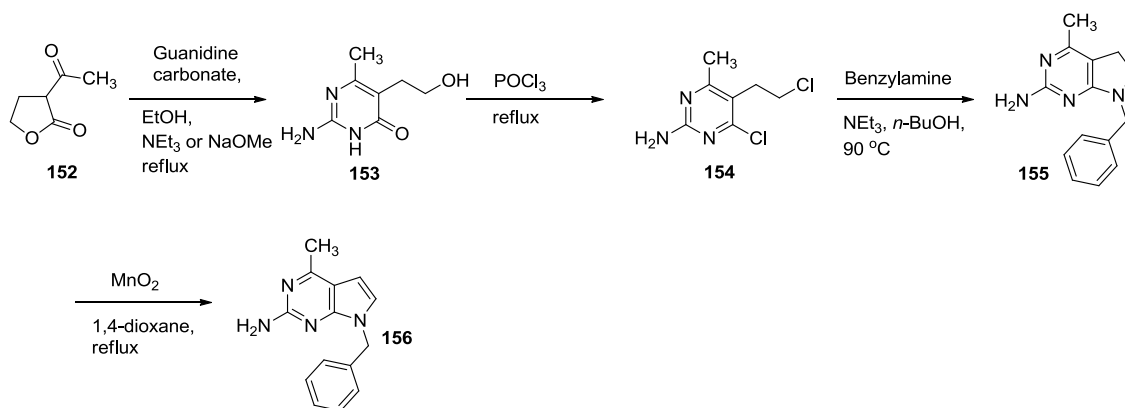


Taylor *et al.*³²⁰ synthesized methyl 4-(2-(2-amino-6-methyl-4-oxo-4,7-dihydro-3*H*-pyrrolo[2,3-*d*]pyrimidin-5-yl)ethyl)benzoate **151** (Scheme 19) by a Fisher-Indole approach. Reaction of 2-amino-6-hydrazinylpyrimidin-4(3*H*)-one **148** with one equivalent of methyl 4-(4-oxopentyl)benzoate **149** in 2-methoxyethanol under reflux afforded the requisite intermediate **150** in 84% yield. The key cyclization step was accomplished by thermolysis of **150** in refluxing diphenyl ether under argon. This

regioselective process provided the pyrrolo[2,3-*d*]pyrimidine **151** in 61% yield.

Gangjee *et al.*²²⁹ reported the synthesis of 7-benzyl-4-methyl-7*H*-pyrrolo[2,3-*d*]pyrimidin-2-amine **156** (Scheme 20) from 2-acetylbutyrolactone **152** by a modification of an earlier synthetic route described by Badaway *et al.*³²¹ Heating **152** and guanidine carbonate at reflux in absolute EtOH in the presence of either NEt₃ or NaOMe afforded intermediate **153** in 57 - 69% yields.

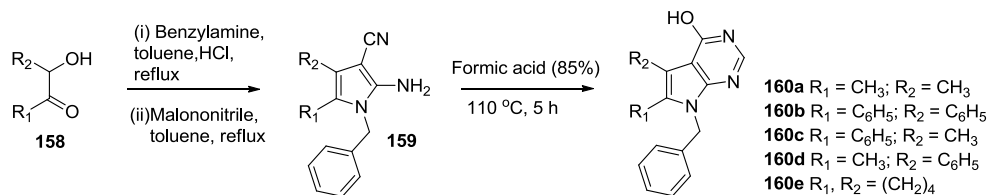
Scheme 20. Synthesis of 7-benzyl-4-methyl-7*H*-pyrrolo[2,3-*d*]pyrimidin-2-amine



Reaction of **153** by heating with phosphorus oxychloride at reflux gave the corresponding chloro derivative **154** which was condensed with benzylamine under basic conditions at reflux in *n*-BuOH to give the tetrahydro pyrrolo[2,3-*d*]pyrimidine **155** in 50% yield. Oxidation of **155** with MnO₂ afforded 7-benzyl-4-methyl-7*H*-pyrrolo[2,3-*d*]pyrimidin-2-amine **156** in 50% yield.

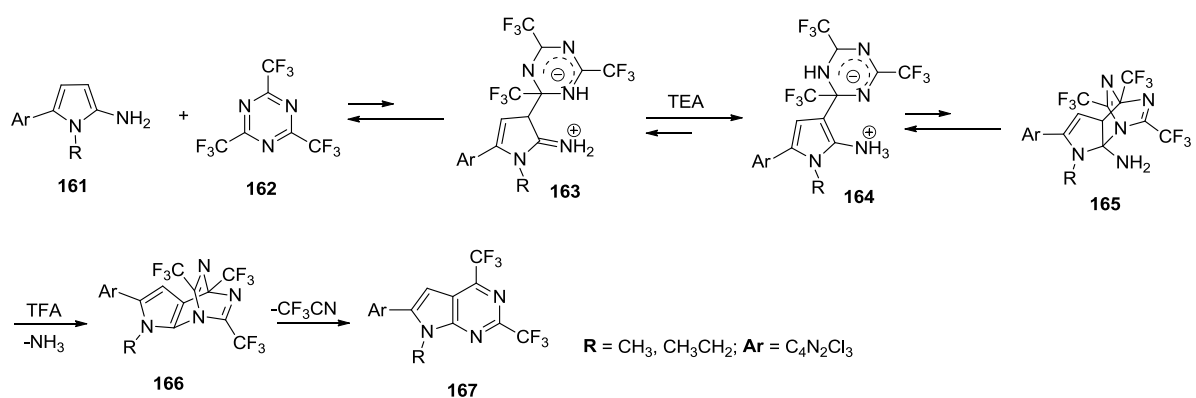
B. 2. 2. From substituted pyrroles

Scheme 21. Synthesis of pyrrolo[2,3-*d*]pyrimidines from 1-benzyl-2-amino-3-cyanopyrroles



Traxler *et al.*¹⁸⁶ reported the synthesis of a series of pyrrolo[2,3-*d*]pyrimidines (Scheme 21) starting from substituted α -hydroxy ketones **158**. Ketones **158** were converted to substituted 1-benzyl-2-amino-3-cyanopyrroles **159** by treatment with benzylamine at reflux in toluene and further condensation with malononitrile in toluene at reflux. Cyanopyrroles **159** underwent condensation with 85% formic acid at reflux to provide the target **160a-e**.

Scheme 22. Conversion of a 2-amino pyrroles to pyrrolo[2,3-*d*]pyrimidines



De Rosa *et al.*³²² reported the conversion of a 2-amino pyrroles to the corresponding pyrrolo[2,3-*d*]pyrimidines **167** (Scheme 22). The 2-amino pyrroles **161** on reaction with 2,4,6-tris(trifluoromethyl)-1,3,5-triazine **162** gives the pyrrolo[2,3-

d]pyrimidine **167**. According to the proposed mechanism, (Scheme 22) the initially formed unstable intermediate **163** converts to a zwitterion intermediate **164** in presence of base triethylamine. Compound **164** undergoes a cascade reaction to provide **165**. The cycloadduct **165** eliminates ammonia to form pyrrole **166**, which undergoes a retro Diels-Alder reaction to give the target pyrrolo[2,3-*d*]pyrimidines **167**.

C. STATEMENT OF THE PROBLEM

The present section deals with design and synthesis of inhibitors and molecular modeling studies in the following four areas:

C.1. ANTIFOLATES

- A. Selective pJDHFR inhibitors as anti-opportunistic agents and molecular modeling studies in pJDHFR and tGDHFR homology models.
- B. Development of a tGTS homology model, docking studies and topomer CoMFA studies with bicyclic tGTS inhibitors.

C.2. RECEPTOR TYROSINE KINASE INHIBITORS

- C. Inhibition of multiple receptor tyrosine kinases as potential antiangiogenic agents, molecular modeling studies of multiple kinase inhibitors with EGFR, VEGFR2 and a PDGFR- β homology model and topomer CoMFA studies with bicyclic RTK inhibitors.

C.3. COLCHICINE SITE BINDING ANTI-MITOTIC AGENTS

- D. Novel colchicine site tubulin binding agents as antimitotic agents and molecular modeling studies of colchicine site binding agents reported in our laboratory.

C.1. ANTIFOLATES

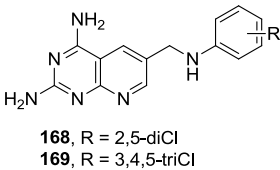
Selective pjDHFR inhibitors as anti-opportunistic agents and molecular modeling studies in pjDHFR and tgDHFR homology models.

C.1.1. Selective pjDHFR inhibitors as anti-opportunistic agents

Opportunistic infections caused by *Pneumocystis jirovecii* can cause pneumocystic pneumonia (PcP) in immunocompromised patients.^{323, 324} *P. jirovecii* is the most prevalent infection in HIV-AIDS patients³²⁴ and is a growing concern in non-HIV patients.³²⁵ Current therapeutic agents for treatment of PcP include SMX (targeting DHPS) and TMP (targeting DHFR). Although TMP-SMX is an effective first line therapy, the combination is limited by severe toxicity.³²⁵ Additional limiting factors include lack of selectivity (TMP or PTX), development of resistance (sulfa drug component), require co-administration of leucovorin (with TMQ or PTX) and have shown limited utility in severe cases (TMQ/leucovorin). Attempts to treat PcP with TMP alone either therapeutically or prophylactically often fail. Results from studies attempting to link this failure to mutations in pjDHFR have been inconclusive.^{51, 326, 327} Thus, agents that combine the potency of TMQ or PTX and the selectivity of TMP in a single agent are highly desirable in a clinical setting. Agents reported in the literature thus far lack these characteristics and remain a significant challenge in the treatment of opportunistic infections. Additionally, single agents that can target multiple opportunistic infectious agents would be highly desirable and would significantly reduce the patient burden, increase compliance and reduce the treatment costs by reducing the need for multiple treatment regimens.

1	--MVGSLNCIVAVSQNMGIKNGDLWPPLRNEFRYFQRMITT---SSVEGQNVLVIMGK	55	P00374	DYR_HUMAN
1	MDWQKSLTLIALTILSRIGLKNLDPWK-LKSDMMFFSRVTSGLLVTRSTGQNVLMGR	59	Q9UUP5	Q9UUP5_PNEJI
1	MNQKSLTLIALTTTSYGIGRSNSLPWK-LKKEISYFKRVISFVPFTDFSFMNVLVLMGR	59	P16184	DYR_PNECA
	** .***: . *** .*** *:..*: **:			:**::*
56	KTWFSIPEKRNRLPKGRINLVLSRELKEPPQGAHFLSRSLDALKLTEQP---ELANKVDM	112	P00374	DYR_HUMAN
60	KTWESLPAHSRPLKNRINVVISRQEVLDDGGAYHARSLDADALLLSQIYDSTSQTQLNR	119	Q9UUP5	Q9UUP5_PNEJI
60	KTWESLPLQRPRLPKGRINNVITRNESLDLGNGIHSAKSLDHAELELYRTYGESESSVQINR	119	P16184	DYR_PNECA
	*** : * : **** **:*: : . . :****.* * :			:::
113	VWIVGGSSVYKEAMNHGHLKLFLVTRIMQDFESDTFFPEIDLEKYKLL-----PE	162	P00374	DYR_HUMAN
120	FVFIGGGLYKAAMEHSRLNRIIATVIHNEVDCEVFPIDFRSSQSCLPWRKQDHSVLEA	179	Q9UUP5	Q9UUP5_PNEJI
120	IFVFIGGLYKAAHDHPKLDRI MATI IYKDICHCVFFLKFRDKEWSSVKKKHSDLES	179	P16184	DYR_PNECA
	:::*:.** ***: ::*. * : ..*.*.*** ..			
163	YPG--VLSDVQEEKGIKYKFVYEYKND	187	P00374	DYR_HUMAN
180	WVGSKVPQGKINENGFIYEFEMNWIRDI	206	Q9UUP5	Q9UUP5_PNEJI
180	WVGTKVPFHGINEDGFDEYEFEMWTRDL	206	P16184	DYR_PNECA
	: * * * : * : * * * : *			

Pneumocystis carinii (pc) had been previously misidentified as the causative agent of pneumocystis pneumonia in humans. Cody *et al.*⁴⁸ reported that pcDHFR and pjDHFR differ by around 38% in their sequence (Figure 48) with 79 residues differing overall. Of these, 9 residues differ in the active site of pjDHFR compared to hDHFR and pcDHFR.⁹¹ Current DHFR inhibitors such as TMP and MTX were shown to inhibit pcDHFR and pjDHFR with different IC₅₀s.⁴⁸



Gangjee *et al.*^{74, 80, 330-334} and others^{44, 284, 301, 335-338} have previously reported DHFR inhibitors of diverse chemical classes that target DHFR from opportunistic infections such as *P. carinii*, *P. jirovecii*, and *T. gondii* in an attempt to design agents that can target the

DHFR from these species potently and selectively over hDHFR. Gangjee *et al.*³³³ reported a series of pyrido[2,3-*d*]pyrimidine compounds in which the 2,5-dichlorophenyl substituted compound **168** (Figure 49) was the most selective inhibitor of both pcDHFR and tgDHFR. In this series compounds with an electron withdrawing group in the side chain phenyl ring afforded better inhibition of pcDHFR than compounds with electron donating groups. Additionally, Cody *et al.*^{48, 91} reported that **168** displayed potent and selective inhibition of pjDHFR (K_i pjDHFR = 2.7 nM, K_i hDHFR = 24.4 nM; 9.0 fold selective) while showing approximately 2.3 fold selectivity for pcDHFR (K_i pcDHFR = 6.3 nM). In the same series, the 3,4,5-trichlorophenyl substituted pyrido[2,3-*d*]pyrimidine **169** (Figure 49) also showed good selectivity and potency against pjDHFR. Very recently Cody *et al.*⁹¹ have reported the X-ray crystal structures of **168** with hDHFR and its Q35K and Q35S/N64F variants.

While several high resolution X-ray crystal structures of pcDHFR have been reported in the literature, there are no reported crystal structures of pjDHFR. Hence, molecular modeling studies of **168** in pjDHFR required the generation of a homology model.

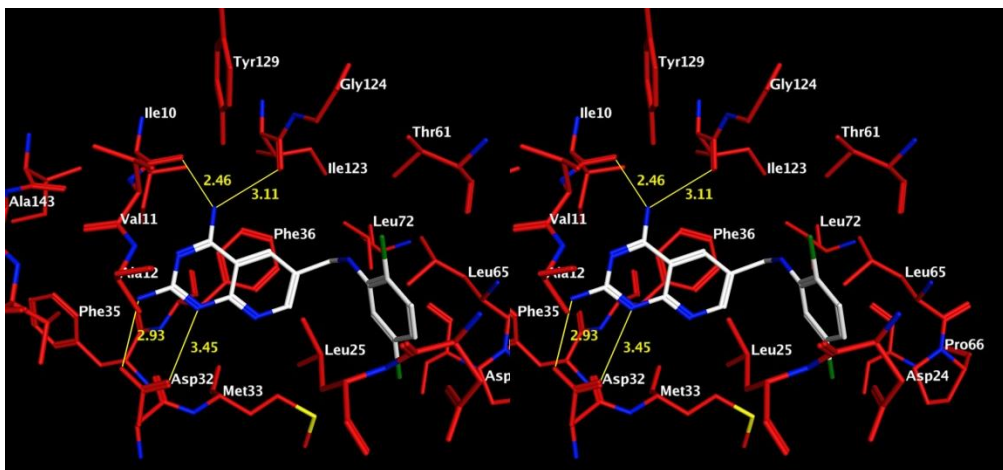


Figure 50. Stereoview. Docked pose of **168** in the active site of the homology model for pjDHFR.

Figure 50 shows the docked pose of **168** in the active site of a pjDHFR homology model generated using pcDHFR as the template. In this pose the protonated N1 and 2-NH₂ of **168** interact in an ionic bond with Asp32. This bidentate ionic bond with a conserved acid residue has been observed in most DHFR crystal structures.^{31, 32, 40, 53} The 4-NH₂ moiety forms hydrogen bonds with the backbone of Ile10 and Ile123. The pyrido[2,3-*d*]pyrimidine scaffold is stabilized by a pi-stacking interaction with Phe36 and with side chain carbon atoms of Met33 and Leu25. The 2',5'-dichlorophenyl side chain of **168** resides in a hydrophobic pocket formed by the side chains of Leu25, Thr61, Ser64, Leu65, Pro66 and Ser69. In this model the 2'-Cl of **168** is oriented towards the side chain OH of Thr61 (3.4 Å) and could form stabilizing Cl...O halogen bonding³³⁹ interactions. Alternate low energy docked poses (not shown) of **168** (within 2 kcal/mol of the pose described in Figure 50) show the formation of a hydrogen bond between the side chain NH of **168** and Ile123 in the pocket.

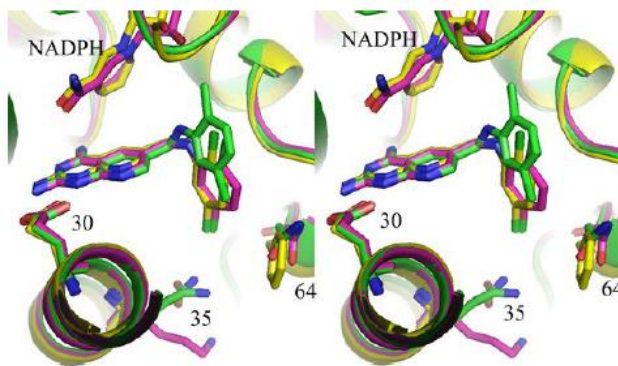


Figure 51. Stereoview. Docked pose of **168** in the pjDHFR homology model (Cody *et al.*⁹¹)

Cody *et al.*⁹¹ recently reported the docked conformation (Figure 51) of **168** in a pjDHFR homology model. With the exception of the orientation of the 2',5'-diCl phenyl side, the model described in Figure 50 matches the model reported by Cody *et al.* In their model Cody *et al.*⁹¹ reported that the 5'-Cl atom is oriented toward Pro66 and Ser69. Poses

similar to the one described by Cody *et al.* were also obtained within 1 kcal/mol of the docked pose of **168** described in Figure 50 above.

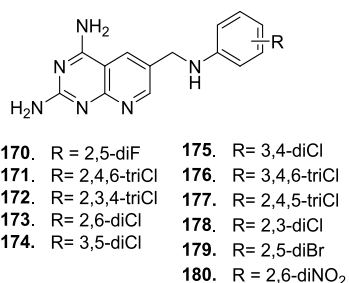


Figure 52. Structures of target compounds **170 – 180**

Hence compounds **170 – 180** (Figure 52) were designed to determine the effect of the nature and position of the electron withdrawing substituents on the terminal phenyl ring on potency and selectivity against pjDHFR.

The 2',5'-diF substituted compound **170** was previously synthesized in the Gangjee laboratory.³⁴⁰ Biological evaluation studies for **170** indicate that it displays excellent potency (pjDHFR IC₅₀ 0.057 μ M) and selectivity (around 280-fold) for pjDHFR over hDHFR. Hence, bulk synthesis of **170** was performed to enable testing in an animal model.

Docking studies performed with **170 – 180** in the pjDHFR homology model indicate that the proposed compounds retain the key binding interactions seen in the docked conformation of the lead **168**. An example of the docking is shown in Figure 51, which shows the docked conformation of **173** in the pjDHFR homology model.

Figure 53 shows the docked pose of the target **173** in the active site of a pjDHFR homology model generated using pcDHFR as the template. In this pose the protonated N1 and 2-NH₂ of **173** interact in an ionic bond with Asp32.

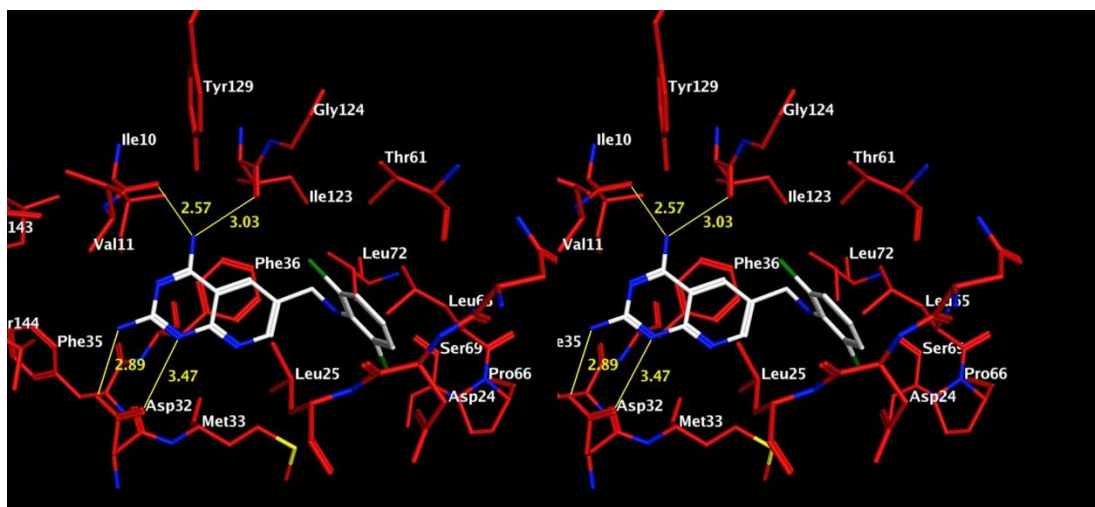


Figure 53. Stereoview. Docked pose of **173** in the active site of the homology model for pjDHFR.

This bidentate ionic bond with a conserved acid residue has been observed in most DHFR crystal structures. The 4-NH₂ moiety forms hydrogen bonds with the backbone of Ile10 and Ile123. The pyrido[2,3-*d*]pyrimidine scaffold is stabilized by a pi-stacking interaction with Phe36 and with side chain carbon atoms of Met33 and Leu25. The 2',6'-dichlorophenyl moiety of **173** resides in the hydrophobic pocket formed by the side chains of Leu25, Thr61, Ser64, Leu65, Pro66 and Ser69. In contrast to **168**, the 2',6'-dichlorophenyl ring of **173** shows a different orientation relative to the pyrido[2,3-*d*]pyrimidine scaffold. This is probably a reflection of the influence of the substitution pattern on the ring and/or interaction of the halogen atoms with the amino acids in the binding pocket and could perhaps influence the binding potency and/or selectivity of these compounds against pjDHFR. The docked conformations of other compounds in this series are presented in the Appendix.

C.1.1.2. Design of novel inhibitors: 2,4-Diamino-6-(thioaryl)methylpyrido[2,3-*d*]pyrimidines and 2,4-Diamino-6-(oxoaryl)methylpyrido[2,3-*d*]pyrimidines as pjDHFR inhibitors

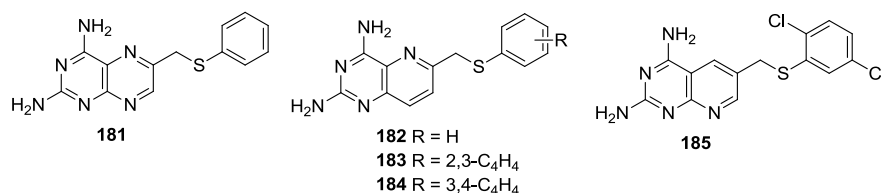


Figure 54. Structures of compounds **181** – **185**

Piper *et al.*³⁴¹ and Queener *et al.*³⁴² reported **181** (Figure 54) as a highly selective compound against both pcDHFR and tgDHFR with selectivity ratios (vs rLDHFR) of 25.9 and 319, respectively. However **181** lacked potency against pcDHFR (9.5 mM) and tgDHFR (0.77 mM). In addition, **181** lacked potency in cell culture, possibly due to a combination of weak DHFR inhibition and lack of cell penetration. Gangjee *et al.*³⁴³ later designed **182** – **184** (Figure 54) as 2,4-diamino-8-deaza analogues of **181**. cLogP calculations of **182** – **184** indicated that these compounds should display improved cell penetration due to improved clogP values compared to **181**. Compound **182** displayed marginally improved potency compared to **181** against pcDHFR and tgDHFR but lacked the selectivity of **181**, thereby demonstrating the importance of N8 for selectivity. Gangjee *et al.*³⁴⁴ later reported **185** (Figure 54) as a part of a series of analogs designed to explore the importance of the N5 for potency and/or selectivity towards pcDHFR or tgDHFR. Compound **185** displayed potent inhibition of pcDHFR (IC₅₀ 5.9 μM, about 2-fold better than TMP), it lacked selectivity against hDHFR (IC₅₀ 5.9 μM). The inhibitory activity of **185** against pjDHFR is not known. Compound **185** is an analogue of **168**, which displayed

potent and selective inhibition of pjDHFR.

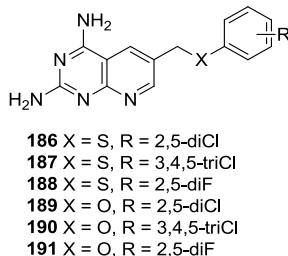


Figure 55. Structures of target compounds **186 – 191**

Target compounds **186 – 191** (Figure 55) were designed as analogs of **185** to study the influence of the nature of the linker on pjDHFR activity. Sulfur is a larger atom than oxygen and the C-S-C bond angle is shorter (98 °) as compared to a C-O-C bond angle (112 °). Thus replacing the sulfur atom of **185** with oxygen in **189** changes the bond angle between the 6-position CH₂ and the terminal substituted phenyl ring and could change the orientation of the terminal phenyl ring relative to the heterocycle that could affect the bound conformation of these molecules in the pjDHFR active site. Compound **187** and **190** were designed based on **169** which showed excellent potency and selectivity against pjDHFR in the study reported by Cody *et al.*⁴⁸ Compounds **188** and **191** were designed based on the 2,5-diF containing compound **170** which has displayed excellent potency and selectivity against pjDHFR and would serve to examine the influence of the nature of the linker on potency and/or selectivity for pjDHFR. Docking studies were carried out for **186 – 191** with the homology model of pjDHFR in order to predict their binding modes in the enzyme.

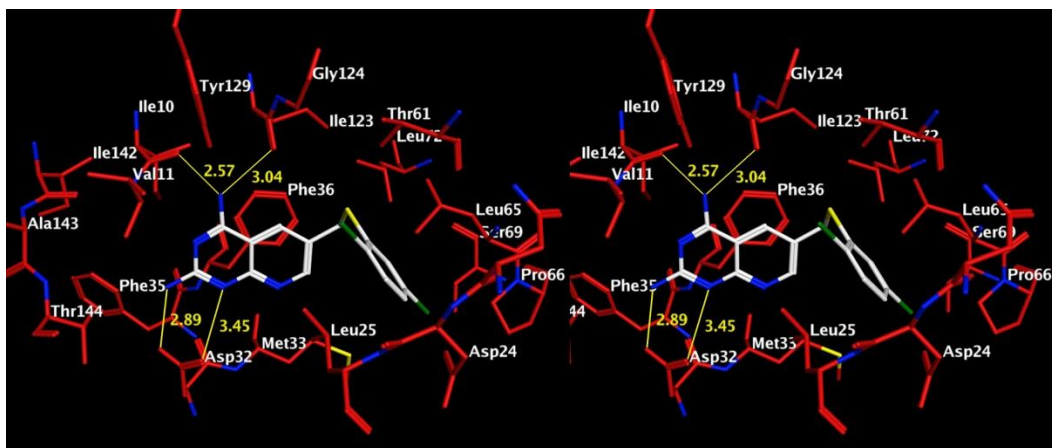


Figure 56. Stereoview. Docked pose of **186** in the active site of the homology model for pjDHFR.

Figure 56 shows the docked conformation of **186** in the pjDHFR homology model. In this pose **186** retains the key interactions of the pyrido[2,3-*d*]pyrimidine scaffold with the enzyme as seen with the lead compound **168** (Figure 50). The key difference between the docked pose of **186** compare to **168** lies in the orientation of the 2,5-dichlorophenyl moiety in the hydrophobic pocket. For **186**, the chlorine atoms can form hydrophobic interactions with the side chain atoms of Leu25, Leu65, Thr61 and Ile123 in the binding pocket, but are not seen to interact with the hydroxyl group of Thr61 where it could form halogen bonds.^{345, 346} These differences in orientation of the terminal substituted phenyl ring of these compounds could, perhaps, influence the interactions of these compounds in pjDHFR and could, in turn, affect their potency and/or selectivity against pjDHFR. The docked conformations of other compounds in this series are presented in the Appendix.

C.1.1.3. Molecular Modeling Studies with pjDHFR

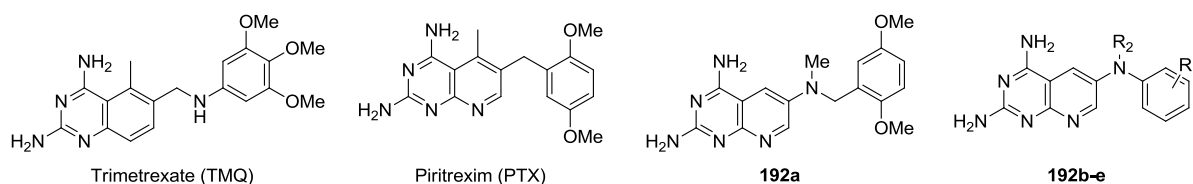
C.1.1.3.1 Development of a homology model

There are no known crystal structures of pjDHFR. Hence a homology model was

generated in order to perform modeling studies. A Basic Local Alignment Search Tool (BLAST)³⁴⁷ search of the primary amino acid sequence of pjDHFR indicated high homology (61%) between pjDHFR and pcDHFR (Figure 48). In addition, multiple high resolution (< 2 Å) crystal structures of pcDHFR bound to various non classical antifolates have been reported in the PDB (details of selected crystal structures in Table 1). Hence, homology models for pjDHFR were built based on the X-ray crystal structure of pcDHFR. Recently Cody *et al.*⁹¹ reported the generation of a homology model of pjDHFR using the crystal structure of pcDHFR as a template. After validation, the pjDHFR homology model was used for docking studies of compounds **170** – **180** (Figure 52), compounds **186** – **191** (Figure 55) and other compounds synthesized by Gangjee *et al.*

C.1.1.3.2 Docking studies with 6-substituted amino-pyrido[2,3-*d*]pyrimidine-2,4-diamines **192b-e** with a pjDHFR homology model

Table 8: Structures and inhibitory concentrations (IC₅₀, nM) of **192a**⁷² and **192b-e**³⁴⁸ against pjDHFR, pcDHFR and hDHFR



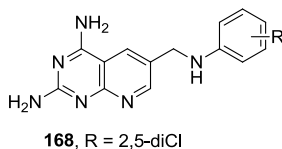
Comp.	R ₁	R ₂	pjDHFR	pcDHFR	hDHFR	Hu/Pj
192a				84	8500	
192b	H	Me	2.2	75.5	57	25.6
192c	H	H	300	2300	193	0.6
192d	3,4,5-triF	Me	4.1	228	148	35.4
192e	3,4,5-triF	H	866	8980	3070	3.5

Gangjee *et al.*³⁴⁸ described the synthesis and biological evaluation of **192b-e** (Table 8). Transposition of the 5-methyl group of PTX and TMQ to the N9-position in pyrido[2,3-*d*]pyrimidine analogs improves potency as well as selectivity against pathogen DHFR.³³⁰ Compound **192a**⁷² exhibits 100-fold selectivity for pcDHFR over hDHFR. A crystal structure of **192a** with hDHFR showed that the N9-methyl moiety is **not** in hydrophobic contact with any hydrophobic side chain of hDHFR.³⁴⁹ In addition, molecular modeling studies of **192a** in pcDHFR suggested that the N9-methyl moiety of **192a** interacts with both Ile123 and Ile65 of pcDHFR. These additional interactions of the N9-methyl moiety of **192a** with pcDHFR compared to the lack of similar interactions with hDHFR could be responsible, in part, for the increased potency and selectivity of **192a** for pcDHFR compared with hDHFR. Hence compounds **192b-e** (Table 8) were designed by incorporating an N9-methyl group. This methyl group was anticipated to interact with Ile123 of pcDHFR (and also with the corresponding Ile123 of pjDHFR) and not with the shorter Val115 in hDHFR in a similar way as that of **192b**. Hence docking studies were carried out with **192b** in the pcDHFR active site (PDB: 1LY3⁸⁹) using LeadIT 1.3.0.¹³¹

The *N*-Me compounds **192b** and **192d** displayed potent and selective pjDHFR inhibitory activity.³⁴⁸ The corresponding *N*-desmethyl compounds **192c** and **192e** displayed significantly less potency against pjDHFR.³⁴⁸ Docking studies were performed in the pjDHFR homology model in an attempt to provide a molecular basis for the observed activities of **192b-e** in pjDHFR and the importance of the *N*-Me group in **192b** and **192e**.

C.1.1.3.3. Docking studies with TMP and 168 in wild type and F36C L65P double mutant pjDHFR models:

Table 9³⁵⁰: Ki values (M) against wild type pjDHFR and F36C L65P double mutant resistant pjDHFR



	Wild type pjDHFR (M)	F36C L65P Mutated pjDHFR (M)
Trimethoprim	3.5×10^{-8}	1.7×10^{-5}
168	2.7×10^{-9}	2×10^{-8}

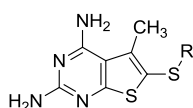
Recent studies have demonstrated the emergence of drug-resistant forms of TMP related to mutations in pcDHFR and pjDHFR.^{91, 338} One such mutation that confers resistance in pjDHFR towards TMP is the F36C L65P double mutation.⁹¹ DHFR inhibitors that retain their activity or atleast show reduced sensitivity to these mutations are, therefore, of immense interest. The results in Table 9 show that **168** only loses around 10-fold inhibitory activity in the F36C L65P double mutant as compared to the 1000-fold loss in inhibitory activity exhibited by TMP for the same mutation. There are no crystal structures of pjDHFR. Thus it was of interest to develop a homology model of the double mutant form of pjDHFR in order to perform docking studies with **168** in an attempt to provide a molecular basis for the observed activity of **168** against the double mutant pjDHFR.

C.1.1.3.3. Docking Studies of 5-Methyl-6-(substituted thio)-thieno[2,3-*d*]pyrimidine-2,4-diamines **193a-j** with a pjDHFR homology model

Compound **193d** (Table 10) was synthesized as part of a series of 5-methyl-6-(substituted thio)-thieno[2,3-*d*]pyrimidine-2,4-diamines **193a-j** (Table 10) by Gangjee *et*

*al.*³⁵¹ and displayed 0.27 μM inhibition (IC_{50}) of pjDHFR. While **193a-j** were not selective for pcDHFR over rIDHFR, compound **193f** displayed 6-fold selectivity for pjDHFR over hDHFR and about 20-fold selectivity for pjDHFR over rIDHFR. Docking studies were hence performed for **193f** to provide a possible molecular basis for the observed activity/selectivity of **193f** against pjDHFR to be utilized for the design of potent and selective inhibitors of pjDHFR.

Table 10: Biological activities of **193a-j** against pcDHFR, tgDHFR, rIDHFR, pjDHFR and hDHFR



193a R = Ph
193b R = 4-OMe-Ph
193c R = 2,6-di-CH₃-Ph
193d R = 3,4-di-CH₃-Ph
193e R = 2,5-di-OMe-Ph
193f R = 3,4-di-OMe-Ph
193g R = 3,4,5-tri-OMe-Ph
193h R = 4-NO₂-Ph
193i R = 3,4-di-Cl-Ph
193j R = 1-Naphthyl

Compound	Inhibition concentration (IC_{50} , μM)				Selectivity ratio ($\text{IC}_{50}/\text{IC}_{50}$)		
	<i>pcDHFR</i>	<i>tgDHFR</i>	<i>pjDHFR</i>	rat	rl/pc	rl/tg	rl/pj
193a	6.7	2.7		1.4	0.21	0.52	
193b	7.3	3.2		8.6	1.18	2.69	
193c	1.9	0.63		0.88	0.46	1.4	
193d	5.2	2.4		4.9	0.94	2.04	
193e	1.7	0.25		0.33	0.19	1.32	
193f	1.63	0.282	0.27	1.64	1	5.82	20.42
193g	5.9	0.99		1.8	0.31	1.85	
193h	4.9	3.4		7.1	1.45	2.09	
193i	4.4	5.1		5	1.14	0.98	
193j	10.2	2.99		3	0.29	1	
TMQ	0.042	0.01		0.00	0.07	0.3	
TMP	12	2.8		180	14	65	

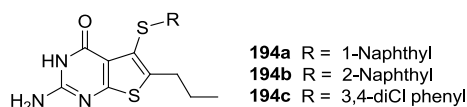
Inhibitory concentrations (IC_{50} , μM) against isolated DHFR^a and selectivity ratios^b of **194a-j**

^a These assays were carried out at 37 °C under conditions of substrate (90 μM dihydrofolic acid) and cofactor (119 μM NADPH) in the presence of 150 mM KCl. ^b Selectivity Ratios [(IC_{50} rIDHFR)/(IC_{50} pcDHFR) and (IC_{50} rIDHFR)/(IC_{50} tgDHFR)]

modeling studies, to better understand the molecular reasons for potency and selectivity of analogs and to provide a template for drug design for *T. gondii* inhibitors. Multiple high resolution (< 2 Å) crystal structures of the DHFR segment of *C. hominis* have been reported in the PDB. Hence, a homology model for tgDHFR was built based on the X-ray crystal structure of ChDHFR. Very recently Pacheo Homen *et al.*³⁵³ reported the generation of a homology model of tgDHFR using the crystal structure of *P. vivae* DHFR as a template. After validation, the tgDHFR homology model was used for docking studies of compounds **194a-c**³⁵¹ (Table 11) synthesized in our laboratory.

C.1.2.2. Molecular Modeling Studies of 2-Amino-4-oxo-5-arylthio-substituted-6-propyl thieno[2,3-*d*]pyrimidines **194a-c** with a tgDHFR homology model

Table 11: Structure of **194a-c** and inhibition concentration (IC₅₀, μM) against isolated TS.³⁵¹



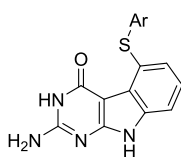
Compound	DHFR (μM)			DHFR selectivity (rl/tg)
	Human ^b	<i>E. coli</i> ^c	<i>T. gondii</i> ^d	
194a	17.0	> 17 (0)	0.017	1000
194b	> 2.6 (0)	> 2.6 (0)	0.023	>113
194c	2.2	> 25 (17)	0.02	110
PMX ^e	6.6	230	0.43	15
PDDF ^f	1.9	23	0.22	8.6
MTX	0.02	0.0088	0.033	0.6
Trimethoprim	>340 (22)	0.01	6.8	>50

^aThe percent inhibition was determined at a minimum of four inhibitor concentrations within 20% of the 50% point. The standard deviations for determination of 50% points were within $\pm 10\%$ of the value given. ^b Kindly provided by Dr. J. H. Freisheim, Medical College of Ohio, Toledo, OH. ^c Kindly provided by Dr. R. L. Blakley, St. Jude Children's hospital, Memphis TN. ^d Kindly provided by Dr. Karen Anderson, Yale Univerisy, New Haven CT. ^e Kindly provided by Dr. Chuan Shih, Eli Lilly and Co. ^f Kindly provided by Dr. M. G. Nair, University of South Alabama.

Compounds **194a-c** (Table 11) were reported by Gangjee *et al.*³⁵¹ as DHFR inhibitors in an attempt to explore the effects of substitution at the 6-position of the thieno[2,3-*d*]pyrimidine scaffold. DHFR inhibitory activities of **194a-c** showed that these compounds exhibit remarkable selectivities among DHFRs from different species. Compound **194a** in this series showed a 1000-fold selectivity against tgDHFR over hDHFR, which is better than any compound known in the literature. It was therefore of interest to perform docking studies to elucidate the probable binding mode and the molecular reasons for the observed selectivity for compounds in this series in order to design potent and selective agents against tgDHFR.

Development of a tgTS homology model, docking studies and topomer CoMFA studies with bicyclic tgTS inhibitors.

C.1.3.1. Molecular modeling studies of 2-Amino-4-oxo-5-arylthio-substituted pyrimido[4,5-*b*]indoles **194d-j with *T. gondii* thymidylate synthase**



194d Ar = phenyl	194h Ar = 4'-ClPh
194e Ar = 2'-naphthyl	194i Ar = 3',4'-diClPh
194f Ar = 1'-naphthyl	194j Ar = 4'-FPh
194g Ar = 4'-CH ₃ Ph	194k Ar = 4'-OCH ₃ Ph

Table 12. Inhibitory concentrations of **194a-d** (IC₅₀, μ M) against TS and DHFR

Compd	TS				DHFR		
	Human	<i>E.</i>	<i>T.</i>	Selectivity	Human	<i>E. coli</i>	<i>T.</i>
194d	0.21	>23	0.012	17.5	>27	>27	14
194e	2.7	>27	0.13	20.8	>32	>32	13
194f	0.27	>2.7	0.027	10	>27	27	2.7
194g	1.3	>25	0.13	10	>30	>30	11
194h	0.26	>14	0.1	2.6	28	28	2.8
194i	0.12	1.4	0.1	1.2	>27	27	2.2
194j	1.8	>2.6	0.65	2.8	>31	>31	4.6
194k	0.75	25	0.23	3.3	>30	>30	15
RTX	0.38	5.7	1.8	0.2	0.21	0.016	0.17
PMX	9.5	76	2.8	3.4	6.6	230	0.46
MTX	29	90	18	1.6	0.022	0.0066	0.011

Compounds **194d-k** (Table 12) were reported by Gangjee *et al.*³⁵⁴ as tricyclic TS inhibitors to explore the effects of substitution at the 5-position of the pyrimido[4,5-*b*]indole scaffold. TS inhibitory activities of **194d-k** showed that these compounds were highly potent for tgTS. Compound **194e** in this series showed a 21-fold selectivity against tgTS over hTS, which is better than standards PMX and RTX used in this study. TS is a highly conserved enzyme across species, thus the selectivity of **194d-g** was a novel and unexpected discovery. To our knowledge these were the first and only tgTS selective and potent inhibitors known. It was therefore of interest to perform docking studies to elucidate the probable binding mode and reasons for the selectivity for compounds in this series particularly to design potent and selective tgTS inhibitors.

C.1.4. Topomer CoMFA Analysis of Bicyclic Inhibitors of *T. gondii* Thymidylate Synthase

Topomer CoMFA applies conventional CoMFA methodologies to fragments attached to a central core. By definition, fragments have at least one open valence (point of attachment to the core), which can be fixed in Cartesian space and can be used to align other fragments.^{275, 276} Topomers provide a reproducible way of generating consistent, automatic alignments. Additionally, ligands assembled from shape similar fragment sets tend to share biological activities.²⁷⁷ Topomer CoMFA is thus insensitive to the initial conformation of the molecules, which is a major limitation of traditional CoMFA methodology.²⁷⁷

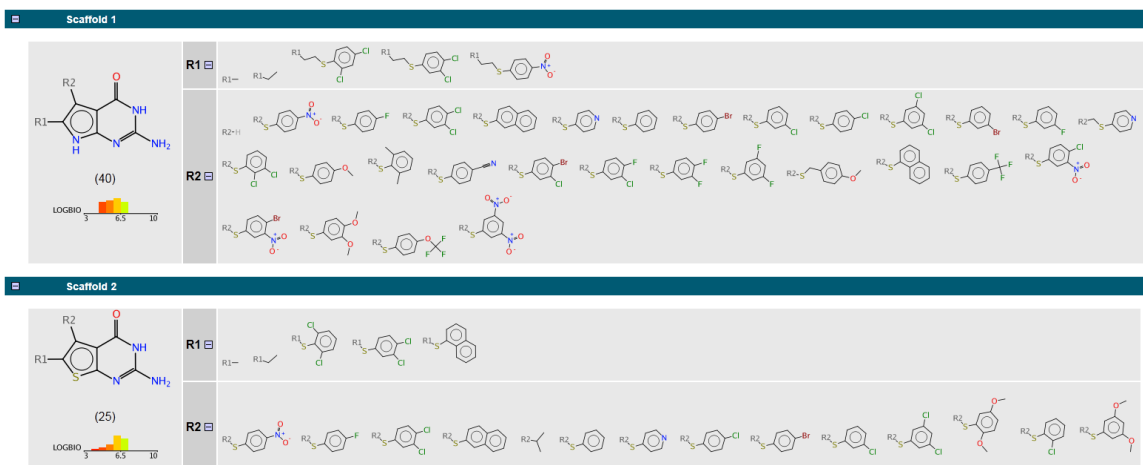


Figure 58: General structures of bicyclic non-classical pyrrolo[2,3-*d*]pyrimidines and thieno[2,3-*d*]pyrimidines for topomer CoMFA analysis

Gangjee *et al.* have reported the synthesis and biological activities against hTS and tgTS of > 100 bicyclic non-classical pyrrolo[2,3-*d*]pyrimidines^{312, 355-365} and thieno[2,3-*d*]pyrimidines^{351, 359, 362, 363, 366} containing a 2-amino-4-oxo moiety (Figure 58). Of these, 85 compounds were identified for which discrete biological activities against

hTS and/or tgTS were reported in the literature. There are no previous literature reports of CoMFA studies of these compounds.

While X-ray crystal structures have been resolved for non-classical inhibitors bound to hTS, there were no crystal structures of tgTS when this work was initiated, either in its apo form or bound to inhibitors. In the absence of structural data for tgTS, it was of interest to develop a homology model of tgTS in order to perform docking studies to gain an understanding of the binding modes of tgTS inhibitors. Additionally, a topomer CoMFA analysis of the bicyclic inhibitors could be used in order to derive a 3D-QSAR model which could be used in conjunction with docking studies to gain an understanding of the binding modes of these bicyclic compounds in tgTS and/or provide insight into the molecular basis of selectivity of some inhibitors for tgTS over hTS in order to rationally design potent and selective tgTS inhibitors.

C.2. RECEPTOR TYROSINE KINASE INHIBITORS

Inhibition of multiple receptor tyrosine kinases as potential antiangiogenic agents, molecular modeling studies of multiple kinase inhibitors with EGFR, VEGFR2 and a PDGFR- β homology model and topomer CoMFA studies with bicyclic RTK inhibitors

C.2.1. Inhibition of multiple RTKs

Receptor tyrosine kinases play a critical role in tumor development. Antitumor agents that inhibit tumor induced angiogenesis by the inhibition of RTKs have been discussed in details in section A. 1. There are multiple reports in the literature regarding the use of RTK inhibitors as monotherapy^{367, 368} for cancer or the use of multiple RTK inhibitors either as single agents or in combination with other chemotherapeutic agents.³⁶⁹⁻³⁷¹

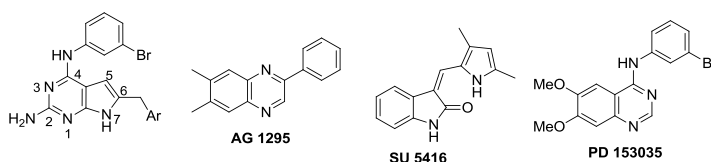
Single RTK targeting provides specificity and reduces off-target inhibition of other RTKs and could thus lower toxicity. However, the use of RTK inhibitors as monotherapy has been associated with development of alternate signaling pathway(s) to continue angiogenesis, thereby developing resistance to specific RTK inhibitors.¹⁵⁰ Additionally, crosstalk has been implicated between EGFR and other growth factor receptors involved in tumor development, aiding tumor survival.³⁷² It has been shown that inhibition of VEGF signaling had no effect on the growth of large tumors because other angiogenic factors like bFGF can substitute for VEGF.³⁷³ Treatments targeting a single RTK would be a less attractive option for tumor control in most patients. Thus

there is now a paradigm shift towards targeting multiple RTKs involved in angiogenesis rather than targeting single RTKs. Targeting multiple RTKs overcome possible resistance and reduce alternative pathways for tumor growth.^{369, 370}

Since RTKs are present in endothelial cells (VEGFR, PDGFR), tumor cells (FGFR, PDGFR), and pericytes/ smooth muscle cells (FGFR, PDGFR), inhibition of more than one RTK can provide synergistic effects against solid tumors.¹⁵⁰ Combination therapy targeting VEGFR-2 (endothelial cell inhibition) along with PDGFR- β inhibition (pericytes inhibition) has been shown to increase the antiangiogenic effect even in the often intractable, late state of solid tumors.^{374, 375} Thus targeting both VEGFR-2 and PDGFR- β simultaneously is a desirable goal for antiangiogenic agents that have cytostatic and perhaps cytotoxic activity.

C.2.2. Design and Synthesis of 2-Amino-4-substituted-6-arylmethyl-7H-pyrrolo[2,3-d]pyrimidines as RTK inhibitors

Table 13: Structure and IC₅₀ (μ M) values of kinase inhibition, A 431 cytotoxicity and inhibition of CAM assay



Comp	Ar	EGFR	VEGFR 2	PDGFR- β	A431	CAM
195	2-MePh	9.19 \pm 1.8	0.25 \pm 0.04	>50	1.21 \pm 0.42	1.21 \pm 0.23
196	2,4- diCl	0.23 \pm 0.06	28.11 \pm 9.9	17 \pm 5.6	2.8 \pm 1.1	10.8 \pm 3.2
	PD153035	0.24 \pm 0.042			12.6 \pm 2.9	
	AG 1295			6.2 \pm 1.6		
	SU5416		2.43 \pm 0.32		19.2 \pm 4.2	0.032 \pm 0.005
	Cisplatin				8.2	

Gangjee *et al.*¹⁷⁹ reported *N*⁴-(3-bromophenyl)-6-(substituted benzyl) pyrrolo[2,3-*d*]pyrimidines, **195-196** (Table 13) as a part of a series of compounds that target multiple RTKs. These compounds were tested in tumor cells known to over express high levels of EGFR, VEGFR2 and PDGFR- β . Compound **195** exhibited toxicity against A431 cells (cell lines that depend on EGFR for survival)³⁷⁶ at values 10-fold better than the standard compound **SU5416** used in this assay. In addition, **195** also demonstrated a VEGFR-2 inhibition 10-fold better than the standard agent semaxinib. Compound **196** inhibited EGFR and A431 cell lines at concentrations which were comparable to or 5-fold better than the standard **SU5416**. Thus, these compounds demonstrated multiple RTK inhibitory potency in a single molecule. It was also determined that the potencies and/or selectivities of compounds in this series were sensitive to the substitution patterns at either the 4- and/or 6-positions of the pyrrolo[2,3-*d*]pyrimidine scaffold.

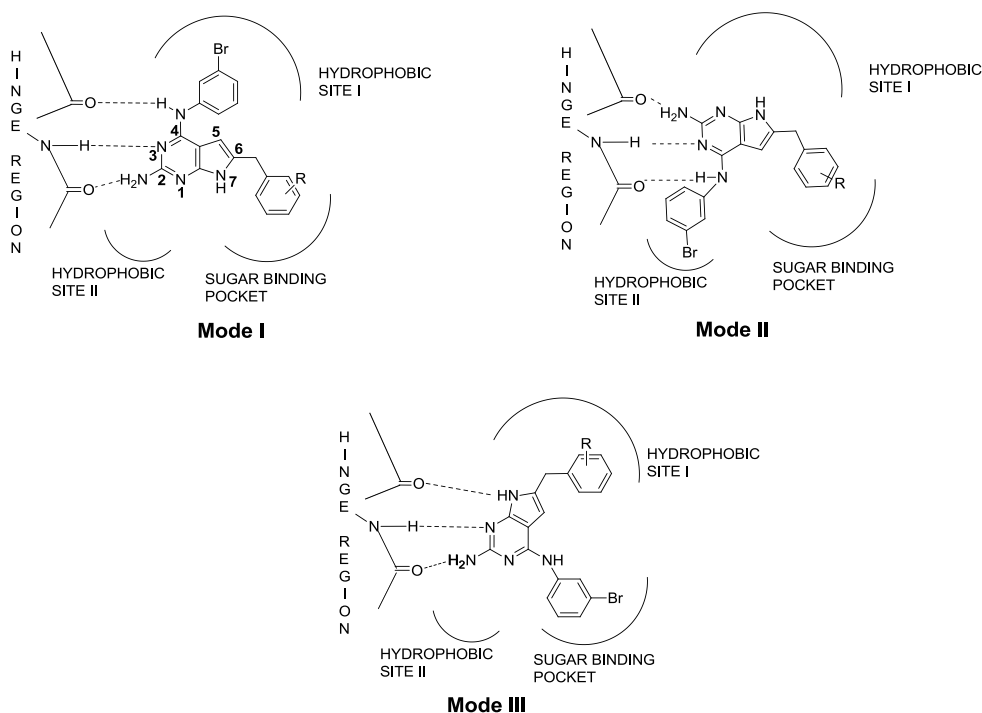


Figure 59:¹⁸³ Proposed binding modes for pyrrolo[2,3-*d*]pyrimidine RTK inhibitors

Figure 59¹⁸³ depicts the general pharmacophore model for the binding of **196a-b** in the ATP binding pocket of RTKs. In this general pharmacophore model it was envisioned that compounds like **195-196** could bind in Mode I where the 2-NH₂, N3 and the 4-NH groups could form hydrogen bonds to the hinge region of RTKs or in Mode II (flipped mode, formed by rotating the compound 180° around the 2-NH₂-C2 axis) where the hinge region hydrogen bonds are formed by the 2-NH₂ and pyrrole NH groups or in Mode III (flipped mode, formed by rotating the compound 180° around the 2-NH₂-C2 axis) where the hinge region hydrogen bonds are formed by the 2-NH₂, N1 and pyrrole NH groups. These binding modes permit the 4-bromophenyl and the 6-benzyl groups to occupy either Hydrophobic Site I or the Sugar binding pocket depending on the binding mode. Additional binding modes where the 4- or the 6-position substituent on the heterocycle occupy Hydrophobic Site II can be envisioned. The presence of such multiple binding modes could explain, in part, the multiple RTK inhibition observed with **195-196** and other analogs.

C.2.2.1. Design of 2-Amino-4-substituted-6-aryl pyrrolo[2,3-*d*]pyrimidines

Compounds **197-210** (Figure 58) were designed based on **195-196** as the lead compounds. These compounds contain, in place of the 4-NH linker group of **195-196**, an isosteric replacement such as S (**197, 198**), CH₂ (**201, 202**) or O (**205, 206**). This replacement of the linker atom with a CH₂, O- or an S- linker alters the hydrogen bonding nature of the atom (neutral or donor vs. acceptor) at the 4-position.

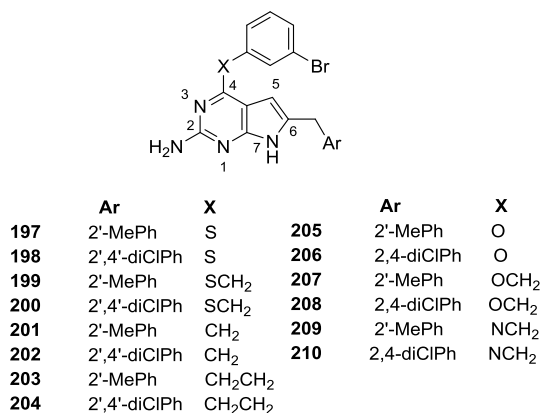


Figure 60: Proposed pyrrolo[2,3-*d*]pyrimidine RTK inhibitors

In Mode I of the proposed binding model of **195-196** in the ATP binding site (Figure 59), the 4-NH moiety forms hydrogen bonding with the hinge region of ATP. Thus, replacement of the 4-NH moiety with either a CH₂- or S- or O- would be expected to affect potential hydrogen bonding in the binding pocket, influence the binding modes of these compounds in the different RTKs and, therefore, affect the potency and/or selectivity of these compounds against the tested RTKs.

Isosteric replacements at the 4-position also alter the bond angle between the bromophenyl ring and the pyrrolo[2,3-*d*]pyrimidine scaffold (Figure 61) and can influence the relative orientations of the bromophenyl ring and the heterocycle in the bound conformation. Additionally, changing the bond angle would permit scanning the binding pockets (Hydrophobic site I or the Sugar binding pocket in Figure 59) for the 4-position substitution and, thereby, influence either the potency and/or selectivity of these compounds against the tested RTKs.

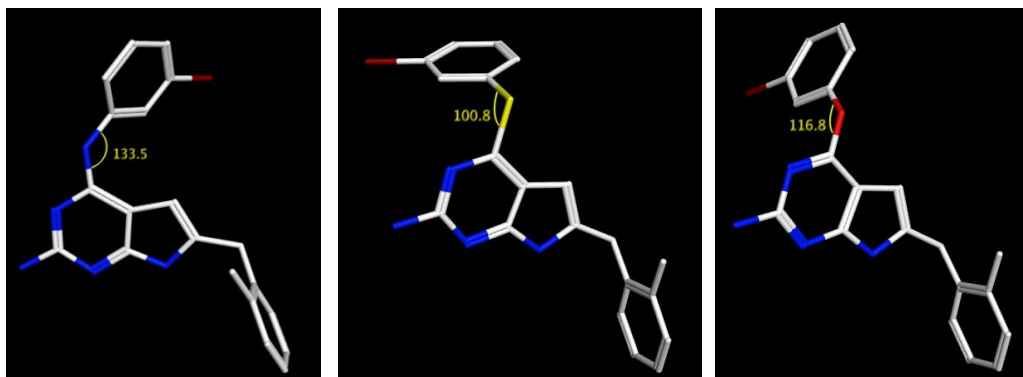


Figure 61: Comparison of C-N-C, C-S-C and C-O-C bond angles in energy minimized conformations of **195**, **197** and **205** respectively.

Compounds **199**, **200**, **203**, **204**, **207-210** (Figure 60) were designed to study the influence of the chain length at the 4-position on potency and/or selectivity of these compounds. Increasing the chain length of the 4-position substitution to two atoms compared to **197**, **198**, **201**, **202**, **205**, **206** and **195-196** respectively permits greater flexibility for the bromophenyl group relative to the pyrrolo[2,3-*d*]pyrimidine scaffold. This could, in turn, permit the bromophenyl group to bind deeper in the ATP binding site (Hydrophobic site I or the Sugar binding pocket in Figure 59) and could influence the potency and/or selectivity against the tested RTKs. Additionally, the increased chain length of these compounds could influence the binding modes of these compounds by influencing the binding interaction with the gatekeeper residue^{377, 378} in the hinge region, and thereby influence potency and/or selectivity against RTKs.

Compounds **197-210** retain the 3'-bromophenyl substitution at the 4-position and either the 2'-methylbenzyl or 2',4'-dichlorobenzyl substitution at the 6-position of the pyrrolo[2,3-*d*]pyrimidine scaffold from the lead compounds **195-196** in order to facilitate comparison.

C.2.3. Molecular Modeling Studies with RTKs

Multiple high resolution X-ray crystal structures have been reported for EGFR (Table 6) and VEGFR2 (Table 7) bound to various inhibitors. Docking studies were performed using X-ray crystal structures for EGFR and VEGFR2 for selected RTK inhibitors discovered and synthesized in our laboratory for prediction of their binding mode(s) in the kinase(s) of interest and/or explanation of observed biological activity. No crystal structures have been reported for PDGFR- β . Hence, homology models were generated for PDGFR- β for use in docking studies for prediction of binding modes of active compounds generated in our laboratory with the aim of understanding, at a molecular level, the interactions with the RTK to provide a template for the design of more potent analogs. Docking studies were performed using either MOE or LeadIT. Verification of the docking software was performed by redocking the crystal structure ligand into the active site using the same methodology used for docking of the compounds of interest and calculating the RMSD value of the best docked pose(s) compared to the crystal structure pose. In all cases, the optimized settings provided RMSD values of $< 2 \text{ \AA}^{94}$ for the best docked pose of the redocked ligand compared to its crystal structure pose.

C.2.3.1. Molecular modeling studies with proposed compounds 197-210 in EGFR

Docking studies were carried out using Flexx 3.1.2 and the proposed molecules in the ATP binding pocket of VEGFR2 and EGFR in order to validate the hypothesis that altering the linker moiety between the bromophenyl ring and the heterocyclic scaffold could alter hydrogen bonding to the hinge region and/or bound conformation of the

bromophenyl ring in the active site. As a representative example, the docked conformations of **195**, **197**, **205** and **207** in EGFR (PDB: 1M17¹⁹²) are discussed below (Figures 60a-d). Docked conformations of the other proposed analogs in EGFR and VEGFR2 are discussed in the Appendix.

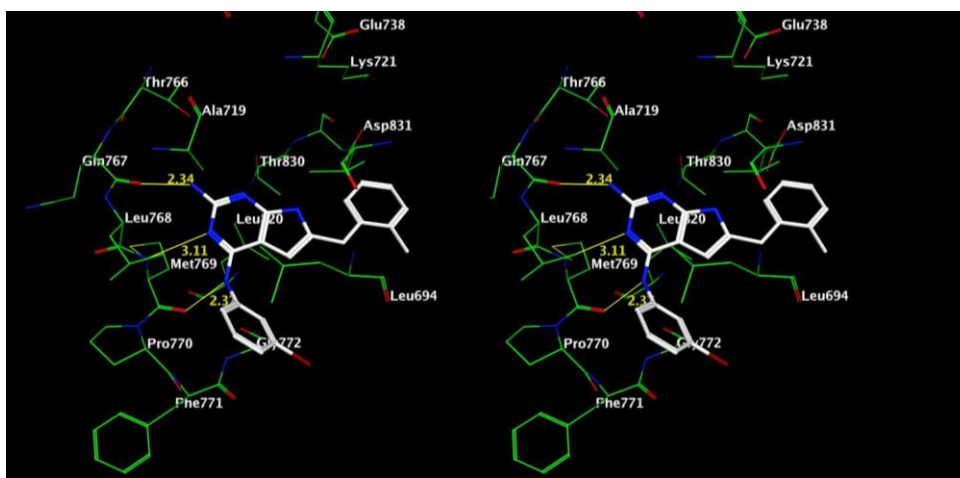


Figure 62: Stereoview. Docked conformation of **195** in the ATP binding pocket of EGFR.

In its docked conformation, **195** (Figure 62) binds in the ATP binding pocket of EGFR with the pyrrolo[2,3-*d*]pyrimidine occupying the adenine binding site in the pocket. Three hydrogen bonds are formed between the 2-NH₂, N3 and 4-NH moieties of **195** with hinge region amino acids Gln767 and Met769. This binding mode is analogous to a flipped version of proposed binding mode I (Figure 59). In the docked pose, the positions of the 4- and the 6- substitutions have been interchanged compared to proposed binding mode I. In this orientation, the bromophenyl moiety of **195** binds in Hydrophobic region II and interacts with the side chains of Pro770 and Phe771. The 6-(2'-methylbenzyl) moiety is oriented towards the back of the pocket and interacts with the side chain atoms of Leu694, Thr830 and Asp831 in the pocket. The docked score of **195**

was -24.78 kJ/mol.

The docked conformation of **197** (Figure 63) shows the compound in a flipped mode (analogous to binding mode II, Figure 59) compared to the docked conformation of **195**, in order to maintain the three hydrogen bonds between the compound (2-NH₂, N1 and the pyrrole NH moieties) and the hinge region amino acids. This change in the docked conformation also causes an exchange in the placement of the 4- and 6-position substitutions of **197** compared to **195**. The docked score of **197** was - 24.78 kJ/mol, comparable to **195**.

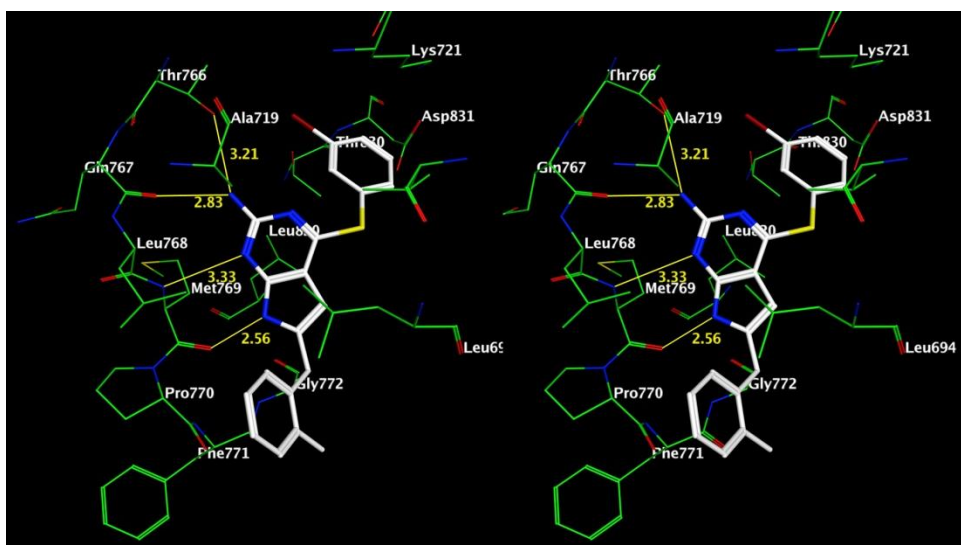


Figure 63: Stereoview. Docked conformation of **197** in the ATP binding pocket of EGFR

In contrast, **205** docks similar to the lead compound **195** in the ATP binding site of EGFR. However, the replacement of the 4-NH of **195** with an O-linker causes the loss of a hydrogen bond with the hinge region. This loss of a hydrogen bond is reflected in the lower docked score of **205** in EGFR (- 21.526 kJ/mol) compared to **195**.

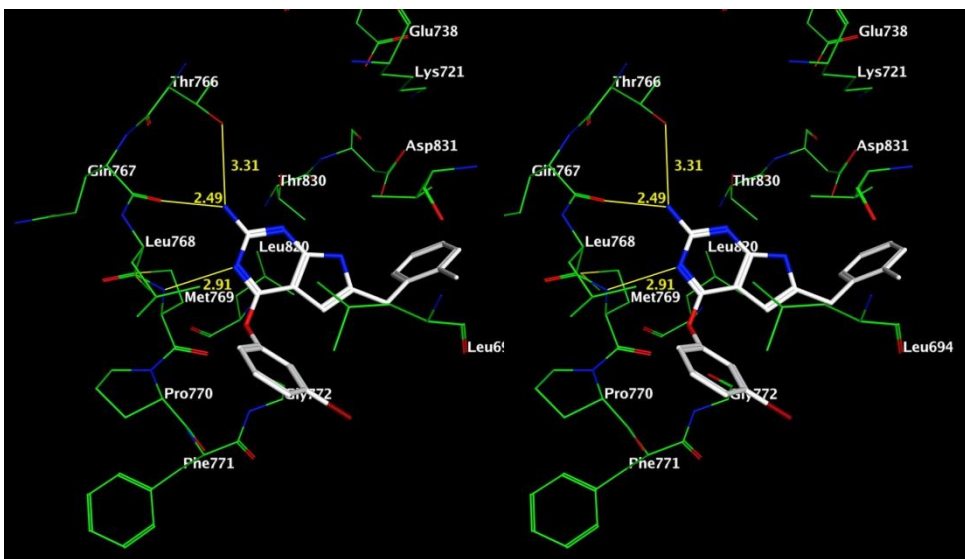


Figure 64: Stereoview. Docked conformation of **205** in the ATP binding pocket of EGFR.

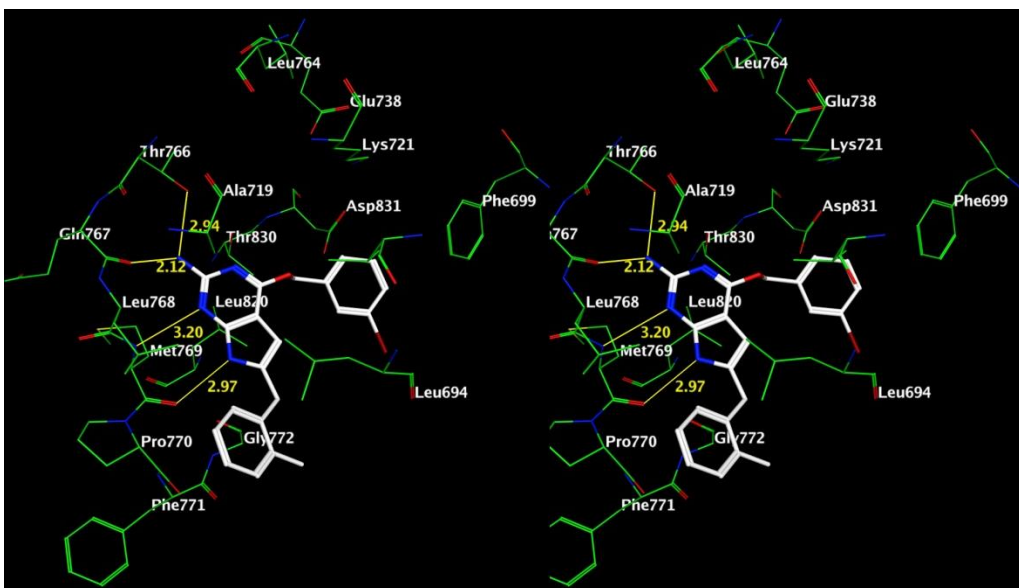


Figure 65: Stereoview. Docked conformation of **207** in the ATP binding pocket of EGFR.

The docked conformation of **207** in the EGFR pocket is similar to the docked pose of **197** (Figure 63) with the 2-NH₂, N1 and pyrrole NH moieties forming hydrogen bonds with the hinge region amino acids (Gln767, Met769 and side chain OH of Thr766). In addition, due to the longer 4-OCH₂- linker, the bromophenyl moiety binds deeper in

the hydrophobic pocket where it can form additional interactions with Phe699. The docking score of **207** was - 30.154 kJ/mol, significantly better than the docked score of **205** and better than the docked score of the lead **195**.

Similar results were seen with the docked conformations of the other proposed analogs (Appendix 1). The docking studies indicate that the docked conformations and the docking scores of the proposed compounds are sensitive to the nature of the linker. These differences could perhaps influence the kinase potency and/or selectivity of compounds in this series and provides justification for the synthesis and evaluation.

C.2.3.2. Development of a PDGFR- β homology model.

Compound **196** and other analogs reported by Gangjee *et al.*^{183, 379-382} show potent inhibition of PDGFR- β . It was therefore of interest to perform docking studies in an attempt to elucidate the probable binding mode of these compounds in PDGFR- β . At the time of initiation of molecular modeling studies against PDGFR- β , there were no reported crystal structures of PDGFR- β . In 2010 Shim *et al.*³⁴² reported the 2.3 Å X-ray crystal structure of a complex of PDGF- β with the first three Ig domains of PDGFR- β . There are no reported crystal structures of PDGFR- β with inhibitors bound to the ATP binding site.

```

1      -----LVLGRTLGSGAFGQ      14  P09619  PGFRB_HUMAN
1      ---QKPMYEVQ--WKVVEEINGNNVYIDPTQLPYDHKWEFFRNRLSFGKTLGAGAFGK      54  1PKG:A|PDBID|CHAIN|SEQUENCE
1      ---QKPMYEVQ--WKVVEEINGNNVYIDPTQLPYDHKWEFFRNRLSFGKTLGAGAFGK      54  1PKG:B|PDBID|CHAIN|SEQUENCE
1      HKYKKQFRYESQLQMVTGSSDNEYFYVDFREYEDLKWEFFRENLEFGKVLGSGAFGK      60  1RJB:A|PDBID|CHAIN|SEQUENCE
1      -----KFWWEDAEVFPRETLKLVRLGAGAGAGE      28  1QPD:A|PDBID|CHAIN|SEQUENCE
1      -----MVAGVSEYELPEDRWELPRDRLVLGKPLGEGAFGQ      36  1FGI:A|PDBID|CHAIN|SEQUENCE
1      -----MVAGVSEYELPEDRWELPRDRLVLGKPLGEGAFGQ      36  1FGI:B|PDBID|CHAIN|SEQUENCE
      * : . * * * * :

15     VVEATAGHLSHSQ--ATMKVAVKMLKSTARSEKQALMSSELKIMSHLGPLNINVNLLGAC      72  P09619  PGFRB_HUMAN
55     VVEATAYGLIKSD--AAMTVAVKMLKPSAHLTEREALMSSELKVLSYLGNHMNIVNLLGAC      112  1PKG:A|PDBID|CHAIN|SEQUENCE
113    VVEATAYGLIKSD--AAMTVAVKMLKPSAHLTEREALMSSELKVLSYLGNHMNIVNLLGAC      112  1PKG:B|PDBID|CHAIN|SEQUENCE
61     VMNATAYGISKTG--VSIQVAVKMLKEKADSSEREALMSSELKMTQLGSHENIVNLLGAC      118  1RJB:A|PDBID|CHAIN|SEQUENCE
29     VVMGYNG-----HTKVAVKSLKQGSMS--PDAFLAEANLMKQLQ--HQRLVRLY-AV      76  1QPD:A|PDBID|CHAIN|SEQUENCE
37     VVLAEAIGLDKDKPNRVTKVAVKMLKSDATEKDLSDLISEMEMMKMIGKHNIINLLGAC      96  1FGI:A|PDBID|CHAIN|SEQUENCE
37     VVLAEAIGLDKDKPNRVTKVAVKMLKSDATEKDLSDLISEMEMMKMIGKHNIINLLGAC      96  1FGI:B|PDBID|CHAIN|SEQUENCE
      * . * * * * : . : : * : : : * : : : * : : : * : : :

73     TKGGPYIYITEYCRYGDLVDVLRNKHKT-----NESFVLSYMDLVGFS      115  P09619  PGFRB_HUMAN
113    TIGGPTLVITEYCCYGDLLNFLRKRDSEFICSKTS-----PAIMEDDELALDLEDLSFS      167  1PKG:A|PDBID|CHAIN|SEQUENCE
113    TIGGPTLVITEYCCYGDLLNFLRKRDSEFICSKTS-----PAIMEDDELALDLEDLSFS      167  1PKG:B|PDBID|CHAIN|SEQUENCE
119    TLGGPIYLIIEYCCYGDLLNFLRSKREKFSDEIEYENQKRLSEEDLNLVTFEDLLCFA      178  1RJB:A|PDBID|CHAIN|SEQUENCE
77     VTQEPYIYITEYMGNSLVDFLTSPG-----IKLTINKLLDMA      115  1QPD:A|PDBID|CHAIN|SEQUENCE
97     TQDGPLVIVVEYASKGNLREYLQARRPPGLEYS--YNP-----SHNPEEQLSKDLVSCA      149  1FGI:A|PDBID|CHAIN|SEQUENCE
97     TQDGPLVIVVEYASKGNLREYLQARRPPGLEYS--YNP-----SHNPEEQLSKDLVSCA      149  1FGI:B|PDBID|CHAIN|SEQUENCE
      . * : * * * * : * : : : * : : : * : : :

116    YQVANGMEFLASKNCVHRDLAARNVLICEGLVKICDFGLARDIMRDSNYISKGSTFLPL      175  P09619  PGFRB_HUMAN
168    YQVAKGMFLASKNCIHRDLAARNILLTHGRITKICDFGLARDIKNDSNYVVGKARLFPV      227  1PKG:A|PDBID|CHAIN|SEQUENCE
168    YQVAKGMFLASKNCIHRDLAARNILLTHGRITKICDFGLARDIKNDSNYVVGKARLFPV      227  1PKG:B|PDBID|CHAIN|SEQUENCE
179    YQVAKGMFLFEKSCVHRDLAARNVLVTHGKVVKICDFGLARDIMSDSNVYVGRNARLPV      238  1RJB:A|PDBID|CHAIN|SEQUENCE
116    AQIAEGMAFIEERNYIHRDLAARNILVSDTLSCKIADPGLARLIE-DAEYTAGAKFPFI      174  1QPD:A|PDBID|CHAIN|SEQUENCE
150    YQVARGMEYLASKNCIHRDLAARNVLVTEEDNVKMIADPGLARDIHHIDYKKTINGRLFPV      209  1FGI:A|PDBID|CHAIN|SEQUENCE
150    YQVARGMEYLASKNCIHRDLAARNVLVTEEDNVKMIADPGLARDIHHIDYKKTINGRLFPV      209  1FGI:B|PDBID|CHAIN|SEQUENCE
      * : * * * : : . : * * * * : * : : . * : * * * * : * : : :

176    KWMAPESIFNSLYTTLSDVWSFGILLWEIFTLGGTPYFELPMNEQFYNAIKRGYRMAQPA      235  P09619  PGFRB_HUMAN
228    KWMAPESIFNCVYTFESDVWSYGIIFLWELFSLGSSPYPGMFVDSKFKYKMIKEGFRMLSPE      287  1PKG:A|PDBID|CHAIN|SEQUENCE
228    KWMAPESIFNCVYTFESDVWSYGIIFLWELFSLGSSPYPGMFVDSKFKYKMIKEGFRMLSPE      287  1PKG:B|PDBID|CHAIN|SEQUENCE
239    KWMAPESLFEGIYTIKSDVWSYGIIFLWELFSLGVNYPGIPVDANFYKLIQNGFKMDQPF      298  1RJB:A|PDBID|CHAIN|SEQUENCE
175    KWTAPALINYGTFITKSDVWSFGILLWEIFTLVTHGRIPYRGMTNPE-VIQNLERGVMVRPD      233  1QPD:A|PDBID|CHAIN|SEQUENCE
210    KWTAPALFDRIYTHQSDVWSFGVLLWEIFTLGGSPYPGVFPVEE-LFKLLKEGHRMDKPS      268  1FGI:A|PDBID|CHAIN|SEQUENCE
210    KWTAPALFDRIYTHQSDVWSFGVLLWEIFTLGGSPYPGVFPVEE-LFKLLKEGHRMDKPS      268  1FGI:B|PDBID|CHAIN|SEQUENCE
      * * * * : : * * * * : * : : * : * : : * : : : * : : : * : : :

236    HASDEIYEIMQKCEWEKFEIRPPFSQVLVLLERLL-----      270  P09619  PGFRB_HUMAN
288    HAPAEYMDIMKTCDWDADPLKRPTFKQIVQLIEKQISESTNHI-----      329  1PKG:A|PDBID|CHAIN|SEQUENCE
288    HAPAEYMDIMKTCDWDADPLKRPTFKQIVQLIEKQISESTNHI-----      329  1PKG:B|PDBID|CHAIN|SEQUENCE
299    YATEIYIIMQSCWAFDSKRPSEFPNLTSLGQCLADAEAEAMYQNV      344  1RJB:A|PDBID|CHAIN|SEQUENCE
234    NCPEELYQLMRLCNKERPEDRPTFDYLRSLVEDFFTEGQYQPP      279  1QPD:A|PDBID|CHAIN|SEQUENCE
269    NCTNELYMMRDCHNAVPSQRPTFKQLVEDLDRIVALTSNQE-----      310  1FGI:A|PDBID|CHAIN|SEQUENCE
269    NCTNELYMMRDCHNAVPSQRPTFKQLVEDLDRIVALTSNQE-----      310  1FGI:B|PDBID|CHAIN|SEQUENCE
      . * : * * : * * * : * : : * : : :

```

Figure 66: Sequence alignment of PDGFR- β (P09619), FLT3 (PDB: 1PKG), FLT-3 kinase (PDB: 1RJB), LCK (PDB: 1QPD) and FGFR (PDB: 1FGI)

The 1106 amino acid sequence PDGFR- β has been reported. (Uniprot ID: P09619). A BLASTP search using MOE 2007.09³⁸³ indicated that the kinase domain amino acid sequence (amino acids 600-962) shows high sequence similarity with chain A of the c-KIT kinase complex (FLT3) (PDB: 1PKG³⁸⁴), chain A of FLT-3 kinase (PDB: 1RJB³⁴⁷, E-value: 1e-88), chain A of the lymphocyte-specific kinase LCK (PDB: 1QPD³⁸⁵) and chain A of Fibroblast Growth Factor Receptor (PDB: 1FGI³⁸⁶) as shown in the sequence alignment file above (Figure 66). Thus, a homology model was generated using MOE 2007.09 and validated for performing docking studies with PDGFR- β .

C.2.3.3. Docking Studies with N⁴-(3-bromophenyl)-7-(substituted benzyl)-7H-pyrrolo[2,3-*d*]pyrimidine-2,4-diamines as potential multiple RTK inhibitors.

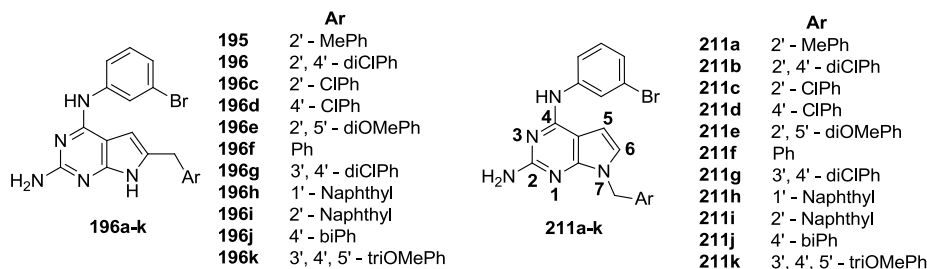


Figure 67. N⁴-(3-bromophenyl)-7-(substituted benzyl)-7H-pyrrolo[2,3-*d*]pyrimidine-2,4-diamines **211a-k** as potential multiple RTK inhibitors.

Compounds **211a-k** (Figure 67) were reported by Gangjee *et al.*³⁸⁰ as analogs obtained by transposition of the 6-position substitutions of lead compounds **195**, **196** and **196c-k** to the 7-position of the pyrrolo[2,3-*d*]pyrimidine scaffold. A general pharmacophore model with five predicted binding modes for compounds **211a-k** was proposed (Figure 68) that would enable inhibition of an increased spectrum of RTKs compared to the previously reported³⁸⁷ parent 6-benzyl substituted series.

In binding mode I, the N⁴-(3-bromophenyl) is accommodated in Hydrophobic region I. The 7-benzyl group interacts with the Sugar binding pocket. Three hydrogen bonds can be made with the hinge region *via* the 2-NH₂, N3 and 4-NH groups. In binding mode 2, the interactions in the hinge region and Hydrophobic region I are conserved. The 7-benzyl group in this mode lies in Hydrophobic region II. A 180 ° rotation of the C2–NH₂ bond in binding mode 1 produces an orientation of the molecule as depicted in binding mode 3. In this mode, the 7-benzyl group is accommodated in Hydrophobic region I, and the 3-bromoaniline lies in the Sugar binding pocket.

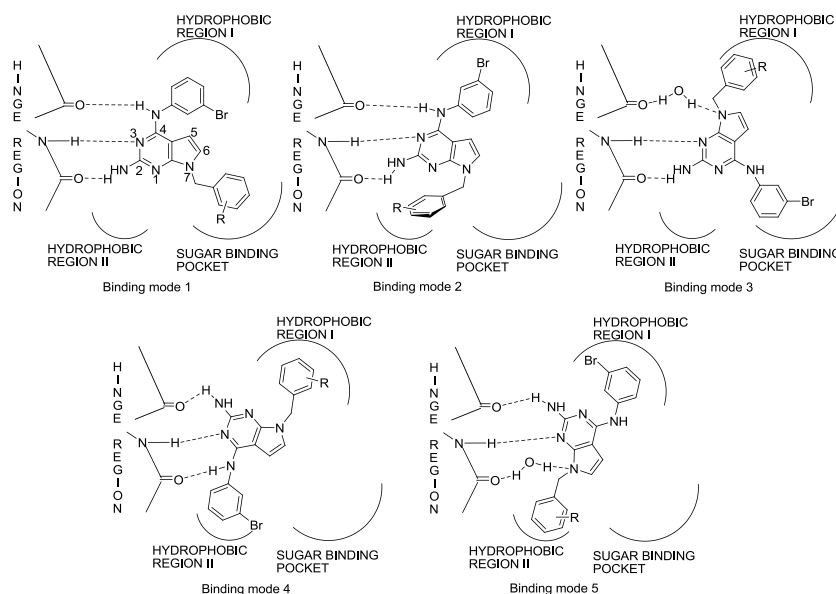


Figure 68.³⁸⁰ General pharmacophore model of pyrrolo[2,3-*d*]pyrimidines with five potential binding modes.

Three hydrogen bonds in the hinge region are formed. The N7-nitrogen is proposed to interact with the hinge region carbonyl via a water molecule bridge. Rotating the molecule in binding mode 1 by 180 ° along the hydrogen bond formed between the N3 of the molecule (hydrogen bond acceptor) and the NH at the hinge region (hydrogen bond donor), results in binding mode 4. In this mode, the 3-bromoaniline is placed in Hydrophobic region II and the 7-benzyl group lies in Hydrophobic region I. Three hydrogen bonds with the hinge region are conserved. Rotating the molecule in binding mode 3 by 180 ° along the hydrogen bond formed between the N3 of the molecule (hydrogen bond acceptor) and the NH at the hinge region (hydrogen bond donor), results in binding mode 5. In this mode, the 3-bromoaniline is accommodated in Hydrophobic region I while the N7 benzyl interacts with Hydrophobic region II. While three hydrogen bonds are proposed in the hinge region, the N7 nitrogen presumably interacts with the

hinge carbonyl via a water molecule bridge.

Molecular modeling studies were carried out for **211c** (Figure 67) and its corresponding 6-position substituted lead compound **196c** (Figure 67) in VEGFR2, EGFR and a homology model of PDGFR- β as an example to determine if the binding modes proposed in Figure 68 could be observed *in silico* and to determine the binding mode preference, if any, of compounds with substitutions at the 6- and the 7-position of the pyrrolo[2,3-*d*]pyrimidine scaffold.

C.2.3.4. Molecular modeling studies of 2-amino-4-*m*-bromoanilino-6-arylmethyl-7H-pyrrolo[2,3-*d*]pyrimidines as tyrosine kinase inhibitors

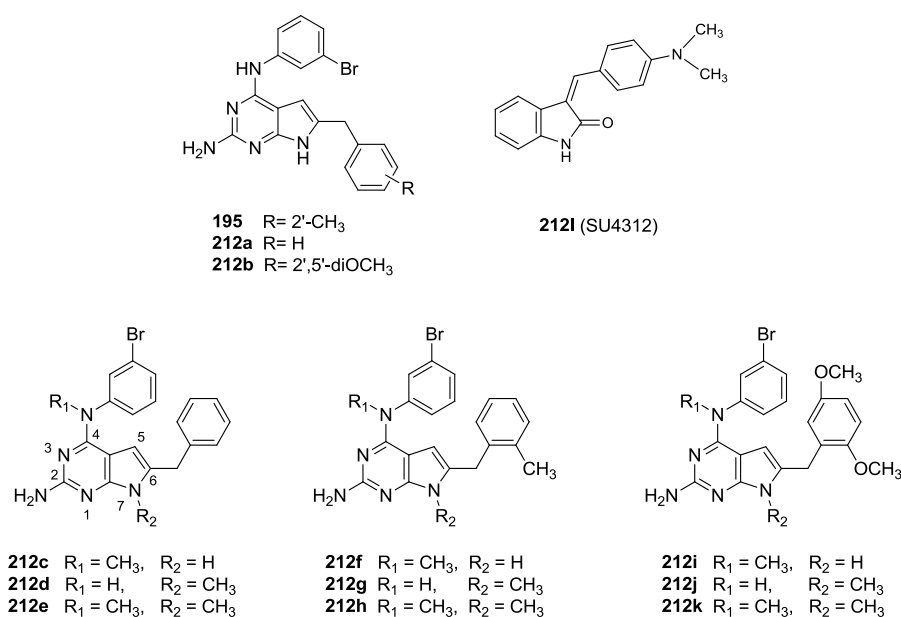


Figure 69.¹⁸³ Structures of lead compounds (**195**, **212a-b**) and analogues (**212c-k**)

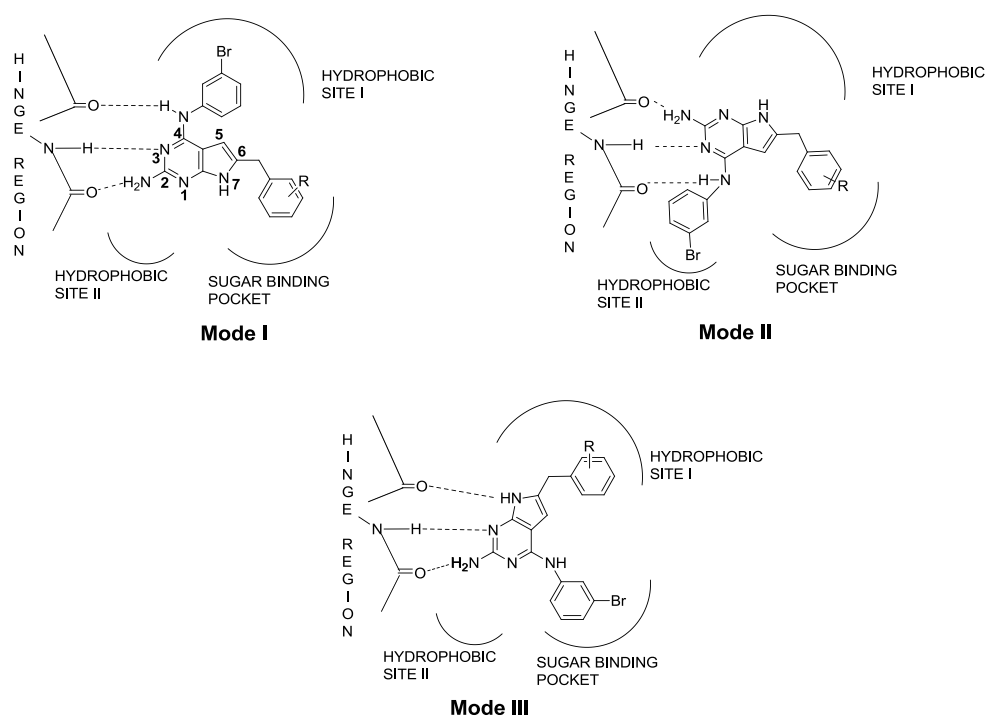


Figure 70:¹⁸³ Proposed binding modes for pyrrolo[2,3-*d*]pyrimidine RTK inhibitors

Gangjee *et al.*¹⁸³ reported the synthesis and biological evaluation against selected RTKs of a series of 2-amino-4-*m*-bromoanilino-6-benzyl pyrrolo[2,3-*d*]pyrimidines **212c-k** (Figure 69) as analogs of lead compounds **195** and **212a-b**.³⁸⁷ As proposed in the general pharmacophore model in Figure 70, compounds such as **195** and **212a-b** could adopt multiple binding modes in the ATP binding site of RTKs. It was envisioned that these hypothetical binding modes could be substantiated by the deliberate introduction of methyl groups at strategic positions on the scaffold. Thus, analogs of the three most potent previously reported lead compounds **195**, **212a-b** were designed by introduction of methyl groups at either the 4-N (**212c-e**) or N7 (**212f-h**) or both the 4-N and N7-positions (**212i-k**). Thus if the compounds adopted either Mode I and/or Mode II (Figure 70) for binding and the 4-NH was necessary for binding, compounds **212c**, **212e-f**, **212h-i** and **212k** should be poorly active. However, if the compounds bound in Mode III (Figure 70)

and the N7-H was necessary for binding, compounds **212d-e**, **212g-h**, **212j-k** should be poorly active. If however, all three modes were possible, only compounds **212e**, **212h** and **212k** should be poorly active since they would be unable to form H-bonds at both the 4-N and N7 positions. In addition, methylation at the N7- and/or the 4-N could also influence the conformation of the 4- and/or 6-substituent relative to the pyrrolo[2,3-*d*]pyrimidine scaffold and could also, in part, influence the potency and selectivity of the methylated compounds compared with the parent compounds.¹⁸³

Table 14.¹⁸³ IC₅₀ values (μM) of kinase inhibition, A431 cytotoxicity, and inhibition of the CAM assay of **195**, **212a-k**.

Compound	EGFR	VEGFR-	PDGFR-	A431	CAM
195	1.67	>50	>50	31.8	ND
212a	9.19	0.25	>50	1.21	1.21
212b	12.62	0.62	8.92	>50	1.32
212c	53.1	89.2	>500	45.7	1.56
212d	>200	>200	2.8	27.9	6.22
212e	253.6	>200	71.7	50.9	2.6
212f	31.2	>200	34.8	>500	0.93
212g	12.8	116.3	>500	204.3	3.0
212h	1.2	>200	>500	226.3	1.6
212i	143.5	>200	1.3	197.4	0.83
212j	>200	>200	348.0	35.6	3.3
212k	0.5	>200	>500	94.1	2.05
58	0.23				
212l			3.75		
Semaxanib		12.9			0.04
Cisplatin				10.6	18.2
Erlotinib	1.2	124.7	83.1		29.1
Sunitinib	172.1	18.9	12.2		1.3

The results from the biological evaluation of **212c-k** along with standard compounds **58**, **212l** (SU4312, Figure 69), semaxanib, cisplatin, erlotinib and sunitinib

are shown in Table 14.¹⁸³ These results indicate that methylation of the 4-NH and/or the 7-NH influences both the specificity and potency of RTK inhibition. Dimethylation of both the 4-N and N7 positions afforded improved whole cell EGFR inhibition compared to clinically used erlotinib. Mono methylation at the 4-N or N7 position led to improved whole cell PDGFR- β cytotoxicity compared to clinically used sunitinib. Thus docking studies were performed with **212c-k** in EGFR, VEGFR-2 and the PDGFR- β homology model to explain the molecular basis of the observed RTK inhibition.

C.2.3.5. Molecular Modeling Studies of 5- Substituted Pyrimido[4,5-*b*]indoles in a PDGFR- β Homology Model

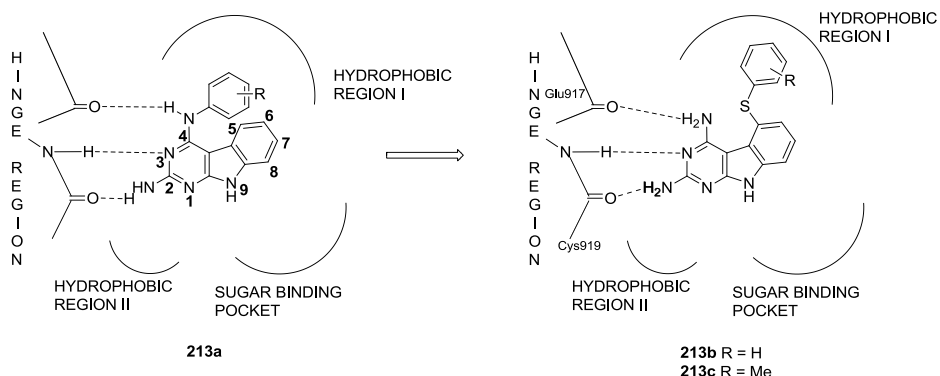


Figure 71.³⁷⁹ Design and structures of pyrimido[4,5-*b*]indoles **213b-c**.

Gangjee *et al.*³⁷⁹ reported **213b-c** (Figure 71) as agents with combination chemotherapy potential in a single molecule. Compounds **213b-c** were designed as agents with RTK, TS and as antitumor agents. Tricyclic compounds like **213a** have been reported³⁸⁸ in the literature as potent RTK inhibitors.³⁸⁸ In a general RTK model (Figure 71)^{179, 389-391} the 2-NH₂, N3 and 4-anilino nitrogen of **213a** form hydrogen bonds with the hinge region. In addition, the 4-anilino moiety lies in Hydrophobic region 1, and the

tricyclic scaffold binds in the purine binding pocket of ATP.^{186, 388} It was envisioned that transposing the phenyl ring from the 4-position of **213a** to the 5-position of the tricyclic scaffold in **213b-c** retains its binding to Hydrophobic region 1 and simultaneously allows hydrogen bonds with the hinge region. Thus compounds **213b-c** were expected to maintain RTK inhibitory activity. In addition, moving the phenyl ring from the 4- to the 5-position reveals a 2,4-diaminopyrimidine motif on the tricyclic scaffold that has shown³⁷⁹ to be highly conducive for DHFR and/or TS inhibition.

Table 15.³⁷⁹ IC₅₀ Values (μM) of kinase inhibition and A431 cytotoxicity assay of **213b-c**.

Compd	EGFR	VEGFR-2	PDGFR-β	A431 Cytotoxicity
213b	15.07 ± 3.1	22.6 ± 4.5	2.8 ± 0.42	49.2 ± 4.7
213c	10.41 ± 1.2	56.3 ± 7.1	40.3 ± 5.1	14.1 ± 2.0
PD153035	0.23 ± 0.05			
Semaxinib		12.9 ± 2.9		
DMBI			3.75 ± 0.31	
Cisplatin				10.6 ± 3.5

The kinase inhibitory activities of **213b-c** are shown in Table 15. It was seen that **213b-c** were potent inhibitors of VEGFR-2 and PDGFR-β with RTK inhibitory activities comparable or better than the standards (except **213c** for PDGFR-β). Thus docking studies were performed with **213b** in the PDGFR-β homology model to explain the molecular basis of its potent PDGFR-β inhibition.

C.2.4. Topomer CoMFA Analysis of Bicyclic Inhibitors of Multiple Receptor

Tyrosine Kinases

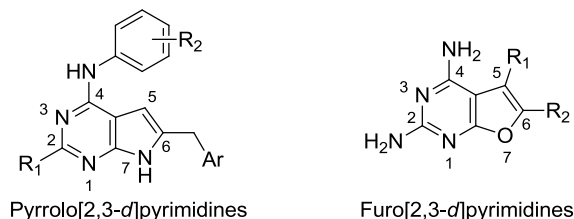


Figure 72. General structures of pyrrolo[2,3-*d*]pyrimine and furo[2,3-*d*]pyrimidine based RTK inhibitors

Gangjee *et al.* have previously reported the design, synthesis and biological evaluation of a series of RTK inhibitors based on either a pyrrolo[2,3-*d*]pyrimidine^{182, 183, 379, 380, 387, 392-394} or a furo[2,3-*d*]pyrimidine^{395, 396} scaffold (Figure 72). Since the objective of the development of these compounds was multiple RTK inhibition in a single molecule, a general pharmacophore model of the ATP binding site was used in the design of the compounds rather than a specific crystal structure of the ATP binding site of an RTK.^{379, 380, 387} Gangjee *et al.*¹⁸³ also reported molecular modeling studies to support multiple potential binding modes for these compounds in the ATP binding site of RTKs, which would enable multiple RTK inhibition.

A topomer CoMFA analysis of bicyclic pyrrolo[2,3-*d*]pyrimine and furo[2,3-*d*]pyrimidine based RTK inhibitors has not been previously reported. There are no literature reports of CoMFA/ topomer CoMFA analysis of single molecules with multiple RTK potential to determine structural features that are conducive to multiple RTK inhibitory potential.

A topomer CoMFA analysis of a compound set results in the development of 3-D steric and electrostatic maps. Thus, analysis of the pyrrolo[2,3-*d*]pyrimine and furo[2,3-*d*]pyrimidine RTK inhibitors would afford steric and electrostatic maps for individual kinases (EGFR, VEGFR2 and PDGFR- β) against which the compounds were tested. Since all the pyrrolo[2,3-*d*]pyrimine and furo[2,3-*d*]pyrimidine RTK inhibitors included in this study were designed as ATP-site kinase binders, comparison of the electrostatic and steric maps should reveal areas of similarity between the maps (common pharmacophore element) which could be used to identify regions in the molecules that contribute to multiple kinase inhibition and further drug design of molecules with multiple RTK inhibitory potential.

On the other hand, identification of the differences between the 3-D steric and electrostatic maps of the different kinases were anticipated to help identify structural features in the molecules which could be explored to enhance selectivity for a kinase or selected kinases.

C.3.COLCHICINE SITE BINDING ANTI-MITOTIC AGENTS

Novel colchicine site tubulin binding agents as antimitotic agents and molecular modeling studies of colchicine site binding agents reported by Gangjee *et al.*

C.3.1. Design of 2-amino-4-substituted-5-thioaryl-6-methyl-7-substituted pyrrolo[2,3-*d*]pyrimidines as colchicine site binding agents

Microtubules play a vital role in mitosis and cell division and are a particularly attractive target for drug development, particularly as anticancer agents. Antimitotic agents such as paclitaxel, vincristine and vinblastine among others have been successfully used

clinically in the treatment of various cancers. However, the utility of such agents are often limited by the emergence of resistant cell lines.³⁹⁷ Drug resistance to antimitotic agents is primarily caused by overexpression of Pgp and MRP1, which are unidirectional efflux pumps that transport drug molecules from the inside of the cells to the exterior. Both vinca alkaloids and paclitaxel are substrates of Pgp, leading to a reduction in their concentration in the cancer cells, thereby leading to resistance. Methods to overcome these resistance mechanisms include co-administration of agents that target the efflux pumps or the use of compounds that are not substrates of these pumps, such as epothilones.^{234-237, 239} A novel mechanism for targeting resistant cells, discovered by Gangjee *et al.*,²⁶⁶ was the development of cytotoxic agents which reverse drug resistance.

Compounds **214a-d** were discovered by Gangjee *et al.*²⁶⁶ and displayed excellent antimitotic properties and reversed drug resistance, by restoring tumor cell sensitivity to other antimitotics to which the tumor cells had become resistant.

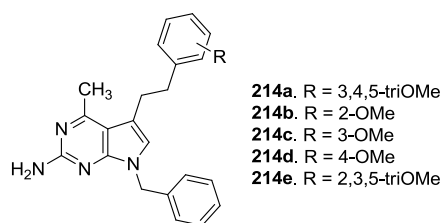


Figure 73. Structures of pyrrolo[2,3-*d*]pyrimines **214a-e**.

Compound **214a** (Figure 73) was the most potent compound in this series in the NCI-60 preclinical tumor cell line panel and inhibited tumor cells 7 to 10 fold better than **214b** (Figure 73). However, **214b** demonstrated effective reversal of Pgp-mediated resistance to vinblastine in the NCI/ADR cell lines.²⁶⁶ Other analogs in this series showed reduced effectiveness in both inhibition of tumor cells and reversal of drug resistance to

vinblastine. Additionally, while **214a,b** and other analogs in this series did not reverse the MRP1 mediated resistance to vincristine in MCF7/VP cells, they themselves were not substrates for MRP1. In **214a-d**, removal of the *N*7-benzyl group led to poor antimitotic activity. Efforts to determine the binding site of these compounds²⁶⁶ indicated that the compounds did not bind to the known binding sites on tubulin (vinca, colchicine or the taxol binding site) and probably bind to a novel site on tubulin.²⁶⁶ Further optimization of the phenethyl side chain²⁷⁰ by nine analogs with di-, tri- or tetra-methoxy or chloro substitutions on the phenyl ring led to compounds that showed improved cytotoxicity against the resistant tumor cells, NCI/ADR and MCF-7/VP, in culture. This study by Gangjee *et al.*²⁶⁶ led to the discovery of **214e** (Figure 73) which reversed both Pgp-mediated as well as MRP1-mediated resistance to clinically used antimitotic agents while simultaneously displaying antimitotic mediated antitumor activity.²⁷⁰

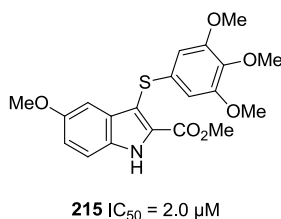


Figure 74. Structures of pyrrolo[2,3-*d*]pyrimines **215**.

Methyl 3-[(3',4',5'-trimethoxyphenyl)thio]-5-methoxy-1*H*-indole-2-carboxylate **215** was reported by De Martino *et al.*³⁹⁸ as the most active compound in a series of arylthioindoles that displayed excellent inhibitory activity against tubulin polymerization and of the growth of MCF-7 human breast carcinoma cells. Compound **215** was the most potent derivative, (IC₅₀ 2.0 μM) and was 1.6 times more active than colchicine, equipotent as combretastatin A-4 (CSA4) and showed potent inhibition of the growth of MCF-7 cells (IC₅₀ 13 nM). Preliminary SAR studies indicated that introduction of the 2-

methoxycarbonyl function on the indole scaffold improved potency by 2-fold. Oxidation of the sulfur atom to the sulfone led to inactive compounds. The 3',4',5'-trimethoxyphenyl group attached to the sulfur atom provided the best activity. Introduction of the methoxy group at the 5-position of indole led to a 7-fold improvement in the inhibition of tubulin polymerization activity of **215** compared to the 5-H compound. It was also reported that tubulin polymerization was less sensitive to substitutions at the 5-position. The proposed binding mode³⁹⁸ of **215** in the colchicine binding site of tubulin (Figure 75) shows that the trimethoxy ring of **215** interacts with Cys β 241 and adopts a conformation similar to the C-ring of DAMA-colchicine. Additionally, the indole NH was proposed to interact with the backbone carbonyl of Thr α 179 in the active site.

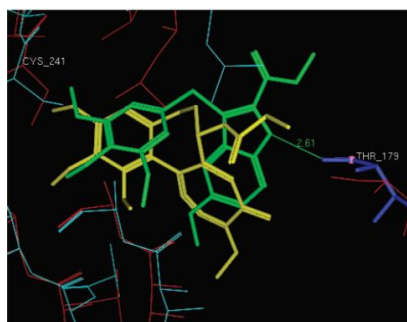


Figure 75. Superimposition of the proposed binding mode of **215** (green) with DAMA-colchicine (yellow) in the colchicine binding site.³⁹⁸

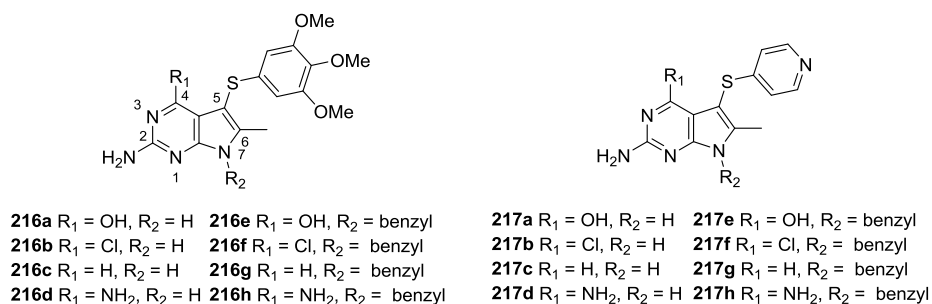


Figure 75a. Structures of target compounds **216a-h** and **217a-h**.

Compounds **216a-h** retain design elements from **214a**, the most potent compound in that series and introduce design elements from **215**. The larger sulfur atom in the 5-S

linker in **216a-h** mimics the ethyl linker in **214a**. Additionally, trimethoxyphenyl ring in **216a-h** is conformationally more restricted as compared to the flexibility afforded by the 2-atom linker to which the corresponding trimethoxyphenethyl ring in **214a** is attached. Additional conformation restriction on the trimethoxyphenyl ring is afforded by the presence of the 6-Me group in **216a-h**, which is absent in **214a** and its analogs. Varying the nature of substituent on the 4-position of **216a-h** explores the influence of substitutions at this position on the biological activity. Thus, 4-OH (**216a**, **216e**) and 4-NH₂ (**216d**, **216h**) groups could form hydrogen bonds in the binding site. Compounds with a 4-H group (**216c**, **216g**) would provide information about the importance of substitutions at the 4-position of these molecules. The 4-Cl compounds (**216b**, **216f**) mimic the 4-Me group of **214a**. The pyrrole NH in **216a-d** mimics the indole NH in **215**. Compounds **217a-h** vary in the nature of the aryl group linked to the sulfur atom. The electron poor 4-pyridyl group is in contrast to the electron rich trimethoxyphenyl ring in **216a** and **216a-h**. In addition, the protonatable pyridyl group could aid in increasing the water solubility of these compounds and the formation of acid salts.

C.3.2. Molecular Modeling Studies in the Colchicine Binding Site of Tubulin.

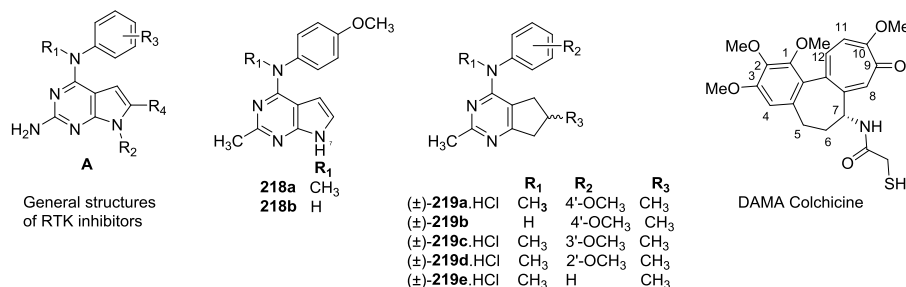


Figure 76. Structures of tubulin inhibitors **218a,b** and **219a-e**.

Table 16.⁵⁰ IC₅₀ values for inhibition of proliferation of MDA-MB-435 cells and EC₅₀s for

cellular microtubule loss.

Cmpd	IC ₅₀ ±SD (MDA-MB-435)	EC ₅₀ for microtubule depolymerization
218a	183 ± 3.4 nM	5.8 µM
218b	>10 µM	> 40 µM
(±)- 219a •HCl	17.0 ± 0.7 nM	56 nM
(±)- 219b	>10 µM	> 40 µM
(±)- 219c •HCl	153 ± 11.1 nM	3.0 µM
(±)- 219d •HCl	ND	> 40 µM
(±)- 219e •HCl	2.7 ± 0.3 µM	> 40 µM

Compounds **218a**, **b** (Figure 76) and (±)-**219a**•HCl (Figure 76) were originally designed by Gangjee *et al.*^{50, 394} as a part of a series of RTK inhibitors based on the general structure A (Figure 76) to determine the binding modes of these compounds in RTK. Compounds **218a**, **b** and (±)-**219a**•HCl did not show RTK inhibition (evaluated against EGFR, VEGFR-1 VEGFR-2 and PDGFR-β),²⁶⁹ but in the preclinical screening program of the National Cancer Institute in its 60 tumor cell line panel, **218a** inhibited the proliferation of most of the 60 cancer cell lines with a GI₅₀ < 500 nM and (±)-**219a**•HCl inhibited the proliferation of the majority of the 60 cell lines with GI₅₀ <30 nM.^{272, 399} A COMPARE analysis^{267, 269} indicated that the mechanism of action of these compounds could involve binding to tubulin. Further biological evaluation of **218a** and (±)-**219a**•HCl⁵⁰ showed dramatic reorganization of the interphase microtubule network and caused formation of aberrant mitotic spindles and mitotic accumulation when measured by flow cytometry, similar to the effects of colchicine and Combretastatin A-4 phosphate (CA4P). In further mechanistic studies, **218a** and (±)-**219a**•HCl was shown to inhibit the polymerization of purified bovine brain tubulin about as well as CA4P and inhibited [3H]colchicine binding to the protein.⁵⁰

To determine the structural requirements for the 4'-OMe and N4-Me moieties for activity, compounds **218b** and (\pm)-**219b**-(\pm)-**219e** were synthesized. The results from the biological evaluation (Table 16) indicated that a methyl substitution on the 4-aniline N is critical for activity in both scaffolds. In addition, the 4'-OMe moiety is important for potent activity. Transposition of the methoxy group from the 4'-position to either the 3'- (in (\pm)-**219c**·HCl) or 2'- (in (\pm)-**219d**·HCl), was detrimental to activity. The critical importance of *N*-Me and 4'-OMe for inhibitory activity of these compounds remains unexplained. Hence, docking studies were hence performed with **218a** and **219a** to predict their bound conformations and binding interactions with residues in the colchicine binding site of tubulin.

A 3.5 Å X-ray crystal structure of the colchicine binding site of tubulin bound to DAMA-colchicine (Figure 75, PDB: 1SA0)²³² has been resolved. It was of further interest to determine if the predicted bound conformation of **218a** and (\pm)-**219a** could explain the observed SAR for microtubule depolymerization for the compounds in this series. Docking studies of other compounds reported by the Gangjee laboratory were similarly performed and are reported in the Appendix

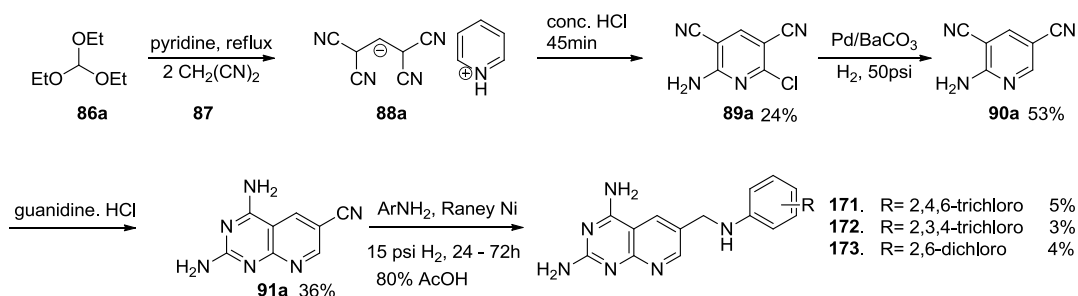
D. CHEMICAL DISCUSSION

D.1. ANTIFOLATES

D.1.1. Synthesis of novel pjDHFR inhibitors

D.1.1.1. Synthesis of novel 2,4-diamino-6-(arylaminomethyl)pyrido[2,3-*d*]-pyrimidines

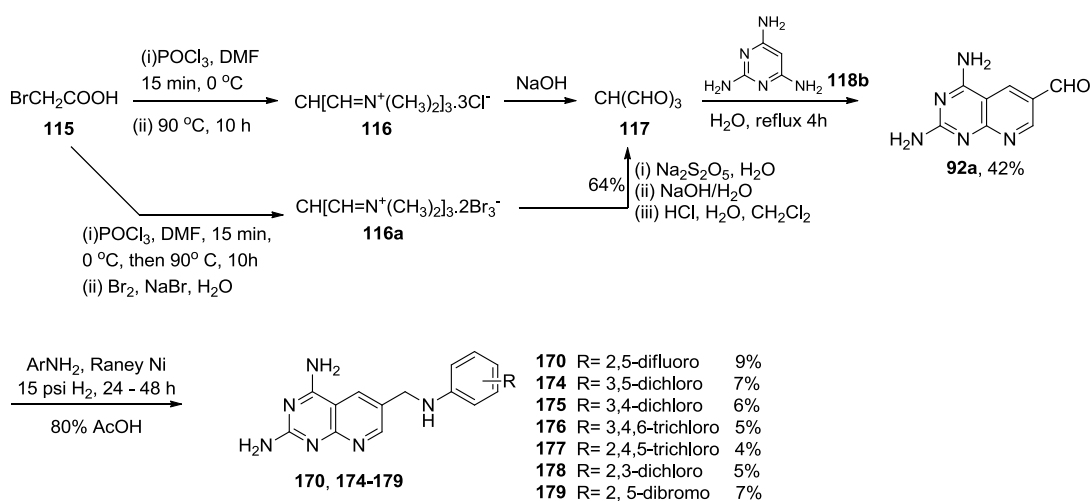
Scheme 23: Synthesis of target compounds **171** – **173**



The syntheses of target compounds **171** – **173** (Scheme 23) were performed using methods described by Gangjee *et al.*³³³ and involved the reductive amination of the key intermediate 2,4-diaminopyrido[2,3-*d*]pyrimidine-6-carbonitrile **91a** with the appropriately substituted aniline. Intermediate **91a** was prepared, in turn, by a method previously reported by Piper *et al.*²⁸⁴ and modified by Gangjee *et al.*⁴⁰⁰ Condensation of triethyl orthoformate with malononitrile using pyridine as a solvent followed by treatment with concentrated HCl at 80 °C afforded the cyclized intermediate 2-amino-6-chloropyridine-3,5-dicarbonitrile **89a** in 24% yield over two steps. Reductive dechlorination of **89a** in the presence of 5% palladium on barium carbonate with hydrogen at 50 psi afforded 2-aminopyridine-3,5-dicarbonitrile **90a**. Cyclization of **90a** with guanidine afforded the key bicyclic intermediate **91a** in 36% yield. Reductive

amination with the appropriate aniline in a Paar hydrogenation apparatus in presence of Raney nickel and hydrogen at atmospheric pressure afforded compounds **171-173**. The poor yields of the reaction could be accounted for by the electron withdrawing nature of the anilines and/or steric hinderance due to the presence of ortho-substitution on the aniline and is consistent with similar results previously reported (3 – 16% yields) by Gangjee *et al.*³³³ Chromatographic separation of the target compounds presented significant challenges due to the presence of tailing impurities ($R_f \sim 0.15 - 0.22$) near the product ($R_f \sim 0.25 - 0.28$ using 5:1:0.1 CHCl_3 : MeOH : NH_4OH as the solvent system) necessitating repeated column separation. Additionally, several target compounds in this series tend to stick to the silica gel leading to band widening during separation, resulting in fractions with mixtures of compounds and a reduction in the reaction yield. Attempts to reduce sticking of the compound to the silica gel column by using basic alumina as the stationary phase or neutralization of the slight acidic nature of silica gel by packing the column with a 1% NH_4OH solution in CHCl_3 were unsuccessful.

Scheme 24: Modified synthesis of **170**, **174 – 179**



The long synthetic route (Scheme 23) and the tedious isolation of the intermediates and the target compounds prompted a search for alternate routes to access

these compounds. It was envisioned that 2,4-diaminopyrido[2,3-*d*]pyrimidine-6-carbaldehyde **92a** could be used as the reductive amination partner with the substituted anilines to afford the target compounds. Intermediate **92a** is also presumably formed *in situ* during the reductive amination of **91a**²⁹⁵ (Scheme 23) and reacts with the substituted aniline present in solution to afford the desired compounds. Thus, the direct synthesis of **92a** could avoid an additional *in situ* hydrolysis step necessary for the reaction to proceed in Scheme 23.

The synthesis of **92a** was performed using methods described by Temple *et al.*²⁹⁵ and involves the condensation of triformylmethane **117** with 2,4,6-triaminopyrimidine **118b** under mild conditions. The synthesis of triformylmethane **117** was carried out using a method initially reported by Arnold *et al.*⁴⁰¹ and involved the reaction of bromoacetic acid **115** with an *N,N*-DMF-POCl₃ complex resulting in the formation of an intermediate quaternary salt **116** which underwent hydrolysis in presence of base (NaOH) to afford **117** which was used without purification. Literature methods^{295, 401} of purification of **117** involve formation of an intermediate diperchlorate salt which can be recrystallized from acetonitrile. Neutralization of the diperchlorate salt with 4N NaOH and subsequent sublimation of the isolated crude material affords pure **117**.

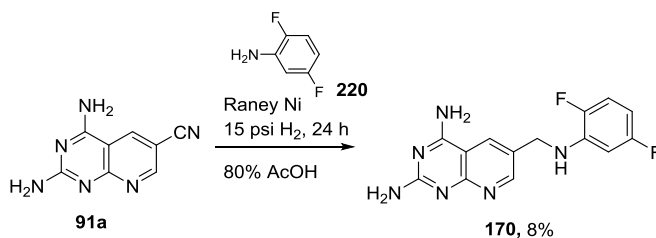
A modified procedure reported by Buděšínský *et al.*⁴⁰² was utilized for the synthesis of pure **117**. The procedure involves the formation of the bisperbromide **116a** as the intermediate. Compound **116a** was synthesized by the reaction of bromoacetic acid with *N,N*-DMF and POCl₃, decomposition of the reaction mixture using ice and precipitation of the orange colored salt using an aqueous mixture of bromine and sodium bromide. The crude salt was purified by dissolving it in acetonitrile, filtration and

reprecipitation by addition of 1,2-dichloroethane. Triformylmethane **117** was synthesized from the salt **116a** by addition of sodium metabisulfite to a cooled suspension of **116a** in water followed by basification with NaOH, neutralization with conc. HCl and extraction with CH₂Cl₂ in 64% yield over four steps.

Reaction²⁹⁵ of crude **117** with 2,4,6-triaminopyrimidine **118b** to afford **92a** proceeds with comparable efficiency (36 – 42% yield) with both, pure and crude **117**. Hence, reactions carried out for the bulk synthesis of the key intermediate **92a** were performed using crude **117**. Compound **92a** was then treated with appropriate anilines under reductive amination conditions^{333, 403} to provide the target compounds **170**, **174** – **179** in 4 – 9% yields. Though the isolated yield of the target compounds was comparable to the method described in Scheme 23, the modified reaction sequence led to a reduction in the number of steps in the reaction sequence, reduced isolation of intermediates, and thus greatly improved the ease of access of the target compounds.

D.1.1.2. Bulk synthesis of lead compound **170**

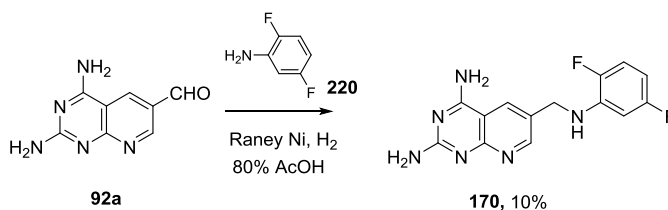
Scheme 25: Synthesis of lead compound **170** from **91a**



Compound **170** was initially synthesized from **91a** utilizing the method described in Scheme 23, analogous to the method described for the synthesis of **171** – **173**. This method involved a long reaction sequence, tedious chromatographic separation and poor yields. Hence it was necessary to find an alternate synthetic route to access **170**. Initial

attempts to synthesize **170** in bulk were carried out using methods described in Scheme 24 using reductive amination of **92a** with 2,5-difluoroaniline **220** in a Paar hydrogenator using 15 psi hydrogen as the reductant as shown in Scheme 25. Extending the reaction time to 48 or 72 h did not significantly improve the yield of **170** and led to increased formation of polar impurities, presumably (2,4-diamino-pyrido[2,3-*d*]pyrimidin-6-yl)methanol formed by the reduction of the intermediate aldehyde **92a** prior to the formation of the Schiff base intermediate by reaction with 2,5-difluoroaniline. Similarly, increasing the pressure of hydrogen in the Paar hydrogenation vessel to 35 or 50 psi to shorten the reaction time led to increased formation of (2,4-diaminopyrido[2,3-*d*]pyrimidin-6-yl)methanol with no improvement in the yield of the desired target compound.

Scheme 26: Synthesis of **170** from **92a**



	H ₂ Pressure	Time	Yield
1	15 psi	24 h	10%
2	35 psi	8 h	8%
3	50 psi	4 h	3%
4	50 psi	8 h	9%
5	15 psi	48 h	11%
6	15 psi	72 h	10%

In an attempt to improve the yield of **170**, reductive amination was attempted using the aldehyde compound **92a** and 2,5-difluoroaniline **220** using a Paar hydrogenator under varying H₂ pressure and reaction time (Scheme 26). Reactions were carried out

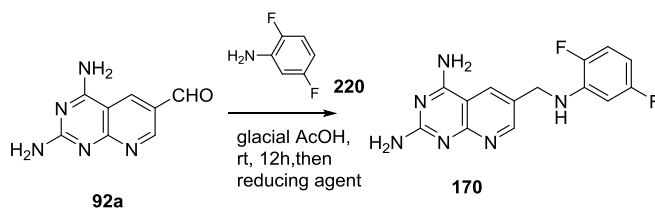
using 0.5 mmol **92a** and 1 mmol of **220**. There was no significant improvement in yield over those obtained in Scheme 25. Increasing the pressure of H₂ to 35 psi (entry 2) led to a reduction in reaction time to 8 h. Increasing the reaction time at 35 psi of H₂ led to significant increase in the polar side products. Increasing the H₂ pressure to 50 psi (entries 3 and 4) did not increase the yield of **170** but caused increased polar side products. Increasing the reaction time at 15 psi of H₂ to 48 h or 72 h did not improve the yields.

Synthesis of **170** using stepwise reductive amination

Abdel-Magid *et al*⁴⁰⁴ state that “A reductive amination reaction is described as a *direct reaction* when the carbonyl compound and the amine are mixed with the proper reducing agent without prior formation of the intermediate imine or iminium salt. A *stepwise* or *indirect reaction* involves the preformation of the intermediate imine followed by reduction in a separate step.” A stepwise reductive amination was utilized in an attempt to improve reaction yields. A variety of reducing agents have been reported in the literature including sodium borohydride, sodium cyanoborohydride, sodium triacetoxyborohydride, borane-pyridine complex, borohydride exchange resin, Ti(OiPr)₄/NaBH₃CN and NaBH₄/Mg(ClO₄)₂.⁴⁰⁵ Based on literature reports,^{406, 407} it was anticipated that the use of a reducing agent should afford **170** in a stepwise manner from the intermediate imine resulting from the reaction of **92a** and **220** (Scheme 26). A stepwise reductive amination approach would have the added advantage of ease of scalability, enables the reaction to be performed safely under normal laboratory conditions without the use of specialized hardware such as the Paar hydrogenator, and avoids the use of high pressure hydrogen gas and avoids the use of toxic, expensive and

pyrophoric metals such as Raney Ni.

Scheme 27: Optimization of reductive amination conditions



	Reductant	Eq. of reductant	Time	Result
1	NaBH ₄	1.5	12 h	Trace amounts
2	NaBH ₄	1.5	24 h	Multiple close spots on TLC
3	NaBH ₃ CN	1.5	12 h	7%
4	Na(CH ₃ COO) ₃ BH	1.5	12 h	11%
5	Na(CH ₃ COO) ₃ BH	1.5	24 h	12%
6	Na(CF ₃ COO) ₃ BH	1.5	24 h	6%
7	Na(CH ₃ COO) ₃ BH	3	24 h	14%
8	Na(CH ₃ COO) ₃ BH	5	24 h	12%

A series of reactions carried out to optimize the reducing agent for the reaction is described in Scheme 27 above. One of the most commonly employed reducing agents for reductive amination is sodium borohydride. The reaction was performed by stirring a mixture of **92a** and **220** in glacial AcOH for 12h at room temperature to permit formation of the intermediate imine, addition of the reducing agent and continued stirring for an additional 12 – 24 h. The use of 1.5 equivalents of NaBH₄ as the reducing agent led to the formation of trace amounts of **170** on TLC after 12 h. Increasing the reaction time to 24 h led to the formation of multiple close spots on TLC which could not be separated using silica gel chromatography under gravity or flash chromatography.

Sodium cyanoborohydride is a milder reducing agent than NaBH₄ and has been successfully employed in reductive amination procedures due to its stability in acidic

conditions (\sim pH 3). It is soluble in polar solvents such as MeOH and shows different selectivities at different pH values. At low pH (\sim 3) NaBH_3CN reduces aldehydes and ketons effectively and at higher pH (\sim 6) it reduces imines more effectively than aldehydes.^{404, 407} Hence, NaBH_3CN was attempted as a reducing agent. This reaction (entry 4, 7% yield) showed improved yields compared to NaBH_4 and provided the impetus for a further scan of reducing agents. The reaction with sodium triacetoxyborohydride (entries 5 and 6, 11-12% yield) showed better yields compared to reactions with NaBH_4 or NaBH_3CN . Reactions with sodium trifluoroacetoxyborohydride (entry 7, 6% yield) showed poorer yields compared to $\text{Na}(\text{CH}_3\text{COO})_3\text{BH}$. Increasing the amount of $\text{Na}(\text{CH}_3\text{COO})_3\text{BH}$ to 3- or 5-equivalents led to marginal improvement in yield. It was seen that the best yields were obtained by the use of 3 equivalents of $\text{Na}(\text{CH}_3\text{COO})_3\text{BH}$ with a reaction time of 24 h at room temperature.

The formation of large amounts of polar baseline impurities relative to the desired compound spot (TLC), presumably due to the competing reduction of the aldehyde group³⁴⁴ of **170** indicated that the rate limiting step could be the formation of the intermediate imine. The reversible addition of the aldehyde **92a** and **220** leads to the formation of a hydroxylamine addition product, which undergoes dehydration to form an iminium ion which is the target of the reductant. (Figure 77).

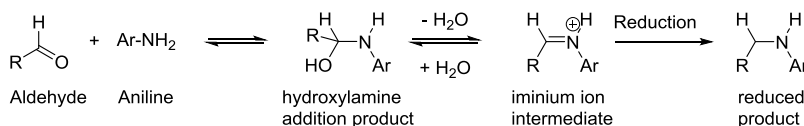
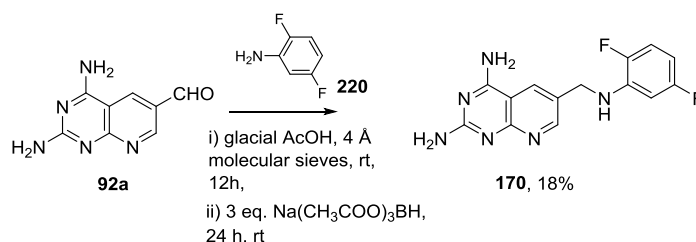


Figure 77: Reductive amination mechanism

Thus, removal of water from the reaction was anticipated to aid in the formation of the iminium intermediate and could help in improving yields. Activated 4 Å molecular sieves have been used to scavenge water in reductive amination reactions.⁴⁰⁵⁻⁴⁰⁷

Scheme 28: Optimized reaction conditions for synthesis of **170**



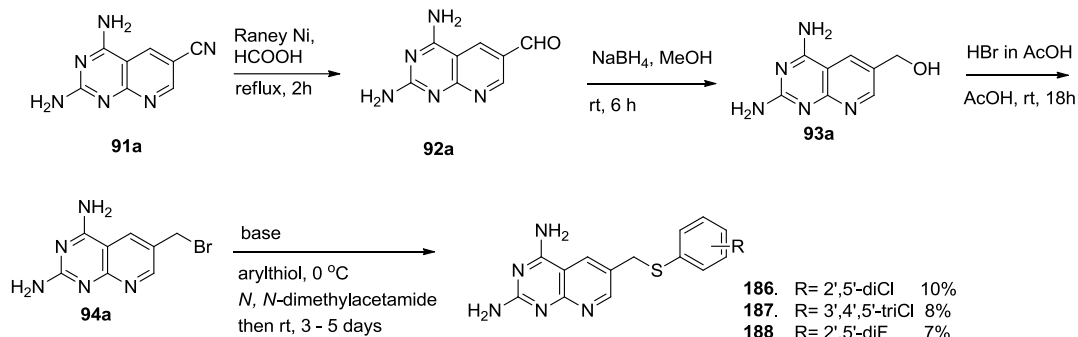
Addition of 4 Å molecular sieves to the reaction (Scheme 28) led to improved yields (18%). The optimized reaction conditions involved addition of 3 eq. of Na(CH₃COO)₃BH in divided portions **170**. Although the reaction in Scheme 28 was much cleaner, the presence of trailing impurities necessitated multiple column chromatographic separations. Separations were aided by the use of Combiflash separation (12g or 24g Teledyne Isco columns, CHCl₃: MeOH, 0 – 15% gradient elution).

A total of 750 mg of **170** was synthesized for biological evaluation studies using this methodology.

D.1.1.2. Synthesis of novel 2,4-diamino-6-[(arylthio)methyl]pyrido[2,3-*d*]pyrimidines

The synthesis of 2,4-diamino-6-[(arylthio)methyl]pyrido[2,3-*d*]pyrimidine compounds **186 - 188** (Scheme 29) was performed from the key bromo intermediate **94a** using methods described by Gangjee *et al.*³⁴⁴ The aldehyde intermediate **94a** was obtained by the hydrolysis of the nitrile group of **91a** using Raney Ni and formic acid at reflux³⁴⁴ or by using methods²⁹⁵ described in Scheme 24.

Scheme 29: Synthesis of 2,4-diamino-6-[(aryltio)methyl]pyrido[2,3-*d*]pyrimidines **186** - **188**



	R	Base	Result
1	2',5'-diCl	K ₂ CO ₃	Trace amount
2	2',5'-diCl	NEt ₃	4%
3	2',5'-diCl	NaH	10%
4	3',4',5'-triCl	NEt ₃	8%
5	3',4',5'-triCl	NaH	6%
6	2'5'-diF	NaH	6%
7	2',5'-diF	NEt ₃	7%

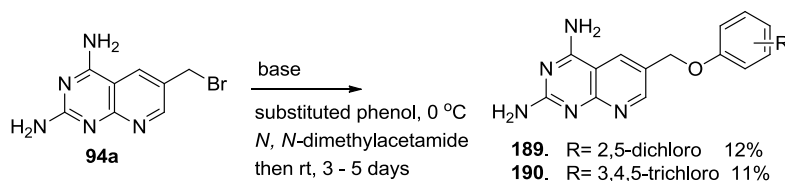
Reduction of the aldehyde group of **91a** using NaBH₄ in MeOH afforded the alcohol **92a** which was brominated using HBr/AcOH in AcOH to give the bromo intermediate **93a**. Nucleophilic displacement of the bromo group of **93a** with appropriate arylthiols using either sodium hydride, potassium carbonate or triethylamine as the base and *N,N*-dimethylacetamide as the solvent afforded the target compounds **186** and **187**. The use of K₂CO₃ as the base afforded trace amounts of compound while the use of either NEt₃ or NaH afforded compounds **186** - **188** in 6-10% yields.

Compounds **189** and **190** were synthesized by the nucleophilic displacement of the bromo intermediate **94a** using either K₂CO₃, NEt₃ or NaH as the base and *N,N*-dimethylacetamide or *N,N*-dimethylformamide as the solvent (Scheme 30). Improved reaction yields were observed when NaH was used as the base compared to K₂CO₃ or

NEt₃. The reaction involved stirring the phenol with the base at 0 °C to form the phenoxide anion followed by dropwise addition of **94a** dissolved in the solvent. The reaction was then allowed to warm to rt and stirred for 3-5 days. The reaction was monitored by TLC and was quenched when multiple side products began to appear in the reaction mixture.

D.1.1.3. Synthesis of novel 2,4-diamino-6-[(aryloxo)methyl]pyrido[2,3-*d*]pyrimidines

Scheme 30: Synthesis of 2,4-diamino-6-[(aryloxo)methyl]pyrido[2,3-*d*]pyrimidines **189** - **191**



	R	Base	Result
1	2',5'-diCl	K ₂ CO ₃	8%
2	2',5'-diCl	NEt ₃	4%
3	2',5'-diCl	NaH	12%
4	3,4,5-triCl	K ₂ CO ₃	6%
5	3',4',5'-triCl	NEt ₃	8%
6	3',4',5'-triCl	NaH	11%
7	2'5'-diF	K ₂ CO ₃	complex mixture
8	2',5'-diF	NEt ₃	complex mixture
9	2',5'-diF	NaH	complex mixture

D.1.1.4. Docking studies with pyrido[2,3-*d*]pyrimidines in *pc*DHFR and *pj*DHFR

D.1.1.4.1. Docking Studies with *pc*DHFR

Protein and ligand preparation prior to docking:

Docking studies were performed for **192a** using the 1.90 Å crystal structure of *pc*DHFR (PDB: 1LY3⁸⁹) complexed with 2,4-diamino-6-[*N*-(2',5'-dimethoxybenzyl)-*N*-

methylamino] quinazoline, (COQ, Figure 20). The active site was defined by a sphere of 6.5 Å near the ligand. Protein preparation prior to docking was performed using the LigX functionality in MOE 2008.10.⁴⁰⁸ LigX is a graphical interface and collection of procedures for conducting interactive ligand modification and energy minimization in the active site of a flexible receptor. In LigX calculations, the receptor atoms far from the ligand are constrained and not allowed to move while receptor atoms in the active site of the protein are allowed to move but are subject to tether restraints that discourage gross movement. The procedure was performed with the default settings. The process of protein preparation using LigX involves addition of hydrogen atoms according to the ionization state of the atoms of the molecule/protein loaded. The heavy atoms are then fixed and a brief energy minimization is carried out to refine the positions of the added hydrogen atoms. The receptor atoms are then tethered during geometry optimization so that they do not deviate too much from their initial coordinates and then energy minimized using the Amber99 forcefield. Ligands used for docking were sketched in MOE, minimized and exported as an SDF file.

Docking:

Docking of ligands into the pcDHFR active site was performed using LeadIT 1.3.0.⁴⁰⁹ Polar hydrogen atoms of amino acids with a polar side chain (Asn23, Ser24, Tyr35, Thr61, Ser64, Tyr129 and Thr144) were not constrained, thereby permitting free rotation. Base placement of fragments for docking was carried out using triangle matching. Default parameters were used for scoring and clash handling. The maximum number of solutions per iteration and the maximum number of solution per fragmentation

were set to 500. Ten poses were obtained per molecule. Docking processes were repeated to ensure reproducibility of the docked conformations. The docked poses were exported to MOE 2008.10, rescored using the affinity dG scoring system, refined using the forcefield system and rescored using London dG scoring system. The binding poses were also visualized using the ligplot utility in MOE and the Poseview utility in LeadIT 1.3.0.

Validation of docking software:

The crystal structure of the inhibitor, 2,4-diamino-6-[*N*-(2',5'-dimethoxybenzyl)-*N*-methylamino]quinazoline from PDB: 1LY3, was sketched, prepared and docked into the pcDHFR active site as described above. The best docked pose displayed and RMSD of 1.072 Å compared to the crystal structure ligand, thereby validating LeadIT 1.3.0 for our docking purposes. Docking studies with **192b** were performed similarly.

Docking studies with *N*6-methyl-*N*6-phenylpyrido[2,3-*d*]pyrimidine-2,4,6-triamine, **192b, in pcDHFR**

Docking studies of **192b** in the pcDHFR active site (PDB: 1LY3) were performed using LeadIT 1.3.0. Figure 78 shows the best scoring pose of **192b** in the pcDHFR active site. In this pose, the protonated N1 and 2-NH₂ of **192a** interact in an ionic bond with Glu32. This bidentate ionic bond with a conserved acid residue has been observed in most DHFR crystal structures.^{22, 31, 32, 53} The 4-NH₂ moiety forms hydrogen bonds with the backbone of Ile10 and Ile123.

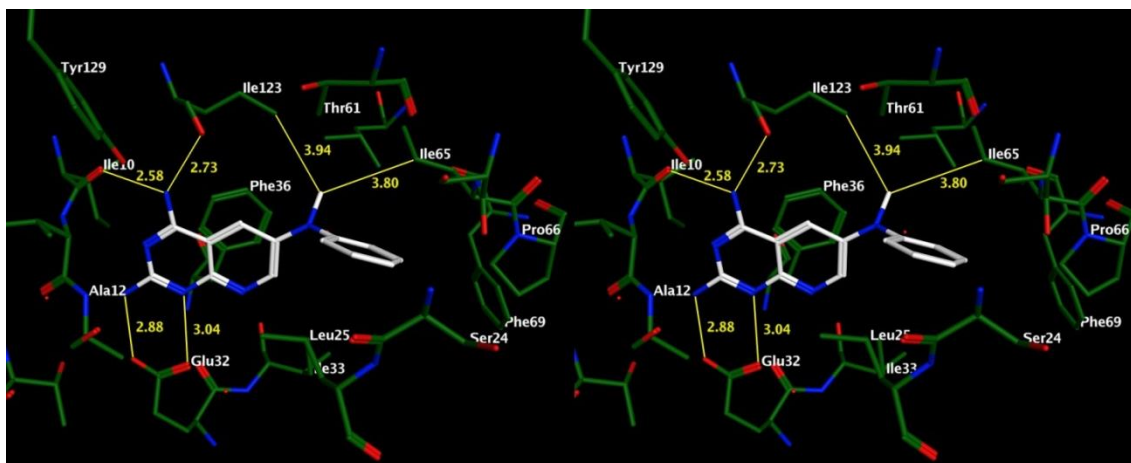


Figure 78: Stereoview. Docked pose of **192b** in pcDHFR binding pocket (PDB: 1LY3⁸⁹).

The pyrido[2,3-*d*]pyrimidine scaffold is stabilized by a pi-stacking interaction with Phe36 and with side chain carbon atoms of Met33 and Leu25. The N9-methyl group of **192b** was 3.94 Å from the terminal methyl group of Ile123 of pcDHFR. In hDHFR, the corresponding Val115, being shorter by one carbon, may not interact with the N9-methyl group. This was expected to improve selectivity as well as potency of these compounds against pcDHFR (and pjDHFR) over hDHFR. In addition the N9-methyl group of **192b** was 3.8 Å away from side chain Ile65 in pcDHFR, and could improve potency by hydrophobic interactions. The N9-methyl group also restricts the number of possible conformations of the side chain phenyl group compared to the N9-H, thus perhaps increasing selectivity.³³² The docked score of **192b** in pcDHFR was -42.416 kJ/mol. Thus docking studies corroborate the proposed interactions of the N9-methyl group in pcDHFR and lend credence to the importance of the N9-group in the design of selective inhibitors of pcDHFR (and pjDHFR) over hDHFR as previously observed by Gangjee *et al.*³³²

D.1.1.4.2. Homology model of pjDHFR

There is currently no known crystal structure of pjDHFR. Thus, a homology model was hence built to evaluate the binding of **192b-e** in pjDHFR. The 206 amino acid sequence of the folate domain was obtained from the UniProt database (ID: Q9UUP5_PNEJI [Q9UUP5]). A BLAST search for the pjDHFR sequence showed high sequence identity with pcDHFR, (61% sequence identity). The BLAST search was carried out on the Uniprot website (www.uniprot.org) using default settings (Threshold: 10; Matrix: Auto; Gapped Hits: Yes).

Alignment of the sequences was performed using clustalw program as implemented on the Uniprot website. The sequence alignment between pjDHFR and pcDHFR (Figure 46) shows a high degree of similarity between the two sequences and makes pcDHFR a valid template for model generation.

Homology model building: MOE 2008.10

The primary pjDHFR FASTA sequence was loaded into MOE 2008.10. Template identification was performed using the BLASTP module implemented in MOE 2008.10 using the default settings and indicated that the pcDHFR crystal structure (PDB: 2FZI⁴⁴) shares high homology with pjDHFR (E value: $1e^{-65}$). The E-value is an estimate of the likelihood of the score arising due to chance, with low E-values preferred over higher values. Thus, the high sequence identity between pjDHFR and pcDHFR (61%) and the availability of high quality crystal structures of pcDHFR in the PDB makes it a valid template for building the pjDHFR homology models. The homology model was built with MOE 2008.10 using the 1.60Å crystal structure of pcDHFR as a template (PDB:

2FZI, chain A). Sequence alignment was performed using MOE_Align using the ‘actual secondary structure’ option in MOE.

Model validation:

The model returned from the software was evaluated using structure assessment tools (Ramachandran plot, Protein Structure Analysis (ProSA),^{410, 411} Procheck,⁴¹² Anolea,⁴¹³ Gromos,⁴¹⁴ and QMEAN⁴¹⁵) as implemented on the Swiss-Model website.⁴¹⁶

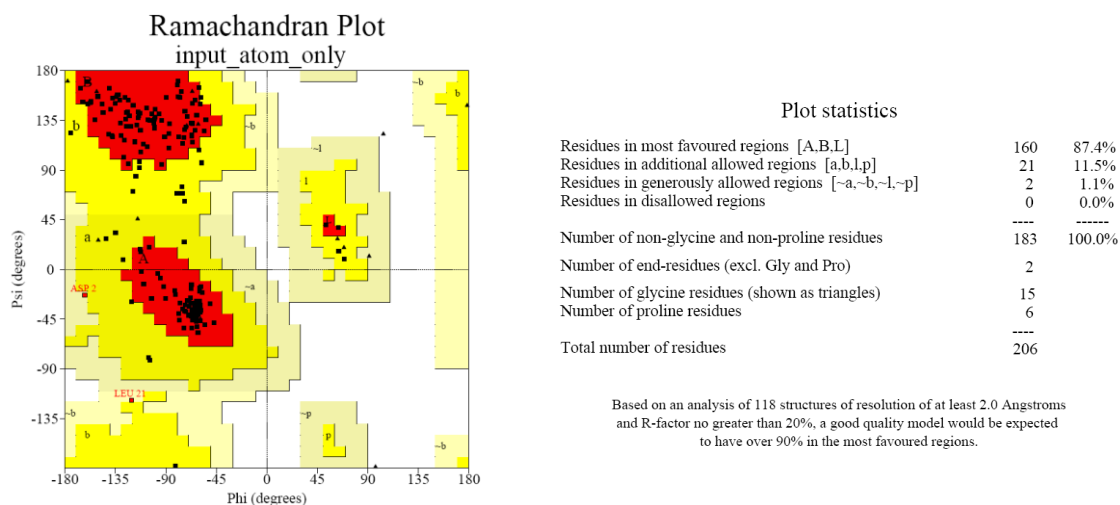


Figure 79: Ramachandran plot and Procheck analysis of the pjDHFR homology model generated using MOE 2008.10

- a) **Ramachandran plot** (Figure 79): A Ramachandran plot generated for the pjDHFR model showed that, with the exception of Asp2, all the residues have acceptable geometries. Since Asp2 is distant from the active site, and was not expected to influence the docking studies, modeling studies were performed without any additional refinements.

b) **Procheck**⁴¹² (Figure 79): A Procheck analysis of the model indicated 87.5% of residues in the most favored regions, 11.5% residues in additional allowed regions, 1% in the generously allowed regions and 0% residues in the disallowed region.

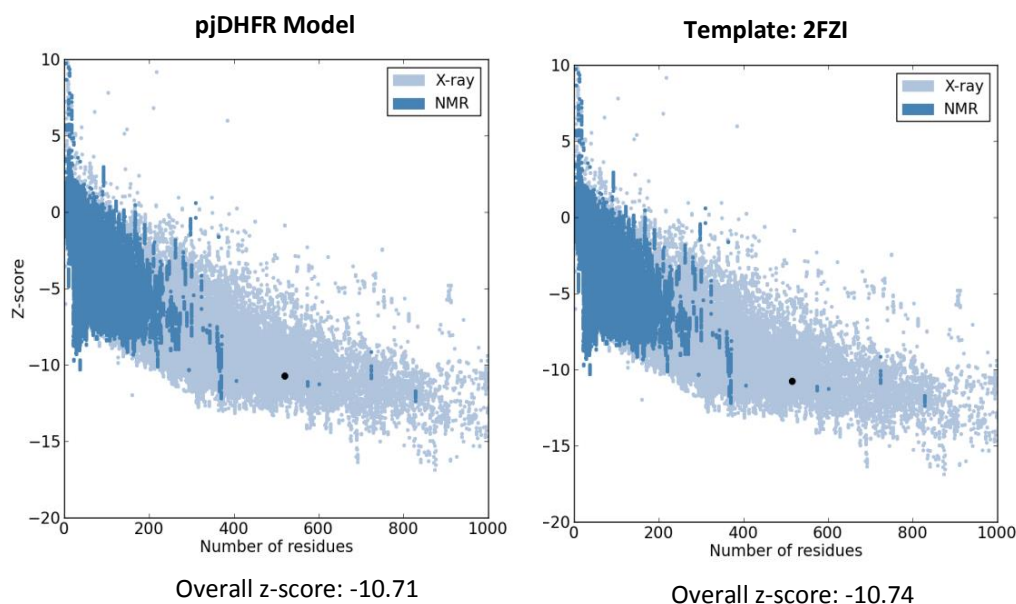


Figure 80: ProSA analysis of the pjDHFR homology model generated using MOE 2008.10.

c) **Protein Structure Analysis (ProSA):**^{410, 411} ProSA calculates an overall quality score (z-score) for a specific input structure. A plot of local quality scores points to problematic parts of the model. The z-score estimates the overall model quality (Figure 80). The Z-score of the input model is plotted along with the z-scores of all experimentally determined protein chains in PDB. In this plot, groups of structures from different sources (X-ray, NMR) are distinguished by different colors (Figure 80). ProSA can be used to check whether the z-score of the input model is within the range of scores typically found for native proteins of similar size with a score outside a range characteristic for native proteins indicating

probable structural errors. The ProSA analysis of the pjDHFR model fell within the range of z-scores of experimentally determined structures.

Details of validation including Anolea,⁴¹³ Gromos,⁴¹⁴ and QMEAN⁴¹⁵ are provided in the experimental section. The results from these studies confirmed the validity of the pjDHFR model for docking studies.

Active site definition and docking to the *pj*DHFR model

The pjDHFR homology model prepared in MOE was superimposed on the X-ray crystal structure of pcDHFR (PDB: 2FZI, chain A) and NADPH and DH3 (2,4-diamino-5-[3',4'-dimethoxy-5'-(5-carboxyl-1-pentynyl)]benzyl pyrimidine), the co-crystallized ligand in 2FZI, were added to the model. The active site was defined by a sphere of 6.5 Å near the ligand. Docking of ligands to the pjDHFR model was performed using LeadIT 1.3.0. as described below.

Validation of the docking system

The pjDHFR structure was obtained by means of homology modeling using pcDHFR as template. Hence, the validation of LeadIT 1.3.0 as suitable docking systems for pjDHFR was carried out by redocking the native ligand in the X-ray crystal structure of pcDHFR (PDB: 2FZI,⁴⁴ chain A). The protein was prepared as mentioned above. The ligand was built and minimized in MOE. The docking procedure in LeadIT 1.3.0 was constrained to the active site of the protein. Polar hydrogen atoms of amino acids with a polar side chain (Ser37, Thr61, Ser64, Ser69, Tyr129, Thr144) were not constrained,

thereby permitting free rotation. Base placement of fragments for docking was carried out using triangle matching. Default parameters were used for scoring and clash handling. The maximum number of solutions per iteration and the maximum number of solution per fragmentation were set to 500. Ten poses were obtained per molecule. Docking processes were repeated to ensure reproducibility of the docked conformations. The best docked pose of the ligand had an RMSD of 0.941 compared to the crystal structure. Thus, LeadIT 1.3.0 was validated for docking studies with the proposed analogs.

Homology model building using automated servers:

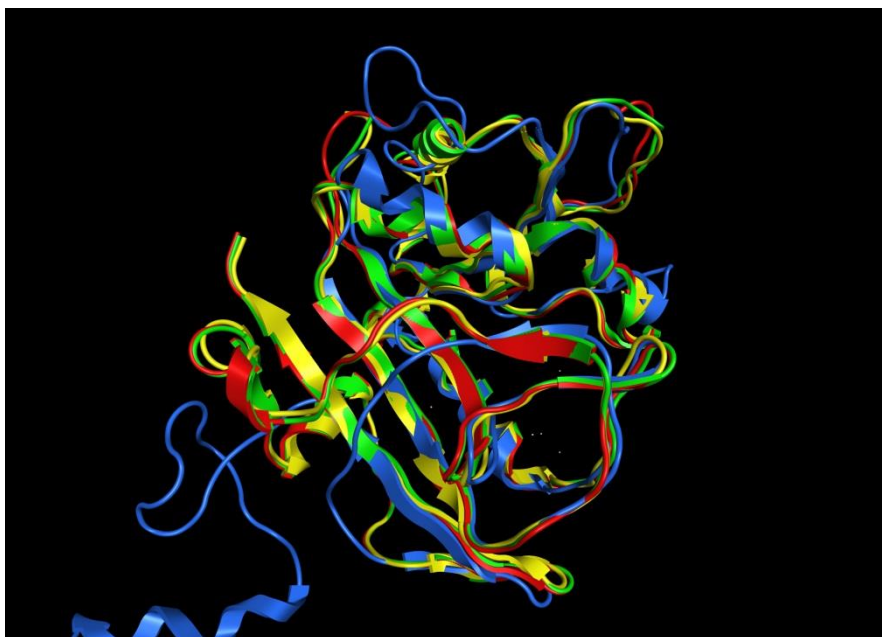


Figure 81: Ribbon rendition of the superimposition of pJDHFR homology models generated using MOE 2008.10 (red), Swiss-Model⁴¹⁷⁻⁴¹⁹ (green), Phyre2⁴²⁰ (yellow) and CPHmodel 3.0⁴²¹ (blue). RMSD between models = 0.955 Å. The model generated using MOE 2008.10 was used for docking studies described below.

In addition to the model generated using MOE, additional homology models were generated using automated homology modeling servers to validate the model from MOE. Model generation using the automated servers was performed by submitting the pJDHFR amino acid sequence to the servers (Swiss-Model⁴¹⁷⁻⁴¹⁹, Phyre2⁴²⁰ and CPHmodel 3.0⁴²¹). The process was carried out using the respective default settings for all three servers. The homology models returned from the three servers was overlaid with the model built using MOE 2008.10 (Figure 81). All the four homology models show good overlap with RMSD between models of 0.955 Å.

D.1.1.4.3. Docking studies with the pJDHFR homology model

D.1.1.4.3.1. Docking studies with *N*6-methyl-*N*6-(3,4,5-trifluorophenyl)pyrido[2,3-*d*]pyrimidine-2,4,6-triamine, **192d, in pJDHFR**

Docking studies were performed for **192b-e** (Table 8) using LeadIT 1.3.0. The docked pose of **192d**, which displays the highest selectivity (35-fold, Table 8) is described here. The docking procedure was identical to that described above for the validation of the software. The binding poses were visualized using the ligplot utility in MOE 2008.10 and the Poseview utility in LeadIT 1.3.0.

Figure 82 shows the best docked pose of **192d** (white) in the folate binding site of the pJDHFR model. In this pose the protonated N1 and 2-NH₂ of **192d** interact in an ionic bond with Asp32. This bidentate ionic bond with a conserved acid residue has been observed in most DHFR crystal structures. The 4-NH₂ moiety forms hydrogen bonds with the backbone of Ile10. The pyrido[2,3-*d*]pyrimidine scaffold is stabilized by a pi-stacking interaction with Phe36 and with side chain carbon atoms of Met33 (not shown) and Leu25.

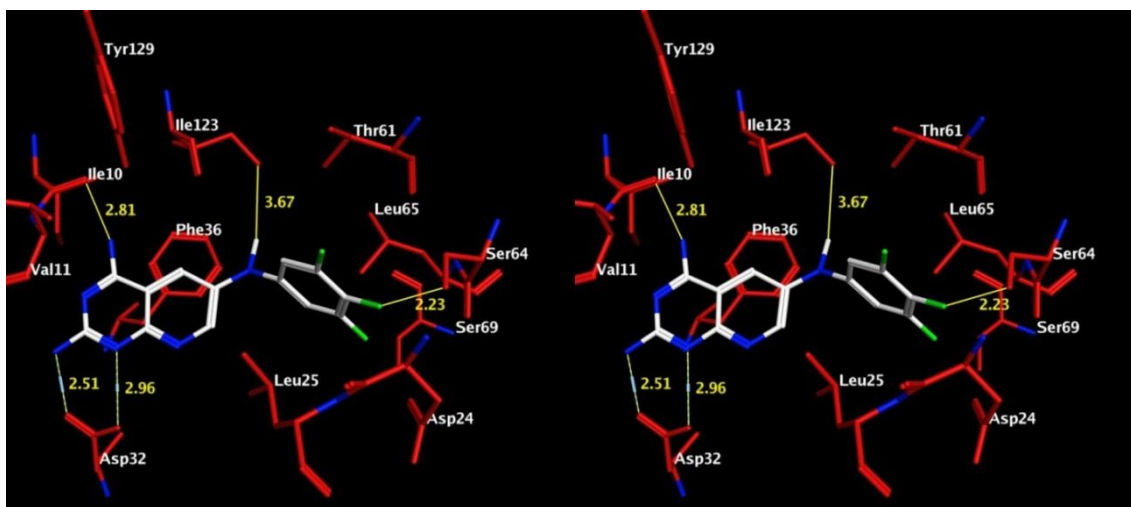


Figure 82: Stereoview. Docked pose of **192d** in the pjDHFR homology model.

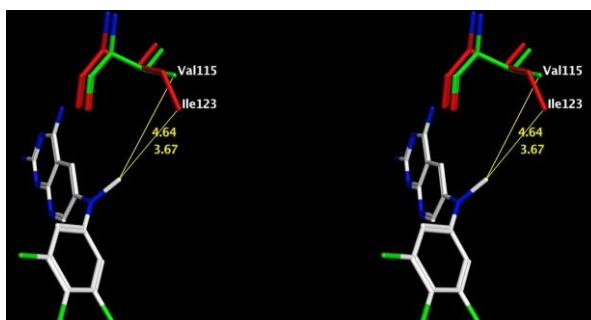


Figure 83: Stereoview. N-Me of **192d** interacts with Ile123 (pjDHFR model, red) but not as well with Val115 (superimposed hDHFR⁴²², green)

The 3'-F of **192d** interacts with the hydroxyl moiety of Ser64. The N9-Me moiety of **192d** is oriented towards the hydrophobic pocket formed by Ile123, Leu72 and Leu65 and interacts specifically with Ile123. The docking score of **192d** was -8.594 kcal/mol for pjDHFR compared with -8.412 kcal/mol for hDHFR. With the exception of the trifluoro groups, **192b** makes similar binding with pjDHFR as compared to **192d**. It was of interest to explain the potency and selectivity of **192b** and **192d** (compared to **192c** and **192e** respectively) for pjDHFR. From the IC₅₀ values in Table 8 for the two pairs **192b** and **192c**; and **192d** and **192e** it is evident that the N9-Me moiety makes about a 300- and a

200-fold difference in potency for pjDHFR respectively, indicating that the N-Me group must contribute significantly to the increased potency. There are two important consequences of adding the Me group on the N9. The first one is the interaction of the N9-Me with Ile123 in *pj*DHFR (Figure 83). This interaction would not exist for the N9-H analogs, **192c** and **192e** from modeling studies. The second is that the N9-Me restricts the available low energy conformations (50 conformations, calculated using Sybyl X 1.2⁴²³) the molecule can adopt compared with the unhindered N9-H (94 conformations, calculated using Sybyl X 1.2). Thus it is perhaps easier for **192b** and **192d** to adopt the bound conformation than it is for **192c** and **192e** and results, in part, to the increased IC₅₀ of **192b** and **192d** over **192c** and **192e**. In addition to potency, the selectivity of **192b** and **192d** for pjDHFR over hDHFR are superior to that of **192c** and **192e**. Thus, the N-Me moiety must also play a significant role in the high selectivity of **192b** and **192d** for pjDHFR over hDHFR compared to **192c** and **192e**. In pjDHFR the N9-Me moiety is 3.67 Å away from the longer Ile123 compared to hDHFR where it is 4.64 Å away from the shorter Val115. These superimpositions of the docked structure of **192d** in the pjDHFR homology model and hDHFR crystal structure (Figure 82) and the highly productive interaction of the N9-Me with Ile123 at 3.67 Å and the lack of productive interaction of the N9-Me with the shorter Val115 of hDHFR also provides, in part, a molecular explanation of the pjDHFR selectivity of **192d** over hDHFR. Thus the docking study validates the structural rationale for selectivity of **192b** and **192d**.

Conformational analysis

Low energy conformers of **192b-e** were generated using the Systematic Search option in Sybyl X 1.3⁴²³ using 5 ° increments.

D.1.1.4.4. Docking studies of 168 in the F36C L65P double mutant pJDHFR

homology model

D.1.1.4.4.1. Generation of F36C L65P double mutant pJDHFR model

The F36C L65P double mutant pJDHFR model was generated from the pJDHFR model used in the docking studies of **192b-e**. using the ‘mutate’ option in MOE 2010.10. The resultant double mutant model was minimized using the Amber99 forcefield. The protein geometry was verified using Ramachandran plots to ensure absence of outliers in the putative active site of the protein. Docking studies were carried out using TMP and **168** in the wild type and mutated pJDHFR homology models. Preparation of the ligands and the docking studies were performed as described earlier.

D.1.1.4.4.2. Docking of TMP in the pJDHFR model

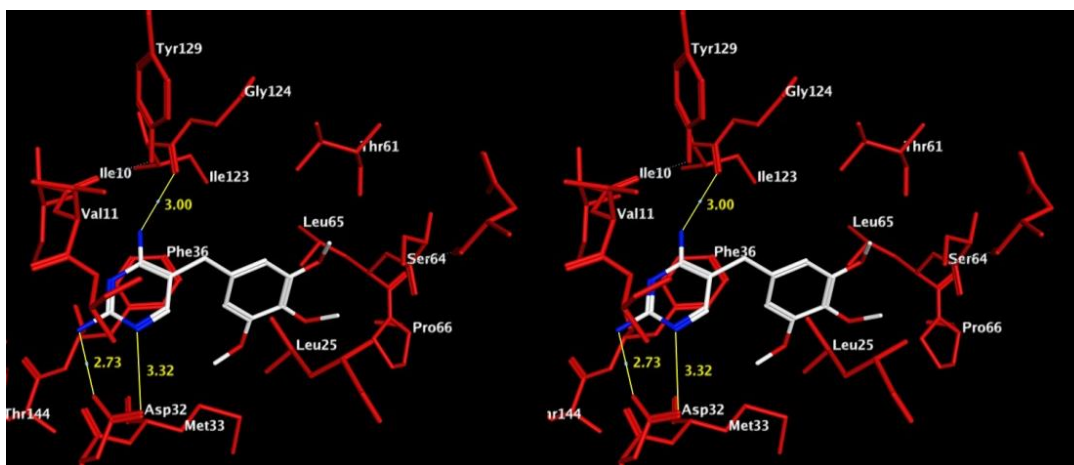


Figure 84: Stereoview. Docked pose of TMP in the pJDHFR homology model.

Figure 84 shows the best docked pose of TMP (white) in the folate binding site of the pJDHFR model. In this pose the protonated N1 and 2-NH₂ of TMP interact in an ionic bond with Asp32. The 4-NH₂ group of TMP can form a hydrogen bond with the backbone of Gly124. The pyrimidine scaffold is stabilized by a pi-stacking interaction

with Phe36 and with side chain carbon atoms of Met33. The 3',4',5'-methoxyphenyl moiety of TMP can form hydrophobic interactions with the side chain atoms of Leu25, Ser64, and Leu65. The docking scores of TMP were -5.832 kcal/mol with MOE 2010.10 and -23.023 kJ/mol with LeadIT 2.0.1.

D.1.1.4.4.3. Docking of TMP in the F36C L65P double mutant pjDHFR model

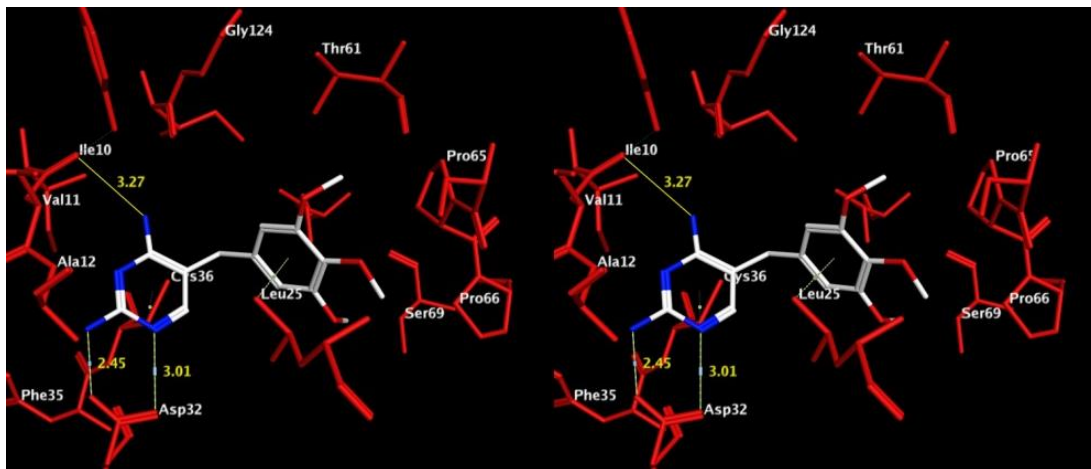


Figure 85: Stereoview. Docked structure of TMP in the F36C L65P double mutant pjDHFR homology model.

Figure 85 shows the best docked pose of TMP (white) in the folate binding site of the F36C L65P double mutant pjDHFR active site model. This docked pose maintains ionic bond between the protonated N1 and 2-NH₂ of TMP and Asp32 as is seen in the docked pose of TMP in the unmutated enzyme model (Figure 84). The 4-NH₂ group of TMP can form a hydrogen bond with the backbone of Ile10. Mutation of Phe36 with Cys36 causes a loss of the stacking interactions seen in the unmutated enzyme and could explain, in part, the loss of activity of TMP against the mutated enzyme. The 3',4',5'-methoxyphenyl moiety of TMP can form hydrophobic interactions with the side chain atoms of Leu25, Ser69, and Pro65. The docking scores of TMP were -4.555 kcal/mol

with MOE 2010.10 and -16.367 kJ/mol with LeadIT 2.0.1.

D.1.1.4.4.4. Docking of **168** in the pjDHFR model

The docked pose of **168** (Figure 86) retains the ionic bond with Asp32 as is seen for TMP. The bicyclic scaffold of **168** is stabilized by a pi-stacking interaction with Phe36 and with side chain carbon atoms of Met33 and Leu25. The aryl side chain of **168** can form hydrophobic interactions with the side chain atoms of Leu25, Thr61, Ser64, and Leu65 and Pro66. The docking score of **168** was -6.491 kcal/mol with MOE 2010.10 and -24.638 kJ/mol with LeadIT 2.0.1.

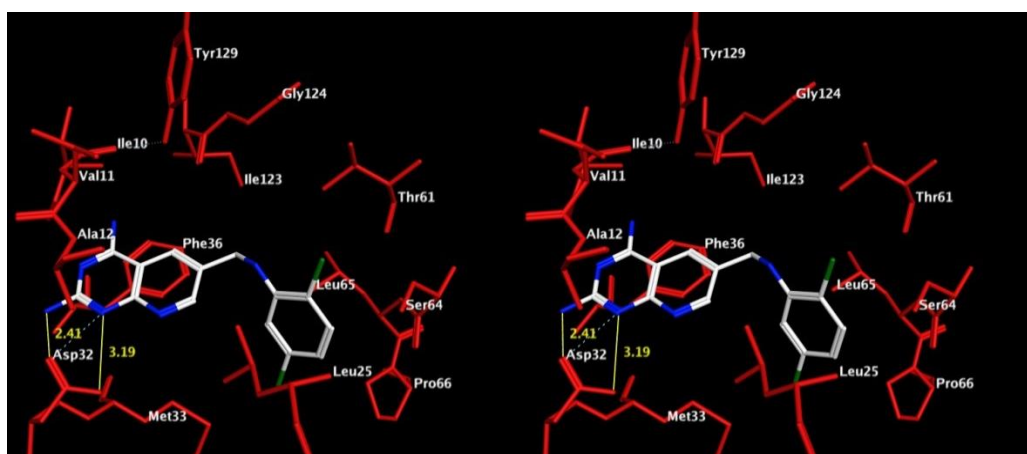


Figure 86: Stereoview. Docked structure of **168** in the pjDHFR homology model.

D.1.1.4.4.5. Docking of **168** in the F36C L65P double mutant pjDHFR model

Figure 87 shows the best docked pose of **168** (white) in the folate binding site of the double mutant pjDHFR active site model. The best docked pose of **168** in the folate binding site of the F36C L65P double mutant pjDHFR active site model retains the ionic bond of the bicyclic scaffold with Asp32. The bicyclic scaffold is placed deeper into the

binding pocket which permits the formation of a hydrogen bond with the side chain hydroxy moiety of Thr144.

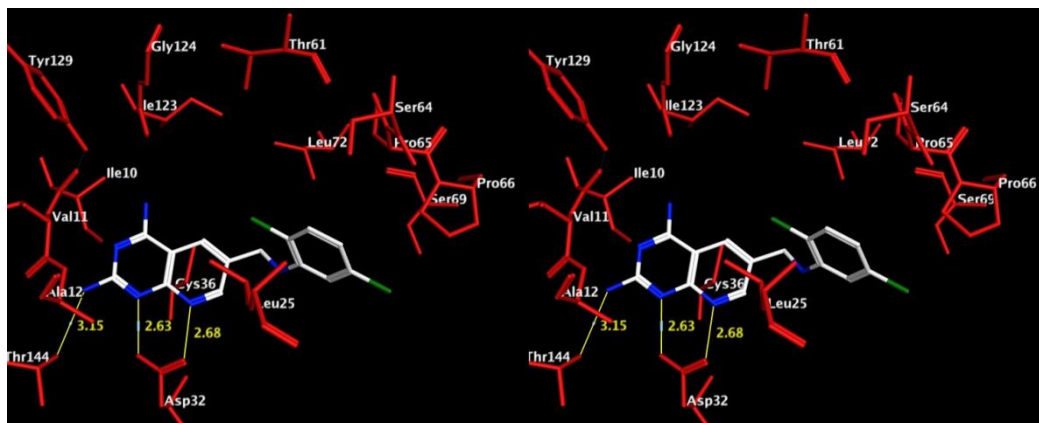


Figure 87: Stereoview. Docked structure of **168** in the double mutant pjDHFR homology model. pjDHFR homology model.

This additional hydrogen bond, which is not observed in the docked pose of **168** in the non-mutated enzyme, could offset the loss of stacking interactions between the bicyclic scaffold and Phe65 in the non-mutated enzyme. Additional hydrophobic interactions between the scaffold and the side chain carbon atoms of Leu25, Met33 and Cys36 help to stabilize the docked pose of **168**. This additional hydrophobic stabilization is less likely with the monocyclic pyrimidine scaffold of TMP in the mutated enzyme. The aryl side chain **168** maintains hydrophobic interactions with the side chain atoms of Leu25, Thr61, Ser64, and Leu65 and Pro66 as is seen with in the docked pose with the

non-mutated enzyme. Thus, a combination of an additional hydrogen bond and maintenance of hydrophobic interactions of the bicyclic scaffold and the aryl side chain provides, in part, a molecular explanation for the maintenance of potency of **168** against the F36C L65P double mutant pjDHFR. The docking score of **168** was -6.026 kcal/mol with MOE 2010.10 and -23.155 kJ/mol with LeadIT 2.0.1.

Docking of **192d** in the F36C L65P double mutant pjDHFR model

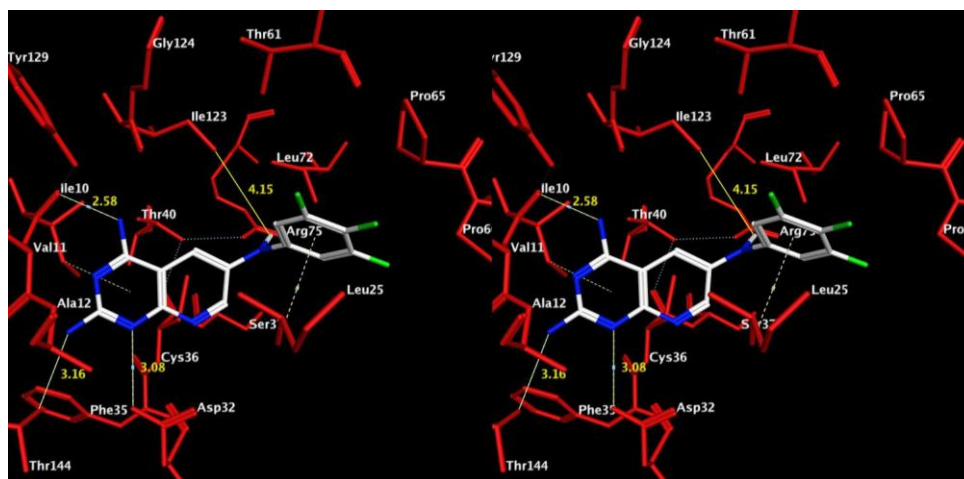


Figure 88: Stereoview. Docked structure of **192d** in the double mutant pjDHFR homology model.

Figure 88 shows the best docked pose of **192d** in the folate binding site of the F36C L65P double mutant pjDHFR active site model. In this pose the protonated N1 of **192d** forms the ionic bond with Asp32 while the 2-NH₂ group forms a hydrogen bond with the side chain hydroxy of Thr144. The pyrido[2,3-*d*]pyrimidine scaffold forms hydrophobic interactions with the side chain carbon atoms of Leu25, Met33 and Cys36. The 3',4',5'-trifluorophenyl side chain of **192d** is oriented similar to the docked conformation of **192d** in the non-mutated enzyme (Figure 86) and forms hydrophobic interactions with Leu25, Thr61 (not shown) Pro65 and Pro66. The docking score of **192d** was -8.145 kcal/mol with MOE 2010.10 and -30.969 with LeadIT 2.0.1.

Table 17: Docking scores for the best docked pose of TMP and **168**

	Wild type pjDHFR		F36C L65P Mutated pjDHFR	
	LeadIT 2.0.1	MOE 2010.10	LeadIT 2.0.1	MOE 2010.10
Trimethoprim	-23.023	-5.832	-16.367	-4.555
168	-24.638	-6.491	-23.155	-6.026

The homology model of pjDHFR and its mutated resistant form (F36C, L65P) could thus be used in docking studies to explain the significant loss of activity of TMP compared to **168** on the basis of the loss of the stacking interaction of Phe36 with the single pyrimidine ring of trimethoprim. Compound **168** has a bicyclic system and is able to compensate for most of the loss of this interaction in the mutated resistant pjDHFR via to a combination of a reinforced ionic bond between the protonated N1 and N8 nitrogens and Asp32, an additional hydrogen bond and maintenance of hydrophobic interactions of the bicyclic scaffold and the aryl side chain moiety. This is not possible with the monocyclic TMP docked into the resistant mutant pjDHFR. There is good correlation between the docking scores of **168** and TMP using both LeadIT 2.0.1 and MOE 2010.10 and their biological activities against wild type and double mutant pjDHFR. This further validates the homology models generated in this study.

D.1.1.4.5. Docking studies with 5-Methyl-6-thioaryl-thieno[2,3-*d*]pyrimidines in pjDHFR

Figure 89 shows the best docked pose of **193f** (Table 10) in the folate binding site of the pjDHFR model. In this pose the protonated N1 and 2-NH₂ of **193f** interact in an ionic bond with Asp32. This bidentate ionic bond with a conserved acid residue has been observed in most DHFR crystal structures. High scoring docked poses where a single bond between the 2-NH₂ of **193f** and Asp32 were observed, but were not considered in

these molecular modeling studies because such bindings deviate from the bidentate bond that is generally observed for 2,4-diamino substituted antifolates binding to a variety of DHFRs in their crystal structure.⁴²²

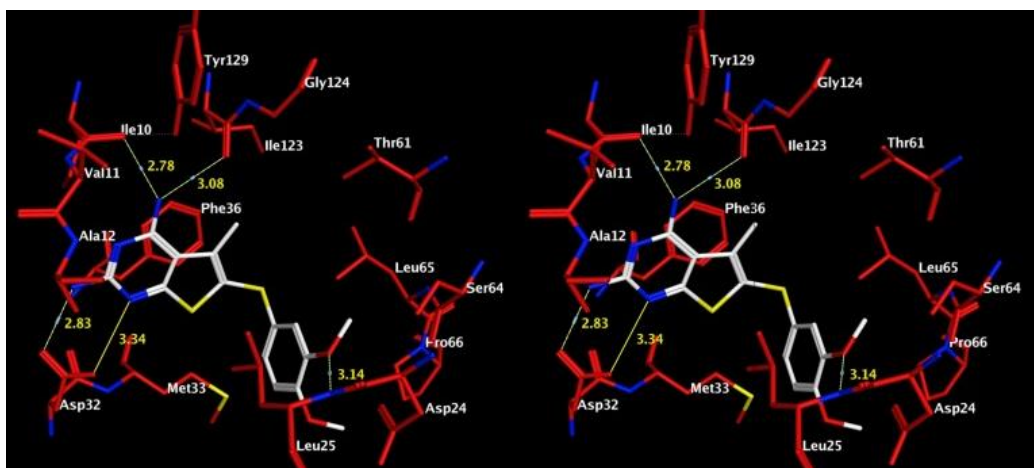


Figure 89. Stereoview. Docked pose of **193f** (white) in the pjDHFR active site model.

The 4-NH₂ moiety forms hydrogen bonds with the backbone of Ile10 and Val123. The thieno[2,3-*d*]pyrimidine scaffold is stabilized by a pi-stacking interaction with Phe36 and with the side chain carbon atoms of Ile10, Leu25 and Met33. The 5-Me moiety of **193f** is oriented towards a small hydrophobic pocket formed by Ile123, Leu72 and Leu65. The 3'-OMe forms a hydrogen bond with the backbone amide of Leu25. The 3',4'-dimethoxyphenyl side chain of **193f** is stabilized by hydrophobic interactions with the side chain of Leu25, Met33 and Leu65. This orientation of the 3',4'-dimethoxyphenyl side chain affords severe steric clashes with Phe31 in hDHFR (Figure 90). This forces a change in the docked conformation of the 3',4'-dimethoxyphenyl side chain in hDHFR that is detrimental to binding and translates to the lower overall docked score of **193f** in hDHFR (-6.132 kcal/mol) compared to pjDHFR (-6.663 kcal/mol). This docked score difference is reflected in the 19-fold selectivity of **193f** for pjDHFR. Figure 90 shows the

steric clash of the Ar side chain with Phe31 (hDHFR) superimposed on Met33 (pjDHFR) where there is no hinderance.

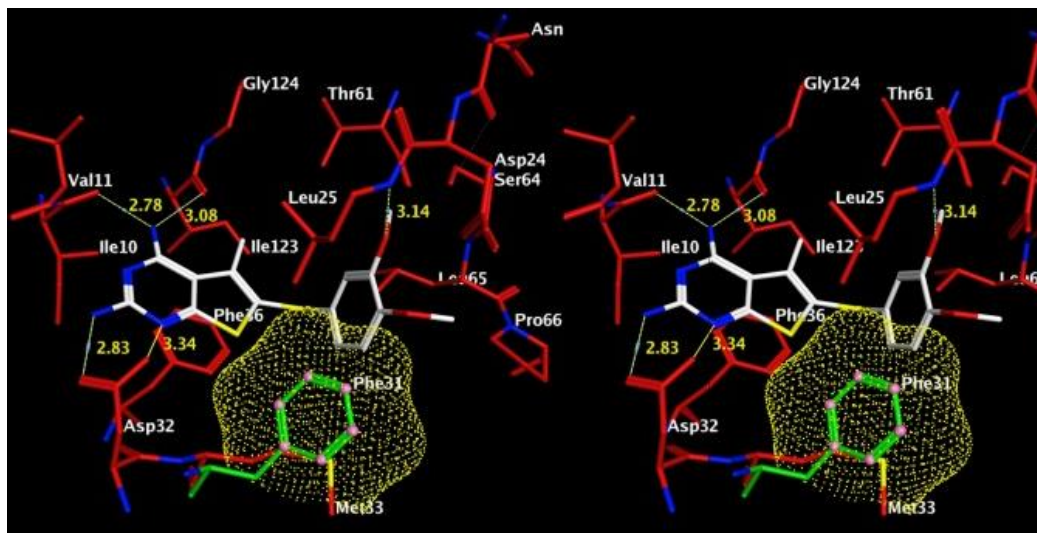


Figure 90. Stereoview. Steric clash of phenyl side chain of **193f** with Phe31 in hDHFR

D.1.2. Molecular modeling studies with tgDHFR

D.1.2.1 tgDHFR homology model

When this work was initiated there was no known crystal structure of tgDHFR. A homology model was hence built for evaluating the binding of **194a-c** (Table 11) in tgDHFR. The amino acid sequence of the dihydrofolate domain of the bifunctional enzyme was obtained from the Uniprot database (ID:DRTS_TOXGO [Q07422]).

Homology model building with automated comparative protein modeling servers

The amino acid sequence for tgDHFR (amino acids 1-300) obtained from the Uniprot website was submitted to four automated comparative protein modeling servers (Swiss-Model⁴¹⁷⁻⁴¹⁹, M4T Server⁴²⁴, 3D-Jigsaw⁴²⁵ and Proteus2⁴²⁶). Modeling was performed in

the automated mode. The crystal structure templates used by the modeling servers for the generation of the models were bifunctional DHFR-TS crystal structures from *T. cruzi* (PDB:2H2Q⁴²⁷, Swiss-Model, M4T Server, 3D-Jigsaw; 33% sequence identity) and *P. falciparum* (PDB:1J3I⁹², Proteus2, 31% sequence identity). Ramachandran plots were generated for all the homology models returned. The models returned by the servers showed an average of four outlying amino acid residues. All the observed outlying amino acid residues were distant (>8 Å away) from the putative folate binding pocket and were not expected to influence the docking results.

Homology model building with MOE 2009.10

A homology model was also built using MOE 2009.10⁴²⁸ using the crystal structure of the bifunctional DHFR-TS from *T. cruzi* (PDB: 2H2Q, chain A) as the template. Sequence alignment was performed using MOE_Align using the ‘actual secondary structure’ option in MOE. The final homology model returned by the program was subjected to further energy minimization using Amber99 as the forcefield and a 0.5 RMS gradient. A Ramachandran plot of the model showed the presence of seven outlying residues (Phe29, Ala125, Glu136, Tyr138, Asp186, Ile229 and Lys231). The outlying amino acids were locally energy minimized using the Amber99 forcefield. The model was imported into Sybyl X and refined using the Fix Bumps functionality available within Sybyl X.

D.1.2.2. Docking studies with the tgDHFR homology model.

Active site definition

The models returned were superposed with *P. falciparum* DHFR (PDB:1J3I) and the crystal structure ligand (6,6-dimethyl-1-[3-(2,4,5-trichlorophenoxy)propoxy]-1,6-dihydro-1,3,5-triazine-2,4-diamine, WR99210)⁹² and NADPH were added to the model. Protein preparation prior to docking was performed using the LigX functionality in MOE 2009.10. LigX is a graphical interface and collection of procedures for conducting interactive ligand modification and energy minimization in the active site of a flexible receptor. In LigX calculations, the receptor atoms far from the ligand are constrained and not allowed to move while receptor atoms in the active site of the protein are allowed to move but are subject to tether restraints that discourage gross movement. The procedure was performed with the default settings. The process of protein preparation using LigX involves addition of hydrogen atoms according to the ionization state of the atoms of the molecule/protein loaded. The heavy atoms are then fixed and a brief energy minimization is carried out to refine the positions of the added hydrogen atoms. The receptor atoms are then tethered during geometry optimization so that they do not deviate too much from their initial coordinates and then energy minimized using the Amber99 forcefield.

Ligands were built using the molecule builder function in MOE and were energy minimized to their local minima using the MMF94X forcefield to a constant of 0.05 kcal/mol. Ligands were docked into the active site of the prepared protein using the docking suite as implemented in Flexx 3.1.2. The active site was defined by a sphere of 6.5 Å near the WR99210 ligand. The docking was performed using Alpha triangle base placement method. Around 50 poses were returned for each compound at the end of each docking run. The docked poses were imported into MOE 2009.10 and manually examined in the binding pocket to ensure quality of docking and to confirm absence of

steric clashes with the amino acid residues of the binding pocket. The docked poses were scored using the affinity dG scoring system refined using the forcefield system and rescored using London dG scoring system implemented in MOE. The binding poses were also visualized using the ligplot utility as in MOE.

Validation of the docking system

Validation of Flexx⁴²⁹ as a suitable docking system was carried out using two docking studies. In the first study, the X-ray crystal structure of *P. falciparum* DHFR (1J3I⁹²) was used for docking WR99210, the native ligand in the crystal structure. The protein was prepared as mentioned above. The ligand was built and minimized in MOE. Docking was carried out with Flexx as described above. The best docked pose of WR99210 had an RMSD of 1.1782 Å compared to the crystal structure ligand. The docked pose of WR99210 maintained all the contacts exhibited by the crystal structure ligand. The best docked pose of WR99210 had a score of -6.291 kcal/mol.

Docking studies with compounds 194a-b

Compounds **194a-b** (Table 11) were docked into the tgDHFR model as representative examples for compounds in this series using Flexx as described above. The docked poses were scored in MOE and ranked on the basis of the scores. The best docked poses of **194a-b** showed high consistency in terms of the conformation of the ligands in the active site (Figure 92, and the protein-ligand contacts made as a result of the orientation. The best docked pose of **194a** had a score of -6.861 kcal/mol while the best docked pose of **194b** had a score of -6.742 kcal/mol. The slight difference in the scores of the two compounds reflects the observed difference in the tgDHFR inhibitory potencies of the two compounds.

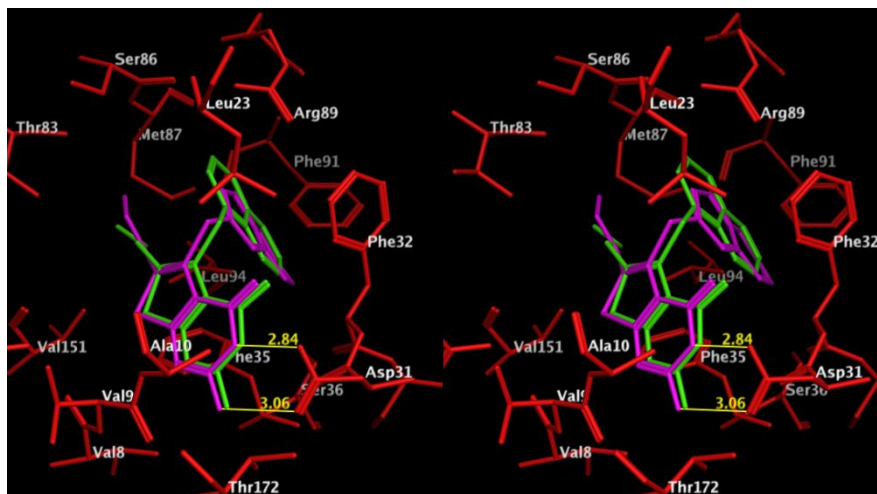


Figure 91. Stereoview. Superimposition of docked pose of **194a** (green) and **194b** (purple) in the active site of the tgDHFR model showing similar docked conformations.

Figure 92 shows the docked pose of **194a** in the folate binding site of the tgDHFR model. In this pose, the 2-NH₂ and N3 moieties of **194a** interact with Asp31. The thieno[2,3-*d*]pyrimidine ring pi-stacks with Phe35 further stabilizing this pose. The 1-naphthyl ring of **194a** is placed in the hydrophobic pocket formed by Phe32, Phe91, Leu23 and Met87. The naphthyl ring forms pi-stacking interactions with Phe32.

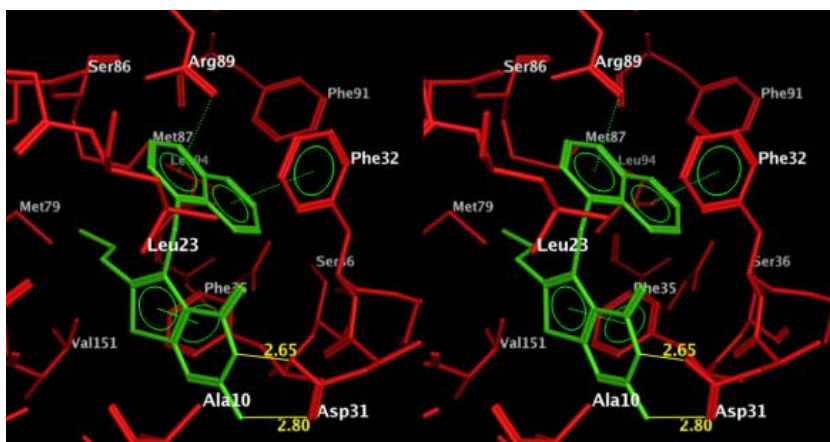


Figure 92. Stereoview. Docked pose of **194a** (green) in the active site of the tgDHFR model

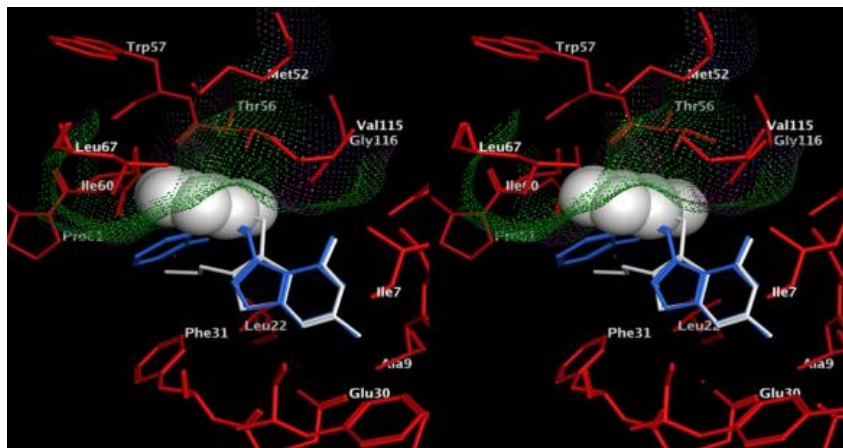


Figure 93. Stereoview. . Superimposition of **194a** (white) on the furo[2,3-*d*]pyrimidine ligand (blue) in hDHFR. (PDB: 3K45³⁵⁹). The naphthyl ring of **194a** (space fill) shows steric clashes with molecular surface near Ile60 and Leu67 (represented in dots) suggesting poor inhibition of hDHFR as observed for **194a**.

Importantly, the 1-naphthyl moiety is involved in a cation-pi interaction⁴³⁰ with the protonated Arg89 stabilizing the docked conformation. The propyl side chain forms hydrophobic interactions with Met79, Met87 and Val151. The propyl side chain also aids in orienting the naphthyl ring correctly in the hydrophobic pocket and its interactions with Arg89. Docking of **194a-b** in hDHFR (PDB id: 3K45³⁵⁹) resulted in docked poses outside the folate binding site. Superimposition of the thieno[2,3-*d*]pyrimidine ring of **194a** on the furo[2,3-*d*]pyrimidine ring of the bound ligand in 3K45 indicated steric clashes with the side chain of Ile60 and Leu67 in hDHFR (Figure 93), which could explain, in part, the decreased activity of **194a-b** against hDHFR.

D.1.3. Molecular modeling studies with *T. gondii* thymidylate synthase

D.1.3.1. Development of a tgTS homology model:

When this work was initiated there was known crystal structure of tgTS, hence a homology model was built using the automated comparative protein modeling server SWISSMODEL⁴¹⁶⁻⁴¹⁹ and using MOE 2010.10⁴³¹ for evaluating the binding of **194d-k** (Table 12) in tgTS. Docking studies were performed using LeadIT 2.1.0¹³¹ and Sybyl-X 1.2.⁴²³

Homology model building

tgTS is a part of a bifunctional DHFR-TS enzyme, as is seen with the TS domains of other apicomplexan parasites. The sequence for the TS portion (Uniprot id: Q07422, amino acids 322 – 610) was obtained from the Uniprot website. Modeling using the Swissmodel server⁴¹⁶ was done using the automated mode.

An alternate model was generated using the homology model module of MOE 2010.10. Two models using the bifunctional DHFR-TS crystal structures of *Trypanosoma cruzi* (PDB: 2H2Q)⁴³² or wild type *Plasmodium falciparum* (PDB: 1J3I)⁹² were generated using the homology builder module as implemented in MOE.

Sequence alignment:

1	MSLFKIRMPETVAEGTRLALRAFSLVVAVDEHGGIGDGRSIPWNVP-EDMKFFRDLTTKL	59	Q27793	DRTS_TRYCR
1	-----	0	P13100	TYSY_PNECA
1	-----MOKPVCLVVAMTPKRGIGINNGLPWPHLTTDFKHFSRVTKIT	42	Q07422	DRTS_TOXGO
1	-----	0	P04818	TYSY_HUMAN
60	-----RGKNVKPS---PAKRNAVVMGRKTWDSIPPFRPLPGRNLNVVL	99	Q27793	DRTS_TRYCR
1	-----	0	P13100	TYSY_PNECA
43	PEEASRLNGWLPRKFAKTGDSGLSPSPVGKRFNAVVMGRKTWESMPRKFRPLVDRLNIVV	102	Q07422	DRTS_TOXGO
1	-----	0	P04818	TYSY_HUMAN
100	SSTLTTHQLLDGLPDEEKRNLHADSIVAVNGGLEQALRLLASPNYTPSIETVYCIGGGSV	159	Q27793	DRTS_TRYCR
1	-----	0	P13100	TYSY_PNECA
103	SSSLKEEDIAAEKPPQAEQG----QVRVVCASLPAALSL-LEEEYKDSVDQIFVVGAGL	156	Q07422	DRTS_TOXGO
1	-----	0	P04818	TYSY_HUMAN
160	YAEALRPPCVHLLQAIYRTTIRASESSCSVFFRV-----	193	Q27793	DRTS_TRYCR
1	-----	0	P13100	TYSY_PNECA
157	YEAALSLGVASH---LYIT-RVAREFPCDVFFPAFPDDILSNKSTAAQAAAPAESVFVP	212	Q07422	DRTS_TOXGO
1	-----	0	P04818	TYSY_HUMAN
194	--PESGTEAAA-----	202	Q27793	DRTS_TRYCR
1	-----	0	P13100	TYSY_PNECA
213	FCPELGREKDNEATYRPIFISKTFSDNGVPYDFVLEKRRKTTDDAATAEPSNAMSSLTST	272	Q07422	DRTS_TOXGO
1	-----	0	P04818	TYSY_HUMAN
203	-----GIEWQRETISEELTSANGNETKYFEKLIPNRREEEQYLS	242	Q27793	DRTS_TRYCR
1	-----MVNAEEQQYLN	11	P13100	TYSY_PNECA
273	REITPVHGLQAPSSAAAIAPVLAWMDEEDRK---KREQELIRAVPHVHFRGHEEFQYLD	329	Q07422	DRTS_TOXGO
1	---MPVAGSELPRRPL--PP---AAQE-----RDAEPRPPHGLQYLG	35	P04818	TYSY_HUMAN
	* **			
243	LVDRIIREGNVHKDRIGVGILSIFGAQ-MRFSLRNNRLPLLTIKRVFWRGVCEELLWFLR	301	Q27793	DRTS_TRYCR
12	LVQYIINHGEDRPDRGTGTLSVFAPSPKFSLRNKTFLPLTIKRVFIRGVIEELLWFIR	71	P13100	TYSY_PNECA
330	LIADIINNGRTMDDRTGTVGVISKFGCT-MRYSL-DQAFPLLTIKRVFWKGVLEELLWFIR	387	Q07422	DRTS_TOXGO
36	QIQHILRCGVRKDDRTGTGTLSVFGMQ-ARYSL-RDEFPLLTIKRVFWKGVLEELLWFIK	93	P04818	TYSY_HUMAN
	: *: * * * * *: * * * * : * * * * : * * * * * : * * * * * :			
302	GETYAKKLSDKGVHIWDDNGSRAFLDSRGLTEYEEMDLGPVYGFQWRHFGAAYTHHDANY	361	Q27793	DRTS_TRYCR
72	GETDSLKLREKNIHIWDANGSREYLDISGLTKRQEGDLGPIYGFQWRHFGAEYIDCKTNY	131	P13100	TYSY_PNECA
388	GDTNANHLSEKGVKIWDKNVTRFLDSRNLPHREVGDIGPGYGFQWRHFGAAYKDMHTDY	447	Q07422	DRTS_TOXGO
94	GSTNAKELSSKGVKIWDANGSRDFLDSLGFSTREEGDLGPVYGFQWRHFGAEYRDMESDY	153	P04818	TYSY_HUMAN
	* * : * * * : * * * * : * * * * : * * * * * * * * * * * :			
362	DGQGVDDQIKAVETLKTNPDDRMLFTAWNPSALPRMALPPCHLLAQFYVS-----NGE	415	Q27793	DRTS_TRYCR
132	IGQGVDDQLANIIQKIRTSPYDRRLILSAWNPADLEKMALPPCHMFCQFYVHIPSNHRPE	191	P13100	TYSY_PNECA
448	TGQGVDDQLKNVIQMLRTNPDDRMLTAWNPAALDEMALPPCHLLCQFYVN-----DQKE	502	Q07422	DRTS_TOXGO
154	SGQGVDDQLQRVIDTIKTNPDDRRIIMCAWNPRLPLMALPPCHALCQFYVV-----N-SE	207	P04818	TYSY_HUMAN
	*****: : : : * * * * * : * * * * * * * * * * * * * * * *			
416	LSCMLYQRSCDMGLGVFPFNIAASYALLTILIAKATGLRPGELVHTLGDAHVYSNHVEPCNE	475	Q27793	DRTS_TRYCR
192	LSCQLYQRSCDMGLGVFPFNIAASYALLTCMIAHVCDLDPGDFIHMVGDCHIYKDHIQALQQ	251	P13100	TYSY_PNECA
503	LSCIMYQRSCDVGLGVFPFNIAASYLLTLMVAHVCNLKPKEFIHFMGNTHVYTNHVEALKE	562	Q07422	DRTS_TOXGO
208	LSCQLYQRSGDMGLGVFPFNIAASYALLTYMIAHITGLKPGDFIHTLGDAHIYLNHIEPLKI	267	P04818	TYSY_HUMAN
	*** : *** :			
476	QLKRVPRAPFYLVFRE--REFLEDYEEGDMEVIDYAPYPPISMKMAV	521	Q27793	DRTS_TRYCR
252	QLTRSPRPFPITLSLNR--ITDIEDFTLDDFNQNYHPYETIKMKMSI	297	P13100	TYSY_PNECA
563	QLRREPRFPPIVNIILNKERIKEIDFTAEDFEVVGYPVPHGRIQMEMAV	610	Q07422	DRTS_TOXGO
268	QLQREPRFPFKIRILRK--VEKIDDFKAEDFQIEGYNPHPTIKMEMAV	313	P04818	TYSY_HUMAN
	** * * * * : : . . : * * : * * : * * * * :			

Figure 94. Sequence alignment of *T. cruzi* TS (DRTS_TRYCR),⁴³³ pcTS (TYSY_PNECA),⁴³⁴ tgTS (DRTS_TOXGO),⁴³⁵ and hTS (TYSY_HUMAN)⁴³⁶ using Clustal W.⁴³⁷

The resulting models were minimized using Amber99 forcefield. Superimposition of the resulting models indicated high overall similarities and a C α -RMSD of 0.855 Å (Figure 95).



Figure 95. Ribbon diagram of the superimposition of homology models generated using T. cruzi (blue), T. cruzi (brown) and swissmodel (magenta) showing good overlap of the models. C α -RMSD: 0.855 Å

Model validation:

The model returned from the software was evaluated using structure assessment tools (Ramachandran plot, ProSA,^{410, 411} Procheck,⁴¹² Anolea,⁴¹³ Gromos,⁴¹⁴ and QMEAN⁴¹⁵) as implemented on the Swissmodel server.⁴¹⁶

- a) **Ramachandran plot** (Figure 96): A Ramachandran plot generated for the pJDHFR model showed that, with the exception of Glu580, all the residues have acceptable geometries. Since Glu580 is distant from the active site, and is not expected to influence the docking studies, modeling studies were performed without any additional refinements.

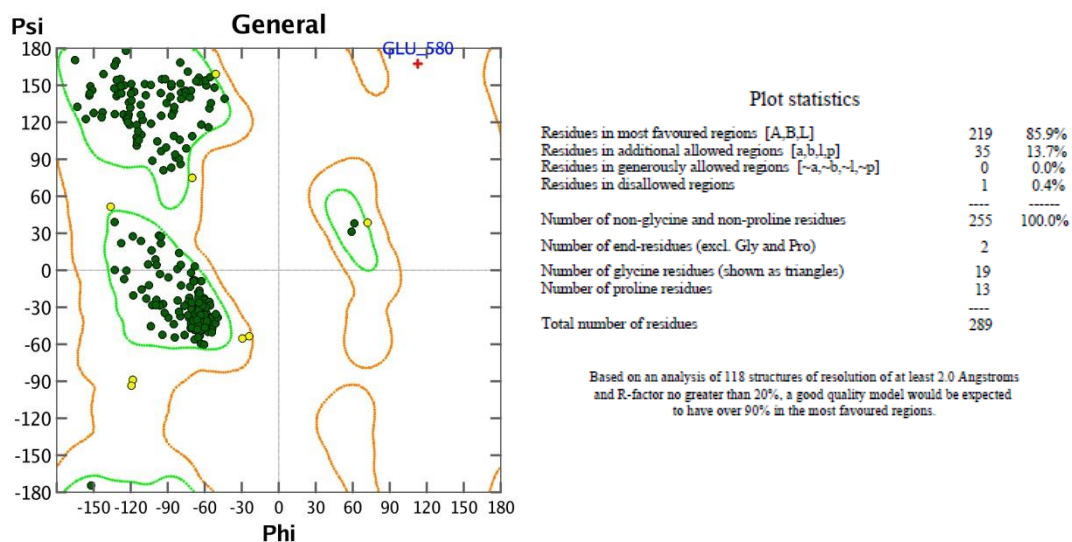


Figure 96: Ramachandran plot and Procheck analysis of the tgTS homology model generated using MOE 2008.10

- b) **Procheck**⁴¹² (Figure 96): A Procheck analysis of the model indicated 85.9% of residues in the most favored regions, 13.7% residues in additional allowed regions, 0% in the generously allowed regions and 0.4% (1 residue, Glu 580) in the disallowed region.

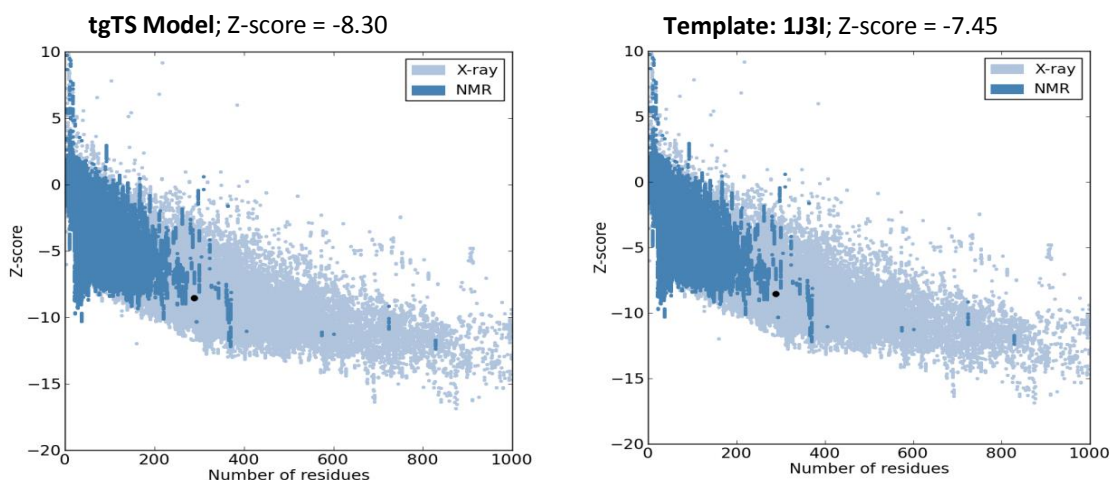


Figure 97: ProSA analysis of the tgTS homology model generated using MOE 2008.10

- c) **ProSA**^{410, 411} ProSA calculates an overall quality score (z-score) for a specific input structure for comparison with the z-scores of all experimentally determined

protein chains in PDB. ProSA can be used to check whether the z -score of the input model is within the range of scores typically found for native proteins of similar size with a score outside a range characteristic for native proteins indicating probable structural errors. The ProSA analysis of the tgTS model (Figure 97) is comparable to the score of the template (PDB: 1J3I) and fell within acceptable limits for z -scores.

- d) Details of validation including Anolea,⁴¹³ Gromos,⁴¹⁴ and QMEAN⁴¹⁵ are provided in the experimental section. The results from these studies confirmed the validity of the tgTS model for docking studies.

D.1.3.2. Docking studies with the tgTS homology model

Active site definition and docking to the tgTS model

The tgTS homology model prepared in MOE was homology aligned and superimposed on the X-ray crystal structure of tcTS (PDB: 2H2Q⁴²⁷) containing NADP, DUMP and DH3 (2,4-diamino-5-[3',4'-dimethoxy-5'-(5-carboxyl- 1-pentynyl)]benzyl pyrimidine), the co-crystallized ligand in 2H2Q, were added to the model. The active site was defined by a sphere of 6.5 Å near the ligand. Protein preparation prior to docking was performed using the LigX functionality in MOE 2010.10. The procedure was performed with the default settings. The process of protein preparation using LigX involves addition of hydrogen atoms according to the ionization state of the atoms of the molecule/protein loaded. The heavy atoms are then fixed and a brief energy minimization is carried out to refine the positions of the added hydrogen atoms. The receptor atoms are then tethered during geometry optimization so that they do not deviate too much from

their initial coordinates and then energy minimized using the Amber99 forcefield.

Ligands used for docking were sketched in MOE, minimized and exported as an SDF file.

Docking of ligands to the tgTS model were performed using LeadIT 1.3.0¹³¹ and MOE 2010.10.⁴³¹ The docking procedure in LeadIT 1.3.0 was constrained to the active site of the protein. Polar hydrogen atoms of amino acids with a polar side chain were not constrained, thereby permitting free rotation. Base placement of fragments for docking was carried out using triangle matching. Default parameters were used for scoring and clash handling. The maximum number of solutions per iteration and the maximum number of solution per fragmentation were set to 500. Ten poses were obtained per molecule. Docking processes were repeated to ensure reproducibility of the docked conformations. The docked poses were exported to MOE 2010.10, rescored using the affinity dG scoring system, refined using the forcefield system and rescored using London dG scoring system. The binding poses were also visualized using the ligplot utility in MOE and the Poseview utility in LeadIT 1.3.0.

Ligands were docked into the active site of the prepared protein using the docking suite as implemented in MOE. The docking was restricted to the active site pocket residues using the Alpha triangle placement method. Refinement of the docked poses was carried out using the Forcefield refinement scheme and scored using the Affinity dG scoring system. Around 30 poses were returned for each compound at the end of each docking run. The docked poses were examined in the binding pocket to confirm absence of steric clashes with the amino acid residues of the binding pocket. The docked poses were scored using the affinity dG scoring system, refined using the forcefield system and

rescored using London dG scoring system. The binding poses were also visualized using the ligplot utility in MOE.

Validation of the docking system

The tgTS structure was obtained by means of homology modeling using tcTS as template. Hence, the validation of LeadIT and MOE as suitable docking systems for tgTS were carried out by redocking the native ligand in the X-ray crystal structure of tcTS (PDB: 2H2Q). The protein was prepared as mentioned above. The ligand was built and minimized in MOE. Docking was carried out with LeadIT and MOE as described above. The best docked pose of the ligand had an RMSD of 0.941 Å in LeadIT and 1.036 Å in MOE compared to the crystal structure. Thus, LeadIT and MOE were validated and were chosen for docking studies with the proposed analogs.

D.1.3.3. Molecular modeling studies of 2-Amino-4-oxo-5-arylthio-substituted pyrimido[2,3-*d*]indoles 194d-j with *T. gondii* thymidylate synthase

D.1.3.3.1. Docking of 194e in the tgTS homology model

Figure 98 shows the best docked pose of **194e** (white) in the binding site of the tgTS model. In this pose N3 forms a hydrogen bond with Asp553. The pyrido[4,5-*b*]indole scaffold is stabilized by hydrophobic interactions with Ile402, Trp403, Asn406, Leu486, Leu516, Met608 and Ala609. The 2-naphthyl moiety of **194e** forms hydrophobic interactions with Phe374, Ile402, Leu516 and Phe520. Specifically, the second ring of the 2-naphthyl moiety forms hydrophobic interactions with Phe374. This additional

interaction of **194e** and the 1-naphthyl analog **194f** with tgTS Phe374 compared to a lack of similar interaction of the phenyl analog **194d** (Figure 88) explains, in part, the 10-fold improved potency of **194e** and 5-fold for **194f** for tgTS over **194d**. The docking score of **194e** was -25.942 kJ/mol.

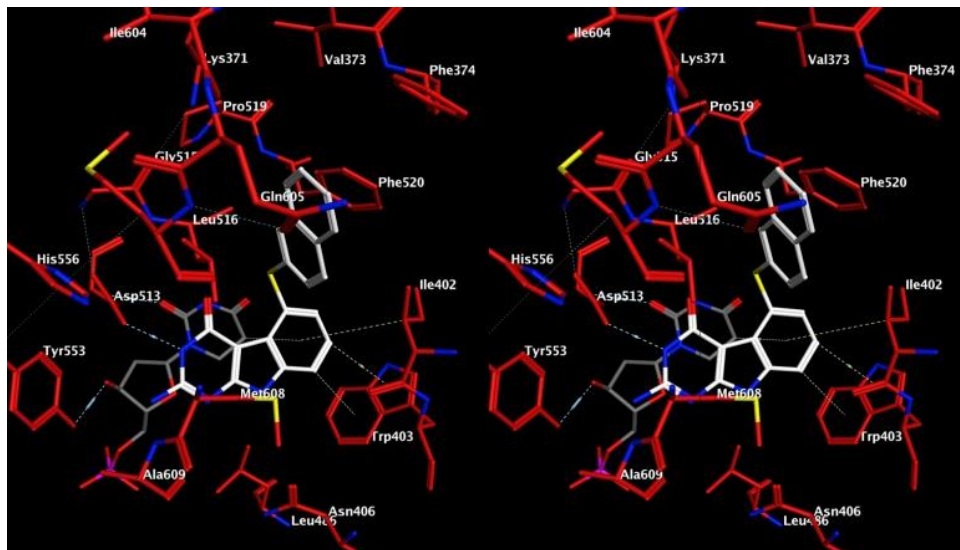


Figure 98. Stereoview. Docked pose of **194e** (white) in the tgTS homology model

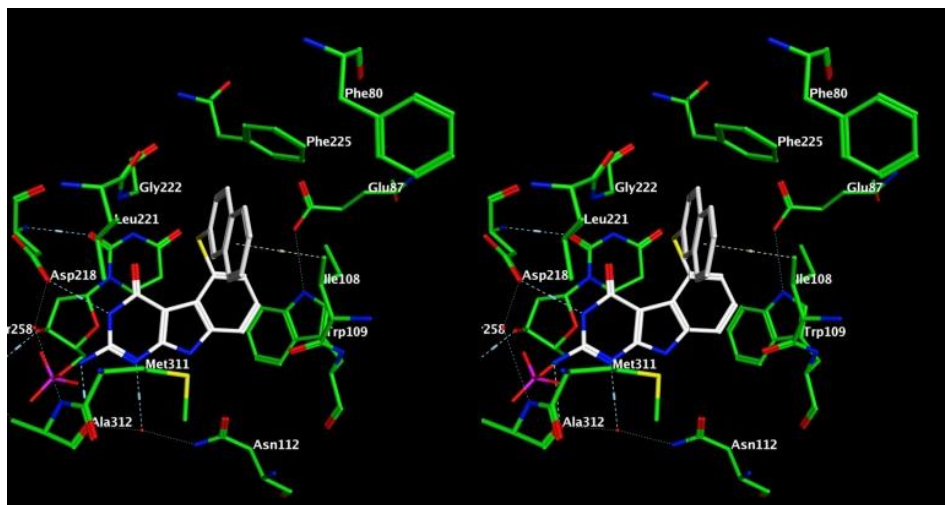


Figure 99. Stereoview. Docked pose of **194e** (white) in hTS (PDB: 1JU6⁴³⁸)

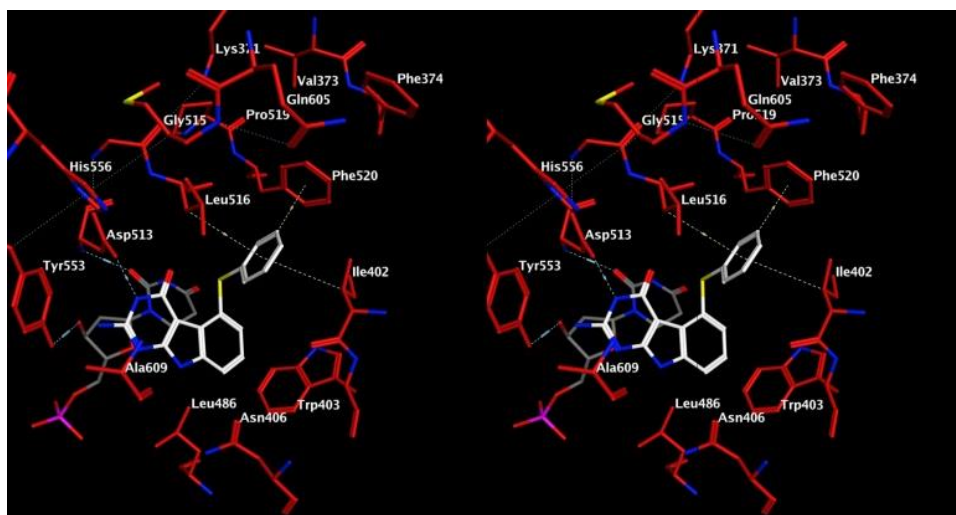


Figure 100. Stereoview. Docked pose of **194d** (white) in the tgTS active site homology model.

The 5-thiophenyl ring of **194d** does not extend far enough in the binding pocket to interact with Phe374 (Figure 100). The amino acid corresponding to Phe374 in hTS is Phe80 and is found to be oriented away from the binding pocket in the hTS crystal structure (PDB: 1JU6⁴³⁸) (Figure 99), and would not interact with the 2-naphthyl moiety of **194e** in its docked pose (Figure 99) and provides, in part, an explanation for the significant selectivity of **194e** for tgTS over hTS (Table 12). There are indications in the literature⁴³⁹ that this region of Phe374 coincides with Ala287 of the *C. hominis* TS structure and is a region previously identified^{440, 441} as a possible target for species selective drug design.

D.1.3.3.2. X-ray crystal structure of **194d** in tgTS



Figure 101. Ribbon depiction of the superimposition of the docked pose of **194d** in the tgTS homology model (white) and the X-ray crystal structure (red, PDB: 4KY4)³⁵⁴ of **194d** in tgTS. C α RMSD = 0.68 Å

The X-ray crystal structure of **194d** in tgTS was recently published. (PDB: 4KY4)³⁵⁴ Superimposition of the docked pose of **194d** in the tgTS homology model and its X-ray crystal structure (Figure 101) showed remarkable similarity between the predicted and the crystal structure of tgTS. (C α RMSD = 0.68 Å). Further, the predicted bound conformation of **194d** and its crystallized conformation show strong similarities, serving to validate the docking software and docking protocol for future use in designing

inhibitors that target tgTS. The crystal structure pose of **194d** shows all binding interactions seen in its predicted binding pose. A closer look at the binding pocket (Figure 102) shows that, with the exception of Phe374 and Arg603 (not shown), the predicted conformation of the binding pocket residues matches their crystal structure conformation. As predicted, Phe374 does not interact with **194d**.

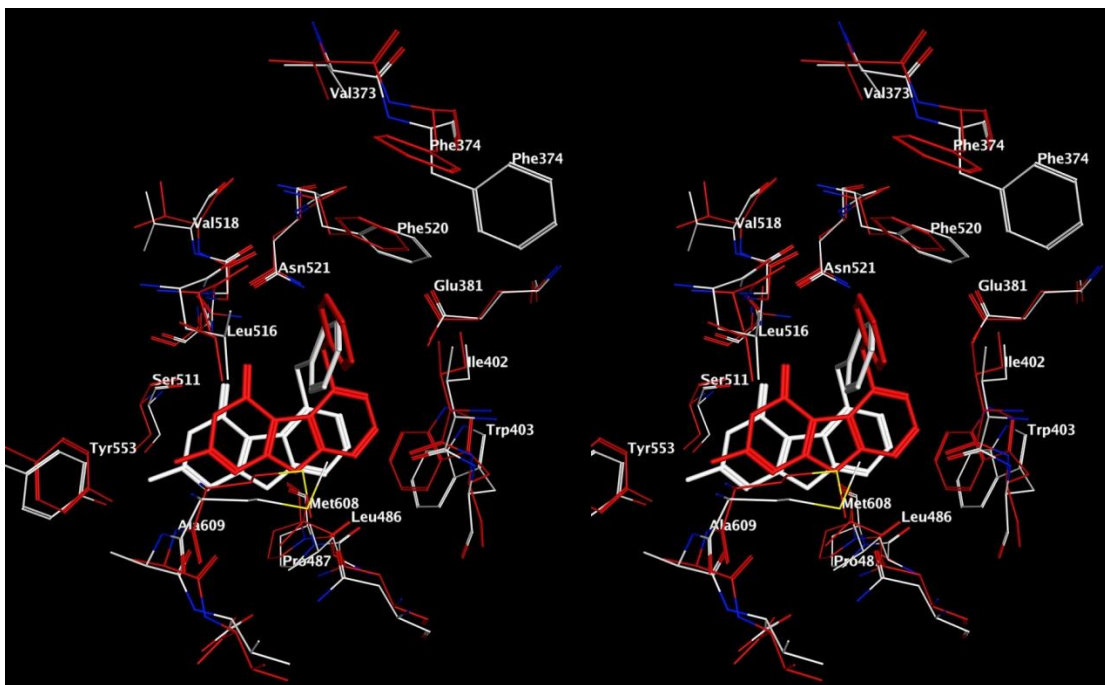


Figure 102. Superimposition of the docked conformation of **194d** in the tgTS homology model (white) and its X-ray crystal structure (red, PDB: 4KY4)³⁵⁴ in the tgTS binding pocket.

D.1.3.3.3. Docking of compound **194f** in the tgTS homology model

Figure 103 shows the docked pose of **194f** in the tgTS active site model. The docked pose of **194f** is similar to the docked pose of **194e** (Figure 98) and retains interactions described for **194e** in its docked pose. The docking score of **194f** was - 22.996 kJ/mol. The X-ray crystal structure of **194f** was recently published (PDB: 4KYA).³⁵⁴ Superimposition of the docked conformation of **194f** in the tgTS homology

model and its X-ray crystal structure³⁵⁴ (Figure 103) in the tgTS binding pocket shows that the predicted interactions of the tricyclic scaffold of **194f** are maintained. However, the crystal structure conformation of the 1'-naphthyl moiety of **194f** is rotated by about 115° relative to the predicted conformation of the 1'-naphthyl moiety. This occurs, presumably, due to the alternate position of the side chains of Phe374 and Arg603 in the crystal structure compared to their predicted side chain conformations in the homology model. The predicted and actual conformation of the backbone residues of Phe374 and Arg603 closely match. It is interesting to note that the predicted relative distance between the side chains of Arg603 and Phe374 is similar to that seen in the homology model of the active site. (Figure 105)

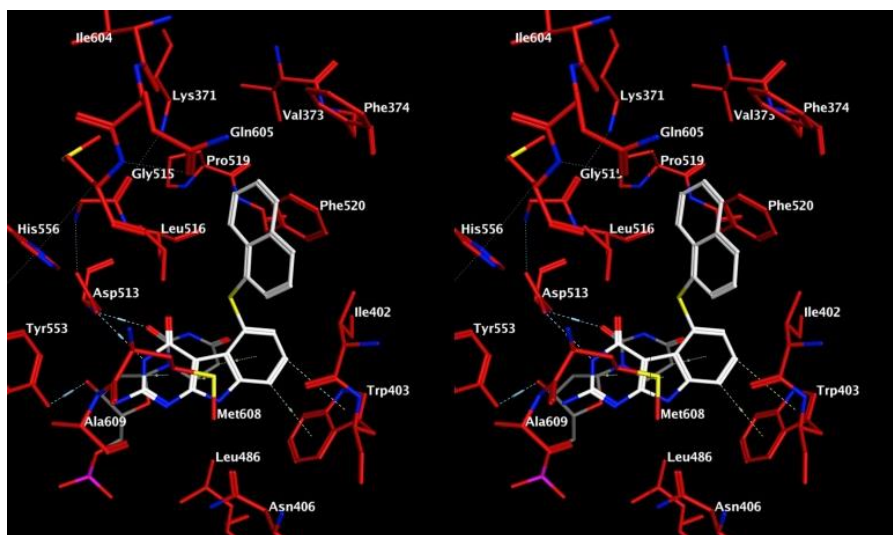


Figure 103. Stereoview. Docked pose of **194f** (white) in the tgTS active site homology model.

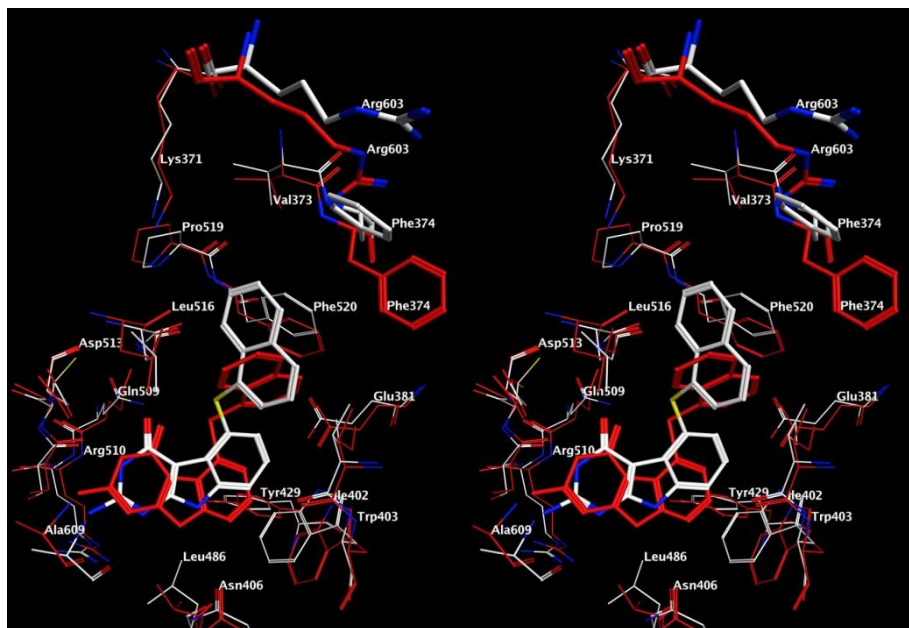


Figure 104. Stereoview. Superimposition of the docked conformation of **194f** in the tgTS homology model (white) and its X-ray crystal structure (red, PDB: 4KY4).³⁵⁴

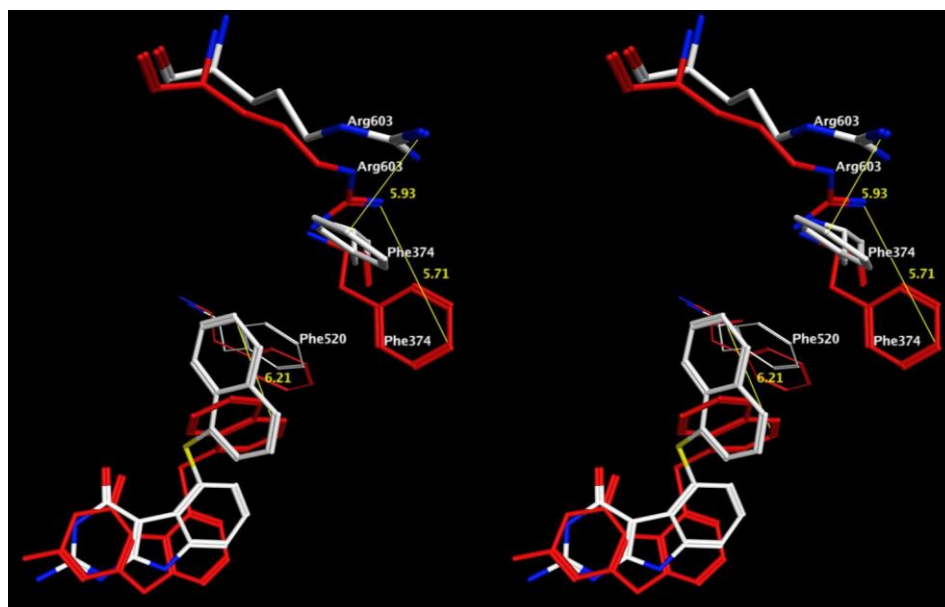


Figure 105. Stereoview. Difference in the predicted (white) and crystal structure (red)³⁵⁴ conformations of the 1'-naphthyl of **194f** and the side chains of Phe374 and Arg603 in tgTS.

The strong correlation between the predicted and bound conformations of **194e** and **194f** provides validation for the utility of the docking software and protocols used in this study for design of future analogs against tgTS.

D.1.3.4. Topomer CoMFA analysis of bicyclic inhibitors of hTS and tgTS

The advantages of using topomer CoMFA over traditional CoMFA are described above in the Biochemical Review section. Importantly, topomer CoMFA methods are sensitive only to the aligned 3D topomer fragments, and do not have any receptor requirements. Hence, it was used for the 3D QSAR analysis of tgTS or hTS inhibitors previously reported in our laboratory to elucidate steric and/or electronic features that lead to potent activity against either hTS or tgTS. Since the compounds used in this study for generating the Topomer CoMFA model share a bicyclic 6-5 (pyrrolo[2,3-*d*]pyrimidine or a thieno[2,3-*d*]pyrimidine) core, the differences in biological activity against hTS or tgTS probably originate from differences in the substitutions on the bicyclic core. Topomer CoMFA calculations were performed using Sybyl X 1.2⁵ on a Windows platform.

D.1.3.4.1. Data Set for Topomer CoMFA Analysis

Gangjee *et al.*^{312, 355-365} have reported the synthesis and biological activities against hTS and tgTS of >100 bicyclic non-classical pyrrolo[2,3-*d*]pyrimidines and thieno[2,3-*d*]pyrimidines containing a 2-amino-4-oxo moiety (Figure 58). Of these, 85 compounds were identified for which discrete biological activities against hTS and/or tgTS were reported in the literature. There are no previous literature reports of these

compounds in CoMFA studies. The molecules were sketched in MOE 2009.10⁴²⁸ and energy minimized using the MMFF94X forcefield to a constant of 0.05 kcal/mol. The molecules were imported into a Sybyl database followed by addition of Gasteiger-Huckel charges. The biological activities were added to the table and were converted to the corresponding log values for use in the model generation. The compounds showed an approximate 3 log unit range in their activities against hTS or tgTS. Approximately 20% of these compounds were used for generation of a test set while the rest of the molecules were used in the training set.

D.1.3.4.2. Fragmentation for Topomer CoMFA Generation.

The pyrrolo[2,3-*d*]pyrimidine and thieno[2,3-*d*]pyrimidine inhibitors used in this study vary in the nature of the substituents on either the 5- or the 6- position. Hence, three different methods were used to fragment these inhibitors: Fragmentation using the ‘Split in two’ option at either the 5- or the 6- positions (Figure 2 A, B) and fragmentation involving a common bicyclic scaffold (Figure 2 C) with two substituents (R₁, R₂) attached at the 5- and 6- positions respectively of the scaffold. The resulting fragments were stored in separate Sybyl tables.

Model Generation: Topomer CoMFA models were generated using the biological evaluation data for hTS and tgTS for each of the three sets generated by the above fragmentation schemes.

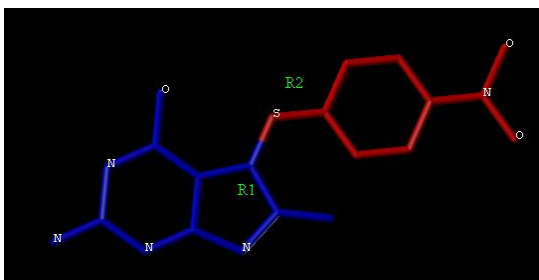


Figure 106A. Method A

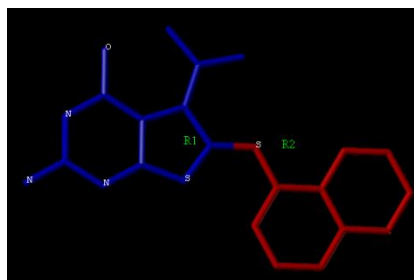


Figure 106B. Method B

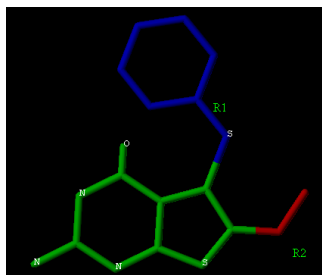


Figure 106C. Method C

Figure 106: Fragmentation methods for compounds used in this study: (A) Split in two – substitutions at the 5-position. (B) Split in two – substitutions at the 6-position. (C) Two substitutions (R_1 , blue and R_2 , red) on the core scaffold (green)

D.1.3.4.3. Topomer CoMFA Models:

The Topomer CoMFA descriptors derived above were used as explanatory variables, and the pIC_{50} values were used as the target variable in PLS regression analyses to derive 3D QSAR models using the implementation in the SYBYL package. The conventional correlation coefficient r^2 and its standard error (r^2 stderr), the cross-validated r^2 (q^2) and its standard error, (q^2 stderr) were subsequently computed for the final models. Additionally, the Y-intercept value for the PLS analysis (intercept) was returned by the program. Adding the R-group contributions to this value gives the predicted activity value.

D.1.3.4.4. Statistical data for analysis of tgTS inhibitors

Table 18a: Topomer CoMFA Statistics – tgTS

	Method A	Method B	Method C
Conventional r^2	0.942	0.772	0.907
r^2 std. err.	0.23	0.38	0.28
Cross-validated r^2 (q^2)	0.778	0.648	0.814
q^2 std. err.	0.44	0.47	0.4
Intercept	4.19	5.25	6.4
Opt. no. components	8	4	2

The training set for generation of a Topomer CoMFA model had a total of 65 compounds and the test set contained 20 compounds. A total of three models were generated using Topomer CoMFA using the fragment databases generated by Methods A - C. The key statistical parameters associated with these models are shown in Table 18a. The CoMFA model generated by splitting the molecule into two (Method A) afforded slightly better conventional and cross-validated r^2 values compared to the models generated by the other two methods. Figure 107.

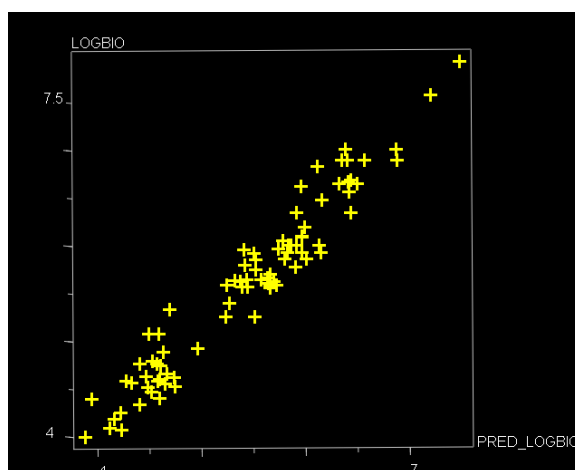


Figure 107. CoMFA predictions for the training set of tgTS inhibitors using Method A

All three models showed satisfactory cross-validated r^2 values ($q^2 > 0.5$) and were used to predict the activities of the test set and showed good predictive abilities. The

CoMFA predictions for the training set for Method A is shown in

D.1.3.4.5. Statistical data for analysis of hTS inhibitors

Table 18b: Topomer CoMFA Statistics – hTS

	Method A	Method B	Method C
Conventional r^2	0.909	0.786	0.91
r^2 std. err.	0.25	0.38	0.38
Cross-validated r^2 (q^2)	0.759	0.652	0.647
q^2 std. err.	0.4	0.49	0.28
Intercept	4.63	5.58	4.58
Opt. no. components	7	5	6

A total of three Topomer CoMFA models were generated, as in the previous case, using the fragment databases generated by Methods A - C. The key statistical parameters associated with these models are shown in Table 18b. The CoMFA models generated by splitting the molecule into two (Method A) and by considering two substitutions on the core afforded comparable conventional and cross-validated r^2 values compared to the model generated by method B. All three models showed satisfactory cross-validated r^2 values ($q^2 > 0.5$). The CoMFA predictions for the training set for Method C is shown in Figure 108.

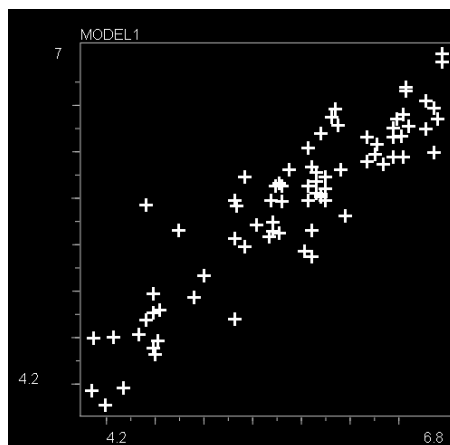


Figure 108. CoMFA predictions for the training set of tgTS inhibitors using Method C

D.1.3.4.6. Using the topomer CoMFA model to explain tgTS SAR

The The Stdev*coefficient contour maps generated using the CoMFA model generated using method A (described above) can be used to provide a possible explanation for the observed gain in potency for tgTS activity between two inhibitors from a series of thieno[2,3-*d*]pyrimidine inhibitors⁴⁴² shown below.

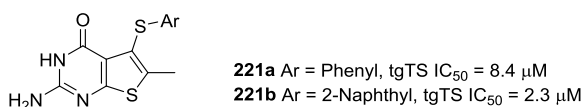


Figure 109. Structures and biological activities of **221a-b**.

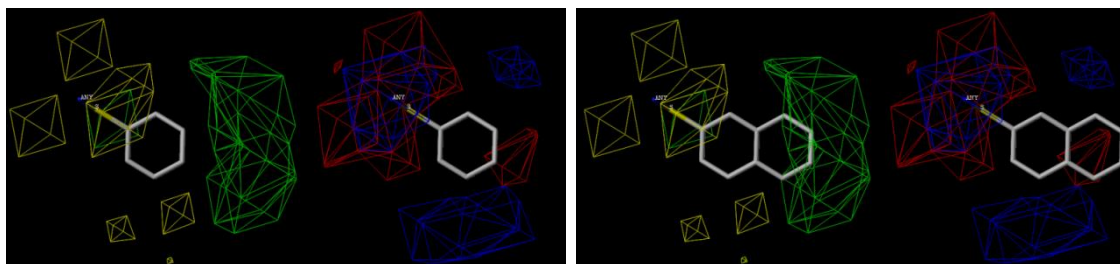


Figure 110. Topomer CoMFA maps representing steric and electrostatic contributions for **221a** (left) and **221b** (right). Steric maps: green – steric bulk favored, yellow - steric bulk disfavored; Electrostatic maps: red – negative charge favored, blue – positive charge favored.

The synthesis and biological evaluation of **221a-b** (Figure 109) was described by Gangjee *et al.*⁴⁴² Figure 110 represent StDev*Coeff maps that represent steric and electrostatic contributions of the substitutions and shows where variability in the molecule's fields can explain differences in the activities of the molecules. In these maps, the regions in green favor steric bulk while regions in yellow disfavor steric bulk. The regions in red and blue represent electrostatic contributions with regions in blue favoring

positive charge while red regions favor negative charge. As can be seen in Figure 110 (left), the phenyl substitutions in **221a** do not reach the large hydrophobic region in green where the addition of bulk is favorable. This region is occupied by the naphthyl ring of **221b** (Figure 110, right) and can perhaps explain the increase in potency of **221b** as compared to **221a**.

D.1.3.4.7. Using the topomer CoMFA model to explain tgTS selectivity:

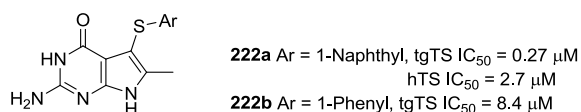


Figure 111. Structures and biological activities of **222a-b** against tgTS and hTS.

The synthesis and biological evaluation of **222a-b** (Figure 111) was described by Gangjee *et al.*³⁵⁸ The 1-naphthyl substituted **222b** compound displays a 10-fold selectivity for tgTS over hTS and shows a 4-fold increased activity over the phenyl substituted compound **222a**. Figures 96a-b display the Topomer COMFA maps representing steric and electrostatic contributions for **222** in the hTS and tgTS models respectively.

These maps suggest that the region where the 5-thioaryl substituent binds in hTS and tgTS differs in its ability to tolerate bulk. Subsequently, the 5-naphthyl substituent of **222** is able to access the larger region in green in tgTS (steric bulk favored) over the yellow region (steric bulk disfavored) in hTS.

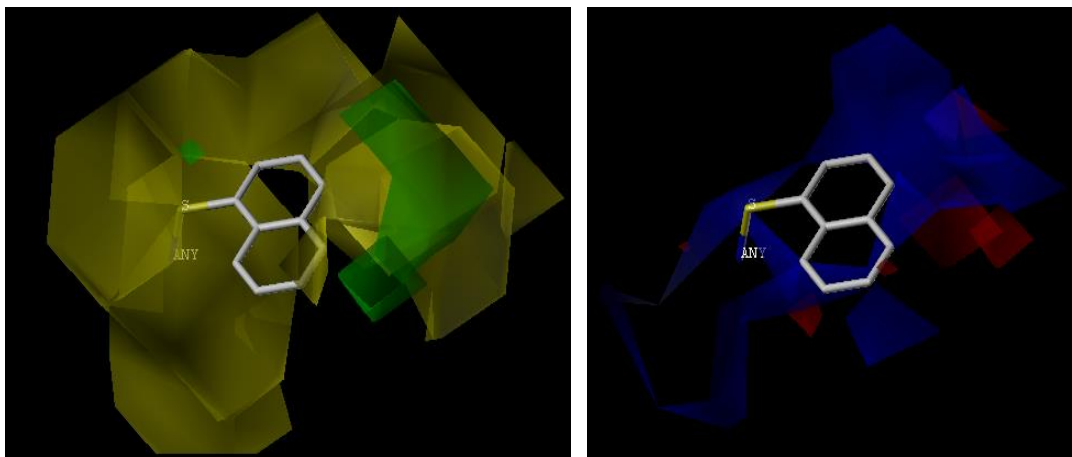


Figure 112. Topomer COMFA maps representing steric and electrostatic contributions for **222b** in the hTS model. Steric maps: green – steric bulk favored, yellow - steric bulk disfavored; Electrostatic maps: red – negative charge favored, blue – positive charge favored.

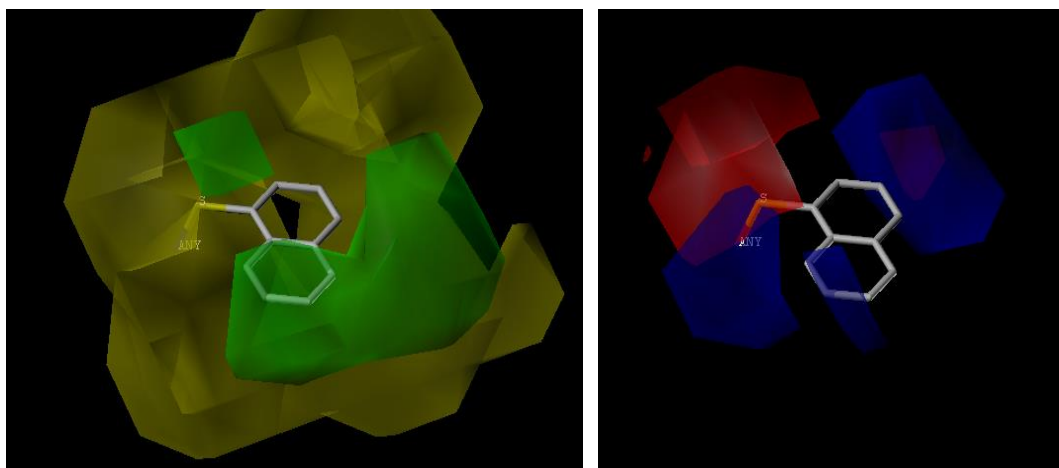


Figure 113. Topomer COMFA maps representing steric and electrostatic contributions for **222b** in the tgTS model. Steric maps: green – steric bulk favored, yellow - steric bulk disfavored; Electrostatic maps: red – negative charge favored, blue – positive charge favored.

This can explain, in part, the higher potency of **222** for tgTS over hTS. Similar findings (Figure 114-115) were also seen in case of the StDev*Coeff maps for **194a-b** (Table 12), thereby providing further evidence that supports the validity of the topomer CoMFA models generated.

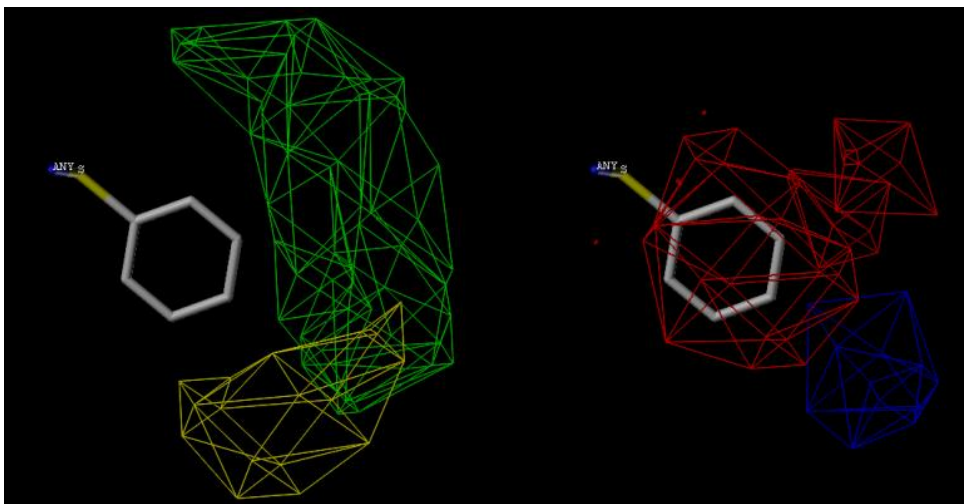


Figure 114. Topomer COMFA maps representing steric and electrostatic contributions for **222a** in the tgTS model. Steric maps: green – steric bulk favored, yellow – steric bulk disfavored; Electrostatic maps: red – negative charge favored, blue – positive charge favored.

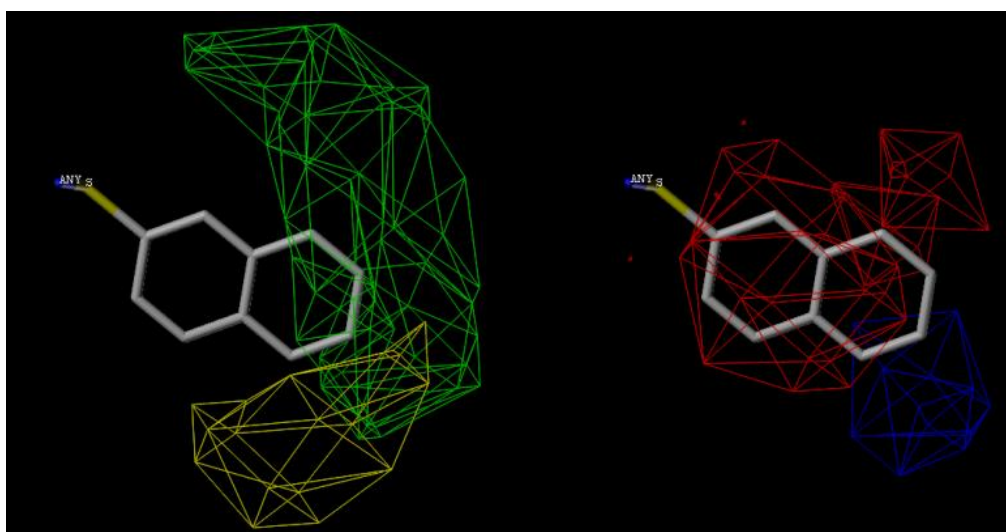


Figure 115. Topomer COMFA maps representing steric and electrostatic contributions for **222b** in the tgTS model. Steric maps: green – steric bulk favored, yellow - steric bulk disfavored; Electrostatic maps: red – negative charge favored, blue – positive charge favored.

D.1.3.4.8. Comparing Docking Studies with the Topomer CoMFA Model

Docking studies were performed with **222b** in the tgTS homology model to ascertain if a molecular basis could be found to explain the observed SAR. In addition, docking studies could be used to determine which amino acids in the tgTS active site, if any, are responsible for the interactions predicted by the topomer CoMFA model.

Docking studies were performed using LeadIT 2.1.0 using the procedures described for **194** in the tgTS homology model above.

Figure 116 shows the best docked pose of **222b** (white) in the binding site of the tgTS model. In this pose the N3 forms a hydrogen bond with Asp513. The thieno[2,3-*d*]pyrimidine scaffold is stabilized by hydrophobic interactions with Ile402, Trp403, Asn406, Leu486 and Leu516, Met608 and Ala609. The 2-naphthyl moiety forms hydrophobic interactions with Ile402, Leu516 and Phe520.

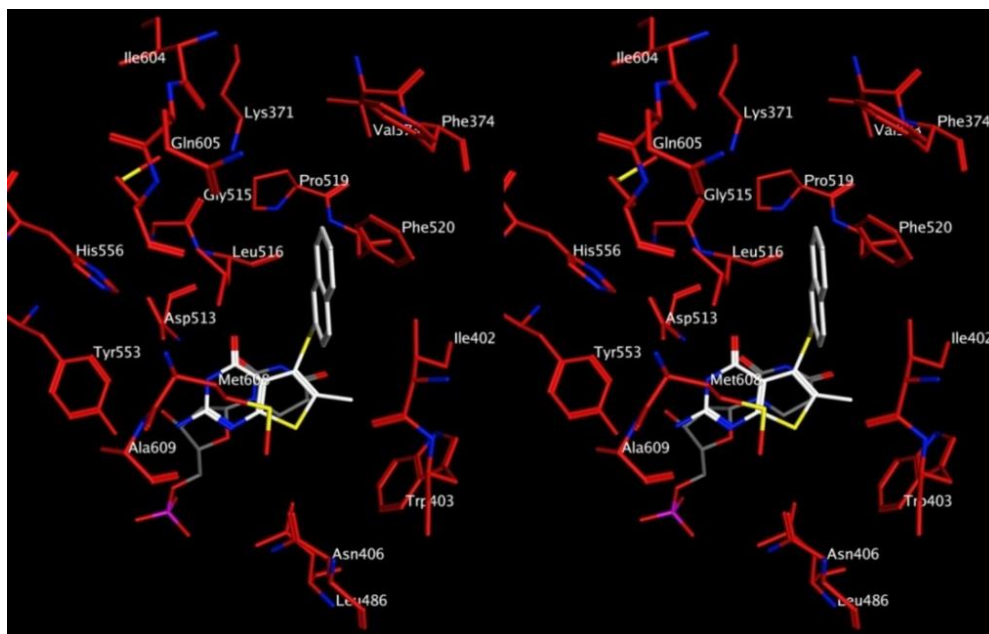


Figure 116. Stereoview. Docked pose of **222b** (white) in the active site of the tgTS homology model.

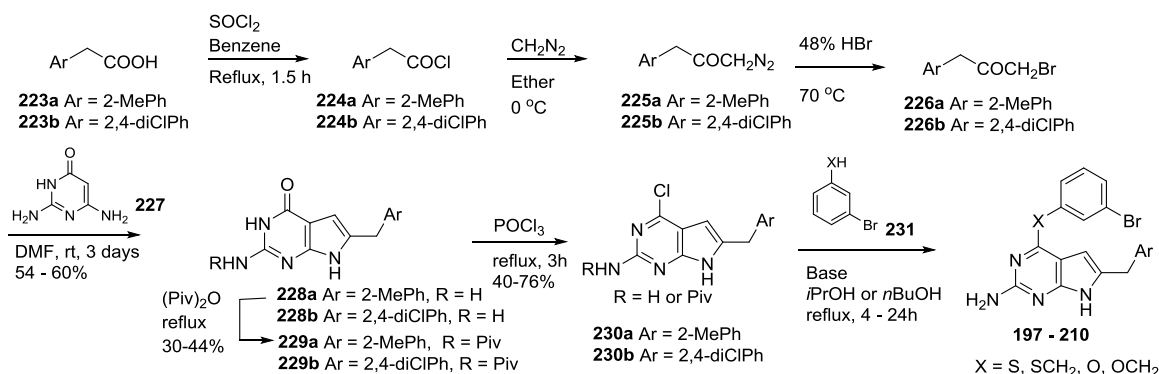
Additional hydrophobic interactions afforded by the second ring in the 2-naphthyl

moiety with Phe520 could explain, in part, the 4-fold gain in potency of **222b** compared to **222a**. There are indications in the literature⁴³⁹ that this region of Phe374/Phe520 coincides with Ala287 of *C. hominis* TS structure and is a region previously identified^{440, 441} as a possible target for species selective drug design.

D.2.RECEPTOR TYROSINE KINASE INHIBITORS

D.2.1. Synthesis of 2-Amino-4-substituted-6-arylmethyl-7H-pyrrolo[2,3-*d*]pyrimidines as RTK inhibitors

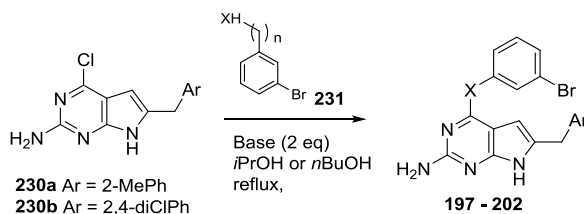
Scheme 31: Synthesis of 2-amino-4-substituted-6-arylmethyl-7H-pyrrolo[2,3-*d*]pyrimidines **197-210**



Scheme 31 shows the route utilized in the synthesis of target compounds **197 – 210**. The target compounds were synthesized by a nucleophilic displacement of the chloro group of the key intermediate **230a-b**³⁸⁷ with the corresponding bromothiols, phenols or amines **231** under basic conditions using isopropanol or butanol as the solvent under reflux conditions. The key intermediates **230a-b** were synthesized using literature methods reported by Gangjee *et al.*³⁸⁷ The corresponding substituted phenyl acetic acids **223a-b** were heated with SOCl_2 at reflux to afford the acid chlorides **224a-b** which were used without purification. Treating the acid chlorides **224a-b** with freshly prepared diazomethane³⁸⁷ afforded the α -diazoketones **225a-b** which were further treated with a 48% aqueous HBr solution to afford the α -bromomethyl benzyl ketones **226a-b** which were used without purification. Etheral diazomethane was prepared under basic

conditions using literature methods³⁸⁷ from *N*-nitroso-*N*-methyl urea or *N*-methyl-*N*-nitroso-*p*-toluenesulfonamide (Diazald). Since *N*-nitroso-*N*-methyl urea has been reported to be toxic, carcinogenic and a potent mutagen,⁴⁴³ large scale preparation (5-10 mmol scale) of ethereal diazomethane was carried out using Diazald. Condensation of **226a-b** with 2,6-diamino-4-oxo-pyrimidine **231** afforded the desired 2-amino-4-oxo-6-substituted benzyl pyrrolo[2,3-*d*]pyrimidines **228a-b** in 54-60% yields. Pivaloyl protection of the 2-NH₂ group gave compounds **229a-b**. Treatment of **229a-b** with POCl₃ at reflux afforded the key 2-amino-4-chloro-6-substituted benzyl pyrrolo[2,3-*d*]pyrimidines **230a-b**. Significantly improved yields (65-76%) were obtained on chlorination of the pivaloyl protected 2-amino-4-oxo-6-substituted benzyl pyrrolo[2,3-*d*]pyrimidines **229a-b** compared to the unprotected compounds **228a-b** as has been previously reported.³⁸⁷ The protected compounds showed significantly improved solubility in organic solvents such as CHCl₃ and MeOH which improved their purification using normal phase column chromatography compared to the unprotected analogs.

Scheme 32: Synthesis of target compounds **197-200**



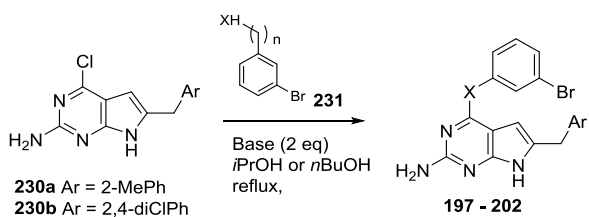
The synthesis of **197-202** by nucleophilic displacement of the chloro group of **230a-b** by the thiol moiety of **231** is shown in Scheme 32. Different bases such as NEt₃, K₂CO₃, Cs₂CO₃ and *t*BuOK were used in order to deprotonate the thiol for the nucleophilic displacement. The reactions were carried out with 2 eq. of base. The best

yields were obtained on using K₂CO₃ as the base for 3-bromobenzene thiol (entries 1-7) and using *t*BuOK as the base for (3-bromophenyl)methanethiol (entries 8-15).

	Comp.	Ar	X	n	Time (h)	Base	Solvent	Yield (%)
1	197	2-MePh	S	0	4	K ₂ CO ₃	<i>i</i> PrOH	34
2	198	2,4- diClPh	S	0	4	K ₂ CO ₃	<i>i</i> PrOH	30
3	197	2-MePh	S	0	4	Cs ₂ CO ₃	<i>i</i> PrOH	12
4	198	2,4- diClPh	S	0	24	Cs ₂ CO ₃	<i>i</i> PrOH	22
5	197	2-MePh	S	0	4	NEt ₃	<i>i</i> PrOH	12
6	198	2,4- diClPh	S	0	4	NEt ₃	<i>i</i> PrOH	Trace
7	198	2,4- diClPh	S	0	24	NEt ₃	<i>i</i> PrOH	8
8	197	2-MePh	S	1	4	NEt ₃	<i>i</i> PrOH	N/A
9	199	2-MePh	S	1	24	NEt ₃	<i>i</i> PrOH	Trace
10	199	2-MePh	S	1	4	<i>t</i> BuOK	<i>n</i> BuOH	21
11	199	2-MePh	S	1	24	<i>t</i> BuOK	<i>n</i> BuOH	24
12	200	2,4- diClPh	S	1	4	K ₂ CO ₃	<i>i</i> PrOH	5
13	200	2,4- diClPh	S	1	4	K ₂ CO ₃	<i>n</i> BuOH	15
14	199	2-MePh	S	1	4	K ₂ CO ₃	<i>i</i> PrOH	6
15	200	2,4- diClPh	S	1	4	<i>t</i> BuOK	<i>n</i> BuOH	25

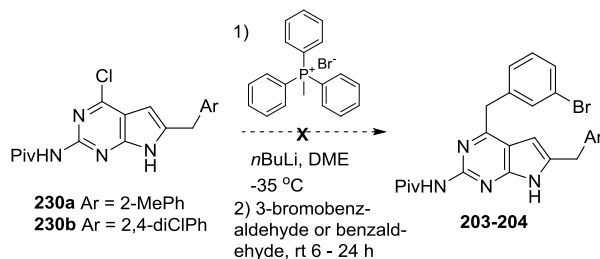
The choice of base was based on literature precedence.^{390, 391} Increasing the reaction time led to modest improvements in yields in some cases (eg. entries 10, 11). Changing the solvent from *i*PrOH to *n*BuOH permitted increasing the reaction temperature and facilitated improved yields. Conducting the reaction under microwave conditions did not lead to an appreciable improvement in yields. Similar yields were obtained when the pivoloyl protected 4-chloro compounds were treated with the corresponding thiols under basic conditions. Deprotection of the pivaloyl group occurred by heating the intermediates with 15% KOH in 1,4-dioxane for 12 h.³⁸⁷ Compounds **205** – **210** (Scheme 33) were synthesized using nucleophilic displacement of the 4-Cl of **230a** or **230b** similar to the synthesis of **197** – **200** described above.

Scheme 33: Synthesis of target compounds 205-210



	Comp.	Ar	X	n	Time (h)	Base	Solvent	Yield (%)
1	205	2-MePh	O	0	24	K ₂ CO ₃	<i>i</i> PrOH	18
2	206	2,4- diClPh	O	0	24	K ₂ CO ₃	<i>i</i> PrOH	22
3	205	2-MePh	O	0	24	Cs ₂ CO ₃	<i>i</i> PrOH	Trace
4	206	2,4- diClPh	O	0	24	Cs ₂ CO ₃	<i>i</i> PrOH	Trace
5	207	2-MePh	O	1	4	K ₂ CO ₃	<i>i</i> PrOH	N/A
6	207	2-MePh	O	1	12	K ₂ CO ₃	<i>i</i> PrOH	N/A
7	207	2-MePh	O	1	24	<i>t</i> BuOK	<i>i</i> PrOH	Trace
8	208	2,4- diClPh	O	1	24	<i>t</i> BuOK	<i>i</i> PrOH	Trace
9	207	2-MePh	O	1	24	<i>t</i> BuOK	<i>n</i> BuOH	11
10	208	2,4- diClPh	O	1	24	<i>t</i> BuOK	<i>n</i> BuOH	10
11	209	2-MePh	NH	1	4	-	<i>i</i> PrOH	N/A
12	209	2-MePh	NH	1	24	-	<i>i</i> PrOH	N/A
13	209	2-MePh	NH	1	24	-	<i>n</i> BuOH	N/A
14	209	2-MePh	NH	1	24	NEt ₃	<i>n</i> BuOH	Trace
15	209	2-MePh	NH	1	24	K ₂ CO ₃	<i>i</i> PrOH	8
16	210	2,4- diClPh	NH	1	24	K ₂ CO ₃	<i>i</i> PrOH	13

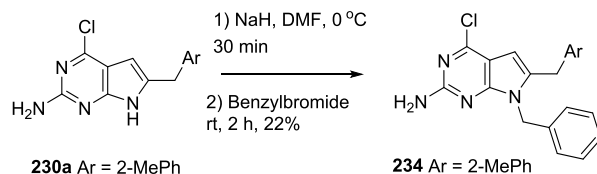
Scheme 34: Attempted synthesis of 203-204



Attempts to synthesize the one-carbon linked compounds **203-204** using a Wittig reaction³⁹⁰ (Scheme 34) afforded a complex, inseparable mixture of compounds. Repeating the reaction using benzaldehyde as a model system also failed to provide the 4-benzyl substituted analogs. The reaction failed to proceed as expected when it was carried

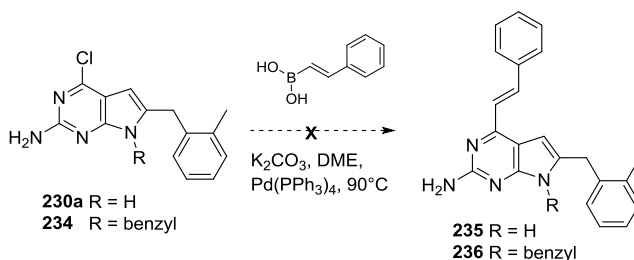
out using the dipivaloyl protected analog of **230a**. In order to rule out complications in the reaction due to the deprotonation of the acidic pyrrole NH of **230a-b**, the corresponding N-7 benzyl protected analog (**234**) of **230a**³⁸⁰ was synthesized (Scheme 35) in 22% yield.

Scheme 35: Synthesis of target compound **234**



Attempts to repeat the Wittig reaction described in Scheme 34 provided a complex mixture of compounds which were not separable using normal phase chromatography or flash chromatography. Increasing the reaction time from 6 to 24 h led to an increase in the number of spots on TLC. Changing the reaction solvent to DMF did not change the proportion of the side products.

Scheme 36: Attempted synthesis of target compound **235**



Attempts to synthesize the two-carbon linked analogs **235** and **236** using Suzuki coupling³⁹⁰ of either **230a** or its N7-benzyl protected analog **234** with styrylboronic acid as the coupling partner (Scheme 36) did not afford the desired compounds. Increasing the reaction time from 12 to 24 h or 48 h led to increasing side products which could not be separated using column chromatography.

D.2.2. Molecular modeling studies with RTKs

D.2.2.1 Homology model of PDGFR- β

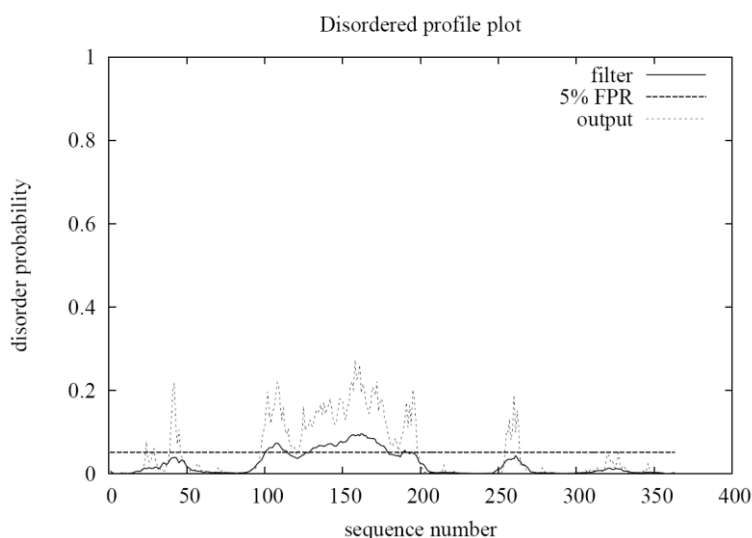


Figure 117. DISOPRED analysis of PDGFR- β kinase domain amino acid sequence.

There is currently no known crystal structure of PDGFR- β . A homology model was hence built for performing molecular modeling studies. The amino acid sequence (amino acids 600 – 962) of the PDGFR- β kinase domain was obtained from the Uniprot database (Uniprot ID:PGFRB_HUMAN [P09619]). A BLASTP search implemented in MOE 2007.09³⁸³ indicated that chain A of the 2.90 Å c-KIT kinase complex (PDB: 1PKG³⁸⁴, chain A) shows high sequence similarity with PDGFR- β (E-value: 1e -58). A homology model was then built using MOE 2007.09 and the structure of c-KIT kinase complex (PDB: 1PKG, chain A) as the template.

As has been reported earlier in the literature,³³⁹ a DISOPRED 2.0⁴⁴⁴ analysis of the PDGFR- β amino acid sequence was performed to predict the ordered and disordered regions. The results from this analysis (Figure 117) predicted amino acids 700 – 792 were

disordered.

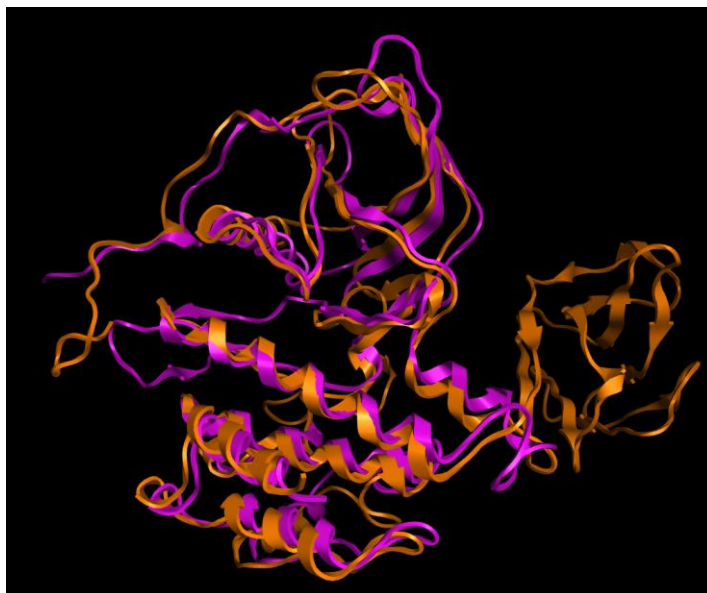


Figure 118. Superimposition of the PDGFR- β homology model (brown) with the c-KIT crystal structure (magenta). The disordered amino acids of PDGFR do not superimpose with the crystal structure.

The disordered amino acids were accounted for during the model building step by using the ‘actual secondary structure’ option in MOE 2007.09. Using literature methods, i.e. truncation of the disordered region, provided models similar to that seen with the models generated using the ‘actual secondary structure’ option in MOE 2007.09. The final homology model returned by the program was subjected to further energy minimization using Amber99 as the forcefield and a 0.5 RMS gradient. Figure 118 shows the superimposition of the PDGFR- β homology model with the c-KIT crystal structure template.

Model validation:

The model generated using MOE 2007.09 was evaluated using structure assessment tools (Ramachandran plot, Protein Structure Analysis (ProSA),^{410, 411} Anolea,⁴¹³ Gromos,⁴¹⁴ and QMEAN⁴¹⁵) as implemented on the Swiss-Model website.⁴¹⁶

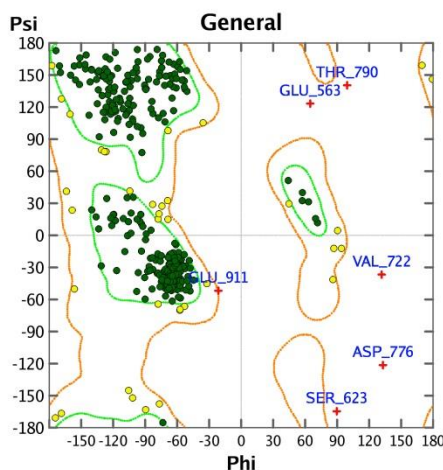


Figure 119. Ramachandran plot of the PDGFR- β homology model.

- a) **Ramachandran plot** (Figure 119): A Ramachandran plot of the model showed the presence of six outlying residues (Glu563, Ser 623, Val722, Asp776, Thr790 and Glu911). Initial efforts to resolve the structure of the outlying residues by tethered energy minimization steps led to the generation of different outlying residues. A tethered global energy minimization for the protein did not resolve the outlying residues. Attempts to use different software such as Sybyl X to prepare the protein did not give satisfactory results. Since these residues are not in the proximity of the purported ATP binding site and are tethered during the docking process, they are not expected to influence the docked conformations of the compound. Hence, the model was used without further refinement.

b) **Protein Structure Analysis (ProSA):**^{410, 411} ProSA calculates an overall quality score (z-score) for a specific input structure for comparison with the z-scores of all experimentally determined protein chains in PDB. The ProSA analysis of the PDGFR- β model (Figure 120) is comparable to the score of the template (PDB: 1PKG, chain A) and fell within acceptable limits for z-scores.

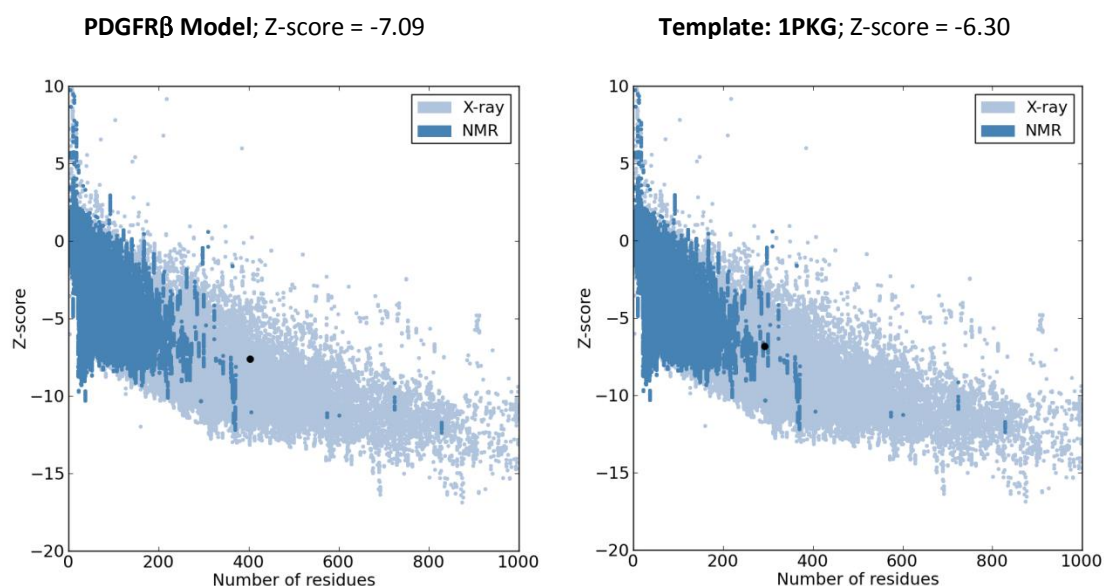


Figure 120. ProSA analysis of the PDGFR- β homology model.

Docking studies were performed using the docking suite of MOE 2007.09. After addition of hydrogen atoms, the protein was then “prepared” using the LigX function in MOE. LigX is a graphical interface and collection of procedures for conducting interactive ligand modification and energy minimization in the active site of a flexible receptor. In LigX calculations, the receptor atoms far from the ligand are constrained and not allowed to move while receptor atoms in the active site of the protein are allowed to move but are subject to tether restraints that discourage gross movement. The procedure

was performed with the default settings. Ligands were built using the molecule builder function in MOE and were energy minimized to its local minima using the MMF94X forcefield to a constant of 0.05 kcal/mol.

Ligands were docked into the active site of the prepared protein using the docking suite as implemented in MOE. The docking was restricted to the active site pocket residues using Alpha triangle placement method. Refinement of the docked poses was carried out using the Forcefield refinement scheme and scored using Affinity dG scoring system. About 30 poses were returned for each compound at the end of each docking run. The docked poses were manually examined in the binding pocket to ensure quality of docking and to confirm absence of steric clashes with the amino acid residues of the binding pocket. The binding poses were also visualized using the ligplot utility as implemented in MOE 2007.09.

D.2.2.2. Docking Studies with *N*⁴-(3-bromophenyl)-7-(substituted benzyl)-7*H*-pyrrolo[2,3-*d*]-pyrimidine-2,4-diamines as potential multiple RTK inhibitors.

Table 19.³⁸⁰ IC₅₀ values (μM) of kinase inhibition and the A431 cytotoxicity assay of **195**, **196a-k** and **211a-k**.

Compd	PDGFR-β	VEGFR-2	VEGFR-1	EGFR	A431
195	>50	0.25±0.04	>50	9.19±1.8	1.21±0.42
196	17.0±5.6	28.11±9.9	>50	0.23±0.06	2.8±1.1
196c	>50	5.58±0.69	26.8±4.1	4.31±1.75	>50
196d	>50	8.28±0.69	42.7±6.1	17.42±3.9	28.6±5.1
196e	8.92±1.6	0.62±0.21	31.1±5.8	12.62±3.3	>50
196f	>50	>50	>50	1.67±0.3	31.8±6.3
196g	>50	>50	>50	19.77±5.6	33.5±6.2
196h	>50	5.08±0.83	19.2±4.3	>50	>50
196i	>50	>50	15.2±2.9	1.24±0.21	33.2±5.9
196j	>50	5.97±0.78	>50	6.16±1.2	23.5±5.2
196k	14.7±3.4	9.42±1.9	>50	>50	42.1±18.5

Compd	PDGFR- β	VEGFR-2	VEGFR-1	EGFR	A431
211a	159.6 \pm 26.3	113.4 \pm 17	129.3 \pm 20.4	113.3 \pm 18.9	15.7 \pm 2.8
211b	34.2 \pm 4.4	>200	138.1 \pm 24.2	>200	15.3 \pm 1.9
211c	1.5 \pm 0.21	17.9 \pm 2.4	126.3 \pm 19.1	>200	88.4 \pm 10.2
211d	>500	65.3 \pm 7.9	79.9 \pm 8.4	99.9 \pm 18.6	16.1 \pm 2.2
211e		>200	>200	69.2 \pm 6	40.6
211f	>500	23.8 \pm 3.0	99.3 \pm 10.3	166.4 \pm 20.6	50.4 \pm 5.9
211g	229.6 \pm 37.1	64.5 \pm 7.8	118.6 \pm 11.4	>200	19.2 \pm 3.0
211h	129.3 \pm 21.1	14.9 \pm 2.1	150 \pm 22.1	>200	36.3 \pm 4.9
211i	212.4 \pm 16.2	22.9 \pm 2.9	50.8 \pm 6.2	>200	20.4 \pm 3.5
211j	129.1 \pm 20.5	22.9 \pm 10.7	>200	>200	13.3 \pm 20.5
211k	1.8 \pm 0.29	25.7 \pm 4.6	156.5 \pm 25	>200	39.0 \pm 6.8

Table 19³⁸⁰ shows the results from the biological evaluation studies for **195**, **196**, **196c-k** and **211a-c** (Figure 69) against selected RTKs. Molecular modeling studies were performed for **196c** and its corresponding analogue **211c** as representative examples from this set.

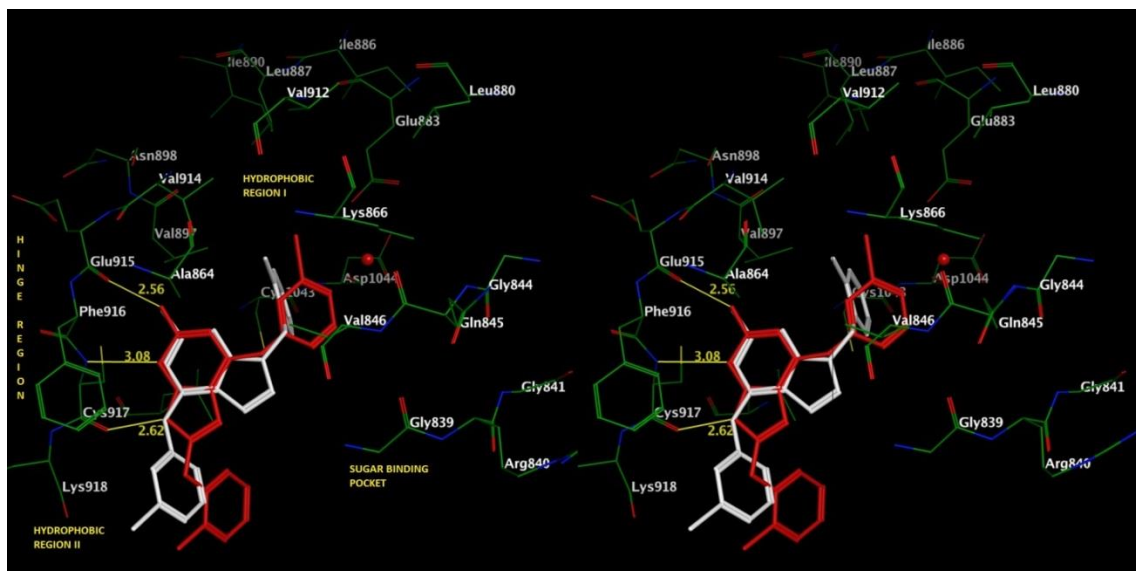


Figure 121.³⁸⁰ Stereoview. Superimposition of docked poses of **196c** (red) and **211c** (white) in the ATP binding site of VEGFR2. (PDB: 1YWN)

Molecular modeling studies³⁸⁰ were carried out using Flexx 3.1.2⁴⁴⁵ and MOE

2008.10⁴⁰⁸ in VEGFR2 (pdb code 1YWN)²⁰⁰ and a homology model of PDGFR β .⁴⁴⁶

Figures 121 and 122 depict the docked poses of **196c** (Figure 67) and its regioisomer **211c** (Figure 73) as a representative study in VEGFR2 and the homology model of PDGFR β . Figure 121 shows the superimposition of the best scored docked poses of **196c** (red) and **211c** (white) in the ATP binding site of VEGFR-2. The binding site of ATP competitive inhibitors in RTKs consists of a hinge region, two hydrophobic binding sites (Hydrophobic Region I and II) and a Sugar binding pocket (Figure 121) as described previously.^{179, 186, 390, 447} Compounds **196c** and **211c** adopt different docked conformations in the active site. The pyrrolo[2,3-*d*]pyrimidine ring of **196c** occupies the adenine binding portion of the ATP binding site. The 2-NH₂ moiety forms a hydrogen bond with the backbone carbonyl oxygen of Glu915 in the hinge region while the N3 and 4-anilino NH are involved in hydrogen bonds with the backbone of Cys917 in the hinge region. Additional hydrophobic interactions of the pyrrolo[2,3-*d*]pyrimidine ring with Leu1033 (not labeled) can stabilize the docked pose. In this pose, the N7-benzylic substitution extends towards Hydrophobic region I and is involved in interactions with Val846, Ala864, Val897 and Val914. The N7-benzylic substitution also interacts with the side chain carbon atoms of Glu883 and Cys1043. The *N*4-(3-bromophenyl) is extended towards Hydrophobic region II and interacts with the side chains of Phe916, Leu838(not shown) and Leu1033 (not shown).

In contrast, the pyrrolo[2,3-*d*]pyrimidine scaffold of **196c** docks³⁸⁰ in a flipped conformation compared to **211c** described above that permits the formation of three hydrogen bonds with the hinge region (Figure 3). The 2-NH₂, N1 and pyrrole NH of **196c** form hydrogen bonds with the backbone of Glu915 and Cys917. Additionally, the

pyrrolo[2,3-*d*]pyrimidine scaffold forms hydrophobic interactions with Leu838 (not shown), Val846, Ala864, Val897 and Leu1033 (not shown). This pose causes the *N*4-(3-bromophenyl) moiety to bind in Hydrophobic region I where it interacts with Val846, Ala864, Leu887, Val897, Val912 and Val914. Additional hydrophobic interactions with the side chain carbon atoms of Lys866 and Glu883 stabilize this docked pose. The 6-benzylic substitution extends towards Hydrophobic region II and forms interactions with Leu838 (not shown), side chain atoms of Phe916, Cys917, Lys918 and Gly920 (not shown). Thus, molecular modeling and docking studies suggest that the 7-benzylic substitution forces **211c** to adopt a binding mode different from that docked for the 6-benzylic compound **196c** in VEGFR2.

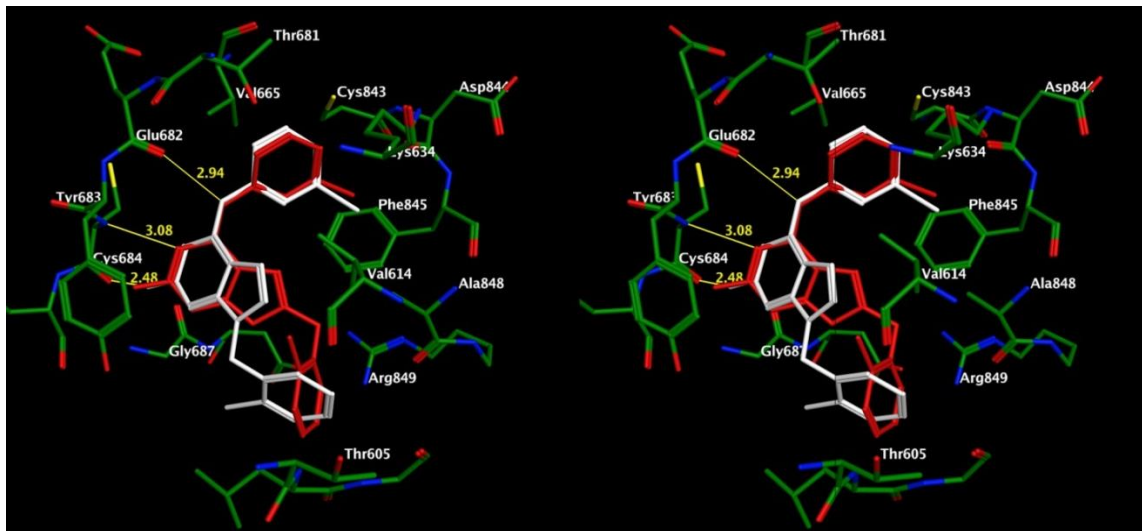


Figure 122.³⁸⁰ Stereo view. Docked pose of **196c** (red) and **211c** (white) in the putative binding site of the PDGFR β homology model.

There is no reported crystal structure of PDGFR β bound to a ligand. Hence a homology model of PDGFR β was built using the structure of c-KIT kinase complex (PDB: 1PKG) as a template.³⁷⁹ Docking studies³⁸⁰ were performed with **196c** and **211c** as

described above for VEGFR-2. Compound **104** binds to the ATP binding site of PDGFR β with the pyrrolo[2,3-*d*]pyrimidine portion occupying the adenine binding site (Figure 122). Three hydrogen bonds with the hinge region are maintained in this binding mode. The aniline NH hydrogen bonds with the backbone of Cys684 while the N3 and 2-NH₂ moieties form hydrogen bonds with Glu682. This pose causes the bromophenyl moiety to bind in Hydrophobic region I and form hydrophobic interactions with Val614, Ala632 (not shown), Val665 and Leu833 (not shown) and with the side chain carbon atoms of Lys634 and Thr681. The N7-benzyl substituent lies in the Sugar binding pocket and interacts with Leu606 (not shown), Val614, Val615 (not shown) and Ala848. The best scored pose of **196e** binds similar to the binding pose seen with **196c** in PDGFR β . The 6-benzylic substituent of **196e** accesses the same region accessed by the 7-benzylic substituent of **211e**, however in a different conformation as shown in Figure 122. It was interesting to note that alternate binding modes³⁸⁰ of **211e** that scored 1-2 kcal/mol higher than the best docked pose indicate different bound conformations of the 7-benzylic substituent (Figure 123). In the alternate binding mode, the 7-benzylic substituent accesses Hydrophobic region II instead of the sugar binding pocket as is seen in the bound conformation in Figure 123 where it interacts with Phe916 and Leu938 (not shown). Compound **196e**, which has a 6-benzylic substituent cannot access Hydrophobic region II in the poses seen in Figures 103 and 104. These binding modes suggested that the presence of multiple docked poses could lead to differences in the activity and/or selectivity of these compounds against different kinases as compared to the parent compounds **195** and **196**.

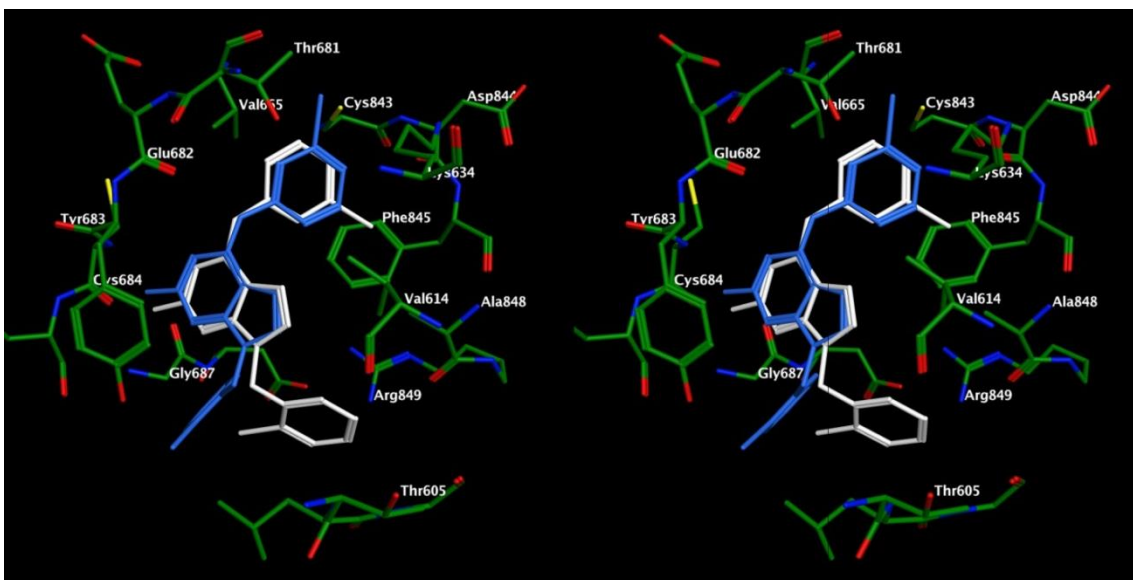


Figure 123.³⁸⁰ Stereoview. Superimposition of the best scored pose (white) and alternate docked pose (blue) of **211e** in the putative binding site of PDGFR β .

D.2.2.3. Molecular modeling studies of 2-Amino-4-*m*-bromoanilino-6-arylmethyl-7*H*-pyrrolo[2,3-*d*]pyrimidines as Tyrosine Kinase Inhibitors

D.2.2.3.1. Docking studies in EGFR.

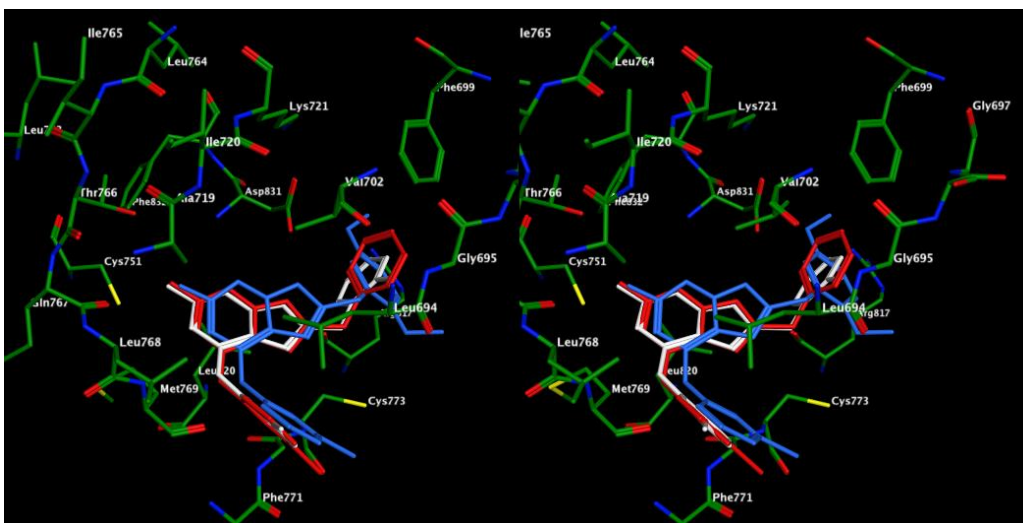


Figure 124.¹⁸³ Stereoview. Overlay of docked poses of **195** (red), **212a** (white) and **212b** (blue) in EGFR active site (PDB: 1M17).

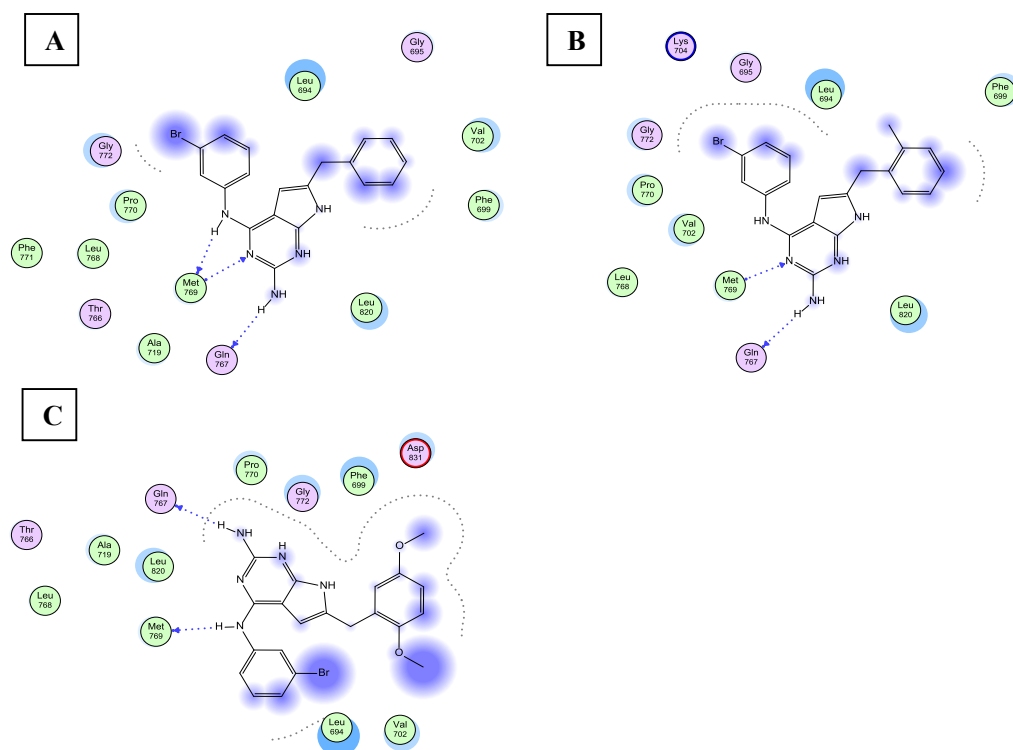


Figure 125.¹⁸³ Ligand interaction plots of docked poses of **195** (red), **212a** (white) and **212b** (blue) in EGFR active site

Compounds **212c-k** were evaluated for activity against cells overexpressing EGFR, VEGFR-2 or PDGFR- β (Table 14).¹⁸³ Molecular modeling studies were performed with the lead compounds **195**, **212a-b** and their corresponding analogues **212c-k** in an attempt to provide a molecular basis for the observed SAR for these compounds.

In an attempt to explain the activity for **212c-k** against EGFR in the whole cell assay, docking studies were performed¹⁸³ using Flexx 3.1.2 and the X-ray crystal structure of the 4-anilinoquinazoline inhibitor erlotinib in EGFR (PDB ID: 1M17).¹⁹² Multiple low energy binding modes were seen for all the docked compounds. The

binding modes presented in Figure 124 for **195**, **212a-b** were observed to be within 2 kcal/mol of the lowest energy pose and permits comparison between the proposed binding modes of the three molecules. All the molecules form hydrogen bonds with the hinge region using the 2-NH₂ moiety. Hinge region hydrogen bonds with the 4-NH is observed for **195** and **212b** but not **212a**. Additional hydrogen bonding using the N3-nitrogen is seen for **195** and **212a** but not for **212b**. This explains, in part, the greater potency of **195** against EGFR compared with **212a** and **212b**. The anilino rings of the three compounds reside in Hydrophobic site II and can interact with Leu694, Leu768 and Pro770. The 6-benzyl moieties of the molecules extend into the Sugar binding pocket and interact with Leu694, Phe699 and Val702. The altered conformations of the side chain benzyl ring in **212a** due to the 2'-Me and in **212b** due to the 2',5'- diOMe cause the benzyl ring to extend away from Val702, reducing the extent of hydrophobic interaction of these molecules. Ligand interaction plots for **195**, **212a-b** are shown in Figure 125.¹⁸³

Docked poses¹⁸³ of the 4-N methylated compound **212c** in EGFR show the loss of hydrogen bonding to the backbone of Met769 afforded by the 4-NH group in the lead compound **195** (Figures 126 and 127). Additionally, **212c** is oriented farther from the hinge region as compared to **195** to accommodate the 4-N methyl group. This results in the loss of a hydrogen bond of the N3-nitrogen with the backbone NH of Met769. Additional binding interactions afforded by other portions of **212c** are similar to those seen in the docked pose of **195**. This loss in H-bonding of the N3 in **212c** could explain, in part, its reduction in whole cell activity against EGFR as compared to **195** which lacks the 4-N methyl group.¹⁸³

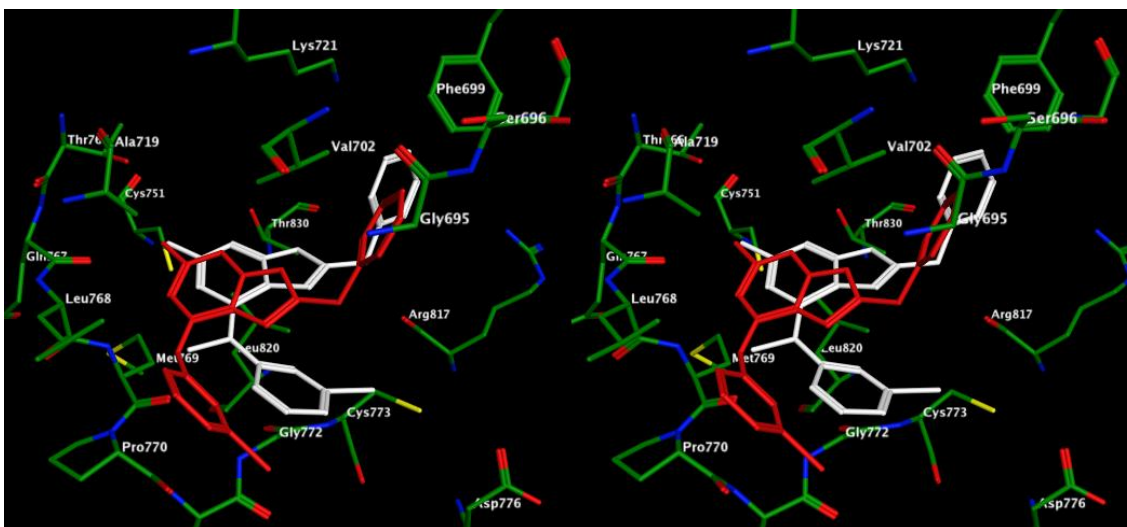


Figure 126.¹⁸³ Stereoview. Overlay of docked poses of **195** (red) and **212c** (white) in EGFR active site.

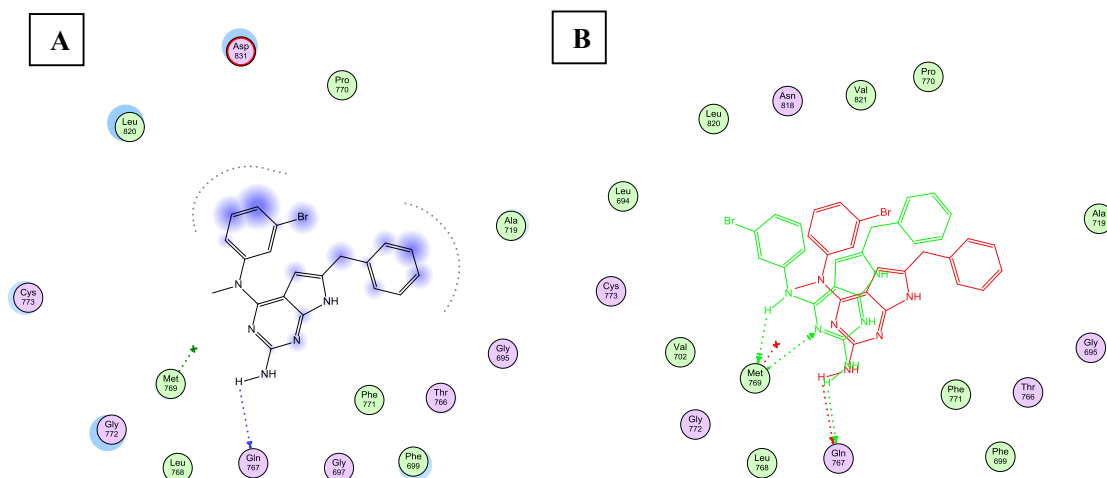


Figure 127.¹⁸³ (A) Ligand interaction plots of docked pose of **212c** in the EGFR active site. (B) Overlay of ligand interaction plots of docked poses of **212c** (red) and **195** (green) in the EGFR active site. Generated using MOE 2009.10

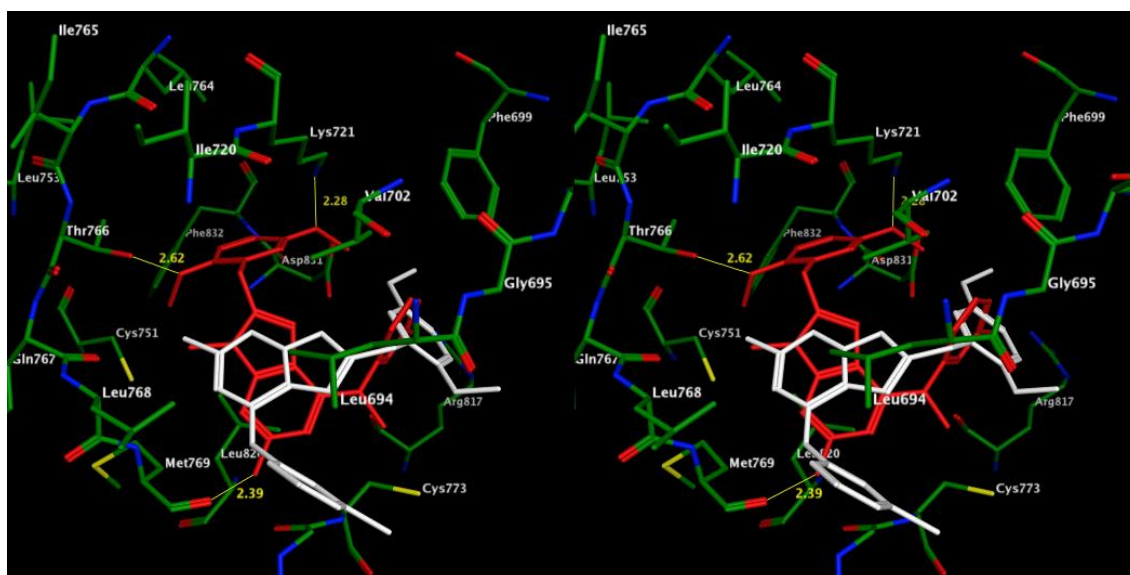


Figure 128.¹⁸³ Stereoview. Overlay of docked poses of **212k** (red) and **212b** (white) in EGFR active site

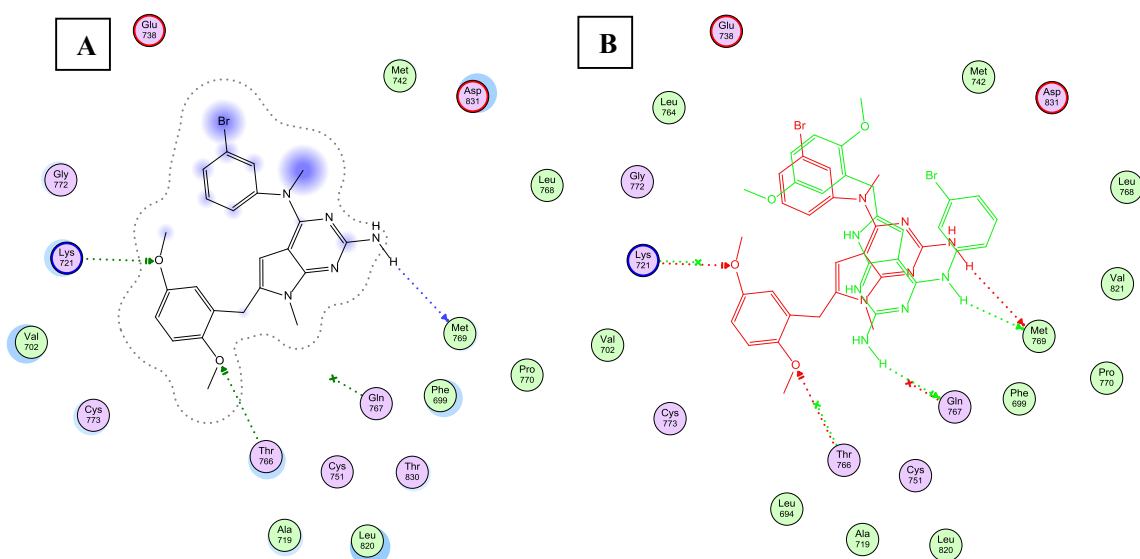


Figure 129.¹⁸³ (A) Ligand interaction plots of docked pose of **212k** in the EGFR active site. (B) Overlay of ligand interaction plots of docked poses of **212k** (red) and **212b** (green) in the EGFR active site.

When comparing the N4, N7-dimethylated compounds **212e**, **212h** and **212k**, it was noted¹⁸³ that the whole cell activity of the compounds increase with increasing size of

the substitution on the 6-benzyl ring. Docking studies with **212k** (Figures 128 and 129) indicated that this compound adopts a binding mode different from that seen with the docked poses of **195**, **212a-b**. In the docked pose of **212k** (Figure 128), the 2-NH₂ moiety is involved in the lone hinge region hydrogen bond. The N4 and N7-methyl groups alter the conformation of the molecule and cause the aniline portion to bind to Hydrophobic site I. The 2',5'-dimethoxybenzyl side chain accesses the Sugar binding pocket and is placed in a hydrophobic site formed by Leu694, Phe699 and Val702. The 2',5'-dimethoxy moieties provide additional hydrogen bonds with Thr766 and Lys721. The conformational change due to N4, N7-dimethylation and additional interactions due to the nature and orientation of the benzyl side chain could be expected to compensate for the loss of hydrogen bonding by either the N4 or N7 nitrogen atom and contribute to the increased potency of **212k** against EGFR in whole cell assays compared with **212b**.

All the mono- and di-methylated derivatives were comparatively inactive against VEGFR-2 in whole cell assays suggesting that, for VEGFR-2 inhibition in whole cells, both the N4- and N7- protons are important for binding and necessary for activity. Whether this reflects space requirements or hydrogen bond donor ability at the N4- and/or N7-positions is not clear.¹⁸³

D.2.2.3.2. Docking studies in PDGFR- β

The 4-N-methyl compound, **212i**, was the most potent analogue in this series and was about 7-fold more potent than its lead analogue **212b** in the PDGFR- β whole cell assay. Molecular modeling studies¹⁸³ were performed using Flexx 3.1.2 with the homology model of PDGFR- β as described above in an attempt to explain the increased

activity of **212i** compared with **212b** in the whole cell assays for PDGFR- β .

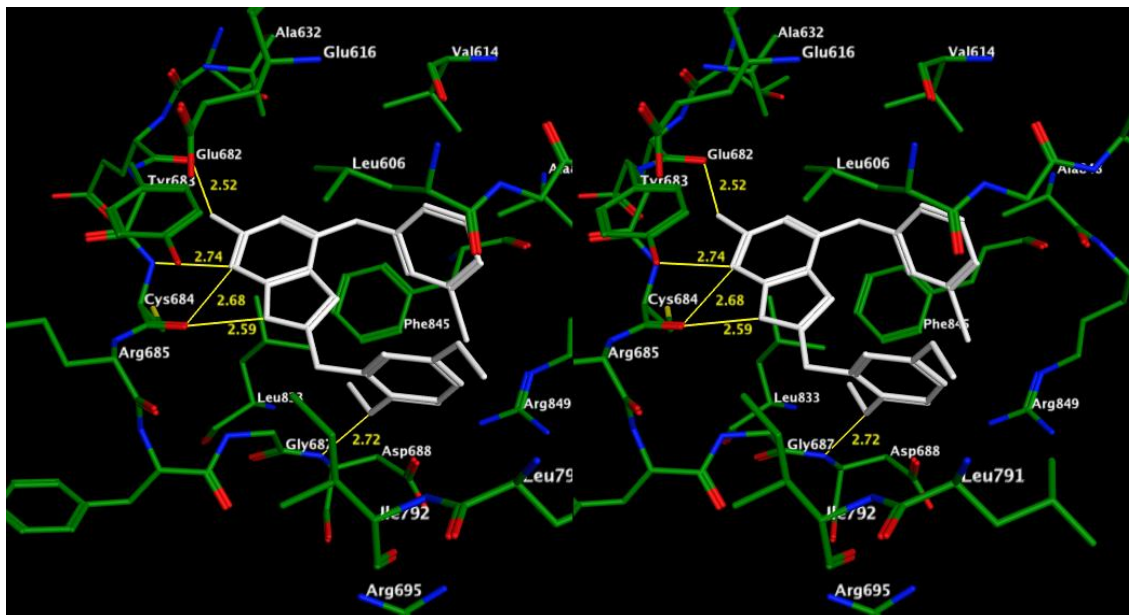


Figure 130.¹⁸³ Stereoview. Docked pose of **212b** (white) in PDGFR- β homology model.

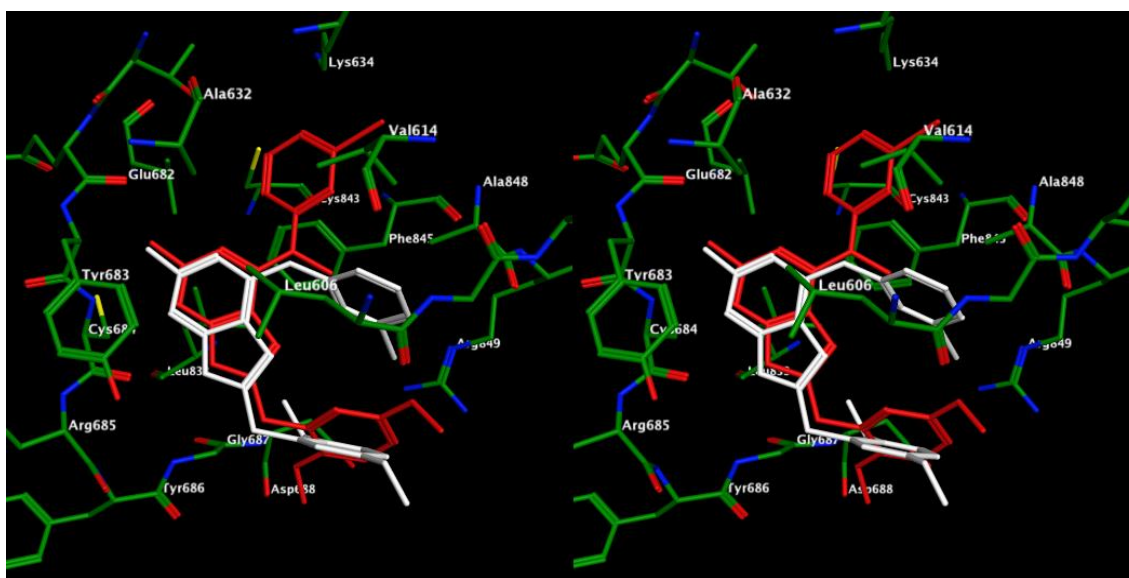


Figure 131.¹⁸³ Stereoview. Overlay of docked poses of **212i** (red) and **212b** (white) in PDGFR- β homology model.

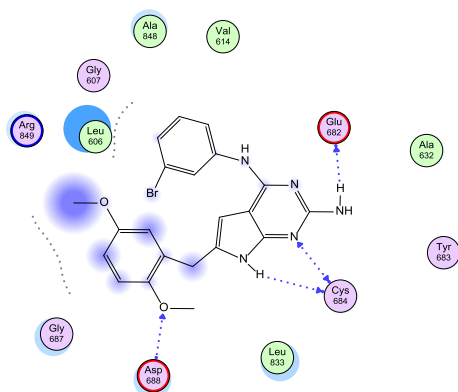
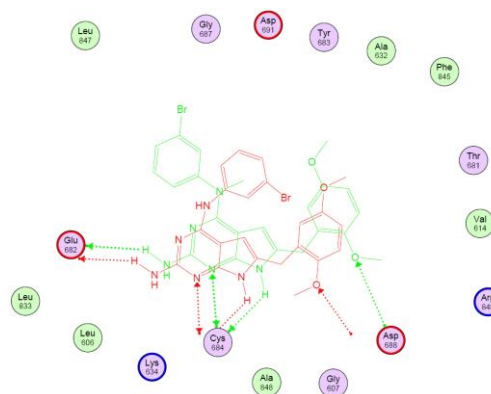
A**B**

Figure 132.¹⁸³ (A) Ligand interaction plots of docked pose of **212b** in the PDGFR-β model.

(B) Overlay of ligand interaction plots of docked poses of **212b** (red) and **212i** (green) in the PDGFR-β model.

Figure 130 shows the best docked pose of **212b** within 2 kcal/mol of the lowest energy pose in the purported ATP binding site of the PDGFR-β homology model. In this pose¹⁸³ the pyrrolo[2,3-*d*]pyrimidine ring of **212b** rests in the Adenine binding region and forms hydrogen bonds with Glu682 and Cys684 in the hinge region via the N1-, 2-NH₂ and N7- nitrogen atoms. These interactions serve to anchor the molecule and permit the anilino moiety to bind in Hydrophobic site I where it can interact with Ala848, Val614 and Leu606. The 2'-OMe substituent forms a hydrogen bond with the backbone of Asp688. The docked pose of **212i** in the homology model (Figure 131) also maintains these interactions seen in the docked pose of **212b**. In addition, **212i**, which is methylated at the N4, binds in a mode which orients the aniline ring deeper in Hydrophobic Site I. The bromophenyl residues can form hydrophobic interactions with Val614, Leu606, Val665 (not shown), Phe845 and Ala848 and the side chain of Lys634. Additionally, the methyl group on the N4 can form hydrophobic interactions with Val614 and Ala848 and

provide additional stabilization of the pose. Together, these interactions could account, in part, for the improvement in activity of **212i** over the lead compound **212b**. Figure 132 shows the ligand interaction plots¹⁸³ for **212b** and **212i** in the active site of the PDGFR- β homology model.

Molecular modeling studies thus indicate the presence of multiple low energy binding modes for these molecules and explain, in part, the potent activities of **212f**, **212i** and **212k**.¹⁸³ Thus, while general activity trends can be observed, it would be challenging to predict the preferred binding modes for these compounds in receptor tyrosine kinases on the basis of molecular modeling and docking studies.

D.2.2.4. Molecular Modeling Studies of 5- Substituted Pyrimido[4,5-*b*]indoles in a PDGFR- β Homology Model

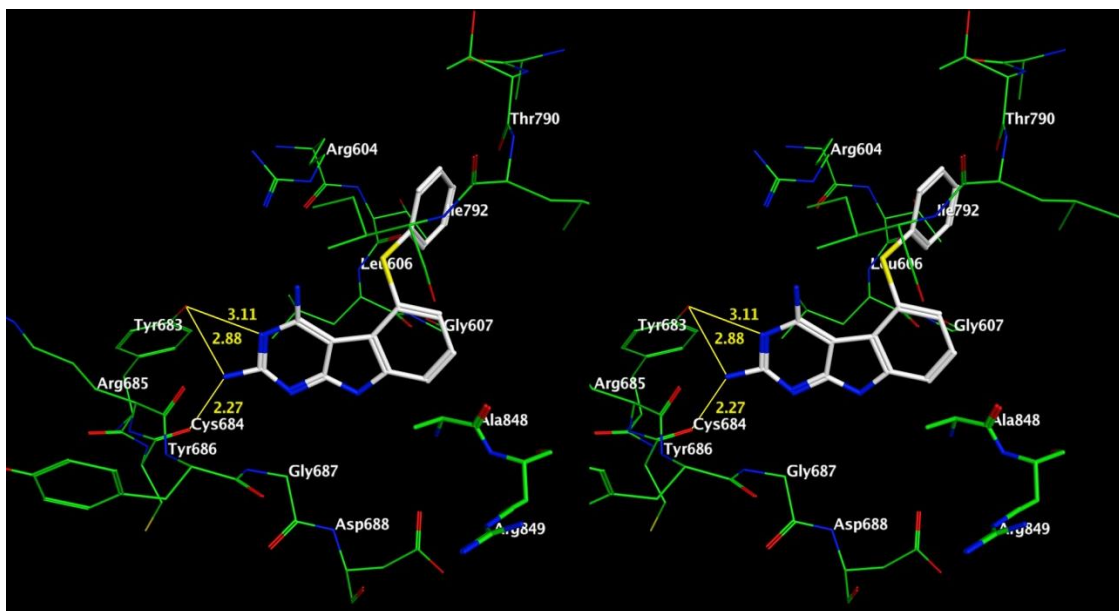


Figure 133.³⁷⁹ Stereoview of the docked pose of **213b** in the putative PDGFR- β active site model.

Results from the biological evaluation studies of tricyclic compounds **213b-c** against cells overexpressing EGFR, VEGFR-2 or PDGFR- β are shown in Table 15.³⁷⁹ Molecular modeling studies were carried out using Flexx 3.1.2⁴⁴⁵ and MOE 2008.10⁴⁰⁸ in VEGFR2 (PDB: 1YWN)²⁰⁰ and a homology model of PDGFR- β ³⁷⁹ to explain the molecular basis of its potent PDGFR- β inhibition.

Docking studies were performed using the energy minimized structure of **213b** in a homology model of PDGFR- β .³⁷⁹ The homology model of PDGFR- β was generated as described above. Figure 133 depicts the best docked pose of **213b** in the homology model of PDGFR- β . In this figure, the 2- and 4- NH₂ groups of **213b** form hydrogen bonds with the backbone residues of the hinge region (Tyr683, Cys684). Additionally, the 5-S-Ph is involved in a cation-pi interaction (10-15 kcal/mol stabilization) with the protonated Arg604. Figure 133 thus provides a working model for binding to PDGFR- β .

D.2.3. CoMFA analysis of pyrrolo[2,3-*d*]pyrimidines and furo[2,3-*d*]pyrimidines as multiple receptor tyrosine kinase inhibitors

The use of traditional CoMFA methods is time-consuming and is very sensitive to the initial preparatory steps of molecular alignment and conformer selection.⁴⁴⁸ The dearth of crystal structures of EGFR and VEGFR2 bound to ligands which bear close structural similarity to the molecules of our interest make the selection of the active or “receptor bound conformation” for alignment of our compounds challenging. Additionally, there are no reported crystal structures for PDGFR- β bound to ligands, thus severely limiting the applicability of conventional CoMFA methods for this analysis.

Topomer CoMFA⁴²³ minimizes the preparation needed for 3D QSAR analysis through an entirely objective and consistent set of alignment rules. Topomer CoMFA generates a 3D QSAR by: (a) splitting the molecules into fragments; (b) topomerically aligning each fragment; (c) calculating steric and electrostatic field descriptor values for the topomerically aligned fragments; and (d) creating a CoMFA table with the field descriptor values. The correlation among the molecules can then be analyzed using steric and electrostatic contour displays. Since Topomer CoMFA methods are sensitive only to the aligned 3D topomer fragments, and do not have any receptor requirements, it was used for the 3D QSAR analysis of our RTK inhibitors. Since the compounds used for generating the Topomer CoMFA model share either a pyrrolo[2,3-*d*]pyrimidine or a furo[2,3-*d*]pyrimidine scaffold, the differences in activity probably originate from the differing portions of the structures. i. e., the nature of the substitution on the scaffold. Topomer CoMFA calculations were performed using Sybyl X 1.1.1⁴²³ on a Windows platform.

D.2.3.1. Data Set and Biological Activity.

Gangjee *et al.* have previously reported the design and synthesis and biological evaluation of a series of RTK inhibitors based on either a pyrrolo[2,3-*d*]pyrimidine^{182, 183, 379, 380, 387, 392-394} or a furo[2,3-*d*]pyrimidine^{395, 396} scaffold (Figure 72). The molecules used in the model generation were sketched using the molecule builder in MOE 2009.10⁴²⁸ and energy minimized using the MMFF94x forcefield to a constant of 0.05 kcal/mol. The molecules were imported into a Sybyl database followed by addition of Gasteiger-Huckel charges. The biological activities were added to the table and were

converted to the corresponding log values for use in the model generation. The compounds showed an approximately 3 log unit range in their activities against EGFR, VEGFR2 and PDGFR- β . Approximately 20% of these compounds were used for generation of a test set while the rest of the molecules were used in the training set.

D.2.3.2. Alignment of compounds:

The energy minimized structures of the 60 compounds (structures and CoMFA data presented in the attached excel sheet) were aligned using MOE 2009.10 using the flexible align option in MOE in the default settings. The resultant aligned structures are shown in Figure 134.

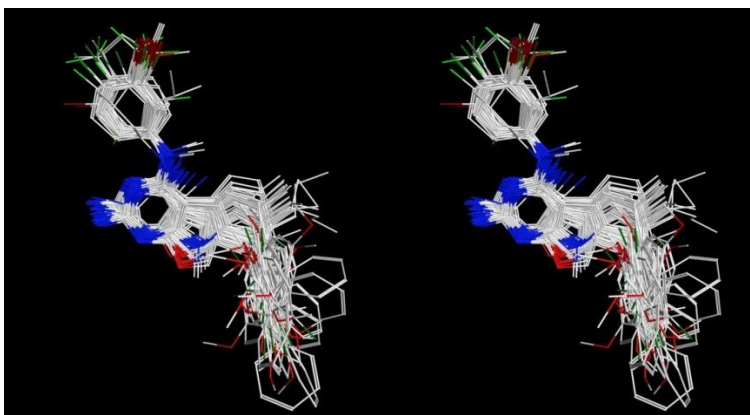
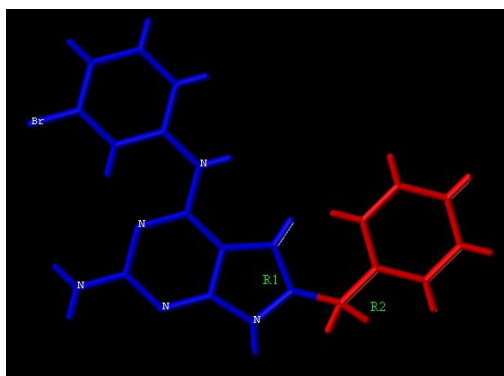


Figure 134: Results from the flexible alignment of the 60 compounds using MOE 2009.10

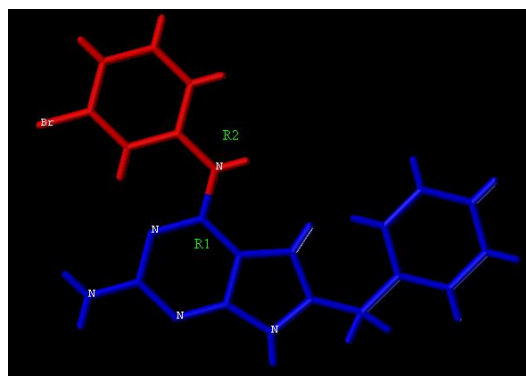
Fragmentation for Topomer CoMFA Generation.

The pyrrolo[2,3-*d*]pyrimidine inhibitors used in this study vary in the nature of the substituents on either the 4- or the 6- position. Three different methods were used to fragment the pyrrolo[2,3-*d*]pyrimidine inhibitors: Fragmentation using the ‘Split in two’ option at either the 4- or the 6- positions (Figures 113 A, B) and fragmentation involving a common pyrrolo[2,3-*d*]pyrimidine scaffold (Figure 135 C) with two substituents (R_1 , R_2)

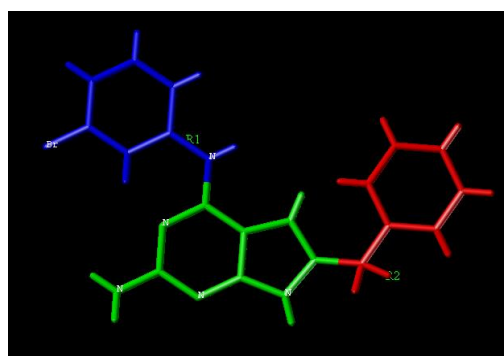
attached at the 4- and 6- positions respectively of the scaffold. Since the reported furo[2,3-*d*]pyrimidine inhibitors used in this study varied only in the nature of the substituents on the 5- position of the scaffold, the molecules, only the ‘Split in two’ option was used in the generation of fragments for the furo[2,3-*d*]pyrimidines. (Figure 135 D). The resulting fragments were stored in separate Sybyl tables.



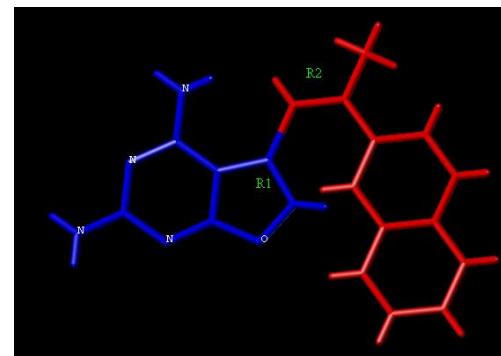
Method A



Method B



Method C



Method D

Figure 135: Fragmentation methods for pyrrolo[2,3-*d*]pyrimidines (A – C) and furo[2,3-*d*]pyrimidines (D). (A, B, D) – two fragments. R1: blue, R2: red. (C) – Two substitutions (R₁, blue and R₂, red) on the core scaffold (green).

D.2.3.3. Model Generation: Topomer CoMFA models were generated using the biological evaluation data for EGFR, VEGFR2 and PDGFR- β for each of the four fragment sets generated by the above fragmentation schemes.

D.2.3.4. Results:

The Topomer CoMFA descriptors derived above were used as explanatory variables, and the pIC₅₀ values were used as the target variable in PLS regression analyses to derive 3D QSAR models using the implementation in the SYBYL package. The conventional correlation coefficient r^2 and its standard error (r^2 stderr), the cross-validated r^2 (q^2) and its standard error, (q^2 stderr) were subsequently computed for the final models. Additionally, Y-intercept value for the PLS analysis (intercept) was returned by the program. Adding the R-group contributions to this value gives the predicted activity value.

D.2.3.4.1. Statistical data for analysis of pyrrolo[2,3-*d*]pyrimidines

The training set for generation of a Topomer CoMFA model had a total of 48

compounds and the test set contained 12 compounds. A total of nine models were generated using Topomer CoMFA using the fragment databases generated for the pyrrolo[2,3-*d*]pyrimidine scaffold by Methods A - C. The key statistical parameters associated with these models are shown in Tables 20 - 22. In general, for the pyrrolo[2,3-*d*]pyrimidine scaffold, CoMFA models generated by splitting the molecule into two (Tables 20 and 21) afforded slightly better conventional and cross-validated r^2 values compared to the models generated by considering two substitution positions on the pyrrolo[2,3-*d*]pyrimidine scaffold. (Table 22) In all nine cases, the models which showed satisfactory cross-validated r^2 values ($q^2 > 0.5$) were used to predict the activities of the test set and showed good predictive abilities.

Table 20: Model generated from fragments using Method A

	Kinase		
	EGFR	VEGFR2	PDGFR- β
Conventional r^2	0.895	0.794	0.819
r^2 stderr	0.422	0.354	0.447
Cross-validated r^2 (q^2)	0.529	0.552	0.468
q^2 stderr	0.47	0.332	0.387
Intercept	4.62	4.48	3.6
Opt. no. components	6	5	4

All three models returned from the analysis of fragments developed by Method A (Table 20) showed good conventional r^2 values. Satisfactory cross-validated r^2 values ($q^2 > 0.5$) were obtained for models generated for EGFR and VEGFR2.

Table 21: Model generated from fragments using Method B

	Kinase		
	EGFR	VEGFR2	PDGFR- β
Conventional r^2	0.834	0.954	0.611
r^2 stderr	0.38	0.411	0.243
Cross-validated r^2 (q^2)	0.58	0.504	0.41

q² stderr	0.293	0.317	0.329
Intercept	5.04	4.06	4.02
Opt. no. components	4	4	3

Models returned from the analysis of fragments developed by Method B (Table 21) showed good conventional r^2 values for EGFR and VEGFR2 but not PDGFR- β . Satisfactory cross-validated r^2 values ($q^2 > 0.5$) were obtained for models generated for EGFR and VEGFR2.

Models returned from the analysis of fragments developed by Method C (Table 22) showed r^2 values lower than those obtained by Methods A and B. However, satisfactory cross-validated r^2 values ($q^2 > 0.5$) were obtained for models generated for EGFR and VEGFR2.

Table 22: Model generated from fragments using Method C

	Kinase		
	EGFR	VEGFR2	PDGFR-β
Conventional r^2	0.755	0.715	0.682
r^2 stderr	0.223	0.281	0.326
Cross-validated r^2 (q^2)	0.521	0.50	0.322
q² stderr	0.233	0.29	0.42
Intercept	4.1	4.5	4.1
Opt. no. components	3	3	4

EGFR: Method A, which generated the fragment database by splitting the molecule in two at the 4-position of the pyrrolo[2,3-*d*]pyrimidine scaffold afforded the best conventional r^2 (0.895, Table 20) and also gave a satisfactory internal cross-validated q^2 at 0.529 (Optimum number of components, ONC = 6).

VEGFR2: Method B, which generated the fragment database by splitting the molecule in two at the 6-position of the pyrrolo[2,3-*d*]pyrimidine scaffold afforded the best conventional r^2 (0.954, Table 21) and also gave a satisfactory internal cross-validated q^2

at 0.504 (ONC = 4).

PDGFR- β : The model obtained by Method A provided the best conventional r^2 (0.819, Table 20). All the three models generated failed to provide a satisfactory internal cross-validated $q^2 > 0.5$ with the best q^2 value of 0.468 returned by Method A (Table 22).

D.2.3.4.2. Statistical data for analysis of furo[2,3-*d*]pyrimidines

All three kinase models generated for the furo[2,3-*d*]pyrimidine scaffold showed conventional r^2 values lower than those returned for the corresponding kinases for the pyrrolo[2,3-*d*]pyrimidine scaffold. The graph of the actual vs. predicted activities indicated 8 – 10 outlying molecules. Removal of the outlying molecules improved the conventional r^2 values but did not significantly improve the cross-validated r^2 values.

Table 23: Model generated from fragments using Method D

	Kinase		
	EGFR	VEGFR2	PDGFR- β
Conventional r^2	0.799	0.715	0.688
r^2 stderr	0.454	0.39	0.402
Cross-validated r^2 (q^2)	0.489	0.446	0.387
q^2 stderr	0.36	0.36	0.294
Intercept	4.12	4.08	3.64
Opt. no. components	5	4	4

An analysis of the biological activities indicated that a bias towards less active compounds in the database could account, in part, for the failure of the method to provide satisfactory q^2 values. Refinement of the model will be performed after the biological evaluation results of molecules with further variations at different locations of this scaffold are obtained.

The Stdev*coefficient Contour Maps

The CoMFA model which provided the best results for the three kinases tested for

the pyrrolo[2,3-*d*]pyrimidine scaffold were used to construct the stdev*coefficient contour maps for the most active fragments (R_1 , shown on top in each figure and R_2 , shown below R_1 in each figure) for each kinase. (Figures 114 - 116). In the CoMFA steric field, the green (sterically favorable) and yellow (sterically unfavorable) contours represent 80% and 20% level contributions, respectively. The CoMFA electrostatic contour map for kinase inhibitory activity is depicted alongside the steric contour map. The red (negative charge favorable) and blue (negative charge unfavorable) contours in the CoMFA electrostatic field represent 80% and 20% level contributions, respectively.

An analysis of the Stdev*coefficient contour maps indicates similarities and differences between the steric and electrostatic requirements at the R_1 and R_2 positions among the three kinases. These observed similarities and differences at a fragment level could be explored for the generation of new analogs with multiple kinase inhibition.

Thus, topomer CoMFA analysis models that correlate the 3D chemical structures of 60 pyrrolo[2,3-*d*]- pyrimidines and 49 furo[2,3-*d*]pyrimidines synthesized in our laboratory and their inhibitory potencies for EGFR, VEGFR2 and PDGFR- β were developed.

Fragments were generated from the molecules by either splitting the molecule into two for both scaffolds or by considering substitutions at the 4- or 6- positions of the pyrrolo[2,3-*d*]pyrimidine scaffold. Models generated for the pyrrolo[2,3-*d*]pyrimidines showed good conventional r^2 values and satisfactory cross-validated r^2 (q^2) values. The models generated for furo[2,3-*d*]pyrimidines showed reasonable conventional r^2 values

but not q^2 values.

Comparison of the topomer CoMFA maps for pyrrolo[2,3-*d*]pyrimidines (Figure 136 – 138) show differences in the steric and/or electronic requirements among the three RTKs. These differences could be used, in conjunction with other medicinal chemistry techniques and docking studies to modulate the selectivity and/or potency of designed small molecule inhibitors with multiple RTK inhibitory potential against the three RTKs.

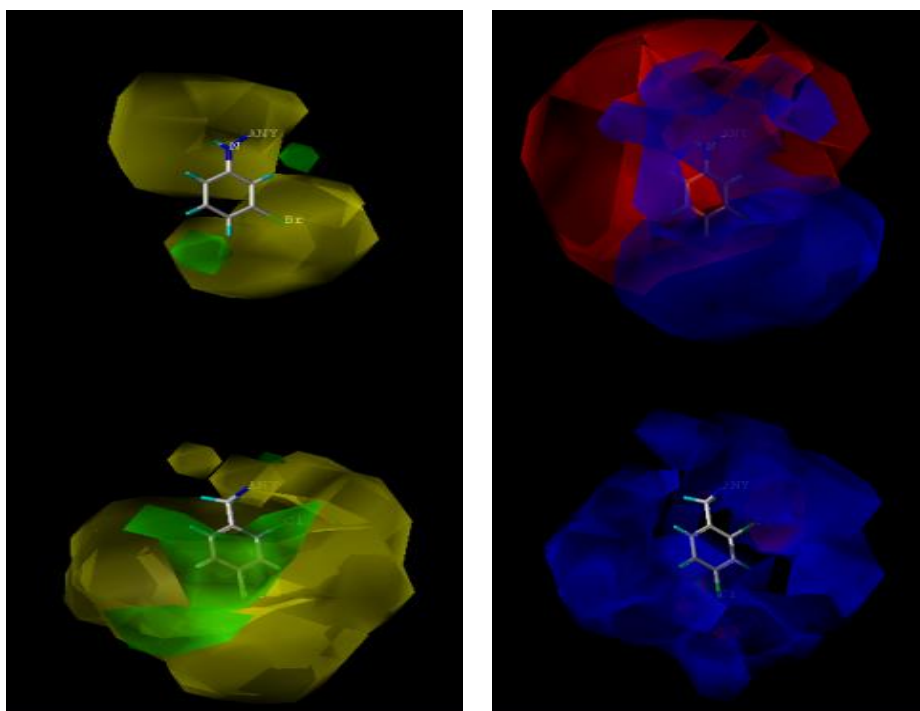


Figure 136. Stdev*coefficient contour maps for EGFR

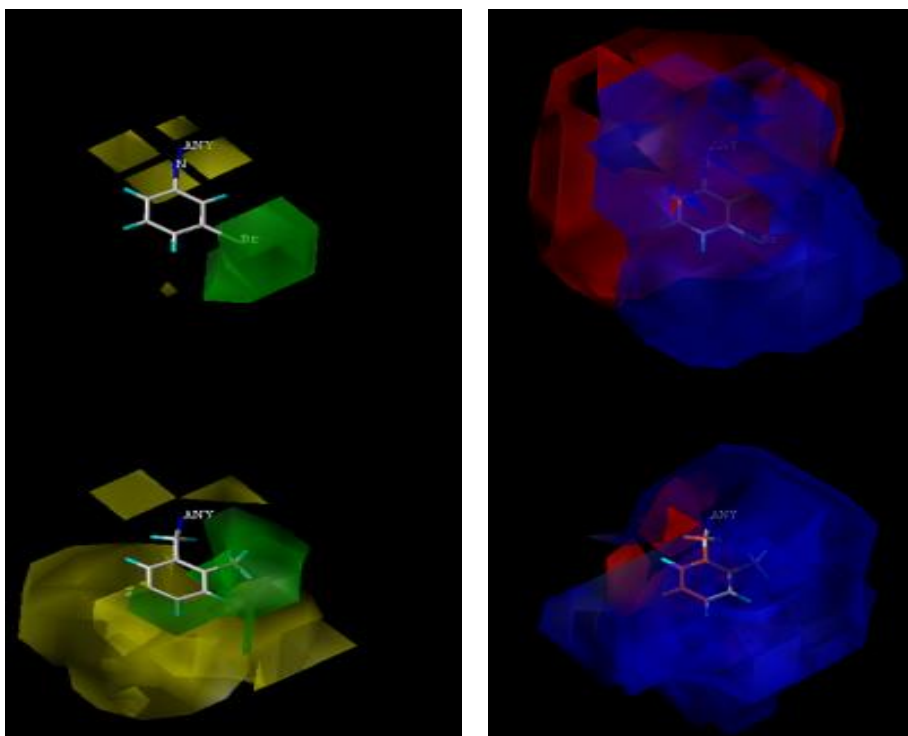


Figure 137. Stdev*coefficient contour maps for VEGFR2

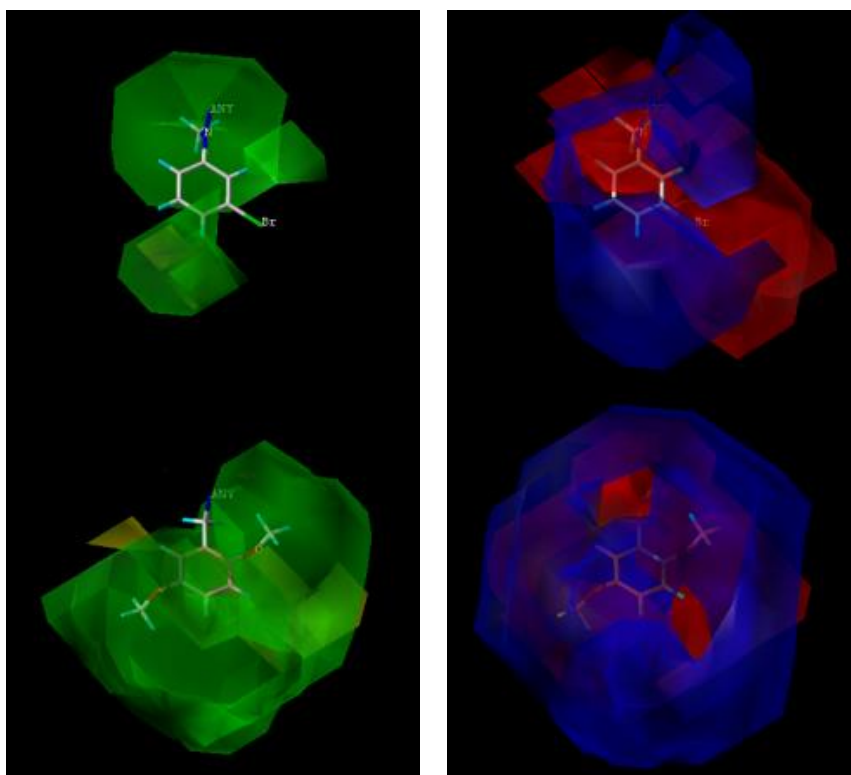
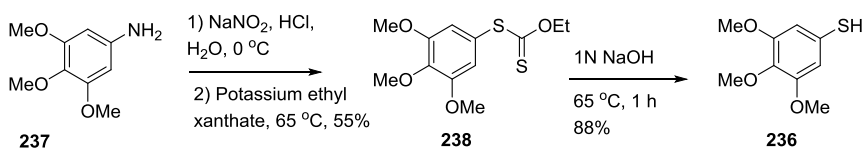


Figure 138. Stdev*coefficient contour maps for PDGFR β

D.3.COLCHICINE SITE BINDING ANTI-MITOTIC AGENTS

D.3.1. Synthesis of novel 2-amino-4-substituted-5-thioaryl-6-methyl-7-substituted pyrrolo[2,3-*d*]pyrimidines as colchicine site binding agents

Scheme 37: Synthesis of compound **236**

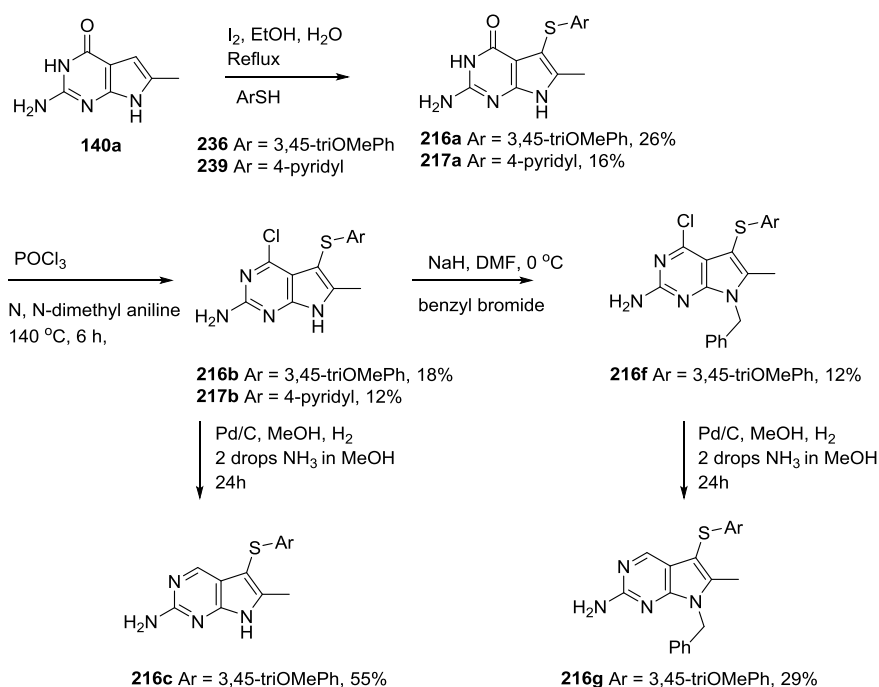


The common synthetic intermediate 3,4,5-trimethoxybenzene thiol **236** was synthesized by a Sandmeyer reaction using reported literature methods⁴⁴⁹ as shown in Scheme 37. 3,4,5-Trimethoxyaniline **237** was diazotized using NaNO₂ in a 10% HCl solution at 0 °C. The diazonium salt was treated with potassium ethyl xanthate at 65 °C to

afford the xanthate salt **238** which was purified using chromatography (silica gel, 10% EtOAc in hexanes). Basic hydrolysis of the xanthate **238** afforded the desired thiol **236** in 88% yield.

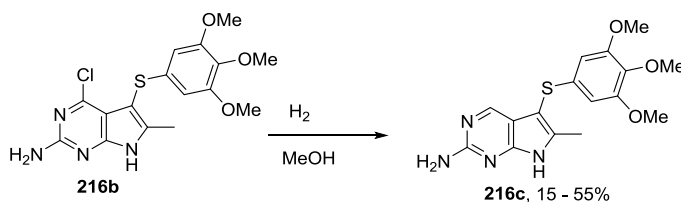
Scheme 38 shows the synthetic route used for **216a-c**, **216f-g**. 2-Amino-4-oxo-6-methyl pyrrolo[2,3-*d*]pyrimidine **140a** was synthesized according to the literature procedure reported by Gangjee *et al.*,³¹² shown previously in Scheme 16. Compound **140a** was subjected to oxidative thiolation^{103, 312, 450, 451} with 3,4,5-trimethoxybenzene thiol **236** in the presence of iodine at reflux using a 5:1 mixture of EtOH and H₂O as the solvent to afford compound **216a** in 26% yield. The absence of the 5-H proton peak and presence of the corresponding aromatic and methoxy peaks in the ¹H NMR confirmed that the substitution had occurred as anticipated.

Scheme 38: Synthesis of compounds **216a-c**, **216f-g**, **217a-c**, **217f-g**



Chlorination³⁵⁷ of **216a** by treatment with POCl₃ at reflux in presence of *N,N*-dimethylaniline afforded the chloro compound **216b** in 26% yield. Chlorination was confirmed by ¹H NMR by the disappearance of the lactam NH peak at δ 10.46 and deshielding of the other proton peaks. Reductive dehalogenation of **216b** using 10% palladium on activated carbon and hydrogen at atmospheric pressure afforded **216c**. Reductive dehalogenation was confirmed by ¹H NMR by the appearance of an additional peak at δ 8.46 corresponding to the 4-H. Conditions attempted to optimize the conversion of **216b** to **216c** are listed in Scheme 39 below. Deprotonation of the pyrrole NH of **216b** with NaH and subsequent reaction with benzyl bromide³⁸⁰ gave the target compound **216f** in 12% yield. Reductive dehalogenation of **216f** using conditions identical to that used for the synthesis of **216c** afforded the N7-benzyl protected target compound **217g** in 29% yield. The 4-pyridylthiol substituted compounds **217a-c** and **217f-g** were synthesized using a similar process as described for the synthesis of **217a-c** and **217f-g** above. 2-Amino-6-methyl-5-(pyridin-4-ylthio)-3,7-dihydro-4*H*-pyrrolo[2,3-*d*]pyrimidin-4-one **217a** was synthesized according to the procedure reported by Gangjee *et al.*³⁵⁵

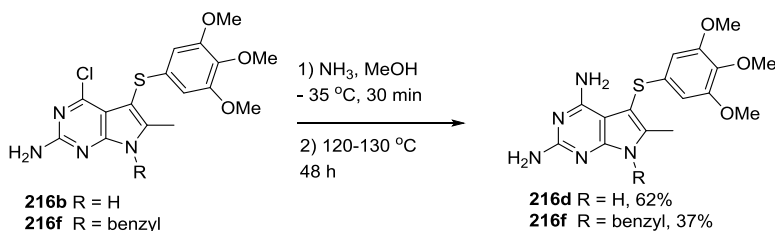
Scheme 39. Optimization of reaction conditions for conversion of **216b** to **216c**



	Catalyst	H ₂ pressure	Time (h)	Yield (%)
1	10% Pd/C	15 psi	4	15
2	10% Pd/C	15 psi	12	25
3	10% Pd/C	15 psi	24	40
3	10% Pd/C with 2 drops NH ₃ in MeOH	15 psi	24	40
4	10% Pd/C	35 psi	12	50
5	10% Pd/C	50 psi	6	40
6	30% Pd/C	15 psi	12	28
7	30% Pd/C	15 psi	24	40

Reductive dehalogenation of **216b** to **216c** was carried out using H₂ in a Paar hydrogenation apparatus in presence of Pd/C as a catalyst. Initial attempts were carried out using 10% Pd/C at atmospheric pressure for 4 h led to partial conversion of **216b** to **216c** and a 15% isolated yield of **216c**. Increasing the reaction time improved the reaction yield. Complete conversion of **216b** required recharging the reaction vessel with an additional equivalent of the catalyst after 12 h. Increasing the H₂ pressure to 35 or 50 psi did not lead to a significant increase in the yield of **216c**. Using 30% Pd/C as the catalyst gave similar yields as using 10% Pd/C as the catalyst. Addition of 2 drops of a solution of ammonia in methanol to the reaction mixture and recharging the catalyst after 12 h provided the best yield of 55% for the conversion of **216b** to **216c**.

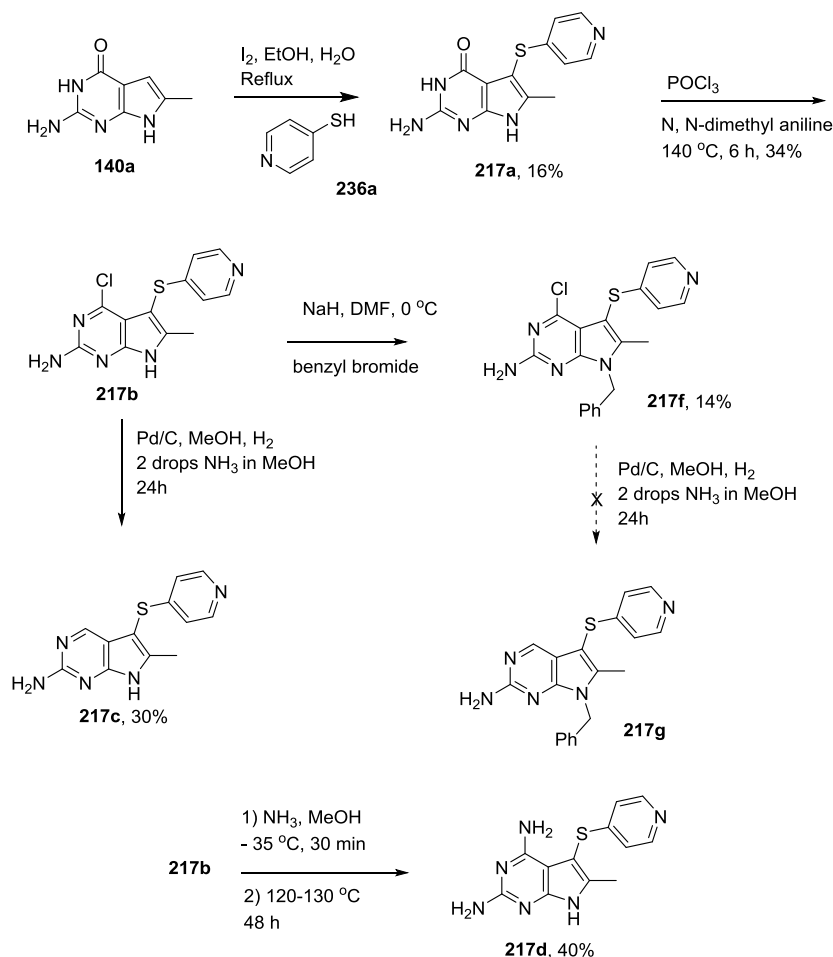
Scheme 40: Synthesis of target compounds **216d** and **216h**



Compounds **216d** and **216h** were synthesized from compounds **216b** and **216d** respectively by the nucleophilic displacement of the chloro groups by ammonia in a

sealed vessel reaction.³⁵⁷ The presence of an additional amino peak at δ 5.22 in the ^1H NMR confirmed that the displacement had taken place.

Scheme 41: Synthesis of target compounds **217a-h**



Synthesis of target compounds **217a-h** from the common synthon **140a** is shown in Scheme 40. Oxidative thiolation³¹² of **140a** with commercially available thiol **236a** in presence of I₂ in an EtOH:H₂O (5:1) mixture at reflux afforded the 5-substituted target compound **217a** in 34% yield. Chlorination of the 4-oxo moiety of **217a** was carried out by heating a mixture of **217a** in POCl₃ at reflux in presence of *N,N*-dimethylaniline to afford target compound **217b** in 30% yield. Abstraction of pyrrole NH proton with NaH and subsequent nucleophilic displacement³⁸⁰ with benzyl bromide afforded the target

compound **217f** in 14% yield. While reductive dechlorination of **217b** in a Paar hydrogenation apparatus with hydrogen at 15 psi afforded target compound **216c** in 30% yield, attempts to synthesize target compound **217g** from the corresponding chloro compound **216f** afforded a complex mixture which could not be separated using gravity or flash chromatography. Attempts to increase the ratio of Pd/C from 1 eq. to 2 or 3 eq. increasing reaction time or performing the hydrogenation at higher pressure (35 or 50 psi) did not afford a cleaner reaction, presumably due to debenzylation of **217g** under the reaction conditions. Compound **217d** was synthesized from **217b** by the nucleophilic displacement of the 4-Cl of **216b** by ammonia in a sealed vessel reaction, similar to the synthesis of **216b** (Scheme 41).

D.3.2. Molecular Modeling Studies in the Colchicine Binding Site of Tubulin.

In an attempt to provide a molecular basis of the remarkable activity of the *N*-Me analogs **218a** and (\pm)-**219a** (Figure 76) and the inactivity of the *N*-desmethyl analogs **218b** and (\pm)-**219b** (Figure 76), we have modeled compounds **218a** – **219e** (Figure 76) into the colchicine binding site.^{50, 399} The X-ray crystal structure of tubulin at 3.58 Å resolution was obtained from the protein database (PDB ID 1SA0).²³² This crystal structure contains the $\alpha\beta$ dimers of tubulin complexed with *N*-deacetyl-*N*-(2-mercaptoacetyl)colchicine (DAMA colchicine), a close structural analog of colchicine. The binding of colchicine to the tubulin dimer has been described in the literature.^{243, 452, 453} Colchicine binds to β tubulin at its interface with α tubulin. The colchicine site has dimensions of ~ 10 Å x ~ 10 Å x ~ 4 -5 Å and is composed of strands S8 and S9, loop T7 and helices H7 and H8 from the β subunit and loop T5 from the α subunit of tubulin.²³²

Thr α 179 and Val α 181 in the α -tubulin subunit form hydrogen bonds with colchicine.

Additionally, Cys β 241 forms a hydrogen bond with the oxygen atom of the 3-OMe in the A-ring of colchicine. Additional hydrophobic stabilization is afforded by side chain atoms of Val α 181 and Met β 259. The carbonyl group of the A-ring also H-bonds with Lys β 352.

Docking studies⁵⁰ were performed using the docking suite of MOE 2008.10.

Details of the docking protocol used are provided in the experimental section. Multiple low-energy conformations (within 1kcal/mol of the best pose) were obtained on docking (*R*)-**219a** and other analogs.

D.3.2.1. Docking of (*R*)- and (*S*)-219a in the colchicine binding site of tubulin.

Docking of (*R*)-219a in the colchicine binding site of tubulin.

The multiple docked poses can be explained by the large volume of the active site (10 Å x 10 Å x 4-5 Å).²³² Figure 139 shows the docked conformation of (*R*)-**219a** which was selected as a working model for the docking of compounds **218a,b** and **219a-e** on the basis of their structural similarity to the bound conformation of DAMA-colchicine. The pose in Figure 139 for (*R*)-**219a** was ranked 4th in the results and had a score (-6.838 kcal/mol) within 1 kcal/mol of the best scored pose.^{50, 399}

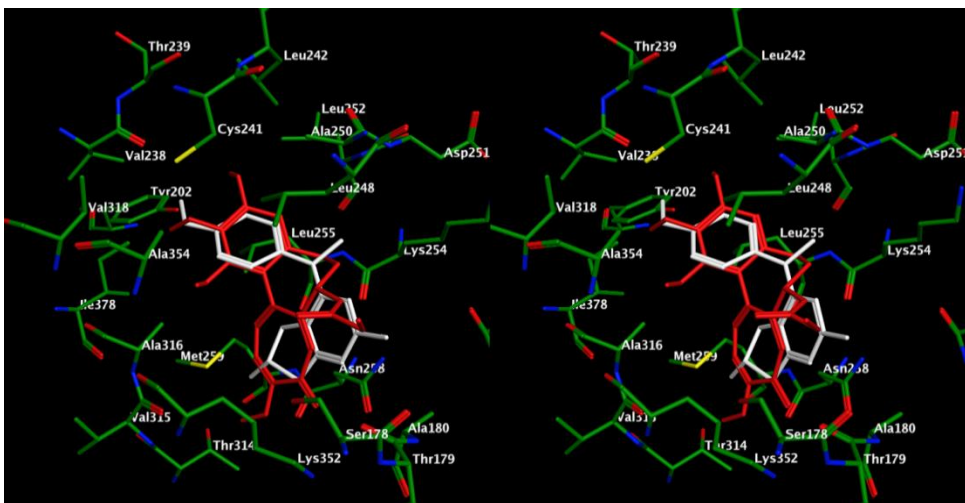


Figure 139:^{50, 399} Stereoview. Docked pose of (*R*)-**219a** (white) overlaid with DAMA colchicine (red) in the colchicine binding site of tubulin.

Comparison of the docked conformation of (*R*)-**219a**^{50, 399} and the crystal structure conformation of DAMA colchicine shows overlap of the 4'-OMe phenyl group of (*R*)-**219a** with the tri-OMe containing A-ring of DAMA colchicine (Figure 139). In this pose the 4'-OMe of (*R*)-**219a** overlaps with the 3'-OMe group in the A ring of DAMA colchicine. Similar interactions of -OMe groups with Cys β 241, as observed in Figure 139, have been reported in the literature.²⁴³ The conformation of (*R*)-**219a** depicted in Figure 139 permits the formation of a hydrogen bond between Cys β 241 and the oxygen atom of the 4'-OMe of (*R*)-**219a** as is observed with the 3'-OMe group of DAMA colchicine in its X-ray crystal structure with tubulin. The phenyl ring of (*R*)-**219a** mimics the A ring of colchicine and is involved in hydrophobic interactions with amino acids from β -tubulin (Leu β 248, Ala β 250, Leu β 255, Ala β 316). Additionally, the methyl group from 4'-OMe could also interact with the side chain of Ile β 378 and/or with the side chain of Val β 318.

The N-Me group of (*R*)-**219a** occupies a region in space in proximity to the C5 and C6 atoms of the B-ring of DAMA-colchicine. In this orientation the *N*-Me group is involved in hydrophobic interactions with the side chain C atoms of Lys β 254 and Ala β 250. An additional hydrophobic interaction between the *N*-Me moiety of (*R*)-**219a** and the side chain C-atom of Leu β 248 also occurs due to the flexible nature of the protein (measured distance between *N*-Me and side chain C of Leu β 248 is 4.21 Å). These interactions could assist in stabilization of the docked conformation of (*R*)-**219a** and could partly explain the remarkable difference in activity of the *N*-desmethyl analog, (*R*)-**219b**, of **219a** which would lack these additional interactions (Figure 140). The *N*-Me also aids in maintaining the relative conformations of the cyclopenta[*d*]pyrimidine and the phenyl rings of *R*-**219a**. While similar docked poses were observed for **219b**, the docked poses of compounds with the *N*-Me group consistently scored higher (~1 kcal/mol) than those of compounds that lacked the *N*-Me group.⁵⁰

The cyclopenta[*d*]pyrimidine of (*R*)-**219a** ring partially overlaps with the C-ring of DAMA colchicine and is stabilized by hydrophobic interactions with side chains C atoms of Leu β 255, Asn β 258 and Lys β 252. The C7 of (*R*)-**219a** overlaps the C9 carbonyl C of DAMA colchicine. The C2 methyl group of (*R*)-**219a** is involved in a hydrophobic interaction with Ala α 180 (4.35 Å) while the C6-methyl group of (*R*)-**219a** is involved in hydrophobic interactions with Val α 181 and Ala β 316. There was no significant difference in the binding poses and the docked scores of (*R*)-**219a** (-6.838 kcal/mol) and (*S*)-**219a** (-6.945 kcal/mol) due to the difference in the chirality of the C6-Me group (Figure 141).

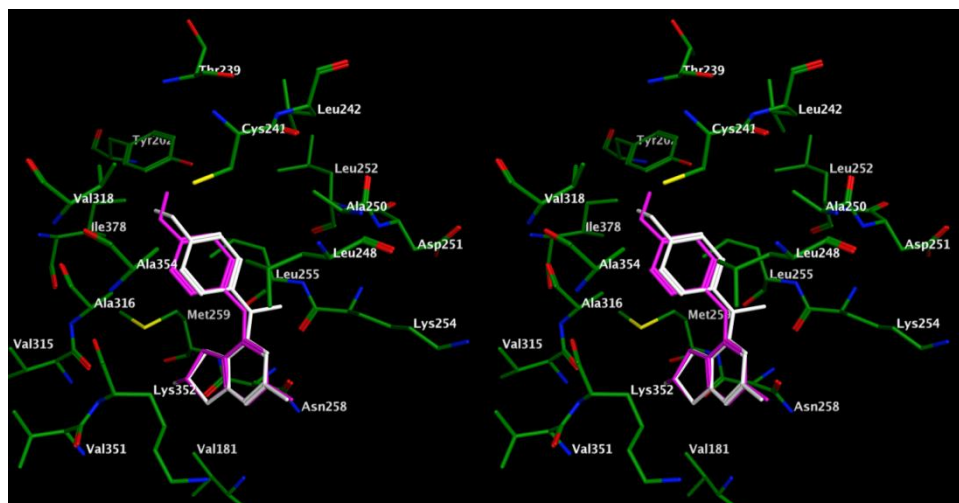


Figure 140:⁵⁰ Stereoview. Superimposition of the docked poses of (*R*)-**219a** (white) and **219b** (magenta) in the colchicine binding site of tubulin.

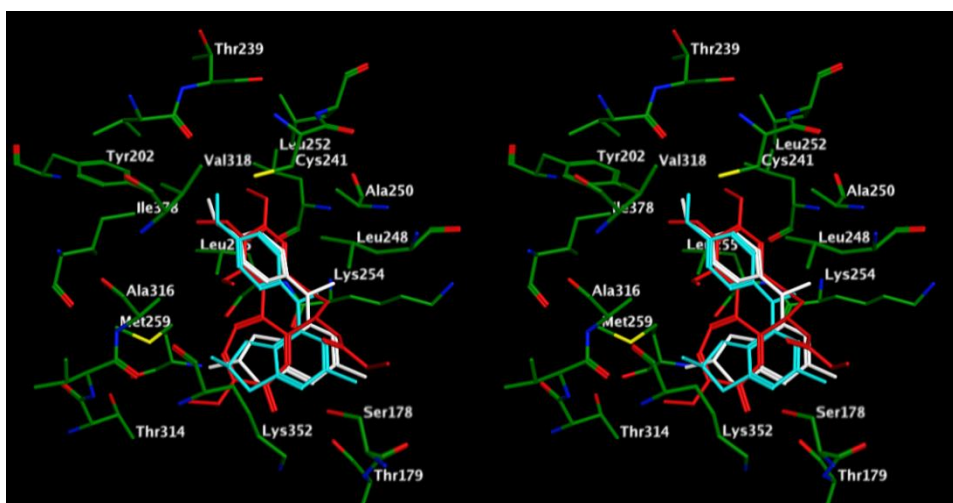


Figure 141:⁵⁰ Stereoview. Superimposition of the docked poses of (*R*)-**219a** (white), (*S*)-**219a** (cyan) and DAMA colchicine (red) in the colchicine binding site of tubulin.

While this work was in progress a series of quinazolines⁴⁵⁴⁻⁴⁵⁷ and thieno[3,2-*d*]pyrimidines⁴⁵⁸ as potent apoptosis inducers were published. These reports suggest a similar function for the *N*-methyl moiety, but do not provide details about the binding modes of the quinazolines and/or thieno[3,2-*d*]pyrimidines.

Molecular modeling suggests that the binding interactions afforded by the 4'-OMe group on the anilino ring also plays an important part in dictating the potency of these compounds against tubulin. Deletion or moving the 4'-OMe moiety results in a significant loss of activity. However, molecular modeling does not provide a reason(s) for the loss of potency of (\pm)-**219d** compared to (\pm)-**219a**. We speculate that the loss of potency could be explained either by the loss of interactions by the 4'-OMe moiety of **219a** and/or the additional conformational restriction of the anilino ring by a combination of *N*-methylation and the 2'-OMe moiety of **219d** on the phenyl ring or both.^{50, 400}

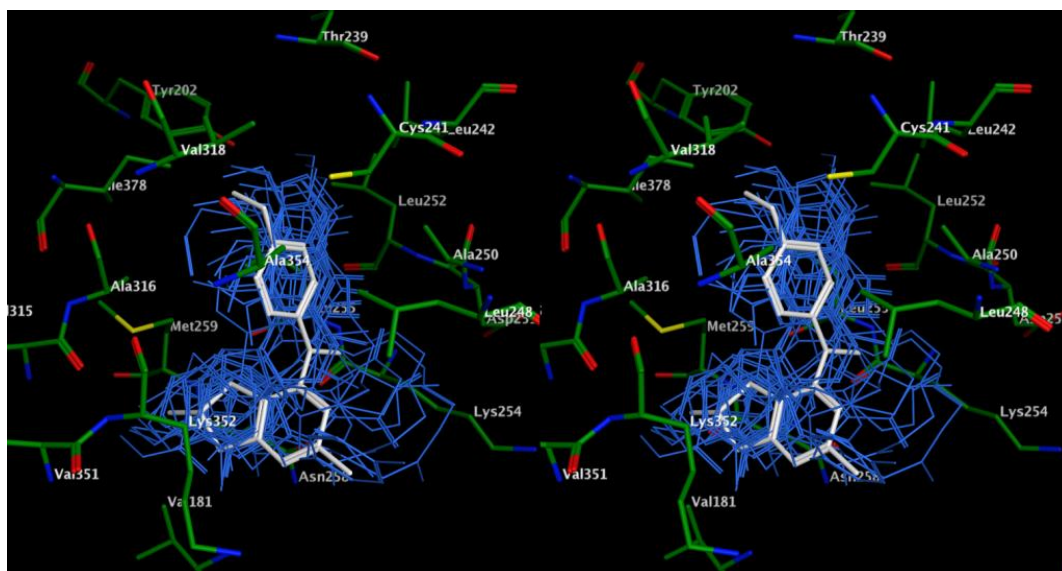


Figure 142:⁵⁰ Stereoview. Docking mode of (*R*)-**219a** (white) overlaid with docked poses of 15 ligands²⁴³ (blue) in the colchicine binding site of tubulin.

Comparison of the binding mode of compounds (*R*)-**219a** to the reported binding modes²⁴³ of 15 known tubulin inhibitors that bind to the colchicine site were carried out. As an example, (*R*)-**219a** retains the key binding interactions exhibited by the known tubulin inhibitors and is in a conformation consistent with those for the reported compounds (Figure 142).

D.3.2.1. Molecular dynamics calculations

While there was no significant difference in the binding poses and docked scores of (*R*)-**219a** (-6.838 kcal/mol) and (*S*)-**219a** (-6.945 kcal/mol) due to the chirality of the C6-Me group in the initial docking study, the biological evaluation studies of the two isomers (Table 23) indicated that (*S*)-**219a** showed higher potency towards tubulin in vitro assays. It was therefore of interest to perform molecular dynamics studies in order to further probe the reasons for the difference in activities between the two enantiomers.

Table 23:⁴⁵⁹ Biological activities of (*R*)-**219a** and (*S*)-**219a**

Cmpd	IC ₅₀ ± SD (nM)			IC ₅₀ ± SD (nM)		
	SKOV3	SKOV-3	Rr ^a	HeLa	WTβIII	Rr ^b
		MDR-1-				
(<i>R,S</i>)-	34.5 ± 1.4	60.9 ± 4.4	1.8	37.3 ± 4.1	23.9 ± 1.7	0.6
(<i>S</i>)-1•HCl	16.4 ± 1.6	62.6 ± 6.7	3.8	19.0 ± 0.9	13.3 ± 0.5	0.7
(<i>R</i>)-1•HCl	85.9 ± 4.5	119.8 ±	1.4	92.9 ± 5.6	67.7 ± 1.3	0.7
Paclitaxel	2.95 ± 0.07	4,875 ±	1,622	13.8 ± 0.13	9/05 ± 51.1	6.6
CA4	6.05 ± 0.61	22.0 ± 6.9	3.6	4.09 ± 0.05	4.02 ± 0.26	0.98

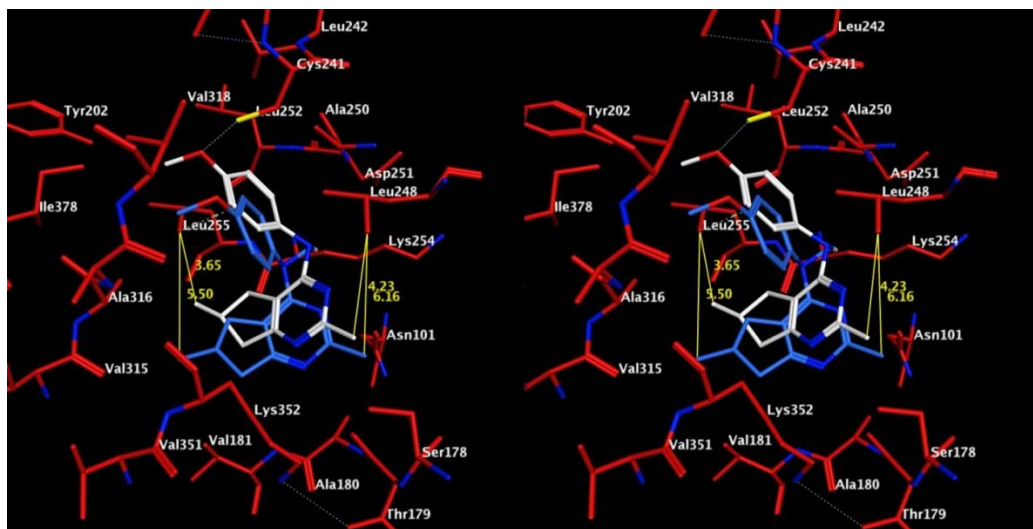


Figure 143. Stereo view. Superimposition of the final docked conformations of (*R*)-**219a** (blue) and (*S*)-**219a** (white) in the colchicine site of tubulin.

Subjecting the docked poses of (*R*)-**219a** and *S*-**219a** to an unconstrained molecular dynamics protocol in MOE 2010.10 (heating the system from 0° to 300° K followed by equilibration, production for 500 ps and cooling to 0° K) revealed differences in the final conformations of docked poses of the *R*- and *S*-enantiomers in the colchicine site as shown in Figure 143. Compound *S*-**219a** is bound in a more favorable conformation in the colchicine binding pocket as compared to *R*-**219a**, which permits the formation of hydrophobic interactions between C2-Me and Leuβ248, and C6-Me and Leuβ255 for *S*-**219a**. The corresponding C2- and C6-Me moieties of *R*-**219a** do not form these hydrophobic interactions with Leuβ248 and Leuβ255 respectively. These hydrophobic interactions could explain, in part, the improvement in the IC₅₀ value of *S*-**219a** compared to *R*-**219a** against isolated tubulin. Prediction of the binding energies of the docked conformations of *R*-**219a** and *S*-**219a** using the Hyde module in LeadIT 2.0.1⁴⁶⁰ indicated a greater contribution of the C6-Me group of the *S*-enantiomer (-6.5 kJ/mol) towards the total binding energy (-28 kJ/mol) of *S*-**219a** as compared to the corresponding C6-Me moiety of *R*-**219a** (-5.1 kJ/mol) towards the total binding energy of *R*-**219a** (-25kJ/mol).

E. SUMMARY

The results from this work are reported into two sections listed below: synthesis of bicyclic heterocyclic molecules and molecular modeling studies.

Synthesis of bicyclic heterocyclic molecules:

Following structural classes of compounds have been designed, synthesized and studied as inhibitors of pJ DHFR, RTKs and tubulin:

4. 2,4-Diamino-6-(substituted-aryl)methylpyrido[2,3-*d*]pyrimidines
5. 4-((3-bromophenyl)linked)-6-(substituted-benzyl)-7*H*-pyrrolo[2,3-*d*]pyrimidin-2-amines
6. 6-methyl-5-((substitutedphenyl)thio)-7*H*-pyrrolo[2,3-*d*]pyrimidin-2-amines

From these projects a total of thirty five new compounds (excluding intermediates) were synthesized and characterized and were submitted for various biological assays. Results from these biological evaluation studies will be presented in due course. These compounds are as follows:

1. **170** 6-(((2,5-difluorophenyl)amino)methyl)pyrido[2,3-*d*]pyrimidine-2,4-diamine
2. **171** 6-(((2,4,6-trichlorophenyl)amino)methyl)pyrido[2,3-*d*]pyrimidine-2,4-diamine
3. **172** 6-(((2,3,4-trichlorophenyl)amino)methyl)pyrido[2,3-*d*]pyrimidine-2,4-diamine
4. **173** 6-(((2,6-dichlorophenyl)amino)methyl)pyrido[2,3-*d*]pyrimidine-2,4-diamine
5. **174** 6-(((3,5-dichlorophenyl)amino)methyl)pyrido[2,3-*d*]pyrimidine-2,4-diamine
6. **175** 6-(((3,4-dichlorophenyl)amino)methyl)pyrido[2,3-*d*]pyrimidine-2,4-diamine

7. **176** 6-(((3,4,6-trichlorophenyl)amino)methyl)pyrido[2,3-*d*]pyrimidine-2,4-diamine
8. **177** 6-(((2,4,5-trichlorophenyl)amino)methyl)pyrido[2,3-*d*]pyrimidine-2,4-diamine
9. **178** 6-(((2,3-dichlorophenyl)amino)methyl)pyrido[2,3-*d*]pyrimidine-2,4-diamine
10. **179** 6-(((2,5-dibromophenyl)amino)methyl)pyrido[2,3-*d*]pyrimidine-2,4-diamine
11. **180** 6-(((2,6-dinitrophenyl)amino)methyl)pyrido[2,3-*d*]pyrimidine-2,4-diamine
12. **186** 6-(((2,5-dichlorophenyl)thio)methyl)pyrido[2,3-*d*]pyrimidine-2,4-diamine
13. **187** 6-(((3,4,5-trichlorophenyl)thio)methyl)pyrido[2,3-*d*]pyrimidine-2,4-diamine
14. **188** 6-(((2,5-difluorophenyl)thio)methyl)pyrido[2,3-*d*]pyrimidine-2,4-diamine
15. **189** 6-((2,5-dichlorophenoxy)methyl)pyrido[2,3-*d*]pyrimidine-2,4-diamine
16. **190** 6-((3,4,5-trichlorophenoxy)methyl)pyrido[2,3-*d*]pyrimidine-2,4-diamine
17. **191** 6-((2,5-difluorophenoxy)methyl)pyrido[2,3-*d*]pyrimidine-2,4-diamine
18. **197** 4-((3-bromophenyl)thio)-6-(2-methylbenzyl)-7*H*-pyrrolo[2,3-*d*]pyrimidin-2-amine
19. **198** 4-((3-bromophenyl)thio)-6-(2,4-dichlorobenzyl)-7*H*-pyrrolo[2,3-*d*]pyrimidin-2-amine
20. **199** 4-((3-bromobenzyl)thio)-6-(2-methylbenzyl)-7*H*-pyrrolo[2,3-*d*]pyrimidin-2-amine
21. **200** 4-((3-bromobenzyl)thio)-6-(2,4-dichlorobenzyl)-7*H*-pyrrolo[2,3-*d*]pyrimidin-2-amine
22. **205** 4-(3-bromophenoxy)-6-(2-methylbenzyl)-7*H*-pyrrolo[2,3-*d*]pyrimidin-2-amine

23. **206** 4-(3-bromophenoxy)-6-(2,4-dichlorobenzyl)-7*H*-pyrrolo[2,3-*d*]pyrimidin-2-amine
24. **207** 4-((3-bromobenzyl)oxy)-6-(2-methylbenzyl)-7*H*-pyrrolo[2,3-*d*]pyrimidin-2-amine
25. **208** 4-((3-bromobenzyl)oxy)-6-(2,4-dichlorobenzyl)-7*H*-pyrrolo[2,3-*d*]pyrimidin-2-amine
26. **209** *N*4-(3-bromobenzyl)-6-(2-methylbenzyl)-7*H*-pyrrolo[2,3-*d*]pyrimidine-2,4-diamine
27. **210** *N*4-(3-bromobenzyl)-6-(2,4-dichlorobenzyl)-7*H*-pyrrolo[2,3-*d*]pyrimidine-2,4-diamine
28. **216a** 2-Amino-6-methyl-5-((3,4,5-trimethoxyphenyl)thio)-3,7-dihydro-4*H*-pyrrolo[2,3-*d*]pyrimidin-4-one
29. **216b** 4-chloro-6-methyl-5-((3,4,5-trimethoxyphenyl)thio)-7*H*-pyrrolo[2,3-*d*]pyrimidin-2-amine
30. **216c** 6-methyl-5-((3,4,5-trimethoxyphenyl)thio)-7*H*-pyrrolo[2,3-*d*]pyrimidin-2-amine
31. **216d** 6-methyl-5-((3,4,5-trimethoxyphenyl)thio)-7*H*-pyrrolo[2,3-*d*]pyrimidine-2,4-diamine
32. **216e** 2-amino-7-benzyl-6-methyl-5-((3,4,5-trimethoxyphenyl)thio)-3,7-dihydro-4*H*-pyrrolo[2,3-*d*]pyrimidin-4-one
33. **216f** 7-benzyl-4-chloro-6-methyl-5-((3,4,5-trimethoxyphenyl)thio)-7*H*-pyrrolo[2,3-*d*]pyrimidin-2-amine

34. **216g** 7-benzyl-6-methyl-5-((3,4,5-trimethoxyphenyl)thio)-7*H*-pyrrolo[2,3-*d*]pyrimidin-2-amine
35. **216h** 7-benzyl-6-methyl-5-((3,4,5-trimethoxyphenyl)thio)-7*H*-pyrrolo[2,3-*d*]pyrimidine-2,4-diamine

In addition, bulk synthesis of the potent lead compound **170** (750 mg) was carried out to facilitate *in vivo* evaluation.

During the bulk synthesis of **170**, the following synthetic improvements were achieved successfully including:

1. Use of a scalable alternate route to synthesize the advanced intermediate **92a** (Scheme 24) in one pot. This intermediate was used without purification without significantly affecting the yield or purity of the reductive amination step needed for synthesis of **170**.
2. Use of mild reductive amination in presence of molecular sieves improved the yield of **170** from 7% to 18% and reduced the amounts of side products generated which are challenging to separate. Use of benchtop reductive amination instead of reductive amination using a Paar-hydrogenation vessel is easily scalable, permits parallel synthesis of multiple analogs from the common intermediate **92a**, and eliminates the use of hydrogen gas for reduction.

Docking Studies

Docking studies were performed using LeadIT, MOE, Sybyl or Flexx for the target compounds listed above and for other compounds reported by Gangjee *et al.* against the

following targets:

5. Dihydrofolate reductase: human, *P. carinii*, *P. jirovecii* and *T. gondii*.
6. Thymidylate synthase: human and *T. gondii*.
7. Receptor tyrosine kinases: VEGFR2, EGFR and PDGFR- β
8. Colchicine binding site of tubulin.

There are no reported crystal structures for pjDHFR and PDGFR- β . At the time this work was initiated there were no reported crystal structures for tgDHFR and tgTS. Hence homology models were generated for these targets using MOE and validated using tools available from the Swissmodel website in order to perform molecular modeling studies. Models generated using MOE were validated by comparison with homology models generated independently using various automated homology modeling servers available online. The X-ray crystal structures of tgTS complexed with **194d** and **194f** were very recently published. The tgTS homology model generated in this study and employed to design novel agents shows remarkable similarity with the recently published X-ray crystal structures ($C\alpha$ RMSD = 0.68-0.72 Å). (Figure 101) At the time this work was initiated, there were no previously reported homology models against pjDHFR. A novel homology model was generated for the F36C L65P double mutant form of pjDHFR, which is resistant to standard therapeutic agents such as TMP.

Docking studies were performed to provide a molecular basis for the observed activity of target compounds against DHFR, RTKs or tubulin. Results from these studies support structure-based and ligand-based medicinal chemistry efforts in order to improve potency

and/or selectivity of analogs of the docked compounds against these targets. Key findings from the docking studies against selected targets are listed below:

1. **pjDHFR homology model:** Docking studies of **192d** (Figure 83) against pjDHFR suggest that the interaction of *N*-Me of **192d** Ile123 in pjDHFR but not with Val115 in hDHFR, and conformational restriction of the terminal aniline moiety by the *N*-Me group could explain, in part, the 300-fold improvement in potency of **192d** against pjDHFR compared to the des-methyl compound **192e**. Docking studies suggest that steric clash with the larger Phe31 in hDHFR compared to the smaller Met33 in pjDHFR (Figure 90) explain, in part, the 19-fold selectivity of **193f** for pjDHFR over hDHFR.
2. **F36C L65P double mutant pjDHFR homology model:** Docking studies were used to explain, in part, the 10-fold loss of potency of **168** against F36C L65P double mutant pjDHFR and the 1000-fold loss of potency of standard TMP against F36C L65P double mutant pjDHFR compared to wild-type pjDHFR.
3. **tgDHFR homology model:** Docking studies of **194a-b** (Figure 91) in the tgDHFR homology model suggest that the bulky naphthyl moiety in these compounds is better accommodated in the larger binding pocket of tgDHFR instead of the smaller pocket in hDHFR, and explains, in part, the decreased activity of **194a-b** against hDHFR.
4. **tgTS homology model:** Docking studies of **194d-j** in the tgTS homology model suggest that additional interaction of the second ring of the 2-naphthyl moiety of **194e** and the 1-naphthyl analog **194f** with tgTS Phe374 compared to a lack of similar interaction of the phenyl analog **194d** (Figure 88) explains, in part, the 10-

fold improved potency of **194e** and 5-fold for **194f** for tgTS over **194d**.

Comparison of the predicted docked pose (Figure 102) and the recently published X-ray crystal structure of **194e** in tgTS show that the key interactions predicted by the docking studies are maintained. This provides validation for the utility of the docking software and protocols used in this study for design of analogs of these compounds against tgTS.

5. **RTKs:** Results from docking studies of three series of bicyclic and tricyclic inhibitors against VEGFR2, EGFR and PDGFR- β homology model suggest that the target compounds can have multiple distinct low-energy binding poses in the ATP-binding pocket of these RTKs. In some cases the docking studies could explain, in part, the observed activity of the target compounds against RTKs. Findings from these docking studies provide validation for the original design hypothesis by Gangjee *et al.* of multiple binding modes of a single agent as a means of achieving multiple kinase inhibition in a single molecule. However, the presence of multiple distinct binding modes reduces the predictive utility of these models for novel compounds against the target RTKs.
6. **Colchicine binding site of tubulin:** Results from docking studies suggest that the cyclopenta[*d*]pyrimidines (*R*)-**219** and (*S*)-**219** and other compounds in the series bind in the colchicine binding site of tubulin with the 4-methoxyphenyl moiety of **219** mimicking the A-ring of the crystal structure ligand DAMA-colchicine and the cyclopenta[*d*]-pyrimidine scaffold mimicking the C-ring of DAMA-colchicine. The N4-Me mimicks the C5-C6 bridge of DAMA-colchicine and helps maintain the relative orientation of the cyclopenta[*d*]pyrimidine scaffold

and the 4-methoxyphenyl moiety. The 4'-OMe moiety of **219** overlaps the 3-OMe of DAMA-colchicine. These findings explain, in part, the molecular basis of the importance of both, the N-Me and 4'-OMe moieties in compounds of this series.

Topomer CoMFA models:

1. **tgTS and hTS:** Topomer CoMFA provides a useful method for generating 3D-QSAR models that are insensitive to the initial structural alignment between molecules used for model generation. Topomer CoMFA models were developed for tgTS and hTS using a set of 85 bicyclic non-classical pyrrolo[2,3-*d*]pyrimidines and thieno[2,3-*d*]pyrimidines using their tgTS and/or hTS inhibitory data reported by Gangjee *et al.* The resultant tgTS topomer CoMFA maps representing steric and electronic contributions could be used to explain the potency difference between compounds **221a** and **221b**. Comparison of topomer tgTS and hTS CoMFA maps show that the tgTS model is more tolerant to bulk compared to the hTS model, and could explain, in part, the 10-fold tgTS selectivity of **222a** and **222b** over hTS. The tgTS topomer CoMFA model was further validated by docking **222b** in a tgTS homology model and identifying Phe374/Phe520 as residues which could interact with the bulky naphthyl ring of **222b**.
2. **RTKs:** Topomer CoMFA models were developed for a set of 60 RTK inhibitors with either a pyrrolo[2,3-*d*]pyrimidine or a furo[2,3-*d*]pyrimidine scaffold by using their whole-cell inhibitory data against EGFR, VEGFR2 and PDGFR- β . Statistically significant models ($q^2 > 0.3$) were developed for the pyrrolo[2,3-

d]pyrimidine dataset but could not be developed for the furo[2,3-*d*]pyrimidine dataset, possibly due to the low number of furo[2,3-*d*]pyrimidines for which biological data could be obtained. Comparing the topomer CoMFA maps for pyrrolo[2,3-*d*]pyrimidines show differences in the steric and/or electronic requirements among the three RTKs, and could be used, in conjunction with other medicinal chemistry approaches, to modulate the selectivity and/or potency of inhibitors with multiple RTK inhibitory potential.

Drug design efforts that involve virtual library screening using these topomer CoMFA models in conjunction with traditional medicinal chemistry techniques and docking are currently underway.

List of publications resulting from research presented in this manuscript:

- Mitchell-Ryan, S.; Wang, Y.; Raghavan, S.; Ravindra, M. P.; Hales, E.; Orr, S.; Cherian, C.; Hou, Z.; Matherly, L. H.; Gangjee, A. Discovery of 5-Substituted Pyrrolo[2,3-*d*]pyrimidine Antifolates as Dual Acting Inhibitors of Glyciniamide Ribonucleotide Formyltransferase and 5-Amino-4-imidazole Carboxamide Ribonucleotide Formyltransferase and de novo Purine Nucleotide Biosynthesis Inhibitors: Implications of AMPK Activation and Anti-Tumor Activity. **2013**, *In progress*.
- Wang, Y.; Cherian, C.; Orr, S.; Mitchell-Ryan, S.; Hou, Z.; Raghavan, S.; Matherly, L.; Gangjee, A. Tumor-Targeting with Novel Non-Benzoyl 6-Substituted Straight Chain Pyrrolo[2,3-*d*]pyrimidine Antifolates via Cellular Uptake by Folate Receptor α and Inhibition of de novo Purine Nucleotide Biosynthesis. **2013**, *J. Med. Chem.* DOI: 10.1021/jm401139z
- Gangjee, A.; Zhao, Y.; Raghavan, S.; Rohena, C.; Mooberry, S. L.; Hamel, E. Structure-activity relationships and in vitro evaluation of the potent cytotoxic anti-microtubule agent *N*-(4-methoxyphenyl)-*N*-2,6-trimethyl-6,7-dihydro-5*H*-cyclopenta[*d*]pyrimidin-4-aminium chloride and its analogues as antitumor agents. *J. Med. Chem.* **2013**, 56, 6829–6844. DOI: 10.1021/jm400086g.

- Gangjee, A.; Namjoshi, O.; Raghavan, S.; Queener, S. F.; Kisliuk, R. L.; Cody, V. Design, synthesis and molecular modelling of novel pyrido[2,3-*d*]pyrimidine analogs as antifolates: Application of Buchwald-Hartwig aminations of heterocycles. *J. Med. Chem.* **2013**, *56*, 4422–4441. DOI: 10.1021/jm400086g.
- Gangjee, A.; Zaware, N.; Raghavan, S.; Disch, B. C.; Thorpe, J. E.; Bastian, A.; Ihnat, M. A. Synthesis and biological activity of 5-chloro-*N*4-substituted phenyl-9H-pyrimido[4,5-*b*]indole-2,4-diamines as vascular endothelial growth factor receptor-2 inhibitors and antiangiogenic agents. *Bioorg. Med. Chem.* **2013**, *21*, 1857-1864. DOI: 10.1016/j.bmc.2013.01.040
- Gangjee, A.; Zaware, N.; Devambatla, R.; Raghavan, S.; Westbrook, C.; Dybdal-Hargreaves, N. F.; Hamel, E.; Mooberry, S. L. Synthesis of *N*4-(Substituted phenyl)-*N*4-alkyl/desalkyl-9H-pyrimido[4,5-*b*]indole-2,4-diamines and Identification of New Microtubule Disrupting Compounds that are Effective against Multidrug Resistant Cells. *Bioorg. Med. Chem.* **2013**, *21*, 891 – 902. DOI: 10.1016/j.bmc.2012.12.010
- Gangjee, A.; Zaware, N.; Raghavan, S. *N*4-(3-bromophenyl)-7-(substituted benzyl) pyrrolo[2,3-*d*]pyrimidines as Potent Multiple Receptor Tyrosine Kinase Inhibitors: Design, Synthesis, and In vivo Evaluation. *Bioorg. Med. Chem.* **2012**, *20*, 2444-2454. DOI: 10.1016/j.bmc.2012.01.029
- Gangjee, A.; Zaware, N.; Raghavan, S. Single Agents with Designed Combination Chemotherapy Potential: Synthesis and Evaluation of Substituted Pyrimido[4,5-*b*]indoles as Receptor Tyrosine Kinase and Thymidylate Synthase Inhibitors and as Antitumor Agents . *J. Med. Chem.* **2010**, *53*, 1563-1578. DOI: 10.1021/jm9011142
- Gangjee, A.; Zhao, Y.; Raghavan, S.; Ihnat, M. A.; Disch, B. C. Design, Synthesis and Evaluation of 2-Amino-4-m-bromoanilino-6-arylmethyl-7H-pyrrolo[2,3-*d*]pyrimidines as Tyrosine Kinase Inhibitors and Antiangiogenic Agents. *Bioorg. Med. Chem.* **2010**, *18*, 5261-5273. DOI: 10.1016/j.bmc.2010.05.049
- Gangjee, A.; Zhao, Y.; Lin, L.; Raghavan, S.; Mooberry, S. L. Synthesis and Discovery of Water Soluble, Antitumor, Antimitotics that Bind to the Colchicine Site on Tubulin and Circumvent Pgp and β -III Tubulin Tumor Resistance. *J. Med. Chem.*, **2010**, *53*, 8116–8128. DOI: 10.1021/jm101010n

F. EXPERIMENTAL

Melting points were determined on a Mel-Temp II melting point apparatus with FLUKE 51 K/J thermocouple and are uncorrected. Nuclear magnetic resonance spectra for proton (^1H) were recorded on a Bruker 300MHz spectrometer or Bruker 400MHz spectrometer. The chemical shift values were expressed in ppm (parts per million) relative to tetramethylsilane as internal standard; s = singlet, d = double, t = triplet, q = quartet, m = multiplet, br = broad singlet. Nuclear magnetic resonance spectra for carbon (^{13}C NMR) were recorded on a Bruker 400MHz NMR spectrometer. The relative integrals of peak areas agreed with those expected for the assigned structures. High-resolution mass spectra (HRMS) were recorded on a MICROMASS AUTOSPEC (EBE Geometry) double focusing mass spectrometer (Electron Impact – EI) or Waters Q-TOF (quadrupole/time-of-flight tandem instrument) mass spectrometer (Electro-Spray Ionization – ESI). Thin-layer chromatography (TLC) was performed on WHATMAN UV254 silica gel plates with a fluorescent indicator, and the spots were visualized under 254 and/or 365 nm illumination. Proportions of solvents used for TLC were by volume. Column chromatography was performed on 230-400 mesh silica gel purchased from ThermoFisher Scientific. All evaporations were carried out under reduced pressure using a rotary evaporator. Analytical samples were dried under reduced pressure (0.2 mmHg) in an Chem-Dry drying apparatus over P_2O_5 at 50-80 °C. Elemental analysis was performed by Altantic Microlabs, Norcross, GA. Element compositions are within $\pm 0.4\%$ of calculated values. Fractional moles of water or organic solvents frequently found in some analytical samples could not be prevented despite 24-48 h of drying under reduced pressure (0.1 torr) and were confirmed where possible by their presence in the ^1H NMR

spectra. All solvents and chemicals were purchased from Strem Chemicals Inc., Sigma-Aldrich Chemical Co. or Fisher Scientific. All of the chemicals and the solvents were used as received.

Synthesis of 6-((substituted-phenylamino)methyl)pyrido[2,3-*d*]pyrimidine-2,4-diamines

General procedure for synthesis of 170 – 173

Compounds **170 – 173** (Scheme 23) were synthesized using literature methods³³³ from the common synthons **91a** or **92a** and the corresponding anilines. Compounds **91a**³³³ or **92a**²⁸⁴ were synthesized according to literature methods. To a solution of the substituted aniline in 70–80% acetic acid were added **91a** and Raney Ni. The mixture was hydrogenated in a Parr hydrogenation apparatus at atmospheric pressure and room temperature for 6 h. TLC analysis using solvent A (5:1:0.1 CHCl₃:MeOH:NH₄OH) or solvent B (6:1 CHCl₃:MeOH) showed the disappearance of the starting material and the appearance of a product spot along with a spot for the alcohol which resulted from an over-reduction of the nitrile **91a** or aldehyde **92a**. The mixture was treated with Norit® and filtered through Celite®. To the acidic filtrate was added 1–3 g of silica gel, and the solvent was evaporated to afford a silica gel plug. Alternatively, the acidic filtrate was evaporated and the residue dissolved in 50 mL of warm ethanol. The solution was adjusted to pH 8 using 1 N Na₂CO₃ and the resulting crude precipitate filtered. The crude product was stirred in hot methanol and filtered, to the filtrate was added 1–3 g of silica gel, and the solvent was evaporated to afford a silica gel plug. The resulting plug was applied to a 2.2 × 24 cm silica gel column and eluted with solvent C

(6:1:0.1CHCl₃:MeOH;NH₄OH) or solvent D (5:1 CHCl₃:MeOH). Fractions containing pure product (TLC) were pooled and evaporated to afford analytically pure compounds **170–191**.

6-(((2,5-Difluorophenyl)amino)methyl)pyrido[2,3-*d*]pyrimidine-2,4-diamine (170)

Compound **170** was synthesized from intermediate **91a** (0.50 g, 2.64 mmol), 2,5-fluoroaniline (0.68 g, 5.2 mmol), and Raney Ni (2.0 g) in 100 mL of 80% acetic acid for 48 h and purified by column chromatography using solvent D to afford a yellow solid (0.07 g, 9%): mp > 232 °C dec; TLC *R_f* 0.2 in solvent D; ¹H NMR (DMSO-*d*₆) δ 4.38 (d, 2 H, CH₂), 6.26–6.33 (m, 3 H, 2-NH₂ and NH, exch.), 6.58 (m, 2 H, 2',4'-H), 7.26 (t, 1 H 3'-H), 7.49 (br, 2 H, 4-NH₂, exch), 8.49 (s, 1 H, 5-H), 8.58 (d, 1 H, 7-H). HR-MS: C₁₄H₁₂F₂N₆: calcd. mass 302.1092, found mass 302.1091.

6-(((2,4,6-Trichlorophenyl)amino)methyl)pyrido[2,3-*d*]pyrimidine-2,4-diamine (171)

Compound **171** was synthesized from intermediate **91a** (0.25 g, 1.3 mmol), 2,4,6-trichloroaniline (0.52 g, 2.6 mmol), and Raney Ni (1.0 g) in 100 mL of 80% acetic acid for 48 h and purified by column chromatography using solvent D to afford a brown solid (0.02 g, 5%): mp > 240 °C dec; TLC *R_f* 0.2 in solvent D; ¹H NMR (DMSO-*d*₆) δ 4.35 (d, 2 H, CH₂), 6.26–6.33 (m, 3 H, 2-NH₂ and NH, exch.), 7.26 (d, 2 H 3',5'-H), 7.49 (br, 2 H, 4-NH₂, exch), 8.49 (s, 1 H, 5-H), 8.58 (d, 1 H, 7-H). HR-MS: C₁₄H₁₁N₆Cl₃: calcd. mass 368.0111, found mass 368.0106.

6-(((2,3,4-Trichlorophenyl)amino)methyl)pyrido[2,3-*d*]pyrimidine-2,4-diamine (172)

Compound **172** was synthesized from intermediate **91a** (0.25 g, 1.3 mmol), 2,3,4-

trichloroaniline (0.52 g, 2.6 mmol), and Raney Ni (1.0 g) in 100 mL of 80% acetic acid for 48 h and purified by column chromatography using solvent D to afford a brown solid (0.01 g, 3%): mp > 240 °C dec; TLC *R_f* 0.2 in solvent D; ¹H NMR (DMSO-*d*₆) δ 4.38 (d, 2 H, CH₂), 6.33–6.36 (m, 3 H, 2-NH₂ and NH, exch.), 6.41 (d, 1 H 6'-H), 7.09 (d, 1 H 5'-H), 7.46 (br, 2 H, 4-NH₂, exch), 8.49 (s, 1 H, 5-H), 8.56 (d, 1 H, 7-H). HR-MS: C₁₄H₁₁N₆Cl₃: calcd. mass 368.0111, found mass 368.0121.

6-(((2,6-Dichlorophenyl)amino)methyl)pyrido[2,3-*d*]pyrimidine-2,4-diamine (173)

Compound **173** was synthesized from intermediate **91a** (0.25 g, 1.32 mmol), 2,6-dichloroaniline (0.42 g, 2.6 mmol), and Raney Ni (1.0 g) in 100 mL of 80% acetic acid for 48 h and purified by column chromatography using solvent B to afford a yellow solid (0.02 g, 4%): mp > 230 °C dec; TLC *R_f* 0.25 in solvent A; ¹H NMR (DMSO-*d*₆) δ 4.38 (d, 2 H, CH₂), 6.26–6.33 (m, 3 H, 2-NH₂ and NH, exch.), 6.89 (m, 1 H, 2',4'-H), 7.31–7.33 (m, 2 H 3', 5'-H), 7.49 (br, 2 H, 4-NH₂, exch), 8.36 (s, 1 H, 5-H), 8.63 (d, 1 H, 7-H). HR-MS: C₁₄H₁₂N₆Cl₂: calcd. mass 334.0500, found mass 334.0488.

6-(((3,5-Dichlorophenyl)amino)methyl)pyrido[2,3-*d*]pyrimidine-2,4-diamine (174)

Compound **174** was synthesized from intermediate **92a** (0.25 g, 1.32 mmol), 3,5-dichloroaniline (0.44 g, 2.6 mmol), and Raney Ni (1.0 g) in 100 mL of 80% acetic acid for 48 h and purified by column chromatography using solvent B to afford a yellow solid (0.035 g, 7%): mp > 236 °C dec; TLC *R_f* 0.2 in solvent A; ¹H NMR (DMSO-*d*₆) δ 4.37 (d, 2 H, CH₂), 6.26–6.33 (m, 3 H, 2-NH₂ and NH, exch.), 6.89 (m, 1 H, 2',4'-H), 7.28–7.33 (m, 1 H 4'-H), 7.59 (br, 2 H, 4-NH₂, exch), 8.36 (s, 1 H, 5-H), 8.63 (d, 1 H, 7-H). HR-MS: C₁₄H₁₂N₆Cl₂: calcd. mass 334.0500, found mass 334.0512.

6-(((3,4-Dichlorophenyl)amino)methyl)pyrido[2,3-*d*]pyrimidine-2,4-diamine (175)

Compound **175** was synthesized from intermediate **92a** (0.25 g, 1.32 mmol), 3,4-dichloroaniline (0.44 g, 2.6 mmol), and Raney Ni (1.0 g) in 100 mL of 80% acetic acid for 48 h and purified by column chromatography using solvent B to afford a yellow solid (0.03 g, 6%): mp > 235 °C dec; TLC *R_f* 0.23 in solvent A; ¹H NMR (DMSO-*d*₆) δ 4.36 (d, 2 H, CH₂), 6.28–6.31 (m, 3 H, 2-NH₂ and NH, exch.), 6.90 (m, 1 H, 6'-H), 7.28–7.33 (m, 2 H 4', 5'-H), 7.56 (br, 2 H, 4-NH₂, exch), 8.34 (s, 1 H, 5-H), 8.61 (d, 1 H, 7-H). HR-MS: C₁₄H₁₂N₆Cl₂: calcd. mass 334.0500, found mass 334.0502.

6-(((3,4,6-Trichlorophenyl)amino)methyl)pyrido[2,3-*d*]pyrimidine-2,4-diamine (176)

Compound **176** was synthesized from intermediate **92a** (0.25 g, 1.32 mmol), 3,4-dichloroaniline (0.44 g, 2.6 mmol), and Raney Ni (1.0 g) in 100 mL of 80% acetic acid for 48 h and purified by column chromatography using solvent B to afford a brown solid (0.03 g, 6%): mp > 265 °C dec; TLC *R_f* 0.23 in solvent A; ¹H NMR (DMSO-*d*₆) δ 4.26 (d, 2 H, CH₂), 6.31 (br, 2 H, 2-NH₂, exch.), 6.78 – 6.83 (m, 2 H, 6'-H, NH exch.), 7.47 (s, 1 H 5'-H), 7.56 (br, 2 H, 4-NH₂, exch), 8.30 (s, 1 H, 5-H), 8.58 (d, 1 H, 7-H). HR-MS: C₁₄H₁₁N₆Cl₃: calcd. mass 368.0111, found mass 368.0116.

6-(((2,4,5-Trichlorophenyl)amino)methyl)pyrido[2,3-*d*]pyrimidine-2,4-diamine (177)

Compound **177** was synthesized from intermediate **92a** (0.25 g, 1.32 mmol), 3,4-dichloroaniline (0.44 g, 2.6 mmol), and Raney Ni (1.0 g) in 100 mL of 80% acetic acid for 48 h and purified by column chromatography using solvent B

to afford a brown solid (0.03 g, 6%): mp > 265 °C dec; TLC *R_f* 0.23 in solvent A; ¹H NMR (DMSO-*d*₆) δ 4.26 (d, 2 H, CH₂), 6.31 (br, 2 H, 2-NH₂, exch.), 6.78 – 6.83 (m, 2 H, 6'-H, NH exch.), 7.47 (s, 1 H 5'-H), 7.56 (br, 2 H, 4-NH₂, exch), 8.30 (s, 1 H, 5-H), 8.58 (d, 1 H, 7-H). HR-MS: C₁₄H₁₁N₆Cl₃: calcd. mass 368.0111, found mass 368.0112.

6-(((2,3-Dichlorophenyl)amino)methyl)pyrido[2,3-*d*]pyrimidine-2,4-diamine (178)

Compound **178** was synthesized from intermediate **92a** (0.25 g, 1.32 mmol), 3,4-dichloroaniline (0.44 g, 2.6 mmol), and Raney Ni (1.0 g) in 100 mL of 80% acetic acid for 48 h and purified by column chromatography using solvent A to afford a yellow solid (0.03 g, 6%): mp > 233 °C dec; TLC *R_f* 0.23 in solvent D; ¹H NMR (DMSO-*d*₆) δ 4.36 (d, 2 H, CH₂), 6.28–6.31 (m, 3 H, 2-NH₂ and NH, exch.), 6.90 (m, 1 H, 6'-H), 7.28–7.33 (m, 2 H 4', 5'-H), 7.56 (br, 2 H, 4-NH₂, exch), 8.34 (s, 1 H, 5-H), 8.61 (d, 1 H, 7-H). HR-MS: C₁₄H₁₂N₆Cl₂: calcd. mass 334.0500, found mass 334.0505.

6-(((2,5-Dibromophenyl)amino)methyl)pyrido[2,3-*d*]pyrimidine-2,4-diamine (179)

Compound **179** was synthesized from intermediate **92a** (0.25 g, 1.32 mmol), 3,4-dichloroaniline (0.44 g, 2.6 mmol), and Raney Ni (1.0 g) in 100 mL of 80% acetic acid for 48 h and purified by column chromatography using solvent A to afford a yellow solid (0.03 g, 6%): mp > 233 °C dec; TLC *R_f* 0.23 in solvent D; ¹H NMR (DMSO-*d*₆) δ 4.37 (d, 2 H, CH₂), 6.26–6.33 (m, 3 H, 2-NH₂ and NH, exch), 6.56 (m, 2 H, 2',4'-H), 7.24 (t, 1 H 3'-H), 7.49 (br, 2 H, 4-NH₂, exch), 8.49 (s, 1 H, 5-H), 8.58 (d, 1 H, 7-H). HR-MS: C₁₄H₁₂N₆Br₂: calcd. mass 421.9490, found mass 421.9501.

6-(((2,6-dinitrophenyl)amino)methyl)pyrido[2,3-*d*]pyrimidine-2,4-diamine (**180**)

Compound **180** was synthesized from intermediate **92a** (0.25 g, 1.32 mmol), 3,4-dichloroaniline (0.44 g, 2.6 mmol), and Raney Ni (1.0 g) in 100 mL of 80% acetic acid for 48 h and purified by column chromatography using solvent A to afford a yellow solid (0.03 g, 6%): mp > 233 °C dec; TLC *R_f* 0.23 in solvent D; ¹H NMR (DMSO-*d*₆) δ 4.37 (d, 2 H, CH₂), 6.26–6.33 (m, 3 H, 2-NH₂ and NH, exch), 6.56 (m, 2 H, 2',4'-H), 7.24 (t, 1 H 3'-H), 7.49 (br, 2 H, 4-NH₂, exch), 8.49 (s, 1 H, 5-H), 8.58 (d, 1 H, 7-H). HR-MS: C₁₄H₁₂N₆O₄ calcd. mass 356.0982, found mass 356.0969.

General procedure for bulk synthesis of **170**

A mixture of intermediate **92a** (0.50 g, 2.64 mmol) and 2,5-fluoroaniline (0.68 g, 5.2 mmol) in 20 mL of 80% acetic acid was stirred for 12 h in presence of activated 4 Å molecular sieves. Sodium triacetoxyborohydride (1.68 g, 7.93 mmol) was added in divided portions to the mixture, with the first half being added at 12 h and the other at 24 h after initiation of the reaction. The reaction was monitored by TLC (5:1 CHCl₃:MeOH). At the end of the reaction, the solution was filtered by filter paper to remove the molecular sieves and concentrated in vacuo. To the concentrated acidified solution was added silica gel (1 – 3 g) and a plug was formed by evaporation. The resulting plug was applied to a 2.2 × 24 cm silica gel column and eluted with solvent C (6:1:0.1 CHCl₃:MeOH;NH₄OH). Fractions containing pure product (TLC) were pooled and evaporated to afford analytically pure **170** as yellow solid (0.13 g, 14%): mp > 232 °C dec; TLC *R_f* 0.2 in solvent D; ¹H NMR (DMSO-*d*₆) δ 4.38 (d, 2 H, CH₂), 6.26–6.33 (m, 3 H, 2-NH₂ and NH, exch.), 6.58 (m, 2 H, 2',4'-H), 7.26 (t, 1 H 3'-H), 7.49 (br, 2 H, 4-NH₂, exch), 8.49

(s, 1 H, 5-H), 8.58 (d, 1 H, 7-H).

General procedure for the synthesis of compounds 186-191.

Compounds **186** – **191** were synthesized from intermediate **94a**. Intermediate **94a** was synthesized from **91a** using literature methods.³⁴⁴ To a cooled solution (0–5 °C) of the appropriate arylthiol dissolved in *N,N*-dimethyl acetamide or *N,N*-dimethyl formamide was added sodium hydride, triethyl amine or potassium carbonate. The solution was stirred under nitrogen for 15 min before intermediate **94a** was added. The reaction was allowed to warm to room temperature and stirred for 24 h under nitrogen. The desired product precipitated out of solution. The yellow solid was filtered and washed with water, ethanol and ether. Thin layer chromatographic analyses were performed in two solvent systems using solvent A (5:1:0.1 CHCl₃:MeOH:NH₄OH) or solvent B (6:1 CHCl₃:MeOH). The crude precipitate was re-dissolved in warm *N,N*-dimethylformamide and 1 g of silica gel added to this solution and the solvent was evaporated to afford a plug of silica gel for column chromatographic purification. The crude product silica gel plug was loaded onto a silica gel column and eluted with solvent D (5:1 CHCl₃:MeOH). Fractions shown by thin layer chromatography to contain pure product were pooled and evaporated to afford a light yellow solid. The solid was washed with water, ethanol and ether. All solids were dried in vacuum with the aid of phosphorous pentoxide.

6-(((2,5-dichlorophenyl)thio)methyl)pyrido[2,3-*d*]pyrimidine-2,4-diamine (186)

Compound **186** was synthesized from intermediate **94a** (0.25 g, 1 mmol) and 2,5-dichlorobenzenethiol (0.21 g, 1.2 mmol) using NaH (0.035 g, 1.5 mmol) as the base in 10 mL of *N,N*-dimethyl formamide as the solvent using the general method described above and purified by column chromatography using solvent D. Compound **186** was obtained as

a yellow solid (0.03 g, 10%): mp > 243 °C dec; TLC *R_f* 0.56 in solvent A; ¹H NMR (DMSO-*d*₆) δ 4.39 (s, 2 H, CH₂), 6.68 (s, 2 H, 2-NH₂ exch.), 6.56 (m, 2 H, 2',4'-H), 7.24-7.49 (m, 3 H 3',4',5'-H), 7.84 (br, 2 H, 4-NH₂, exch), 8.49 (s, 1 H, 5-H), 8.68 (d, 1 H, 7-H). HR-MS: C₁₄H₁₁Cl₂N₅S: calcd. mass 351.0112, found mass 351.0108.

6-(((3,4,5-trichlorophenyl)thio)methyl)pyrido[2,3-*d*]pyrimidine-2,4-diamine (187)

Compound **187** was synthesized from intermediate **94a** (0.25 g, 1 mmol) and 3,4,5-trichlorobenzenethiol (0.25 g, 1.2 mmol) using NaH (0.035 g, 1.5 mmol) as the base in 10 mL of *N,N*-dimethyl formamide as the solvent using the general method described above and purified by column chromatography using solvent D. Compound **187** was obtained as a yellow solid (0.03 g, 10%): mp > 246 °C dec; TLC *R_f* 0.59 in solvent A; ¹H NMR (DMSO-*d*₆) δ 4.22 (d, 2 H, CH₂), 6.31 (br, 2 H, 2-NH₂ exch.), 6.78-6.82 (m, 2 H, 2',6'-H), 7.49 (br, 2 H 4-NH₂ exch.), 8.30 (d, 1 H, 5-H), 8.58 (d, 1 H, 7-H) HR-MS: C₁₄H₁₀Cl₃N₅S: calcd. mass 384.9722, found mass 384.9716.

6-(((2,5-difluorophenyl)thio)methyl)pyrido[2,3-*d*]pyrimidine-2,4-diamine (188)

Compound **188** was synthesized from intermediate **94a** (0.25 g, 1 mmol) and 2,5-difluorobenzenethiol (0.15 g, 1.2 mmol) using NaH (0.035 g, 1.5 mmol) as the base in 10 mL of *N,N*-dimethyl formamide as the solvent using the general method described above and purified by column chromatography using solvent D. Compound **188** was obtained as a yellow solid (0.03 g, 10%): mp > 240°C dec; TLC *R_f* 0.23 in solvent D; ¹H NMR (DMSO-*d*₆) δ 4.37 (d, 2 H, CH₂), 6.28 (br, 2 H, 2-NH₂ exch.), 6.56 (m, 2 H, 2',4'-H), 7.24 (t, 1 H 3'-H), 7.49 (br, 2 H, 4-NH₂, exch), 8.49 (s, 1 H, 5-H), 8.58 (d, 1 H, 7-H). HR-MS:

C₁₄H₁₁F₂N₅S: calcd. mass 319.0703, found mass 319.0711.

6-((2,5-dichlorophenoxy)methyl)pyrido[2,3-*d*]pyrimidine-2,4-diamine (**189**)

Compound **189** was synthesized from intermediate **94a** (0.25 g, 1 mmol) and 2,5-dichlorophenol (0.25 g, 1.2 mmol) using K₂CO₃ (0.2 g, 1.5 mmol) as the base in 10 mL of *N,N*-dimethyl formamide as the solvent using the general method described above and purified by column chromatography using solvent D. Compound **189** was obtained as a light yellow solid (0.026 g, 8%): mp > 230 °C dec; TLC *R_f* 0.23 in solvent D; ¹H NMR (DMSO-*d*₆) δ 4.37 (d, 2 H, CH₂), 6.26 (br, 2 H, 2-NH₂ exch), 6.56 (m, 2 H, 2',4'-H), 7.24 (t, 1 H 3'-H), 7.49 (br, 2 H, 4-NH₂, exch), 8.49 (s, 1 H, 5-H), 8.58 (d, 1 H, 7-H). HR-MS: C₁₄H₁₁Cl₂N₅O: calcd. mass 335.0341, found mass 335.0344.

6-((3,4,5-trichlorophenoxy)methyl)pyrido[2,3-*d*]pyrimidine-2,4-diamine (**190**)

Compound **190** was synthesized from intermediate **94a** (0.25 g, 1 mmol) and 3,4,5-trichlorophenol (0.23 g, 1.2 mmol) using NaH (0.035 g, 1.5 mmol) as the base in 10 mL of *N,N*-dimethyl formamide as the solvent using the general method described above and purified by column chromatography using solvent D. Compound **190** was obtained as a yellow solid (0.038 g, 11%): mp > 236 °C dec; TLC *R_f* 0.23 in solvent D; ¹H NMR (DMSO-*d*₆) δ 4.23 (d, 2 H, CH₂), 6.34 (br, 2 H, 2-NH₂ exch.), 6.78-6.83 (m, 2 H, 2',6'-H), 7.50 (br, 2 H 4-NH₂ exch.), 8.31 (d, 1 H, 5-H), 8.58 (d, 1 H, 7-H) HR-MS: C₁₄H₁₀Cl₃N₅O: calcd. mass 368.9951, found mass 368.9960.

General Procedure for the Synthesis of **228a,b**

Compounds **228a,b** were synthesized using reported literature methods.³⁸⁷ A solution of substituted phenyl acetic acids (5 mmol) in 5 mL of dry toluene and 5 mL of

thionyl chloride was heated at reflux for 1 h and the colorless solution was evaporated in vacuo. The resulting acid chloride was dissolved in 10 mL of ether and added dropwise with stirring to 30 mL of ethereal diazomethane (about 13 mmol, made from 20 mmol of *N*-nitroso-*N*-methyl urea)⁴⁶¹ at 0–5 °C. The yellow solution was allowed to stand at room temperature for 1 h, then 5 mL of 47.5% aqueous HBr was added drop wise to the solution and the yellow mixture was heated at 70–80 °C (oil bath) for 1 h. The reaction was cooled to room temperature and the ether layer was separated, washed with water (10 mL), saturated NaHCO₃ aqueous solution (10 mL) and water (10 mL) and dried (anhydrous Na₂SO₄). The solution was evaporated to afford the α -bromomethyl benzyl ketones **226a-b** which were used in the next step without further purification.

The α -bromomethyl benzyl ketones **226a-b** was placed in a 50-mL flask with an equivalent amount of 2,6-diaminopyrimidin-4-one **227** and 5 mL dry DMF was added to form a clear solution. The mixture was stirred at room temperature for 3 days. After 1 day the reaction mixture darkened and at the third day of the reaction, a solid could be precipitated out in some cases. To the reaction mixture was added 1 g of silica gel and the solvent was evaporated in vacuo to afford a dry plug. This plug was placed on the top of 45×150 mm silica gel column and eluted with CHCl₃/MeOH (gradient elution, 2% MeOH in CHCl₃, and 5% MeOH in CHCl₃). Fractions containing the product (TLC) were pooled and evaporated to afford the pure 2-amino-4-oxo-6-substituted benzyl pyrrolo[2,3-*d*]pyrimidines **228a-b**.

2-Amino-4-oxo-6-(2-methylbenzyl)-pyrrolo[2,3-*d*]pyrimidine 228a

1-bromo-3-(2-methylphenyl)-acetone **226a** was obtained from 2-methylphenylacetic acid (0.75 g, 5 mmol) using the general procedure described above as

a yellow oil (0.64 g, 56%). Rf : 0.55 (Hexane/EtOAc, 3:1). ¹H NMR (CDCl₃): δ 2.25 (s, 3H, CH₃), 3.85 (s, 2H, CH₂), 3.95 (s, 2H, CH₂), 7.10–7.22 (m, 4H, Ph–H).

Using the general procedure described above, compound **226a** (1 g, 4.2 mmol) reacted with an equivalent amount of 2,6-diaminopyrimidin-4-one **227** to afford compound **228a** (400 mg, 51%) as a yellow solid. Mp: 287 °C. (Lit.³⁸⁷ 290 °C) TLC Rf 0.56 (CHCl₃/CH₃OH, 5:1). ¹H NMR (DMSO-*d*₆): δ 2.32 (s, 3H, CH₃), 3.90 (s, 2H, CH₂), 5.85 (s, 1H, C5-CH), 6.03 (s, 2H, NH₂, exch.), 7.14–7.28 (m, 4H, Ar–H), 10.10 (s, 1H, NH, exch.), 10.94 (s, 1H, NH).

2-Amino-4-oxo-6-(2,4-dichlorobenzyl)-pyrrolo[2,3-*d*]pyrimidine 228b

1-bromo-3-(2,4-dichlorophenyl)-acetone **226b** was obtained from 2,4-dichlorophenylacetic acid (1.02 g, 5 mmol), using the general procedure described above as a white solid (0.68 g, 50%). Mp: 71–73 °C. (Lit.³⁸⁷ 70 – 73 °C). TLC Rf 0.60 (Hexane/EtOAc, 3:1). ¹H NMR (CDCl₃): δ 3.95 (s, 2H, CH₂), 4.05 (s, 2H, CH₂), 7.20–7.45 (m, 3H, Ar–H).

Using the general procedure described above, compound **226b** (700 mg, 2.5 mmol) was reacted with an equivalent amount of 2,6-diaminopyrimidin-4-one **227** to afford the compound **228b** (430 mg, 43%) as a yellow solid. Mp: 265 °C. TLC Rf 0.51 (CHCl₃/CH₃OH, 5:1). ¹H NMR (DMSO-*d*₆): δ 3.94 (s, 2H, CH₂), 5.85 (s, 1H, C5-CH), 7.25–7.60 (m, 3H, Ar–H), 8.24 (s, br., 2H, NH₂, exch.), 10.60 (s, 1H, NH, exch.), 11.20 (s, 1H, NH, exch.).

General procedure for the synthesis of compounds 230a-b

2-Amino-4-oxo-6-substitued-pyrrolo[2,3-*d*]pyrimidines **228a** or **228b** (about 1 mmol), 5 mL of POCl₃ and 0.1 mL of PhNMe₂ were placed in a 50-mL round-bottom flask. The mixture was heated to reflux and kept stirring for 4 h. After evaporation of the excess of POCl₃, crushed ice was added to the mixture. The reaction mixture was neutralized with NH₃·H₂O (pH 7, tested with a pH paper), and extracted with CHCl₃ (3×50 mL). The organic phase was combined and dried with Na₂SO₄. Concentration of the chloroform layer afforded a brown solid that was re-dissolved in chloroform (2–3 mL) and was placed to the top of a 15×150 mm column and eluted with 0.1% methanol in chloroform. Alternatively, a silica gel plug was formed using around 500mg of silica gel and was placed on top of the column for chromatography. Fractions containing the product were pooled and evaporated to afford pure 2-amino-4-chloro-6-substitued-pyrrolo[2,3-*d*]pyrimidine **230a-b**.

2-Amino-4-chloro-6-(2-methylbenzyl)-pyrrolo[2,3-*d*]pyrimidine 230a

Compound **230a** was synthesized from 2-amino-4-oxo-6-(2-methylbenzyl)-pyrrolo[2,3-*d*]pyrimidine **228a** (200 mg, 0.78 mmol) using the general procedure described above to afford **230a** 64 mg (29%) as a light yellow solid. Mp: 250-252 °C (Lit.³⁸⁷ 250 °C).

TLC *R_f* 0.53 (CHCl₃/CH₃OH, 10:1). ¹H NMR (DMSO-*d*₆): δ 3.91 (s, 2H, CH₂), 5.69 (s, 1H, C5-CH), 6.42 (s, 2H, NH₂), 7.13–7.16 (m, 4H, Ar-H), 11.46 (s, 1H, NH).

2-Amino-4-chloro-6-(2,4-dichlorobenzyl)-pyrrolo[2,3-*d*]pyrimidine 35b

Compound **230b** was synthesized from 2-amino-4-oxo-6-(2,4-dichlorobenzyl)-pyrrolo[2,3-*d*]pyrimidine **228b** (300 mg, 0.97 mmol) using the general procedure

described above to afford 107 mg (32%) of **230b** as a light yellow solid. Mp: >250 °C (Lit.³⁸⁷ >255 °C) . TLC *R_f* 0.5 (CHCl₃/CH₃OH, 10:1). ¹H NMR (DMSO-*d*₆): δ 4.17 (s, 2H, CH₂), 5.82 (s, 1H, C5-CH), 6.48 (s, 2H, NH₂), 7.33–7.66 (m, 3H, Ar–H), 11.53 (s, 1H, NH).

General method for synthesis of 197-200, 205-210

Compounds **197-200**, **205-210** were synthesized from the nucleophilic displacement of the 4-chloro moiety of intermediates **230a-b**. Intermediates **230a-b** were synthesized using literature methods.⁴⁶² To a cooled solution (0–5 °C) of 3-bromobenzenethiol, 3-bromophenol, (3-bromophenyl)methanethiol, (3-bromophenyl)methanol or (3-bromophenyl)methanamine in *i*PrOH or *n*BuOH was added 2 eq. of base (sodium hydride, triethyl amine or potassium carbonate). The solution was stirred under nitrogen for 30 min before intermediate **230a** or **230b** was added. The reaction was allowed to warm to room temperature and stirred for 24 h under nitrogen. To the solution was added 1-3 g of silica gel was added to the mixture concentrated in vacuo to afford a plug of silica gel for column chromatographic purification. Thin layer chromatographic analyses were performed in two solvent systems using solvent A (5:1:0.1 CHCl₃:MeOH:NH₄OH) or solvent B (10:1 CHCl₃:MeOH). The crude product silica gel plug was loaded onto a silica gel column and eluted with solvent D (5:1 CHCl₃:MeOH). Fractions shown by thin layer chromatography to contain pure product were pooled and evaporated to afford a solid. The solid was washed with water, ethanol and ether. All solids were dried in vacuum with the aid of phosphorous pentoxide.

**4-((3-bromophenyl)thio)-6-(2-methylbenzyl)-7*H*-pyrrolo[2,3-*d*]pyrimidin-2-amine
(197)**

Compound **197** was synthesized from intermediate **230a** (0.2 g, 0.75 mmol) and 3-bromobenzenethiol (0.27 g, 1.5 mmol) using K₂CO₃ (0.2 g, 1.5 mmol) as the base in 10 mL of *i*PrOH as the solvent using the general method described above and purified by column chromatography using solvent D. Compound **189** was obtained (11 mg, 18%) as an off white solid. Mp: 241–243 °C. TLC R_f 0.49 (CHCl₃/CH₃OH, 10:1). ¹H NMR (DMSO-*d*₆): δ 2.27 (s, 3H, CH₃), 3.89 (s, 2H, CH₂), 4.36 (s, 2H, CH₂) 5.72 (s, 2H, NH₂ exch.), 5.98 (s, 1H, C5-CH), 7.04–7.20 (m, 6H, Ar-H), 7.99–8.09 (m, 2H, Ar-H), 8.88 (s, 1H, NH, exch.), 10.91 (s, 1H, NH, exch.) Anal. (C₂₀H₁₇N₄BrS): Cal. C: 56.48, H: 4.03, N: 13.17. Found C: 56.45, H: 3.98, N: 13.13.

**((3-bromophenyl)thio)-6-(2,4-dichlorobenzyl)-7*H*-pyrrolo[2,3-*d*]pyrimidin-2-amine
(198)**

Compound **198** was synthesized from intermediate **230b** (0.2 g, 0.75 mmol) and 3-bromobenzenethiol (0.27 g, 1.5 mmol) using K₂CO₃ (0.2 g, 1.5 mmol) as the base in 10 mL of *i*PrOH as the solvent using the general method described above and purified by column chromatography using solvent D. Compound **198** was obtained (11 mg, 18%) as an off white solid. Mp: 237–239 °C. TLC R_f 0.49 (CHCl₃/CH₃OH, 10:1). ¹H NMR (DMSO-*d*₆): δ 2.27 (s, 3H, CH₃), 3.89 (s, 2H, CH₂), 5.73 (s, 2H, NH₂), 5.98 (s, 1H, C5-CH), 7.04–7.20 (m, 6H, Ar-H), 7.99–8.09 (m, 2H, Ar-H), 8.87 (s, 1H, NH), 10.91 (s, 1H, NH). Anal. (C₂₀H₁₇N₄BrS): Cal. C: 56.48, H: 4.03, N: 13.17. Found C: 56.45, H: 3.98, N: 13.13.

**4-((3-bromobenzyl)thio)-6-(2-methylbenzyl)-7*H*-pyrrolo[2,3-*d*]pyrimidin-2-amine
(199)**

Compound **199** was synthesized from intermediate **230a** (0.2 g, 0.75 mmol) and 3-bromobenzenethiol (0.29 g, 1.5 mmol) using *t*BuOK (0.16 g, 1.5 mmol) as the base in 10 mL of *i*PrOH as the solvent using the general method described above and purified by column chromatography using solvent D. Compound **189** was obtained (62 mg, 24%) as an off white solid. Mp: 226–228 °C. TLC R_f 0.52 (CHCl₃/CH₃OH, 10:1). ¹H NMR (DMSO-*d*₆): δ 2.29 (s, 3H, CH₃), 3.85 (s, 2H, CH₂), 5.72 (s, 2H, NH₂), 5.91 (s, 1H, C5-CH), 7.08–7.35 (m, 6H, Ar-H), 7.94–8.03 (m, 2H, Ar-H), 10.93 (s, 1H, NH). Anal. (C₂₁H₁₉N₄BrS): Cal. C: 57.41, H: 4.03, N: 12.75. Found C: 57.45, H: 4.28, N: 12.71.

**4-((3-bromobenzyl)thio)-6-(2,4-dichlorobenzyl)-7*H*-pyrrolo[2,3-*d*]pyrimidin-2-amine
(200)**

Compound **200** was synthesized from intermediate **230b** (0.2 g, 0.6 mmol) and 3-bromobenzenethiol (0.25 g, 1.2 mmol) using *t*BuOK (0.14 g, 1.2 mmol) as the base in 10 mL of *n*BuOH as the solvent using the general method described above and purified by column chromatography using solvent D. Compound **189** was obtained (44 mg, 15%) as an off white solid. Mp: 231–233 °C. TLC R_f 0.52 (CHCl₃/CH₃OH, 10:1). ¹H NMR (DMSO-*d*₆): δ 3.96 (s, 2H, CH₂), 5.91 (s, 2H, NH₂ exch), 6.04 (s, 1H, C5-CH), 7.08–7.45 (m, 5H, Ar-H), 7.91–8.02 (m, 2H, Ar-H), 11.03 (s, 1H, NH). Anal. (C₂₀H₁₅N₄Cl₂BrS 0.35H₂O): Cal. C: 48.60, H: 3.06, N: 11.34. Found C: 47.88, H: 3.04, N: 11.12.

4-(3-bromophenoxy)-6-(2-methylbenzyl)-7H-pyrrolo[2,3-*d*]pyrimidin-2-amine (205)

Compound **205** was synthesized from intermediate **230a** (0.2 g, 0.75 mmol) and 3-3-bromophenol (0.17 g, 1.5 mmol) using K₂CO₃ (0.16 g, 1.5 mmol) as the base in 10 mL of *i*PrOH as the solvent using the general method described above and purified by column chromatography using solvent D. Compound **205** was obtained (66 mg, 22%) as an off white solid. Mp: > 239 °C dec. TLC R_f 0.49 (CHCl₃/CH₃OH, 10:1). ¹H NMR (DMSO-*d*₆): ¹H NMR (DMSO-*d*₆): δ 2.26 (s, 3H, CH₃), 3.84 (s, 2H, CH₂), 5.72 (s, 2H, NH₂), 5.99 (s, 1H, C5-CH), 6.85–7.14 (m, 6H, Ar-H), 7.94–8.03 (m, 2H, Ar-H), 10.93 (s, 1H, NH). Anal. (C₂₀H₁₇N₄BrO): Cal. C: 58.69, H: 4.19, N: 13.69. Found C: 58.88, H: 4.03, N: 13.55.

4-(3-bromophenoxy)-6-(2,4-dichlorobenzyl)-7H-pyrrolo[2,3-*d*]pyrimidin-2-amine (206)

Compound **206** was synthesized from intermediate **230b** (0.2 g, 0.75 mmol) and 3-3-bromophenol (0.21 g, 1.5 mmol) using K₂CO₃ (0.14 g, 1.5 mmol) as the base in 10 mL of *n*BuOH as the solvent using the general method described above and purified by column chromatography using solvent D. Compound **205** was obtained (66 mg, 22%) as an off white solid. Mp: > 240 °C dec. TLC R_f 0.49 (CHCl₃/CH₃OH, 10:1). ¹H NMR (DMSO-*d*₆): δ 4.00 (s, 2H, CH₂), 5.84 (s, 2H, NH₂ exch.), 6.02 (s, 1H, C5-CH), 7.09–7.63 (m, 5H, Ar-H), 8.04–8.22 (m, 2H, Ar-H), 10.99 (s, 1H, NH exch.). Anal. (C₁₉H₁₃N₄BrCl₂O 0.15H₂O): Cal. C: 49.17, H: 2.82, N: 12.07. Found C: 48.67, H: 2.63, N: 11.76.

**4-((3-bromobenzyl)oxy)-6-(2-methylbenzyl)-7*H*-pyrrolo[2,3-*d*]pyrimidin-2-amine
(207)**

Compound **207** was synthesized from intermediate **230a** (0.2 g, 0.75 mmol) and 3-3-(3-bromophenyl)methanol (0.27 g, 1.5 mmol) using *t*BuOK (0.16 g, 1.5 mmol) as the base in 10 mL of *n*BuOH as the solvent using the general method described above and purified by column chromatography using solvent D. Compound **207** was obtained (32 mg, 11%) as an off white solid. Mp: 228–231 °C. TLC R_f 0.49 (CHCl₃/CH₃OH, 10:1). ¹H NMR (DMSO-*d*₆): δ 2.35 (s, 3H, CH₃), 3.88 (s, 2H, CH₂), 4.42 (s, 2H, CH₂) 5.74 (s, 2H, NH₂ exch.), 6.01 (s, 1H, C5-CH), 7.05–7.43 (m, 6H, Ar-H), 8.00–8.10 (m, 2H, Ar-H), 8.91 (s, 1H, NH, exch.), 10.94 (s, 1H, NH, exch.) Anal. (C₂₁H₁₉N₄BrO 0.35MeOH): Cal. C: 59.58, H: 4.52, N: 13.24. Found C: 58.77, H: 6.64, N: 12.76.

**4-((3-bromobenzyl)oxy)-6-(2,4-dichlorobenzyl)-7*H*-pyrrolo[2,3-*d*]pyrimidin-2-amine
(208)**

Compound **208** was synthesized from intermediate **230b** (0.2 g, 0.61 mmol) and 3-3-(3-bromophenyl)methanol (0.23 g, 1.2 mmol) using *t*BuOK (0.14 g, 1.2 mmol) as the base in 10 mL of *n*BuOH as the solvent using the general method described above and purified by column chromatography using solvent D. Compound **207** was obtained (32 mg, 11%) as an off white solid. Mp: 240–242 °C. TLC R_f 0.49 (CHCl₃/CH₃OH, 10:1). ¹H NMR (DMSO-*d*₆): δ 4.02 (s, 2H, CH₂), 4.59 (s, 2H, CH₂) 5.76 (s, 2H, NH₂ exch.), 6.02 (s, 1H, C5-CH), 7.12–7.78 (m, 5H, Ar-H), 7.98–8.06 (m, 2H, Ar-H), 10.98 (s, 1H, NH, exch.) Anal. (C₂₀H₁₅N₄BrCl₂O 0.05H₂O): Cal. C: 50.24, H: 3.16, N: 11.72. Found C: 50.11, H: 3.02, N: 11.34.

***N*4-(3-bromobenzyl)-6-(2-methylbenzyl)-7*H*-pyrrolo[2,3-*d*]pyrimidine-2,4-diamine (209)**

Compound **209** was synthesized from intermediate **230a** (0.2 g, 0.75 mmol) and (3-bromophenyl)methanamine (0.27 g, 1.5 mmol) using *t*BuOK (0.16 g, 1.5 mmol) as the base in 10 mL of *n*BuOH as the solvent using the general method described above and purified by column chromatography using solvent D. Compound **209** was obtained (23 mg, 8%) as an off white solid. Mp: 218–221 °C. TLC R_f 0.49 (CHCl₃/CH₃OH, 10:1). ¹H NMR (DMSO-*d*₆): δ 2.27 (s, 3H, CH₃), 3.89 (s, 2H, CH₂), 4.36 (s, 2H, CH₂) 5.72 (s, 2H, NH₂ exch.), 5.98 (s, 1H, C5-CH), 7.04–7.20 (m, 6H, Ar-H), 7.99–8.09 (m, 2H, Ar-H), 8.88 (s, 1H, NH, exch.), 10.91 (s, 1H, NH, exch.) HRMS (C₂₁H₂₀N₅Br 0.35MeOH): calcd. mass 421.0902, found mass 421.0960.

***N*4-(3-bromobenzyl)-6-(2,4-dichlorobenzyl)-7*H*-pyrrolo[2,3-*d*]pyrimidine-2,4-diamine (210)**

Compound **209** was synthesized from intermediate **230b** (0.2 g, 0.6 mmol) and (3-bromophenyl)methanamine (0.22 g, 1.2 mmol) using *t*BuOK (0.14 g, 1.2 mmol) as the base in 10 mL of *n*BuOH as the solvent using the general method described above and purified by column chromatography using solvent D. Compound **209** was obtained (40 mg, 13%) as an off white solid. Mp: 224–227 °C. TLC R_f 0.49 (CHCl₃/CH₃OH, 10:1). ¹H NMR (DMSO-*d*₆): δ 4.01 (s, 2H, CH₂), 4.62 (s, 2H, CH₂) 5.81 (s, 2H, NH₂ exch.), 6.04 (s, 1H, C5-CH), 7.05–7.64 (m, 5H, Ar-H), 8.00–8.09 (m, 2H, Ar-H), 8.91 (s, 1H, NH, exch), 10.98 (s, 1H, NH, exch.). HRMS (C₂₁H₂₀N₅Br 0.35MeOH): calcd. mass 474.1870, found mass 474.1902.

2-Amino-6-methyl-3,4-dihydro-4-oxo-7H-pyrrolo[2,3-*d*]pyrimidine (**140a**).

Compound **140a** was synthesized using literature methods.³¹² A suspension of 2,6-diamino-4-hydroxypyrimidine (1.26 g, 10 mmol) in 25 mL of water containing sodium acetate (0.82 g, 10 mmol) was heated to 100 °C until it formed a clear solution. Chloroacetone (0.79 mL, 10 mmol) was added to this solution in one lot, following which a precipitate began to form within 10 min. The reaction mixture was heated with stirring at 100 °C for an additional 4 h, cooled to 0 °C, and filtered to afford 1.05 g (63%) of **140a** as a slight pink colored solid: mp > 260 °C (lit.³¹² > 260 °C); TLC R_f 0.37 (CHCl₃/MeOH, 4:1); ¹H NMR (DMSO-*d*₆) δ 2.14 (s, 3H, 6-CH₃), 5.83 (s, 1H, 5-CH), 5.98 (bs, 2H, 2-NH₂), 10.15 (bs, 1H, 7-NH), 10.78 (bs, 1H, 3-NH).

3,4,5-Trimethoxybenzenethiol (**236**).

Compound **236** was synthesized from xanthate **238** using literature methods.⁴⁴⁹ Xanthate **238** was synthesized from 3,4,5-trimethoxyaniline **237**. Aniline **237** (0.97 g, 5.44 mmol) was dissolved in MeOH (10 mL) and 10% aqueous HCl and was then cooled to 0 °C. A solution of sodium nitrite (0.5 g, 7.25 mmol) in H₂O (20 mL) was added dropwise over 1 h. The reaction mixture was stirred at 0 °C for an additional 15 min at which time the solution was added to a solution of potassium ethyl xanthate (1.73 g, 10.8 mmol) in H₂O (50 mL) at 65 °C. After the mixture was stirred for 15 min, the reaction was cooled to 25 °C. The resulting mixture was extracted with EtOAc (3 \times 20 mL) and the combined organic extracts were washed with brine (20 mL), dried (Na₂SO₄), and concentrated in vacuo. Flash column chromatography of the residue (silica gel, 10% EtOAc in hexanes) afforded xanthate **238** (0.72 g, 51%). R_f 0.36 (EtOAc: hexanes 1:5);

^1H NMR (CDCl_3) δ 6.72 (s, 2 H, ArH), 4.60 (q, 2 H, OCH_2), 3.86 (s, 3 H, OCH_3), 3.84 (s, 6 H, OCH_3), 1.33 (t, 3 H, CH_3)

A solution of xanthate **238** (0.7 g, 2.43 mmol) in 1N NaOH (20 mL) was heated under reflux for 8 h. The solution was concentrated under vacuum, water (75 mL) was added, and the solution was extracted with ether (3×25 mL). The ether extracts were discarded. The aqueous layer was cooled in an ice bath and acidified to pH 1-2 with 6N H_2SO_4 . The oil that separated was extracted with ether (3×25 mL). The ether layer was washed with water (3×25 mL) and dried over anhydrous Na_2SO_4 . Ether was removed under vacuum to afford a crude oil that contained **236**, and was used without further purification.

General procedure for synthesis of **216a**, **217a**

To a solution of **140a** (2.0 mmol) in a mixture of ethanol/water (2:1, 90 mL) was added the appropriate thiophenol (4.0 mmol) and the reaction mixture was heated to 100-110 $^\circ\text{C}$. At this point, I_2 (4.0 mmol) was added and the heating was continued with stirring for a total of 3 hours. To this mixture was added excess $\text{Na}_2\text{S}_2\text{O}_7$ and concentrated under reduced pressure. To the resulting residue was added some silica gel and MeOH and the solution was evaporated to dryness to afford a plug which was loaded on top of a column and eluted with a gradient of 1-5% MeOH in CHCl_3 . Fractions containing the desired spot (TLC) were pooled and evaporated to dryness. The resulting residue was recrystallized from MeOH, filtered and dried to obtain the desired compound.

2-Amino-6-methyl-5-((3,4,5-trimethoxyphenyl)thio)-3,7-dihydro-4H-pyrrolo[2,3-*d*]pyrimidin-4-one (216a).

Compound **140a** (0.330g, 2 mmol) was reacted with **236** (0.8 g, 4 mmol) in presence of I₂ (1 g, 4 mmol) using the method described above to afford **216a** (194 mg, 26%) as an off-white solid. Mp > 240 °C dec.; TLC *R_f* 0.44 (CHCl₃/MeOH, 5:1, with 2 drops of NH₄OH); ¹H NMR (DMSO-*d*₆) δ 2.19 (s, 3H, 6-CH₃), 3.82 (s, 3H, OCH₃), 3.84 (s, 6H, OCH₃) 6.15 (bs, 2H, 2-NH₂ exch.), δ 6.53 (s, 2H, C₆H₄), 10.46 (s, 1H, 3-NH), 11.48 (s, 1 H, 7-NH). Anal. (C₁₆H₁₈N₄O₄S 0.1H₂O) C, H, N: Cal. C: 53.03, H: 5.01, N: 15.46. Found C: 52.61, H: 4.88, N: 15.34.

2-Amino-6-methyl-5-(pyridin-4-ylthio)-3,7-dihydro-4H-pyrrolo[2,3-*d*]pyrimidin-4-one (217a).

Compound **140a** (0.330g, 2 mmol) was reacted with pyridine-4-thiol **239** (0.45 g, 4 mmol) in presence of I₂ (1 g, 4 mmol) using the method described above to afford **217a** (94 mg, 16%) as a brown solid. mp> 242 °C (lit.³⁵⁵ >250 °C, dec.); TLC *R_f* 0.27 (CHCl₃/MeOH, 5:1, with 2 drops of NH₄OH); ¹H NMR (DMSO-*d*₆) δ 2.17 (s, 3 H, 6-CH₃), 6.14 (s, 2 H, 2-NH₂ exch.), 6.93 (d, 2 H, 3', 5'-CH), 8.26 (d, 2 H, 2', 6'-CH), 10.46 (s, 1 H, 3-NH exch.), 11.53 (s, 1 H, 7-NH exch.).

General method for synthesis of 216b and 217b

2-Amino-4-oxo-6-substitued-pyrrolo[2,3-*d*]pyrimidine **216a** or **217a** (about 1 mmol), 5 mL of POCl₃ and 0.1 mL of PhNMe₂ were placed in a 50-mL round-bottom flask. The mixture was heated to reflux and kept stirring for 4 h. After evaporation of the excess of

POCl₃, ice-cold water was added and the reaction mixture was neutralized with NH₃·H₂O. The precipitated solid was collected by filtered, and the filtrate was extracted with CHCl₃ (3×50 mL). The organic phase was combined and dried (Na₂SO₄). Concentration of the chloroform afforded additional solid compounds. The solids thus obtained were dissolved in methanol, then 1 g silica gel was added and removed the solvent in vacuo to afford a dry plug. The plug was placed on the top of a 15×150 mm column and eluted with 2% methanol in chloroform. Fractions containing the product were pooled and evaporated to afford pure **216b** or **217b** respectively.

4-Chloro-6-methyl-5-((3,4,5-trimethoxyphenyl)thio)-7H-pyrrolo[2,3-*d*]pyrimidin-2-amine (216b)

Reaction of **216a** (0.36 g, 1 mmol) with 5 mL POCl₃ in presence 0.1 mL of PhNMe₂ using the method described afforded **216b** (53 mg, 18%) as a brown solid. mp> 250 °C, dec.; TLC *R_f* 0.51 (CHCl₃/MeOH, 5:1, with 2 drops of NH₄OH) ¹H NMR (DMSO-*d*₆) δ 2.19 (s, 3H, 6-CH₃), 3.78 (s, 3H, OCH₃), 3.83 (s, 6H, OCH₃) 6.15 (bs, 2H, 2-NH₂, exch.), δ 6.53 (s, 2H, C₆H₄), 11.84 (s, 1 H, 7-NH, exch.). Anal. (C₁₆H₁₇ClN₄O₃S 0.1MeOH) C, H, N: Cal. C: 50.46, H: 4.50, N: 14.71. Found C: 50.83, H: 4.34, N: 14.12.

4-Chloro-6-methyl-5-(pyridin-4-ylthio)-7H-pyrrolo[2,3-*d*]pyrimidin-2-amine (217b)

Reaction of **217a** (0.27 g, 1 mmol) with 5 mL POCl₃ in presence 0.1 mL of PhNMe₂ using the method described afforded **217b** (35 mg, 12%) above as a tan solid. mp> 250 °C, dec.; TLC *R_f* 0.36 (CHCl₃/MeOH, 5:1, with 2 drops of NH₄OH); ¹H NMR

(DMSO-*d*₆) δ 2.17 (s, 3 H, 6-CH₃), 6.21 (s, 2 H, 2-NH₂ exch.), 6.94 (d, 2 H, 3', 5'-CH), 8.24 (d, 2 H, 2', 6'-CH), 11.53 (s, 1 H, 7-NH exch.).

6-methyl-5-((3,4,5-trimethoxyphenyl)thio)-7H-pyrrolo[2,3-*d*]pyrimidin-2-amine (216c)

To a solution of **216b** (150 mg, 0.4 mmol) was in 20 mL MeOH in a Paar hydrogenation vessel was added 10% Pd/C (500 mg) and the mixture subjected to hydrogenation at 15 psi of hydrogen. The reaction was continued till the appearance of a new spot (TLC) and consumption of the starting material spot. The reaction was stopped and the mixture filtered through celite to remove Pd/C. The celite was washed with MeOH (2 x 20 mL) and the washing combined with the filtrate. To this, 1 g of silica gel was added and the solvent removed in vacuo to afford a silica gel plug. This plug was placed on the top of a 15×150 mm column and eluted with 2% methanol in chloroform. Fractions containing the product were pooled and evaporated to afford pure **216c** (73 mg, 55%) as a light brown solid. Mp > 238 °C, dec.; TLC *R*_f 0.4 (CHCl₃/MeOH, 5:1, with 2 drops of NH₄OH) ¹H NMR (DMSO-*d*₆) δ 2.19 (s, 3H, 6-CH₃), 3.78 (s, 3H, OCH₃), 3.83 (s, 6H, OCH₃) 6.19 (bs, 2H, 2-NH₂, exch.), 6.53 (s, 2H, C₆H₄), 8.46 (s, 1H, 4-H), 11.82 (s, 1 H, 7-NH, exch.). Anal. (C₁₆H₁₈N₄O₃S) C, H, N: Cal. C: 55.48, H: 5.24, N: 16.17. Found C: 55.82, H: 5.14, N: 16.16.

6-Methyl-5-((3,4,5-trimethoxyphenyl)thio)-7H-pyrrolo[2,3-*d*]pyrimidine-2,4-diamine (216d)

To a Parr bomb apparatus was added 10 ml methanol and cooled in a dry ice-acetone bath. To this solution was added ammonia gas for 30 minutes along with

continuous stirring. Compound **216b** (100 mg, 0.26 mmol) was added to this saturated solution of ammonia in methanol following which the bomb was tightly sealed and placed in an oil bath at 135 °C with continuous stirring for 48 hours. At this point TLC indicated the disappearance of the starting material and formation of one major spot at R_f 0.41 (CHCl₃/MeOH 5:1). The reaction was stopped at this point and the solution transferred to a 100 ml round bottom flask. The excess ammonia was allowed to evaporate and 2 grams of silica gel was added to this solution following which the methanol was evaporated and the plug obtained. This plug was placed on the top of a 15×150 mm column and eluted with 2% methanol in chloroform. Fractions containing the product were pooled and evaporated to afford pure **216d** (58mg, 62%) of as an off-white solid. mp 243-246 °C; TLC R_f 0.38 (CHCl₃/MeOH, 5:1, with 2 drops of NH₄OH) ¹H NMR (DMSO-d₆) δ 2.17 (s, 3H, 6-CH₃), 3.78 (s, 3H, OCH₃), 3.84 (s, 6H, OCH₃) 5.22 (bs, 2H, 4-NH₂, exch.) 6.20 (bs, 2H, 2-NH₂, exch.), δ 6.53 (s, 2H, C₆H₄), 10.44 (s, 1 H, 7-NH, exch.) HRMS (C₁₆H₁₉N₅O₃S) : calcd. mass 361.1209, found mass 361.1212.

2-Amino-7-benzyl-6-methyl-5-((3,4,5-trimethoxyphenyl)thio)-3,7-dihydro-4H-pyrrolo[2,3-*d*]pyrimidin-4-one (216e)

To a round bottomed flask was added **216a** (100 mg, 0.4 mmol) and dissolved in 5 ml of DMF. The solution was cooled to 0 °C and sodium hydride (10 mg, 0.4 mmol) was added. After stirring at 0 °C for 1 hour, benzylbromide (81 mg, 0.48 mmol) was added. The reaction was continued at rt till the appearance of a new spot (TLC) after which the reaction was quenched with water. The water phase was extracted with chloroform. The organic phase was dried over sodium sulfate and evaporated under reduced pressure. The residue was dissolved in methylene chloride, 250 mg silica gel was

added to the solution which was then evaporated to dryness to form a plug. The silica gel plug obtained was loaded onto a silica gel column and eluted with 1% methanol in chloroform. Fractions corresponding to the product (TLC) were pooled and evaporated to dryness under reduced pressure to afford **216e** (16 mg, 12%) as a light brown solid. mp > 250 °C, dec.; TLC R_f 0.5 (CHCl₃/MeOH, 5:1, with 2 drops of NH₄OH) Mp > 240 °C dec.; TLC R_f 0.48 (CHCl₃/MeOH, 5:1, with 2 drops of NH₄OH); ¹H NMR (DMSO-*d*₆) δ 2.19 (s, 3H, 6-CH₃), 3.82 (s, 3H, OCH₃), 3.84 (s, 6H, OCH₃) 5.30 (s, 2H CH₂) 6.15 (bs, 2H, 2-NH₂ exch.), 6.53 (s, 2H, C₆H₄), 7.22–7.31 (m, 4H, C₆H₅) 7.49–7.51 (m, 1H, C₆H₅), 10.46 (s, 1H, 3-NH exch). HR-MS: C₂₃H₂₄N₄O₄S: calcd. mass 452.1518, found mass 452.1511.

7-benzyl-4-chloro-6-methyl-5-((3,4,5-trimethoxyphenyl)thio)-7H-pyrrolo[2,3-*d*]pyrimidin-2-amine (216f)

Compound **216b** when reacted with benzyl bromide using conditions described for the synthesis of **216e** afforded **216f** (16 mg, 12%) as a light brown solid. mp > 250 °C, dec.; TLC R_f 0.55 (CHCl₃/MeOH, 5:1, with 2 drops of NH₄OH) ¹H NMR (DMSO-*d*₆) δ 2.19 (s, 3H, 6-CH₃), 3.82 (s, 3H, OCH₃), 3.84 (s, 6H, OCH₃) 5.30 (s, 2H CH₂) 6.19 (bs, 2H, 2-NH₂ exch.), 6.53 (s, 2H, C₆H₄), 7.26–7.33 (m, 4H, C₆H₅) 7.48–7.51 (m, 1H, C₆H₅). HR-MS: C₂₃H₂₃ClN₄O₃S: calcd. mass 470.1179, found mass 470.1160.

7-benzyl-6-methyl-5-((3,4,5-trimethoxyphenyl)thio)-7H-pyrrolo[2,3-*d*]pyrimidin-2-amine (216g)

Treatment of **216f** with 10% Pd/C and hydrogen at 15 psi using a Paar hydrogenator and conditions used for the synthesis of **216e** afforded **216f** (16 mg, 12%)

as a light brown solid. mp > 240 °C, dec.; TLC R_f 0.4 (CHCl₃/MeOH, 5:1, with 2 drops of NH₄OH) ¹H NMR (DMSO-*d*₆) δ 2.21 (s, 3H, 6-CH₃), 3.81 (s, 3H, OCH₃), 3.83 (s, 6H, OCH₃) 5.28 (s, 2H CH₂) 5.86 (s, 1H 4-H) 6.19 (bs, 2H, 2-NH₂ exch.), 6.53 (s, 2H, C₆H₄), 7.26–7.33 (m, 4H, C₆H₅) 7.48–7.51 (m, 1H, C₆H₅). HR-MS: C₂₃H₂₄N₄O₃S: calcd. mass 436.1569, found mass 436.1560.

7-benzyl-6-methyl-5-((3,4,5-trimethoxyphenyl)thio)-7H-pyrrolo[2,3-*d*]pyrimidine-2,4-diamine (216h)

Treatment of **216g** with a saturated solution of ammonia in methanol in a paar bomb apparatus and conditions used for the synthesis of **216d** afforded **216f** (16 mg, 12%) as a light brown solid. mp > 250 °C, dec.; TLC R_f 0.6 (CHCl₃/MeOH, 5:1, with 2 drops of NH₄OH) ¹H NMR (DMSO-*d*₆) δ 2.19 (s, 3 H, 6-CH₃), 3.65 (s, 6 H, OCH₃), 3.79 (s, 3 H, OCH₃), 5.30 (s, 2H, CH₂) 6.19 (bs, 2 H, 2-NH₂), 6.56 (d, 1 H, 5'-CH). 7.22–7.31 (m, 4H, Ar-H) 7.49–7.51 (m, 2H, Ar-H). HR-MS: C₂₃H₂₅N₅O₃S: calcd. mass 451.1678, found mass 451.1680.

Validation of homology models:

In addition to Ramachandran plots, Procheck and ProSA analysis, the following model validation tests were carried out for the three homology models generated.

1. pJDHFR homology model

Errat2 analysis.⁴¹⁶ The program works by analyzing the statistics of non-bonded interactions between different atom types. A single output plot is produced that gives the value of the error function vs. position of a 9-residue sliding window and can be compared with statistics from highly refined structures to give confidence limits.

Program: ERRAT2
 File: /var/www/html/Services/ERRAT/DATA/3340240.pdb
 Chain#:1
 Overall quality factor*: 94.118

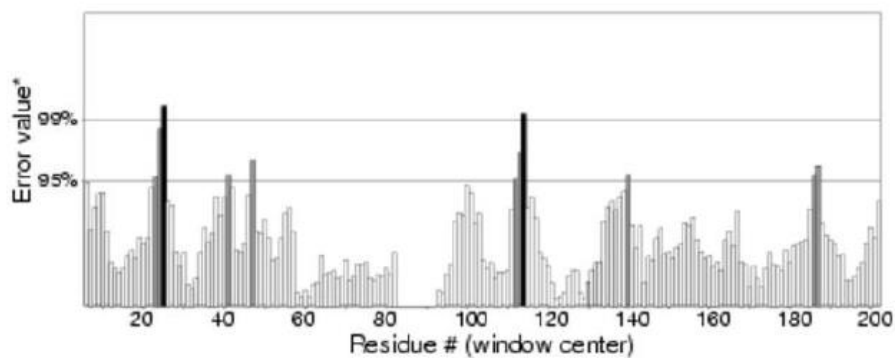


Figure E1. Errat2 analysis of the pjDHFR homology model

QMEAN

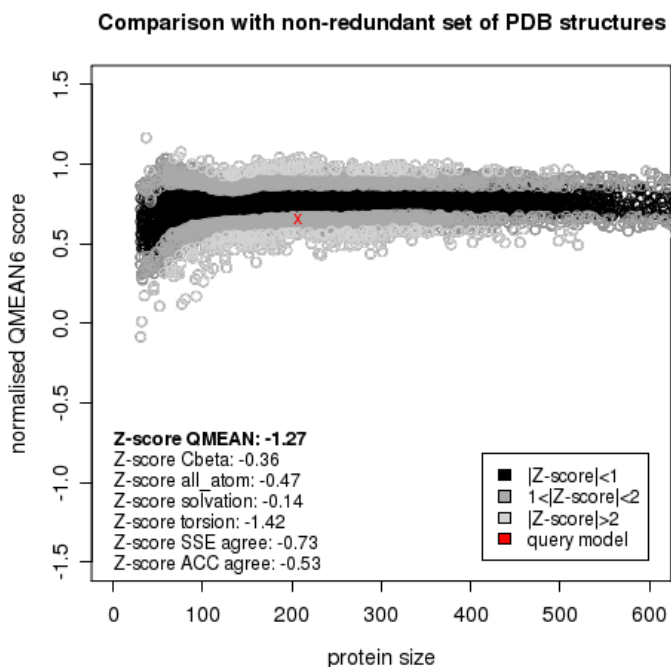


Figure E2. Comparison of the overall Qmean score of the pjDHFR homology model with PDB structures

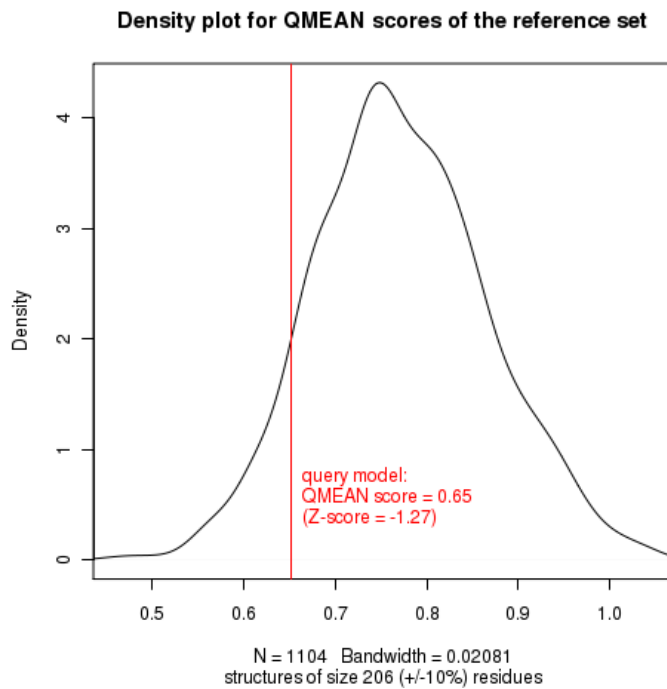


Figure E3. Comparison of the overall Qmean score of the pjDHFR homology model with PDB structures

QMEAN⁴¹⁶ is a composite scoring function which is able to derive both global (i.e. for the entire structure) and local (i.e. per residue) error estimates based on a single model.

tgDHFR homology model analysis

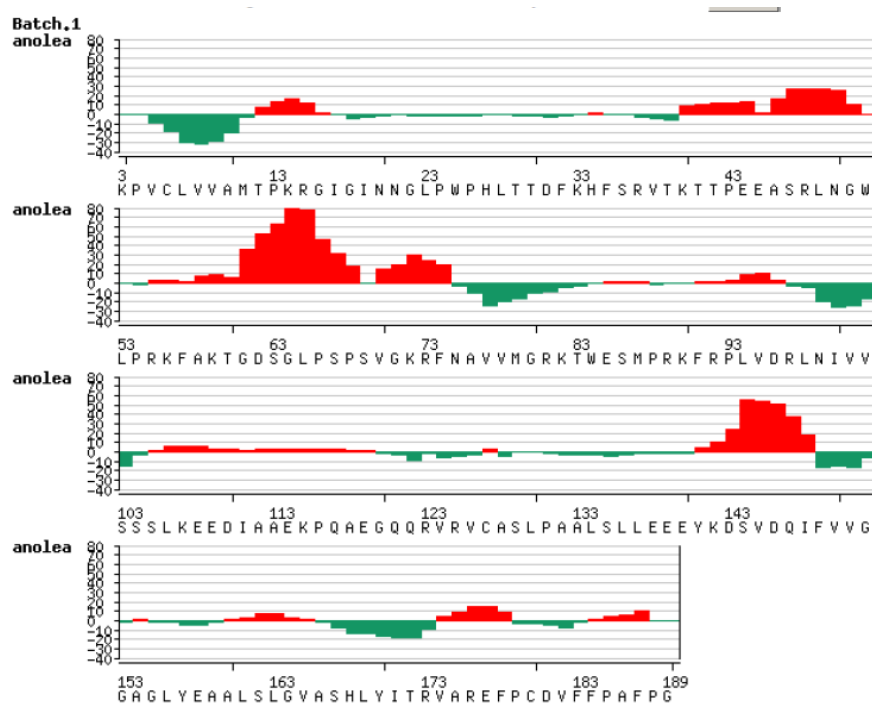
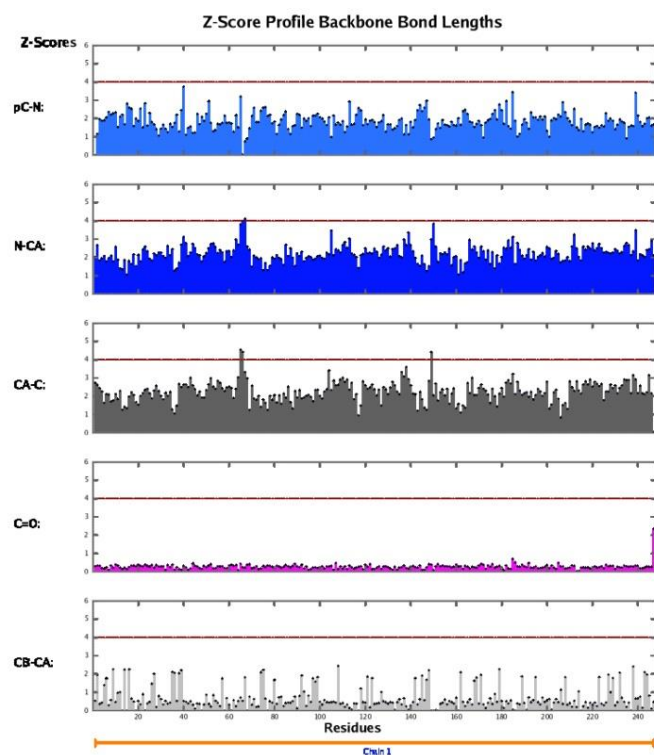
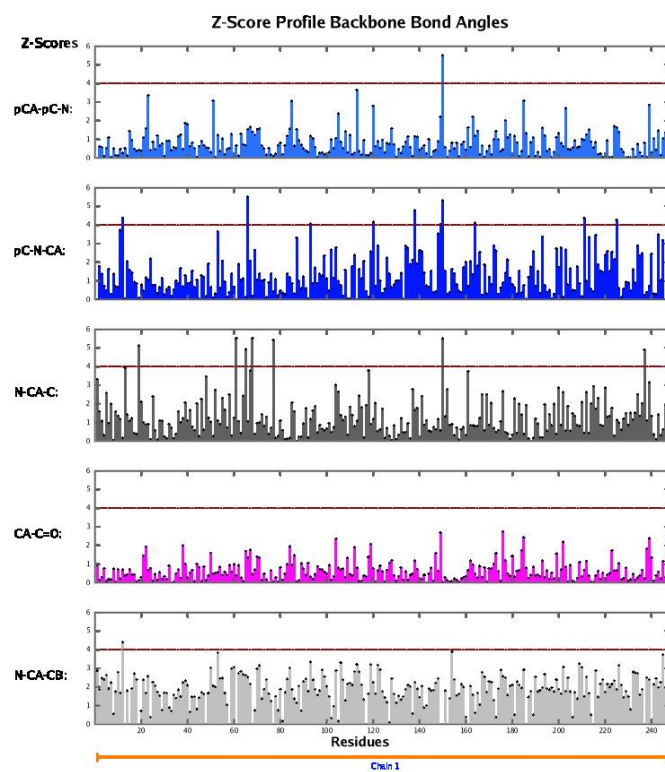


Figure E4: ANOLEA analysis of the tgDHFR homology model

ANOLEA evaluation:

The atomic empirical mean force potential ANOLEA⁴¹⁶ is used to assess packing quality of the models. The program performs energy calculations on a protein chain, evaluating the "Non- Local Environment" (NLE) of each heavy atom in the molecule. The y-axis of the plot represents the energy for each amino acid of the protein chain. Negative energy values (in green) represent favourable energy environment whereas positive values (in red) unfavourable energy environment for a given amino acid. Energy minimization was performed to minimize the unfavorable energy regions of the model.



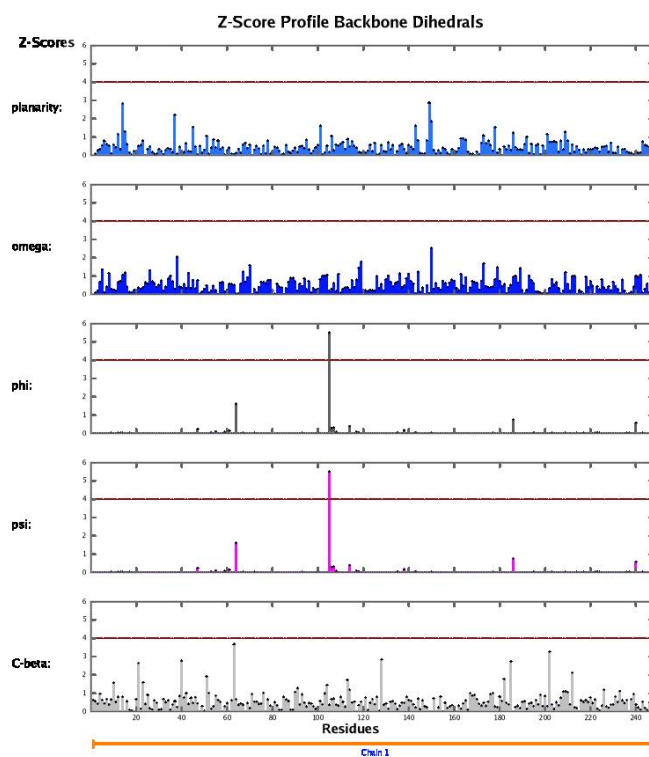


Figure E5: Z-score analysis of the bond angles, backbone length and dihedral angles of the tgDHFR homology model.

Z-score analysis⁴¹⁶ of the the bond angles, backbone length and dihedral angles of the tgDHFR homology model indicate that the values lie within acceptable range.

G. BIBLIOGRAPHY

1. <http://www.uniprot.org/uniprot/P00374>. Accessed 07/15/2013.
2. Cossins, E. A. The fascinating world of folate and one-carbon metabolism. *Can. J. Bot.* **2000**, *78*, 691-708.
3. Melse-Boonstra, A.; De Bree, A.; Verhoef, P.; Bjorke-Monsen, A. L.; Verschuren, W. M. M. Dietary monoglutamate and polyglutamate folate are associated with plasma folate concentrations in Dutch men and women aged 20-65 years. *J. Nutr.* **2002**, *132*, 1307-1312.
4. McKillop, D. J.; Pentieva, K.; Daly, D.; McPartlin, J. M.; Hughes, J.; Strain, J. J.; Scott, J. M.; McNulty, H. The effect of different cooking methods on folate retention in various foods that are amongst the major contributors to folate intake in the UK diet. *Br. J. Nutr.* **2002**, *88*, 681-688.
5. Murphy, M.; Keating, M.; Boyle, P.; Weir, D. G.; Scott, J. M. The elucidation of the mechanism of folate catabolism in the rat. *Biochem. Biophys. Res. Commun.* **1976**, *71*, 1017-24.
6. Kamen, B. Folate and antifolate pharmacology. *Semin. Oncol.* **1997**, *24*, S18/30-S18/39.
7. Blakley, R. L. *The Biochemistry of Folic Acid and Related Pteridines (Frontiers of Biology)* **1969**; *13*, 569 pp.
8. Matherly, L. H.; Goldman, I. D. Membrane transport of folates. *Vitam. Horm. (San Diego, CA, U. S.)* **2003**, *66*, 403-456.
9. Matherly, L. H.; Hou, Z.; Deng, Y. Human reduced folate carrier: Translation of basic biology to cancer etiology and therapy. *Cancer Metastasis Rev.* **2007**, *26*, 111-128.
10. Salazar, M. D. A.; Ratnam, M. The folate receptor: What does it promise in tissue-targeted therapeutics? *Cancer Metastasis Rev.* **2007**, *26*, 141-152.
11. Hilgenbrink, A. R.; Low, P. S. Folate receptor-mediated drug targeting: From therapeutics to diagnostics. *J. Pharm. Sci.* **2005**, *94*, 2135-2146.
12. Qiu, A.; Jansen, M.; Sakaris, A.; Min, S. H.; Chattopadhyay, S.; Tsai, E.; Sandoval, C.; Zhao, R.; Akabas, M. H.; Goldman, I. D. Identification of an intestinal folate transporter and the molecular basis for hereditary folate malabsorption. *Cell*, **2006**, *127*, 917-928.
13. Stankova, J.; Lawrance, A. K.; Rozen, R. Methylenetetrahydrofolate reductase (MTHFR): a novel target for cancer therapy. *Curr. Pharm. Des.* **2008**, *14*, 1143-1150.
14. Moran, R. G. Roles of folylpolyglutamate synthetase in therapeutics with tetrahydrofolate antimetabolites: an overview. *Semin. Oncol* **1999**, *26*, 24-32.
15. Gangjee, A.; Elzein, E.; Kothare, M.; Vasudevan, A. Classical and nonclassical antifolates as potential antitumor, antipneumocystis and antitoxoplasma agents. *Curr. Pharm. Des.* **1996**, *2*, 263-280.
16. Calvert, H. An overview of folate metabolism: features relevant to the action and toxicities of antifolate anticancer agents. *Semin. Oncol* **1999**, *26*, 3-10.
17. Jackman, A. L.; Editor. *Antifolate Drugs in Cancer Therapy*. 1999; p 456 pp.
18. Schnell, J. R.; Dyson, H. J.; Wright, P. E. Structure, dynamics, and catalytic

- function of dihydrofolate reductase. *Annu. Rev. Biophys. Biomol. Struct.* **2004**, *33*, 119-140.
19. Costi, M. P.; Ferrari, S. Update on antifolate drugs targets. *Curr. Drug Targets* **2001**, *2*, 135-166.
 20. Jackson, R. C. Antifolate drugs: past and future perspectives. *Antifolate Drugs Cancer Ther.* **1999**, 1-12.
 21. Costi, M. P.; Ferrari, S.; Venturelli, A.; Calo, S.; Tondi, D.; Barlocco, D. Thymidylate synthase structure, function and implication in drug discovery. *Curr. Med. Chem.* **2005**, *12*, 2241-2258.
 22. Bag, S.; Tawari, N. R.; Degani, M. S.; Queener, S. F. Design, synthesis, biological evaluation and computational investigation of novel inhibitors of dihydrofolate reductase of opportunistic pathogens. *Bioorg. Med. Chem.* **2010**, *18*, 3187-3197.
 23. Marr, K. A. Delayed opportunistic infections in hematopoietic stem cell transplantation patients: a surmountable challenge. *ASH Education Program Book*, **2012**, 265-270.
 24. Kelly, M. N.; Shellito, J. E. Current understanding of Pneumocystis immunology. *Future Microbiol.* **2009**, *5*, 43-65.
 25. Catherinot, E.; Lanternier, F.; Bougnoux, M.-E.; Lecuit, M.; Couderc, L.-J.; Lortholary, O. *Pneumocystis jirovecii* Pneumonia. *Infect. Dis. Clin. N. Am.* **2010**, *24*, 107-138.
 26. Ong, E. Common AIDS-associated opportunistic infections. *Clinical Medicine* **2008**, *8*, 539-543.
 27. Anderson, A. C. Targeting DHFR in parasitic protozoa. *Drug Discov. Today* **2005**, *10*, 121-128.
 28. *Glide*, 5.0; Schrödinger, LLC, New York, NY, 2008.
 29. Anderson, A. C. Winning the arms race by improving drug discovery against mutating targets. *ACS Chem. Biol.* **2012**, *7*, 278-288.
 30. Bolstad, D. B.; Bolstad, E. S. D.; Wright, D. L.; Anderson, A. C. Dihydrofolate reductase inhibitors: developments in antiparasitic chemotherapy. *Expert Opin. Ther. Pat.* **2008**, *18*, 143-157.
 31. Gangjee, A.; Jain, H. D.; Kurup, S. Recent advances in classical and non-classical antifolates as antitumor and antiopportunistic infection agents: part I. *Anti-Cancer Agents Med. Chem.* **2007**, *7*, 524-542.
 32. Gangjee, A.; Jain, H. D.; Kurup, S. Recent advances in classical and non-classical antifolates as antitumor and antiopportunistic infection agents: Part II. *Anti-Cancer Agents Med. Chem.* **2008**, *8*, 205-231.
 33. Colbry, N. L.; Elslager, E. F.; Werbel, L. M. Folate antagonists. 21. Synthesis and antimalarial properties of 2,4-diamino-6-(benzylamino)pyrido[3,2-*d*]pyrimidines. *J. Med. Chem.* **1985**, *28*, 248-52.
 34. Miwa, T.; Hitaka, T.; Akimoto, H.; Nomura, H. Novel pyrrolo[2,3-*d*]pyrimidine antifolates: synthesis and antitumor activities. *J. Med. Chem.* **1991**, *34*, 555-60.
 35. Shih, C.; Gossett, L. S. The synthesis of N-{2-amino-4-substituted [(pyrrolo[2,3-*d*]pyrimidin-5-yl)ethyl]benzoyl}-L-glutamic acids as antineoplastic agents. *Heterocycles* **1993**, *35*, 825-41.
 36. www.pdb.org, accessed 10/10/2013
 37. Blakley, R. L.; Appleman, J. R. Recent advances in the study of dihydrofolate

- reductase. *Chem. Biol. Pteridines*, 1986, *Pteridines Folic Acid Deriv., Proc. Int. Symp. Pteridines Folic Acid Deriv.: Chem., Biol. Clin. Aspects*, 8th **1986**, 769-88.
38. Freisheim, J. H.; Matthews, D. A. The comparative biochemistry of dihydrofolate reductase. *Folate Antagonists Ther. Agents* **1984**, *1*, 69-131.
 39. Oefner, C.; D'Arcy, A.; Winkler, F. K. Crystal structure of human dihydrofolate reductase complexed with folate. *Eur. J. Biochem.* **1988**, *174*, 377-85.
 40. Davies, J. F., II; Delcamp, T. J.; Prendergast, N. J.; Ashford, V. A.; Freisheim, J. H.; Kraut, J. Crystal structures of recombinant human dihydrofolate reductase complexed with folate and 5-deazafolate. *Biochemistry* **1990**, *29*, 9467-79.
 41. Matthews, D. A.; Bolin, J. T.; Burrige, J. M.; Filman, D. J.; Volz, K. W.; Kaufman, B. T.; Beddell, C. R.; Champness, J. N.; Stammers, D. K.; Kraut, J. Refined crystal structures of *Escherichia coli* and chicken liver dihydrofolate reductase containing bound trimethoprim. *J. Biol. Chem.* **1985**, *260*, 381-91.
 42. Champness, J. N.; Achari, A.; Ballantine, S. P.; Bryant, P. K.; Delves, C. J.; Stammers, D. K. The structure of *Pneumocystis carinii* dihydrofolate reductase to 1.9 Å resolution. *Structure* **1994**, *2*, 915-24.
 43. Cody, V.; Galitsky, N.; Rak, D.; Luft, J. R.; Pangborn, W.; Queener, S. F. Ligand-induced conformational changes in the crystal structures of *Pneumocystis carinii* dihydrofolate reductase complexes with folate and NADP. *Biochemistry* **1999**, *38*, 4303-4312.
 44. Cody, V.; Pace, J.; Chisum, K.; Rosowsky, A. New insights into DHFR interactions: Analysis of *Pneumocystis carinii* and mouse DHFR complexes with NADPH and two highly potent 5-(ω -carboxy(alkyloxy) trimethoprim derivatives reveals conformational correlations with activity and novel parallel ring stacking interactions. *Proteins: Struct., Funct., Bioinf.* **2006**, *65*, 959-969.
 45. Graffner-Nordberg, M.; Kolmodin, K.; Åqvist, J.; Queener, S. F.; Hallberg, A. Design, synthesis, and computational affinity prediction of ester soft drugs as inhibitors of dihydrofolate reductase from *Pneumocystis carinii*. *Eur. J. Pharma. Sci.* **2004**, *22*, 43-54.
 46. Ma, L.; Kovacs, J. A. Expression and characterization of recombinant human-derived *Pneumocystis carinii* dihydrofolate reductase. *Antimicrob. Agents Chemother.* **2000**, *44*, 3092-3096.
 47. Mori, S.; Sugimoto, M. *Pneumocystis jirovecii* infection: an emerging threat to patients with rheumatoid arthritis. *Rheumatology* **2012**, *51*, 2120-2130.
 48. Cody, V.; Chisum, K.; Pope, C.; Queener, S. F. Purification and characterization of human-derived *Pneumocystis jirovecii* dihydrofolate reductase expressed in Sf21 insect cells and in *Escherichia coli*. *Protein Expression Purif.* **2005**, *40*, 417-423.
 49. Roos, D. S. Primary structure of the dihydrofolate reductase-thymidylate synthase gene from *Toxoplasma gondii*. *J. Biol. Chem.* **1993**, *268*, 6269-6280.
 50. Gangjee, A.; Lin, X.; Biondo, L. R.; Queener, S. F. CoMFA analysis of tgDHFR and rLDHFR based on antifolates with 6-5 fused ring system using the all-orientation search (AOS) routine and a modified cross-validated r^2 -guided region selection (q^2 -GRS) routine and its initial application. *Bioorg. Med. Chem.* **2010**, *18*, 1684-1701.
 51. Chan, D. C. M.; Anderson, A. C. Towards species-specific antifolates. *Curr. Med.*

- Chem.* **2006**, *13*, 377-398.
52. Kovacs, J. A.; Allegra, C. J.; Masur, H. Characterization of dihydrofolate reductase of *Pneumocystis carinii* and *Toxoplasma gondii*. *Exp. Parasitol.* **1990**, *71*, 60-68.
 53. Tawari, N. R.; Bag, S.; Degani, M. S. A review of molecular modelling studies of dihydrofolate reductase inhibitors against opportunistic microorganisms and comprehensive evaluation of new models. *Curr. Pharm. Des.* **2011**, *17*, 712-751.
 54. Gready, J. E. Dihydrofolate reductase: binding of substrates and inhibitors and catalytic mechanism. *Adv. Pharmacol. Chemother.* **1980**, *17*, 37-102.
 55. Subramanian, S.; Kaufman, B. T. Interaction of methotrexate, folates, and pyridine nucleotides with dihydrofolate reductase: calorimetric and spectroscopic binding studies. *Proc. Natl. Acad. Sci. U. S. A.* **1978**, *75*, 3201-3205.
 56. Stockman, B. J.; Nirmala, N. R.; Wagner, G.; Delcamp, T. J.; DeYarman, M. T.; Freisheim, J. H. Methotrexate binds in a nonproductive orientation to human dihydrofolate reductase in solution, based on NMR spectroscopy. *FEBS Lett.* **1991**, *283*, 267-9.
 57. Gavrin, L. K.; Saiah, E. Approaches to discover non-ATP site kinase inhibitors. *Med. Chem. Comm* **2013**, *4*, 41.
 58. Cody, V.; Galitsky, N.; Luft, J. R.; Pangborn, W.; Blakley, R. L.; Gangjee, A. Comparison of ternary crystal complexes of F31 variants of human dihydrofolate reductase with NADPH and a classical antitumor furopyrimidine. *Anticancer Drug Des* **1998**, *13*, 307-15.
 59. Dams, T.; Auerbach, G.; Bader, G.; Jacob, U.; Ploom, T.; Huber, R.; Jaenicke, R. The crystal structure of dihydrofolate reductase from *Thermotoga maritima*: Molecular features of thermostability. *J. Mol. Biol.* **2000**, *297*, 659-672.
 60. Stammers, D. K.; Champness, J. N.; Beddell, C. R.; Dann, J. G.; Eliopoulos, E.; Geddes, A. J.; Ogg, D.; North, A. C. T. The structure of mouse L1210 dihydrofolate reductase-drug complexes and the construction of a model of human enzyme. *FEBS Lett.* **1987**, *218*, 178-84.
 61. Sutherland, J. J.; Weaver, D. F. Three-dimensional quantitative structure-activity and structure-selectivity relationships of dihydrofolate reductase inhibitors. *J. Comput.-Aided Mol. Des.* **2004**, *18*, 309-331.
 62. Cody, V.; Galitsky, N.; Rak, D.; Luft, J. R.; Pangborn, W.; Queener, S. F. Ligand-induced conformational changes in the crystal structures of *Pneumocystis carinii* dihydrofolate reductase complexes with folate and NADP⁺. *Biochemistry* **1999**, *38*, 4303-4312.
 63. Yu, Z.; Jacobson, M. P.; Friesner, R. A. What role do surfaces play in GB models? A new-generation of surface-generalized born model based on a novel gaussian surface for biomolecules. *J. Comput.Chem.* **2006**, *27*, 72-89.
 64. Agrawal, V. K.; Sohgaure, R.; Khadikar, P. V. QSAR studies on biological activity of piritrexim analogues against pc DHFR. *Bioorg. Med. Chem.* **2002**, *10*, 2919-2926.
 65. Kovalevskaya, N.; Smurnyy, Y.; Polshakov, V.; Birdsall, B.; Bradbury, A.; Frenkiel, T.; Feeney, J. Solution Structure of Human Dihydrofolate Reductase in its Complex with Trimethoprim and NADPH. *J. Biomol. NMR* **2005**, *33*, 69-72.
 66. Pitts, C.; Yin, J.; Bowen, D.; Maxwell, C.; Southerland, W. Interaction energy

- analysis of nonclassical antifolates with *Pneumocystis carinii* dihydrofolate reductase. *Int. J. Mol. Sci.* **2002**, *3*, 1188-1202.
67. Mattioni, B. E.; Jurs, P. C. Prediction of dihydrofolate reductase inhibition and selectivity using computational neural networks and linear discriminant analysis. *J. Mol. Graphics Modell.* **2003**, *21*, 391-419.
 68. Masur, H. P.; Tuazon, C. U.; Ogata-Arakaki, D.; Kovacs, J. A.; Katz, D.; Hilt, D.; Simmons, T.; Feuerstein, I.; Lundgren, B. Salvage trial of trimetrexate-leucovorin for the treatment of cerebral toxoplasmosis in patients with AIDS. *J. Infect. Dis.* **1993**, *167*, 1422-1426.
 69. Sattler, F. R. F.; Davis, R.; Nichols, L.; Shelton, B.; Akil, B.; Baughman, R.; Hughlett, C.; Weiss, W.; Boylen, C. T. Trimetrexate with leucovorin versus trimethoprim-sulfamethoxazole for moderate to severe episodes of *Pneumocystis carinii* pneumonia in patients with AIDS: a prospective, controlled multicenter investigation of the AIDS Clinical Trials Group Protocol 029/031. *J. Infect. Dis.* **1994**, *170*, 165-172.
 70. Paulsen, J. L.; Anderson, A. C. Scoring ensembles of docked protein:ligand interactions for virtual lead optimization. *J. Chem. Inf. Model.* **2009**, *49*, 2813-2819.
 71. Liu, J.; Bolstad, D. B.; Bolstad, E. S. D.; Wright, D. L.; Anderson, A. C. Towards new antifolates targeting eukaryotic opportunistic infections. *Eukaryotic Cell* **2009**, *8*, 483-486.
 72. Gangjee, A.; Vasudevan, A.; Queener, S. F.; Kisliuk, R. L. 2,4-Diamino-5-deaza-6-substituted pyrido[2,3-*d*]pyrimidine antifolates as potent and selective nonclassical inhibitors of dihydrofolate reductases. *J. Med. Chem.* **1996**, *39*, 1438-46.
 73. Kovacs, J. A.; Allegra, C. J.; Swan, J. C.; Drake, J. C.; Parrillo, J. E.; Chabner, B. A.; Masur, H. Potent antipneumocystis and antitoxoplasma activities of piritrexim, a lipid-soluble antifolate. *Antimicrob. Agents Chemother.* **1988**, *32*, 430-433.
 74. Gangjee, A.; Adair, O. O.; Pagley, M.; Queener, S. F. N9-Substituted 2,4-diaminoquinazolines: synthesis and biological evaluation of lipophilic inhibitors of *Pneumocystis carinii* and *Toxoplasma gondii* dihydrofolate reductase. *J. Med. Chem.* **2008**, *51*, 6195-6200.
 75. Suling, W. J.; Seitz, L. E.; Pathak, V.; Westbrook, L.; Barrow, E. W.; Zywno-Van-Ginkel, S.; Reynolds, R. C.; Piper, J. R.; Barrow, W. W. Antimycobacterial activities of 2,4-diamino-5-deazapteridine derivatives and effects on mycobacterial dihydrofolate reductase. *Antimicrob. Agents. Chemother.* **2000**, *44*, 2784-2793.
 76. Rosowsky, A.; Chen, H.; Fu, H.; Queener, S. F. Synthesis of new 2,4-diaminopyrido[2,3-*d*]pyrimidine and 2,4-diaminopyrrolo[2,3-*d*]pyrimidine inhibitors of *Pneumocystis carinii*, *Toxoplasma gondii*, and *Mycobacterium avium* dihydrofolate reductase. *Bioorg. Med. Chem.* **2003**, *11*, 59-67.
 77. Gangjee, A.; Vasudevan, A.; Queener, S. F.; Kisliuk, R. L. 2,4-diamino-5-deaza-6-substituted pyrido[2,3-*d*]pyrimidine antifolates as potent and selective nonclassical inhibitors of dihydrofolate reductases. *J. Med. Chem.* **1996**, *39*, 1438-1446.

78. Gangjee, A.; Devraj, R.; Queener, S. F. Synthesis and dihydrofolate reductase inhibitory activities of 2,4-diamino-5-deaza and 2,4-diamino-5,10-dideaza lipophilic antifolates. *J. Med. Chem.* **1997**, *40*, 470-478.
79. Gangjee, A.; Adair, O. O.; Queener, S. F. Synthesis and biological evaluation of 2,4-diamino-6-(arylaminoethyl)pyrido[2,3-*d*]pyrimidines as inhibitors of *Pneumocystis carinii* and *Toxoplasma gondii* dihydrofolate reductase and as antiopportunistic infection and antitumor agents. *J. Med. Chem.* **2003**, *46*, 5074-5082.
80. Gangjee, A.; Adair, O.; Queener, S. F. Synthesis of 2,4-Diamino-6-(thioarylthiomethyl)pyrido[2,3-*d*]pyrimidines as dihydrofolate reductase inhibitors. *Bioorg. Med. Chem.* **2001**, *9*, 2929-2935.
81. Barf, T.; Kaptein, A. Irreversible protein kinase inhibitors: balancing the benefits and risks. *J. Med. Chem.* **2012**, *55*, 6243-6262.
82. Graczyk, P. P. Gini Coefficient: A new way to express selectivity of kinase inhibitors against a family of kinases. *J. Med. Chem.* **2007**, *50*, 5773-5779.
83. Edman, J. C.; Edman, U.; Cao, M.; Lundgren, B.; Kovacs, J. A.; Santi, D. V. Isolation and expression of the *Pneumocystis carinii* dihydrofolate reductase gene. *Proc. Natl. Acad. Sci.* **1989**, *86*, 8625-8629.
84. Cody, V.; Galitsky, N.; Luft, J. R.; Pangborn, W.; Gangjee, A.; Devraj, R.; Queener, S. F.; Blakely, R. L. Comparison of ternary complexes of *Pneumocystis carinii* and wild-type human dihydrofolate reductase with coenzyme NADPH and a novel classical antitumor furo[2,3-*d*]pyrimidine antifolate. *Acta Crystallogr., Sect. D: Biol. Crystallogr.* **1997**, *D53*, 638-649.
85. Jain, P.; Soni, L. K.; Gupta, A. K.; Kashkedikar, S. G. QSAR analysis of 2,4-diamino pyrido[2,3-*d*]pyrimidines and 2,4-diaminopyrrolo[2,3-*d*]pyrimidines as dihydrofolate reductase inhibitors. *Ind. J. Biochem. Biophys.* **2005**, *42*, 315 - 320.
86. Karaman, M. W.; Herrgard, S.; Treiber, D. K.; Gallant, P.; Atteridge, C. E.; Campbell, B. T.; Chan, K. W.; Ciceri, P.; Davis, M. I.; Edeen, P. T.; Faraoni, R.; Floyd, M.; Hunt, J. P.; Lockhart, D. J.; Milanov, Z. V.; Morrison, M. J.; Pallares, G.; Patel, H. K.; Pritchard, S.; Wodicka, L. M.; Zarrinkar, P. P. A quantitative analysis of kinase inhibitor selectivity. *Nat. Biotech.* **2008**, *26*, 127-132.
87. Xu, W.; Harrison, S. C.; Eck, M. J. Three-dimensional structure of the tyrosine kinase c-Src. *Nature* **1997**, *385*, 595-602.
88. Graffner-Nordberg, M.; Marelus, J.; Ohlsson, S.; Persson, Å.; Swedberg, G.; Andersson, P.; Andersson, S. E.; Åqvist, J.; Hallberg, A. Computational Predictions of Binding Affinities to Dihydrofolate Reductase: Synthesis and Biological Evaluation of Methotrexate Analogues. *J. Med. Chem.* **2000**, *43*, 3852-3861.
89. Cody, V.; Galitsky, N.; Luft, J. R.; Pangborn, W.; Queener, S. F.; Gangjee, A. Analysis of quinazoline and pyrido[2,3-*d*]pyrimidine N9-C10 reversed-bridge antifolates in complex with NADP⁺ and *Pneumocystis carinii* dihydrofolate reductase. *Acta Crystallogr., Sect. D: Biol. Crystallogr.* **2002**, *D58*, 1393-1399.
90. Cody, V.; Luft, J. R.; Pangborn, W.; Gangjee, A.; Queener, S. F. Structure determination of tetrahydroquinazoline antifolates in complex with human and *Pneumocystis carinii* dihydrofolate reductase: correlations between enzyme selectivity and stereochemistry. *Acta Crystallogr., Sect. D: Biol. Crystallogr.*

- 2004**, D60, 646-655.
91. Cody, V.; Pace, J.; Queener, S. F.; Adair, O. O.; Gangjee, A. Kinetic and structural analysis for potent antifolate inhibition of pneumocystis jirovecii, *Pneumocystis carinii* and human dihydrofolate reductase (DHFR) and their active site variants. *Antimicrob. Agents Chemother.* **2013**, *57*, 2669-2677.
 92. Yuvaniyama, J.; Chitnumsub, P.; Kamchonwongpaisan, S.; Vanichtanankul, J.; Sirawaraporn, W.; Taylor, P.; Walkinshaw, M. D.; Yuthavong, Y. Insights into antifolate resistance from malarial DHFR-TS structures. *Nat. Struct. Mol. Biol.* **2003**, *10*, 357-365.
 93. Popov, V. M.; Yee, W. A.; Anderson, A. C. Towards in silico lead optimization: scores from ensembles of protein/ligand conformations reliably correlate with biological activity. *Proteins* **2007**, *66*, 375-87.
 94. Corbeil, C.; Williams, C.; Labute, P. Variability in docking success rates due to dataset preparation. *J. Comput.-Aided Mol. Des.* **2012**, *26*, 775-786.
 95. Rykunov, D.; Steinberger, E.; Madrid-Aliste, C. J.; Fiser, A. Improved scoring function for comparative modeling using the M4T method. *J Struct Funct Genomics* **2009**, *10*, 95-99.
 96. Kollman, P. Free energy calculations: Applications to chemical and biochemical phenomena. *Chem. Rev.* **1993**, *93*, 2395-2417.
 97. Böhm, H.-J.; Stahl, M. The Use of Scoring Functions in Drug Discovery Applications. In *Reviews in Computational Chemistry*, John Wiley & Sons, Inc.: **2003**; pp 41-87.
 98. Graffner-Nordberg, M.; Kolmodin, K.; Åqvist, J.; Queener, S. F.; Hallberg, A. Design, synthesis, computational prediction, and biological evaluation of ester soft drugs as inhibitors of dihydrofolate reductase from *Pneumocystis carinii*. *J. Med. Chem.* **2001**, *44*, 2391-2402.
 99. Graffner-Nordberg, M.; Kolmodin, K.; Åqvist, J.; Queener, S. F.; Hallberg, A. Design, synthesis, computational prediction, and biological evaluation of ester soft drugs as inhibitors of dihydrofolate reductase from *Pneumocystis carinii*. *J. Med. Chem.* **2001**, *44*, 2391-2402.
 100. Morris, G. M.; Huey, R.; Lindstrom, W.; Sanner, M. F.; Belew, R. K.; Goodsell, D. S.; Olson, A. J. AutoDock4 and AutoDockTools4: Automated docking with selective receptor flexibility. *J. Comput.Chem.* **2009**, *30*, 2785-2791.
 101. Gorse, A. D.; Gready, J. E. Molecular dynamics simulations of the docking of substituted N5-deazapterins to dihydrofolate reductase. *Protein Eng.* **1997**, *10*, 23-30.
 102. Jacobson, M. P.; Pincus, D. L.; Rapp, C. S.; Day, T. J.; Honig, B.; Shaw, D. E.; Friesner, R. A. A Hierarchical approach to all-atom protein loop prediction. *Proteins* **2004**, *55*, 351-367.
 103. Gangjee, A.; Lin, X. CoMFA and CoMSIA analyses of *Pneumocystis carinii* dihydrofolate reductase, *Toxoplasma gondii* dihydrofolate reductase, and rat liver dihydrofolate reductase. [Erratum to document cited in CA142:369701]. *J. Med. Chem.* **2006**, *49*, 2850.
 104. Harrison, P. T.; Scott, J. E.; Hutchinson, M. J.; Thompson, R. Site-directed mutagenesis of Varicella-zoster virus thymidylate synthase. Analysis of two highly conserved regions of the enzyme. *Eur. J. Biochem.* **1995**, *230*, 511-16.

105. www.pdb.org
106. Berman, H. M.; Westbrook, J.; Feng, Z.; Gilliland, G.; Bhat, T. N.; Weissig, H.; Shindyalov, I. N.; Bourne, P. E. The Protein Data Bank. *Nucleic Acids Res.* **2000**, *28*, 235-242.
107. Davisson, V. J.; Sirawaraporn, W.; Santi, D. V. Expression of human thymidylate synthase in Escherichia coli. *J. Biol. Chem.* **1989**, *264*, 9145-8.
108. Carreras, C. W.; Santi, D. V. The catalytic mechanism and structure of thymidylate synthase. *Annu. Rev. Biochem.* **1995**, *64*, 721-62.
109. Gmeiner, W. H. Novel chemical strategies for thymidylate synthase inhibition. *Curr. Med. Chem.* **2005**, *12*, 191-202.
110. Matthews, D. A.; Villafranca, J. E.; Janson, C. A.; Smith, W. W.; Welsh, K.; Freer, S. Stereochemical mechanism of action for thymidylate synthase based on the x-ray structure of the covalent inhibitory ternary complex with 5-fluoro-2'-deoxyuridylate and 5,10-methylenetetrahydrofolate. *J. Mol. Biol.* **1990**, *214*, 937-48.
111. Gangjee, A.; Devraj, R.; McGuire, J. J.; Kisliuk, R. L. 5-Arylthio substituted 2-amino-4-oxo-6-methylpyrrolo[2,3-d]pyrimidine antifolates as thymidylate synthase inhibitors and antitumor agents. *J. Med. Chem.* **1995**, *38*, 4495-502.
112. Gangjee, A.; Mavandadi, F.; Kisliuk, R. L.; McGuire, J. J.; Queener, S. F. 2-Amino-4-oxo-5-substituted-pyrrolo[2,3-d]pyrimidines as nonclassical antifolate inhibitors of thymidylate synthase. *J. Med. Chem.* **1996**, *39*, 4563-4568.
113. Gangjee, A.; Dubash, N. P.; Kisliuk, R. L. Synthesis of novel, nonclassical 2-amino-4-oxo-6-(arylthio)ethylpyrrolo[2,3-d]pyrimidines as potential inhibitors of thymidylate synthase. *J. Heterocyclic Chem.* **2001**, *38*, 349-354.
114. Gangjee, A.; Yu, J.; Kisliuk, R. L. 2-Amino-4-oxo-6-substituted-pyrrolo[2,3-d]pyrimidines as potential inhibitors of thymidylate synthase. *J. Heterocyclic Chem.* **2002**, *39*, 833-840.
115. Gangjee, A.; Mavandadi, F.; Kisliuk, R. L.; Queener, S. F. Synthesis of classical and a nonclassical 2-amino-4-oxo-6-methyl-5-substituted pyrrolo[2,3-d]pyrimidine antifolate inhibitors of thymidylate synthase. *J. Med. Chem.* **1999**, *42*, 2272-2279.
116. Gangjee, A.; Mavandadi, F.; Queener, S. F. Conformationally restricted tricyclic analogues of lipophilic pyrido[2,3-d]pyrimidine antifolates. *J. Heterocycl. Chem.* **2001**, *38*, 213-220.
117. Folkman, J. Tumor angiogenesis: therapeutic implications. *N Engl J Med* **1971**, *285*, 1182-1186.
118. Hanahan, D.; Weinberg, R. A. The hallmarks of cancer. *Cell* **2000**, *100*, 57-70.
119. Quesada, A. R.; Munoz-Chapuli, R.; Medina, M. A. Anti-angiogenic drugs: from bench to clinical trials. *Med. Res. Rev.* **2006**, *26*, 483-530.
120. He, L.; Hristova, K. Physical-chemical principles underlying RTK activation, and their implications for human disease. *Biochim. Biophys. Acta, Biomembr.* **2012**, *1818*, 995-1005.
121. Gasparini, G. The rationale and future potential of angiogenesis inhibitors in neoplasia. *Drugs* **1999**, *58*, 17-38.
122. Kerbel, R. S. A cancer therapy resistant to resistance. *Nature* **1997**, *390*, 335-6.
123. Johnson, G. L.; Lapadat, R. Mitogen-activated protein kinase pathways mediated

- by ERK, JNK, and p38 protein kinases. *Science* **2002**, 298, 1911-1912.
124. Blume-Jensen, P.; Hunter, T. Oncogenic kinase signaling. *Nature* **2001**, 411, 355-365.
 125. Sharma, P. S.; Sharma, R.; Tyagi, T. Receptor tyrosine kinase inhibitors as potent weapons in war against cancers. *Curr. Pharm. Des.* **2009**, 15, 758-776.
 126. Gunby, R. H.; Sala, E.; Tartari, C. J.; Puttini, M.; Gambacorti-Passerini, C.; Mologni, L. Oncogenic fusion tyrosine kinases as molecular targets for anti-cancer therapy. *Anti-Cancer Agents Med. Chem.* **2007**, 7, 594-611.
 127. Sawyer, T. K.; Wu, J. C.; Sawyer, J. R.; English, J. M. Protein kinase inhibitors: breakthrough medicines and the next generation. *Expert Opin. Investig. Drugs* **2013**, 22, 675-678.
 128. Plate, K. H.; Breier, G.; Weich, H. A.; Mennel, H. D.; Risau, W. Vascular endothelial growth factor and glioma angiogenesis: Coordinate induction of VEGF receptors, distribution of VEGF protein and possible In vivo regulatory mechanisms. *Int. J. Cancer* **1994**, 59, 520-529.
 129. Buchdunger, E.; Cioffi, C. L.; Law, N.; Stover, D.; Ohno-Jones, S.; Druker, B. J.; Lydon, N. B. Abl protein-tyrosine kinase inhibitor STI571 inhibits in vitro signal transduction mediated by c-Kit and platelet-derived growth factor receptors. *J. Pharmacol. Exp. Ther.* **2000**, 295, 139-145.
 130. Druker, B. J.; Tamura, S.; Buchdunger, E.; Ohno, S.; Segal, G. M.; Fanning, S.; Zimmermann, J.; Lydon, N. B. Effects of a selective inhibitor of the Abl tyrosine kinase on the growth of Bcr-Abl positive cells. *Nature Med* **1996**, 2, 561-566.
 131. Hynes, N. E.; Lane, H. A. ERBB receptors and cancer: the complexity of targeted inhibitors. *Nature Rev. Cancer* **2005**, 5, 341-354.
 132. Gorden, K. J.; Mesbah, P.; Kolesar, J. M. EGFR inhibitors as first-line therapy in EGFR mutation-positive patients with NSCLC. *J. Oncol. Pharm. Pract.* **2012**, 18, 245-249.
 133. Kim, K. J.; Li, B.; Winer, J.; Armanini, M.; Gillett, N.; Phillips, H. S.; Ferrara, N. Inhibition of vascular endothelial growth factor-induced angiogenesis suppresses tumor growth in vivo. *Nature* **1993**, 362, 841-844.
 134. Millauer, B.; Longhi, M. P.; Plate, K. H.; Shawver, L. K.; Risau, W.; Ullrich, A.; Strawn, L. M. Dominant-negative inhibition of Flk-1 suppresses the growth of many tumor types in vivo. *Cancer Res.* **1996**, 56, 1615-20.
 135. Brown, L. F.; Berse, B.; Jackman, R. W.; Tognazzi, K.; Manseau, E. J.; Senger, D. R.; Dvorak, H. F. Expression of vascular permeability factor (vascular endothelial growth factor) and its receptors in adenocarcinomas of the gastrointestinal tract. *Cancer Res.* **1993**, 53, 4727-35.
 136. Shaheen, R. M.; Davis, D. W.; Liu, W.; Zebrowski, B. K.; Wilson, M. R.; Bucana, C. D.; McConkey, D. J.; McMahon, G.; Ellis, L. M. Antiangiogenic therapy targeting the tyrosine kinase receptor for vascular endothelial growth factor receptor inhibits the growth of colon cancer liver metastasis and induces tumor and endothelial cell apoptosis. *Cancer Res.* **1999**, 59, 5412-5416.
 137. Takahashi, A.; Sasaki, H.; Kim, S. J.; Tobisu, K.-i.; Kakizoe, T.; Tsukamoto, T.; Kumamoto, Y.; Sugimura, T.; Terada, M. Markedly increased amounts of messenger RNAs for vascular endothelial growth factor and placenta growth factor in renal cell carcinoma associated with angiogenesis. *Cancer Res.* **1994**, 54,

- 4233-7.
138. Luttun, A.; Tjwa, M.; Moons, L.; Wu, Y.; Angelillo-Scherrer, A.; Liao, F.; Nagy, J. A.; Hooper, A.; Priller, J.; De Klerck, B.; Compennolle, V.; Daci, E.; Bohlen, P.; Dewerchin, M.; Herbert, J.-M.; Fava, R.; Matthys, P.; Carmeliet, G.; Collen, D.; Dvorak, H. F.; Hicklin, D. J.; Carmeliet, P. Revascularization of ischemic tissues by PlGF treatment, and inhibition of tumor angiogenesis, arthritis and atherosclerosis by anti-Flt1. *Nat. Med.* **2002**, *8*, 831-840.
 139. Quintas-Cardama, A.; Cortes, J. Therapeutic Options Against BCR-ABL1 T315I-Positive Chronic Myelogenous Leukemia. *Clin. Cancer Res.* **2008**, *14*, 4392-4399.
 140. Yang, F.-C.; Ingram, D. A.; Chen, S.; Zhu, Y.; Yuan, J.; Li, X.; Yang, X.; Knowles, S.; Horn, W.; Li, Y.; Zhang, S.; Yang, Y.; Vakili, S. T.; Yu, M.; Burns, D.; Robertson, K.; Hutchins, G.; Parada, L. F.; Clapp, D. W. Nfl-Dependent Tumors Require a Microenvironment Containing Nfl+/- and c-kit-Dependent Bone Marrow. *Cell* **2008**, *135*, 437-448.
 141. Gorre, M. E.; Mohammed, M.; Ellwood, K.; Hsu, N.; Paquette, R.; Rao, P. N.; Sawyers, C. L. Clinical resistance to STI-571 cancer therapy caused by BCR-ABL gene mutation or amplification. *Science* **2001**, *293*, 876-880.
 142. Chan, S. K.; Gullick, W. J.; Hill, M. E. Mutations of the epidermal growth factor receptor in non-small cell lung cancer - Search and destroy. *Eur. J. Cancer* **2006**, *42*, 17-23.
 143. Gazdar, A. F.; Shigematsu, H.; Herz, J.; Minna, J. D. Mutations and addiction to EGFR: the Achilles 'heel' of lung cancers? *Trends Mol. Med.* **2004**, *10*, 481-486.
 144. Ji, H.; Zhao, X.; Yuza, Y.; Shimamura, T.; Li, D.; Protopopov, A.; Jung, B. L.; McNamara, K.; Xia, H.; Glatt, K. A.; Thomas, R. K.; Sasaki, H.; Horner, J. W.; Eck, M.; Mitchell, A.; Sun, Y.; Al-Hashem, R.; Bronson, R. T.; Rabindran, S. K.; Discafani, C. M.; Maher, E.; Shapiro, G. I.; Meyerson, M.; Wong, K.-K. Epidermal growth factor receptor variant III mutations in lung tumorigenesis and sensitivity to tyrosine kinase inhibitors. *Proc. Natl. Acad. Sci. U. S. A.* **2006**, *103*, 7817-7822.
 145. Johnson, B. E.; Jaenke, P. A. Epidermal Growth Factor Receptor Mutations in Patients with Non-Small Cell Lung Cancer. *Cancer Res.* **2005**, *65*, 7525-7529.
 146. Kobayashi, S.; Boggon, T. J.; Dayaram, T.; Jaenke, P. A.; Kocher, O.; Meyerson, M.; Johnson, B. E.; Eck, M. J.; Tenen, D. G.; Halmos, B. EGFR mutation and resistance of non-small-cell lung cancer to gefitinib. *N. Engl. J. Med.* **2005**, *352*, 786-792.
 147. Lynch, T. J.; Bell, D. W.; Sordella, R.; Gurubhagavatula, S.; Okimoto, R. A.; Brannigan, B. W.; Harris, P. L.; Haserlat, S. M.; Supko, J. G.; Haluska, F. G.; Louis, D. N.; Christiani, D. C.; Settleman, J.; Haber, D. A. Activating mutations in the epidermal growth factor receptor underlying responsiveness of non-small-cell lung cancer to gefitinib. *N. Engl. J. Med.* **2004**, *350*, 2129-2139.
 148. Paez, J. G.; Jaenke, P. A.; Lee, J. C.; Tracy, S.; Greulich, H.; Gabriel, S.; Herman, P.; Kaye, F. J.; Lindeman, N.; Boggon, T. J.; Naoki, K.; Sasaki, H.; Fujii, Y.; Eck, M. J.; Sellers, W. R.; Johnson, B. E.; Meyerson, M. EGFR Mutations in Lung Cancer: Correlation with Clinical Response to Gefitinib Therapy. *Science* **2004**, *304*, 1497-1500.

149. Pao, W.; Miller, V.; Zakowski, M.; Doherty, J.; Politi, K.; Sarkaria, I.; Singh, B.; Heelan, R.; Rusch, V.; Fulton, L.; Mardis, E.; Kupfer, D.; Wilson, R.; Kris, M.; Varmus, H. EGF receptor gene mutations are common in lung cancers from "never smokers" and are associated with sensitivity of tumors to gefitinib and erlotinib. *Proc. Natl. Acad. Sci. U. S. A.* **2004**, *101*, 13306-13311.
150. Faivre, S.; Djelloul, S.; Raymond, E. New paradigms in anticancer therapy: targeting multiple signaling pathways with kinase inhibitors. *Semin. Oncol* **2006**, *33*, 407-420.
151. Hicklin, D. J.; Ellis, L. M. Role of the vascular endothelial growth factor pathway in tumor growth and angiogenesis. *Journal of Clinical Oncology* **2005**, *23*, 1011-1027.
152. Klebl, B. M.; Mueller, G. Second-generation kinase inhibitors. *Expert Opin. Ther. Targets* **2005**, *9*, 975-993.
153. Faivre, S.; Demetri, G.; Sargent, W.; Raymond, E. Molecular basis for sunitinib efficacy and future clinical development. *Nature Rev. Drug Discov.* **2007**, *6*, 734-745.
154. Lowinger, T. B.; Riedl, B.; Dumas, J.; Smith, R. A. Design and discovery of small molecules targeting raf-1 kinase. *Curr. Pharm. Des.* **2002**, *8*, 2269-2278.
155. Sun, L.; Liang, C.; Shirazian, S.; Zhou, Y.; Miller, T.; Cui, J.; Fukuda, J. Y.; Chu, J.-Y.; Nematalla, A.; Wang, X.; Chen, H.; Sistla, A.; Luu, T. C.; Tang, F.; Wei, J.; Tang, C. Discovery of 5-[5-fluoro-2-oxo-1,2-dihydroindol-(3z)-ylidenemethyl]-2,4-dimethyl-1H-pyrrole-3-carboxylic acid (2-diethylaminoethyl)amide, a novel tyrosine kinase inhibitor targeting vascular endothelial and platelet-derived growth factor receptor tyrosine kinase. *J. Med. Chem.* **2003**, *46*, 1116-1119.
156. Tokarski, J. S.; Newitt, J. A.; Chang, C. Y. J.; Cheng, J. D.; Wittekind, M.; Kiefer, S. E.; Kish, K.; Lee, F. Y. F.; Borzilleri, R.; Lombardo, L. J.; Xie, D.; Zhang, Y.; Klei, H. E. The structure of dasatinib (BMS-354825) bound to activated Abl kinase domain elucidates its inhibitory activity against imatinib-resistant Abl mutants. *Cancer Research* **2006**, *66*, 5790-5797.
157. Bikker, J. A.; Brooijmans, N.; Wissner, A.; Mansour, T. S. Kinase Domain Mutations in Cancer: Implications for Small Molecule Drug Design Strategies. *J. Med. Chem.* **2009**, *52*, 1493-1509.
158. Huse, M.; Kuriyan, J. The conformational plasticity of protein kinases. *Cell* **2002**, *109*, 275-282.
159. Liu, Y.; Gray, N. S. Rational design of inhibitors that bind to inactive kinase conformations. *Nat. Chem. Biol.* **2006**, *2*, 358-364.
160. Noronha, G.; Cao, J.; Chow, C. P.; Dneprovskaya, E.; Fine, R. M.; Hood, J.; Kang, X.; Klebansky, B.; Lohse, D.; Mak, C. C.; McPherson, A.; Palanki, M. S. S.; Pathak, V. P.; Renick, J.; Soll, R.; Zeng, B. Inhibitors of ABL and the ABL-T315I mutation. *Curr. Top. Med. Chem.* **2008**, *8*, 905-921.
161. Wood, J. M.; Bold, G.; Buchdunger, E.; Cozens, R.; Ferrari, S.; Frei, J.; Hofmann, F.; Mestan, J.; Mett, H.; O'Reilly, T.; Persohn, E.; Rosel, J.; Schnell, C.; Stover, D.; Theuer, A.; Towbin, H.; Wenger, F.; Woods-Cook, K.; Menrad, A.; Siemeister, G.; Schirner, M.; Thierauch, K.-H.; Schneider, M. R.; Dreves, J.; Martiny-Baron, G.; Totzke, F.; Marme, D. PTK787/ZK 222584, a novel and potent inhibitor of vascular endothelial growth factor receptor tyrosine kinases, impairs vascular

- endothelial growth factor-induced responses and tumor growth after oral administration. *Cancer Res.* **2000**, *60*, 2178-2189.
162. Yun, C.-H.; Mengwasser, K. E.; Toms, A. V.; Woo, M. S.; Greulich, H.; Wong, K.-K.; Meyerson, M.; Eck, M. J. The T790M mutation in EGFR kinase causes drug resistance by increasing the affinity for ATP. *Proc. Natl. Acad. Sci. U. S. A.* **2008**, *105*, 2070-2075.
 163. Zhang, X.; Gureasko, J.; Shen, K.; Cole, P. A.; Kuriyan, J. An allosteric mechanism for activation of the kinase domain of epidermal growth factor receptor. *Cell* **2006**, *125*, 1137-1149.
 164. Zhang, X.; Pickin, K. A.; Bose, R.; Jura, N.; Cole, P. A.; Kuriyan, J. Inhibition of the EGF receptor by binding of MIG6 to an activating kinase domain interface. *Nature* **2007**, *450*, 741-744.
 165. Levinson, N. M.; Kuchment, O.; Shen, K.; Young, M. A.; Koldobskiy, M.; Karplus, M.; Cole, P. A.; Kuriyan, J. A Src-like inactive conformation in the Abl tyrosine kinase domain. *PLoS Biol.* **2006**, *4*, 753-767.
 166. Liao, J. J.-L.; Andrews, R. C. Targeting protein multiple conformations: a structure-based strategy for kinase drug design. *Curr. Top. Med. Chem.* **2007**, *7*, 1394-1407.
 167. Carter, T. A.; Wodicka, L. M.; Shah, N. P.; Velasco, A. M.; Fabian, M. A.; Treiber, D. K.; Milanov, Z. V.; Atteridge, C. E.; Biggs, W. H., III; Edeen, P. T.; Floyd, M.; Ford, J. M.; Grotzfeld, R. M.; Herrgard, S.; Insko, D. E.; Mehta, S. A.; Patel, H. K.; Pao, W.; Sawyers, C. L.; Varmus, H.; Zarrinkar, P. P.; Lockhart, D. J. Inhibition of drug-resistant mutants of ABL, KIT, and EGF receptor kinases. *Proc. Natl. Acad. Sci. U. S. A.* **2005**, *102*, 11011-11016.
 168. Ji, H.; Li, D.; Chen, L.; Shimamura, T.; Kobayashi, S.; McNamara, K.; Mahmood, U.; Mitchell, A.; Sun, Y.; Al-Hashem, R.; Chirieac, L. R.; Padera, R.; Bronson, R. T.; Kim, W.; Janne, P. A.; Shapiro, G. I.; Tenen, D.; Johnson, B. E.; Weissleder, R.; Sharpless, N. E.; Wong, K.-K. The impact of human EGFR kinase domain mutations on lung tumorigenesis and in vivo sensitivity to EGFR-targeted therapies. *Cancer Cell* **2006**, *9*, 485-495.
 169. Liu, Y.; Bishop, A.; Witucki, L.; Kraybill, B.; Shimizu, E.; Tsien, J.; Ubersax, J.; Blethrow, J.; Morgan, D. O.; Shokat, K. M. Structural basis for selective inhibition of Src family kinases by PP1. *Chem. Biol.* **1999**, *6*, 671-678.
 170. Modugno, M.; Casale, E.; Soncini, C.; Rosettani, P.; Colombo, R.; Lupi, R.; Rusconi, L.; Fancelli, D.; Carpinelli, P.; Cameron, A. D.; Isacchi, A.; Moll, J. Crystal structure of the T315I Abl mutant in complex with the aurora kinases inhibitor PHA-739358. *Cancer Res.* **2007**, *67*, 7987-7990.
 171. Young, M. A.; Shah, N. P.; Chao, L. H.; Seeliger, M.; Milanov, Z. V.; Biggs, W. H., III; Treiber, D. K.; Patel, H. K.; Zarrinkar, P. P.; Lockhart, D. J.; Sawyers, C. L.; Kuriyan, J. Structure of the kinase domain of an imatinib-resistant Abl mutant in complex with the aurora kinase inhibitor VX-680. *Cancer Res.* **2006**, *66*, 1007-1014.
 172. Zhou, T.; Parillon, L.; Li, F.; Wang, Y.; Keats, J.; Lamore, S.; Xu, Q.; Shakespeare, W.; Dalgarno, D.; Zhu, X. Crystal structure of the T315I mutant of Abl kinase. *Chem. Biol. Drug Des.* **2007**, *70*, 171-181.
 173. Yun, C.-H.; Boggon, T. J.; Li, Y.; Woo, M. S.; Greulich, H.; Meyerson, M.; Eck,

- M. J. Structures of lung cancer-derived EGFR mutants and inhibitor complexes: mechanism of activation and insights into differential inhibitor sensitivity. *Cancer Cell* **2007**, *11*, 217-227.
174. Beghini, A.; Cairoli, R.; Morra, E.; Larizza, L. *In vivo* differentiation of mast cells from acute myeloid leukemia blasts carrying a novel activating ligand-independent C-kit mutation; *Blood Cells Mol. Dis.* **1998**, *24*, 262-270.
 175. Chompret, A.; Kannengiesser, C.; Barrois, M.; Terrier, P.; Dahan, P.; Tursz, T.; Lenoir, G. M.; Bressac-De Paillerets, B. PDGFRA germline mutation in a family with multiple cases of gastrointestinal stromal tumor. *Gastroenterology* **2004**, *126*, 318-321.
 176. Heinrich, M. C.; Corless, C. L.; Duensing, A.; McGreevey, L.; Chen, C.-J.; Joseph, N.; Singer, S.; Griffith, D. J.; Haley, A.; Town, A.; Demetri, G. D.; Fletcher, C. D. M.; Fletcher, J. A. PDGFRA Activating Mutations in Gastrointestinal Stromal Tumors. *Science* **2003**, *299*, 708-710.
 177. Traxler, P.; Allegrini, P. R.; Brandt, R.; Brueggen, J.; Cozens, R.; Fabbro, D.; Grosios, K.; Lane, H. A.; McSheehy, P.; Mestan, J.; Meyer, T.; Tang, C.; Wartmann, M.; Wood, J.; Caravatti, G. AEE788: A Dual Family Epidermal Growth Factor Receptor/ErbB2 and Vascular Endothelial Growth Factor Receptor Tyrosine Kinase Inhibitor with Antitumor and Antiangiogenic Activity. *Cancer Res.* **2004**, *64*, 4931-4941.
 178. Harris, P. A.; Bolor, A.; Cheung, M.; Kumar, R.; Crosby, R. M.; Davis-Ward, R. G.; Epperly, A. H.; Hinkle, K. W.; Hunter, R. N., III; Johnson, J. H.; Knick, V. B.; Laudeman, C. P.; Luttrell, D. K.; Mook, R. A.; Nolte, R. T.; Rudolph, S. K.; Szewczyk, J. R.; Truesdale, A. T.; Veal, J. M.; Wang, L.; Stafford, J. A. Discovery of 5-[[4-[(2,3-Dimethyl-2H-indazol-6-yl)methylamino]-2-pyrimidinyl]amino]-2-methyl-benzenesulfonamide (Pazopanib), a novel and potent vascular endothelial growth factor receptor inhibitor. *J. Med. Chem.* **2008**, *51*, 4632-4640.
 179. Gangjee, A.; Yang, J.; Ihnat, M. A.; Kamat, S. Antiangiogenic and antitumor agents. Design, synthesis, and evaluation of novel 2-amino-4-(3-bromoanilino)-6-benzylsubstituted pyrrolo[2,3-*d*]pyrimidines as inhibitors of receptor tyrosine kinases. *Bioorg. Med. Chem.* **2003**, *11*, 5155-5170.
 180. Gangjee, A.; Namjoshi, O. A.; Yu, J.; Ihnat, M. A.; Thorpe, J. E.; Warnke, L. A. Design, synthesis and biological evaluation of substituted pyrrolo[2,3-*d*]pyrimidines as multiple receptor tyrosine kinase inhibitors and antiangiogenic agents. *Bioorg. Med. Chem.* **2008**, *16*, 5514-5528.
 181. Gangjee, A.; Namjoshi, O. A.; Ihnat, M. A.; Buchanan, A. The contribution of a 2-amino group on receptor tyrosine kinase inhibition and antiangiogenic activity in 4-anilino-substituted pyrrolo[2,3-*d*]pyrimidines. *Bioorg. Med. Chem. Lett.* **2010**, *20*, 3177-3181.
 182. Gangjee, A.; Kurup, S.; Ihnat, M. A.; Thorpe, J. E.; Shenoy, S. S. Synthesis and biological activity of N 4-phenylsubstituted-6-(2,4-dichloro phenylmethyl)-7H-pyrrolo[2,3-*d*]pyrimidine-2,4-diamines as vascular endothelial growth factor receptor-2 inhibitors and antiangiogenic and antitumor agents. *Bioorg. Med. Chem.* **2010**, *18*, 3575-3587.
 183. Gangjee, A.; Zhao, Y.; Raghavan, S.; Ihnat, M. A.; Disch, B. C. Design, synthesis and evaluation of 2-amino-4-m-bromoanilino-6-arylmethyl-7H-pyrrolo[2,3-

- d*]pyrimidines as tyrosine kinase inhibitors and antiangiogenic agents. *Bioorg. Med. Chem.* **2010**, *18*, 5261-5273.
184. Bridges, A. J. Chemical inhibitors of protein kinases. *Chem. Rev.* **2001**, *101*, 2541-2571.
 185. Traxler, P.; Bold, G.; Frei, J.; Lang, M.; Lydon, N.; Mett, H.; Buchdunger, E.; Meyer, T.; Mueller, M.; Furet, P. Use of a pharmacophore model for the design of EGFR tyrosine kinase inhibitors: 4-(phenylamino)pyrazolo[3,4-*d*]pyrimidines. *J. Med. Chem.* **1997**, *40*, 3601-3616.
 186. Traxler, P. M.; Furet, P.; Mett, H.; Buchdunger, E.; Meyer, T.; Lydon, N. 4-(Phenylamino)pyrrolopyrimidines: Potent and selective, ATP site directed inhibitors of the EGF-receptor protein tyrosine kinase. *J. Med. Chem.* **1996**, *39*, 2285-2292.
 187. Traxler, P.; Frei, J.; Bold, G. Preparation of pyrrolopyrimidines as inhibitors of protein kinases. 97-EP1279727199, 19970113., **1997**.
 188. Garcia-Echeverria, C.; Traxler, P.; Evans, D. B. ATP site-directed competitive and irreversible inhibitors of protein kinases. *Med. Res. Rev.* **2000**, *20*, 28-57.
 189. Wilson, S. M.; Barsoum, M. J.; Wilson, B. W.; Pappone, P. A. Purine nucleotides modulate proliferation of brown fat preadipocytes. *Cell Proliferation* **1999**, *32*, 131-140.
 190. Vu, M. T.; Smith, C. F.; Burger, P. C.; Klintworth, G. K. An evaluation of methods to quantitate the chick chorioallantoic membrane assay in angiogenesis. *Laboratory investigation; a journal of technical methods and pathology* **1985**, *53*, 499-508.
 191. Xu, M.; Yu, L.; Wan, B.; Yu, L.; Huang, Q. Predicting Inactive Conformations of Protein Kinases Using Active Structures: Conformational Selection of Type-II Inhibitors. *PLoS ONE* **2011**, *6*, e22644.
 192. Stamos, J.; Sliwkowski, M. X.; Eigenbrot, C. Structure of the epidermal growth factor receptor kinase domain alone and in complex with a 4-anilinoquinazoline inhibitor. *J. Biol. Chem.* **2002**, *277*, 46265-46272.
 193. Miyamoto, N.; Sakai, N.; Hirayama, T.; Miwa, K.; Oguro, Y.; Oki, H.; Okada, K.; Takagi, T.; Iwata, H.; Awazu, Y.; Yamasaki, S.; Takeuchi, T.; Miki, H.; Hori, A.; Imamura, S. Discovery of N-[5-(2-((cyclopropylcarbonyl)amino)imidazo[1,2-*b*]pyridazin-6-yl)oxy)-2-methylphenyl]-1,3-dimethyl-1H-pyrazole-5-carboxamide (TAK-593), a highly potent VEGFR2 kinase inhibitor. *Bioorg. Med. Chem.* **2013**, *21*, 2333-2345.
 194. McTigue, M.; Murray, B. W.; Chen, J. H.; Deng, Y.-L.; Solowiej, J.; Kania, R. S. Molecular conformations, interactions, and properties associated with drug efficiency and clinical performance among VEGFR TK inhibitors. *Proc. Natl Acad. Sci.* **2012**, *109*, 18281-18289.
 195. Okaniwa, M.; Hirose, M.; Imada, T.; Ohashi, T.; Hayashi, Y.; Miyazaki, T.; Arita, T.; Yabuki, M.; Kakoi, K.; Kato, J.; Takagi, T.; Kawamoto, T.; Yao, S.; Sumita, A.; Tsutsumi, S.; Tottori, T.; Oki, H.; Sang, B.-C.; Yano, J.; Aertgeerts, K.; Yoshida, S.; Ishikawa, T. Design and synthesis of novel DFG-Out RAF/vascular endothelial growth factor receptor 2 (vegfr2) inhibitors. 1. exploration of [5,6]-fused bicyclic scaffolds. *J. Med. Chem.* **2012**, *55*, 3452-3478.
 196. Oguro, Y.; Miyamoto, N.; Okada, K.; Takagi, T.; Iwata, H.; Awazu, Y.; Miki, H.;

- Hori, A.; Kamiyama, K.; Imamura, S. Design, synthesis, and evaluation of 5-methyl-4-phenoxy-5H-pyrrolo[3,2-d]pyrimidine derivatives: Novel VEGFR2 kinase inhibitors binding to inactive kinase conformation. *Bioorg. Med. Chem.* **2010**, *18*, 7260-7273.
197. McTigue, M.; Wickersham, J.; Marrone, T. Crystal Structure Of The Vegfr2 Kinase Domain In Complex With Pf-00337210 (N,2-Dimethyl-6-(7-(2-Morpholinoethoxy) Quinolin-4-Yloxy)Benzofuran-3-Carboxamide). In **2013**.doi: 10.1021/pdb2xir/pdb
 198. Cee, V. J.; Cheng, A. C.; Romero, K.; Bellon, S.; Mohr, C.; Whittington, D. A.; Bak, A.; Bready, J.; Caenepeel, S.; Coxon, A.; Deak, H. L.; Fretland, J.; Gu, Y.; Hodous, B. L.; Huang, X.; Kim, J. L.; Lin, J.; Long, A. M.; Nguyen, H.; Olivieri, P. R.; Patel, V. F.; Wang, L.; Zhou, Y.; Hughes, P.; Geuns-Meyer, S. Pyridyl-pyrimidine benzimidazole derivatives as potent, selective, and orally bioavailable inhibitors of Tie-2 kinase. *Bioorg. Med. Chem. Lett.* **2009**, *19*, 424-427.
 199. Harmange, J.-C.; Weiss, M. M.; Germain, J.; Polverino, A. J.; Borg, G.; Bready, J.; Chen, D.; Choquette, D.; Coxon, A.; DeMelfi, T.; DiPietro, L.; Doerr, N.; Estrada, J.; Flynn, J.; Graceffa, R. F.; Harriman, S. P.; Kaufman, S.; La, D. S.; Long, A.; Martin, M. W.; Neervannan, S.; Patel, V. F.; Potashman, M.; Regal, K.; Roveto, P. M.; Schrag, M. L.; Starnes, C.; Tasker, A.; Teffera, Y.; Wang, L.; White, R. D.; Whittington, D. A.; Zanon, R. Naphthamides as novel and potent vascular endothelial growth factor receptor tyrosine kinase inhibitors: design, synthesis, and evaluation. *J. Med. Chem.* **2008**, *51*, 1649-1667.
 200. Miyazaki, Y.; Matsunaga, S.; Tang, J.; Maeda, Y.; Nakano, M.; Philippe, R. J.; Shibahara, M.; Liu, W.; Sato, H.; Wang, L.; Nolte, R. T. Novel 4-aminofuro[2,3-d]pyrimidines as Tie-2 and VEGFR2 dual inhibitors. *Bioorg. Med. Chem. Lett.* **2005**, *15*, 2203-2207.
 201. Assefa, H.; Kamath, S.; Buolamwini, J. K. 3D-QSAR and docking studies on 4-anilinoquinazoline and 4-anilinoquinoline epidermal growth factor receptor (EGFR) tyrosine kinase inhibitors. *J. Comput.-Aided Mol. Des.* **2003**, *17*, 475-493.
 202. Caballero, J.; Fernandez, M.; Saavedra, M.; Gonzalez-Nilo, F. D. 2D Autocorrelation, CoMFA, and CoMSIA modeling of protein tyrosine kinases' inhibition by substituted pyrido[2,3-d]pyrimidine derivatives. *Bioorg. Med. Chem.* **2008**, *16*, 810-821.
 203. Hyun, K. H.; Kwack, I. Y.; Lee, D. Y.; Park, H. Y.; Lee, B.-S.; Kim, C. K. Ligand-based QSAR studies on the indolinones derivatives as inhibitors of the protein tyrosine kinase of fibroblast growth factor receptor by CoMFA and CoMSIA. *Bull. Korean Chem. Soc.* **2004**, *25*, 1801-1806.
 204. Jiang, Q.; Liao, H.; Yang, Q.; Zan, W.; Zang, Z. Pharmacophore-based 3D-QSAR as a predictive method for the QSAR analysis on a series of potent and selective inhibitors for three kinases of RTK family. *Mol. Simul.* **2010**, *36*, 693-707.
 205. Li, Y.-S.; Zhou, L.; Ma, X. Molecular docking and 3D QSAR studies of substituted 4-amino-1H-pyrazolo[3,4-d]pyrimidines as insulin-like growth factor-1 receptor (IGF1R) inhibitors. *Med. Chem. Res.* **2012**, *21*, 3301-3311.
 206. Lu, X.; Chen, Y.; You, Q. Pharmacophore guided 3D-QSAR CoMFA analysis of amino substituted nitrogen heterocycle ureas as kdr inhibitors. *QSAR Comb. Sci.*

- 2009**, 28, 1524-1536.
207. Parasuk, W.; Parasuk, V.; Wolschann, P. In *3D-QSAR studies of 4-phenylaminoquinazoline derivatives as EGFR tyrosine kinase inhibitor*, **2006**; Computer Aided Drug Design & Development Society in Turkey: 2006; pp 162-163.
 208. Tsakovska, I.; Pinto-Bazurco, M.; Pajeva, I. Receptor tyrosine kinase inhibitors: QSAR and molecular modeling study. *Farmatsiya (Sofia, Bulg.)* **2005**, 52, 11-15.
 209. Wu, X.; Wu, S.; Chen, W.-H. Molecular docking and 3D-QSAR study on 4-(1H-indazol-4-yl) phenylamino and aminopyrazolopyridine urea derivatives as kinase insert domain receptor (KDR) inhibitors. *J. Mol. Model.* **2012**, 18, 1207-1218.
 210. Zhang, Y.; Liu, H.; Jiao, Y.; Yuan, H.; Wang, F.; Lu, S.; Yao, S.; Ke, Z.; Tai, W.; Jiang, Y.; Chen, Y.; Lu, T. De novo design of N-(pyridin-4-ylmethyl)aniline derivatives as KDR inhibitors: 3D-QSAR, molecular fragment replacement, protein-ligand interaction fingerprint, and ADMET prediction. *Mol. Diversity* **2012**, 16, 787-802.
 211. Zhu, L. L.; Hou, T. J.; Chen, L. R.; Xu, X. J. 3D QSAR analyses of novel tyrosine kinase inhibitors based on pharmacophore alignment. *J. Chem. Inf. Comput. Sci.* **2001**, 41, 1032-1040.
 212. Du, J.; Lei, B.; Qin, J.; Liu, H.; Yao, X. Molecular modeling studies of vascular endothelial growth factor receptor tyrosine kinase inhibitors using QSAR and docking. *J Mol Graph Model* **2009**, 27, 642-654.
 213. Conde, C.; Caceres, A. Microtubule assembly, organization and dynamics in axons and dendrites. *Nat Rev Neurosci* **2009**, 10, 319-332.
 214. Horio, T.; Uzawa, S.; Jung, M. K.; Oakley, B. R.; Tanaka, K.; Yanagida, M. The fission yeast $\hat{\Gamma}^3$ -tubulin is essential for mitosis and is localized at microtubule organizing centers. *J. Cell Sci.* **1991**, 99, 693-700.
 215. McIntosh, J. R.; McDonald, K. L. The mitotic spindle. *Sci Am* **1989**, 261, 48-56.
 216. <http://www.britannica.com/EBchecked/media/66085/Stages-of-mitosis>. Accessed 10/10/2013
 217. Margolis, R. L.; Wilson, L. Opposite end assembly and disassembly of microtubules at steady state in vitro. *Cell* **1978**, 13, 1-8.
 218. Mitchison, T.; Kirschner, M. Dynamic instability of microtubule growth. *Nature* **1984**, 312, 237-242.
 219. Desai, A.; Mitchison, T. J. Microtubule polymerization dynamics. *Annu. Rev. Cell Dev. Biol.* **1997**, 13, 83-117.
 220. Howard, J.; Hyman, A. A. Dynamics and mechanics of the microtubule plus end. *Nature* **2003**, 422, 753-758.
 221. Jordan, M. A.; Wilson, L. Microtubules as a target for anticancer drugs. *Nature Rev. Cancer* **2004**, 4, 253-265.
 222. Panda, D.; Goode, B. L.; Feinstein, S. C.; Wilson, L. Kinetic stabilization of microtubule dynamics at steady state by tau and microtubule-binding domains of tau. *Biochemistry* **1995**, 34, 11117-11127.
 223. Panda, D.; Miller, H. P.; Wilson, L. Rapid treadmilling of brain microtubules free of microtubule-associated proteins in vitro and its suppression by tau. *Proc. Natl. Acad. Sci.* **1999**, 96, 12459-12464.
 224. Panda, D.; Miller, H. P.; Wilson, L. Determination of the Size and Chemical

- Nature of the Stabilizing "Cap" at Microtubule Ends Using Modulators of Polymerization Dynamics. *Biochemistry* **2002**, *41*, 1609-1617.
225. Panda, D.; Rathinasamy, K.; Santra, M. K.; Wilson, L. Kinetic suppression of microtubule dynamic instability by griseofulvin: Implications for its possible use in the treatment of cancer. *Proc. Natl. Acad. Sci. U. S. A.* **2005**, *102*, 9878-9883.
 226. Panda, D.; Samuel, J. C.; Massie, M.; Feinstein, S. C.; Wilson, L. Differential regulation of microtubule dynamics by three- and four-repeat tau: Implications for the onset of neurodegenerative disease. *Proc. Natl. Acad. Sci. U. S. A.* **2003**, *100*, 9548-9553.
 227. Cassimeris, L. Accessory protein regulation of microtubule dynamics throughout the cell cycle. *Curr. Opin. Cell Biol.* **1999**, *11*, 134-141.
 228. Panda, D.; Daijo, J. E.; Jordan, M. A.; Wilson, L. Kinetic stabilization of microtubule dynamics at steady state *in vitro* by substoichiometric concentrations of tubulin-colchicine complex. *Biochemistry* **1995**, *34*, 9921-9929.
 229. Gangjee, A.; Yu, J.; Copper, J. E.; Smith, C. D. Discovery of novel antitumor antimetabolic agents that also reverse tumor resistance. *J. Med. Chem.* **2007**, *50*, 3290-3301.
 230. Heald, R.; Nogales, E. Microtubule dynamics. *J. Cell Sci.* **2002**, *115*, 3-4.
 231. Lowe, J.; Li, H.; Downing, K. H.; Nogales, E. Refined structure of alpha beta-tubulin at 3.5 Å resolution. *J. Mol. Biol.* **2001**, *313*, 1045-1057.
 232. Ravelli, R. B. G.; Gigant, B.; Curmi, P. A.; Jourdain, I.; Lachkar, S.; Sobel, A.; Knossow, M. Insight into tubulin regulation from a complex with colchicine and a stathmin-like domain. *Nature* **2004**, *428*, 198-202.
 233. Tozer, G. M.; Kanthou, C.; Parkins, C. S.; Hill, S. A. The biology of the combretastatins as tumour vascular targeting agents. *Int. J. Exp. Pathol.* **2002**, *83*, 21-38.
 234. Cortes, J.; Baselga, J. Targeting the microtubules in breast cancer beyond taxanes: the epothilones. *Oncologist* **2007**, *12*, 271-280.
 235. Bollag, D. M.; McQueney, P. A.; Zhu, J.; Hensens, O.; Koupal, L.; Liesch, J.; Goetz, M.; Lazarides, E.; Woods, C. M. Epothilones, a new class of microtubule-stabilizing agents with a taxol-like mechanism of action. *Cancer Res.* **1995**, *55*, 2325-33.
 236. Lee, F. Y. F.; Borzilleri, R.; Fairchild, C. R.; Kim, S.-H.; Long, B. H.; Reventos-Suarez, C.; Vite, G. D.; Rose, W. C.; Kramer, R. A. BMS-247550: A novel epothilone analog with a mode of action similar to paclitaxel but possessing superior antitumor efficacy. *Clin. Cancer Res.* **2001**, *7*, 1429-1437.
 237. Pronzato, P. New therapeutic options for chemotherapy-resistant metastatic breast cancer: the epothilones. *Drugs* **2008**, *68*, 139-146.
 238. Yang, Y.; Zhao, L.; Wang, Y.-F.; Chang, M.-L.; Huo, C.-H.; Gu, Y.-C.; Shi, Q.-W.; Kiyota, H. Chemical and Pharmacological Research on Plants from the Genus *Senecio*. *Chem. Biodiversity* **2011**, *8*, 13-72.
 239. Wartmann, M.; Altmann, K. H. The biology and medicinal chemistry of epothilones. *Curr. Med. Chem. Anticancer Agents* **2002**, *2*, 123-48.
 240. Jordan, M. A.; Kamath, K. How do microtubule-targeted drugs work? An overview. *Curr. Cancer Drug Targets* **2007**, *7*, 730-742.
 241. Nogales, E.; Wolf, S. G.; Khan, I. A.; Luduena, R. F.; Downing, K. H. Structure of

- tubulin at 6.5 Å and location of the taxol-binding site. *Nature* **1995**, 375, 424-427.
242. Ranaivoson, F. M.; Gigant, B.; Berritt, S.; Joullie, M.; Knossow, M. Structural plasticity of tubulin assembly probed by vinca-domain ligands. *Acta Crystallographica Section D* **2012**, 68, 927-934.
 243. Nguyen, T. L.; McGrath, C.; Hermone, A. R.; Burnett, J. C.; Zaharevitz, D. W.; Day, B. W.; Wipf, P.; Hamel, E.; Gussio, R. A common pharmacophore for a diverse set of colchicine site inhibitors using a structure-based approach. *J. Med. Chem.* **2005**, 48, 6107-6116.
 244. Szakacs, G.; Paterson, J. K.; Ludwig, J. A.; Booth-Genthe, C.; Gottesman, M. M. Targeting multidrug resistance in cancer. *Nature Rev. Drug Discov.* **2006**, 5, 219-234.
 245. Dano, K. Active outward transport of daunomycin in resistant Ehrlich ascites tumor cells. *Biochim. Biophys. Acta, Biomembr.* **1973**, 323, 466-83.
 246. Juliano, R. L.; Ling, V. A surface glycoprotein modulating drug permeability in Chinese hamster ovary cell mutants. *Biochim. Biophys. Acta, Biomembr.* **1976**, 455, 152-162.
 247. Chen, C. J.; Chin, J. E.; Ueda, K.; Clark, D. P.; Pastan, I.; Gottesman, M. M.; Roninson, I. B. Internal duplication and homology with bacterial transport proteins in the *mdr1* (P-glycoprotein) gene from multidrug-resistant human cells. *Cell* **1986**, 47, 381-389.
 248. Ueda, K.; Cardarelli, C.; Gottesman, M. M.; Pastan, I. Expression of a full-length cDNA for the human "MDR1" gene confers resistance to colchicine, doxorubicin, and vinblastine. *Proc Natl Acad Sci* **1987**, 84, 3004-3008.
 249. Gerlach, J. H.; Endicott, J. A.; Juranka, P. F.; Henderson, G.; Sarangi, F.; Deuchars, K. L.; Ling, V. Homology between P-glycoprotein and a bacterial hemolysin transport protein suggests a model for multidrug resistance. *Nature* **1986**, 324, 485-9.
 250. Shen, D. W.; Cardarelli, C.; Hwang, J.; Cornwell, M.; Richert, N.; Ishii, S.; Pastan, I.; Gottesman, M. M. Multiple drug-resistant human KB carcinoma cells independently selected for high-level resistance to colchicine, adriamycin, or vinblastine show changes in expression of specific proteins. *J. Biol. Chem.* **1986**, 261, 7762-7770.
 251. Gros, P.; Croop, J.; Housman, D. Mammalian multidrug resistance gene: complete cDNA sequence indicates strong homology to bacterial transport proteins. *Cell* **1986**, 47, 371-380.
 252. McGrath, T.; Center, M. S. Mechanisms of multidrug resistance in HL60 cells: evidence that a surface membrane protein distinct from P-glycoprotein contributes to reduced cellular accumulation of drug. *Cancer Res.* **1988**, 48, 3959-3963.
 253. Mirski, S. E. L.; Gerlach, J. H.; Cole, S. P. C. Multidrug resistance in a human small cell lung cancer cell line selected in adriamycin. *Cancer Res.* **1987**, 47, 2594-2598.
 254. Cole, S. P. C. Patterns of cross-resistance in a multidrug-resistant small-cell lung carcinoma cell line. *Cancer Chemother. Pharmacol.* **1990**, 26, 250-256.
 255. Cole, S. P. C.; Bhardwaj, G.; Gerlach, J. H.; Mackie, J. E.; Grant, C. E.; Almquist, K. C.; Stewart, A. J.; Kurz, E. U.; Duncan, A. M. V.; Deeley, R. G. Overexpression of a transporter gene in a multidrug-resistant human lung cancer

- cell line. *Science* **1992**, 258, 1650-1654.
256. Tsuruo, T.; Iida, H.; Tsukagoshi, S.; Sakurai, Y. Overcoming of vincristine resistance in P388 leukemia in vivo and in vitro through enhanced cytotoxicity of vincristine and vinblastine by verapamil. *Cancer Res.* **1981**, 41, 1967-1972.
 257. Martin, C.; Berridge, G.; Mistry, P.; Higgins, C.; Charlton, P.; Callaghan, R. The molecular interaction of the high affinity reversal agent XR9576 with P-glycoprotein. *Br. J. Pharmacol.* **1999**, 128, 403-411.
 258. Stewart, A.; Steiner, J.; Mellows, G.; Laguda, B.; Norris, D.; Bevan, P. Phase I trial of XR9576 in healthy volunteers demonstrates modulation of P-glycoprotein in CD56+ lymphocytes after oral and intravenous administration. *Clinical Cancer Res.* **2000**, 6, 4186-4191.
 259. Dantzig, A. H.; Shepard, R. L.; Law, K. L.; Ehlhardt, W. J.; Baughman, T. M.; Bumol, T. F.; Starling, J. J. Reversal of P-glycoprotein-mediated multidrug resistance by a potent cyclopropyldibenzosuberane modulator, LY335979. *Cancer Res.* **1996**, 56, 4171-4179.
 260. Kapoor, K.; Sim, H.; Ambudkar, S. Multidrug Resistance in Cancer: A Tale of ABC Drug Transporters. In *Molecular Mechanisms of Tumor Cell Resistance to Chemotherapy*, Bonavida, B., Ed. Springer New York: **2013**; Vol. 1, pp 1-34.
 261. Nobili, S.; Landini, I.; Mazzei, T.; Mini, E. Overcoming tumor multidrug resistance using drugs able to evade P-glycoprotein or to exploit its expression. *Med. Res. Rev.* **2012**, 32, 1220-1262.
 262. Dantzig, A. H.; de Alwis, D. P.; Burgess, M. Considerations in the design and development of transport inhibitors as adjuncts to drug therapy. *Adv. Drug Delivery Rev.* **2003**, 55, 133-150.
 263. Sandor, V.; Fojo, T.; Bates, S. E. Future perspectives for the development of P-glycoprotein modulators. *Drug Resistance Updates* **1998**, 1, 190-200.
 264. Aller, S. G.; Yu, J.; Ward, A.; Weng, Y.; Chittaboina, S.; Zhuo, R.; Harrell, P. M.; Trinh, Y. T.; Zhang, Q.; Urbatsch, I. L.; Chang, G. Structure of P-glycoprotein reveals a molecular basis for poly-specific drug binding. *Science* **2009**, 323, 1718-1722.
 265. Conlin, A.; Fornier, M.; Hudis, C.; Kar, S.; Kirkpatrick, P. Ixabepilone. *Nature Rev. Drug Discov.* **2007**, 6, 953-954.
 266. Gangjee, A.; Yu, J.; Copper, J. E.; Smith, C. D. Discovery of novel antitumor antimetabolic agents that also reverse tumor resistance. *J. Med. Chem.* **2007**, 50, 3290-3301.
 267. Boyd, M. R. P., K. D.; Rbinstein, L. R. In *Cytotoxic Anticancer Drugs: Models and Concepts for Drug Discovery and Development*; Vleriotte, F. A., Corbett, T. H., Baker, L. H., Eds.; Kluwer Academic: Hingham, MA, **1992**; pp 11-34.
 268. Bai, R.; Paull, K. D.; Herald, C. L.; Malspeis, L.; Pettit, G. R.; Hamel, E. Halichondrin B and homohalichondrin B, marine natural products binding in the vinca domain of tubulin. Discovery of tubulin-based mechanism of action by analysis of differential cytotoxicity data. *J. Biol. Chem.* **1991**, 266, 15882-15889.
 269. Paull, K. D.; Lin, C. M.; Malspeis, L.; Hamel, E. Identification of novel antimetabolic agents acting at the tubulin level by computer-assisted evaluation of differential cytotoxicity data. *Cancer Res.* **1992**, 52, 3892-900.
 270. Gangjee, A.; Namjoshi, O. A.; Keller, S. N.; Smith, C. D. 2-Amino-4-methyl-5-

- phenylethyl substituted-7-N-benzyl-pyrrolo[2,3-*d*]pyrimidines as novel antitumor antimetabolic agents that also reverse tumor resistance. *Bioorg. Med. Chem.* **2011**, *19*, 4355-4365.
271. Gangjee, A.; Kurup, S.; Smith, C. D. Synthesis of 5,7-disubstituted-4-methyl-7*H*-pyrrolo[2,3-*d*]pyrimidin-2-amines as microtubule inhibitors. *Bioorg. Med. Chem.* **2013**, *21*, 1180-1189.
 272. Gangjee, A.; Zhao, Y.; Lin, L.; Raghavan, S.; Roberts, E. G.; Risinger, A. L.; Hamel, E.; Mooberry, S. L. Synthesis and discovery of water-soluble microtubule targeting agents that bind to the colchicine site on tubulin and circumvent pgp mediated resistance. *J. Med. Chem.* **2011**, *54*, 913.
 273. Gangjee, A.; Zhao, Y.; Hamel, E.; Westbrook, C.; Mooberry, S. L. Synthesis and biological activities of (*R*)- and (*S*)-N-(4-methoxyphenyl)-N,2,6-trimethyl-6,7-dihydro-5*H*-cyclopenta[*d*]pyrimidin-4-aminium chloride as potent cytotoxic antitubulin agents. *J. Med. Chem.* **2011**, *54*, 6151-6155.
 274. Gangjee, A.; Pavana, R.; Li, W.; Hamel, E.; Westbrook, C.; Mooberry, S. Novel water-soluble substituted pyrrolo[3,2-*d*]pyrimidines: design, synthesis, and biological evaluation as antitubulin antitumor agents. *Pharmaceutical Res.* **2012**, *29*, 3033-3039.
 275. Jilek, R. J.; Cramer, R. D. Topomers: A Validated Protocol for Their Self-Consistent Generation. *J. Cheml Inf. Comput. Sci.* **2004**, *44*, 1221-1227.
 276. Wendt, B.; Mülbaier, M.; Wawro, S.; Schultes, C.; Alonso, J.; Janssen, B.; Lewis, J. Toluidinesulfonamide Hypoxia-Induced Factor 1 inhibitors: alleviating drug-drug interactions through use of pubchem data and comparative molecular field analysis guided synthesis. *J. Med. Chem.* **2011**, *54*, 3982-3986.
 277. Cramer, R. D.; Clark, R. D.; Patterson, D. E.; Ferguson, A. M. Bioisosterism as a Molecular Diversity Descriptor: Steric Fields of Single "Topomeric" Conformers. *J. Med. Chem.* **1996**, *39*, 3060-3069.
 278. Cramer, R. D. R-group template CoMFA combines benefits of "ad hoc" and topomer alignments using 3D-QSAR for lead optimization. *J. Comput.-Aided Mol. Des.* **2012**, *26*, 805-819.
 279. Sun, X. H.; Guan, J. Q.; Tan, J. J.; Liu, C.; Wang, C. X. 3D-QSAR studies of quinoline ring derivatives as HIV-1 integrase inhibitors. *SAR QSAR Environ. Res.* **2012**, *23*, 683-703.
 280. Ismail, M. A. H.; Abou, E. E. D. A.; Abouzid, K. A. M.; Mahmoud, A. H. Integrated structure-based activity prediction model of benzothiadiazines on various genotypes of HCV NS5b polymerase (1a, 1b and 4) and its application in the discovery of new derivatives. *Bioorg. Med. Chem.* **2012**, *20*, 2455-2478.
 281. Subramanian, G.; Rao, S. N. An integrated computational workflow for efficient and quantitative modeling of renin inhibitors. *Bioorg. Med. Chem.* **2012**, *20*, 851-858.
 282. Gadhe, C. G.; Madhavan, T.; Kothandan, G.; Cho, S. J. In silico quantitative structure-activity relationship studies on P-gp modulators of tetrahydroisoquinoline-ethyl-phenylamine series. *BMC Struct. Biol.* **2011**, *11*, 5.
 283. Wendt, B.; Mulbaier, M.; Wawro, S.; Schultes, C.; Alonso, J.; Janssen, B.; Lewis, J. Toluidinesulfonamide hypoxia-induced factor 1 inhibitors: alleviating drug-drug interactions through use of pubchem data and comparative molecular field

- analysis guided synthesis. *J. Med. Chem.* **2011**, *54*, 3982-3986.
284. Piper, J. R.; McCaleb, G. S.; Montgomery, J. A.; Kisliuk, R. L.; Gaumont, Y.; Sirotnak, F. M. Syntheses and antifolate activity of 5-methyl-5-deaza analogs of aminopterin, methotrexate, folic acid, and N10-methylfolic acid. *J. Med. Chem.* **1986**, *29*, 1080-1087.
 285. Mulvey, D. M.; Cottis, S. G.; Tieckelmann, H. The synthesis of 2,4,6-trisubstituted pyrido[2,3-*d*]pyrimidines from 2-amino-3,5-dicyanopyridine. *J. Org. Chem.* **1964**, *29*, 2903-2907.
 286. Su, T. L.; Huang, J. T.; Burchenal, J. H.; Watanabe, K. A.; Fox, J. J. Synthesis and biological activities of 5-deaza analogs of aminopterin and folic acid. *J. Med. Chem.* **1986**, *29*, 709-715.
 287. Vorbrüggen, H.; Krolikiewicz, K. Amination, III. Trimethylsilanol as Leaving Group, V. Silylation—Amination of Hydroxy N-Heterocycles. *Chemische Berichte* **1984**, *117*, 1523-1541.
 288. DeGraw, J. I.; Tagawa, H. An alternate synthesis of 6-substituted-5-deazapteridines. *J. Heterocycl. Chem.* **1982**, *19*, 1461-3.
 289. Soliman, A. M. Synthesis of novel pyrazolopyridine and pyridopyrimidine derivatives. *J. Heterocyclic Chem.* **2011**, *48*, 592-596.
 290. Duindam, A.; Lishinsky, V. L.; Sikkema, D. J. One Pot Synthesis of 2,6-Dichloro-3,5-dicyanopyridine from Aliphatic Precursors. *Synth. Commun.* **1993**, *23*, 2605-2609.
 291. Davoll, J.; Clarke, J.; Elslager, E. F. Antimalarial substances. 26. Folate antagonists. 4. Antimalarial and antimetabolite effects of 2,4-diamino-6-[(benzyl)amino]pyrido[2,3-*d*]pyrimidines. *J. Med. Chem.* **1972**, *15*, 837-838.
 292. Pochat, F.; Lavelle, F.; Fizames, C.; Zerial, A. Synthesis and experimental antitumor activities of 6-alkyl (or aryl) thio-5-deazapteridines. *Eur. J. Med. Chem.* **1987**, *22*, 135-137.
 293. Pochat, F. Voie d'accès aux amino-5 isoxazoles substitués en 4 par un groupement SR. *Tetrahedron Lett.* **1980**, *21*, 3755-3758.
 294. Harrington, P. J. Synthetic approaches to 5-deaza and 5,10-dideazafolic acid analogs. **1982**.
 295. Temple, C., Jr.; Elliott, R. D.; Montgomery, J. A. Pyrido[2,3-*d*]pyrimidines. The synthesis of the 5-deaza analogs of aminopterin, methotrexate, folic acid, and N10-methylfolic acid. *J. Org. Chem.* **1982**, *47*, 761-764.
 296. Arnold, Z. Synthetic reactions of dimethylformamide. XII. Formylation of some carboxylic acids and their derivatives. *Collect. Czech. Chem. Commun.* **1961**, *26*, 3051-3057.
 297. Stark, E.; Breitmaier, E. 5-Deazapteridines, synthesis and NMR spectra. *Tetrahedron* **1973**, *29*, 2209-17.
 298. Gangjee, A.; Ohemeng, K. A.; Lin, F. T.; Katoh, A. A. Synthesis and antitumor evaluation of some 1,3-disubstituted tetrahydropyrimido[4,5-*c*]isoquinolines. *J. Heterocycl. Chem.* **1986**, *23*, 523-8.
 299. Gangjee, A.; Shi, J.; Queener, S. F.; Barrows, L. R.; Kisliuk, R. L. Synthesis of 5-methyl-5-deaza nonclassical antifolates as inhibitors of dihydrofolate reductases and as potential antipneumocystis, antitoxoplasma, and antitumor agents. *J. Med. Chem.* **1993**, *36*, 3437-43.

300. Gangjee, A.; Devraj, R.; Lin, F. T. Synthesis of 2,4-diamino-5,10-dideaza nonclassical antifolates. *J. Heterocycl. Chem.* **1991**, *28*, 1747-1751.
301. Rosowsky, A.; Chen, H.; Fu, H.; Queener, S. F. Synthesis of new 2,4-Diaminopyrido[2,3-*d*]pyrimidine and 2,4-Diaminopyrrolo[2,3-*d*]pyrimidine inhibitors of *Pneumocystis carinii*, *Toxoplasma gondii*, and *Mycobacterium avium* dihydrofolate reductase. *Bioorg. Med. Chem.* **2003**, *11*, 59-67.
302. Taylor, E. C. Design and synthesis of inhibitors of folate-dependent enzymes as antitumor agents. *Adv. Exp. Med. Biol.* **1993**, *338*, 387-408.
303. Cheung, A. W.-H.; Banner, B.; Bose, J.; Kim, K.; Li, S.; Marcopulos, N.; Orzechowski, L.; Sergi, J. A.; Thakkar, K. C.; Wang, B.-B.; Yun, W.; Zwingelstein, C.; Berthel, S.; Olivier, A. R. 7-Phenyl-pyrido[2,3-*d*]pyrimidine-2,4-diamines: Novel and highly selective protein tyrosine phosphatase 1B inhibitors. *Bioorg. Med. Chem. Lett* **2012**, *22*, 7518-7522.
304. Tumkevicius, S.; Sarakauskaitė, Z.; Masevicius, V. Synthesis of novel thieno- and pyrrolo[2,3-*d*]pyrimidines peri-fused with pyrimidine, 1,4-diazepine and 1,4-thiazepine rings. *Synthesis* **2003**, 1377-1382.
305. Clark, J.; Shahhet, M. S. Synthesis of thieno[2,3-*d*]pyrimidines from 4,6-dichloropyrimidine-5-carboxaldehydes. *J. Heterocyclic Chem.* **1993**, *30*, 1065-1072.
306. Hirota, K.; Shirahashi, M.; Senda, S.; Yogo, M. Pyrimidines. 65. Synthesis of 6-substituted thieno[2,3-*d*]pyrimidine-2,4(1*H*,3*H*)-diones. *J. Heterocyclic Chem.* **1990**, *27*, 717-21.
307. Santilli, A. A.; Dong Han, K.; Wanser, S. V. Thieno[2,3-*d*]pyrimidines. I. New method for the preparation of esters and amides of thieno[2,3-*d*]pyrimidine-6-carboxylic acids. *Journal of Heterocyclic Chemistry* **1971**, *8*, 445-453.
308. Tumkevicius, S. A facile synthesis of 5*H*-1-thia-3,5,6,8-tetraazaacenaphthylenes. *Liebigs Ann.* **1995**, 1703-1705.
309. Tumkevicius, S.; Agrofoglio, L. A.; Kaminskas, A.; Urbelis, G.; Zevaco, T. A.; Walter, O. Synthesis of a novel heterocyclic ring system: 2-thia-3,5,6,7,9-pentaazabenz[*c,d*]azulenes. *Tetrahedron Lett.* **2002**, *43*, 695-697.
310. Tumkevicius, S.; Kaminskas, A.; Kulbokaite, J. A simple synthesis of novel 6,7,8,9-tetrahydro-2-thia-3,5,6,9-tetraazabenz[*c,d*]azulenes. *J. Chem. Res., Synop.* **2000**, 287-289.
311. Wang, Z.; Neidlein, R.; Krieger, C. A new approach to the synthesis of heteroannulated 3,1-oxazin-4-ones from enamino esters and phosgeniminium salts. *Synthesis* **2000**, 255-258.
312. Gangjee, A.; Jain, H. D.; Kisliuk, R. L. Novel 2-amino-4-oxo-5-arylthio-substituted-pyrrolo[2,3-*d*]pyrimidines as nonclassical antifolate inhibitors of thymidylate synthase. *Bioorg. Med. Chem. Lett.* **2005**, *15*, 2225-2230.
313. Linz, S.; Troschuetz, R. Synthesis of 5-[(4-phenylpiperazin-1-yl)methyl]pyrrolo[2,3-*d*]pyrimidine derivatives as potential dopamine D4 receptor ligands. *J. Heterocyclic Chem.* **2007**, *44*, 349-354.
314. Noell, C. W.; Robins, R. K. Aromaticity in heterocyclic systems. II. The application of NMR. in a study of the synthesis and structure of certain imidazo[1,2-*c*]pyrimidines and related pyrrolo[2,3-*d*]pyrimidines. *J. Heterocyclic Chem.* **1964**, *1*, 34-41.

315. Secrist, J. A., III; Liu, P. S. Studies directed toward a total synthesis of nucleoside Q. Annulation of 2,6-diaminopyrimidin-4-one with $\hat{I}\pm$ -halo carbonyls to form pyrrolo[2,3-*d*]pyrimidines and furo[2,3-*d*]pyrimidines. *J. Org. Chem.* **1978**, *43*, 3937-41.
316. Graul, A.; Tracy, M.; Castaner, J. Pemetrexed disodium. Antineoplastic antifolate LY-231514. *Drugs Future* **1998**, *23*, 498-507.
317. Yoneda, F.; Higuchi, M.; Senga, K.; Kanahori, M.; Nishigaki, S. Synthesis and properties of some pyrrolo[2,3-*d*]pyrimidine derivatives. *Chem. Pharm. Bull.* **1973**, *21*, 473-477.
318. Kidwai, M.; Singhal, K.; Rastogi, S. Paal Knorr reaction for novel pyrrolo[2,3-*d*]pyrimidines. *J. Heterocyclic Chem.* **2006**, *43*, 1231-1236.
319. Rodriguez, A. L.; Koradin, C.; Dohle, W.; Knochel, P. Versatile indole synthesis by a 5-endo-dig cyclization mediated by potassium or cesium bases. *Angew. Chem., Int. Ed.* **2000**, *39*, 2488-2490.
320. Taylor, E. C.; Hu, B. A Fischer-indole approach to pyrrolo[2,3-*d*]pyrimidines. *Heterocycles* **1996**, *43*, 323-338.
321. Badawey, E.-S. A. M. Synthesis and in vitro evaluation of some new pyrimidines and related condensed ring systems as potential anticancer agents. *J. Heterocyclic Chem.* **1996**, *33*, 229-233.
322. De Rosa, M.; Arnold, D. Mechanism of the inverse-electron demand Diels-Alder reaction of 2-aminopyrroles with 1,3,5-triazines: detection of an intermediate and effect of added base and acid. *Tetrahedron Lett.* **2007**, *48*, 2975-2977.
323. Kovacs Ja, G. V. J. M. S. M. H. New insights into transmission, diagnosis, and drug treatment of *pneumocystis carinii* pneumonia. *JAMA* **2001**, *286*, 2450-2460.
324. Huang, L.; Cattamanchi, A.; Davis, J. L.; Boon, S. d.; Kovacs, J.; Meshnick, S.; Miller, R. F.; Walzer, P. D.; Worodria, W.; Masur, H.; HIV-Associated Pneumocystis Pneumonia. *Proc. Am. Thoracic Soc.* **2011**, *8*, 294-300.
325. Jain, P.; Yi, S.; Flaherty, P. T. Suzuki–Miyaura cross-coupling of potassium organoborates with 6-sulfonate benzimidazoles using microwave irradiation. *J. Heterocyclic Chem.* **2013**, *50*, E166-E173.
326. Nahimana, A.; Rabodonirina, M.; Bille, J.; Francioli, P.; Hauser, P. M. Mutations of *Pneumocystis jirovecii* dihydrofolate reductase associated with failure of prophylaxis. *Antimicrob. Agents Chemother.* **2004**, *48*, 4301-4305.
327. Nahimana, A.; Rabodonirina, M.; Francioli, P.; Bille, J.; Hauser, P. M. *Pneumocystis jirovecii* dihydrofolate reductase polymorphisms associated with failure of prophylaxis. *J Eukaryot Microbiol* **2003**, *50* Suppl, 656-7.
328. <http://www.uniprot.org/uniprot/Q9UUP5>, accessed 10/10/13
329. <http://www.uniprot.org/uniprot/P16184>. accessed 10/10/13
330. Gangjee, A.; Vasudevan, A.; Queener, S. F. Synthesis and biological evaluation of nonclassical 2,4-diamino-5-methylpyrido[2,3-*d*]pyrimidines with novel side chain substituents as potential inhibitors of dihydrofolate reductases. *J. Med. Chem.* **1997**, *40*, 479-485.
331. Gangjee, A.; Vasudevan, A.; Queener, S. F.; Kisliuk, R. L. 2,4-Diamino-5-deaza-6-substituted pyrido[2,3-*d*]pyrimidine antifolates as potent and selective nonclassical inhibitors of dihydrofolate reductases [Erratum for 1996, Volume 39]. *J. Med. Chem.* **1996**, *39*, 3228.

332. Gangjee, A.; Adair, O.; Queener, S. F. *Pneumocystis carinii* and *Toxoplasma gondii* dihydrofolate reductase inhibitors and antitumor agents: synthesis and biological activities of 2,4-diamino-5-methyl-6-[(monosubstituted anilino)methyl]-pyrido[2,3-*d*]pyrimidines. *J. Med. Chem.* **1999**, *42*, 2447-2455.
333. Gangjee, A.; Adair, O. O.; Queener, S. F. Synthesis and biological evaluation of 2,4-diamino-6-(arylaminoethyl)pyrido[2,3-*d*]pyrimidines as inhibitors of *Pneumocystis carinii* and *Toxoplasma gondii* dihydrofolate reductase and as antiopportunistic infection and antitumor agents. *J. Med. Chem.* **2003**, *46*, 5074-5082.
334. Gangjee, A.; Mavandadi, F.; Queener, S. F. Effect of N9-methylation and bridge atom variation on the activity of 5-substituted 2,4-diaminopyrrolo[2,3-*d*]pyrimidines against dihydrofolate reductases from *Pneumocystis carinii* and *Toxoplasma gondii*. *J. Med. Chem.* **1997**, *40*, 1173-1177.
335. Rosowsky, A.; Chen, H.; Fu, H.; Queener, S. F. Synthesis of new 2,4-diaminopyrido[2,3-*d*]pyrimidine and 2,4-diaminopyrrolo[2,3-*d*]pyrimidine inhibitors of *Pneumocystis carinii*, *Toxoplasma gondii*, and *Mycobacterium avium* dihydrofolate reductase. *Bioorg. Med. Chem.* **2003**, *11*, 59-67.
336. Rosowsky, A.; Fu, H.; Queener, S. F. Synthesis of 2,4-diaminopyrido[2,3-*d*]pyrimidines and 2,4-diaminoquinazolines with bulky dibenz[*b,f*]azepine and dibenzo[*a,d*]-cycloheptene substituents at the 6-position as inhibitors of dihydrofolate reductase from *Pneumocystis carinii*, *Toxoplasma gondii*, and *Mycobacterium avium*. *J. Heterocycl. Chem.* **2000**, *37*, 921-926.
337. Liao, S. Y.; Qian, L.; Lu, H. L.; Shen, Y.; Zheng, K. C. A combined 2D- and 3D-QSAR study on analogues of ARC-111 with antitumor activity. *Mol. Informat.* **2008**, *27*, 740-749.
338. Cody, V.; Pace, J.; Makin, J.; Piraino, J.; Queener, S. F.; Rosowsky, A. correlations of inhibitor kinetics for *Pneumocystis jirovecii* and human dihydrofolate reductase with structural data for human active site mutant enzyme complexes. *Biochemistry* **2009**, *48*, 1702-1711.
339. Mori, Y.; Hirokawa, T.; Aoki, K.; Satomi, H.; Takeda, S.; Aburada, M.; Miyamoto, K.-i. Structure activity relationships of quinoxalin-2-one derivatives as platelet-derived growth factor- β receptor (PDGFR β) inhibitors, derived from molecular modeling. *Chem. Pharm. Bull.* **2008**, *56*, 682-687.
340. Gangjee, A.; Li, W. Unpublished results. **2009**.
341. Piper, J. R.; Ramamurthy, B.; Johnson, C. A.; Otter, G. M.; Sirotiak, F. M. Analogs of 10-Deazaaminopterin and 5-Alkyl-5,10-dideazaaminopterin with the 4-Substituted 1-Naphthoyl Group in the Place of 4-Substituted Benzoyl. *J. Med. Chem.* **1996**, *39*, 614-618.
342. Hye-Ryong Shim, A.; Liu, H.; Focia, P. J.; Chen, X.; Lin, P. C.; He, X. Structures of a platelet-derived growth factor/propeptide complex and a platelet-derived growth factor/receptor complex. *Proc. Natl Acad. Sci.* **2010**, *107*, 11307-11312.
343. Gangjee, A.; Zhu, Y.; Queener, S. F.; Francom, P.; Broom, A. D. Nonclassical 2,4-diamino-8-deazafolate analogs as inhibitors of dihydrofolate reductases from rat liver, *Pneumocystis carinii*, and *Toxoplasma gondii*. *J. Med. Chem.* **1996**, *39*, 1836-1845.
344. Gangjee, A.; Adair, O.; Queener, S. F. Synthesis of 2,4-diamino-6-

- [(arylthio)methyl]pyrido[2,3-*d*]pyrimidines as dihydrofolate reductase inhibitors. *Bioorg. Med. Chem.* **2001**, *9*, 2929-2935.
345. Wilcken, R.; Zimmermann, M. O.; Lange, A.; Joerger, A. C.; Boeckler, F. M. Principles and applications of halogen bonding in medicinal chemistry and chemical biology. *J. Med. Chem.* **2012**, *56*, 1363-1388.
 346. Scholfield, M. R.; Zanden, C. M. V.; Carter, M.; Ho, P. S. Halogen bonding (X-bonding): A biological perspective. *Protein Sci.* **2013**, *22*, 139-152.
 347. Griffith, J.; Black, J.; Faerman, C.; Swenson, L.; Wynn, M.; Lu, F.; Lippke, J.; Saxena, K. The Structural Basis for Autoinhibition of FLT3 by the Juxtamembrane Domain. *Molecular Cell* **2004**, *13*, 169-178.
 348. Gangjee, A.; Namjoshi, O. A.; Raghavan, S.; Queener, S. F.; Kisliuk, R. L.; Cody, V. Design, synthesis and molecular modeling of novel pyrido[2,3-*d*]pyrimidine analogs as antifolates: Application of Buchwald-Hartwig aminations of heterocycles. *J. Med. Chem.* **2013** *56*, 4422-4441.
 349. Gangjee, A.; Vidwans, A. P.; Vasudevan, A.; Queener, S. F.; Kisliuk, R. L.; Cody, V.; Li, R.; Galitsky, N.; Luft, J. R.; Pangborn, W. Structure-based design and synthesis of lipophilic 2,4-diamino-6-substituted quinazolines and their evaluation as inhibitors of dihydrofolate reductases and potential antitumor agents. *J. Med. Chem.* **1998**, *41*, 3426-3434.
 350. *LeadIT 1.3.0*, Biosolve IT: St. Augustin, Germany, www.biosolveit.com.
 351. Gangjee, A.; Adair, O.; Cody, V. Unpublished results.
 352. Gangjee, A.; Zhou, X. Classical and Nonclassical 2-Amino-4-oxo-5-arylthio-substituted-6-propyl thieno[2,3-*d*]pyrimidines as Dual Thymidylate Synthase and Dihydrofolate Reductase Inhibitors and Potential Agent for *Toxoplasma gondii* Infection In 2012.
 353. Pacheco Homem, D.; Flores, R.; Tosqui, P.; de Castro Rozada, T.; Abicht Basso, E.; Gasparotto Junior, A.; Augusto Vicente Seixas, F. Homology modeling of dihydrofolate reductase from *T. gondii* bonded to antagonists: molecular docking and molecular dynamics simulations. *Molecular BioSystems* **2013**.
 354. Altschul, S. F.; Koonin, E. V. Iterated profile searches with PSI-BLAST - a tool for discovery in protein databases. *Trends Biochem. Sci.* **1998**, *23*, 444-447.
 355. Zaware, N.; Sharma, H.; Yang, J.; Devambatla, R. K. V.; Queener, S. F.; Anderson, K. S.; Gangjee, A. Discovery of potent and selective inhibitors of *Toxoplasma gondii* thymidylate synthase for opportunistic infections. *ACS Med. Chem. Lett.* **2013**. ASAP article. doi: 10.1021/ml400208v
 356. Gangjee, A.; Devraj, R.; McGuire, J. J.; Kisliuk, R. L. 5-Arylthio Substituted 2-Amino-4-oxo-6-methylpyrrolo[2,3-*d*]pyrimidine Antifolates as Thymidylate Synthase Inhibitors and Antitumor Agents. *J. Med. Chem.* **1995**, *38*, 4495-502.
 357. Gangjee, A.; Elzein, E.; Kothare, M.; Vasudevan, A. Classical and nonclassical antifolates as potential antitumor, antipneumocystis and antitoxoplasma agents. *Curr. Pharm. Des.* **1996**, *2*, 263-280.
 358. Gangjee, A.; Jain, H. D.; Phan, J.; Kisliuk, R. L. Synthesis of 2-amino-4-oxo-5-substituted benzylthiopyrrolo[2,3-*d*]pyrimidines as potential inhibitors of thymidylate synthase. *J. Heterocycl. Chem.* **2005**, *42*, 165-168.
 359. Gangjee, A.; Jain, H. D.; Phan, J.; Lin, X.; Song, X.; McGuire, J. J.; Kisliuk, R. L. Dual inhibitors of thymidylate synthase and dihydrofolate reductase as antitumor

- agents: design, synthesis, and biological evaluation of classical and nonclassical pyrrolo[2,3-*d*]pyrimidine antifolates. *J. Med. Chem.* **2006**, *49*, 1055-1065.
360. Gangjee, A.; Li, W.; Kisliuk, R. L.; Cody, V.; Pace, J.; Piraino, J.; Makin, J. Design, synthesis, and x-ray crystal structure of classical and nonclassical 2-amino-4-oxo-5-substituted-6-ethylthieno[2,3-*d*]pyrimidines as dual thymidylate synthase and dihydrofolate reductase inhibitors and as potential antitumor agents. *J. Med. Chem.* **2009**, *52*, 4892-4902.
 361. Gangjee, A.; Li, W.; Yang, J.; Kisliuk, R. L. Design, synthesis, and biological evaluation of classical and nonclassical 2-amino-4-oxo-5-substituted-6-methylpyrrolo[3,2-*d*]pyrimidines as dual thymidylate synthase and dihydrofolate reductase inhibitors. *J. Med. Chem.* **2008**, *51*, 68-76.
 362. Gangjee, A.; Mavandadi, F.; Kisliuk, R. L.; Queener, S. F. Synthesis of Classical and a Nonclassical 2-Amino-4-oxo-6-methyl-5-substituted pyrrolo[2,3-*d*]pyrimidine antifolate inhibitors of thymidylate synthase. *J. Med. Chem.* **1999**, *42*, 2272-2279.
 363. Gangjee, A.; Qiu, Y.; Kisliuk, R. L. Synthesis of classical and nonclassical 2-amino-4-oxo-6-benzylthieno[2,3-*d*]pyrimidines as potential thymidylate synthase inhibitors. *J. Heterocycl. Chem.* **2004**, *41*, 941-946.
 364. Gangjee, A.; Qiu, Y.; Li, W.; Kisliuk, R. L. Potent dual thymidylate synthase and dihydrofolate reductase inhibitors: classical and nonclassical 2-amino-4-oxo-5-arylthio-substituted-6-methylthieno[2,3-*d*]pyrimidine antifolates. *J. Med. Chem.* **2008**, *51*, 5789-5797.
 365. Gangjee, A.; Vidwans, A.; Elzein, E.; McGuire, J. J.; Queener, S. F.; Kisliuk, R. L. Synthesis, antifolate, and antitumor activities of classical and nonclassical 2-amino-4-oxo-5-substituted-pyrrolo[2,3-*d*]pyrimidines. *J. Med. Chem.* **2001**, *44*, 1993-2003.
 366. Gangjee, A.; Yu, J.; Kisliuk, R. L. 2-Amino-4-oxo-6-substituted-pyrrolo[2,3-*d*]pyrimidines as potential inhibitors of thymidylate synthase. *J. Heterocycl. Chem.* **2002**, *39*, 833-840.
 367. Zhang, X.; Zhou, X.; Kisliuk, R. L.; Piraino, J.; Cody, V.; Gangjee, A. Design, synthesis, biological evaluation and X-ray crystal structure of novel classical 6,5,6-tricyclic benzo[4,5]thieno[2,3-*d*]pyrimidines as dual thymidylate synthase and dihydrofolate reductase inhibitors. *Bioorg. Med. Chem.* **2011**, *19*, 3585-3594.
 368. Mori, A.; Miyakawa, Y.; Ohashi, E.; Haga, T.; Maegawa, T.; Sajiki, H. Pd/C-Catalyzed chemoselective hydrogenation in the presence of diphenylsulfide. *Org. Lett.* **2006**, *8*, 3279-3281.
 369. Brown, H. C.; Rao, B. C. S. Addition compounds of the alkali metal hydrides. XI. A new aldehyde synthesis-the reduction of acid chlorides by lithium tri-tert-butoxyaluminumhydride. *J. Am. Chem. Soc.* **1958**, *80*, 5377-5380.
 370. Potapova, O.; Laird, A. D.; Nannini, M. A.; Barone, A.; Li, G.; Moss, K. G.; Cherrington, J. M.; Mendel, D. B. Contribution of individual targets to the antitumor efficacy of the multitargeted receptor tyrosine kinase inhibitor SU11248. *Mol. Cancer Therap.* **2006**, *5*, 1280-1289.
 371. King, A. O.; Okukado, N.; Negishi, E. Highly general stereo-, regio-, and chemo-selective synthesis of terminal and internal conjugated enynes by the palladium-catalyzed reaction of alkynylzinc reagents with alkenyl halides. *J. Chem. Soc.*,

- Chem. Commun.* **1977**, 683-684.
372. Huo, S. Highly efficient, general procedure for the preparation of alkylzinc reagents from unactivated alkyl bromides and chlorides. *Org. Lett.* **2003**, *5*, 423-425.
 373. Tabernero, J. The Role of VEGF and EGFR inhibition: implications for combining anti-vegf and anti-egfr agents. *Mol. Cancer Res.* **2007**, *5*, 203-220.
 374. Yoshiji, H.; Harris, S. R.; Thorgeirsson, U. P. Vascular endothelial growth factor is essential for initial but not continued in vivo growth of human breast carcinoma cells. *Cancer Res.* **1997**, *57*, 3924-3928.
 375. Bergers, G.; Song, S.; Meyer-Morse, N.; Bergsland, E.; Hanahan, D. Benefits of targeting both pericytes and endothelial cells in the tumor vasculature with kinase inhibitors. *J. Clin. Invest.* **2003**, *111*, 1287-1295.
 376. Carmeliet, P. Angiogenesis in life, disease and medicine. *Nature* **2005**, *438*, 932-936.
 377. Schilder, R. J.; Hall, L.; Monks, A.; Handel, L. M.; Fornace, A. J., Jr.; Ozols, R. F.; Fojo, A. T.; Hamilton, T. C. Metallothionein gene expression and resistance to cisplatin in human ovarian cancer. *Int. J. Cancer* **1990**, *45*, 416-22.
 378. Badrinarayan, P.; Sastry, G. N. Rational approaches towards lead optimization of kinase inhibitors: the issue of specificity. *Curr. Pharm. Des.* **2013**, *19*, 4714-4738.
 379. Gibbons, D. L.; Priel, S.; Kantarjian, H.; Cortes, J.; Quintas-Cardama, A. The rise and fall of gatekeeper mutations? The BCR-ABL1 T315I paradigm. *Cancer* **2012**, *118*, 293-299.
 380. Gangjee, A.; Zaware, N.; Raghavan, S.; Ihnat, M.; Shenoy, S.; Kisliuk, R. L. Single agents with designed combination chemotherapy potential: synthesis and evaluation of substituted pyrimido[4,5-*b*]indoles as receptor tyrosine kinase and thymidylate synthase inhibitors and as antitumor agents. *J. Med. Chem.* **2010**, *53*, 1563-1578.
 381. Gangjee, A.; Zaware, N.; Raghavan, S.; Yang, J.; Thorpe, J. E.; Ihnat, M. A. N4-(3-Bromophenyl)-7-(substituted benzyl) pyrrolo[2,3-*d*]pyrimidines as potent multiple receptor tyrosine kinase inhibitors: Design, synthesis, and in vivo evaluation. *Bioorg. Med. Chem.* **2012**, *20*, 2444-2454.
 382. Gangjee, A.; Namjoshi, O. A.; Yu, J.; Ihnat, M. A.; Thorpe, J. E.; Bailey-Downs, L. C. N2-Trimethylacetyl substituted and unsubstituted-N4-phenylsubstituted-6-(2-pyridin-2-ylethyl)-7*H*-pyrrolo[2,3-*d*]pyrimidine-2,4-diamines: Design, cellular receptor tyrosine kinase inhibitory activities and in vivo evaluation as antiangiogenic, antimetastatic and antitumor agents. *Bioorg. Med. Chem.* **2013**, *21*, 1312-1323.
 383. Gangjee, A.; Zhao, Y.; Ihnat, M. A.; Thorpe, J. E.; Bailey-Downs, L. C.; Kisliuk, R. L. Novel tricyclic indeno[2,1-*d*]pyrimidines with dual antiangiogenic and cytotoxic activities as potent antitumor agents. *Bioorg. Med. Chem.* **2012**, *20*, 4217-4225.
 384. Molecular Operating environment (MOE 2007.09), C. C. G., Inc., 1255 University Street, Suite 1600, Montreal, Quebec, Canada, H3B 3X3.
 385. Mol, C. D.; Lim, K. B.; Sridhar, V.; Zou, H.; Chien, E. Y. T.; Sang, B.-C.; Nowakowski, J.; Kassel, D. B.; Cronin, C. N.; McRee, D. E. Structure of a c-Kit Product Complex Reveals the Basis for Kinase Transactivation. *J. Biol. Chem.*

- 2003**, 278, 31461-31464.
386. Zhu, X.; Kim, J. L.; Newcomb, J. R.; Rose, P. E.; Stover, D. R.; Toledo, L. M.; Zhao, H.; Morgenstern, K. A. Structural analysis of the lymphocyte-specific kinase Lck in complex with non-selective and Src family selective kinase inhibitors. *Structure* **1999**, *15*, 651-661.
 387. Mohammadi, M.; McMahon, G.; Sun, L.; Tang, C.; Hirth, P.; Yeh, B. K.; Hubbard, S. R.; Schlessinger, J. Structures of the Tyrosine Kinase Domain of Fibroblast Growth Factor Receptor in Complex with Inhibitors. *Science* **1997**, *276*, 955-960.
 388. Gangjee, A.; Yang, J.; Ihnat, M. A.; Kamat, S. Antiangiogenic and antitumor agents. Design, synthesis, and evaluation of novel 2-amino-4-(3-bromoanilino)-6-benzylsubstituted pyrrolo[2,3-*d*]pyrimidines as inhibitors of receptor tyrosine kinases. *Bioorg. Med. Chem.* **2003**, *11*, 5155-5170.
 389. Showalter, H. D. H.; Bridges, A. J.; Zhou, H.; Sercel, A. D.; McMichael, A.; Fry, D. W. Tyrosine Kinase Inhibitors. 16. 6,5,6-Tricyclic Benzothieno[3,2-*d*]pyrimidines and Pyrimido[5,4-*b*]- and -[4,5-*b*]indoles as Potent Inhibitors of the Epidermal Growth Factor Receptor Tyrosine Kinase. *J. Med. Chem.* **1999**, *42*, 5464-5474.
 390. Traxler, P.; Furet, P. Strategies toward the design of novel and selective protein tyrosine kinase inhibitors. *Pharmacol. Therap.* **1999**, *82*, 195-206.
 391. Laufer, S. A.; Domeyer, D. M.; Scior, T. R. F.; Albrecht, W.; Hauser, D. R. J. Synthesis and biological testing of purine derivatives as potential atp-competitive kinase inhibitors. *J. Med. Chem.* **2005**, *48*, 710-722.
 392. Abu Thaher, B.; Koch, P.; Schattel, V.; Laufer, S. Role of the hydrogen bonding heteroatom-Lys53 interaction between the p38 mitogen-activated protein (MAP) kinase and pyridinyl-substituted 5-membered heterocyclic ring inhibitors. *J. Med. Chem.* **2009**, *52*, 2613-2617.
 393. Gangjee, A.; Namjoshi, O. A.; Yu, J.; Ihnat, M. A.; Thorpe, J. E.; Warnke, L. A. Design, synthesis and biological evaluation of substituted pyrrolo[2,3-*d*]pyrimidines as multiple receptor tyrosine kinase inhibitors and antiangiogenic agents. *Bioorg. Med. Chem.* **2008**, *16*, 5514-5528.
 394. Gangjee, A.; Kurup, S.; Ihnat, M. A.; Thorpe, J. E.; Disch, B. N4-Aryl-6-substituted phenylmethyl-7H-pyrrolo[2,3-*d*]pyrimidine-2,4-diamines as receptor tyrosine kinase inhibitors. *Bioorg. Med. Chem.* **2012**, *20*, 910-914.
 395. Gangjee, A. Z., Y.; Ihnat, M. A.; Green, D. and Miller, W. T. In *Synthesis of 2-Amino-4-m-bromoanilino-6-arylmethyl-7H-pyrrolo[2,3-*d*]pyrimidines as Tyrosine Kinase Inhibitors and Antiangiogenic Agents.*, 96th American Association for Cancer Research (AACR) Annual Meeting, Anaheim, CA, April 16-20, 2005; American Association for Cancer Research (AACR): Anaheim, CA, **2005**.
 396. Gangjee, A.; Ye, Z.; Queener, S. F. Synthesis of three carbon atom bridged 2,4-diaminopyrrolo[2,3-*d*]pyrimidines as nonclassical dihydrofolate reductase inhibitors. *J. Heterocycl. Chem.* **2005**, *42*, 1127-1133.
 397. Gangjee, A.; Li, W.; Lin, L.; Zeng, Y.; Ihnat, M.; Warnke, L. A.; Green, D. W.; Cody, V.; Pace, J.; Queener, S. F. Design, synthesis, and X-ray crystal structures of 2,4-diaminofuro[2,3-*d*]pyrimidines as multireceptor tyrosine kinase and dihydrofolate reductase inhibitors. *Bioorg. Med. Chem.* **2009**, *17*, 7324-7336.

398. Stanton, R. A.; Gernert, K. M.; Nettles, J. H.; Aneja, R. Drugs that target dynamic microtubules: A new molecular perspective. *Med. Res. Rev.* **2011**, *31*, 443-481.
399. De Martino, G.; La Regina, G.; Coluccia, A.; Edler, M. C.; Barbera, M. C.; Brancale, A.; Wilcox, E.; Hamel, E.; Artico, M.; Silvestri, R. Arylthioindoles, potent inhibitors of tubulin polymerization. *J. Med. Chem.* **2004**, *47*, 6120-6123.
400. Gangjee, A.; Zhao, Y.; Lin, L.; Raghavan, S.; Roberts, E. G.; Risinger, A. L.; Hamel, E.; Mooberry, S. L. Corrections to Synthesis and Discovery of Water-Soluble Microtubule Targeting Agents that Bind to the Colchicine Site on Tubulin and Circumvent Pgp Mediated Resistance. *J. Med. Chem.* **2011** *53*, 913.
401. Gangjee, A.; Vasudevan, A.; Queener, S. F.; Kisliuk, R. L. 6-Substituted 2,4-Diamino-5-methylpyrido[2,3-*d*]pyrimidines as inhibitors of dihydrofolate reductases from *Pneumocystis carinii* and *Toxoplasma gondii* and as antitumor agents. *J. Med. Chem.* **1995**, *38*, 1778-1785.
402. Arnold, Z.; Budesinsky, M. 2,6,9-Trioxabicyclo[3.3.1]nona-3,7-diene-4,8-dicarbaldehyde, a dissymmetric propeller-like molecule. The structure and chirality proof. *J. Org. Chem.* **1988**, *53*, 5352-3.
403. Buděšínský, M.; Fiedler, P.; Arnold, Z. Triformylmethane: An efficient preparation, some derivatives, and spectra. *Synthesis* **1989**, 858-860.
404. Gangjee, A.; Adair, O. O.; Pagley, M.; Queener, S. F. N9-substituted 2,4-diaminoquinazolines: synthesis and biological evaluation of lipophilic inhibitors of *Pneumocystis carinii* and *Toxoplasma gondii* dihydrofolate reductase. [Erratum to document cited in CA149:425887]. *J. Med. Chem.* **2009**, *52*, 4979.
405. Abdel-Magid, A. F.; Carson, K. G.; Harris, B. D.; Maryanoff, C. A.; Shah, R. D. Reductive amination of aldehydes and ketones with sodium triacetoxyborohydride. studies on direct and indirect reductive amination procedures. *J. Org. Chem.* **1996**, *61*, 3849-3862.
406. Abdel-Magid, A. F.; Mehrman, S. J. A review on the use of sodium triacetoxyborohydride in the reductive amination of ketones and aldehydes. *Org. Process Res. Dev.* **2006**, *10*, 971-1031.
407. Gribble, G. W. Sodium borohydride in carboxylic acid media: a phenomenal reduction system. *Chem. Soc. Rev.* **1998**, *27*, 395-404.
408. Baxter, E. W.; Reitz, A. B. Reductive aminations of carbonyl compounds with borohydride and borane reducing agents. *Org. React.* **2002**, *59*.
409. Molecular Operating environment (MOE 2008.10), C. C. G., Inc., 1255 University Street, Suite 1600, Montreal, Quebec, Canada, H3B 3X3. www.chemcomp.com.
410. Sreshty, M. A. L.; Surolia, A.; Sastry, G. N.; Murty, U. S. Deorphanization of malonyl coa:acp transacylase drug target in *Plasmodium falciparum* (PfFabD) using bacterial antagonists: a piggyback' approach for antimalarial drug discovery. *Mol. Inf.* **2012**, *31*, 281-299.
411. Sippl, M. J. Recognition of errors in three-dimensional structures of proteins. *Proteins: Struct., Funct., Genet.* **1993**, *17*, 355-62.
412. Wiederstein, M.; Sippl, M. J. ProSA-web: interactive web service for the recognition of errors in three-dimensional structures of proteins. *Nucleic Acids Res.* **2007**, *35*, W407-W410.
413. Laskowski, R. A.; MacArthur, M. W.; Moss, D. S.; Thornton, J. M. PROCHECK:

- A program to check the stereochemical quality of protein structures. *J. Appl. Cryst.* **1993**, *26*, 283-291.
414. Melo, F.; Feytmans, E. Assessing protein structures with a non-local atomic interaction energy. *J. Mol. Biol.* **1998**, *277*, 1141-1152.
 415. van Gunsteren, W. H.; Billeter, S. R.; Eising, A. A.; Hünenberger, P.; Krüger, A. E.; Mark, A. E.; Scott, W. R. P.; Tironi, I. G. Biomolecular Simulation: The GROMOS96 Manual and User Guide. In Vdf Hochschulverlag AG an der ETH Zürich: Zürich, Switzerland, **1996**; pp 1 - 1042.
 416. Benkert, P.; Schwede, T.; Tosatto, S. QMEANclust: estimation of protein model quality by combining a composite scoring function with structural density information. *BMC Struct. Biol.* **2009**, *9*, 35.
 417. http://swissmodel.expasy.org/workspace/index.php?func=tools_structureassessment1.
 418. Kiefer, F.; Arnold, K.; Kunzli, M.; Bordoli, L.; Schwede, T. The SWISS-MODEL Repository and associated resources. *Nucleic Acids Res* **2009**, *37*, D387-92.
 419. Bordoli, L.; Kiefer, F.; Arnold, K.; Benkert, P.; Battey, J.; Schwede, T. Protein structure homology modeling using SWISS-MODEL workspace. *Nat Protoc* **2009**, *4*, 1-13.
 420. Arnold, K.; Bordoli, L.; Kopp, J.; Schwede, T. The SWISS-MODEL workspace: a web-based environment for protein structure homology modelling. *Bioinformatics* **2006**, *22*, 195-201.
 421. Kelley, L. A.; Sternberg, M. J. E. Protein structure prediction on the Web: a case study using the Phyre server. *Nat. Protocols* **2009**, *4*, 363-371.
 422. Nielsen, M.; Lundegaard, C.; Lund, O.; Petersen, T. N. CPHmodels-3.0 remote homology modeling using structure-guided sequence profiles. *Nucleic Acids Res.* **2010**, *38*, W576-W581.
 423. Cody, V.; Luft, J. R.; Pangborn, W. Understanding the role of Leu22 variants in methotrexate resistance: comparison of wild-type and Leu22Arg variant mouse and human dihydrofolate reductase ternary crystal complexes with methotrexate and NADPH. *Acta Crystallographica Section D* **2005**, *61*, 147-155.
 424. Tripos Inc., 1699 South Hanley Road, St. Louis, MO 63144.
 425. Fernandez-Fuentes, N.; Rai, B. K.; Madrid-Aliste, C. J.; Eduardo Fajardo, J.; Fiser, A. Comparative protein structure modeling by combining multiple templates and optimizing sequence-to-structure alignments. *Bioinformatics* **2007**, *23*, 2558-2565.
 426. Bates, P. A.; Kelley, L. A.; MacCallum, R. M.; Sternberg, M. J. Enhancement of protein modeling by human intervention in applying the automatic programs 3D-JIGSAW and 3D-PSSM. *Proteins* **2001**, Suppl 5, 39-46.
 427. Montomerie, S.; Cruz, J. A.; Shrivastava, S.; Arndt, D.; Berjanskii, M.; Wishart, D. S. PROTEUS2: a web server for comprehensive protein structure prediction and structure-based annotation. *Nucleic Acids Res.* **2008**, *36*, W202-W209.
 428. Schormann, N.; Senkovich, O.; Walker, K.; Wright, D. L.; Anderson, A. C.; Rosowsky, A.; Ananthan, S.; Shinkre, B.; Velu, S.; Chattopadhyay, D. Structure-based approach to pharmacophore identification, in silico screening, and three-dimensional quantitative structure–activity relationship studies for inhibitors of *Trypanosoma cruzi* dihydrofolate reductase function. *Proteins: Struct., Funct.*

- Bioinf.* **2008**, *73*, 889-901.
429. Molecular Operating environment (MOE 2009.10), C. C. G., Inc., 1255 University Street, Suite 1600, Montreal, Quebec, Canada, H3B 3X3.
 430. Flexx 3.1.2, B. G., Germany. www.biosolveit.com.
 431. Gallivan, J. P.; Dougherty, D. A. Cation- π interactions in structural biology. *Proc. Natl. Acad. Sci. U. S. A.* **1999**, *96*, 9459-9464.
 432. Molecular Operating environment (MOE 2010.10), C. C. G., Inc., 1255 University Street, Suite 1600, Montreal, Quebec, Canada, H3B 3X3. www.chemcomp.com.
 433. Schormann, N.; Senkovich, O.; Walker, K.; Wright, D. L.; Anderson, A. C.; Rosowsky, A.; Ananthan, S.; Shinkre, B.; Velu, S.; Chattopadhyay, D. Structure-based approach to pharmacophore identification, *in silico* screening, and three-dimensional quantitative structure-activity relationship studies for inhibitors of *Trypanosoma cruzi* dihydrofolate reductase function. *Proteins: Struct., Funct., Bioinf.* **2008**, *73*, 889-901.
 434. <http://www.uniprot.org/uniprot/Q27793>. accessed 10/10/2013
 435. <http://www.uniprot.org/uniprot/P04818>. accessed 10/10/2013
 436. <http://www.uniprot.org/uniprot/Q07422>. accessed 10/10/2013
 437. <http://www.uniprot.org/uniprot/P04818>. accessed 10/10/2013
 438. Larkin, M. A.; Blackshields, G.; Brown, N. P.; Chenna, R.; McGettigan, P. A.; McWilliam, H.; Valentin, F.; Wallace, I. M.; Wilm, A.; Lopez, R.; Thompson, J. D.; Gibson, T. J.; Higgins, D. G. Clustal W and Clustal X version 2.0. *Bioinformatics* **2007**, *23*, 2947-2948.
 439. Sayre, P. H.; Finer-Moore, J. S.; Fritz, T. A.; Biermann, D.; Gates, S. B.; MacKellar, W. C.; Patel, V. F.; Stroud, R. M. Multi-targeted antifolates aimed at avoiding drug resistance form covalent closed inhibitory complexes with human and *Escherichia coli* thymidylate synthases. *J. Mol. Biol.* **2001**, *313*, 813-829.
 440. Martucci, W. E.; Vargo, M. A.; Anderson, K. S. Explaining an Unusually Fast Parasitic Enzyme: Folate Tail-Binding Residues Dictate Substrate Positioning and Catalysis in *Cryptosporidium hominis* Thymidylate Synthase. *Biochemistry* **2008**, *47*, 8902-8911.
 441. Almog, R.; Waddling, C. A.; Maley, F.; Maley, G. F.; Van Roey, P. Crystal structure of a deletion mutant of human thymidylate synthase Δ (7-29) and its ternary complex with Tomudex and dUMP. *Protein Sci.* **2001**, *10*, 988-996.
 442. Kamb, A.; Finer-Moore, J. S.; Stroud, R. M. Cofactor triggers the conformational change in thymidylate synthase: implications for an ordered binding mechanism. *Biochemistry* **1992**, *31*, 12876-12884.
 443. Gangjee, A.; Qiu, Y.; Li, W.; Kisliuk, R. L. Potent dual thymidylate synthase and dihydrofolate reductase inhibitors: classical and nonclassical 2-amino-4-oxo-5-arylthio-substituted-6-methylthieno[2,3-*d*]pyrimidine antifolates. *J. Med. Chem.* **2008**, *51*, 5789-5797.
 444. Adelberg, E. A.; Mandel, M.; Ching Chen, G. C. Optimal conditions for mutagenesis by *N*-methyl-*N'*-nitro-*N*-nitrosoguanidine in *Escherichia coli* K12. *Biochem. Biophys. Res. Commun.* **1965**, *18*, 788-795.
 445. Ward, J. J.; McGuffin, L. J.; Bryson, K.; Buxton, B. F.; Jones, D. T. The DISOPRED server for the prediction of protein disorder. *Bioinformatics* **2004**, *20*,

- 2138-2139.
446. Rarey, M.; Kramer, B.; Lengauer, T.; Klebe, G. A fast flexible docking method using an incremental construction algorithm. *J. Mol. Biol.* **1996**, *261*, 470-489.
 447. Gangjee, A.; Zaware, N.; Raghavan, S.; Ihnat, M.; Shenoy, S.; Kisliuk, R. L. Single agents with designed combination chemotherapy potential: synthesis and evaluation of substituted pyrimido[4,5-*b*]indoles as receptor tyrosine kinase and thymidylate synthase inhibitors and as antitumor agents. *J. Med. Chem.* **2010**, *53*, 1563-1578.
 448. Choowongkomon, K.; Sawatdichaikul, O.; Songtawee, N.; Limtrakul, J. Receptor-based virtual screening of EGFR kinase inhibitors from the NCI diversity database. *Molecules* **2010**, *15*, 4041-4054.
 449. Cramer, R. D. Topomer CoMFA: A design methodology for rapid lead optimization. *J. Med. Chem.* **2003**, *46*, 374-388.
 450. Offer, J.; Boddy, C. N. C.; Dawson, P. E. Extending synthetic access to proteins with a removable acyl transfer auxiliary. *J. Am. Chem. Soc.* **2002**, *124*, 4642-4646.
 451. Gangjee, A.; Lin, X. CoMFA and CoMSIA analyses of *Pneumocystis carinii* dihydrofolate reductase, *Toxoplasma gondii* dihydrofolate reductase, and rat liver dihydrofolate reductase. *J. Med. Chem.* **2005**, *48*, 1448-1469.
 452. Gangjee, A.; Lin, X.; Queener, S. F. Design, synthesis, and biological evaluation of 2,4-diamino-5-methyl-6-substituted-pyrrolo[2,3-*d*]pyrimidines as dihydrofolate reductase Inhibitors. *J. Med. Chem.* **2004**, *47*, 3689-3692.
 453. Ravelli, R. B. G.; Gigant, B.; Curmi, P. A.; Jourdain, I.; Lachkar, S.; Sobel, A.; Knossow, M. Insight into tubulin regulation from a complex with colchicine and a stathmin-like domain. *Nature* **2004**, *428*, 198-202.
 454. Bhabatarak Bhattacharyya, D. P. S. G. M. B. Anti-mitotic activity of colchicine and the structural basis for its interaction with tubulin. *Med. Res. Rev.* **2008**, *28*, 155-183.
 455. Kasibhatla, S.; Baichwal, V.; Cai, S. X.; Roth, B.; Skvortsova, I.; Skvortsov, S.; Lukas, P.; English, N. M.; Sirisoma, N.; Drewe, J.; Pervin, A.; Tseng, B.; Carlson, R. O.; Pleiman, C. M. MPC-6827: A small-molecule inhibitor of microtubule formation that is not a substrate for multidrug resistance pumps. *Cancer Res.* **2007**, *67*, 5865-5871.
 456. Sirisoma, N.; Kasibhatla, S.; Pervin, A.; Zhang, H.; Jiang, S.; Willardsen, J. A.; Anderson, M. B.; Baichwal, V.; Mather, G. G.; Jessing, K.; Hussain, R.; Hoang, K.; Pleiman, C. M.; Tseng, B.; Drewe, J.; Cai, S. X. Discovery of 2-Chloro-N-(4-methoxyphenyl)-N-methylquinazolin-4-amine (EP128265, MPI-0441138) as a Potent Inducer of Apoptosis with High In Vivo Activity. *J. Med. Chem.* **2008**, *51*, 4771-4779.
 457. Sirisoma, N.; Pervin, A.; Zhang, H.; Jiang, S.; Willardsen, J. A.; Anderson, M. B.; Mather, G.; Pleiman, C. M.; Kasibhatla, S.; Tseng, B.; Drewe, J.; Cai, S. X. Discovery of N-(4-Methoxyphenyl)-N,2-dimethylquinazolin-4-amine, a Potent Apoptosis Inducer and Efficacious Anticancer Agent with High Blood Brain Barrier Penetration. *J. Med. Chem.* **2009**, *52*, 2341-2351.
 458. Sirisoma, N.; Pervin, A.; Zhang, H.; Jiang, S.; Adam Willardsen, J.; Anderson, M. B.; Mather, G.; Pleiman, C. M.; Kasibhatla, S.; Tseng, B.; Drewe, J.; Cai, S. X.

- Discovery of *N*-methyl-4-(4-methoxyanilino)quinazolines as potent apoptosis inducers. Structure–activity relationship of the quinazoline ring. *Bioorg. Med. Chem. Lett* **2010**, *20*, 2330-2334.
459. Kemnitzer, W.; Sirisoma, N.; May, C.; Tseng, B.; Drewe, J.; Cai, S. X. Discovery of 4-anilino-*N*-methylthieno[3,2-*d*]pyrimidines and 4-anilino-*N*-methylthieno[2,3-*d*]pyrimidines as potent apoptosis inducers. *Bioorg. Med. Chem. Lett* **2009**, *19*, 3536-3540.
 460. Gangjee, A.; Zhao, Y.; Hamel, E.; Westbrook, C.; Mooberry, S. L. Synthesis and Biological Activities of (R)- and (S)-*N*-(4-Methoxyphenyl)-*N*,2,6-trimethyl-6,7-dihydro-5H-cyclopenta[*d*]pyrimidin-4-aminium Chloride as Potent Cytotoxic Antitubulin Agents. *J. Med. Chem.* **2011**, *54*, 6151-6155.
 461. *LeadIT 2.1.3*, Biosolve IT: St. Augustin, Germany, www.biosolveit.com.
 462. Arndt, F. *Org. Synth.* **1943**, Coll. Vol. II, 165.
 463. Gangjee, A.; Yang, J.; Queener, S. F. Novel non-classical C9-methyl-5-substituted-2,4-diaminopyrrolo[2,3-*d*]pyrimidines as potential inhibitors of dihydrofolate reductase and as anti-opportunistic agents. *Bioorg. Med. Chem.* **2006**, *14*, 8341-8351.
 464. Mitchell-Ryan, S.; Wang, Y.; Raghavan, S.; Ravindra, M. P.; Hales, E.; Orr, S.; Cherian, C.; Hou, Z.; Matherly, L. H.; Gangjee, A. Discovery of 5-substituted pyrrolo[2,3-*d*]pyrimidine antifolates as dual acting inhibitors of glycylamide ribonucleotide formyltransferase and 5-aminoimidazole-4-carboxamide ribonucleotide formyltransferase in de novo purine nucleotide biosynthesis: implications of inhibiting 5-amino-4-carboxamide ribonucleotide formyltransferase to AMPK activation and anti-tumor activity. In Duquesne University: **2013**.
 465. Zhang, Y.; Desharnais, J.; Marsilje, T. H.; Li, C.; Hedrick, M. P.; Gooljarsingh, L. T.; Tavassoli, A.; Benkovic, S. J.; Olson, A. J.; Boger, D. L.; Wilson, I. A. Rational Design, Synthesis, Evaluation, and Crystal Structure of a Potent Inhibitor of Human GAR Tfase: 10-(Trifluoroacetyl)-5,10-dideazaacyclic-5,6,7,8-tetrahydrofolic Acid. *Biochemistry* **2003**, *42*, 6043-6056.
 466. Cheong, C.-G.; Wolan, D. W.; Greasley, S. E.; Horton, P. A.; Beardsley, G. P.; Wilson, I. A. Crystal Structures of Human Bifunctional Enzyme Aminoimidazole-4-carboxamide Ribonucleotide Transformylase/IMP Cyclohydrolase in Complex with Potent Sulfonyl-containing Antifolates. *J. Biol. Chem.* **2004**, *279*, 18034-18045.

APPENDIX 1

Validation of docking software and docking studies with compounds listed in the statement of the problem with pjDHFR, tgDHFR, tgTS and RTKs (EGFR and VEGFR2)

Docking studies with pyrido[2,3-*d*]pyrimidines in *pc*DHFR

Validation of LeadIT 1.3.0 for docking in *pc*DHFR:

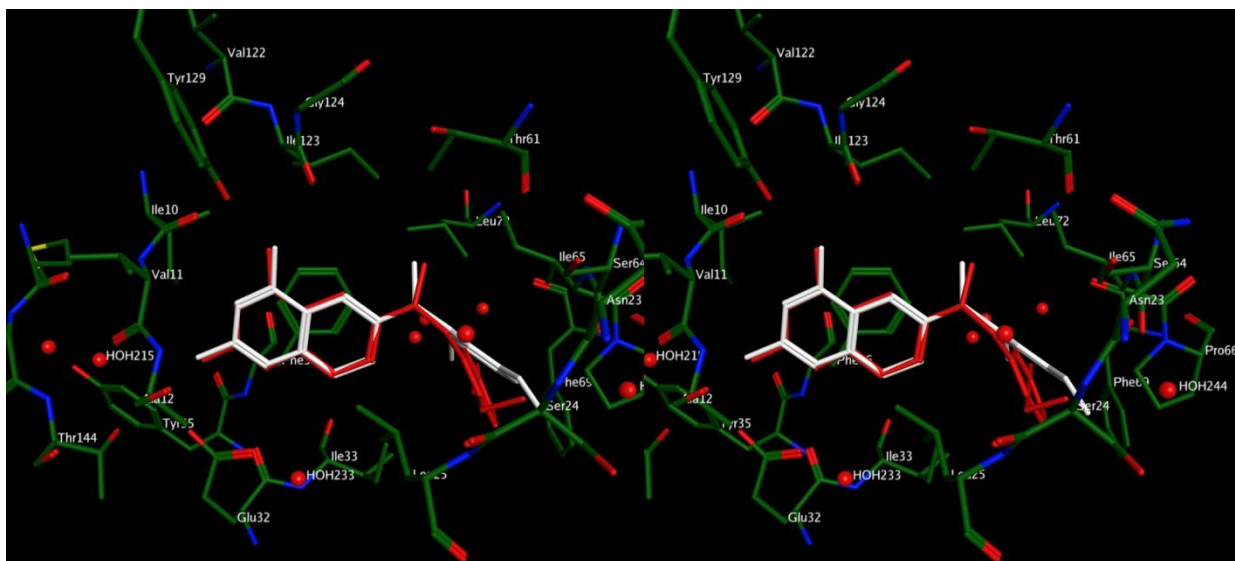


Figure A1. Stereoview. Superimposition of best docked pose (white) and the crystal structure (red) of the native crystal structure ligand of *pc*DHFR (PDB: 1LY3).

Figure A1 shows the best docked pose (white) of 2,4-diamino-6-[*N*-(2',5'-dimethoxybenzyl)-*N*-methylamino] quinazoline superimposed on its crystal structure in *pc*DHFR (PDB: 1LY3). The docking studies were performed using LeadIT 1.3.0 using methods described in the Chemical Discussion section above. As seen in Figure A1, the best docked pose retains the key interactions seen in the crystal structure ligand and has an RMSD of 1.07 Å compared to the crystal structure ligand, thereby validating LeadIT 1.3.0 for docking purposes.

Docking studies with a pjDHFR homology model

Docking studies with target compounds 170 – 180 in pjDHFR

Docking studies with 171:

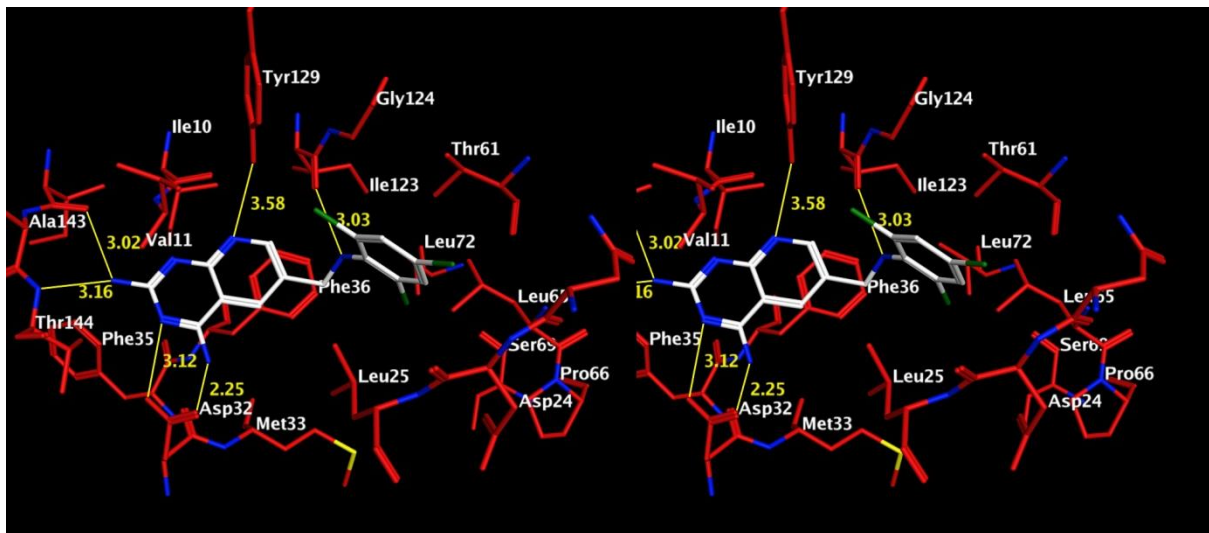


Figure A2. Stereoview. Docked pose of **171** in the active site of the pjDHFR homology model.

Figure A2 shows the docked pose of the target **171** in the active site of a pjDHFR homology model generated using pcDHFR as the template. Compound **171** adopts a flipped conformation in the binding pocket as compared to the docked post of **173** (Figure 55). In its docked pose, the N3 and 4-NH₂ of **171** interact with Asp32. The 2-NH₂ moiety forms hydrogen bonds with the backbone of Ala143 and Thr144. Additional hydrogen bonding is afforded between the pyridine N of **171** and the side chain OH of Tyr129 and between the side chain NH of **171** and the backbone carbonyl of Ile123. The pyrido[2,3-*d*]pyrimidine scaffold is stabilized by a pi-stacking interaction with Phe36 and with side chain carbon atoms of Met33 and Leu25. The 2,4',6'-trichlorophenyl moiety of **171** resides in the hydrophobic pocket formed by the side chains of Leu25, Thr61, Ser64, Leu65, Pro66 and Ser69. The docked score of **171** was -26.67 kJ/mol.

Docking studies with 172:

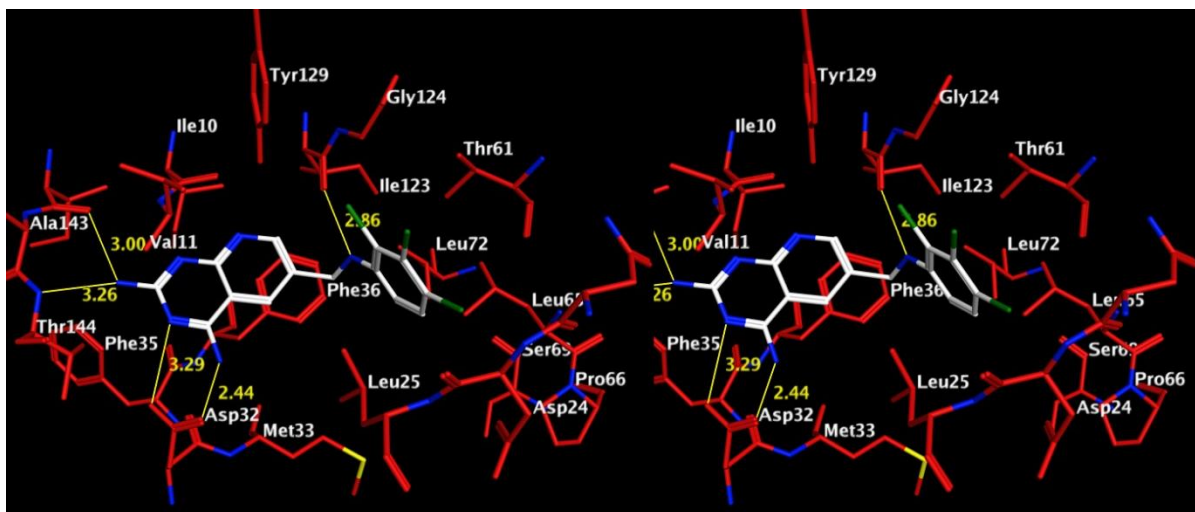


Figure A3. Stereoview. Docked pose of **172** in the active site of the pjDHFR homology model.

Figure A3 shows the docked pose of compound **172** in the active site of a pjDHFR homology model generated using pcDHFR as the template. Compound **172** binds in an orientation similar to that seen in the docked pose of **171** (Figure A2) above. . The docked score of **172** was -28.68 kJ/mol.

Docking studies with 174:

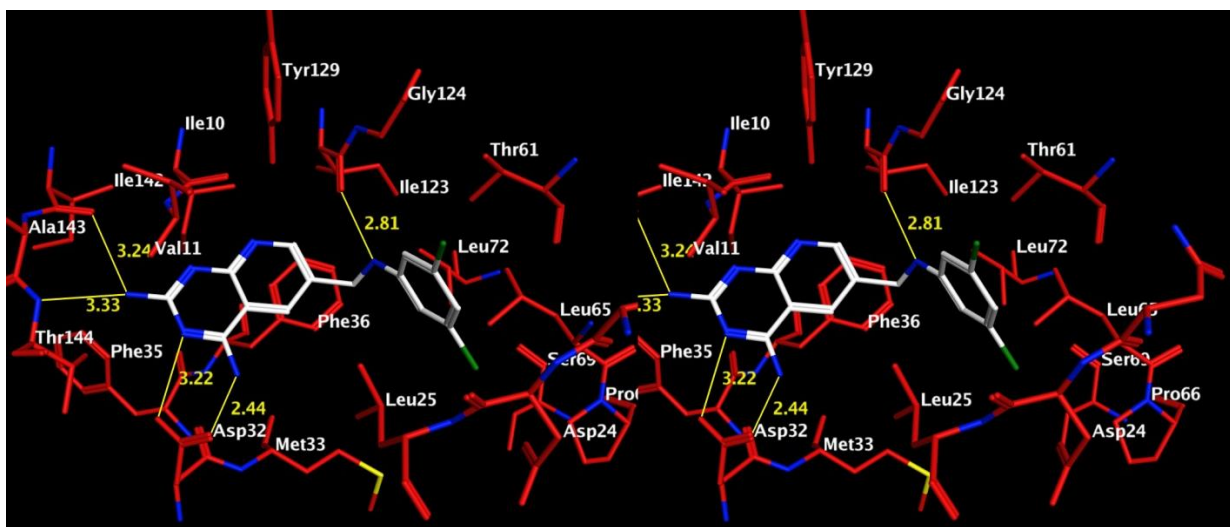


Figure A4. Stereoview. Docked pose of **174** in the active site of the pjDHFR homology model.

Figure A4 shows the docked pose of compound **174** in the active site of a pjDHFR homology model generated using pcDHFR as the template. Compound **174** binds in an orientation similar to that seen in the docked pose of **171** (Figure A2) above. The docked score of **174** was -29.97 kJ/mol.

Docking studies with **175**:

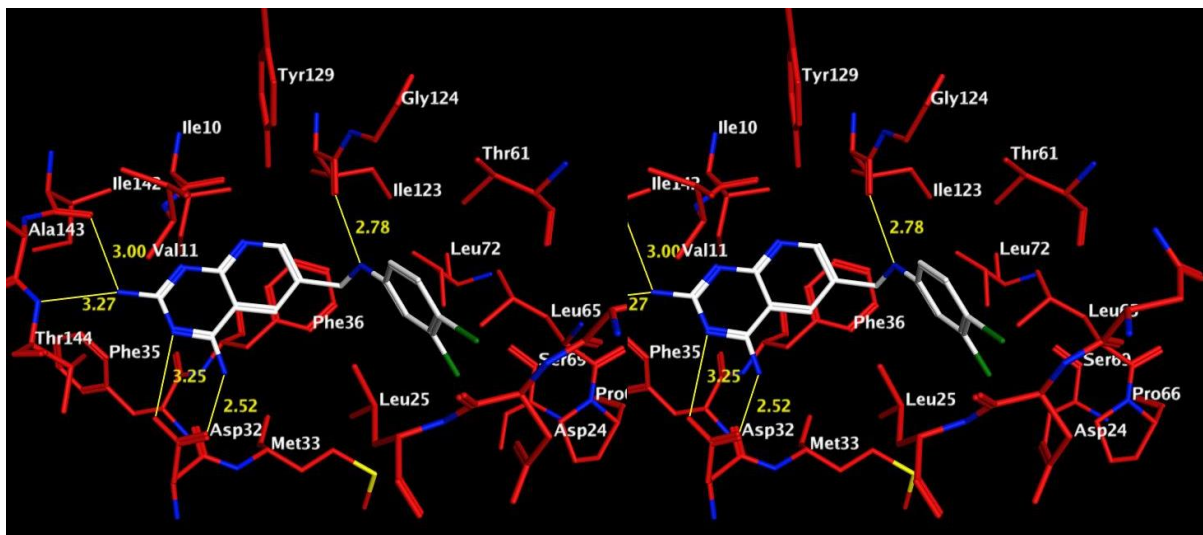


Figure A5. Stereoview. Docked pose of **175** in the active site of the pjDHFR homology model.

Figure A5 shows the docked pose of compound **175** in the active site of a pjDHFR homology model generated using pcDHFR as the template. Compound **175** binds in an orientation similar to that seen in the docked pose of **171** (Figure A2) above. The docked score of **175** was -27.95 kJ/mol.

Docking studies with **176**:

Figure A6 shows the docked pose of compound **176** in the active site of a pjDHFR homology model generated using pcDHFR as the template. Compound **176** binds in an orientation similar to that seen in the docked pose of **171** (Figure A2) above. The docked score of **176** was -28.27 kJ/mol.

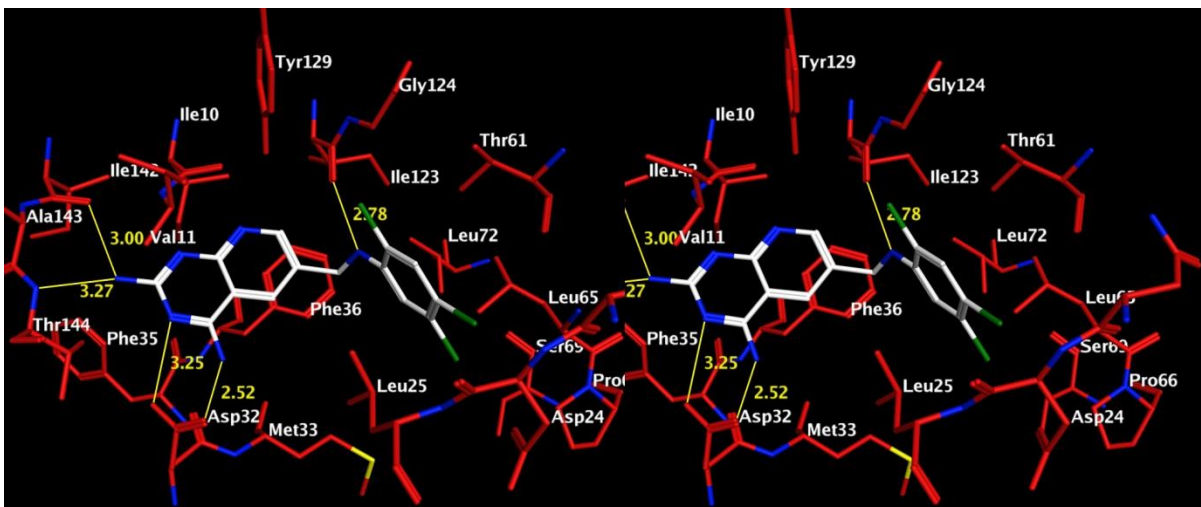


Figure A6. Stereoview. Docked pose of **176** in the active site of the pjDHFR homology model.

Docking studies with **177**:

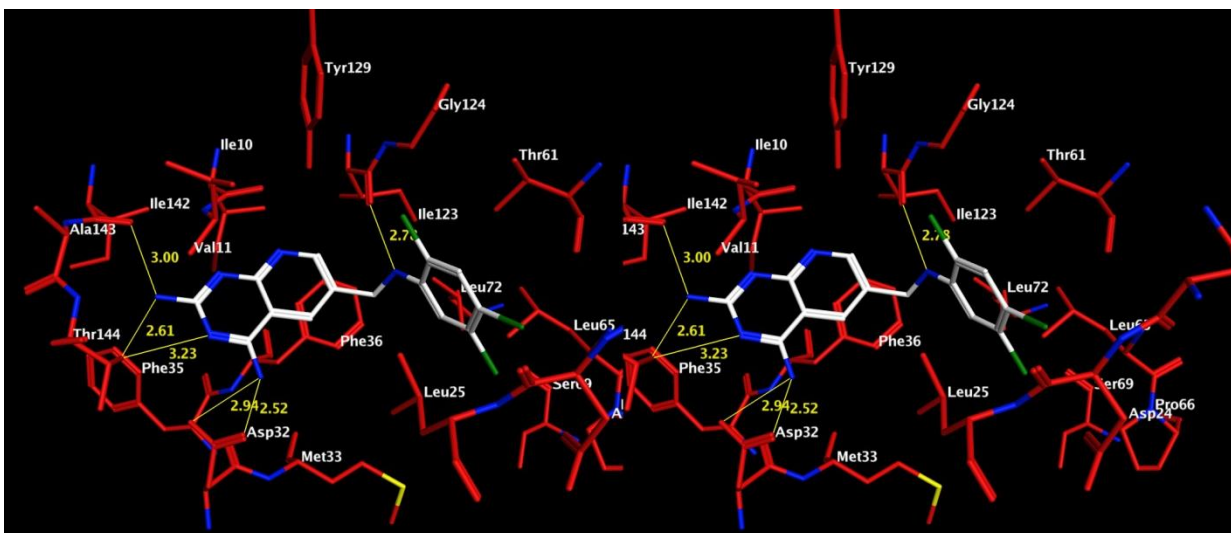


Figure A7. Stereoview. Docked pose of **177** in the active site of the pjDHFR homology model.

Figure A7 shows the docked pose of compound **177** in the active site of a pjDHFR homology model generated using pcDHFR as the template. Compound **177** binds in an orientation similar to that seen in the docked pose of **171** (Figure A2) above. The docked score of **177** was -28.26 kJ/mol.

Docking studies with 178:

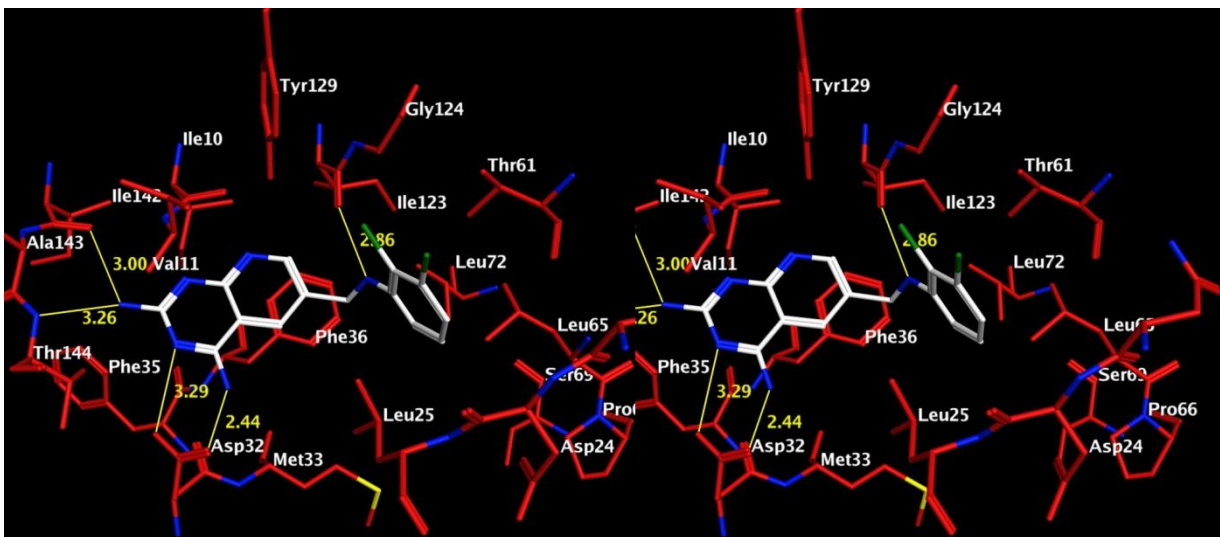


Figure A8. Docked pose of **178** in the active site of the pjDHFR homology model.

Figure A8 shows the docked pose of compound **178** in the active site of a pjDHFR homology model generated using pcDHFR as the template. Compound **178** binds in an orientation similar to that seen in the docked pose of **171** (Figure A2) above. The docked score of **178** was -28.74 kJ/mol.

Docking studies with 180:

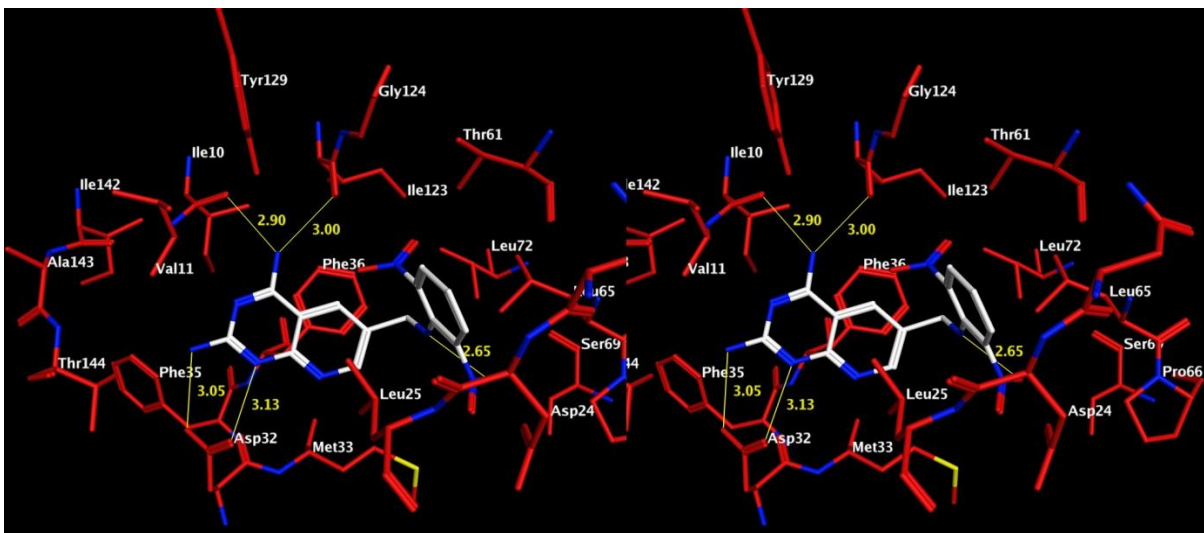


Figure A9. Stereoview. Docked pose of **180** in the active site of the pjDHFR homology model.

Figure A9 shows the docked pose of compound **180** in the active site of a pJDHFR homology model generated using pcDHFR as the template. Compound **180** binds in an orientation similar to that seen in the docked pose of **173** (Figure 53). The docked pose indicates that the side chain NH could form an intramolecular hydrogen bond with the 2'-NO₂ moiety of **180** which can influence the bound conformation of **180** in the pocket. The docked score of **180** was -28.28 kJ/mol.

Molecular modeling studies with 2,4-diamino-6-(thioaryl)methylpyrido[2,3-*d*]pyrimidines and 2,4-Diamino-6-(oxoaryl)methylpyrido[2,3-*d*]pyrimidines as pJDHFR inhibitors

Docking studies with 187:

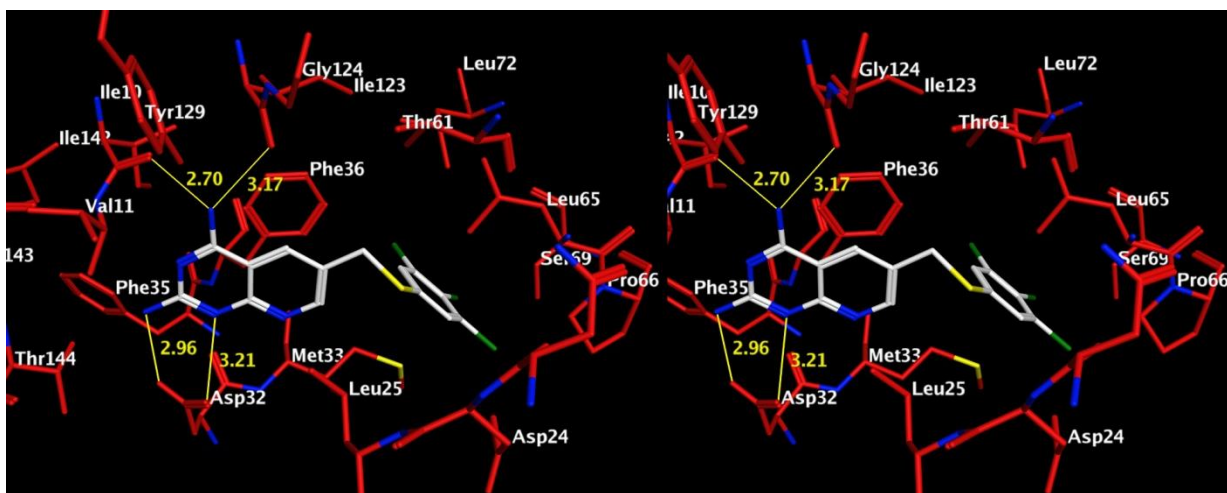


Figure A10. Stereoview. Docked pose of **187** in the active site of the pJDHFR homology model.

Figure A10 shows the docked pose of compound **187** in the active site of a pJDHFR homology model generated using pcDHFR as the template. Compound **187** binds in an orientation similar to that seen in the docked pose of **173** (Figure 53). The docked score of **187** was -23.56 kJ/mol.

Docking studies with 188:

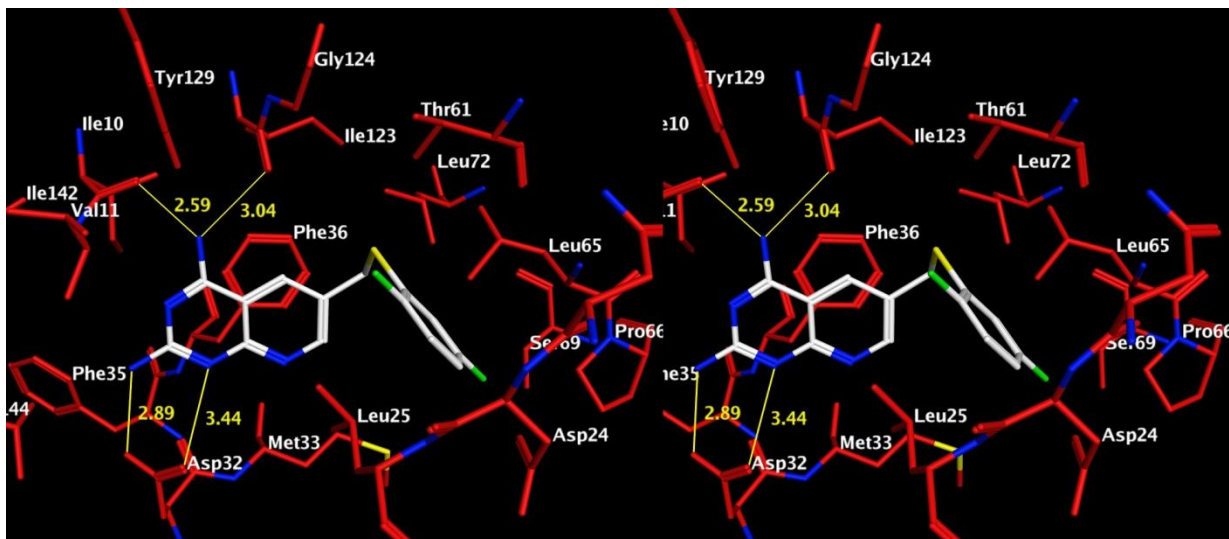


Figure A11. Stereoview. Docked pose of **188** in the active site of the pjDHFR homology model.

Figure A11 shows the docked pose of compound **188** in the active site of a pjDHFR homology model generated using pcDHFR as the template. Compound **188** binds in an orientation similar to that seen in the docked pose of **173** (Figure 53). The docked score of **188** was -25.15 kJ/mol.

Docking studies with 189:

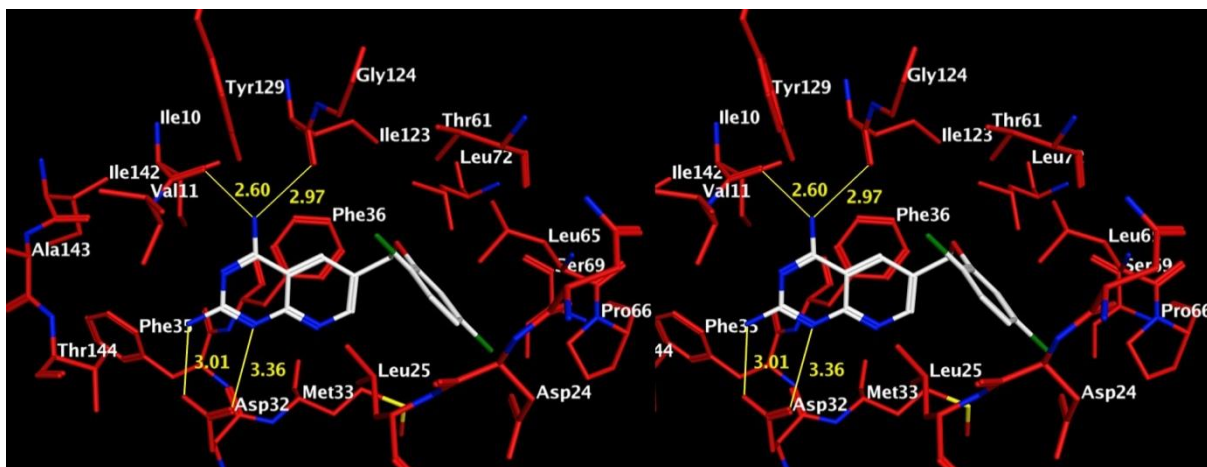


Figure A12. Stereoview. Docked pose of **189** in the active site of the pjDHFR homology model.

Figure A12 shows the docked pose of compound **189** in the active site of a pjDHFR

homology model generated using pcDHFR as the template. Compound **189** binds in an orientation similar to that seen in the docked pose of **173** (Figure 53). The docked score of **189** was -25.8030 kJ/mol.

Docking studies with 190:

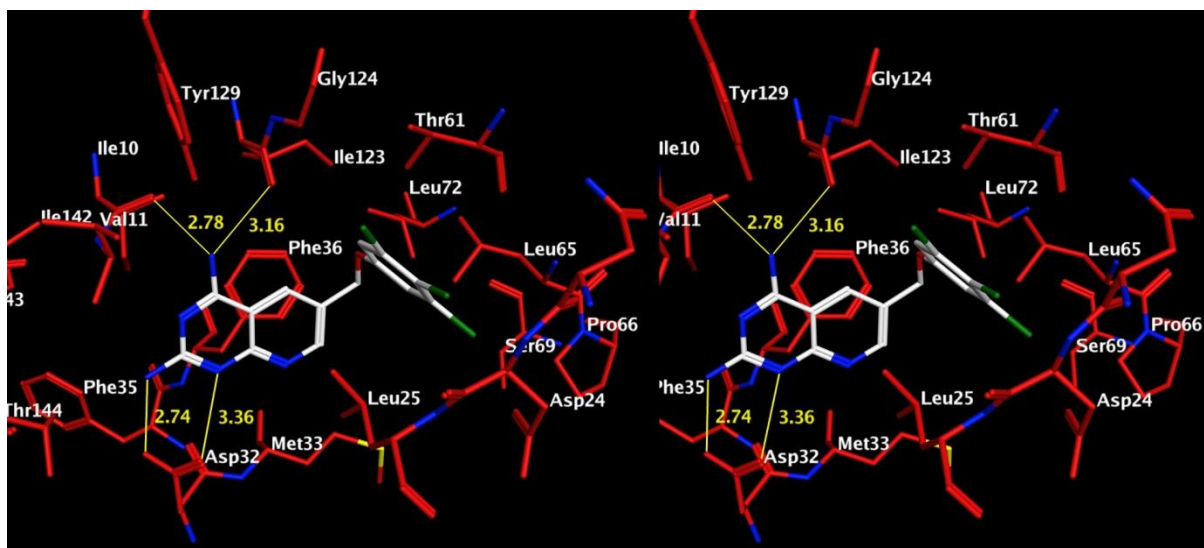


Figure A13. Stereoview. Docked pose of **190** in the active site of the homology model for pjDHFR.

Figure A13 shows the docked pose of compound **190** in the active site of a pjDHFR homology model generated using pcDHFR as the template. Compound **190** binds in an orientation similar to that seen in the docked pose of **173** (Figure 53). The docked score of **190** was -24.0010 kJ/mol.

Docking studies with 191:

Figure A14 shows the docked pose of compound **191** in the active site of a pjDHFR homology model generated using pcDHFR as the template. Compound **191** binds in an orientation similar to that seen in the docked pose of **173** (Figure 53). The docked score of **191** was -25.90 kJ/mol.

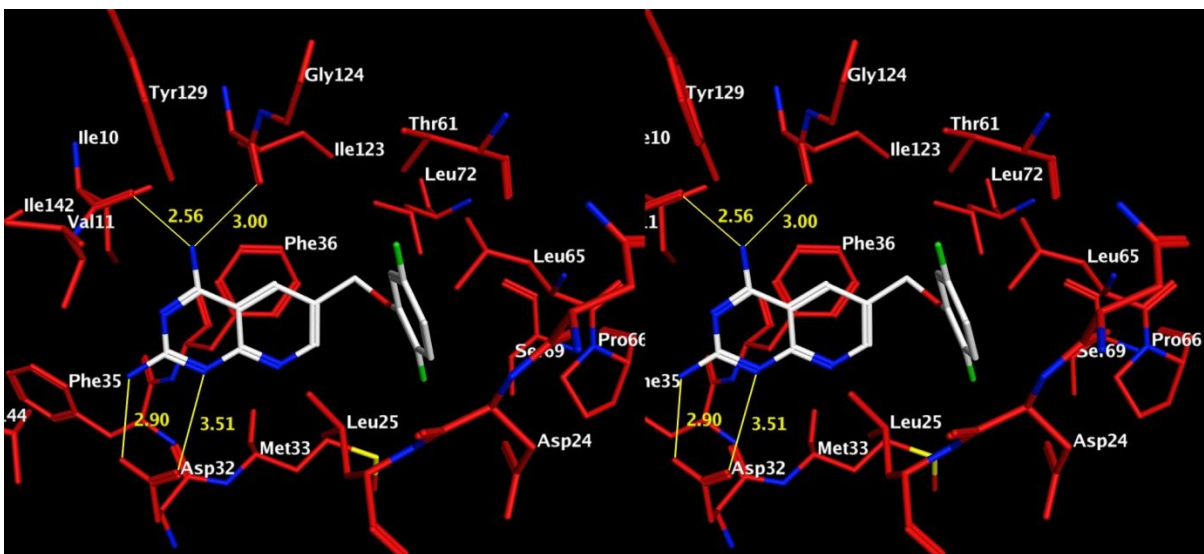


Figure A14. Docked pose of **191** in the active site of the homology model for pjDHFR.

Molecular modeling studies with the tgDHFR homology model

Validation of Flexx 3.1.2 for docking:

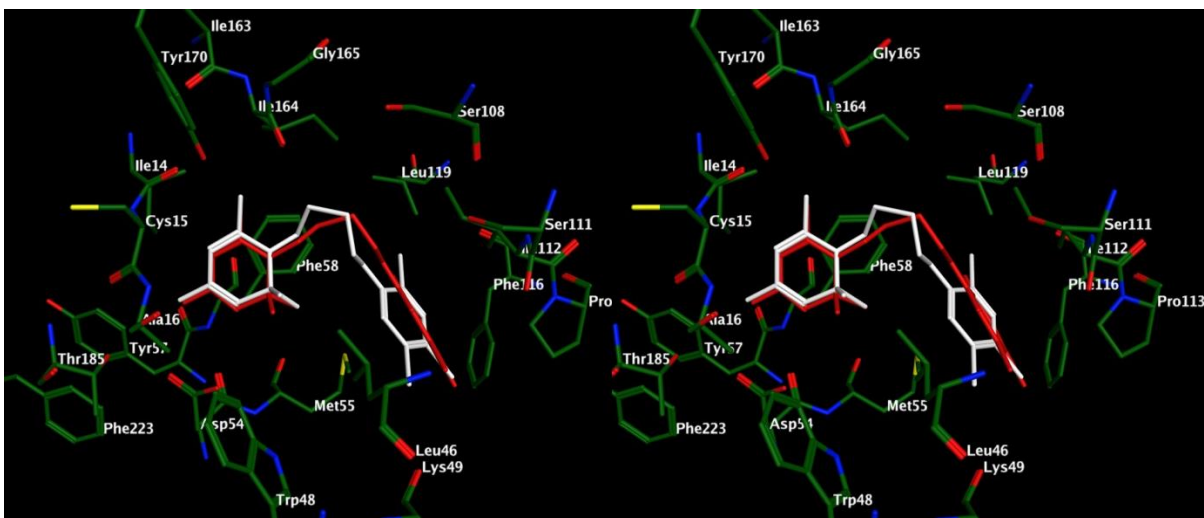


Figure A15. Stereoview. Superimposition of best docked pose (white) and the crystal structure (red) of the native crystal structure ligand of pfDHFR (PDB: 1J3I).

Figure A15 shows the best docked pose (white) of 6,6-dimethyl-1-[3-(2,4,5-trichlorophenoxy)propoxy]-1,6-dihydro-1,3,5-triazine-2,4-diamine (WR99210) superimposed on its crystal structure in pfDHFR (PDB: 1J3I). The docking studies were

performed using Flexx 3.1.2 using methods described in the Chemical Discussion section. As seen in Figure 13, the best docked pose retains the key interactions and the overall bound conformation of WR99210 as seen in the crystal structure and has an RMSD of 1.18 Å compared to the crystal structure ligand, thereby validating Flexx 3.1.2 for docking purposes.

Docking Studies of 2-Amino-4-oxo-5-arylthio-substituted-6-propyl thieno[2,3-*d*]pyrimidines **194c with a tgDHFR homology model**

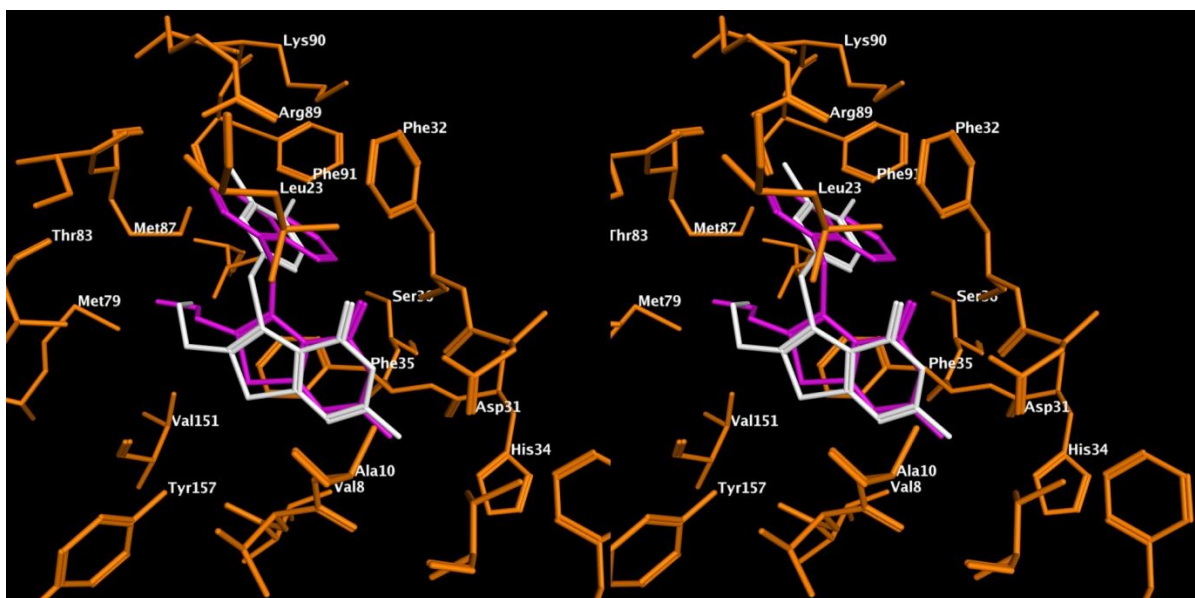


Figure A16. Docked pose of **194c** in the active site of the pjDHFR homology model.

Figure A16 shows the docked pose of compound **194c** in the active site of a pjDHFR homology model generated using pcDHFR as the template. Compound **194c** binds in an orientation similar to that seen in the docked pose of **194a** and **194b** (Figure 92). The 3,4-diCl phenyl moiety in **194c** resides in the binding site occupied by the naphthyl moieties of **194a-b**. The 3,4-diCl phenyl moiety similarly shows steric clashes with hDHFR. This can explain, in part, the selectivity of **194c** towards tgDHFR over

hDHFR. The docked score of **194c** was -6.71 kcal/mol, similar to the docking score of **194b**.

Molecular modeling studies of 2-Amino-4-oxo-5-arylthio-substituted pyrimido[4,5-*b*]indoles **194d-j with *T. gondii* thymidylate synthase**

Docking of **194g in the tgTS homology model**

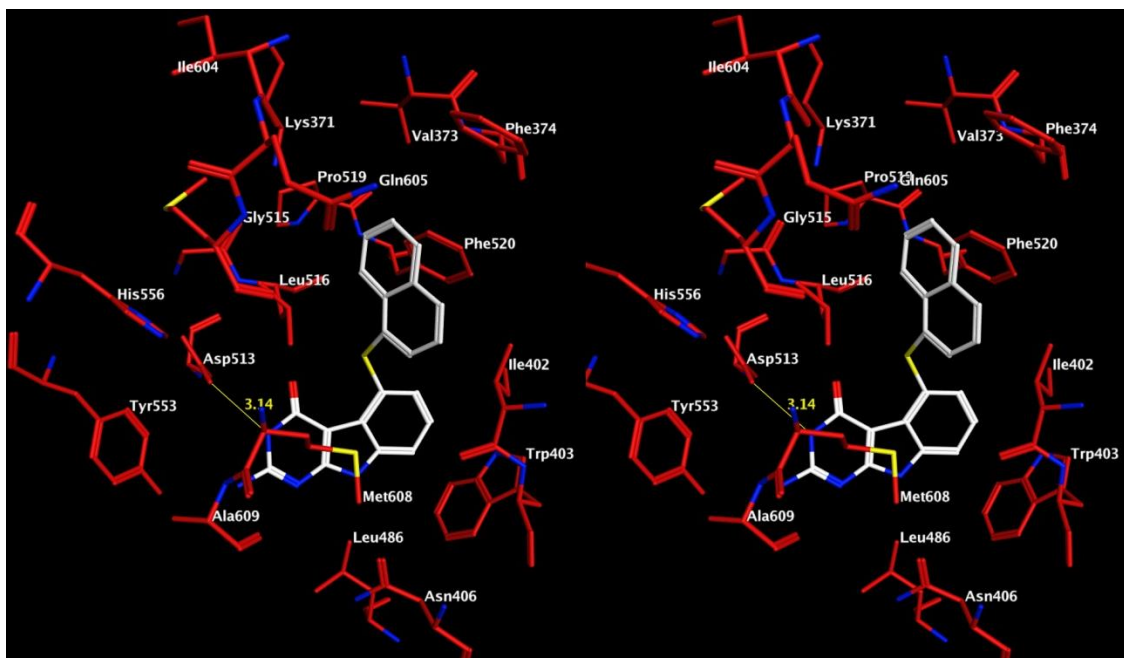


Figure A17. Stereoview. Docked pose of **194g** in the active site of the tgTS homology model

Figure A17 shows the docked pose of **194d** (white) in the folate binding site of the tgDHFR homology model. This docked pose is similar to the docked pose of **194a** in tgTS (Figure82a). The docked score of **194d** was -6.80 kcal/mol, similar to the docking score of **194b**.

Molecular modeling studies of 2-Amino-4-oxo-5-arylthio-substituted pyrimido[2,3-*d*]indoles **194d-j with *T. gondii* dihydrofolate reductase**

Docking of **194d in the tgDHFR homology model**

Figure A18 shows the docked pose of **194d** (white) in the folate binding site of the tgDHFR homology model. The 2-NH₂ and N3 moieties of **194d** form hydrogen bonds with Asp31. The benzene ring in the pyrimido[4,5-*b*]indole scaffold of **194d** affords pi-stacking interactions with Phe35 and additional hydrophobic interactions with Val151. In addition, the 6-S-side chain helps to orient the naphthyl moiety of **194d** into the hydrophobic pocket.

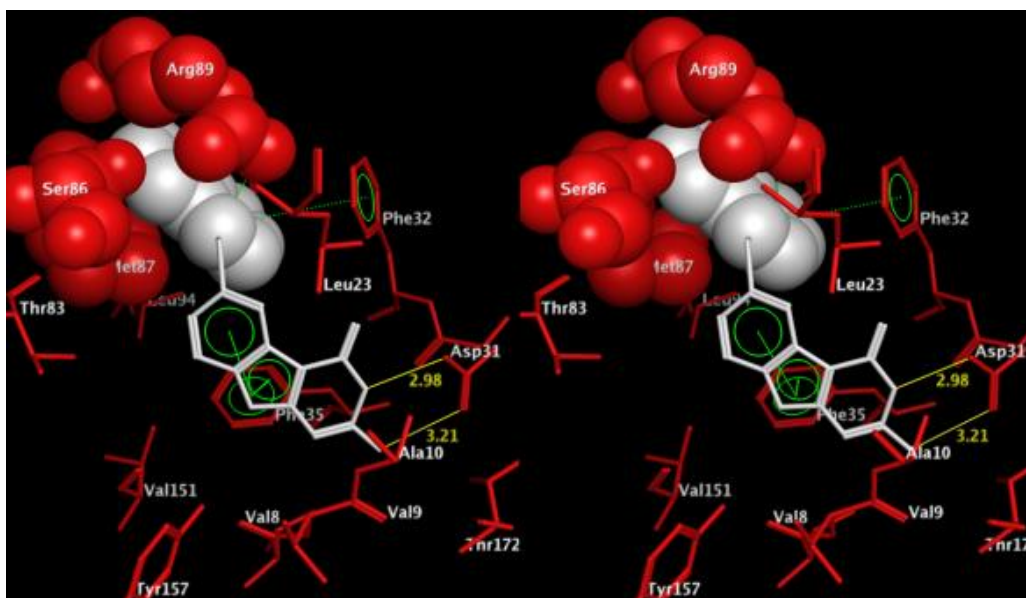


Figure A18. Stereoview. Docked pose of **194d** in the active site of the tgDHFR homology model

The naphthyl side chain of **194d** maintains the cation-pi interaction with Arg89 (or Lys90) and the pi-stacking interaction with Phe32 as is seen with the side chain of **194a**. Docking of **194d** into the active site of hDHFR (PDB: 3K45) did not yield docked poses within the active site. Superimposition of the pyrimidine ring of **194d** on the pyrimidine ring of the bound furo[2,3-*d*]pyrimidine ligand in 3K45 indicated steric clashes with the side chain of Ile60 and Leu67 in hDHFR, which could explain the decreased activity of

194d (Table 12) against hDHFR and hence its selectivity for tgDHFR.

Molecular modeling studies in RTKs

Validation of Flexx 3.1.2 for docking studies with EGFR

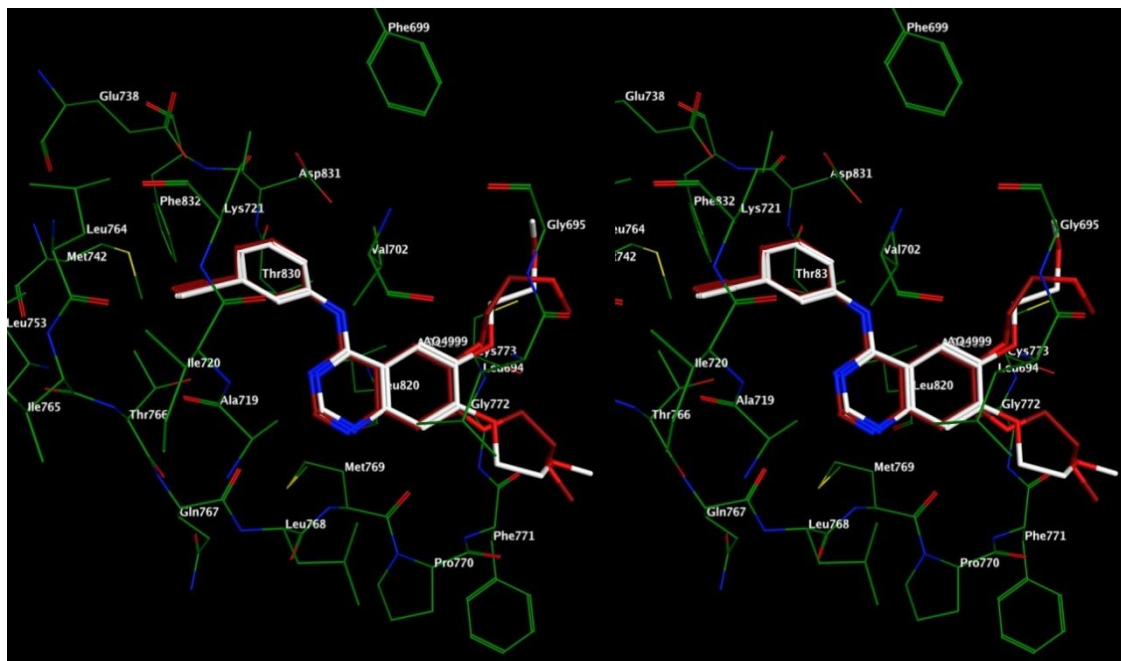


Figure A19. Stereoview. Superimposition of best docked pose (white) and the crystal structure (red) of the native crystal structure ligand of EGFR (PDB:1M17).

Figure A19 shows the best docked pose (white) of erlotinib ([6,7-bis(2-methoxyethoxy)quinazoline-4-yl]-(3-ethynylphenyl)amine) superimposed on its crystal structure in EGFR (PDB: 1M17). The docking studies were performed using Flexx 3.1.2 using methods described in the Chemical Discussion section. As seen in Figure A19, the best docked pose retains the key interactions and the overall bound conformation of erlotinib as seen in the crystal structure and has an RMSD of 0.91 Å compared to the crystal structure ligand, thereby validating Flexx 3.1.2 for docking purposes.

Validation of Flexx 3.1.2 for docking studies with VEGFR2

Figure A20 shows the best docked pose (white) of the furo[2,3-*d*]pyrimidine ligand

superimposed on its crystal structure in VEGFR2 (PDB: 1YWN). The docking studies were performed using Flexx 3.1.2 using methods described in the Chemical Discussion section. As seen in Figure A19, the best docked pose retains the key interactions and the overall bound conformation of erlotinib as seen in the crystal structure and has an RMSD of 0.91 Å compared to the crystal structure ligand, thereby validating Flexx 3.1.2 for docking purposes.

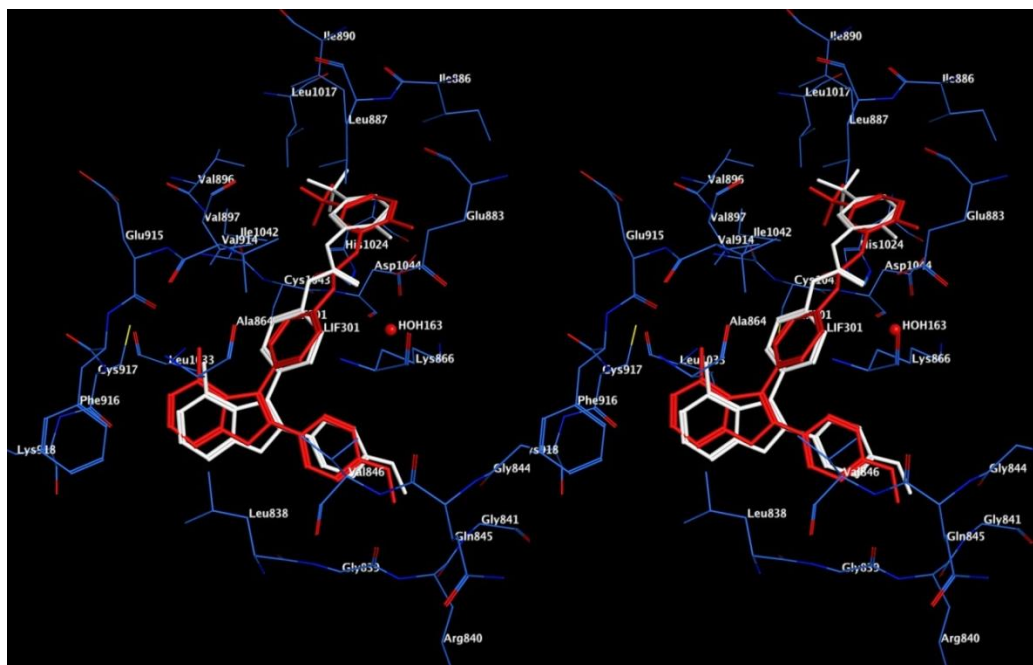


Figure A20. Stereoview. Superimposition of best docked pose (white) and the crystal structure (red) of the furo[2,3-*d*]pyrimidine ligand of VEGFR2 (PDB:1YWN).

Docking studies with lead 196, and target compounds 196 and 200 in EGFR

Docking studies with target compounds **197 – 210** in EGFR were performed using the same settings as those used for lead compounds **195** and **196**.

Docking studies with lead compound 196 in EGFR

Figure A21 shows the docked pose of the lead compound **196** (white) in ATP

binding site of EGFR (PDB: 1M17). This docked pose is similar to the docked pose of **195** in EGFR (Figure 62). The docked score of **196** was -20.43 kJ/mol, similar to the docking score of **195**.

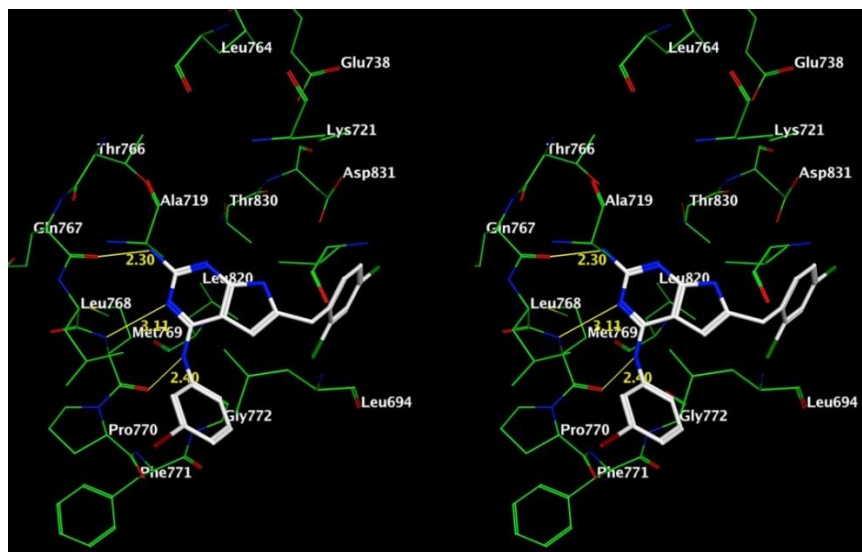


Figure A21. Stereoview. Docked pose of **196** in the ATP binding site of EGFR. (PDB: 1M17)

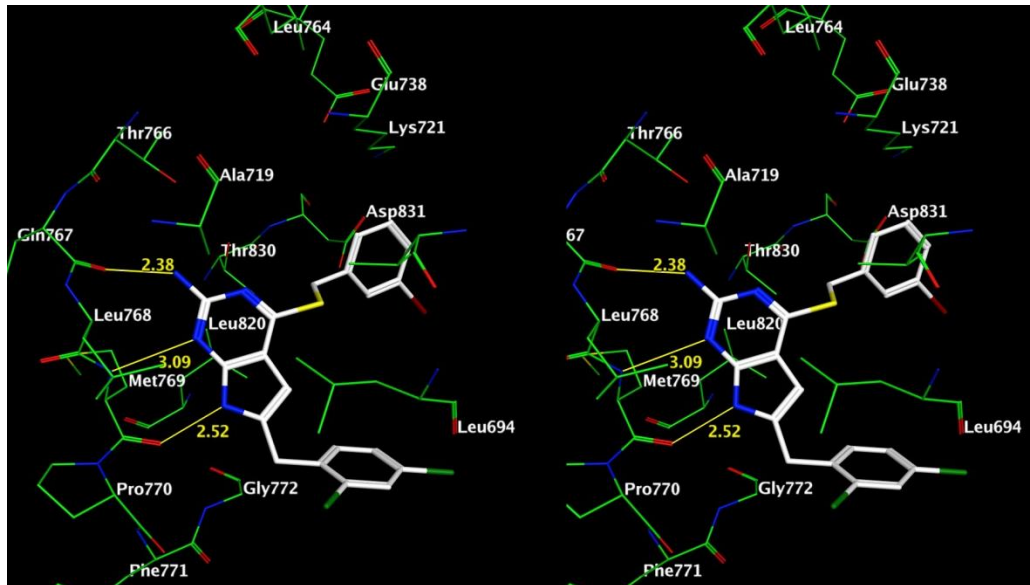


Figure A22. Stereoview. Docked pose of **200** in the ATP binding site of EGFR. (PDB: 1M17)

Figure A22 shows the docked pose of the lead compound **200** (white) in ATP binding site of EGFR (PDB: 1M17). This docked pose is similar to the docked pose of **197**

in EGFR (Figure 63). The docked score of **200** was -22.74 kJ/mol, similar to the score of **195**.

Docking studies with leads **195**, **196**, and target compounds **197** and **210** in VEGFR2

Docking studies with target compounds **197** – **210** in VEGFR2 were performed using the same settings as those used for validation of the docking software. The docked poses of target compounds **197** and **210** are depicted here as illustrative examples.

Docking studies with lead compound **195** in VEGFR2

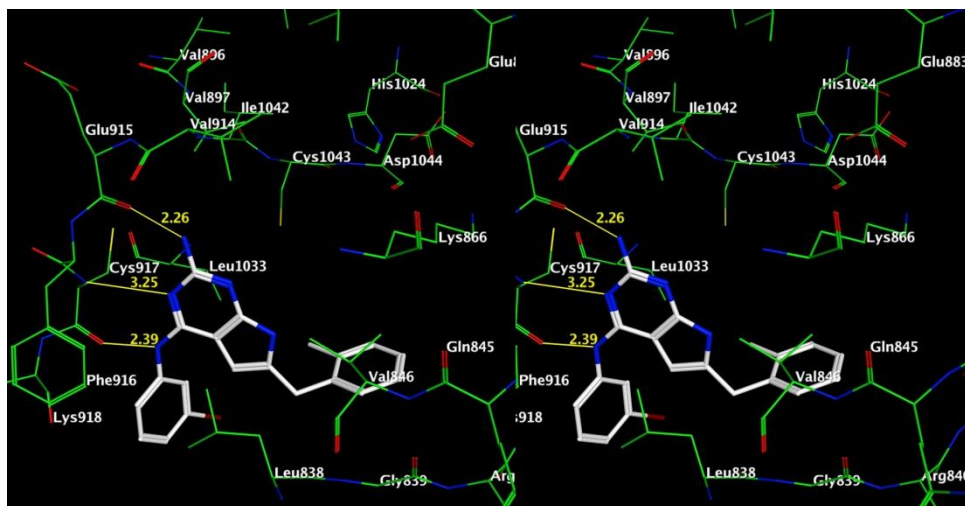


Figure A23. Stereoview. Superimposition of best docked pose (white) of **195** in VEGFR2 (PDB:1YWN).²⁰⁰

Docking studies with lead compound **196** in VEGFR2

Figures A23 and A24 shows two low energy docked poses of the lead compound **195** (within 1 kcal of each other) VEGFR2 (PDB: 1YWN). In both docked poses, **195** binds in the ATP binding site of VEGFR2 and forms three hydrogen bonds with the hinge region residues (Glu915 and Cys917).

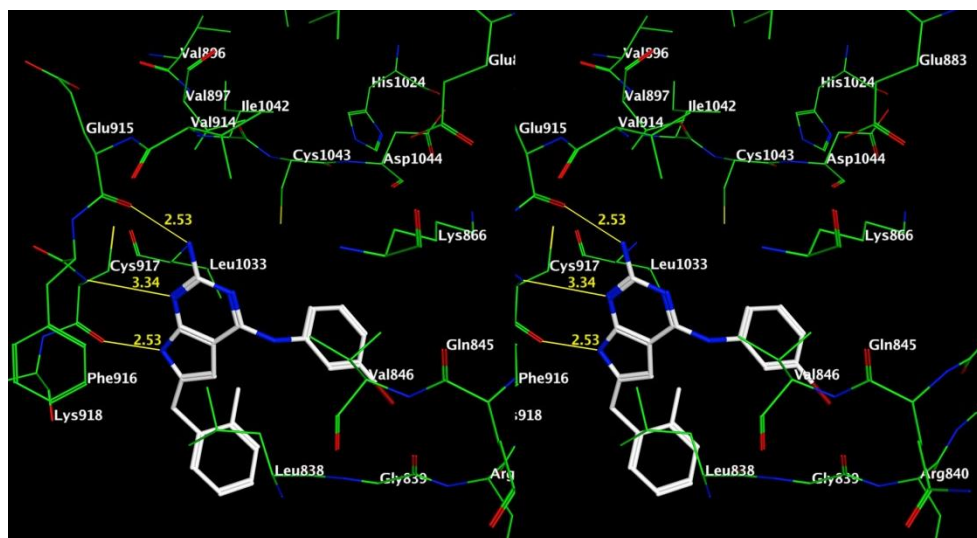


Figure A24. Stereoview. Superimposition of best docked pose (white) of **196** in VEGFR2 (PDB:1YWN).²⁰⁰

In pose 1 (Figure A23), **195** forms hydrogen bonds with the hinge region using the 2-NH₂, N3- and the 4-anilino nitrogen atoms (analogous to the proposed Binding mode 2 in Figure 68) . In contrast, **195** binds analogous to the proposed Binding mode 5 (Figure 68) in Figure A24 and forms hydrogen bonds with the hinge region with its 2-NH₂, N3 and pyrrole NH atoms. The 2'-MePh moiety of **195** binds in the Hydrophobic site 2 of VEGFR2 while the aniline moiety binds in the sugar binding pocket. In pose 2 (Figure A24), **195** binds with the 2'-MePh extending towards the sugar binding pocket and the aniline moiety binding toward Hydrophobic binding site 1. These alternate low-energy binding poses provide a molecular basis of the proposed design idea of multiple binding poses in a single agent. The docking score of **195** in pose 1 was -21.60 kJ/mol while the docking score in pose 2 was -22.80 kJ/mol.

Docking studies with target compound **197** in VEGFR2

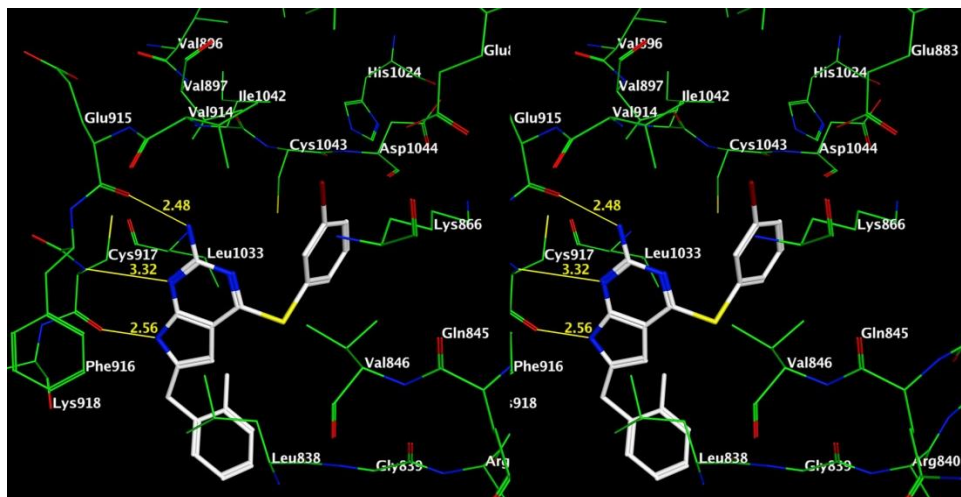


Figure A25. Stereoview. Superimposition of best docked pose (white) of **197** in VEGFR2 (PDB:1YWN).²⁰⁰

Figure A25 shows the docked pose of the target compound **197** in VEGFR2. The docked pose of **197** is similar to that seen in the docked pose of lead **195** in Figure A25. The docked score of **197** in VEGFR2 was -18.74 kJ/mol, lower than that of **195**.

Docking studies with target compound **210** in VEGFR2

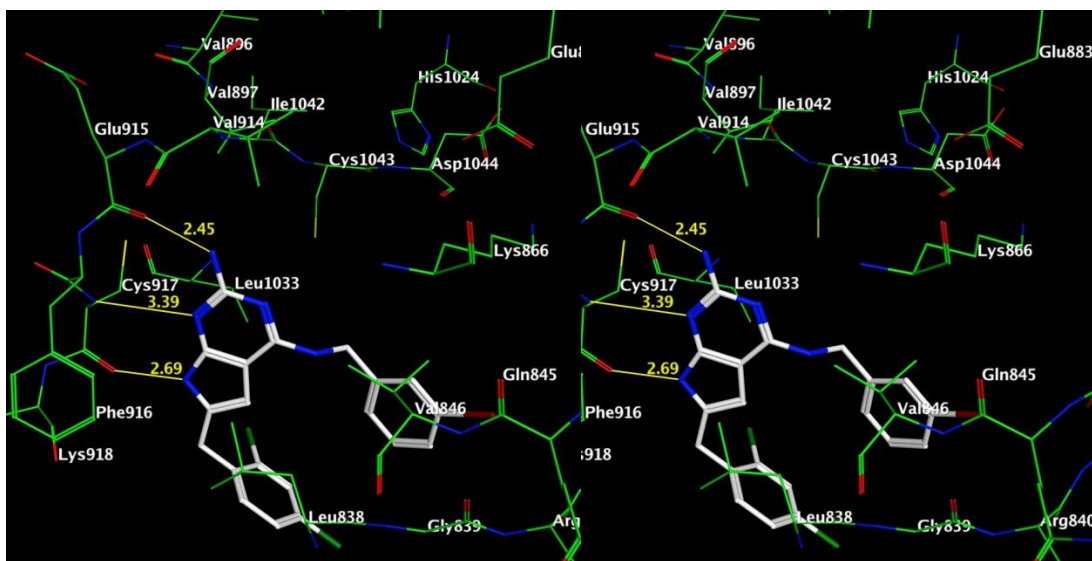


Figure A26. Stereoview. Superimposition of best docked pose (white) of **197** in VEGFR2 (PDB:1YWN).²⁰⁰

Figure A26 shows the docked pose of the target compound **197** in VEGFR2. The docked pose of **197** is similar to that seen in the docked pose of lead **195** in Figure A25. The docked score of **197** in VEGFR2 was -22.61 kJ/mol, comparable to the docked score of **195** in VEGFR2.

APPENDIX 2

Molecular modeling: docking studies of **223d** with GARFTase and AICARFTase

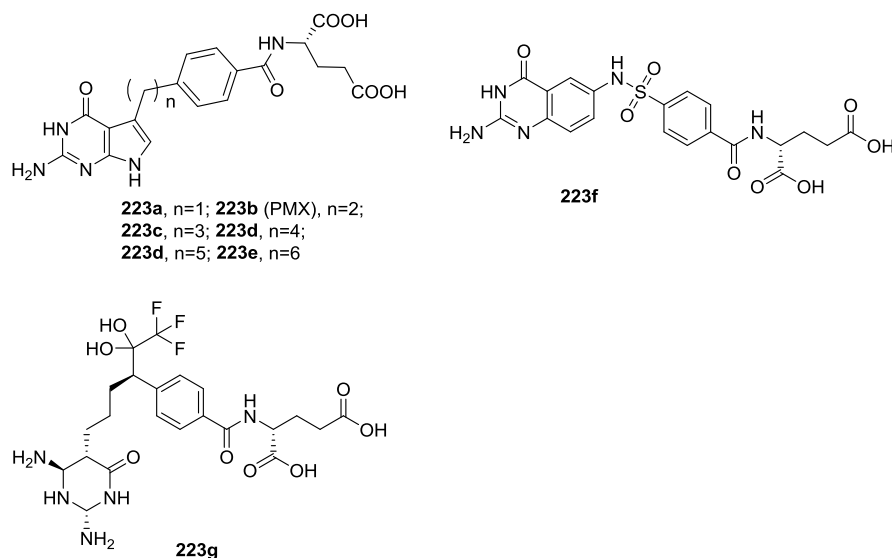


Figure A27. Structures of **223a-g**

Compounds **223a**, **c-e** were reported by Gangjee *et al.*⁴⁶³ Based on the cellular metabolic data, **223d** was seen to inhibit both GARFTase ($IC_{50} = 29.7 \pm 10.6nM$) and AICARFTase in KB cells. Thus molecular modeling studies were performed with **223d** in human GARFTase (PDB ID: 1NJS)⁴⁶⁴ and human AICARFTase (PDB ID: 1PL0)⁴⁶⁵ to determine the molecular basis of the potent activity of **223d** against these enzymes. Molecular modeling of compound **223d** was performed using LeadIT 1.3.0 and the results were visualized using MOE 2011.10. LeadIT 1.3.0 was validated for docking by redocking the native crystal structure ligands 10-CF₃CO-DDACTHF (**223f**)⁴⁶⁴ for human GARFTase and (BW2315U89, BW2315, **223g**)⁴⁶⁵ for AICARFTase into their respective crystal structures afforded docked poses with RMSD $\sim 1\text{\AA}$.

Figure A28 shows the docked pose of **223d** in the human GARFTase active site. The cofactor binding pocket of GARFTase is located at the interface between the N-terminal mononucleotide binding domain and the C-terminal half of the structure. The

binding site for the folate cofactor moiety consists of three parts: the pteridine binding cleft, the benzoylglutamate region, and the formyl transfer region.

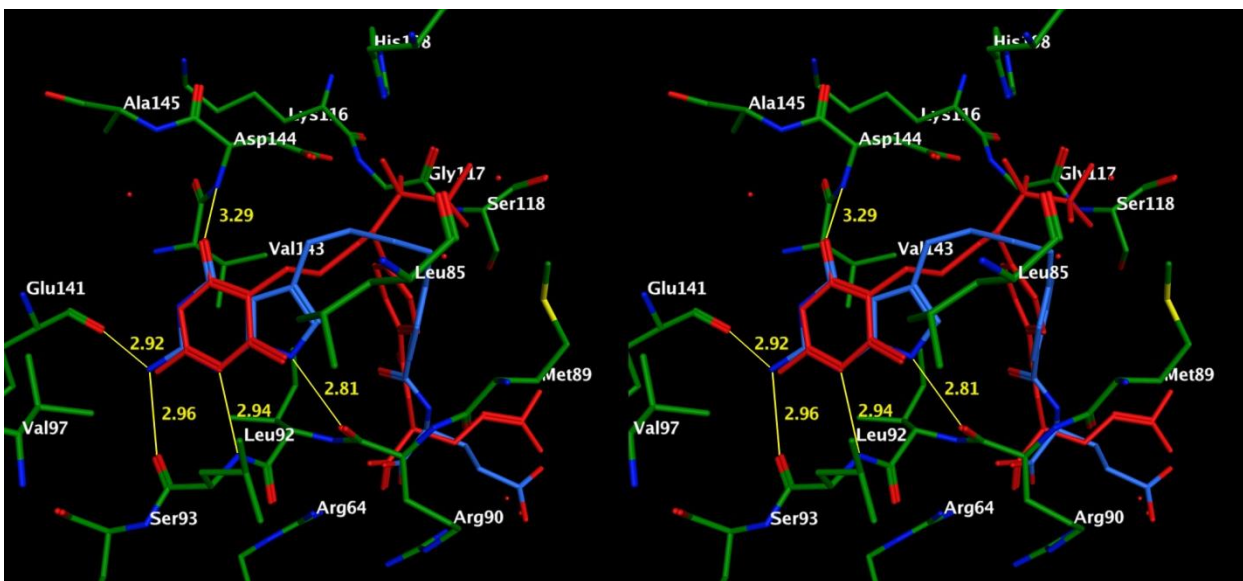


Figure A28. Stereoview. Overlay of the docked pose of **223d** (blue) with 10-CF₃CO-DDACTHF (red) in human GARFTase (PDB ID: 1NJS).⁴⁶⁴

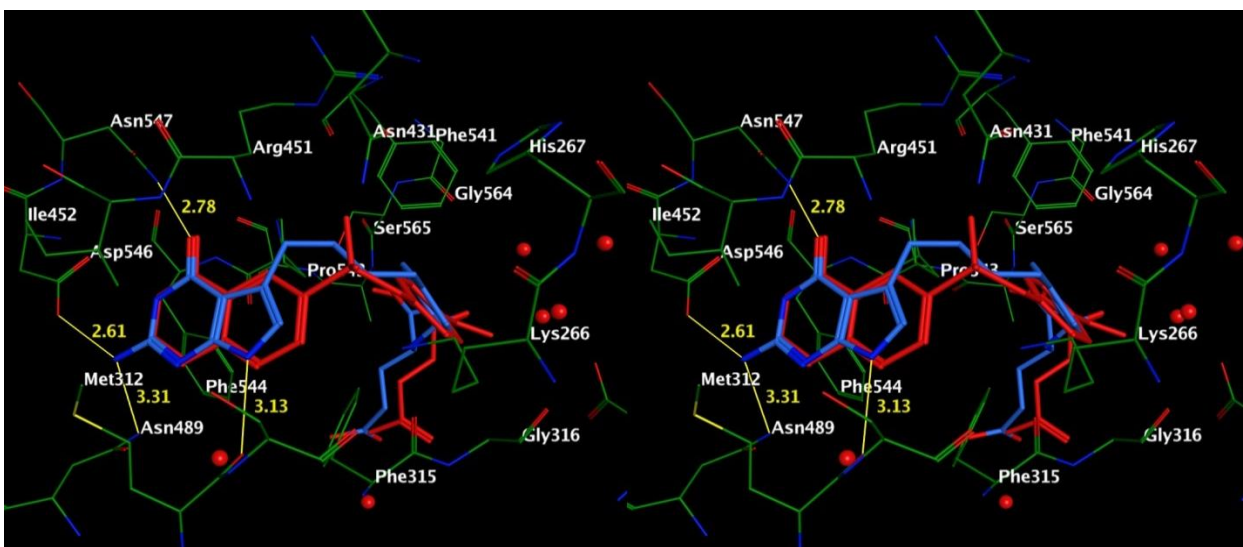


Figure A29. Stereoview. Overlay of the docked pose of **223d** (blue) with **223g** (red) in human AICARFTase (PDB ID: 1PL0).

The docked pose shows the pyrrolo[2,3-*d*]pyrimidine scaffold of **223d** to be buried deep in the active site and to occupy the same location as the diaminopyrimidone

ring in the native crystal structure ligand (10-CF₃CO-DDACTHF). This orientation of the scaffold permits the 2-amino moiety to form hydrogen bonds to the backbone of Glu141 and Ser93. The N1 nitrogen interacts with the backbone of Leu92 to form a hydrogen bond. The 4-oxo moiety forms a hydrogen bond with Asp144 and forms water-mediated hydrogen bonds with Asp142 and Ala140 (not shown).

The molecule is oriented in a manner which aids the *N*7 nitrogen to form a hydrogen bond with Arg90. The pyrrolo[2,3-*d*]pyrimidine scaffold resides in a hydrophobic pocket formed by Leu85, Ile91 (not shown), Leu92, Val97, and the folate binding loop residues 141-146. The flexible 4-atom side chain helps to orient the benzoyl moiety of compound **223d** into the benzoylglutamate region of the protein. The amide NH of the glutamate side chain forms a hydrogen bond with Met89. The α -carboxylic acid of the glutamate side chain interacts with Arg64 and additionally interacts with the backbone of Ile91. The γ -carboxylic acid can form a water-mediated hydrogen bond with Arg90. The interaction of the flexible glutamate side chain is very similar to the interaction network observed for the glutamate side chain of 10-CF₃CO-DDACTHF.

Figure A29 shows the overlay of the docked poses of **223d** (blue) with the crystal structure ligand **223f** (red) (a potent inhibitor) in human AICARFTase (PDB ID: 1PL0). The pyrrolo[2,3-*d*]pyrimidine scaffold of **223d** occupies the same location as the dihydroquinazoline scaffold of **223f**. Analogous to **223f** the 2-NH₂ and N3 nitrogens of **223d** interact with Asp546 while the 4-oxo moiety forms a hydrogen bond with the side chain of Asn547. The *N*7-nitrogen of **223d** forms a hydrogen bond with the backbone of Met312. The pyrrolo[2,3-*d*]pyrimidine scaffold of **223d** forms hydrophobic interactions with Met312, Phe315, Ile452, Pro543 and Phe544. The aryl glutamate section of **223d** is

oriented similar to the phenyl glutamate side chain of **223f**.

These docking results predict that **223d** should bind and inhibit the two folate-dependent purine biosynthetic enzymes (GARFTase and AICARFTase) and were entirely consistent with the results of the *in situ* metabolic assays (not shown).